ALMA MATER STUDIORUM
UNIVERSITÀ DI BOLOGNA

DOTTORATO DI RICERCA IN

MECCANICA E SCIENZE AVANZATE DELL'INGEGNERIA

Ciclo XXXVII

Settore Concorsuale: 09/C1 - MACCHINE E SISTEMI PER L'ENERGIA E L'AMBIENTE

Settore Scientifico Disciplinare: ING-IND/08 - MACCHINE A FLUIDO

MODELLING AND EXPERIMENTATION ON MACHINES AND INTEGRATED SYSTEMS FOR ENERGY CONVERSION AND STORAGE BASED ON WASTE HEAT VALORIZATION

Presentata da: Chiara Poletto

Coordinatore Dottorato:

Prof. Lorenzo Donati

Supervisore:

Prof. Andrea De Pascale

Esame finale anno 2025

Abstract

The increasing global energy demand, alongside unsustainable environmental impacts, presents a significant challenge for modern society. The rising levels of carbon dioxide emissions have contributed to global warming, with the summer of 2022 in Europe marking the hottest on record. Fossil fuels remain the dominant energy source, contributing not only to greenhouse gas emissions but also to local air pollution, which leads to millions of premature deaths annually. Despite ongoing efforts to shift towards a low-carbon economy, the transition is slow, with renewable energy sources making up just 13% of the global energy mix. To tackle climate change and meet rising energy demands, it is essential to reduce the reliance on fossil fuels, increase the use of renewable energy, and improve energy conversion efficiencies. Additionally, recovering low-grade heat sources, such as waste heat from industrial processes, represents a major untapped opportunity for improving energy efficiency. However, the variability of waste heat sources necessitates customized solutions. Technologies like Organic Rankine Cycles (ORCs) – Heat-To-Power (H2P) – and High-Temperature Heat Pumps (HTHPs) – Power-To-Heat (P2H) – show promise in converting and upgrading low-temperature waste heat into useful energy forms. However, optimizing these systems requires advancements in optimal working fluids, implementation of advanced cycle designs, integration with existing thermal systems, development of advanced materials, and integration of digital technologies for system control and monitoring. Carnot batteries (CBs), which combine P2H and H2P technologies for energy storage, represent a promising solution for managing the intermittency of renewable energy sources. However, achieving efficiency and cost-effectiveness in these systems is dependent on improvements in cycle design and material integration. Indeed, high initial costs and long payback periods deter investments in P2H and H2P systems. Furthermore, integrating P2H and H2P systems into existing industrial processes and energy networks requires significant investments and careful planning. The intention of this thesis is to address some of these challenges, contributing to fostering innovation and supporting the deployment of these technologies, aiming for a more sustainable and resilient energy future. To this purpose, this thesis aims to advance understanding and providing practical insights into improving energy efficiency and reducing the environmental impact of P2H and H2P technologies, focusing in particular on experimental data collection, development of reliable models accounting for the system off-design performance, and their integration into complex energy systems. The research includes technological analysis, environmental considerations, and economic assessments. The project is split into two main parts, i.e., “ORC and HTHP for stand-alone electric and thermal energy generation” and “Carnot battery technology integration for energy storage applications”. Distinct methods and models are utilized across the different applications, drawing on both experimental data and insights from scientific literature and manufacturers. The original contributions and key findings of this research are outlined as follows.

Concerning the “ORC and HTHP for stand-alone electric and thermal energy generation” part, it focuses on the application of ORC and HTHP technologies to utilize low-grade heat sources, including renewable energy and industrial waste heat. Key goals include: i) experimentally evaluating ORC's performance in partial evaporation mode, which shows potential for recovering ultra-low-temperature waste heat; ii) investigating ORC performance in residential applications using solar thermal heat and waste heat recovery from data center cooling systems; iii) exploring HTHP technology for energy-intensive industries like ceramic tile manufacturing, where waste heat is upgraded using renewable electricity, and then reused in the production process. An extensive experimental campaign focusing on partial evaporation and wet expansion for ultra-low-temperature heat recovery was conducted using a micro-ORC test bench available at the University of Bologna. The experimental setup, originally designed for dry expansion, was adapted

to test the system's performance, particularly the piston expander, under challenging off-design conditions. The results show that, despite the off-design operation, the system maintains stable performance and continuous power production, achieving vapor quality as low as 0.2 – 0.3 at lower temperatures (40 °C – 60 °C). Higher heat source temperatures (68 °C – 75 °C) lead to increased vapor quality, with optimal performance observed at vapor qualities between 0.8 and 1. The experimental outcomes revealed key insights into the behaviour of the ORC system under partial evaporation conditions, including i) the significant influence of heat source temperature on vaporization pressure, and ii) the improvement of pump efficiency and evaporator effectiveness, with the evaporator showing up to 125 % increased performance compared to dry expansion. However, challenges resulted in the expander's efficiency under lower vapor qualities and at higher temperatures, where performance dropped by up to 19 %. Additionally, high energy consumption by the pump emerged as a concern. Nevertheless, partial evaporation demonstrated potential for improving heat source utilization in ultra-low-temperature heat recovery, positioning it as a valuable off-design condition for ORC systems. An off-design micro-ORC simulation model was recalibrated using experimental data from the University of Bologna's test bench. Developed in MATLAB, the model predicts system performance under various conditions by combining physical equations and empirical correlations. Once validated, the model was applied to assess two low-temperature heat recovery applications: residential solar thermal integration and industrial waste heat recovery from data centers. Both studies include sensitivity analyses to examine the potential of using environmentally friendly working fluids. The first study explores the application of a small-scale ORC system with a solar thermal collector to reduce the electricity consumption of a single-family house. A performance comparison with low-GWP fluids as alternatives to the R134a shows that using R134a, the system can meet approximately 39 % of the annual electricity demand, generating over 1150 kWh of electricity. However, switching to low-GWP fluids like R1234yf and R513A results in a significant drop in electricity production, covering only 16 % and 17.5 % of annual demand, respectively. The second study investigates waste heat recovery in data centers. Experiments simulating typical data center conditions showed second law efficiencies between 5 % and 13 %. Based on the experimental results, the ORC model was recalibrated to optimize the piston expander's volume ratio for improved performance. A numerical parametric analysis was also carried out, comparing the performance of R134a with low-GWP alternatives, including R1234yf and R1234ze(E). While R134a provides the highest power output, R1234ze(E) achieves better second law efficiency (29 %) and higher energy savings, recovering 3 % of server power. The research demonstrates ORC's potential to improve energy efficiency in both residential and industrial applications, with low-GWP fluids reducing environmental impact. An alternative for industrial waste heat recovery usage consists of upgrading the low-temperature waste heat to higher enthalpy content thermal energy that can be reused to address industrial process demand. In this regard, the assessment of HTHP technology application to recover waste heat from ceramic industry energy-intensive stages is presented. More in detail, an innovative energy recovery configuration to preheat air for drying and firing stages by capturing waste heat from these processes is proposed and designed, exploring two configurations that result to recover 75 % and 48 % of process waste heat, respectively. Furthermore, the first configuration allows fuel savings of 13.6 kg/h and reduced CO_2 emissions by 37.5 kg/h per ton of tiles, while the second saves 8.89 kg/h of fuel and cut emissions by 24.4 kg/h per ton of tiles. As a result, HTHP technology is a promising solution to decarbonize energy-intensive industries, offering substantial reductions in energy consumption and emissions by utilizing waste heat efficiently.

Regarding the "Carnot battery technology integration for energy storage applications" part, it focuses on the integration of ORC and HTHP technologies into energy storage systems, specifically Carnot batteries, which can enhance renewable energy penetration. CBs store excess electrical energy as thermal energy and convert it back to electricity when needed, improving grid stability and managing the intermittency of renewable energy sources. The main purposes of this part include: i) developing the acquisition and control system for a new CB prototype connected to the district heating system at the

University of Liège (Belgium), with the goal of implementing efficient management strategies; ii) exploring the integration of CB technology with district heating and photovoltaic systems in a university facility, and optimizing energy management for data center cooling systems: to this aim, a rule-based management strategy was developed to optimize CB operations, supported by experimental data from the University of Liège; iii) assessing a preliminary performance analysis of a Brayton CB, aimed at higher-temperature applications. A two-level acquisition and control system for a reversible HP/ORC Carnot battery test bench at the University of Liège was designed and developed. The lower control level, created with Siemens LOGO! Modular microcontrollers and programmed using LOGO! Soft Comfort software, manages fundamental functions like turning actuators on and off, regulating their operations, and reading sensor signals. The higher-level system, developed in Python, oversees manual and automatic control of the CBs start-up and shut-down procedures for each operating mode, including HP mode, ORC mode, and thermal discharge mode. This level also processes key physical quantities, such as temperature, pressure, and flow rate, which are first captured by the lower-level controllers. A rule-based control strategy was developed in MATLAB to optimize the operation of a reversible HP/ORC CB integrated with a district heating substation and photovoltaic power plant to satisfy a university building thermal and electric energy demand. The control strategy was designed to maximize the economic benefits of the CB over a year, accounting for daily fluctuations in electricity prices from the spot market. By storing thermal energy, the CB reduces early morning thermal demand peaks, enabling the downsizing of the DH substation and resulting in substantial investment savings. Two system configurations, differentiating for HP extracting free waste heat or drawing heat from the district heating substation return branch, were considered. The first configuration shows that the CB reduces the district heating substation size, generating annual savings of approximately € 5000 and achieving a payback period of less than 9 years. However, the second configuration limits HP operation, preventing thermal discharge mode and eliminating positive financial outcomes. The study also explores how specific control rules affect system performance. Furthermore, sensitivity analyses reveal that increasing storage volume significantly impacts district heating substation downsizing but has minimal influence on net economic gains, with 13 m^3 being identified as the optimal storage volume. In contrast, electricity prices play a more critical role, as higher prices reduce economic benefits due to the increased operating costs of the HP. The developed rule-based control strategy was then readapted and applied to a data center cooling system integrated with a photovoltaic power plant, to assess its potential for improving energy efficiency and economic performance. Thermodynamic analysis identifies R1233zd(E) as the optimal working fluid for both HP and ORC cycles, enabling the CB to achieve a roundtrip efficiency of 43 %. The CB uses surplus electricity from the photovoltaic plant for thermal energy storage via the HP, which can later be converted back into electricity using the ORC when renewable energy is insufficient. A sensitivity analysis shows that CB integration can be financially viable, especially in high energy price scenarios. With a 10 m^3 storage capacity, the system generates an additional annual profit of € 7744, with a PB period of about 10 years. Favourable results emerge when the system avoids selling electricity to the grid, reducing the PB to under 5 years and generating an annual economic gain of nearly € 18500. The CB achieves roundtrip efficiencies of over 30 % even at low temperatures and enhances key performance metrics like PUE and ERE in DCs by recovering part of the HP's electric consumption through the ORC. The research concludes by comparing the CB with a simpler alternative that continuously recovers DC waste heat using a stand-alone ORC system, underscoring the advantages of the CB, which not only operates as an energy storage solution but also enhances the overall system's performance, particularly when integrated with renewable energy sources. Eventually, a comprehensive thermodynamic assessment of a closed Brayton CB utilizing supercritical CO_2 as a promising alternative to Rankine-based systems for large-scale applications at higher temperature levels was performed. Two configurations, a base version and a recuperated variant featuring an additional heat exchanger, were compared. The recuperator enables the system to reach higher maximum temperatures, over 500 °C. Detailed parametric analyses were conducted using the THERMOFLEX simulation software to assess both

energy conversion and storage potential under various conditions, providing insights into the system's potential for achieving high thermodynamic performance and flexibility. The recuperated configuration demonstrates higher roundtrip efficiencies, ranging from 20 % to 30 %, mainly due to enhanced temperature differences that improve discharge efficiency. In contrast, the base configuration shows a higher Coefficient of Performance during the inverse cycle, reaching values up to 3.5. This suggests the need for searching a trade-off between higher discharging efficiency in the recuperated system and better charging efficiency in the base configuration, depending on the system's intended use. Furthermore, the cogeneration performance of the system was analysed, allowing the system to meet both thermal and electrical needs, offering greater energy management flexibility. The results suggest that at least 25 % of stored heat must be allocated to thermal use to achieve significant primary energy savings. At higher temperatures, like 350 °C, at least 60 % of energy output must be thermal to deliver positive energy-saving results, highlighting the importance of optimizing heat allocation in cogeneration applications. An economic evaluation completes the technical analysis, exploring the maximum allowable specific investment costs to ensure commercial viability. The economic assessment considers variations in electricity and thermal energy prices. The findings indicate that higher prices for electricity and thermal energy improve the system's economic potential, allowing for a higher maximum specific investment cost. However, the economic performance varies between the two configurations, with the base one primarily influenced by changes in thermal energy prices, and the recuperated affected more by fluctuations in both electricity and thermal energy markets. This highlights the recuperated system's responsiveness to dynamic market conditions, particularly in electricity pricing.

Index

List of contents

Figures

Tables

Nomenclature

Acronyms

ACAES	Adiabatic Compressed Air Energy Storage
BD	Direct Brayton
BI	Inverse Brayton
B-PTES	Brayton Cycle-Based Pumped Thermal Energy Storage
C	Cold side
CAES	Compressed Air Energy Storage
CB	Carnot Battery
CCHP	Combined Cooling Heating and Power
CFC	ChloroFluoroCarbons
CHP	Combined Heating and Power
COP	Coefficient Of Performance
DC	Data Centers
DE	Dry Expansion
DH	District Heating
EES	Electric Energy Storage
EII	Energy-Intensive Industries
ERE	Energy Reuse Effectiveness
EU	European Union
FC	Fuel Cell
GES	Gravity Energy Storage
GT	Gas Turbine
GWP	Global Warming Potential
H	Hot side
HCFC	HydroChloroFluoroCarbons
HFC	HydroFluoroCarbons
HFO	HydroFluoroOlefines
HGS	Heat Generation System
HP	Heat Pump
HT	High Temperature
HTF	Heat Transfer Fluid
HTHP	High-Temperature Heat Pump
HX	Heat Exchanger
H2P	Heat-To-Power
IHX	Internal Heat Exchanger
LAES	Liquified Air Energy Storage
LCOS	Levelized Cost of Storage
LT	Low Temperature
LTHP	Low-Temperature Heat Pump
MTHP	Medium-Temperature Heat Pump
NPV	Net Present Value
ODP	Ozone Depletion Potential
ORC	Organic Rankine Cycle
PB	Payback
PCB	Printed Circuit Board

PE	Partial Evaporation
PE-ORC	Partially Evaporated Organic Rankine Cycle
PHES	Pumped Hydro Energy Storage
PTES	Pumped Thermal Energy Storage
PUE	Power Usage Effectiveness
PV	Photovoltaic
PV-T	Photovoltaic Thermal
P2H	Power-To-Heat
P2P	Power-To-Power
RECB-PTES	Recuperated Brayton Cycle-Based Pumped Thermal Energy Storage
RES	Renewable Energy Sources
RH	Recovery Heat Exchanger
TD	Thermal Discharge
TES	Thermal Energy Storage
TFC	Trilateral Flash Cycle
TI-PTES	Thermally Integrated Pumped Thermal Energy Storage
UHTHP	Ultra High-Temperature Heat Pump
VHTHP	Very High-Temperature Heat Pump
VVT	Variable Valve Time
WHR	Waste Heat Recovery

Chemical Symbols

CH_4	Methane
CO_2	Carbon Dioxide
H_2O	Water
NH_3	Ammonia
sCO_2	Supercritical Carbon Dioxide

Symbols

A	Area (m^2)
BWR	Back Work Ratio (-)
$const$	Constant (-)
C	Cost (€/kWh)
CF	Cash Flow (€/kW/year)
C_I	Investment Cost (€/kW)
COP	Coefficient Of Performance (-)
c_p	Specific Heat at Constant Pressure (J/kg/K)
C^*	Thermal Capacity Ratio (-)
d	Increment of Iterative Variable (-)
day	24-hour day (d)
DPB	Discounted Payback Period (years)
E	Energy (kWh)
E_P	Primary Energy Consumption (J/kg)
f	Frequency (Hz)
FF	Filling Factor (-)
G	Irradiance (W/m^2)
$gain$	Economic gain (€)
GEF	Global Error Function (-)

h	Enthalpy (J/kg)
h_{eq}	Equivalent Working Hours (h)
I_{es}	Energy Saving Index (-)
L	Length (m)
LHV	Lower Heating Value (J/kg)
$lifetime$	Lifespan (years)
$load$	Load (-)
M	Mass (kg)
$\dot{m}$	Mass Flow Rate (kg/s)
N	Rotational Speed (rpm)
NTU	Number of Transfer Units (-)
n_{train}	Number of Data Training (-)
Nu	Nusselt Number (-)
p	Pressure (bar)
Q	Thermal Energy (kWh)
$\dot{Q}$	Thermal Power (W)
R	Revenue (€/kWh)
r	Discount Rate (-)
r_v	Built-in Volume Ratio (-)
s	Entropy (J/kg/K)
$size$	Size (kW)
SPB	Simple Payback Period (years)
T	Temperature (°C)
t	Time (s)
Th_{dis}	Thermal Discharge Logic Variable (-)
U	Heat Transfer Coefficient (W/m²/K)
UA	Global Heat Transfer Coefficient (W/K)
UF	Utilization Factor (-)
V	Volume (m³)
V_s	Displacement (m³)
V_0	Clearance Volume (m³)
$\dot{V}$	Volume Flow Rate (L/s)
W	Specific Work (J/kg)
$\dot{W}$	Power (W)
x	Quality (-)

Greek Letters

α	Convective Heat Transfer Coefficient (W/m²/K)
α_{Th}	Thermal Diffusivity Coefficient (m²/s)
α_v	Intake Stroke Ratio (-)
β	Temperature Coefficient (%/°C)
γ	Rate (-)
γ_G	Irradiance Coefficient (-)
Δ	Difference (-)
δ	Uncertainty (-)
ε	Thermal Effectiveness (-)
η	Efficiency (-)
μ	Viscosity (Pa·s)
ρ	Density (kg/m³)

τ	Investment Period (years)

Subscripts

amb	Ambient
aux	Auxiliaries
ava	Available
ave	Average
calc	Calculated
CB2dem	Demand Satisfied By Carnot Battery
cd	Condenser
ch	Charge
chiller	Chiller
cold	Cold
coll	Collector
comb	Combustion
comp	Compressor
con	Self-Consumption
cooler	Cooler – Cooling Stage
cooling	Cooling System
crit	Critical
dem	Demand
DH,fee	District Heating Investment fee
DH2HP	Fron District Heating To Heat Pump
dis	Discharge
eco	Economizer
el	Electric
el,pur	Electricity Purchase
el,sale	Electricity Sale
em	Electromechanics
ev	Evaporator
ex	Exhaust
exp	Expander
dryer	Dryer – Drying Stage
F	Fuel
fans	Fans
fluid	Fluid
glide	Fluid Temperature Difference Across a Heat Exchanger
grid	Electric Grid
grid2DC	From Electric Grid To Data Center
hot	Hot
i	Index i-th
id	Ideal
II	Second Law
in	Inlet
is	Isentropic
IT	IT Equipment
k	Condensation
kiln	Kiln – Firing Stage
L	Saturated Liquid

light&loss	Light and Energy Distribution Losses
lim	Limit
max	Maximum
meas	Measured
min	Minimum
net	Net
NOCT	Nominal Operating Cell Temperature
nom	Nominal
on	System Operating
op	Operating
out	Outlet
peak	Demand/Production Peaks
pp	Pinch Point
prod	Self-Production
pump	Pump
PV2DC	From Photovoltaic To Data Center
PV2grid	From Photovoltaic To Electric Grid
Q	Thermal Energy
Q,DH	District Heating Heat
ratio	Ratio
rec	Recuperator
ref	Reference
ren	Renewables
reuse	Recovered Thermal Energy
rt	Roundtrip
sat	Saturation
SC	Subcooling
selfcons	Production for Self-Consumption
sens	Sensitivity
sf	Secondary Fluid
SH	Superheating
Sink	Thermal Sink
Source	Thermal Source
sto	Storage
su	Supply
sub	Substation
surplus	Production Surplus
tank	Tank
TH	Thermal User
Th	Thermal
th	Thermodynamic
tile	Ceramic Tiles
tot	Total
TP	Two-phase
turb	Turbine
v	Vaporization
vap	Vaporizer
vol	Volumetric
wall	Wall
wCB	With Carnot Battery Integration

wf	Working Fluid
WH	Waste Heat
woCB	Without Carnot Battery Integration
0	Initial Condition

INTRODUCTION

1. Power-to-Heat and Heat-to-Power energy systems

Summary. This chapter introduces the thesis work by examining the energetic scenario and the context in which the Organic Rankine Cycle (i.e., Heat-to-Power systems) and the High-Temperature Heat Pump (i.e., Power-to-Heat systems) technologies could be integrated, their potential, and the current challenges that hinder their diffusion on the market. In the second part of the chapter, the Carnot battery (i.e., Power-to-Heat-to-Power systems) storage technology is introduced outlining its potential in the upcoming energy scenario and the main challenges that must be faced to push the spread of this technology.

1.1. Low-temperature energy sources into the energetic scenario

The global energy consumption has been continuously increasing and has reached levels that are no longer sustainable from an environmental perspective. In recent decades, the release of increasingly large quantities of carbon dioxide (CO_2) has led to a significant rise in the greenhouse gas emissions and, therefore, in the average temperature of the planet. Every year, the evidence and concern surrounding climate change become increasingly pronounced. Indeed, summer 2022 in Europe marked the warmest on record since 1950, surpassing the previous record set in 2021 by a significant margin [1]. Three-quarters of the world's greenhouse gas emissions stem from the combustion of fossil fuels for energy generation. These fuels also contribute significantly to local air pollution, posing a serious health concern that accounts for at least five million premature deaths annually [2]. Despite a gradual shift towards a low-carbon economy over the past decades, fossil fuels continue to dominate as primary energy source, comprising nearly 77 % of the global primary energy consumption. Traditional biomasses represent about 6 %, nuclear plants account for almost 4 %, and renewable sources cover the remaining 13 % (Figure 1.1 and Figure 1.2) [3].

To meet the challenges posed by climate change and rising energy demand, it is necessary to reduce the global reliance on fossil fuels, scaling up the utilization of renewable energies, and enhancing conversion efficiencies in the exploitation of conventional primary sources. This can be achieved through the adoption of smarter, renewable-focused, integrated, well-regulated, and decentralized energy systems [4].

Over the past few decades, there have been continuous improvements in the thermal energy systems conversion efficiencies. Despite ongoing advancements, these systems encounter limitations imposed by the thermodynamics laws. Currently, state-of-the-art conversion technologies use natural gas and coal in combined cycles, achieving maximum efficiencies exceeding 60% [5]. A cycle conversion efficiency is strongly influenced by factors such as the power plant size. Indeed, typically larger plants enable greater investments in new technologies and materials, which contribute to the plant overall efficiency improvement. A limited number of large plants with distribution through high and medium voltage transmission lines has long been the prevailing model for electricity production. Such a centralized power generation model faces drawbacks including significant transmission losses, high emissions, challenges in rural electrification due to infrastructure costs, waste production, and water usage. As alternative, the distributed power generation model features numerous small plants located closer to users, linked via low voltage lines or directly to consumers. This model offers advantages such as reduced transmission losses, improved blackout management, lower investment costs, rural serviceability, and compatibility with low or zero-carbon sources. Nonetheless, the distributed power generation model presents technical,

economic and regulatory limits in terms of energy management and distribution, cost competitiveness, and limited incentives [6].

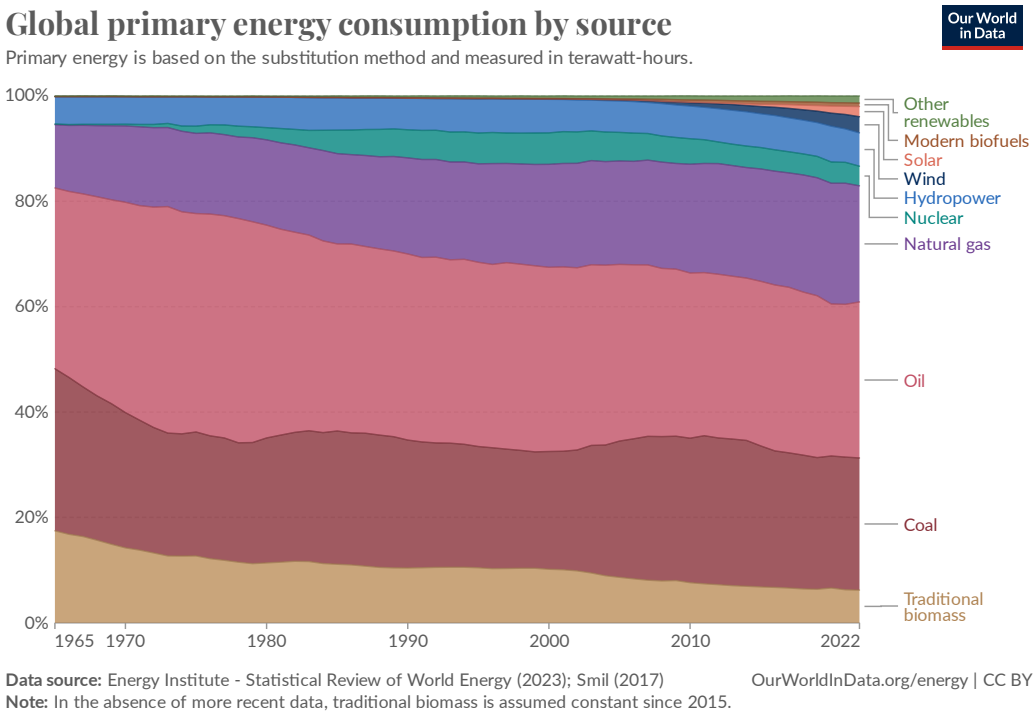

Figure 1.1 - Global primary energy consumption by energy source over the last decades [3].

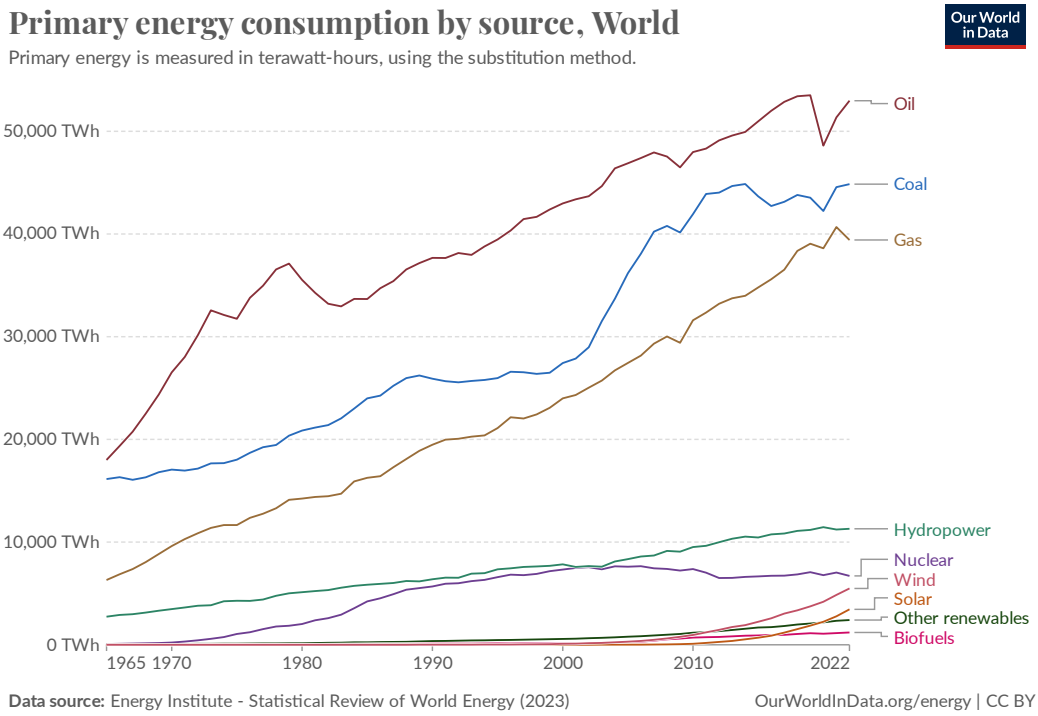

Figure 1.2 - Primary energy consumption by energy source over the last decades [3].

The reduction of the global reliance on fossil fuels can be supported also harnessing low-grade heat sources, both increasing the exploitation of low-temperature renewable heat and recovering low-grade waste heat released in conversion processes. Approximately 50 % of global energy generation is lost as heat due to unavoidable thermodynamic losses during conversion processes [7]. Various waste heat

sources exist, including industrial heat, turbine and engine exhaust heat, solar thermal power, low-enthalpy geothermal power, and biomass heat. The quality of waste thermal sources depends on factors like usability, available power, and temperature. Historically, these sources were deemed useless, but advancements now enable both i) their conversion into electricity through heat recovery engines like organic Rankine cycles (ORCs), ii) their upgrade to produce thermal energy at higher temperature through high-temperature heat pumps (HTHPs). Indeed, significant progress has been achieved in minimizing the amount of heat released into the environment [8]. However, there is still room for enhancing low-grade energy sources harnessing.

1.1.1. Low-grade industrial waste heat recovery

In March 2020, the European Commission underscored the pivotal role of the industry in steering towards a carbon-neutral economy through its publication "A New Industrial Strategy for Europe" [9]. The document highlights the industrial sector's essential role in minimizing its carbon footprint while hastening the shift towards affordable and clean technological solutions. Regulatory policies, public procurement, financial instruments at both European Union (EU) and national levels, along with private sector engagement, are deemed crucial to robustly support endeavours towards achieving carbon neutrality while ensuring the EU industry remains globally competitive. Particularly, attention is directed towards energy-intensive industries (EII) due to their substantial carbon footprints. Despite a notable 30 % reduction in CO_2 emissions from the EU's EII between 1990 and 2018, the conventional practice of fossil fuel combustion for high-temperature processes persists, contributing to approximately half of all emissions [10]. Nowadays, EII expend around one billion euros annually to adhere to the EU emission trading scheme, constituting about 1.4 % of their profits in 2017 [11].

The technologies identified for reducing CO_2 emissions can be categorized into four primary groups, according to the method [11]: i) improving energy efficiency, ii) electrification, iii) substitution of fossil fuels with renewable energy sources (RES) or low-carbon hydrogen (or other synthetic fuels), and iv) carbon capture and storage. Despite the multiplicity of available strategies, the most readily implementable approach involves enhancing energy efficiency through process and technology optimization. Natural gas, considered indispensable in the short term, will continue to serve as the industry's primary fuel during the ongoing energy transition. Additionally, the lack of dedicated infrastructure poses a significant obstacle to the adoption of fuel switching, electrification, and carbon capture. Energy efficiency entails consuming less primary energy without altering the production process itself. Current assessments indicate that, utilizing existing technologies, the technical potential for further energy savings by 2050 falls within the range of 15-25 % [11]. Apart from improving the industrial process technologies, an additional approach consists of reducing the amount of energy wasted to the environment. Indeed, low-grade waste heat constitutes 50 % or more of the overall heat produced in industrial processes [12], including combustion, drying, heating, cooling, chemical processes, wastewater [13]. Low-temperature waste heat is also available from residential facilities such as sewage from residential buildings, hotels, medical facilities, swimming pools and others. The waste heat temperature varies in a wide range according to the industrial process (or residential waste) spanning from 25 °C (e.g., in flat plate collectors) to 400 °C (such as in the flue gases of ceramic production processes) [14]. Consequently, waste heat is categorized as low-, medium-, or high-grade. Even though higher temperatures of waste heat make the recovery process more economically viable [8], approximately 50 % of thermal energy is released as sensible heat, at temperatures below 230 °C [15]. The release of heat into the environment concurs in the disruption of the aquatic ecosystem balance and biodiversity [4]. Consequently, recovering this low-grade thermal energy, which would otherwise be discharged into the environment, provides the double advantage of mitigating the thermal impact on the environment and

curtailing the primary energy consumption (and the associated CO_2 and pollutants production) attributed to industrial operations.

Currently, the industrial sectors producing the highest amount of waste heat are the ceramic, cement, lime and glass (non-metallic mineral) industries, releasing about 85 TWh/year in EU. The iron and steel sectors, together with the paper and pulp industries follow releasing about 50 TWh/year in EU (Figure 1.3) [16]. Most of this industrial waste heat is available at temperatures between 100 and 200 °C, as show in Figure 1.4.

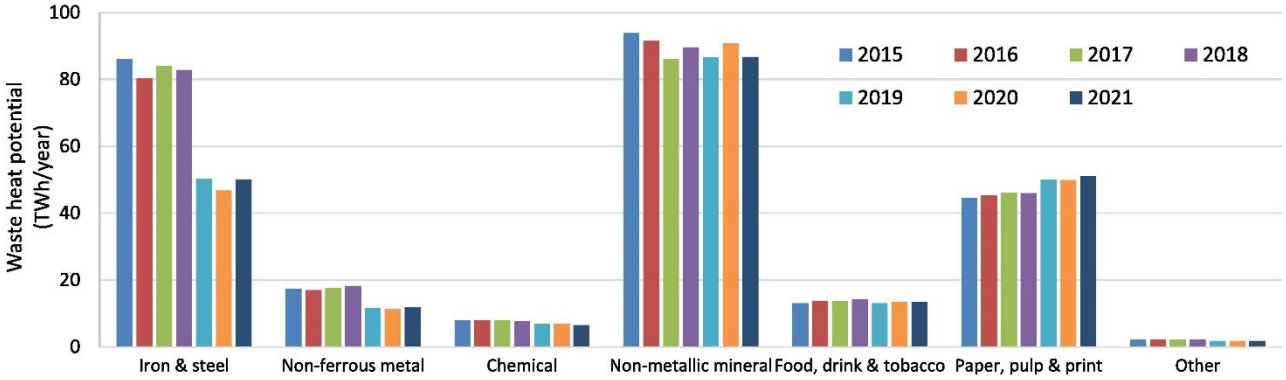

Figure 1.3 - Waste heat potential per EU and United Kingdom industrial branch in the period 2015–2021 [16].

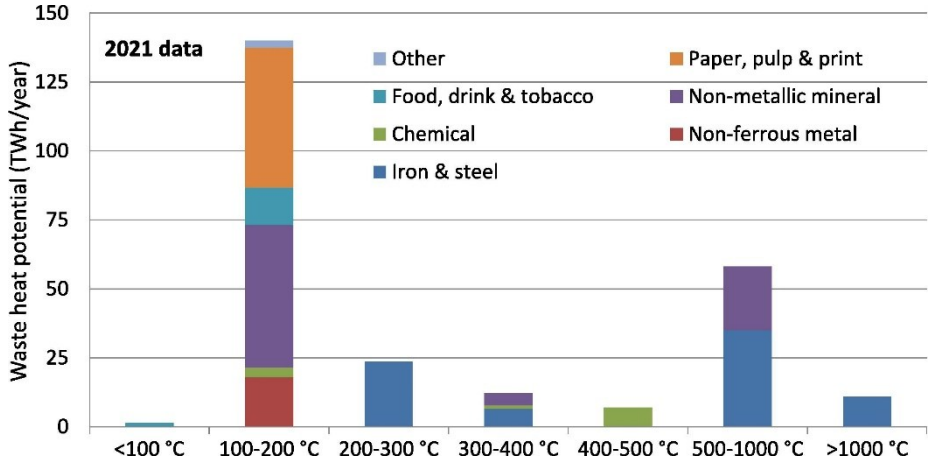

Figure 1.4 - Waste heat potential per temperature band and EU and United Kingdom industrial sector in 2021 [16].

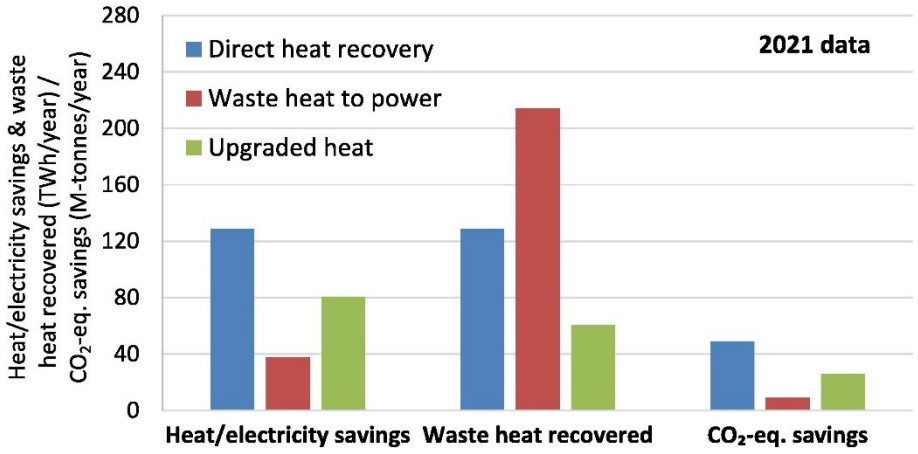

Figure 1.5 - Waste heat recovered, heat/electricity and CO_2-eq savings in EU and United Kingdom in 2021 [16].

There are three ways of recovering waste heat: i) direct heat recovery, ii) waste heat to power, and iii)

waste heat upgrading. The direct heat recovery consists of supplying the heat to another process running at a lower temperature. The waste heat to power relies on using the heat to produce electricity through a thermal cycle (Rankine cycle or Brayton cycle). The waste heat upgrading consists of increasing the temperature of the available heat through a HTHP to supply a process running at a higher temperature. The direct heat recovery provides the highest amount of thermal energy to be used in another process and allows to save the highest amount of equivalent CO_2. On the other hand, the waste heat to power solution exploits the highest amount of waste heat, but it provides the lowest equivalent CO_2 savings (Figure 1.5) [16].

A non-negligible contribution to the world's waste heat production is provided by data centers (DCs). Over the past few decades, DCs have gained a role of primary importance in the information and communication technology field, serving as critical infrastructure for Internet-based services. Beyond mere data storage, they facilitate various functions related to digital data processing, management, and virtual information exchange [17]. Structurally, DCs are comparable to large containers housing organized rows of racks containing modular elements [18].

A significant concern associated with DCs is their substantial energy requirements. According to Koomey [19], servers alone consume over 1.2 % of total energy usage in the United States, 2.5 % in EU [14], and around 0.8 % globally. Cho et al. [20] note a yearly increase of 20 % in DC energy consumption, driven by a 13 % annual rise in servers and a 56 % surge in data storage demand. Recent statistics indicate that in 2017, DCs consumed 416.2 billion kWh of electricity, constituting nearly 2 % of the world's total electricity consumption [21] and approximately 2 % of total greenhouse gas emissions [22] (3 % and 4 %, respectively, within the industry sector [23]).

The high energy intensity of DCs stems partly from the conversion of 99 % of their power into heat, with 70 % of this heat requiring complete removal to ensure safe and reliable operation [20]. According to Ebrahimi et al. [24], a rack with a footprint of 0.65 m^2 must dissipate 30 kW of thermal power, a figure that can double to 60 kW in the case of supercomputer servers filling the rack [25]. As a result, the cooling system requires almost 40 % of the total DC electricity demand (Figure 1.6) [25].

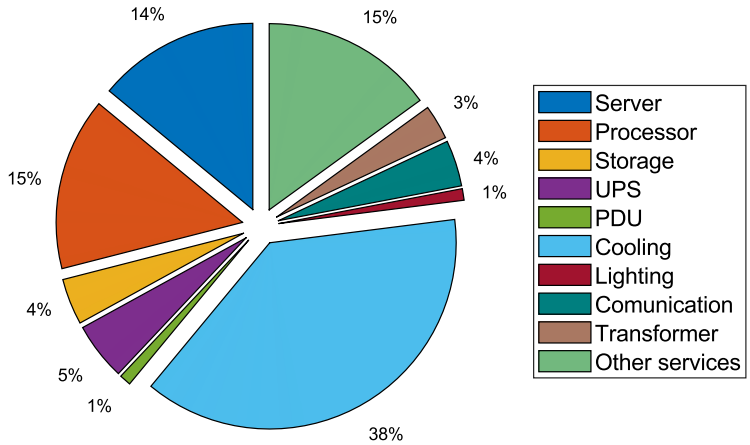

Figure 1.6 - Electricity consumption distribution in data centers [25].

In light of the above, as for the EII processes, also DCs are well suited for coupling with thermal energy recovery technologies, like ORC power plants and HTHPs.

1.1.2. Low-temperature renewable energy sources valorisation and storage

To reduce global greenhouse gas emissions and local air pollution, the world needs to rapidly shift

towards low-carbon sources of energy, i.e., nuclear and renewable technologies. The utilization of RES has seen a global increase, particularly in developed nations (Figure 1.7) where advanced energy policies and substantial investments in low-carbon technologies have been implemented [2]. Figure 1.8 illustrates the global trend in electricity generation from low-carbon sources, including renewables, over the past 57 years. Currently, among RES, hydropower is the most widely adopted, accounting for nearly 4300 TWh/year, followed by wind energy (2100 TWh/year) and solar energy (1300 TWh/year). Other renewables such as geothermal, biomass, wave, and tidal collectively contribute for nearly 800 TWh/year to the global generation. Beyond mitigating pollutant and greenhouse gas emissions, renewable energy offers the distinct advantage of being globally distributed, thus offering a solution to the energy supply challenges faced by rural areas and developing countries.

Based on the provided information, one way to increase and speed up the penetration of the renewables in the global energy scenario is to push towards the exploitation of thermal RES, including solar, geothermal, and biomass.

Indeed, there are alternative methods to harness solar radiation for electricity beyond photovoltaics. One such method involves capturing solar energy to produce thermal energy, which can then be converted into electricity through a thermodynamic cycle. Utilizing simple flat collectors with evacuated tubes, temperatures of up to around 150 °C can be reached at the receiver. Alternatively, specialized systems that concentrate solar radiation into a focal line or point can achieve temperatures as high as 1000 °C, known as concentrating solar power systems. However, the cost of the reflector increases significantly with the desired temperature, making it economically viable primarily for large solar fields.

Geothermal sources encompass a broad spectrum of temperatures, ranging from a few tens of Celsius degrees to 300°C. However, the minimum temperature required for the production of electrical power is technologically set at 80°C, as efficiency drops below this threshold. Geothermal plants extract hot fluid, typically pressurized liquid water up to 100 bar in dominant water hydrothermal sites, or in the form of saturated or superheated steam in dominant steam hydrothermal sites. It's crucial to carefully evaluate pumping consumption in such plants, which often constitutes a significant factor [4]. These energy sources offer key advantages such as programmability and continuous availability, unlike many other renewable sources, thus obviating the need for storage tanks. However, a primary challenge lies in sourcing these sites, with many promising hydrothermal locations situated in remote islands with low energy demand [15].

Biomass is abundantly available in various agricultural and industrial processes, particularly those involving organic waste like the wood industry. It can be combusted to generate thermal energy, which can then be converted into mechanical energy through thermodynamic cycles. While the cost of biomass itself is relatively low, significant investments are required to ensure clean combustion, rendering it less competitive for smaller-scale applications. An alternative approach to direct biomass combustion is gasification, wherein biomass is transformed into synthetic gas (syngas) consisting primarily of combustible fractions such as molecular hydrogen, unburned hydrocarbons, carbon monoxide, and methane, along with inert components like water, carbon dioxide, and molecular nitrogen. The syngas is then purified to remove pollutants, particularly sulphur and nitrogen, before being burned. This results in a highly efficient and clean combustion process. However, gasification necessitates expensive plants and entails high maintenance costs, making it impractical for smaller-scale operations [4]. Similar to geothermal energy, biomass can be harnessed in a programmable and continuous manner, with no concerns regarding geographical availability. Another advantage of biomass combustion is the potential for small-scale cogeneration applications.

Due to their comparable temperature ranges, these low-grade RES can be harnessed using the same technologies utilized for waste heat recovery (WHR), i.e., thermal cycles including organic Rankine and Brayton cycles for the electricity production, and HTHPs for the thermal energy upgrading. Furthermore, these technologies can be combined in more complex systems for increasing the energy efficiency and/or

storing the available energy (e.g., Carnot batteries), particularly beneficial when dealing with renewables, which often lack programmability.

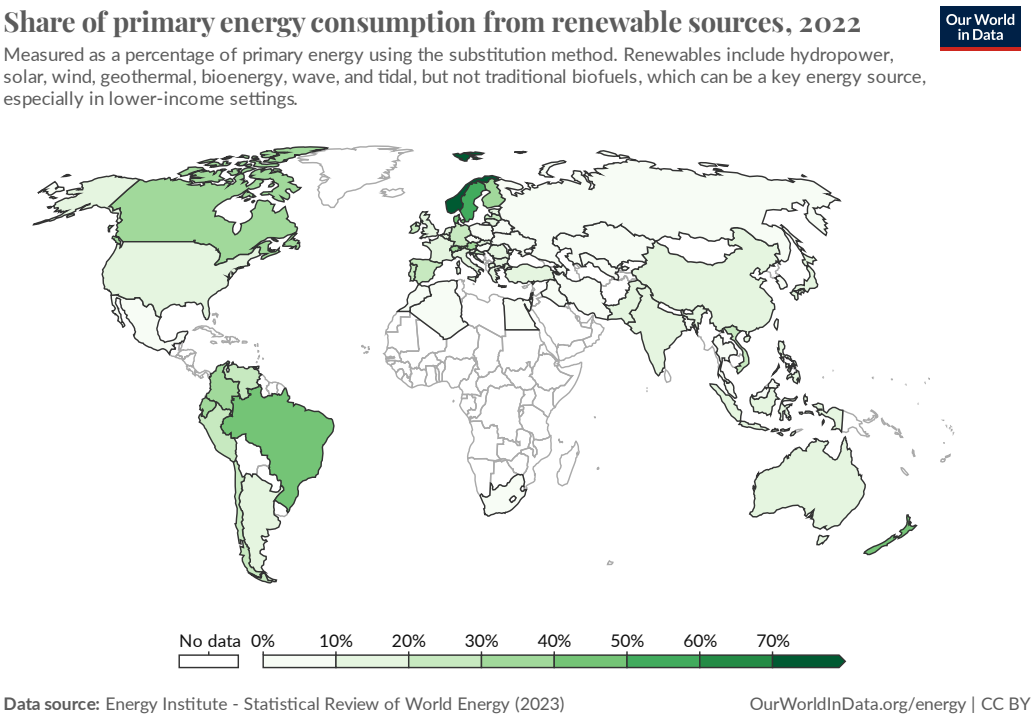

Figure 1.7 - Share of primary energy consumption from renewable energy sources in the world in 2022 [2].

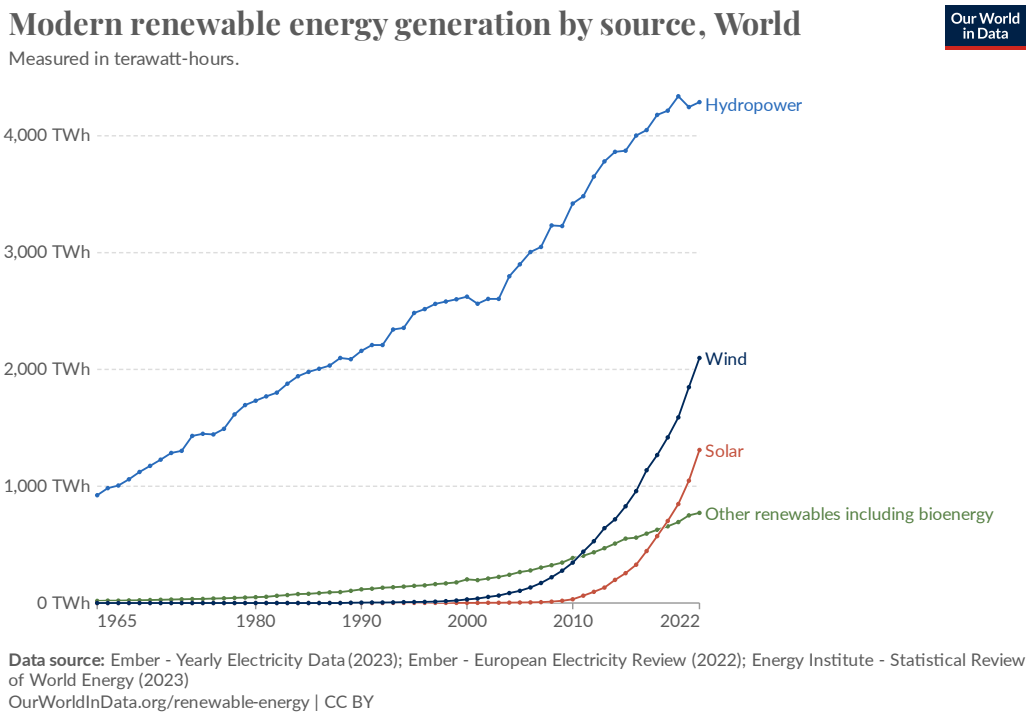

Figure 1.8 - Renewable energy generation trend by source in the world [2].

In conclusion, the combined implementation of waste heat recovery and penetration of renewable sources in the global energy scenario could significantly contribute to the achievement of a sustainable future. This approach would diminish reliance on fossil fuels and decrease emissions of pollutants and

greenhouse gases.

1.2. Organic Rankine Cycle potential for low-grade heat valorisation

Thanks to its simplicity and its capacity to retrofit existing thermal system, ORC technology is suitable to be employed with several low-temperature thermal sources that are in general not valorised and thus wasted to the ambient. The exploitable heat sources involve both low-grade industrial waste heat and low-enthalpy renewable thermal energy sources (i.e., geothermal, solar thermal, biomass).

ORC systems work based on the same thermodynamic principle as traditional water steam Rankine cycle plants (see Figure 1.9(a)). The working fluid, in liquid phase, is pressurized by the feed pump to the high-pressure level of the cycle; then it enters the evaporator, where it undergoes preheating, vaporization, and superheating through thermal energy transferred from an external heat source; subsequently, the working fluid expands to the low-pressure level of the cycle in an expansion machine, producing mechanical work, then converted into electric energy by a generator; eventually the fluid crosses the condenser returning to the liquid phase and closing the thermodynamic cycle. Potentially, efficiency can be enhanced by including a regenerator, which pre-heats the liquid entering the evaporator using the residual sensible heat from the expander exhaust vapor (Figure 1.9(b)).

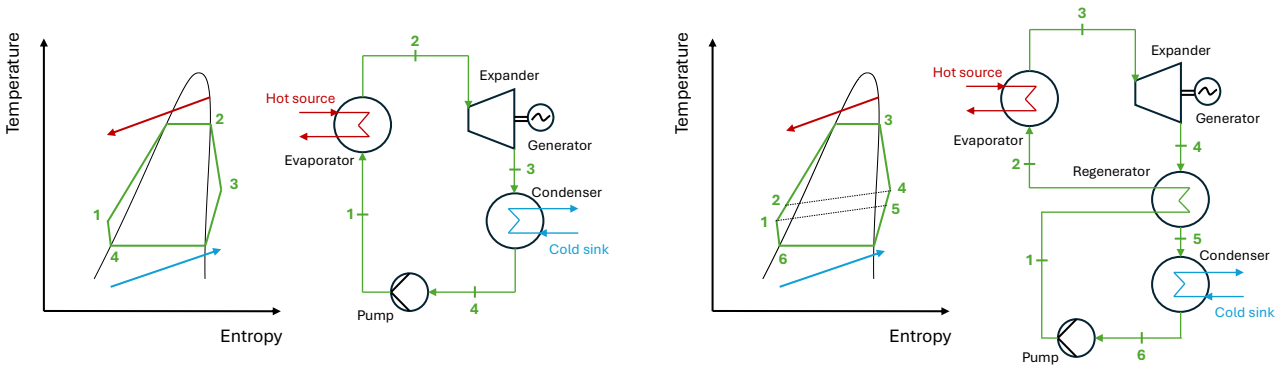

Figure 1.9 - ORC thermodynamic process and layout: (a) simple cycle and (b) recuperated cycle.

The main distinction between a traditional steam Rankine cycle and an ORC lies in the choice of the working fluid, whose different chemical and physical properties, compared to water, significantly impact the system's design.

1.2.1. Working fluid

The first distinction among the fluids is related to the molecular complexity, which determines the heat capacity and the inclination of the saturated vapor curve in the temperature-entropy diagram. A higher molecular complexity, characteristic of the organic fluids, results in a larger heat capacity and in an increase in the slope of the saturated vapor curve. Water, R134a, and MM (as shown in Figure 1.10) are examples of fluids with increasing molecular complexity, and they are called respectively wet (negative slope), isentropic (infinite slope) and dry (positive slope) fluids. The slope of the saturated vapour curve determines the state in which the expansion process occurs. Indeed, a negative slope leads to an expansion occurring in the two-phase zone (wet expansion), while a null or positive slope allows the expansion occurring in the superheated vapour zone (dry expansion).

Since the presence of liquid droplets in the wet expansion can damage the turbine blades, the minimum

vapor quality ensured at the end of expansion is limited to 85%, appropriately superheating the vapor supplied to the turbine. However, the heat transfer coefficient notably decreases in the vapor phase, leading to an increase in the required heat transfer area and, consequently, in the heat exchanger cost. Furthermore, the introduction of superheating requires the availability of a thermal source at a higher temperature, excluding the possibility of exploiting some medium or low temperature thermal sources, such as geothermal or solar. By contrast, isentropic and dry fluids do not necessitate the vapour superheating. However, the more the superheating degree at the end of the expansion rises, the more the cooling load at the condenser increases. This aspect suggests the convenience of adopting a recuperated configuration (Figure 1.9(b)) to recover the exhaust vapour residual heat to preheat the liquid entering the evaporator, reducing the thermal input and increasing the cycle efficiency.

Besides water, another example of wet fluid is ammonia, while most of the organic fluids belong to the isentropic and dry groups (see Figure 1.11).

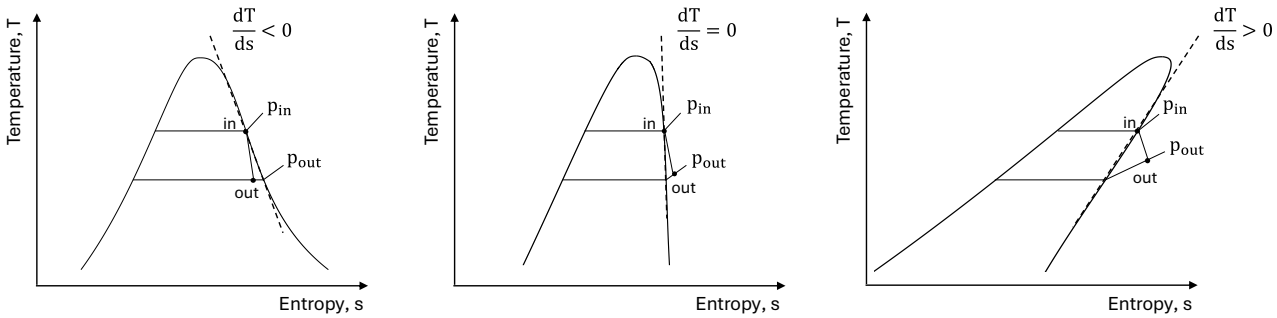

(a) - water (b) - R134a (c) - MM

Figure 1.10 - Saturated vapor curve slope classification: (a) wet fluid, (b) isentropic fluid, and (c) dry fluid.

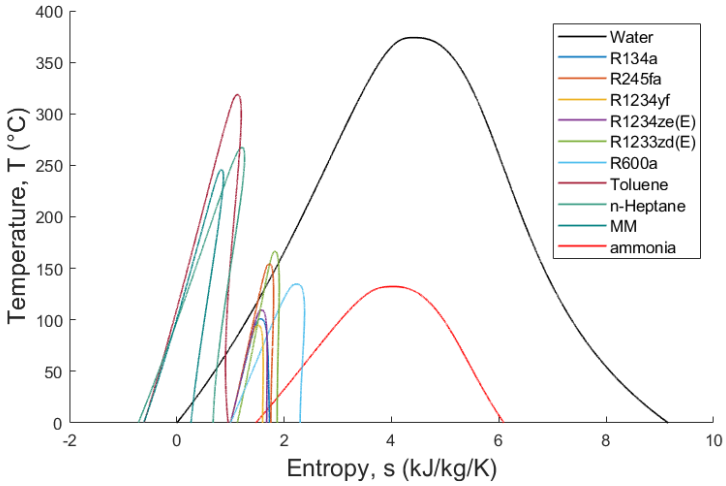

Figure 1.11 - Saturation curves for different categories of fluids.

The critical temperature of the working fluid influences the saturated pressure for a given temperature (Figure 1.12(a)). Higher critical temperatures result in lower condensation pressures, which may complicate plant design and increase costs, if lower than atmospheric pressure. The critical pressure is in the range between 30 and 50 bar, except for siloxanes and water, which have lower and higher critical pressures, respectively (Figure 1.12(b)). Researches [26] indicate that fluids with higher critical temperatures tend to achieve higher cycle efficiency due to their higher pressure ratios and enthalpy drops. However, higher pressure ratios also lead to increased plant complexity and costs, as in water Rankine cycles.

Lower critical temperatures are associated with higher fluid densities (Figure 1.12(c)), which allow to

limit volume flow rates, reducing the pressure drops in the heat exchangers and allowing a smaller expander size. Molecular weight typically increases with critical temperature (Figure 1.12(d)), although different fluid categories may exhibit varying trends. Specifically, hydrocarbons generally have lower molecular weights compared to refrigerants and siloxanes. Hence, high molecular weight fluids may be preferred for simpler and more compact applications.

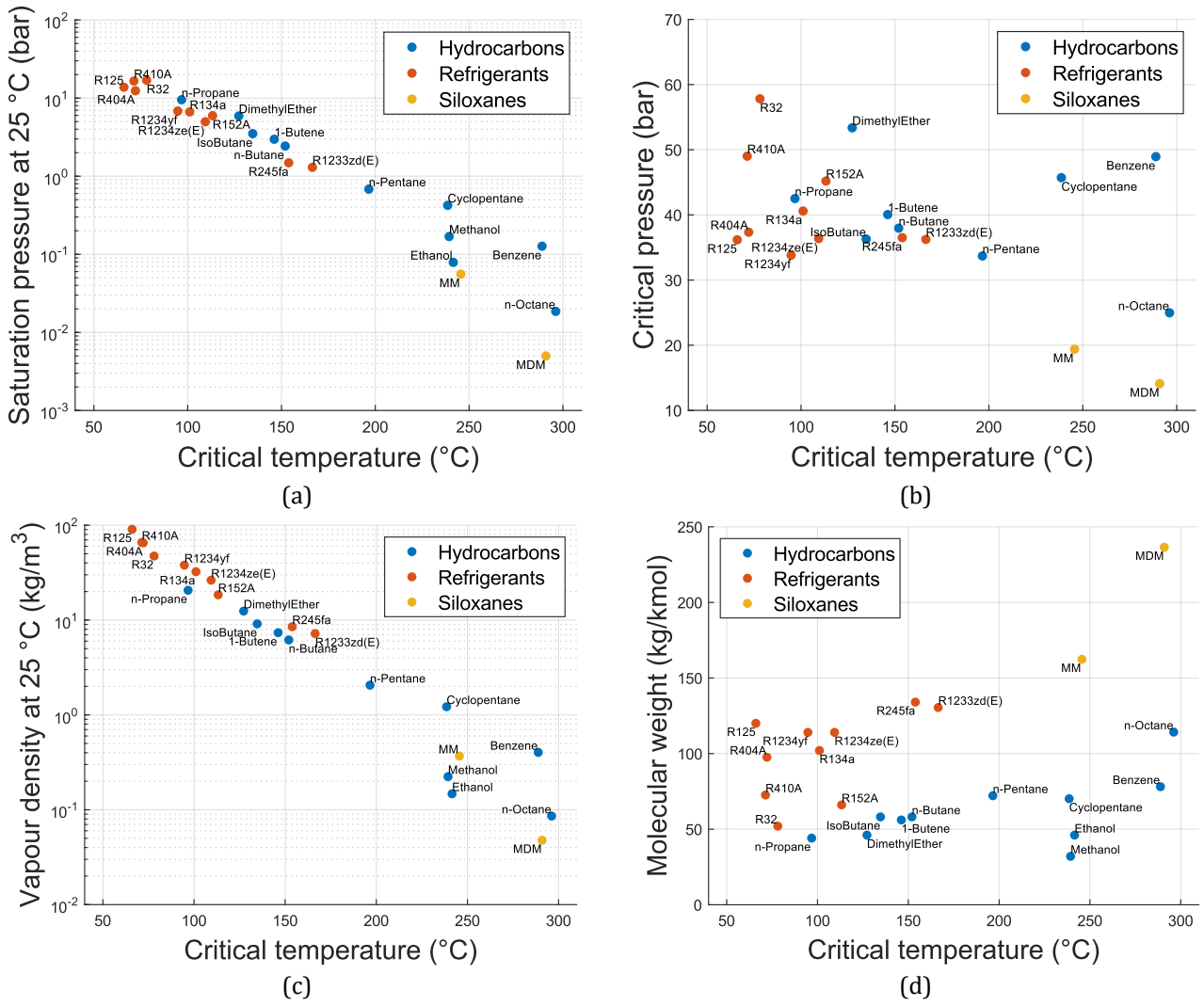

Figure 1.12 - Trend of the (a) saturation pressure, (b) critical pressure, (c) saturated vapor density, and (d) molecular weight of different fluids' families as functions of the critical temperature (properties calculated by means of CoolProp library [27]).

Another crucial aspect to consider in the selection of the working fluid is the environmental impact. In low-temperature applications, high global warming potential (GWP) refrigerants are commonly used due to their thermal compatibility with low-grade heat sources. Refrigerants belonging to the HydroFluoroCarbons (HFCs) category, such as R245fa, R123, and R134a, are frequently employed for these purposes, owing to their low critical temperature which makes them higher performing than other fluids [26]. However, HFCs pose a significant risk to the environment due to their high GWP values and extended atmospheric residence time, which can contribute to the greenhouse effect if released during plant operation. The GWP index facilitates the comparison of the global warming impact of different gases by evaluating their ability to absorb energy and retain it in the atmosphere, slowing the rate at which it is released [28]. The phase-out of high ozone depletion potential (ODP) fluids, such as ChloroFluoroCarbons (CFCs) and HydroChloroFluoroCarbons (HCFCs), has already occurred as a result of the Montreal Protocol.

Table 1.1 reports the value of the GWP and ODP indexes for different categories of refrigerants employed (today and in the past) in ORC applications. The phase-down of GWP refrigerants is ongoing, with regulations like the EU F-Gas Regulation 517/2014 aiming to reduce HFC consumption by 79% by 2030 [29]. This entails transitioning to refrigerants with lower GWP, such as HydroFluoroOlefines (HFOs) [30], which offer similar thermal performance with GWP values close to 1. Researchers in this field face the challenge of identifying suitable replacements for HFCs that meet low GWP requirements while maintaining similar thermal performance, chemical stability, low toxicity and flammability (according to ASHRAE Standard [31]), low cost and wide availability.

Table 1.1 - Environmental properties of different fluids (GWP and ODP calculated by means of CoolProp library [27], safety class available at [32]).

Family		Fluid	GWP	ODP	Safety class
Hydrocarbons (HC)	Alkanes	n-Propane	3	0	A3
		n-Butane	3	0	A3
		n-Pentane	0	0	A3
		n-Octane	0	0	NA
		IsoButane	0	0	A3
		Cyclopentane	0	0	A3
	Alkenes	1-Butene	0	0	NA
		Benzene	0	0	NA
	Alcohols	DimethylEther	1	0	NA
		Methanol	2.8	0	NA
		Ethanol	0	0	NA
Refrigerants	CloroFluoroCarbons (CFC)	R11	4660	1	A1
		R113	5820	1	A1
		R114	8590	1	A1
	HydroCloroFluoroCarbons (HCFC)	R123	79	0.02	B1
	HydroFluoroCarbons (HFC)	R125	3500	0	A1
		R32	675	0	A2L
		R134a	1430	0	A1
		R152A	124	0	A2
		R245fa	1030	0	B1
	HydroFluoroOlefines (HFO)	R1234yf	4	0	A2L
		R1234ze(E)	6	0	A2L
		R1233zd(E)	0	0	A1
	Mixtures	R404A	3900	0	A1
		R410A	2088	0	A1
Siloxanes		MM	0	0	NA
		MDM	0	0	NA
		MD2M	0	0	NA
		MD3M	0	0	NA

1.2.2. Partial-evaporation cycle

Nowadays, ORCs are primarily utilized in the small to medium-size sector, with limited application in the micro-size range (electric power below 50 kW). Ongoing research aims to enhance performance and optimize this category of energy systems. With this aim, besides the selection of the more convenient working fluid for each application already discussed in the previous subsection, the main aspects currently

under research involve: i) the optimization of the expander and pump performance, ii) the development of control strategies to enhance performance under dynamic heat source conditions and off-design operation, and iii) the exploration of non-traditional cycles aimed at improving conversion efficiency.

In particular, concerning the last point, there is growing interest in ORCs utilizing partial evaporation and two-phase expansion (also called wet expansion) due to distinct characteristics making them advantageous for harnessing low-grade heat sources. When expansion occurs entirely in wet conditions, two configurations are typically considered:

a) The trilateral flash cycle (TFC), where the fluid enters the expander as saturated liquid or with a vapor quality below 0.1 (Figure 1.13(a)). In this scenario, the evaporator works as an economizer, heating the fluid to its vaporization temperature, and only flash vapor expands in the expander.
b) The partially evaporated organic Rankine cycle (PE-ORC), where vaporization of the working fluid is halted at a specific vapor quality value (Figure 1.13(b)). Compared to the TFC, a larger portion of fluid vapor is expanded in the expander, with both sensible and latent heat transferred in the evaporator. This approach aims to mitigate some of the drawbacks of the TFC.

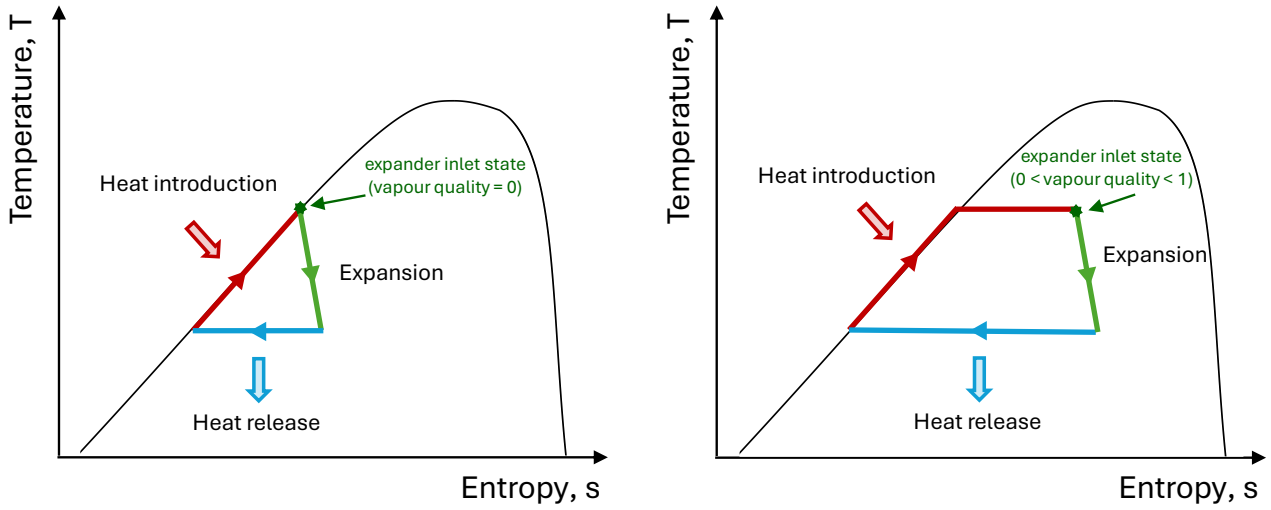

(a) - TFC (b) – PE-ORC

Figure 1.13 - Concept of (a) trilateral flash cycle (TFC) and (b) partially evaporated organic Rankine cycle (PE-ORC).

Interest in studying ORC systems with trilateral cycles or partial evaporation stems from the potential to achieve higher conversion efficiency from heat sources with finite capacity [33]. By reducing or eliminating the isothermal heat of vaporization, a closer temperature match between the heat source and working fluid can be achieved, leading to improved energy utilization and reduced heat transfer losses.

However, it's important to note that expander performance in wet conditions may be inferior compared to dry expansion, resulting in lower power output for a given working fluid mass flow rate. Additionally, two-phase expansion can cause erosion of expander materials, thereby reducing machine lifespan [4]. In this regard, it is recognized that volumetric expanders generally behave better than turbines when subjected to expansion in two-phase conditions [34]. For this reason, partial evaporation approach is particularly advantageous for low-temperature heat sources [35]. Indeed, the positive displacement (or volumetric) expanders are better suited for small-scale ORC units, since they are characterized by lower flow rates, higher pressure ratios, and significantly lower rotational speeds compared to turbo-machines [4]. Positive displacement expanders employed in ORCs include piston, scroll, screw, and vane types. While screw and scroll expanders typically exhibit superior overall performance, piston expanders may be preferred due to their ability to offer larger expansion ratios [36]. Usually, positive displacement expanders are prototypes adapted from existing compressors utilized in the refrigeration industry [4].

1.2.3. Applications, market share, and current challenges

Organic Rankine cycle technology can be advantageous especially in applications with heat source temperatures, typically below 400 °C, and smaller-scale power plants, typically under 10 MW. Such applications encompass renewable sources like geothermal, biomass, solar, as well as WHR from energy-intensive industrial processes [37]. Distinct operating temperatures and plant dimensions are exhibited by various applications (Figure 1.14).

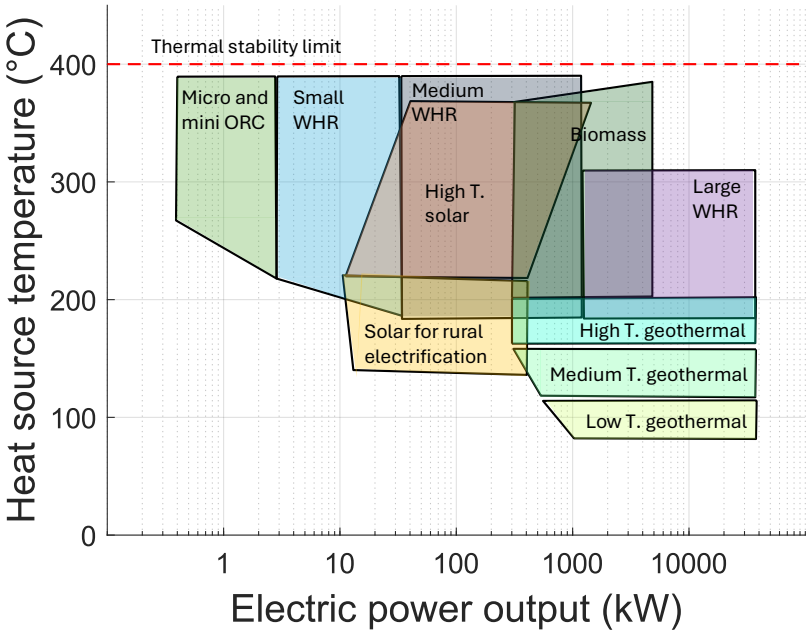

Figure 1.14 - ORC fields of application (data from [37]).

Biomass and geothermal power plants typically range in size from 300 kW to 30 MW, although they operate at different temperature ranges: geothermal plants typically operate below 200 °C, while biomass plants operate above 200 °C. These two types of plants represent a significant portion of the market share, with geothermal plants accounting for 75 % of the global installed ORC capacity, followed by biomass plants at 11 %. WHR applications from gas turbines (GTs) and engines rank third, covering 9 % of the total installed capacity (Figure 1.15(a)). Other WHR applications cover 5 % of the market, while solar power comprises less than 1 % [38]. In WHR applications, waste heat temperatures can range from 200 to 400 °C, with varying enthalpy content influenced by the nature of the heat source and its mass flow rate (Figure 1.14). Depending on the available thermal power magnitude (which determines the ORC power output), WHR applications can be categorized as small, medium, or large WHR systems. Solar power plants sizes typically range between 10 kW and 1 MW, with temperatures limited to 200 °C for rural electrification systems but reaching up to 350 °C in high-temperature solar concentration applications. A more recent and promising application area is micro-generation, although it currently represents a small portion of the market share.

Medium to large-scale ORCs are prevalent in the market and frequently employed for power generation in various industrial heat recovery power plants. With over 340 MW of installed capacity worldwide and an additional 18.5 MW under construction, these systems are well-established. However, their current capacity remains limited compared to their potential [38]. Indeed, ORC technology is highly adaptable for flexible and remote operation due to its characteristics, including a wide part-load regulation range (from 10 to 100 % without issues), straightforward start-stop procedures, minimal maintenance needs, and a compact layout.

Regarding producers (Figure 1.15(b)), ORMAT leads globally with 63 % of the total installed capacity,

trailed by Italian companies Turboden (13 %) and Exergy (11 %) [38]. In the micro-scale ORC systems niche, several small manufacturers are active in the market, including Air Squared (US), Rank (ES), Enogia, Visorc (FI), ElectraTherm (USA), and the Italian Zuccato Energia (IT).

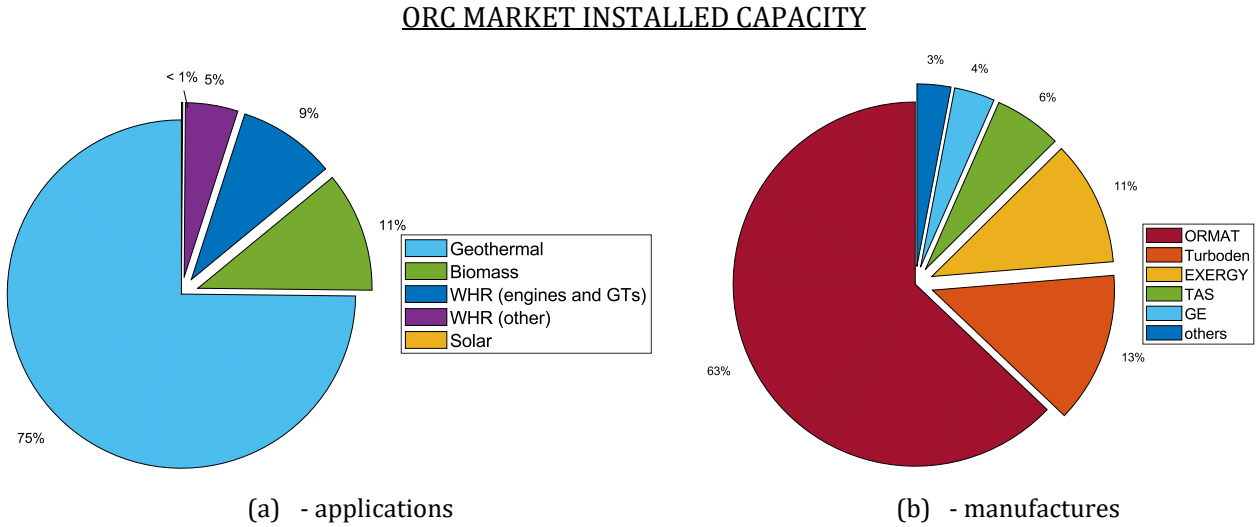

(a) - applications (b) - manufactures

Figure 1.15 - ORC market installed capacity (a) by application and (b) manufacturer (data from [38]).

Trends in technology costs are also depicted in Figure 1.16. Data from Turboden [39] indicate a negative exponential trend in ORC investment costs based on size, particularly for medium to large-scale systems (shown in Figure 1.16). The specific cost decreases with size, from 4000 to less than 2000 €/kW, ranging from 500 kW to 10 MW. However, precise correlations for specific costs at the micro-scale are not yet available. An estimated curve provided by Air Squared [40] follows a similar trend, suggesting a specific cost of around 9000 € for a 1 kW system.

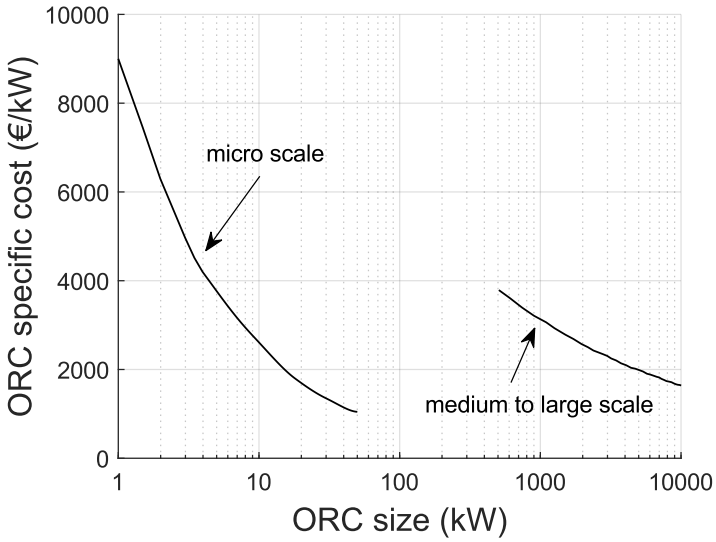

Figure 1.16 - ORC specific cost of investment curves obtained interpolating data for the micro-scale from [40], and for the medium to large-scale from [39], considering a conversion factor of 0.9 between dollars and euros.

Although medium to large-scale ORCs are quite common, this technology remains underutilized compared to its potential [41]. The micro-scale market is particularly penalized due to technological issues, such as i) the low Carnot efficiency due to the small difference between the hot source and cold sink temperature levels, ii) the lack of appropriate expander machines in the commercial market, iii) the critical selection of the working fluid for each application. Furthermore, existing barriers, such as the absence of

green incentives and long-term payback periods, pose a significant risk to investment, and industrial capital budgets are limited, leading companies to prioritize safer investments aligned with their core business activities [13]. Therefore, it is imperative for ORC producers and researchers to explore new solutions to enhance its attractiveness to industries, particularly in sectors poised for expansion with anticipated significant investments in the coming years.

Researchers are increasingly refining techniques for studying these systems. However, most analyses focus only on the on-design regime of operation [42]. Yet, the performance of ORC systems is strongly influenced by the characteristics of the heat source and system design. In WHR applications, heat sources often experience fluctuations and intermittency due to the non-uniform production of industrial processes. This aspect is critical for evaluating system feasibility, despite being commonly overlooked.

1.3. High-Temperature Heat Pump potential for waste heat upgrade

In addition to providing space heating and hot water, there is a considerable need for process heat at different temperature levels (Figure 1.17(a)) in various industries for manufacturing, processing, or refining products. Indeed, the industrial process heat accounts for 19 % of the world total energy demand, contributing to 36.8 % of all emissions related to energy use [43]. This is largely due to the significant reliance on fossil fuel boilers for generating energy in industrial processes (Figure 1.17(b)). To meet global targets set by the International Energy Agency for achieving net-zero greenhouse gas emissions by 2050 [44], industries must transition from fossil fuels to more sustainable solutions and RES. Meanwhile, substantial amounts of low-grade waste heat (< 250 °C) [43] are available from many industrial processes, often without immediate usability. Indeed, the industrial sector current thermal energy recovery rate is below 30 % [45]. Indeed, while high-temperature waste heat is often directly recovered and reutilized to satisfy lower-temperature heat demands, the recovery of medium- and low-temperature waste heat, which constitutes a significant portion of total waste heat, is not widely adopted [45]. Therefore, it is crucial to develop more efficient and environmentally friendly methods to upgrade this unused thermal energy for use in industrial applications.

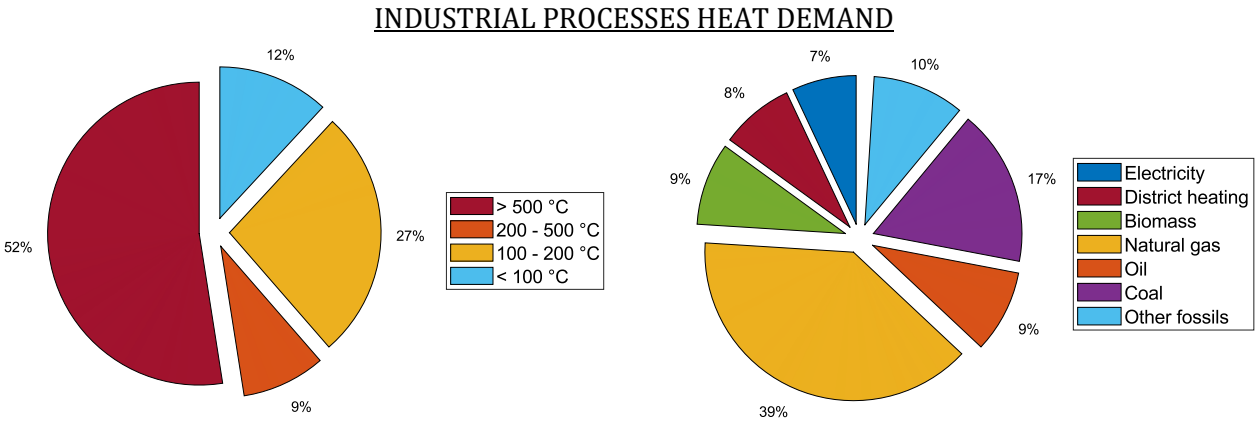

(a) – temperature levels (b) – energy source

Figure 1.17 - Worldwide industrial processes heat demand: (a) temperature levels distribution, and (b) primary energy source (data from [43]).

Using electricity, heat pumps (HPs) can harness "waste heat" available in various processing industries (Figure 1.18(a)), thereby reducing overall energy demand from fossil fuel boilers and consequent emissions, especially when powered by renewable electricity. HP technology is well-established for commercial, residential, district heating, and industrial process heat applications operating below 100 °C,

while HTHP technology remains less established, with limited commercially available units [46]. HPs are categorized based on source and sink temperature levels: HPs can be classified in conventional heat pumps (HP) (source: 0-40 °C; sink: 0-80 °C), high-temperature heat pumps (HTHP) (source: 40-60 °C; sink: 80-100 °C), very high-temperature heat pumps (VHTHP) (source: 60-120 °C; sink: 100-160 °C) [47]. A more recent classification divides the HPs into four groups based on the sink output temperature: low-temperature heat pumps (LTHP) (0-60 °C), medium-temperature heat pumps (MTHP) (60-100 °C), high-temperature heat pumps (HTHP) (100-160 °C), and ultra-high temperature heat pumps (UHTHP) (160-200 °C) [45]. In this thesis, for the sake of simplicity, all the non-conventional HPs (sink temperature higher than 80 °C) are grouped and referred as HTHPs. In EII (Figure 1.18 (b)) such as food processing, paper production, and chemical manufacturing, HTHPs show significant promise for applications such as drying, pasteurization, sterilization, evaporation, and distillation [47]. Furthermore, based on their operating principles, HPs can be categorized into two main types, i.e., compression and absorption. In this thesis, the compression HP technology is investigated to recover low- and medium-temperature waste heat.

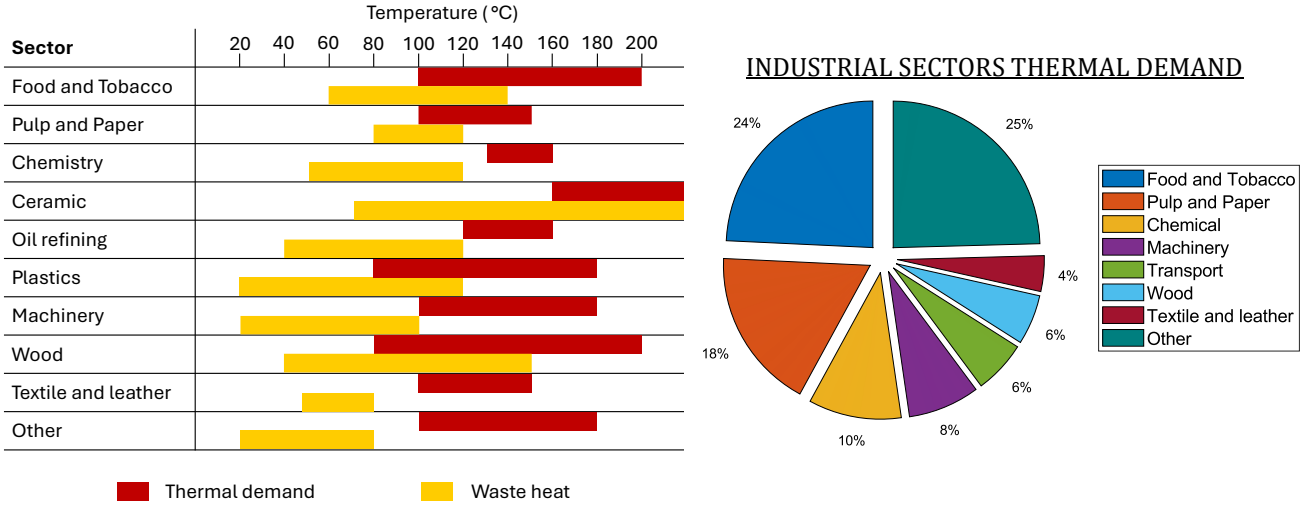

Figure 1.18 – Energy-intensive industrial sectors (a) heat temperature ranges and (b) thermal demand (data from [45], [47], [48], [49]).

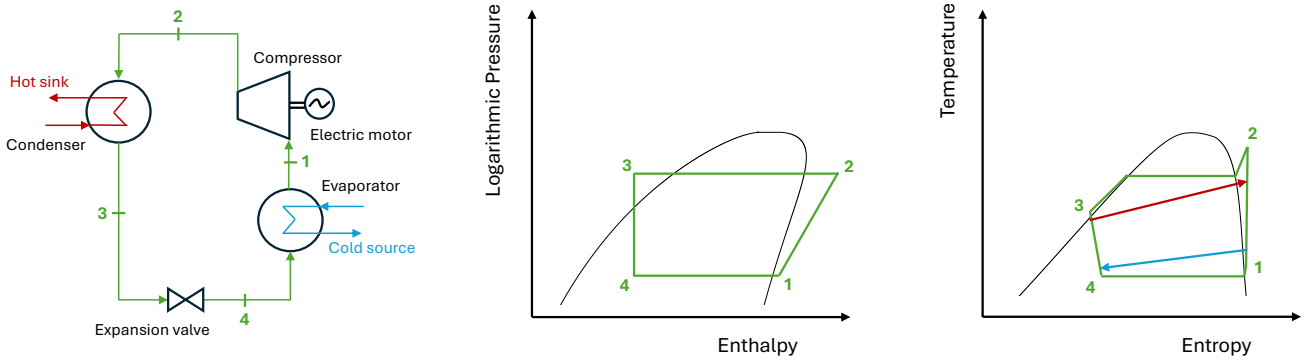

Figure 1.19 - HP base configuration layout and thermodynamic processes.

HP systems operate by absorbing thermal energy into the working fluid from an external heat source, through vaporization at a low-temperature level; the working fluid is then compressed, leading to an increase in pressure and temperature; subsequently the working fluid releases thermal energy at a higher temperature point to an external heat sink, through a condensing process; eventually, to close the cycle, the fluid in liquid phase undergoes an expansion process through an expansion valve, before entering

again the evaporator for the thermal energy absorption stage (see Figure 1.19). Through this process, the waste heat from an industrial process stream or from the environment can be upgraded and utilized in higher-temperature processes, at the cost of the compression work in input to the cycle.

From the base configuration shown in Figure 1.19, in literature more complex layout are investigated with the aim to enhance the performance. In the following subsection, a brief review of the most common configurations and refrigerants is provided.

1.3.1. Configurations and working fluids

HTHP configurations can be grouped in single-stage and multi-stages layouts. Apart from the base layout, single-stages configurations include systems with vapor injection or ejectors to enhance cycle performance, and systems equipped with an economizer and/or an intermediate heat exchanger to increase the temperature lift. Multi-stage configurations utilize more than one compression stage to attain higher output temperatures, at the cost of increased mechanical energy consumption. Among multi-stage systems, cascade heat pumps involve two or more working fluids to achieve higher temperature lift.

More in detail, a base single-stage cycle (Figure 1.19) can achieve a high coefficient of performance (COP) for limited temperature lifts because as temperature lift increases, so do throttling losses. Furthermore, the maximum temperature lift is constrained by the pressure ratio limit of a single compression stage. Typically, the maximum temperature lift in a standard cycle with a single compression stage is around 90–100 °C, with most reported temperature lifts in the range between 30 °C and 50 °C (see for example Ochsner IWWDS, Combitherm HWW, Star Refrigeration Netpump, GEA Grasso FX P [47]).

In single-stage cycles a liquid and vapor separator is often adopted (Figure 1.20(a)) enabling a fully wetted heat transfer surface in the evaporator and reducing the superheat at the compressor, while also preventing liquid refrigerant from entering the compressor [46]. At high discharge temperatures, the use of injection technique can improve the compression performance. This alternative can be applied through liquid refrigerant injection (Figure 1.20(b)) or vapour refrigerant injection (Figure 1.20(c)). In the liquid-cooling injection technology, to prevent overheating of the compressor chamber, liquid from the separator can be tapped to be injected into the suction chamber of the compressor [50]. In the vapour injection, the separator is at an intermediate pressure between the evaporating and condensing pressure levels, and the vapour refrigerant is tapped and injected in the compressor [51]. The single-stage configuration tends to exhibit lower efficiency when dealing with significant temperature lifts. To enhance efficiency, an intermediate heat exchanger (IHX) can be included (Figure 1.20(d)). IHXs are typically positioned between the outlet of the condenser and the outlet of the evaporator. By transferring some heat from the refrigerant exiting the condenser to the refrigerant exiting the evaporator, the refrigerant temperature at the compressor suction is raised. Consequently, a higher compressor discharge temperature can be attained, allowing the heat sink to achieve a higher temperature with an increased compression work [52].

A multi-stage vapor compression system utilizes more than one compressor, offering advantages in increasing temperature lift and enhancing compressor efficiency. Employing multiple compression stages in series (Figure 1.20(e)) helps to maintain compression ratios within optimal ranges and facilitates multi-temperature heat rejection. Additionally, vapor injection is integrated into multi-stage compression to reduce the discharge temperature of each compressor and decrease the consumption of the heat pump system. As the number of stages increases, the multi-stage compression system demonstrates higher energy and exergy efficiency [53]. However, due to its complexity, most studies have focused on theoretical investigations, with only a few experimental prototypes being developed [51].

Parallel systems present two main configurations: parallel compression within a single cycle and two parallel cycles. In the former, the heating capacity is doubled compared to a single-stage compression configuration. In the case of parallel cycles (Figure 1.20(f)), the primary goal is to achieve gradient heat

transfer in heat exchangers. In this setup, the vapour exiting from the evaporator enters the main compressor, which discharges thermal energy at intermediate pressure, while a second compressor is entered by vapour at an intermediate pressure and discharges thermal energy at high pressure. The compressor's efficiency is enhanced due to the low-pressure ratio, resulting in reduced costs.

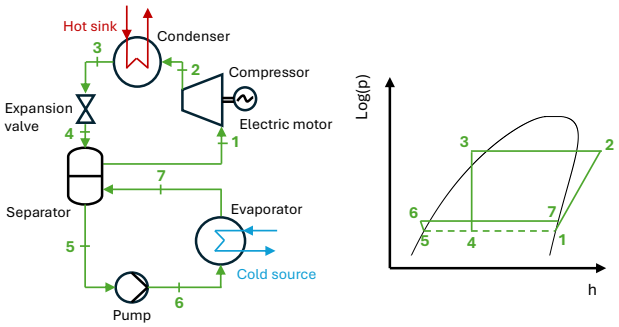

(a) – Single-stage with separator

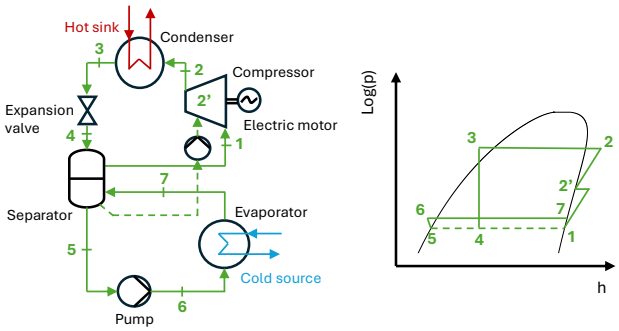

(b) – Single stage with liquid injection

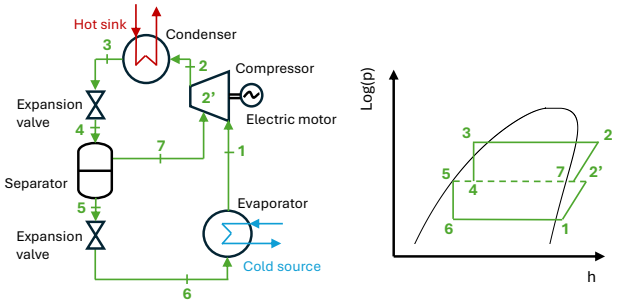

(c) – Single-stage with vapour injection

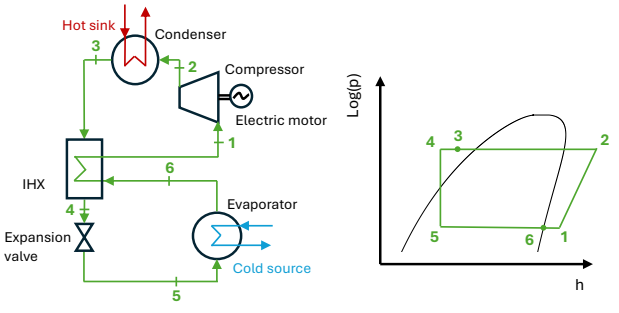

(d) – Single-stage with internal heat exchanger

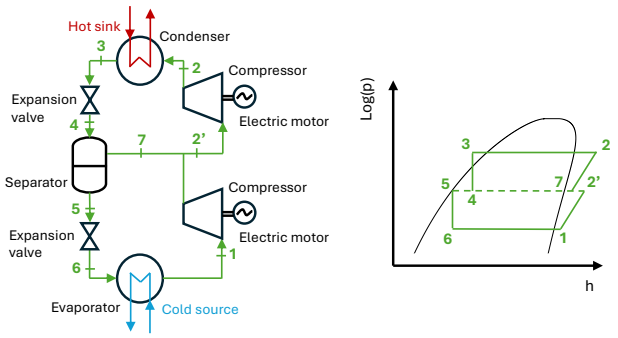

(e) – Double-stage with separator

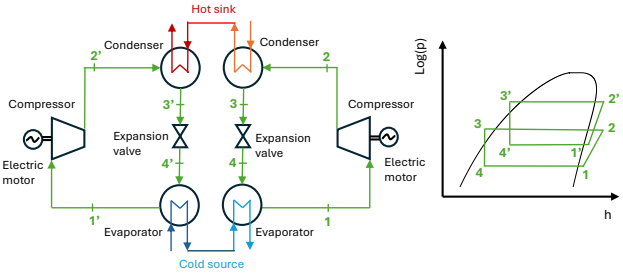

(f) – Double-stage parallel cycle

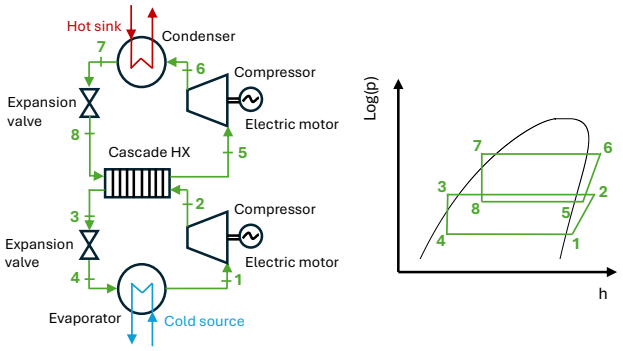

(g) – Cascade system

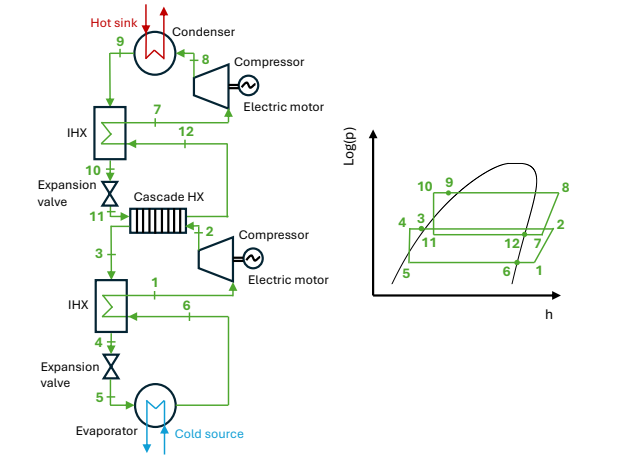

(h) – Cascade system with internal heat exchangers

Figure 1.20 - HTHP layout configurations.

A cascade system comprises two separate operating systems that are interconnected by a cascade heat exchanger, which serves as the evaporator for the upper cycle and the condenser for the lower cycle (Figure 1.20(g)) [54]. Cascade cycles can be equipped with IHX (Figure 1.20(h)) and can combine cycles that utilize different refrigerants for the upper and lower stages [55].

More complex configurations [46] can be obtained by combining the main characteristics of the layouts shown in Figure 1.20. Furthermore, to increase the discharging temperature without reducing the system performance, compression HTHP can be combined with other systems such as adsorption HP or/and solar collectors [51], resulting in hybrid systems.

Regarding the selection of HTHP working fluids, similar considerations to those made in subsection 1.2.1 for ORC systems apply, as i) the employed refrigerants are almost the same (see Table 1.1), and ii) the working fluid choice significantly influences performance, mechanical design, and cost. Key refrigerant properties affecting the COP include viscosity, thermal conductivity, specific heat capacities, heats of vaporization, density, critical temperatures and pressures, and volumetric heating capacity [46]. It is crucial to maintain refrigerant pressure above atmospheric levels at all system stages to prevent air and water vapor entering and ensure compressor lubricant compatibility. Refrigerant performance is strongly dependent on its proximity to critical temperature and pressure: condensing temperature should remain well below the refrigerant's critical temperature for optimal COP. Higher sink temperatures necessitate higher pressures, limited by practical factors such as maximum pressure ratio. Beyond thermodynamic performance, safety and environmental impact are critical factors, since non-toxic and non-flammable as well as zero-ODP and low-GWP refrigerants should be preferable [29].

1.3.2. Applications, market share, and current challenges

The implementation of HTHP into industrial processes can be very attractive either for cost efficiency or for the reduction of carbon emissions within industrial operations. However, the suitability of HTHP for integration into industrial processes varies widely, contingent upon factors such as temperature range, stability, capacity, and the differences in temperature levels between the source and sink sides. Furthermore, the feasibility hinges on the nature of the process (batch or continuous), annual operational hours, and the energy carrier type (fuel or electricity) used to heat the processes, which have a significant techno-economic impact. Furthermore, the economic viability for HTHP integration is strongly dependent on the accessibility to a proper heat source, such as waste heat released by one or more process' stages, recirculated streams within process, or low-cost heat derived from renewable sources (e.g., solar thermal, geothermal, sea water, ambient air) [56].

These integration challenges have limited the HTHP industrial implementations so far. Nonetheless, there is a growing trend of emerging new applications. As shown in Figure 1.21(a), HTHP technology finds its main application in the food sector with 39 % of the HTHPs installed. Indeed, the low-temperature processes within the food industry (Figure 1.18) offer suitable heat sources and sinks for integrating heat pumps. In second place, the district heating sector is responsible of 17 % of the HTHP installations. Additionally, there is recognized potential for HTHP integration in industries like metal processing and automotive manufacturing, which account for 8 % of the HTHP installed number each. Chemical processing also presents promising opportunities (6 % of the HTHP installations). Furthermore, wood and pharma sectors, followed by paper, waste water treatment, mechanical engineering, textiles and plastic industries hold application potential.

Considering the heating capacity (Figure 1.21 (b)), 90 % of the HP units presents heating capacity below 10 MW. More in detail, the 26 % of the installed HTHP can be found for heating capacities of less than 1 MW, 47 % between 1 and 5 MW, 17 % shows heating capacity between 5 and 10 MW, 7 % between 10 and 20 MW, and only 3 % of the HTHP units can provide more than 20 MW of thermal power.

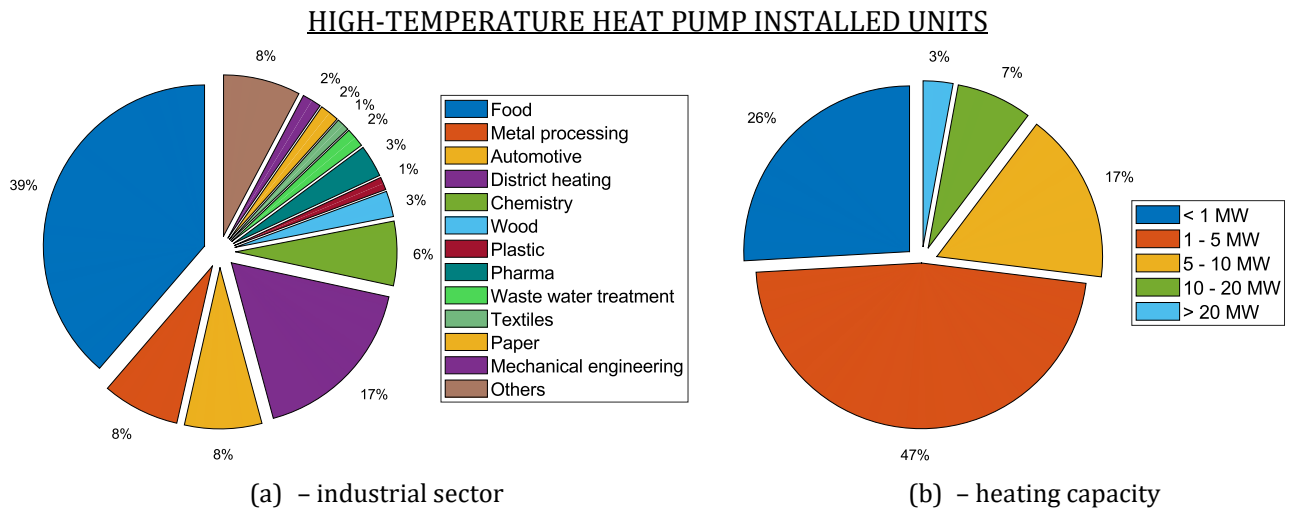

(a) – industrial sector (b) – heating capacity

Figure 1.21 - Industrial HTHP installed units by (a) industrial sector (data from [57]) and (b) heating capacity (data from [56]) distributions.

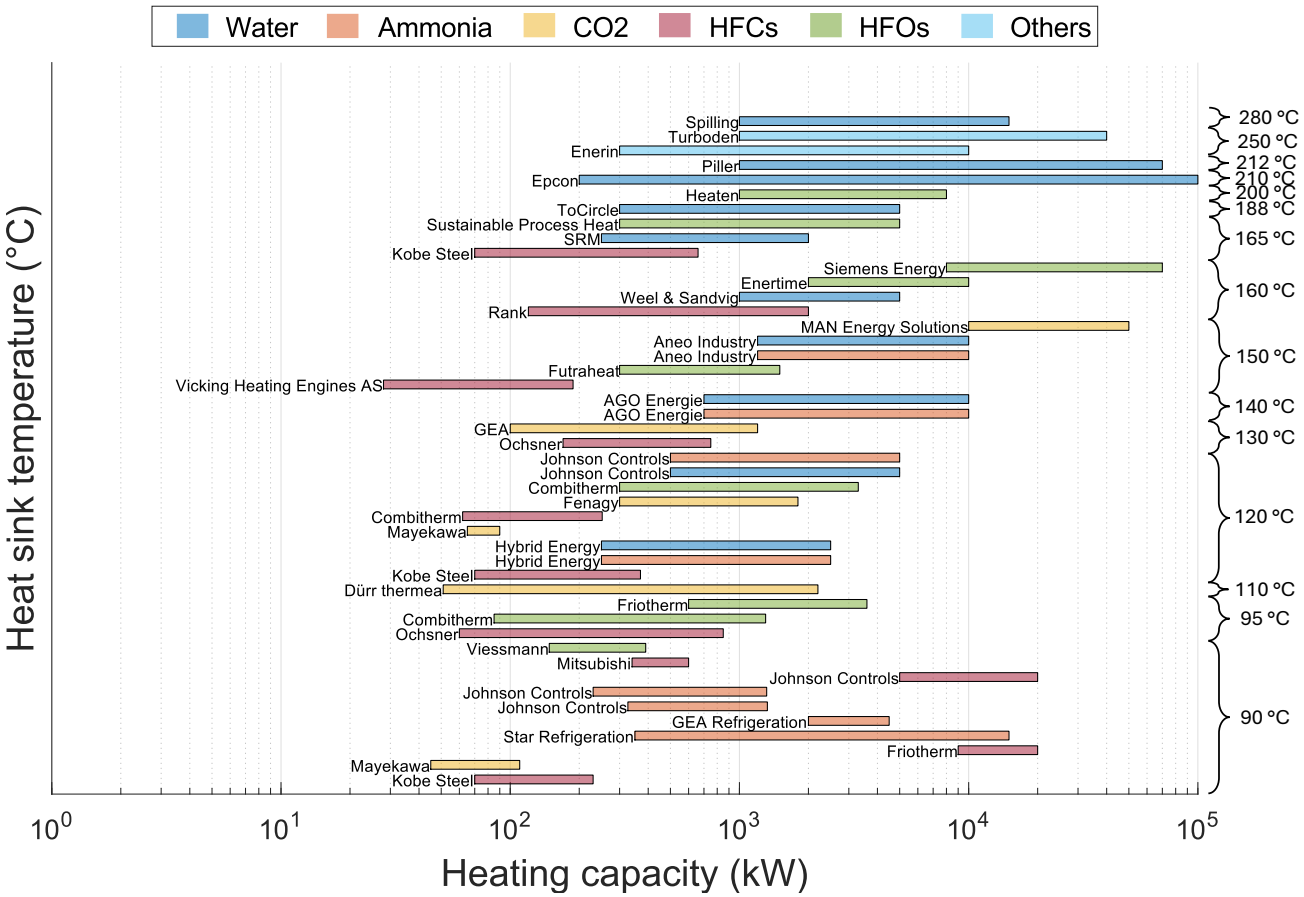

Figure 1.22 - Industrial HTHPs available on the market sorted by their maximum heat sink temperature, heating capacity, and working fluid family (data from [47] and [56]).

The number and the manufactures of HP models with high heat capacities and sink temperatures available on the market has steadily increased in recent years. Figure 1.22 displays the industrial HTHPs currently available on the market, categorized by their maximum heat sink temperature and heating capacity, and the working fluid family adopted by the manufacturer. The maximum sink temperature ranges between 90 and 280 °C, while the heating capacities span from approximately 30 kW to 100 MW.

Regarding the working fluids, ammonia and HFCs are preferred for heat sink temperatures below 90 °C. Between 90 and 165 °C, there is a good number of manufactures working with HFOs and CO_2, other than HFCs and ammonia, while for the highest heat sink temperature range, i.e., above 165 °C water is mostly adopted. The COP values of the industrial HTHPs represented in Figure 1.22 are shown in Figure 1.23(a) as a function of the respective temperature lift (i.e., temperature difference between the hot sink and the cold source) and categorized according to the configuration layout. The COP values range between 1.7 and 5.8 with a temperature lift of 100 to 25 K, respectively. The mean COP of this data set is about 3.3 at an average temperature lift of 62 K. Furthermore, the colormap shows that the second low efficiency of each point (i.e., how much the COP is close to the Carnot COP) ranges between 31 % and 76 %. Figure 1.23(b) shows the sink temperature and the temperature lift reached by the different configurations. As a result, the configuration with the internal heat exchanger allows to reach higher temperature levels at the sink. Figure 1.23 also includes the data collected in experimental research project on HTHPs ongoing worldwide. The maximum value reached by the COP is 7.2 with a temperature lift of 30 K.

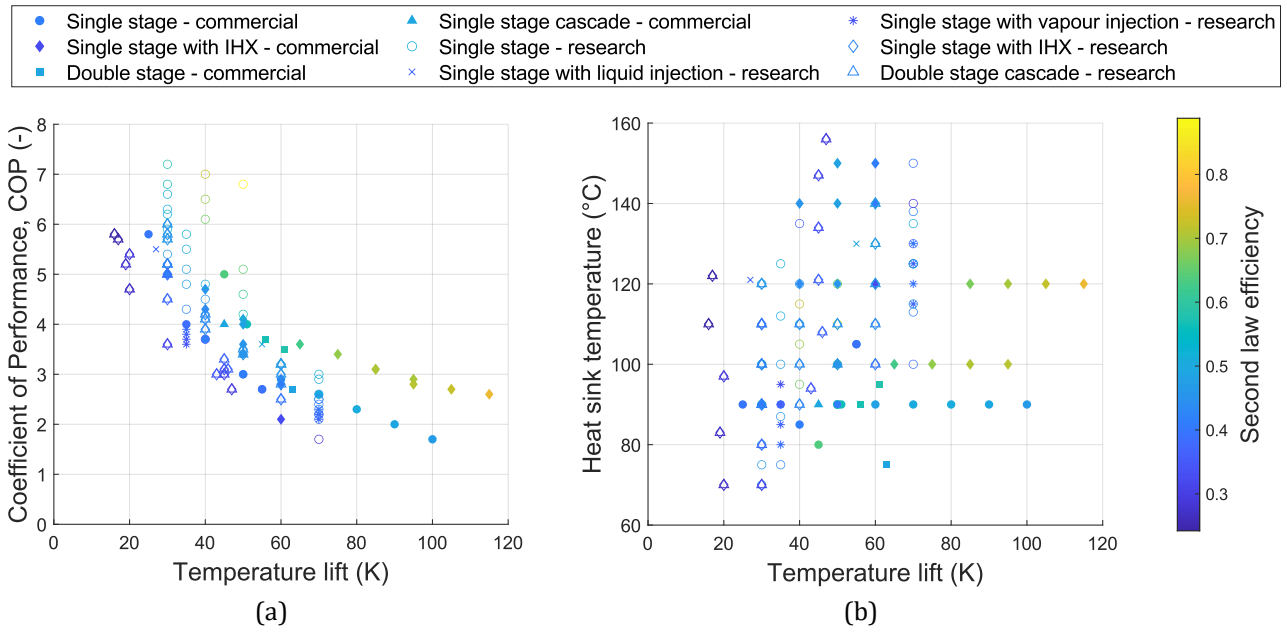

Figure 1.23 - Commercial and research project HTHP (a) COP and (b) heat sink temperature as functions of temperature lift and second low efficiency (data from [47] and [56]).

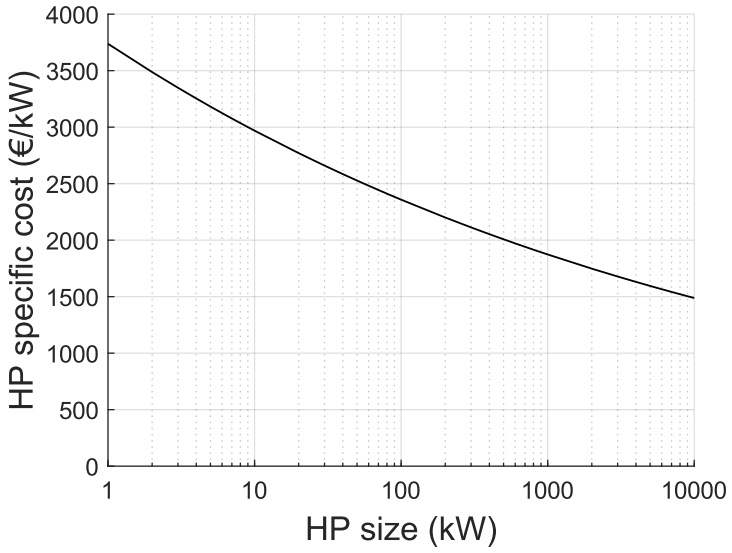

Figure 1.24 - HP specific cost of investment curve as a function of the size obtained interpolating data from [58].

Regarding the industrial HP technology investment costs, Becker [58] proposes a trend as a function of the size (electrical power required by the compression stage), shown in Figure 1.24. This trend is derived from a simple relationship used in industry to roughly estimate the investment cost of an industrial heat pump, also including the installation costs and the necessary equipment. However, the installation costs are strongly dependent on the given process and site, and the specific investment costs are expecting to decrease in the future when the technology readiness level will improve [56].

Despite the significant ecological potential of HTHPs, several barriers hinder their widespread industrial implementation. Key challenges include:

- Awareness and Knowledge: There is a low level of awareness among users, consultants, investors, plant designers, producers, and installers about the technical possibilities and economic feasibility of HTHP applications. Additionally, integrating HTHPs into industrial processes requires tailor-made designs, which can be cost-intensive.
- Economic Barriers: HTHPs often face long payback periods exceeding three years, which is longer than the payback period for gas or oil-fired boilers. Competing heating technologies using fossil fuels at low energy prices further complicate their adoption.
- Technical Limitations: The lack of available refrigerants that operate efficiently at high temperatures with low global warming potential is a significant barrier. Additionally, there is a shortage of pilot and demonstration systems to showcase the technology's potential.
- Regulatory and Policy Issues: Policy uncertainty and the lack of specific regulations for HTHPs hinder their adoption. Many countries have generalized policies for all heating systems, which may not effectively support HTHPs.
- Public Acceptance: Public acceptance is also a challenge, as there are concerns about noise pollution, land subsidence, and water pollution associated with HTHP installations. There is also a general lack of awareness about the financial and environmental benefits of HTHPs.

HTHP technology faces several technical challenges, including:

- Temperature Lift and Efficiency: HTHPs with a low temperature lift are well-developed, but they have not been extensively tested for high sink temperatures. There is a research gap for HTHPs with output temperatures higher than 100°C and a COP greater than 4.
- Component Development: Improving the customization of large-capacity HTHP components, especially compressors, is crucial. Enhancing cooling technology for compressors, motors, and other components is also necessary to ensure safe operation at high temperatures.

To overcome these barriers and enhance the adoption of HTHPs, several initiatives and research directions are being pursued:

- International Energy Agency Programs: The International Energy Agency has conducted several programs to overcome barriers to the large-scale market introduction of industrial heat pumps.
- Research and Development: Continued research is pushing the limits of HTHPs, focusing on increasing the temperature lift and improving system efficiency. Development of new green refrigerants with better characteristics and adaptability for drop-in replacements is a long-term prospect.
- Policy and Financial Support: Government initiatives aim to raise public awareness and provide financial support for HTHP integration. Ensuring adequate financing for HTHP research and development is essential for overcoming economic barriers.
- Technological Innovations: The development of HTHPs with low-GWP refrigerants, higher supply temperatures, improved COP, and large-scale units with heating capacities larger than 1 MW are crucial for future advancements.

The integration of HTHPs in industrial processes has the potential to significantly reduce greenhouse gas emissions and contribute to sustainable energy-efficient heating and cooling. However, addressing the technical, economic, regulatory, and public acceptance challenges is crucial for their widespread adoption. Continued research, policy support, and technological innovations will be key to unlock the full potential of HTHPs in industrial applications.

1.4. Carnot Battery as electric energy storage technology

To achieve carbon neutrality in less than 30 years, a comprehensive transformation of energy systems across key carbon-emitting sectors (i.e., industrial, residential, and transportation) is essential. This transformation hinges on a deep penetration of RES, aiming to nearly eliminate reliance on fossil fuels and achieve net-zero emissions by 2050 [59]. However, the inherent instability and fluctuations of RES pose significant challenges, necessitating advanced solutions to bridge the gap between RES production and energy demand: to this purpose, energy storage technologies gain primary importance.

Among the grid-scale Electric Energy Storage (EES) technologies, none is prevailing because the selection depends on multiple factors specific to each application, and research for effective solutions is ongoing. In this context, the Carnot battery (CB) concept is particularly appealing since it offers advantages such as long cycle life, no geographical constraints, no reliance on fossil fuel streams, and the easy integration with conventional fossil-fuelled power plants or other waste heat sources [60].

The working principle of CBs involves storing electrical energy as thermal energy. During the charging phase, surplus renewable electricity is converted into thermal energy, which is stored in a thermal energy storage (TES) for later use during the discharging phase. Charging occurs when there is excess renewable electricity, while discharging takes place when electricity is needed. As an EES system, a CB primarily stores electrical energy, requiring both an electric input and an electric output of similar magnitude (Figure 1.25).

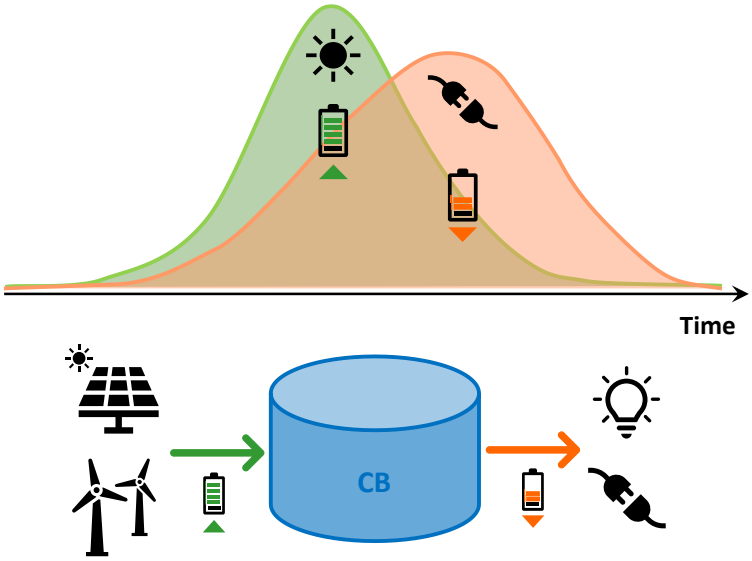

Figure 1.25 - General concept of a Carnot battery.

CBs can be classified into three types [60]: i) Liquified Air Energy Storage (LAES), ii) Pumped Thermal Energy Storage (PTES), and iii) the Lamm-Honigmann process. In LAES technology, electricity is used to liquefy air through compression, cooling, and expansion until it becomes liquid and it is then stored at atmospheric pressure [61]. In PTES (Figure 1.26), electricity is used during the charging phase to let heat flow against a thermal gradient (through an inverse thermodynamic cycle), from a low-temperature (LT) source to a high-temperature (HT) sink. The thermal energy is stored in a HT reservoir until electricity is not demanded. In the discharging phase, the stored thermal energy flows to the LT sink, driving a heat engine that produces mechanical work (direct thermodynamic cycle), which is then converted into electricity [60]. The Lamm-Honigmann process is a flexible thermo-chemical energy storage and conversion system that can be charged and discharged with both heat and electric power. It operates by exploiting the pressure difference between a pure working fluid in thermodynamic equilibrium and a corresponding sorbate with lower equilibrium pressure [62].

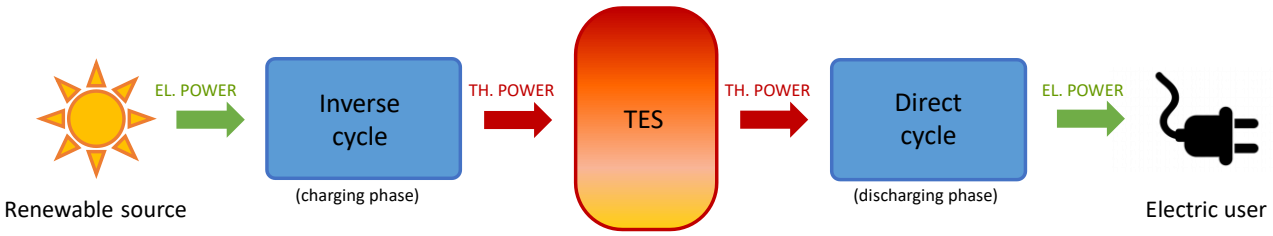

Figure 1.26 - General concept of a Pumped Thermal Energy Storage system.

In this thesis, the PTES technology is mainly discussed and investigated as CB energy storage technology.

1.4.1. Thermally Integrated Pumped Thermal Energy Storage systems

Since the charging phase requires electric input to create a thermal gradient, the availability of recoverable low-grade waste heat can reduce the temperature lift (i.e., the temperature difference between the HT thermal energy reservoir and the LT thermal energy reservoir). Therefore, recoverable waste heat decreases the electric energy required in the inverse cycle to achieve relatively high-temperature thermal energy. This diversification of temperature lift (compare Figure 1.27(a) with Figure 1.27(b)) between the inverse cycle (charging phase) and the direct cycle (discharging phase) improves

conversion efficiencies [63] and overall storage efficiency, also known as roundtrip efficiency [64], which may also overcome 100 %. PTES systems integrated with low-temperature thermal energy sources, such as solar energy, district heating, and waste heat recovery, are called Thermally Integrated PTES (TI-PTES). Ökten and Kurşun [65] conducted a thermodynamic analysis on a TI-PTES combined with an absorption refrigeration cycle, achieving a roundtrip efficiency of 142 %. Frate et al. [66] developed a numerical model of a TI-PTES using Coolprop thermodynamic properties and simulated a roundtrip efficiency of 130 % with the refrigerant R1233zd(E). Su et al. [67] created mathematical models to compare the performance of four CB configurations integrated with geothermal energy, finding that all configurations can achieve a heat-to-power efficiency above 100 %, with the flash HP-ORC configuration being the most efficient, boasting a COP of 6.13 and a heat-to-power efficiency of 137.13 %. Zhang et al. [68] assessed the thermodynamic performance of a Rankine cycle-based CB thermally assisted by steam from a coal-fired power plant, noting that integrating the CB with the thermal power plant increases roundtrip efficiency up to 114.67 %, with a power generation efficiency decrease of less than 3 percentage points and a 1.26 % reduction in carbon emissions.

Another method of thermal integration involves using waste heat as the high-temperature source for the discharging phase, with the low-temperature reservoir storing thermal energy at temperatures below ambient conditions [60] (see Figure 1.27(c)). Xia et al. [69] compared three configurations of cold storage Rankine CBs, finding that including a recuperator in the vapor compression refrigeration unit and a preheater in the ORC unit improves the CB energy, exergy, and economic performance. Bellos [70] proposed an innovative approach using waste heat by first feeding the latent storage with waste heat and then enhancing the charging phase performance by supplying the HP evaporator. Bellos' system performance improvement ranges from 12.37 % to 173.58 %, depending on the waste heat temperature.

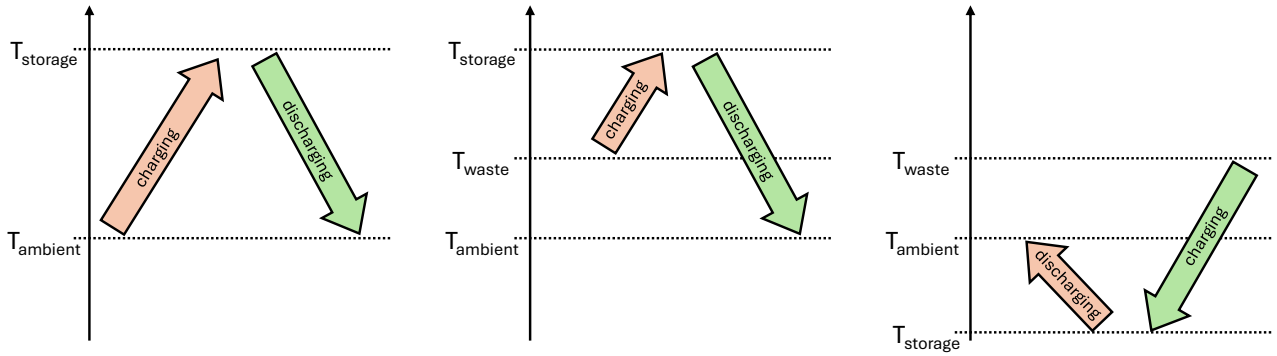

Figure 1.27 - Operating temperature levels of (a) basic Carnot battery, (b) Thermally integrated Carnot battery with high-temperature storage, and (c) Thermally integrated Carnot battery with low-temperature storage.

As both thermal and electric energy flows are involved, CBs can easily be expanded from purely electric energy storage to a combined heat and electricity storage and management system, enabling flexible sector coupling. Indeed, the thermal energy stored may not be entirely reconverted into electricity. Instead, a portion of it can be used to meet thermal demands, thereby introducing greater flexibility in thermal production and consumption [71]. In this regard, Figure 1.28 shows a general example of an integrated system in which the user (e.g., an industrial process) requires electric and thermal energy, generating low-grade waste heat that can be recovered by the CB to enhance the overall system efficiency.

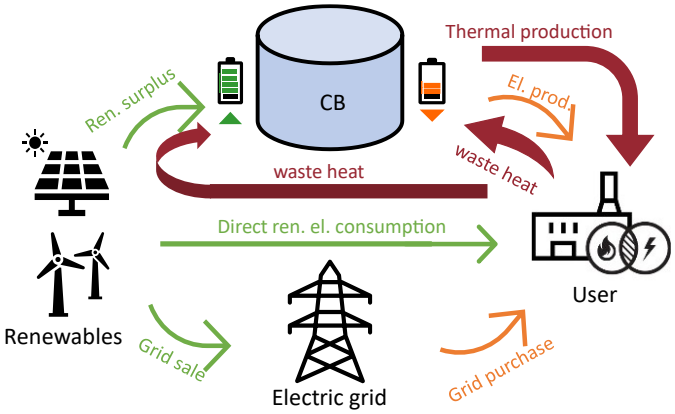

Figure 1.28 - General example of thermal and electric integration of a Carnot battery in a complex energy system.

1.4.2. Pumped Thermal Energy Storage configurations

PTES systems can utilize either the direct/inverse Rankine cycle or the direct/inverse Brayton cycle. Although the roundtrip efficiencies of Rankine and Brayton CBs are similar, their characteristics differ significantly.

In Rankine PTES, the charging phase is carried out by a vapor compression HP, while the discharging phase uses a direct Rankine cycle (Figure 1.29(a)). During the charging phase, the HP compressor increases the working fluid pressure and temperature, allowing to store thermal energy by recovering the heat released during condensation. The stored thermal energy powers the Rankine cycle during the discharging phase, converting it into mechanical energy via a turbine or volumetric expander, and subsequently into electricity through an electric generator [72].

Rankine PTES typically stores energy at lower temperatures than Brayton PTES, with remarkable benefits such as reduced thermal losses and the use of less expensive materials for the components and storage. Various working fluids are used in these systems, including water vapor [73], organic fluids [64], transcritical CO_2 [74], and subcritical NH_3 [75]. Due to the similarities between the HP and the direct Rankine cycle in terms of working fluid and main components, some studies explore Rankine PTES using the same equipment (compressor/expander) and heat exchangers for both charging and discharging phases, significantly reducing investment costs [60]. This setup is known as a reversible heat pump/Rankine cycle system [74]. Yu et al. [76] conducted a thermo-economic comparison of three Rankine-based CB systems: a base configuration, a reversible configuration with separate machines for charging and discharging, and a reversible configuration using a dual-function machine. They found that the third configuration, despite having lower power-to-power and exergy efficiencies, has the lowest levelized cost of storage, 12.3 % and 5.4 % lower than the first and second configurations, respectively.

In Brayton PTES, the working fluid is a gas that operates in a closed-inverse Brayton cycle during charging phases and a closed-direct Brayton cycle during discharging phases (Figure 1.29(b)). During the charging phase, the working fluid is compressed to high pressure and temperature using electrical input, releasing sensible heat to a HT heat reservoir. During the discharging phase, the stored heat is converted back into electricity as the working fluid is heated and then expanded, producing mechanical work that is converted into electric energy through a generator.

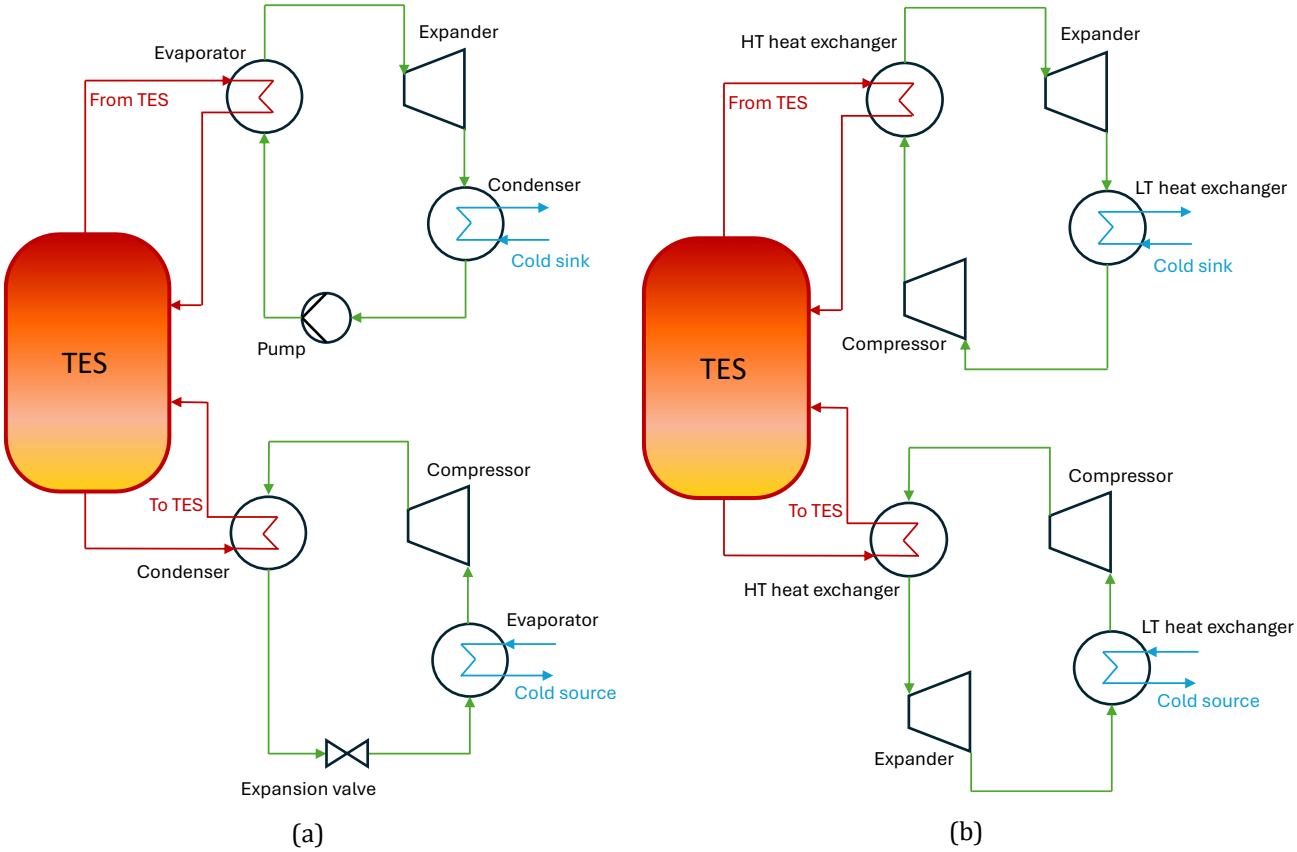

Figure 1.29 – PTES layout: (a) Rankine configuration and (b) Brayton configuration.

Compared to Rankine PTES, the efficiency of Brayton systems is less influenced by the pressure ratio and more affected by the polytropic efficiencies of the machines and the temperature ratio [77]. Promising working fluids for Brayton PTES include monoatomic gases like argon [78] and helium, with helium showing higher round-trip efficiency (56.9 %) compared to argon (39.3 %) [79]. McTigue et al. [80] found that supercritical CO_2 provides higher work ratios and power densities compared to ideal gases. Furthermore, incorporating an electric heater can improve power output and efficiency when using air as the working fluid [81]. Typically, Brayton PTES involves four machines (two compressors and two expanders), each dedicated to the charging or discharging phase, though research has explored the use of reversible compressors and turbines [82]. Alternatively, the same heat exchangers can be used for both phases, even with separate machines for charging and discharging [83].

1.4.3. Grid-scale storage technologies state of the art

The main EES technologies include electrochemical batteries (Li-Ion and flow batteries) [84], supercapacitors [85], flywheels [86], and hydrogen storage technologies combined with fuel cell (FC) systems [87]. Other notable EES technologies are Pumped Hydro Energy Storage (PHES) [88], Gravity Energy Storage (GES) [89], and Compressed Air Energy Storage (CAES) [90]. An advanced version of CAES, called Adiabatic Compressed Air Energy Storage (ACAES) [91], uses separate mechanical and thermal energy storages to increase efficiency up to 70 %, as reviewed by Vecchi et al [61].

Currently, the most widely adopted grid-scale EES technology that has proven to be techno-economically viable is PHES [60], which operates by pumping a fluid to an elevated reservoir during periods of low electricity demand. When discharging, the fluid releases its potential energy through a turbine to generate electricity. CAES has also demonstrated large-scale feasibility, where air is compressed into a hermetic tank or underground reservoir during charging and expanded during discharge. However,

both PHES and CAES require specific geological conditions, limiting their availability. Additionally, their energy density is relatively low (as shown in Table 1.2).

Flow batteries could potentially store large amounts of energy, but they have a relatively short lifespan and rely on rare or expensive materials. Technologies such as LAES and GES are not yet mature and suffer from high energy costs and low energy density. FCs, despite their high energy density, have a limited lifespan and cycle count.

Most grid-scale non-PHES solutions, like lithium batteries, have a high cost-per-capacity unit, making them unaffordable for low power-to-capacity ratio applications. Additionally, according to Gimeno-Gutiérrez and Lacal-Arántegui [92], the easily exploitable additional capacity of PHES is nearly exhausted, necessitating the search for viable alternatives. CAES and ACAES technologies are gaining attention due to the inexpensive storage medium (usually air), but they require pre-existing reservoirs and caves, which are not everywhere available.

Table 1.2 - Performance comparison of different EES technologies (data collected from [89] and [93]).

Technology	Energy density (kWh/m^3)	Power density (kW/m^3)	Power range (MW)	Roundtrip efficiency (%)	Storage time scale	Lifetime (years)	Geographical constraints
PHES	0.13-1.5	0.01-1.5	10-5000	65-87	1-24 h	30-60	Yes
GES	2-5	3	1-20	70-86	1-24 h	25-50	Yes
CAES	3-12	0.5-2	5-1000	50-89	1-168 h	20-40	Yes
LAES	50-80	0.5-2	1.1-200	40-70	1-24 h	20-40	No
PTES	10-200	1-15	8-200	48-75	1-24 h	25-30	No
TI-PTES	10-200	24	8-200	70-200	1-24 h	25-30	No
Li-Ion B.	100-500	500-2000	0-100	85-97	1 h	5-15	No
Flow B.	16-30	<2	0.2-50	65-85	1-24 h	5-15	No
FC	500-3000	>500	0.02-1000	10-50	10 s – 1 w	5-30	No
Flywheel	20-80	1000-2000	0.08-20	85-95	0-3000 s	15	No

In this context, CBs, which are not limited by geographical conditions (Table 1.2), present an interesting alternative to PHES and CAES. Although CBs might have lower conversion efficiencies, they offer benefits such as low specific cost, long lifespan, use of materials with a low environmental footprint, and the ability to integrate with any type of waste heat source, making them valuable grid-scale alternatives.

1.4.4. Applications, market share, and current challenges

Although the European Commission targets 96-99 % decarbonization by 2050, varying RES penetration levels and grid limitations have led some countries to the curtailment of non-dispatchable RES electricity, highlighting the need for effective EES solutions [94]. The Carnot battery system is a promising technology that avoids PHES' and CAES' geographical constraints. Financial analyses, such as those by Smallbone et al. [95] and Benato [81], indicate that CBs can be cost-competitive, particularly with no charging costs, despite lower round-trip efficiency compared to PHS and CAES. Furthermore, PTES can achieve higher efficiencies than LAES systems but have higher capital and levelized costs [96]. When both capital and operational costs are considered, CBs could outperform more expensive systems like molten salt and flow batteries in energy arbitrage scenarios [97].

Heat pumps and heat engines have been around for decades, but PTES technology is still in its early stages. Consequently, much of the work in this field is theoretical, focusing on establishing the technology. One of the earliest breakthroughs was by Howes [98], who demonstrated a small-scale 150 kW device

scalable to a 2 MW, 16 MWh capacity demonstrator plant based on pumped heat energy storage. Recently, with increased efforts to achieve carbon-zero targets, a few experimental studies and pilot-scale projects have been initiated. Table 1.3 presents a comprehensive list of academic and commercial projects pilot-plants.

Table 1.3 - List of academic and commercial projects pilot-plants (integration of data from [99]).

Company/ Institution	**Carnot battery type**	**Size**	**Storage capacity/ Duration**	**Storage material**	**Working fluid**	**Roundtrip efficiency**	**Reference**
Siemens Gamesa, ETES	Resistance heater – steam RC	1 – 100 MW	24 h	Volcanic rock bed~600 C	Water	25 – 40 %	[100]
RWE, Store2Power	Resistance heater – steam RC	100 MW	hours	Molten salt	Water	40 %	[101]
E2S Power	Resistance heater – steam RC	1 – 100 MW	hours	Graphite/ aluminium alloy at 700 C	Water	25 – 40 %	[102]
Spilling	Steam HP/RC	1 MW	hours	Saturated water	Water	N/A	[103]
University of Erlangen-Nürnberg	Reversible HP-ORC	9 – 15 kW	270 kWh	Hot water at 120 °C	R1233zd(E)	17 %	[104]
National Technical University of Athens	Reversible HP-ORC	1.5 kW	N/A	No storage – thermal production at 110 °C	R1234ze(E)	N/A	[105]
Technical University of Munich	Reversible HP-ORC	20 kW	N/A	No storage – thermal production at 140 °C	R1233zd(E)	N/A	[106]
University of Liège	Reversible HP-ORC	1.5 kW	10 kWh	Hot water at 90 °C	R1233zd(E)	72 %	[107]
CHESTER consortium	Separate HP and ORC	10 kW	60 kWh	PCM at 133 °C	R1233zd(E) / R1336mzz(E)	N/A	[108]
FutureBay	Separate HP and ORC	10 kW	hours	Hot water	N/A	80 %	[109]
Climeon	HP-ORC	80 kW	hours	Water	N/A	25-60 %	[110]
TC Mach	HP-ORC	N/A	hours	Stone dust at 120 °C	R1233zd(E)	N/A	[111]
MAN/ABB, ETES	Reversible HP-ORC	50 MW	5 h	Hot water	CO_2	45 %	[112]
Echogen, ETES	Reversible HP-ORC	25 MW	8 h – 250 MWh	Hot sand	CO_2	60 %	[113]
Energydome, CO_2 battery	HP-ORC	10 MW	20 MWh	Liquid CO_2	CO_2	77 %	[114]
Highview	HP-ORC	50 – 350MW	6 h	Liquid air	Air	60 – 70 %	[115]
GE, AMSESS	CO_2 Brayton – Steam cycle	10 – 100 MW	8 h	Molten salt/ water	CO_2 - Water	42 – 62 %	[116]

247Solar, Heat2Power Turbine	Resistance heater – Gas turbine	0.2 – 100 MW	6 – 20 h	Silica sand	Air	30 %	[117]
1414Degrees TESS	Resistance heater – Gas turbine	10 MW	N/A	Silicon alloy, 1414 °C	Air	N/A	[118]
Peregrine Turbine Technologies	Resistance heater – Brayton cycle	1 MW	8 MWh	Graphite – aluminium alloy, 800 °C	CO_2	45 %	[119]
Shanghai Jiao Tong University	Reversible Brayton cycle	20 kW	12.5 kWh	PCM at 331 °C	N/A	37 %	[120]
Isoentropic	Reversible Brayton cycle	150 kW	16 MWh	Crushed rock packed bed	N/A	72 %	[98]
Stiesdal, GridScale	Reversible Brayton cycle	2 MW	100000 MWh	Crushed basalt rock packed bed	N/A	35 – 60 %	[121]
WindTP	Reversible Brayton cycle	3 – 20 MW	100 h	Gravel bed	N/A	85 %	[122]
Enolcon, OPTES	Reversible Brayton cycle	8 MW	80 MWh	Silica sand	N_2, Ar	58 – 66 %	[123]
Malta, Pumped Heat Energy Storage	Recuperated reversible Brayton cycle	10 – 100 MW	0.08 – 1 GWh	Molten salt	N_2, Ar	N/A	[124]

Regarding economic estimations on CBs (Figure 1.30), the cost variability for PTES is significantly higher compared to LAES due to different assumptions about the equipment involved. For Brayton PTES, costs range from 1830 $/kW to 6160 $/kW (Figure 1.30(a)), and from 57 $/kWh to 1570 $/kWh when considering the thermal capacity (Figure 1.30(b)). The high variability in the price is mostly related to the machines: costs increase significantly when using four independent turbomachinery systems instead of two reversible machines [59]. For Rankine-based PTES, power and energy costs range in between 550-9000 $/kW (Figure 1.30(a)) and 157-670 $/kWh (Figure 1.30(b)), respectively [59]. For LAES, costs vary less (it is around 2000 $/kW and 160-670 $/kWh) due to smaller design variations. Power equipment contributes significantly to cost, but heat exchangers also make up a large portion due to high operating pressures [125]. The low cost per unit of stored energy explains the large variations in plant capacities. Rankine PTES shows the lowest Levelized Cost of Storage (LCOS) at around 230 $/MWh, while LAES and Brayton PTES are comparable at 330 and 369 $/MWh, respectively [59]. LCOS values for CB systems are competitive with other storage technologies, with specific durations favouring CB over batteries [126]. Integration of industrial waste heat can further reduce costs.

According to the market perspective provided by Nitsch et al. [127], if significant reductions in either the specific capital expenditure for power or storage costs are achieved, both Brayton and Rankine systems could potentially become competitive options in terms of cost. For lower round-trip efficiency systems, ranging around 55 %, the suitable cost range for their introduction varies from 400 €/kW at 20 €/kWh to 90 €/kW at 55 €/kWh. However, for higher round-trip efficiency solutions (< 75 %), there is more flexibility for accepting higher investment costs, ranging from 400 €/kW at 35 €/kWh to 150 €/kW at 70 €/kWh.

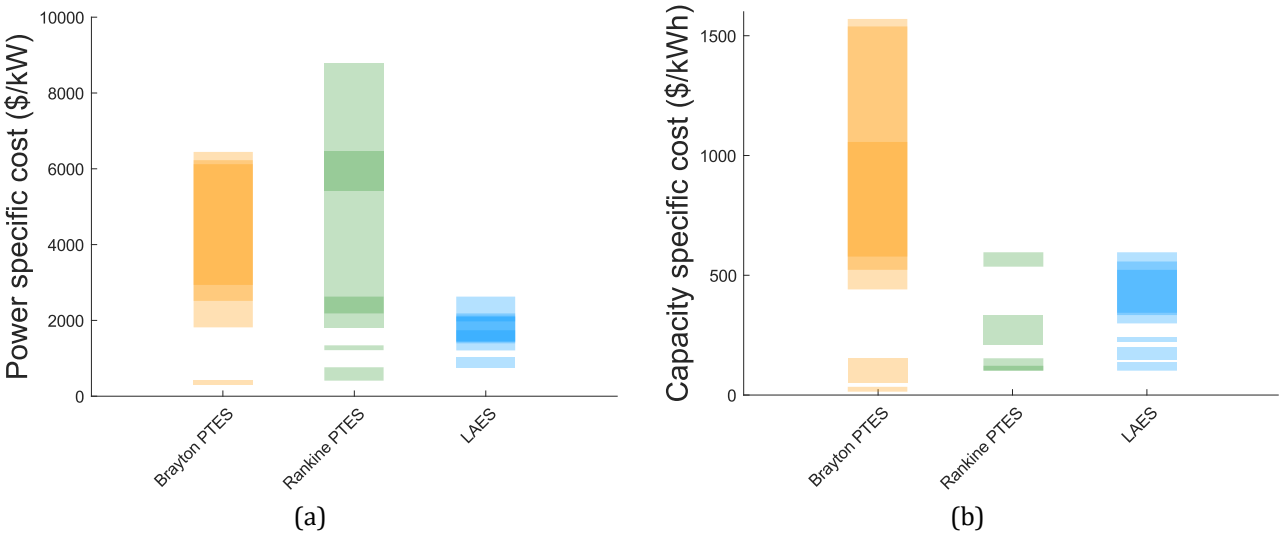

Figure 1.30 – Carnot Batteries specific investment cost according to the system (a) power and (b) capacity (literature data collected by [59]).

Despite current financial and technical challenges, EES implementation is expected to grow rapidly, with technologies like CBs offering cost-effectiveness, long lifespan, and independence from geographical constraints. Indeed, CBs offer unique opportunities for integration with energy systems, thanks to their ability to store hot and cold thermal energy. This integration provides both financial benefits and technical advantages through the provision of power and thermal services.

In terms of power services, CBs can function independently or in conjunction with existing power plants such as coal, natural gas, solar, or nuclear facilities. However, their economic viability depends on factors like local electricity prices, regulations, and tariffs. While CB can compete with traditional batteries in offering services like ancillary support, arbitrage, and peak shaving, challenges such as high operational costs and the need for subsidies in certain markets remain.

CB's integration with thermal streams presents opportunities to improve overall performance by utilizing waste heat. This is particularly relevant in contexts where the electrification of process heat is limited by technology. Waste heat recovery can significantly enhance efficiency and reduce costs. Furthermore, CBs can be employed to retrofit existing power plants, replacing firing chambers with thermal energy storage systems. This supports efforts towards decarbonization and offers cost-effective solutions by reusing existing equipment. Examples include initiatives like Chile's coal phase-out plan and potential retrofits in countries like Germany and the United States. However, the success of such endeavours hinges on the development of regulatory frameworks and private agreements [59].

Despite economic and technical challenges, CB technology holds promise for enhancing energy system flexibility and efficiency. Ongoing research and commercial projects underscore the growing interest and viability of CBs in future energy landscapes.

1.5. Conclusions

The exploration of Power-to-Heat (P2H) and Heat-to-Power (H2P) energy systems presents a compelling opportunity to enhance energy efficiency and sustainability. The primary focus has been on leveraging low-temperature energy sources, both from industrial waste heat and renewable sources. Industrial processes generate substantial amounts of low-grade heat, often released into the environment without any beneficial use. The recovery and utilization of this waste heat through technologies such as the ORC and HTHP offer significant potential for improving energy efficiency and reducing greenhouse gas

emissions.

The ORC technology, in particular, is well-suited for converting low-grade heat into electricity. Its simplicity and adaptability make it a viable solution for various low-temperature heat sources, including industrial waste heat and low-enthalpy renewable sources like geothermal and solar thermal energy. The use of appropriate working fluids and the implementation of advanced cycles, such as the partial-evaporation cycle, can further enhance the efficiency and applicability of ORC systems.

On the other hand, HTHPs provide an effective means of upgrading low-grade waste heat to higher temperatures, making it usable for industrial processes and district heating systems. The development of advanced configurations and the selection of suitable working fluids are critical for optimizing the performance of HTHPs. Despite their potential, the market penetration of HTHPs is still limited, primarily due to high initial costs and technological challenges.

CBs, integrating both P2H and H2P technologies, represent a promising approach for energy storage. These systems store excess electrical energy as thermal energy, which can be converted back to electricity when needed. This dual operability is particularly advantageous for managing the intermittency of RES, enhancing grid stability, and providing a sustainable energy storage solution.

In summary, the penetration into the energetic scenario of P2H and H2P systems, supported by technologies like ORC, HTHP, and CB, can significantly contribute to a sustainable energy future. By maximizing the use of low-grade heat sources and improving energy storage capabilities, these technologies help in reducing reliance on fossil fuels, lowering greenhouse gas emissions, and promoting more efficient and resilient energy systems.

2. Thesis overview

Summary. In this final introduction chapter, the structure of the document is presented, highlighting the original contribution of this thesis with respect to current literature and the main challenges of the topic.

2.1. Current challenges overview

In this final chapter of introduction, open challenges concerning P2H and H2P energy systems are summarized to present the innovative contribution made by this thesis. P2H and H2P systems are crucial for enhancing energy efficiency and integrating RES into the global energy mix. Despite their potential, several challenges hinder P2H and H2P widespread adoption and implementation.

- Technological Challenges and Innovations. The effective recovery and utilization of low-grade industrial waste heat is at the heart of P2H and H2P systems. One significant technological challenge is the variability in the temperature and quality of waste heat sources. Each industrial process generates waste heat with distinct characteristics, necessitating customized solutions. Technologies such as ORC and HTHP have shown promise in converting low-grade heat into useful energy forms. The ORCs, for instance, can convert low-temperature heat into electricity using a suitable working fluid in a closed thermodynamic cycle. However, the efficiency of ORC systems hinges on the selection of optimal working fluids and the implementation of advanced cycle designs like the partial-evaporation cycle. Similarly, HTHPs are pivotal in upgrading low-temperature waste heat to higher temperatures, making it usable for industrial processes and district heating systems. The development of HTHPs faces challenges related to material durability, efficiency at high temperatures, and integration with existing thermal systems. Overcoming these challenges requires advancements in HP technology, including the use of novel working fluids and improved heat exchanger designs. CBs, which integrate P2H and H2P technologies for energy storage, represent a novel approach. These systems store surplus electric energy as thermal energy and convert it back to electricity when required. The dual functionality of CBs is particularly advantageous for managing the intermittency of RES. However, achieving high efficiency and cost-effectiveness in CBs necessitates breakthroughs in thermodynamic cycle design, material science, and system integration.
- Economic and Market Considerations. The economic feasibility of P2H and H2P systems is another critical aspect explored in this thesis. High initial capital costs and long payback periods often deter investment in these technologies. For instance, while HTHPs offer significant energy savings, their market penetration remains limited due to the high costs associated with advanced materials and components needed for high-temperature operations. Economic analysis within this thesis will focus on cost-benefit assessments, potential incentives, and policy frameworks that can enhance the attractiveness of these technologies to investors and stakeholders. The market dynamics of P2H and H2P systems are influenced by various factors, including energy prices, regulatory policies, and the availability of financial incentives. This thesis examines these market conditions and proposes strategies to improve the adoption rates of these systems.
- Infrastructural and Integration Challenges. Integrating P2H and H2P systems into existing industrial and energy infrastructures poses significant challenges. The retrofit of existing facilities to incorporate these systems often requires substantial modifications and investment. For example, integrating ORC systems with industrial processes demands careful planning and adaptation to ensure smooth operation and minimal disruption. Similarly, the deployment of HTHPs in district

heating networks involves challenges related to network compatibility, thermal storage, and operational efficiency. CBs, despite their potential, face integration challenges related to their operational dynamics and interaction with the electrical grid. The efficiency of these batteries depends on their ability to operate flexibly and respond to grid demands. This thesis explores the integration of CBs with RES and grid infrastructure, examining the potential for these systems to provide grid services such as frequency regulation and load balancing.

- Environmental and Sustainability Considerations. The environmental impact of P2H and H2P systems is a critical aspect of this research. These systems have the potential to significantly reduce greenhouse gas emissions by improving energy efficiency and enabling greater use of RES. The thesis evaluates the environmental benefits of deploying these technologies, considering factors such as emission reductions, energy savings, and the potential for contributing to a low-carbon economy.

Continued research and development are essential for advancing the efficiency, cost-effectiveness, and integration capabilities of P2H and H2P systems. Key areas of focus include the development of advanced materials, optimization of thermodynamic cycles, and the integration of digital technologies for improved system control and monitoring. By addressing some of the current challenges and leveraging the opportunities presented by P2H and H2P systems, this thesis aims to contribute to foster innovation and support the deployment of these technologies in the broader goal of achieving a sustainable and resilient energy future.

2.2. Aims and structure

This thesis addresses the aforementioned issues, including the experimental collection of real data, the development of reliable models based on the experimental data, and their integration into complex energy systems. Technological analysis, environmental considerations, and economical investigations are performed.

The document is split into two parts, i.e. “PART I - ORC and HTHP for stand-alone electric and thermal energy generation” and “PART 2 - Carnot battery technology integration for energy storage applications”.

PART I - ORC and HTHP for stand-alone electric and thermal energy generation

The aim of part I of this thesis is to explore the application of ORC and HTHP technologies to different low-grade heat sources both renewables and industrial waste heat. In this sense, the ORC performance is investigated: i) when applied to solar thermal heat source and intended for residential applications; ii) when integrated with data center cooling system for waste heat recovery. HTHP technology is explored when applied to energy-intensive industrial processes, i.e., the ceramic tiles industry, to upgrade the waste heat released by some process stages exploiting renewable electricity and reuse the recover thermal energy to feed the industrial process. The modelling activities on ORC applications were supported by experimental data collected on the micro-ORC prototype located at the University of Bologna. A second objective of this part is to experimentally assess the ORC operation in partial evaporation operation, as a promising advanced cycle for ultra-low-temperature waste heat recovery applications.

The thesis structure for PART I is the following:

- Chapter 3 - Micro-ORC experimental analysis and semi-empirical modelling. This chapter introduces the micro-ORC test bench available at the University of Bologna, detailing its main components and the acquisition and control system. The experimental tests methodology is discussed and the ORC semi-empirical model is described. The chapter also covers the model calibration using experimental data and presents the results of an experimental campaign assessing the system's performance under partial evaporation and wet expansion operation.

- Chapter 4 - Micro-ORC applications for low-grade heat valorisation. This chapter presents two distinct applications of low-temperature kW-sized ORC technology. The first application investigates the ORC integration with a commercial solar thermal collector to satisfy the annual electricity needs of a single-family household. The second application focuses on industrial waste heat recovery, evaluating the feasibility and energy-saving potential of recovering data centers cooling waste heat through a micro-ORC system. A sensitivity analysis by varying the ORC working fluid to explore the potential of low-GWP alternatives is performed in both the studies.
- Chapter 5 - HTHP in the ceramic tiles manufacturing sector. This chapter analyses the use of a HTHP to improve energy efficiency in ceramic tile manufacturing by converting waste heat streams into process heat. Ceramic tile production is an energy-intensive process with significant carbon emissions but also offers opportunities for low-grade thermal energy recovery. The study explores two different waste heat recovery configurations to transform unused waste heat into valuable process heat, reducing natural gas consumption and lowering CO_2 emissions.

PART II - Carnot battery technology integration for energy storage applications

The aim of part II of this thesis is to explore the integration of ORC and HTHP technologies in electric energy storage solutions, namely Carnot batteries, which are implementable in more complex energy systems to push the penetration of renewables in the energy sector. Indeed, CBs offer a promising method for energy storage by converting excess electrical energy into thermal energy and back to electricity when required. This approach effectively manages the intermittency of RES, improves grid stability, and provides a sustainable energy storage solution. In this context, CB technology is applied to i) a university building facility, combined with district heating and photovoltaic panels for smoothing the mismatch between the energy demand and production; ii) a data center cooling system for improving the energy management. Rule-based management strategies are developed and implemented to optimize the CB operation in each explored application. Furthermore, the modelling activity was supported by experimental data collected on the CB prototype located at the Thermodynamics Laboratory of the University of Liège, in Belgium. A second objective of this part is to develop the acquisition and control system of a new CB prototype under construction at the University of Liège, connected to the district heating substation of the Thermodynamics Laboratory building, with the aim to implement the developed CB management strategy simulated in the modelled system. Eventually, the last chapter of this part presents a preliminary performance analysis of a Brayton CB, which address higher temperature levels applications.

The thesis structure for PART II is the following:

- Chapter 6 - Carnot battery reference test benches. This chapter presents the two reversible HP/ORC test benches developed at the Thermodynamics Laboratory of the University of Liège. It details the main components and acquisition/control systems of the facilities. The first test bench, a 1.5 kW-sized prototype, serves as a proof of concept to validate the reversible technology in both HP and ORC modes. The second, a larger 10 kW-sized setup, is under development for integration with the laboratory building's district heating substation, focusing on energy storage and peak shaving. The chapter describes also the control and acquisition system of the 10 kW-sized test rig developed in collaboration with the University of Liège, as part of this thesis.
- Chapter 7 - Thermally integrated Carnot battery combined with district heating. This chapter presents a rule-based control strategy for operating a 10 kWe reversible HP/ORC Carnot battery within an integrated system that includes a district heating substation and a photovoltaic power plant, aimed at optimizing both thermal and electrical demands for a university campus building. The strategy focuses on maximizing economic benefits by using the CB to shave early morning thermal demand peaks, enabling a reduction in district heating substation size and investment costs. Two scenarios are examined: one where the HP draws heat from free waste heat, and another one where it uses the

return branch of the district heating substation. The first scenario shows significant savings, while the second offers no economic gain. The study also evaluates how different factors, such as photovoltaic plant size, storage volume, electricity pricing, and the investment cost of the HP/ORC system, affect the system's techno-economic performance. The results highlight that reducing the district heating substation size is crucial for economic benefits.

- Chapter 8 - Carnot battery thermally integrated with a data center. This chapter explores the integration of a reversible HP/ORC Carnot battery into a data center cooling system powered by photovoltaic electricity. The study includes a thermodynamic performance evaluation to identify the optimal working fluid. Subsequently, the semi-empirical off-design model from the reference CB test bench is utilized within a rule-based control strategy to manage the CB operations, maximizing the economic benefit. A sensitivity analysis examines the impacts of different storage volumes and energy prices. Findings show that CB integration proves economically feasible in scenarios with high energy prices, particularly when selling electricity back to the grid is not an option. Additionally, a comparison with a simpler alternative that recovers DC waste heat using only an ORC system is conducted, demonstrating the ORC-only configuration's lower performance and emphasizing the benefits of the more sophisticated CB system for waste heat recovery.
- Chapter 9 - Combined Heat and Power reversible Brayton PTES system. This chapter compares the thermodynamic performance of a closed Brayton-PTES in base and recuperated configurations. The recuperated version achieves higher temperatures and roundtrip efficiencies, while the base configuration shows a higher COP due to a lower temperature difference. The analysis also includes the system’s cogeneration performance, recognizing that part of the heat stored in the TES can be directly supplied to a thermal user. Eventually, the maximum specific investment cost of the system for both configurations and varying the average electricity and thermal energy prices is evaluated, with the goal of achieving a return on investment within 10 years.

PART I

ORC and HTHP for stand-alone electric and thermal energy generation

3. Micro-ORC experimental analysis and semi-empirical modelling

Summary. This chapter introduces the micro-ORC test bench located at the Micro-cogeneration Laboratory of the University of Bologna. The experimental facility is described in its main components, including the acquisition and control system. The methodology used to perform the experimental tests is discussed, and a detailed description of the semi-empirical model develop to simulate the ORC operation is provided. The model calibration procedure through the experimental data is included. In the last part of the chapter, the experimental campaign performed to assess the system behaviour in strongly off-design conditions, i.e., partial evaporation and wet expansion operation, is presented. The methodology adopted to conduct the tests and the performance results are discussed in detail.

3.1. University of Bologna micro-ORC test bench – experimental setup

As part of this doctoral thesis, the micro-ORC test bench available at the University of Bologna was utilized to carry out experimental campaigns aimed at assessing its performance when paired with very low temperature sources and under specific off-design operating conditions (i.e., partial evaporation and wet expansion). Additionally, the experimental data collected was used to calibrate and validate a detailed semi-empirical model of the micro-ORC, which is extensively employed throughout this thesis to analyse various applications of micro-ORC in both simpler and more complex energy systems.

The micro-ORC test bench is located at the Laboratory of Micro-cogeneration Technologies within the Department of Industrial Engineering at the University of Bologna since the beginning of 2016. Designed and assembled by StarEngine [128], this power plant is intended for residential use and can also function as an off-grid supply system. The development of the test bench, including external heat supply circuits, cold sink circuits, and the acquisition and control system, was completed by UNIBO laboratory personnel.

The following subsections describe the experimental setup of the test bench. For more detailed information about the components and the acquisition system, readers are encouraged to refer to Ottaviano's thesis [129], which focuses on the design of the test rig and the experimental characterization of the prototype. This work, instead, is more focused on the performance assessment of the system under very off-design operating conditions and using experimental data to evaluate the system's feasibility in several applications.

3.1.1. Micro-ORC system layout

The reference micro-ORC test bench has a nominal power of approximately 3 kW [72] and is designed to utilize thermal power from a low-temperature source (below 100 °C) [130]. Due to these characteristics and its compact size (80x85x253 cm), the prototype is primarily intended for residential applications or small-scale industrial uses. A photo of the facility is presented in Figure 3.1, while Figure 3.2 illustrates its layout, consisting of three circuits: the internal ORC circuit and the two external circuits that supply the evaporator and condenser within the system.

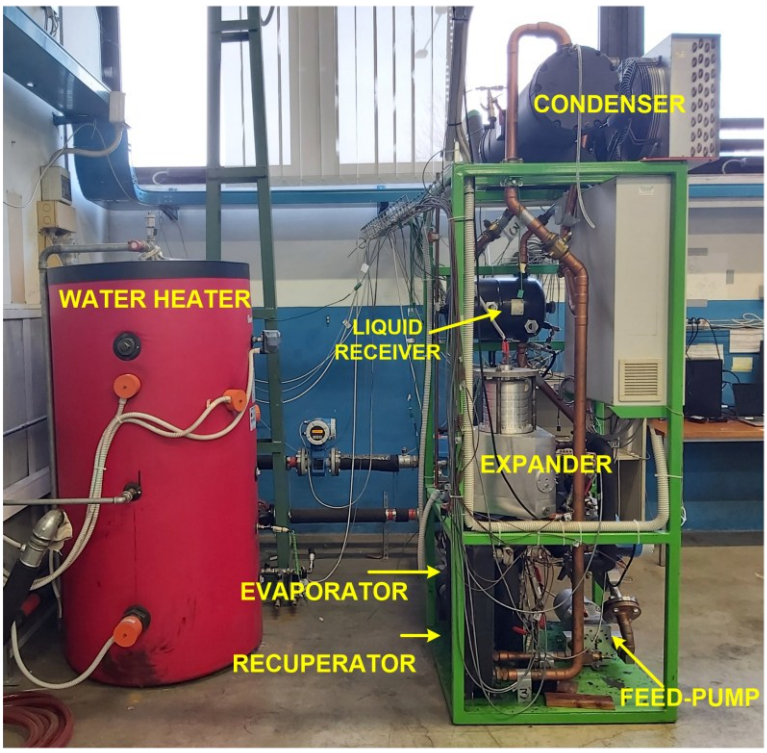

Figure 3.1 - Photo of the micro-ORC facility at the University of Bologna.

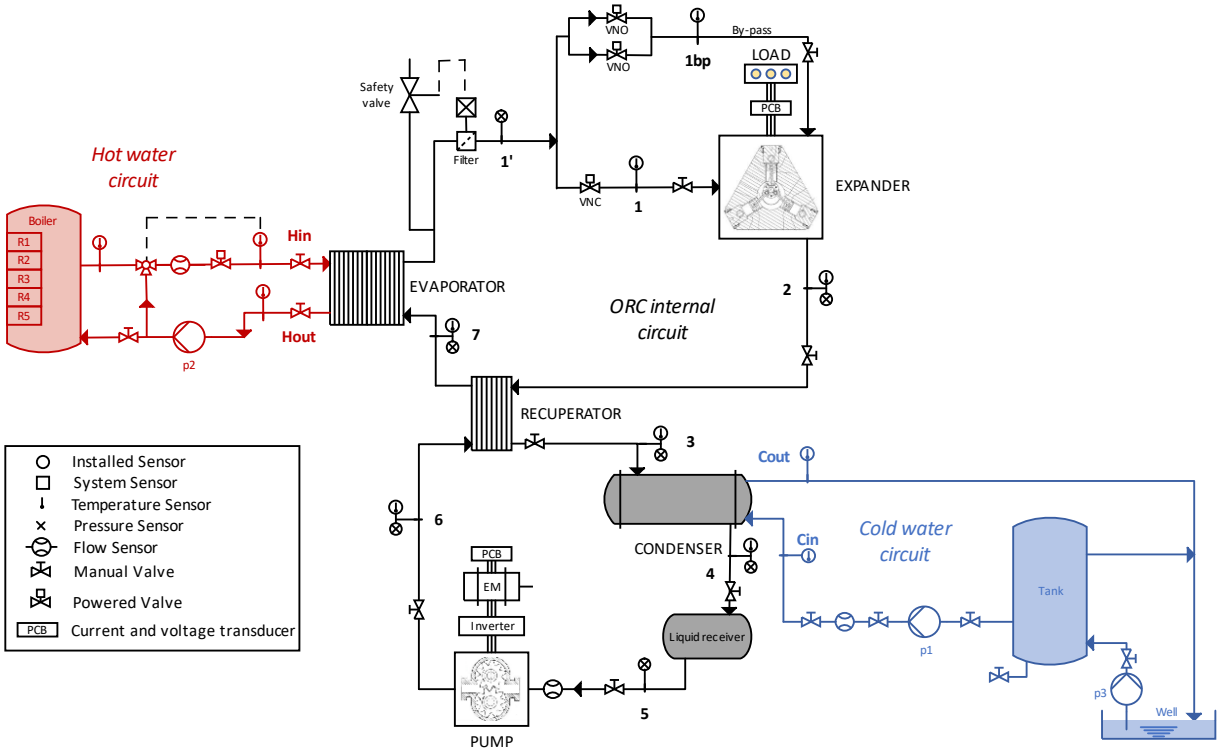

Figure 3.2 – Layout of the micro-ORC facility at the University of Bologna.

The internal ORC circuit, utilizing a recuperative configuration, operates with HFC-134a as the working fluid, holding a total charge of 22 kg. Although as all HFC refrigerants R134a (or Tetrafluoroethane) presents a non-negligible GWP (1430 [131]), it was selected as working fluid because of its

thermodynamic properties (i.e., critical temperature of 101 °C and critical pressure of about 40 bar - R134a thermodynamic characteristics are reported in the diagram in Figure 3.3), chemical and thermal stability, low toxicity and flammability. The quantity of fluid charged within the ORC circuit is a crucial factor influencing system performance. Specifically, overcharging the fluid can simultaneously reduce the phase change heat transfer area of the heat exchangers and raise the cost of the fluid, which can be considerable in certain situations. Conversely, an insufficient charge of working fluid heightens the risk of pump cavitation [129]. In the rotating components of the ORC pump and expander, lubricating oil is mixed with the working fluid in a proportion of 3-6 %.

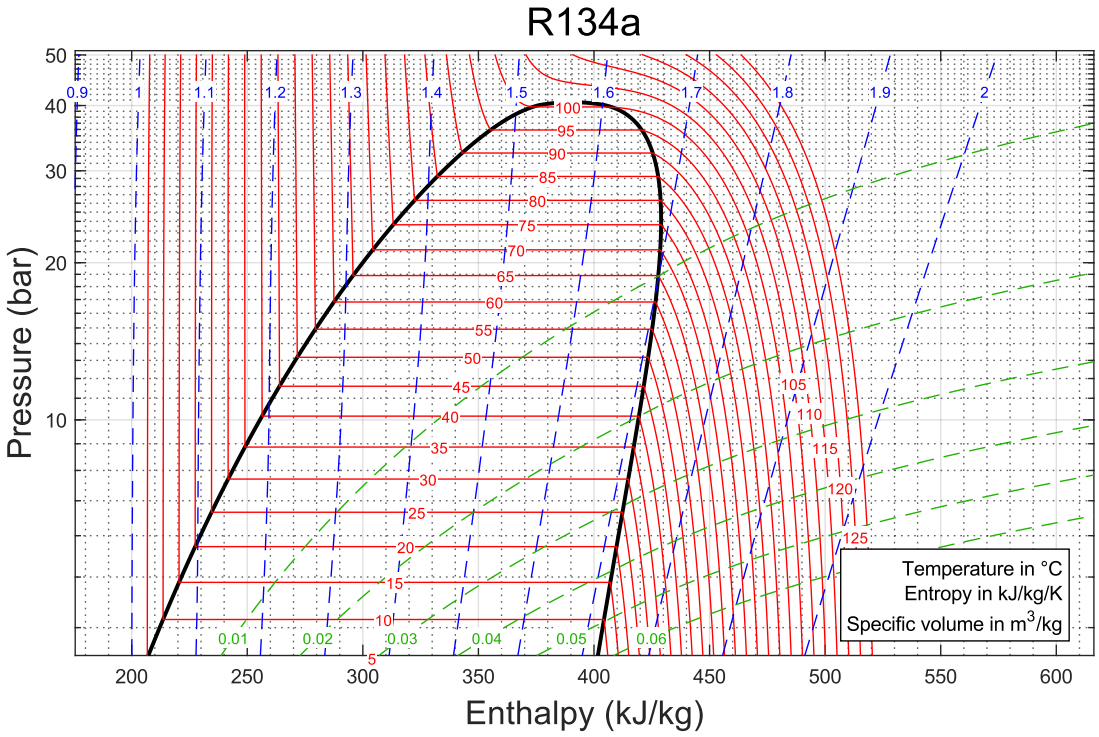

Figure 3.3 - R134a semi-logarithmic pressure-enthalpy thermodynamic diagram (obtained by means of Refprop thermodynamic database [132]).

The ORC circuit consists of seven primary components:

- Reciprocating piston expander. Developed by StarEngine Company [128], the expander prototype features three radial cylinders arranged out of phase by 120 °, each driving the same crankshaft, resulting in a total displacement of 230 cm^3. The machine is directly coupled to a permanent magnet electric generator within a hermetically sealed case, operating at the same rotational speed, ranging from 300 rpm to 1800 rpm.
- External gear pump. Also designed by StarEngine Company, the ORC recirculation pump is directly driven by a three-phase motor via an inverter, allowing variable speeds between 90 rpm and 300 rpm. This setup enables precise control of the working fluid mass flow rate through the circuit.
- Electrical load. The generator is connected to five parallel pure resistive loads, configured in *delta* with the generator output three-phase line. Each load consists of three 200 W light bulbs, and is provided with a separate switch, enabling the simulation of a three-phase load adjustable from 600 W (one load activated) to 3000 W (five loads activated), matching the nominal ORC power output. This configuration allows the expander shaft to balance the generator torque and load resistance, indeed the expander rotational speed is the result of the equilibrium between the driving and the load torque.
- Evaporator. It is commercial brazed plate heat exchanger made of 64 plates of 0.30 mm thick 316L stainless steel brazed in copper. It is fed by hot water from the heat source.

- Recuperator. Similar to the evaporator but made of 19 plates, this heat exchanger recovers residual heat from the expander outlet stream to preheat the liquid at the evaporator inlet. This process enhances thermodynamic efficiency, reducing the need for external heat supply [133]. Additionally, the recuperator increases the average temperature of thermal energy supply and decreases the average temperature of heat release, both of which improve thermodynamic efficiency [134].
- Condenser. It is a commercial shell and tube heat exchanger, fed by well or sink water collected in a tank within the external cooling circuit.
- Liquid receiver. It is a 19-liter tank located between the condenser and the recirculation pump, serving the dual purpose of preventing pump cavitation and acting as a system reintegration point during maintenance operations.

Table 3.1 lists the specifics of the ORC circuit main components.

Table 3.1 - Micro-ORC facility main components' specifics.

Component	Model	Features
Evaporator	ONDA S202	Plate heat exchanger with 64 plates
Recuperator	ONDA S202	Plate heat exchanger with 19 plates
Condenser	ONDA CT292-1100	Shell-and-tube heat exchanger with 4 passages
Expander	Radial piston prototype (STARENGINE [128])	Three radial cylinders at 120 °, displacement = 230 cm^3, direct coupling with generator
Pump	External gear prototype (STARENGINE [128])	Displacement = 50 cm^3, driven by three-phase 1.5 kW asynchronous motor with inverter. Variable speed between 90 rpm and 300 rpm
Generator	Magnetic NGB 145 M-SA	Three-phase permanent magnet synchronous generator, 380 V, 5.2 A, 8 poles
Load	Pure resistive	Five parallel loads, each made of three light bulbs, connected in *delta* with the generator

The heat transfer surfaces of the three heat exchangers were estimated using the available geometric parameters, resulting in 10.21 m^2 for the evaporator, 2.80 m^2 for the recuperator, and 2.85 m^2 for the condenser.

As shown in Figure 3.2, several manual valves are installed all along the circuits for inspection and in case of breakage. In addition, a normally closed valve (VNC) and two normally open valves (VNO) are installed before the expander to allow the cylinders by-pass during the ORC start-up operation: when the organic fluid by-pass the cylinders, it flows through the external casing of the expander increasing the temperature of its surfaces and preventing the machine from thermal stresses. Moreover, a safety valve is installed at the outlet of the evaporator to interrupt the operation in case of unexpected overpressure (higher than 26 bar).

3.1.2. Water circuits

The heat source circuit includes an electric water heater (see Figure 3.2) with a rated thermal power of 42 kW. It consists of a 500-liter tank equipped with five heating elements, each capable of independent activation to control the heat input to the ORC evaporator. The pressure within the hot water circuit is maintained above atmospheric pressure (between 1 and 2 bar) to prevent localized vaporization at high temperatures, which could lead to cavitation in the variable flow centrifugal pump P2. The temperature of the water entering the evaporator can be adjusted using an automatic three-way valve located at the outlet of the heater. This valve mixes hot water with cooler water exiting from the evaporator. The water flow rate is regulated by adjusting a motorized ball valve, in the range between 1.0 l/s and 2.6 l/s.

The cooling system is supplied by cold water extracted from a well by pump P3, or coming from the sink, and stored in a 300 l tank, from which water is circulated to the condenser by the centrifugal pump P1 (see Figure 3.2), with flow rate values from 1.0 l/s to 2.8 l/s. Cooling water temperature strongly depends on ambient conditions, indeed it has been observed that it varies from 16 °C in winter time to 25 °C in summer time.

3.1.3. Acquisition and control system

The test rig's three circuits are equipped with dedicated sensors to measure temperatures, pressures, and flow rates of the organic working fluid and the hot/cold water, as well as to capture the electric power generated by the expander and consumed by the pump motor. The specifications of these measurement devices are detailed in Table 3.2.

Table 3.2 – Micro-ORC facility acquisition hardware's specifics.

Physical quantity	Layout point (Figure 3.2)	Sensor	Calibration range	Output signal	COST accuracy*	Input module
SENSORS						
ORC temperatures	1, 1bp, 2, 3, 3', 4, 6, 7	T-type thermocouple	0–90 °C	±80 mV	±0.5 °C	NI9213-Thermocouple input
Hot water temperatures	Hin, Hout, Hboil	K-type thermocouple	0–90 °C	±80 mV	±0.5 °C	
Cold water temperatures	Cin, Cout					
ORC pressures	1, 6, 7	Pressure transducer	0–30 bar	0–5 V	±0.25 % FS	NI9201-Voltage AI
	2, 3, 4, 5		0–10 bar			
ORC mass flow rate	5	Coriolis mass flow meter	0.05–1.00 kg/s	4–20 mA	±0.3 % RV	NI9203-Current AI
ORC density			10–1300 kg/m3		±0.1 kg/m3	
Hot water flow rate	Hin	Magnetic flow meter	0–6.4 l/s	4–20 mA	±0.5 % RV	
Cold water flow rate	Cin		0–9.8 l/s			
Electric voltage and current	Expander generator and pump motor supply lines	PCB mounted Hall effect voltage and current transducers	0–400 V 0–5A	0–4 V	±0.1 % RV ±0.2 % RV	NI9215-Voltage AI
ACTUATORS						
Hot water flow rate	Hin	Motorized ball valve	0-100 %	0-10 V	-	NI 9263-Voltage AO
Hot water inlet temperature	Hin	Motorized three-way valve	0-100 %	0-10 V	-	NI 9263-Voltage AO
Hot water drain	Hout	Solenoid valve	On-off	Relay	-	NI 9482-Relay output

*Component Off-the-Shelf (COTS) accuracy: it refers to the instrument accuracy as indicated on the data sheet, before individual calibration or calibration of the measurement chain

For a comprehensive thermodynamic characterization and thorough performance analysis of the system, temperature and pressure sensors are positioned at the inlet and outlet of each component in the

internal ORC circuit (the numbers and positions of the sensors are illustrated in Figure 3.2 and detailed in Table 3.2). Temperatures are recorded using T-type thermocouples with mineral insulating sheaths, while pressures are measured with absolute ceramic pressure transducers, with ranges of 0-10 bar for low-pressure and 0-30 bar for high-pressure branches. The working fluid's mass flow rate is measured by a Coriolis flow meter located at the pump inlet. K-type thermocouples are installed on the hot/cold water supply lines at the evaporator and condenser inlet and outlet pipes to measure water temperatures. Two magnetic flow meters determine the volumetric flow rates of water to the evaporator and condenser. All pressure transducers and thermocouples, along with the entire measurement chain (including cables and acquisition devices), are periodically calibrated in the laboratory to minimize uncertainty in performance assessments.

For acquiring the three-phase electric power generated by the expander and consumed by the pump motor, two printed circuit boards (PCBs) with voltage and current transducers were developed in the laboratory. Mechanical output power is not measured directly but is estimated from the electric output power via conversion efficiency. Additionally, the analysis of the AC signal is used to detect the generator frequency and determine the expander shaft's rotational speed.

Temperature, pressure, and flow rate signals are sampled at a frequency of 1 Hz, while current and voltage signals at the expander and pump motor are sampled at 100 kHz and 50 kHz, respectively. All signals are transmitted to a workstation via a National Instrument CompactRIO device, which includes an FPGA chassis with various FPGA modules for analogue input and a real-time embedded controller. Custom real-time data acquisition software was developed in the LabVIEW environment, consisting of two subprograms: Real-time and Host. The Real-time subprogram, running on the CompactRIO processor, handles signal conditioning, conversion of analogue electric signals to physical quantities, and adjustments using calibration equations. The Host subprogram, running on the workstation, serves as the user interface for the acquisition software, graphically displaying measured variables and allowing input variables to be set. It also utilizes the integrated thermodynamic library CoolProp [27] to obtain enthalpy values based on temperature and pressure measurements and to calculate the thermal power transferred in the heat exchangers. Additionally, the Host subprogram continuously monitors the thermodynamic cycle throughout the experimental test campaign.

3.2. Data acquisition and analysis

Although the full experimental characterization of the reference micro-ORC test bench is part of Ottaviano's PhD thesis [129], an overview of the test methodology and of the resulted characterization is provided in this thesis as fundamental basis for the further experimental tests performed as part of the current thesis. Furthermore, the collected experimental data were used to calibrate and validate the system semi-empirical model widely adopted within this thesis and described in the following section of this chapter.

The experimental analysis was carried out under both steady-state and dynamic conditions. However, this thesis focuses solely on the steady-state campaign. Approximately 120 experimental data points were collected under off-design conditions by varying the hot water temperature, the ORC feed pump's rotational speed, and the external load connected to the expander. The test bench's other controlled variables include the hot and cold water flow rates, while the cold water temperature, influenced by ambient conditions, remains unregulated. The measured variables enable the evaluation of performance indices for each component.

3.2.1. Test setup and steady-state detection

The tests were performed under stable conditions for the heat source, cold sink, electric load, and feed-pump frequency. The controlled variables, i.e. the hot water temperature and flow rate, the cold water flow rate, the electric load (nominal impedance), and the feed-pump rotating frequency, were varied systematically, while the cold water temperature varied based on the cold sink used. The user had no direct control over the cold water temperature. Furthermore, the nominal power associated with a certain number of loads does not reflect the actual electric power output of the expander, but the actual load impedance, calculated using electric current and voltage measurements, is always lower than the nominal value of the light bulbs. Lastly, the feed-pump rotating frequency was varied using the inverter that controls the pump motor. For given heat source and cold sink temperatures, and external load, the mass flow rate determines the cycle's operating pressures and thus its power output. The flow rate is proportional to the feed pump's rotational speed, which is managed by the pump's inverter. After each adjustment of an operating variable, the system was waited for reaching stability for over 10 minutes to achieve steady-state conditions.

Detecting steady-state operating intervals is crucial for extracting realistic and significant data from experiments. This helps in tracing the performance maps of the system by evaluating its behaviour under different boundary conditions. During tests, variables are measured at specific acquisition frequencies, resulting in a time-ordered sequence of data. In a strict sense, stationarity implies no variation over time, but this is impractical for experimental data due to noise and disturbances. Thus, a limited variation around the mean value is accepted to consider an interval as steady-state. Once detected, the operating point is obtained by averaging values over the steady-state interval to minimize disturbances' influence (see Figure 3.4). A post-processing algorithm similar to Kim et al. [135] is used. This algorithm compares the variable's value to its moving mean. When the variation falls within an acceptable band, the interval is considered steady-state. The moving mean at the k-th time step is calculated using the latest n values, where n is the size of the time window over which the average is computed. The relative variation is computed as the absolute difference between the variable value and its mean, divided by the mean. Two constraints must be met for the variable to be considered stationary: (i) the relative variation must be below a maximum acceptable threshold, (ii) the duration of the time interval must exceed a minimum duration. The threshold value is chosen based on the signal's characteristics, such as inertia and noise. Smaller thresholds ensure conservative detection but take longer to settle, while larger thresholds allow faster data collection but may include transient data. Suggested thresholds for various variables include 0.5 K for temperature, 2 % for pressure, flow rate, and rotational speed.

For further details about the steady-state detection, the lecturer is invited to consult the thesis of Torricelli [136], more focused on the data elaboration techniques.

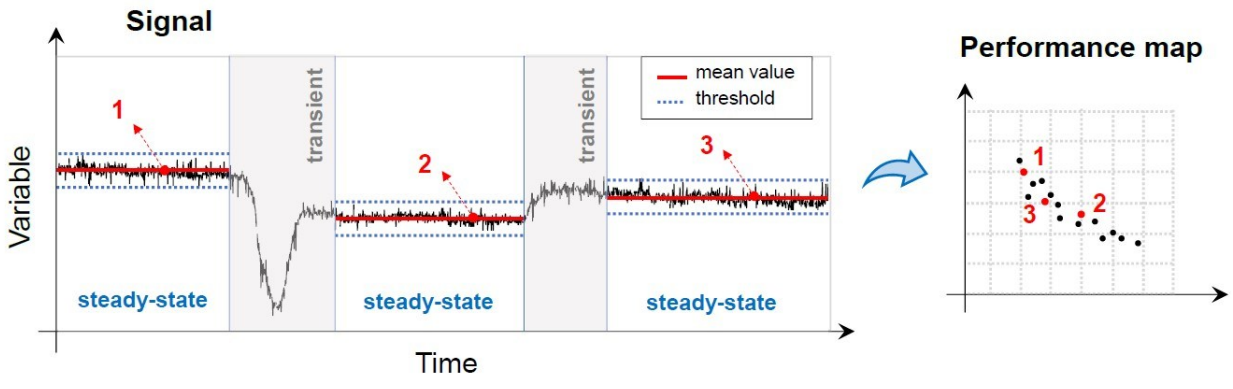

Figure 3.4 - Steady-state detection operating principle [136].

3.2.2. Uncertainty quantification

Assessing the thermodynamic state of the working fluid at each section of the cycle involves inherent uncertainty due to sensor and probe characteristics, installation, and calibration procedures. Additionally, calculated variables are influenced by uncertainties propagated from multiple measurements, as part of the calculation process based on thermal balances and CoolProp library. Each variable and calculation in this process contributes to the overall uncertainty of the calculated state property or performance index.

The uncertainty calculation for ORC performance parameters, as described in [137], follows the procedure outlined in the ISO/IEC Guide 98 and EA-4/02M standards. Uncertainty propagation relies on a classic rule, which allows for the calculation of a variable's uncertainty by considering the uncertainties of all dependent variables. For instance, if y is a variable computed as a function of x and z, the uncertainty of y, δy, is evaluated using Eq. (3-1).

$$\delta y = \sqrt{\left(\frac{\partial y}{\partial x}\right)^2 \delta x^2 + \left(\frac{\partial y}{\partial z}\right)^2 \delta z^2} \tag{3-1}$$

where δx and δz are the uncertainties of x and z, while $\partial y/\partial x$ and $\partial y/\partial z$ are the partial derivatives of y with respect to x and z, respectively.

Three standards distinguish the computation of uncertainty contributions based on accuracy levels:

- Basic Approach. It relies on off-the-shelf accuracy of sensors, probes, and acquisition modules. Accuracy increases with a calibration process using specific calibrators and standard procedures. No calibration process is required, and uncertainty assessment is based on data reported in data sheets.
- Field-Calibrated Approach. Pressure sensors and temperature probes are calibrated on-field using standard procedures, involving pressure calibrators and thermostatic furnaces respectively, in turn calibrated towards a primary laboratory standard certified in agreement with the Italian Accreditation Body (Accredia). This approach considers two uncertainty contributions: reference uncertainty of the certified laboratory standard (type B), and standard deviation of the data set (type A). However, environmental conditions cannot be fully controlled with this approach, and signal noise cannot be eliminated.
- Lab-Scale Approach. In this case, sensors are calibrated under controlled conditions, thus it is possible to eliminate signal noise and control the environmental conditions.

The uncertainty contribution for temperature and pressure measurements varies across the three approaches (Figure 3.5). In the off-the-shelf approach, the acquisition module's measurement performance is the main contributor to uncertainty. In the field-calibrated approach, sensor/probe performance mainly affects uncertainty due to uncontrolled environmental conditions. In the lab-scale approach, the calibrator's accuracy is the primary contributor to the uncertainty chain.

Among these standards, the UNIBO laboratory follows the third approach, where measurement uncertainty is represented by the reference uncertainty of the certified laboratory. Temperature and pressure sensors are periodically calibrated within their operating ranges using certified instruments (MicroCal PM200+ for pressure sensors and Isotech Jupiter 650 for temperature thermocouples). For flow rate sensors, the uncertainty contributions are provided by the manufacturer (component off-the-shelf accuracy).

The uncertainty calculation of thermodynamic properties, such as enthalpy, entropy, density, uniquely dependent on pressure and temperature values, follows the general rule of uncertainty propagation (Eq. (3-1)). The partial derivatives with respect to pressure and temperature are estimated using CoolProp library. The uncertainty for all performance indexes is calculated according to this method, i.e., applying Eq. (3-1).

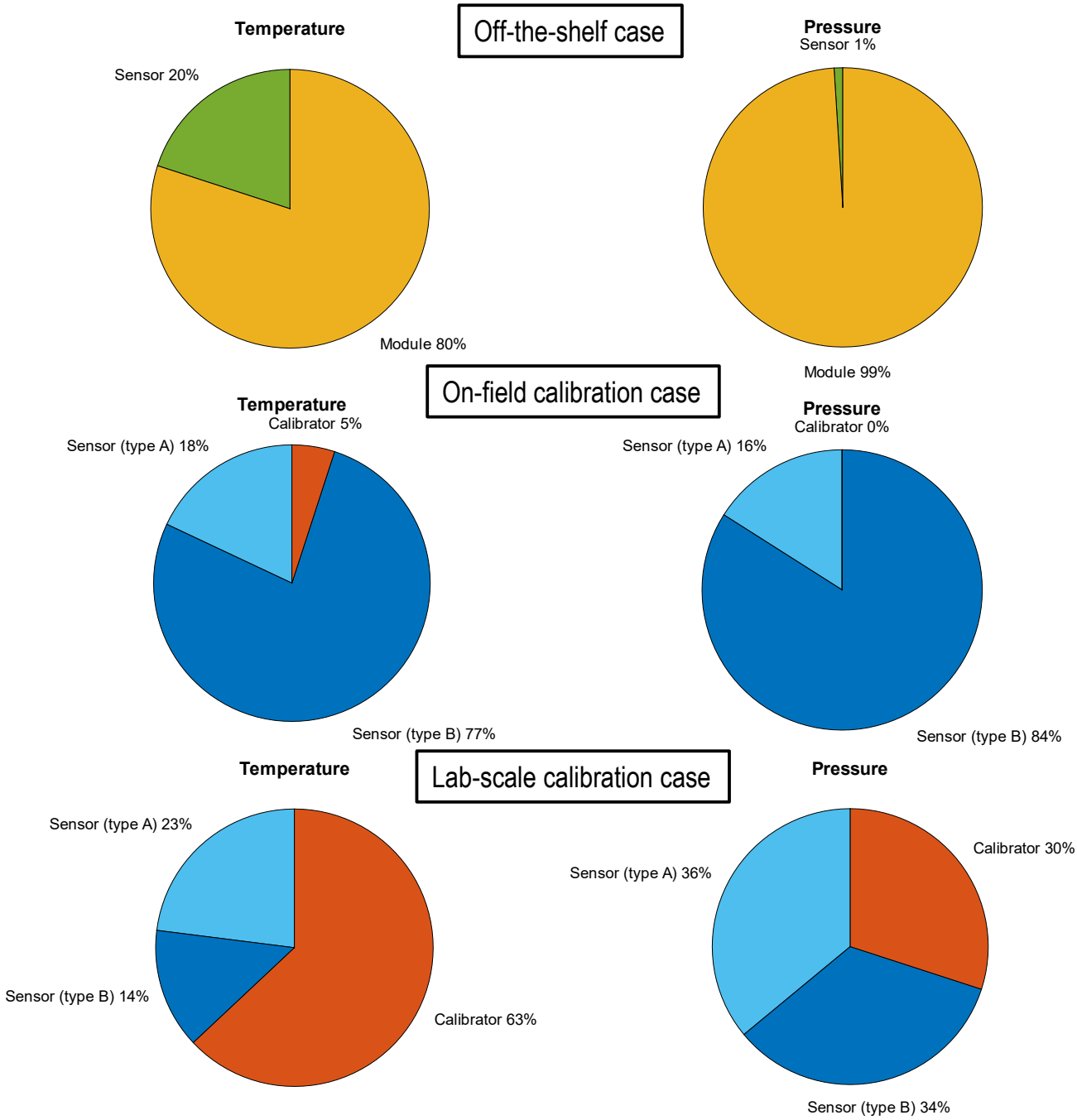

Figure 3.5 - Uncertainty contributions of temperature and pressure measurement chain according to the three standards for uncertainty calculation.

3.2.3. Test bench characterization

The characterization of the reference micro-ORC test bench was conducted under steady-state conditions by adjusting the available control variables across various boundary conditions (see Figure 3.6). The hot water temperature was varied between 65 °C and 85 °C, with a flow rate ranging from 1.3 l/s to 2.7 l/s. The cold water flow rate was adjusted between 1.4 l/s and 2.9 l/s, while the cold water temperature varied based on the cold sink used. When using the water well, the temperature fluctuated with ambient conditions, from 18 °C in winter to 27 °C in summer. With the tap water circuit, the temperature ranged from 8 °C to 16 °C, depending on the season. The electric load was modified in discrete increments, ranging from a minimum of one load (nominal impedance of 288 Ω) to a maximum of five

loads (nominal impedance of 58 Ω). Lastly, the feed-pump rotating frequency was varied between 20 Hz and 55 Hz. The maximum frequency of 60 Hz was not tested due to instability issues at higher frequencies.

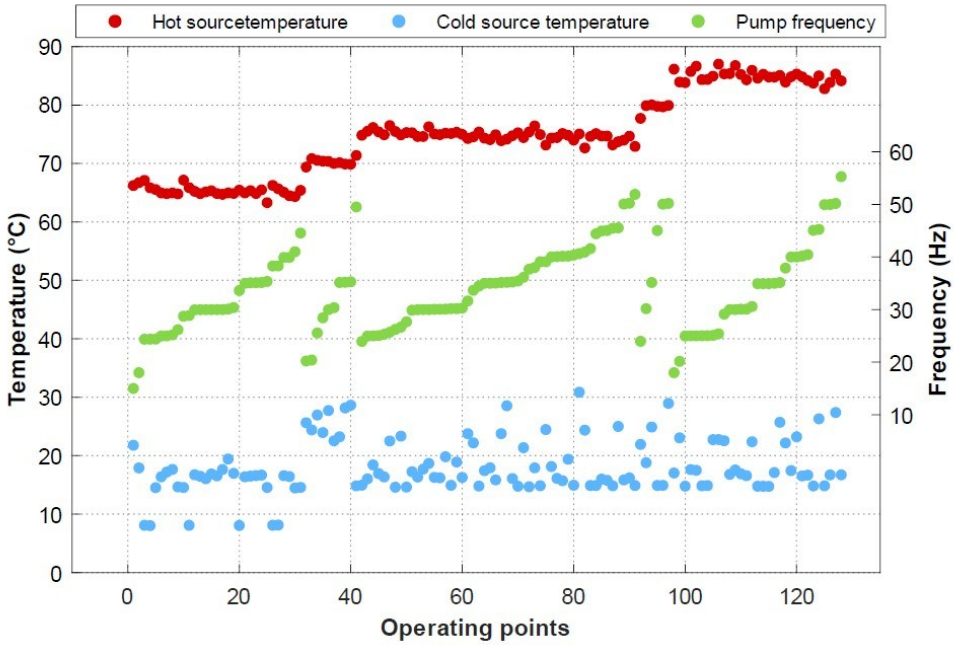

Figure 3.6 - Map of the collected steady-state points for ORC test rig characterization - Controlled variables [136].

As shown in Figure 3.7, the system operation is strongly influenced by the controlled variables. There is a linear correlation between the pump frequency, the working fluid mass flow rate (Figure 3.7(a)) and the power consumption (Figure 3.7(c)) due to the pump of positive displacement type. Increasing the working fluid flow rate, a quasi-linear increase of the evaporating pressure is observed, while the condensing pressure remains almost constat because it depends on the cold sink temperature (Figure 3.7(b)-(d)). The working fluid mass flow rate increase in the range between 0.05 kg/s and 0.22 kg/s corresponds to an increase in the evaporating pressure from 11 to 23 bar. The expander power production increases linearly with the speed following characteristic curves depending on the electric load (Figure 3.7(e)), reaching the maximum value of 1.7 kW. Eventually, the overall system efficiency trend increases with the pressure ratio and the mass flow rate (Figure 3.7(f)).

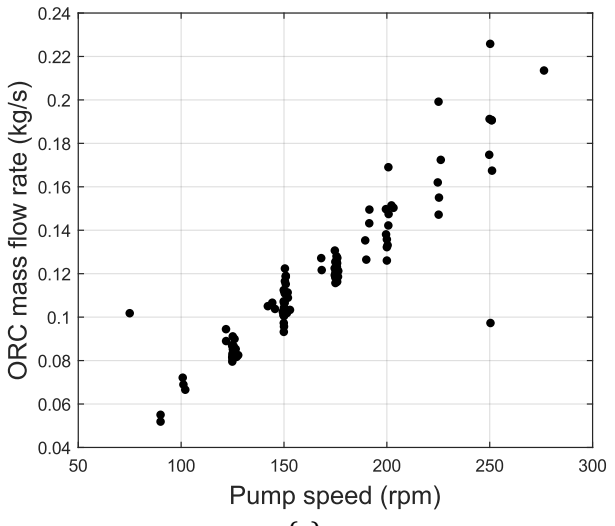

(a)

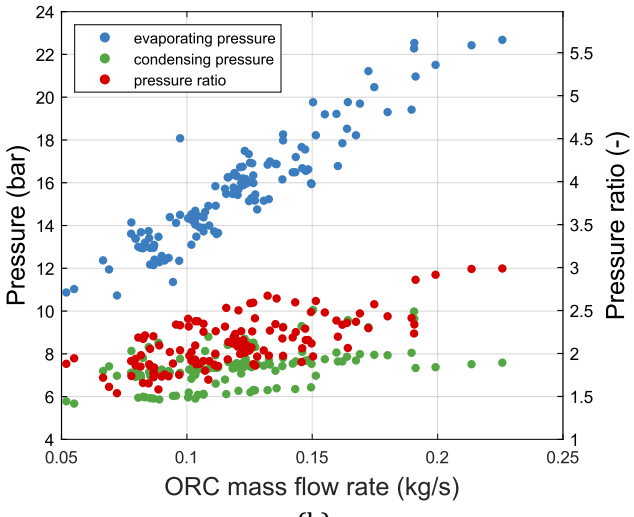

(b)

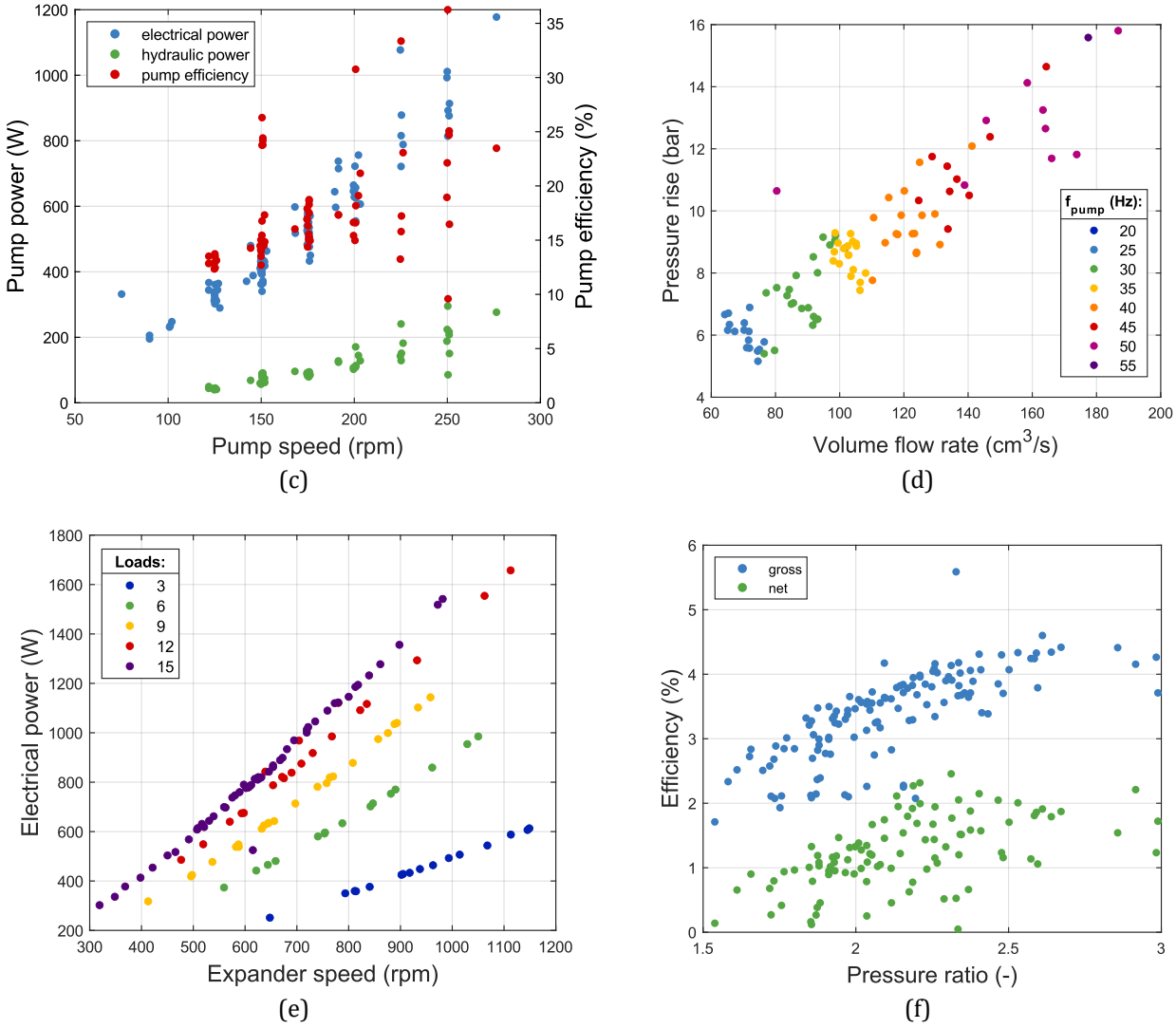

Figure 3.7 - Maps of the collected steady-state points for ORC test rig characterization – Measured variables.

3.3. Semi-empirical modelling approach

A semi-empirical model for the micro-ORC system off-design behaviour simulation was developed by Torricelli [138] and employed to predict the system performance with low-environmental impact working fluids [139]. The availability of a large experimental data set from the reference test bench allowed the development of a robust semi-empirical model of the micro-ORC.

Semi-empirical models offer a balance between black-box and white-box approaches. The black-box method simplifies implementation but lacks detailed process physics, limiting accuracy in extrapolated conditions. Examples include constant-efficiency and polynomial-based models. Conversely, the white-box approach accurately models systems using detailed physical and chemical equations, requiring extensive system knowledge. The semi-empirical approach combines these methods by using both meaningful physical equations and empirical parameters, providing a trade-off between simulation speed, calibration effort, modelling accuracy, and extrapolation capability.

Dickes et al. [140] found that this method is more accurate than constant-efficiency and pure polynomial models for micro-ORC systems. More in detail, the constant-efficiency approach assumes fixed performance parameters regardless of operating conditions, assigning constant volumetric efficiencies to the pump and the expander, and a fixed thermal efficiency to each heat exchanger. The polynomial

regression technique uses quadratic functions to describe performance parameters, accounting for the effects of operating conditions. The semi-empirical method uses a limited set of physical equations, with coefficients optimized to best fit experimental data, to describe the transformations within the components. While the constant efficiency approach is much less accurate than the other two, the polynomial regression approach is very accurate near the operating conditions used for calibration but it becomes unreliable and less accurate when conditions deviate from these. Therefore, the semi-empirical approach is deemed the most reliable in terms of accuracy. However, in terms of computational burden, the first two approaches require significantly less effort than the semi-empirical model. In conclusion, semi-empirical models are best suited for simulating systems under off-design operating conditions despite the challenges in parameter calibration and higher computational demands.

3.3.1. Contribution

In this work, the model proposed by Torricelli has been regained, enhanced, and adapted to investigate system performance when integrated into more complex energy systems. For each application, the model has been recalibrated with new, dedicated experimental data tailored to the specific boundary conditions of the simulated scenarios. When the system operates under highly off-design conditions, such as very low heat source temperatures, even a semi-empirical model loses accuracy due to significant deviations from typical operating conditions. The empirical correlations' simplifications become no more negligible. Recalibrating with experimental data collected under conditions closer to those desired for simulation helps mitigate this issue. For this reason, as part of this thesis, dedicated experimental campaigns were conducted to expand the reference test bench data set, enabling recalibration according to the specific boundary conditions of the simulated applications.

The following subsections provide a brief overview of the methodology adopted to model the ORC system and its main components. For further details, the interested reader is encouraged to refer to Torricelli's doctoral thesis [136]. Finally, the calibration and validation procedures used in the present thesis are discussed.

3.3.2. The system model

The ORC off-design semi-empirical model is developed in MATLAB environment with the alternative integration of the thermodynamic libraries CoolProp [27] or Refprop [132], for the calculation of the thermodynamic properties of the fluids respectively when using pure fluids and mixtures. Indeed, the open-source CoolProp is preferred, when possible, but mixtures simulation often require Refprop database.

The model utilizes a modular approach where each main component of the ORC is modelled individually as a MATLAB function. These components are then interconnected at a high level to simulate the overall cycle behaviour. The thermodynamic properties of the working fluid at the inlet and outlet of each component serve as the inputs and outputs for each sub-model. Figure 3.8 illustrates the system model framework, emphasizing the input and output variables for the entire model and the interactions between the components sub-models. The components sub-models refer to the expander, the ORC pump, the evaporator, the recuperator, and the condenser.

The inputs of the model are the boundary conditions of the system and the variables that can be controlled from the outside: the hot source temperature (TH_{in}) and volumetric flow rate ($\dot{V}H$) at the evaporator inlet, the ambient temperature (T_{amb}), and the cold sink temperature (TC_{in}) at the condenser inlet; whilst the control variables are the superheating level at the expander inlet (ΔT_{SH}), the electric load ($load$), the cold sink volumetric flow rate at the condenser inlet ($\dot{V}C$), and the subcooling level at the

condenser outlet (ΔT_{SC}).

Since the model is formulated as two levels implicit problem, its solution is determined through an iterative process with two iterative variables: the expander inlet temperature (T_1) and the condenser outlet temperature (T_4).

The output variables are the expander output power ($\dot{W}_{exp}$) and its shaft rotational speed (N_{exp}), the pump absorbed power ($\dot{W}_{pump}$) and its frequency (f_{pump}), the thermal input provided at the evaporator ($\dot{Q}_{ev}$), the condenser discharged thermal power ($\dot{Q}_{cd}$), and the thermal power exchanged in the recuperator ($\dot{Q}_{rec}$).

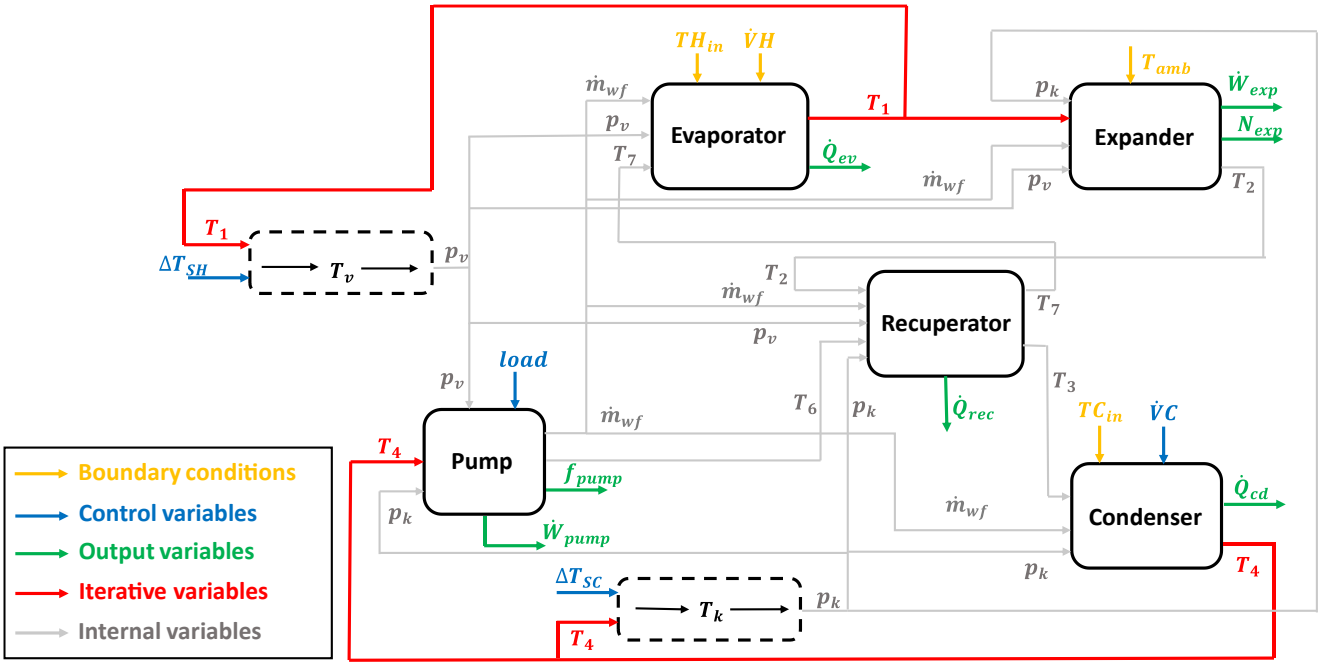

Figure 3.8 - ORC-cycle model block diagram.

3.3.3. Heat exchangers

The three heat exchangers (evaporator, recuperator, and condenser) are modelled using a lumped parameter moving boundary approach [141]. Each heat exchanger is divided into zones corresponding to the different states experienced by the fluid within the component [142]. In each zone, the fluid remains in a single phase throughout its length. This method characterizes each zone by a global heat exchange coefficient U_i and a heat transfer surface area A_i, through which heat transfer occurs [143]. Figure 3.9 shows a schematization of the moving boundary method.

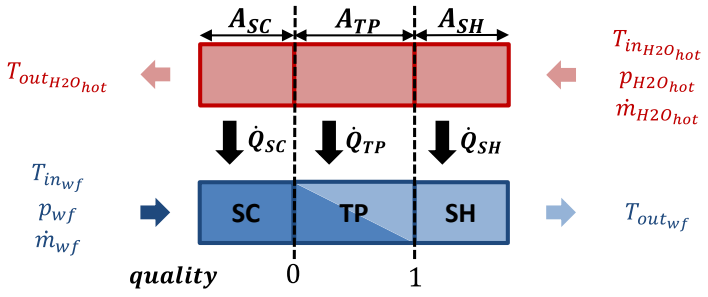

Figure 3.9 - Moving boundary method schematization.

The moving boundary approach is particularly accurate as it accounts for significant variations in the global heat exchange coefficient during phase changes of the fluid. The boundaries between consecutive zones are not fixed but move according to the fluid's physical state, with the only constraint being that the sum of the three A_i must equal the component's geometric surface, a model parameter.

The evaporator and condenser are each divided into three zones (subcooled, two-phase, and superheated), whereas the recuperator is considered as a single heat exchange zone. Differently from the version proposed by Torricelli, in this thesis the heat transfer process in the *i-th* zone ($\dot{Q}_i$) is calculated using the ε-NTU (*Number of Transfer Units*) method, according to the following three equations:

$$\dot{Q}_i = \varepsilon_i \cdot \dot{m}_{hot} \cdot c_{p_{hot_i}} \cdot \left(T_{in_{hot_i}} - T_{in_{cold_i}}\right) \tag{3-2}$$

$$\varepsilon_i = \frac{1-e^{-NTU_i \cdot (1-C_i^*)}}{1-C_i^* \cdot e^{-NTU_i \cdot (1-C_i^*)}} \tag{3-3}$$

$$NTU_i = \frac{U_i A_i}{C_{min_i}} \tag{3-4}$$

where $\dot{m}_{hot} \cdot c_{p_{hot_i}}$ is the thermal capacity of the hottest fluid, and $T_{in_{hot_i}}$ and $T_{in_{cold_i}}$ are the inlet temperature of respectively the hottest and the coldest exchanging fluids. C_i^* is the ratio between the minimum and the maximum thermal capacity.

In the subcooling and superheating zones, the overall heat transfer coefficient considers the convective coefficients on both the working fluid side (α_{wf_i}) and the water side (α_{H2O}), as shown in Eq. (3-5). These coefficients are evaluated using the Dittus-Boelter correlation for forced convection.

$$U_i = \left(\frac{1}{\alpha_{wf_i}} + \frac{1}{\alpha_{H2O}}\right)^{-1} \tag{3-5}$$

In the two-phase zone and the single zone of the recuperator, the global heat transfer coefficient is derived from empirical correlations. Specifically, the correlations for the evaporator and condenser are in the form of Eq. (3-6), while the one for the recuperator follows Eq. (3-7).

$$U_{ev/cd} = U_{ev/cd,ref} \cdot \dot{m}_{wf}{}^{a} \cdot \Delta T_{sat}{}^{b} \cdot \dot{m}_{H2O}{}^{c} \cdot p_{sat}{}^{d} \cdot \Delta h_{sat}{}^{e} \tag{3-6}$$

$$U_{rec} = U_{rec,ref} \cdot \dot{m}_{wf}{}^{a} \cdot \Delta T^{b} \tag{3-7}$$

The reference heat transfer coefficients ($U_{ev/cd/rec,ref}$) and all exponents in these equations are numerically calibrated to match the available experimental data. Eq. (3-6) accounts for the working fluid and water mass flow rates ($\dot{m}_{wf}$ and $\dot{m}_{H2O}$), the saturation pressure (p_{sat}), the temperature difference between the water and the saturation temperature of the working fluid (ΔT_{sat}), and the specific latent heat (Δh_{sat}). Eq. (3-7) considers only the working fluid mass flow rate ($\dot{m}$) and the inlet temperature difference between the two fluid streams (ΔT).

3.3.4. Expander

The reciprocating piston expander model [144], based on the lumped parameter approach introduced

by Glavatskaya in [145], is illustrated in Figure 3.10(a). It simulates the behaviour of the working fluid to determine the outlet thermodynamic conditions and the output electric power. Figure 3.10(b) illustrates the working fluid cycle inside the cylinders in a pressure-volume diagram, which includes fluid admission (1-2), internal expansion (2-4), fluid exhaust (4-5), and re-compression (5-1).

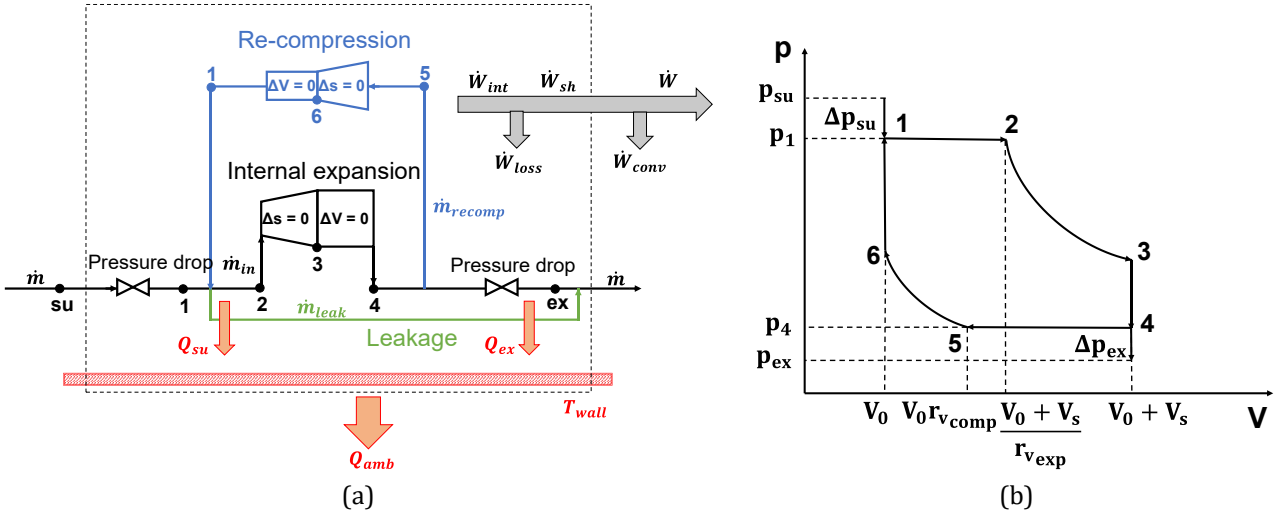

Figure 3.10 - Expander model: (a) lumped parameters scheme, and (b) indicated diagram.

The fluid admission and exhaust processes are modelled in two stages each: the first stage is represented as an isentropic flow through a converging nozzle (Eq. (3-8)), considering only the pressure drop; in the second stage, the pressure is assumed constant while accounting for thermal power dissipation using the ε-NTU method (Eq. (3-9)). A similar equation to Eq. (3-8) is used to estimate the leakage mass flow rate between the cylinder liner wall and the piston.

$$\dot{m}_{wf} = \rho_{su/ex} \cdot A_{su/ex} \cdot \sqrt{2 \cdot \left| h_{su/ex} - h_{wf} \right|} \tag{3-8}$$

$$\dot{Q}_{su/ex} = \varepsilon_{su/ex} \cdot \dot{m}_{wf} \cdot c_p \cdot \left(T_{wf} - T_{wall} \right) \tag{3-9}$$

The internal expansion (and re-compression) is modelled as a sequence of isentropic expansion (compression) followed by constant volume expansion (compression). The output electric power is calculated by reducing the ideal thermodynamic expansion power by various internal losses, including leakages, heat dissipation through the expander wall, under and over-expansion losses, friction, and electro-mechanical conversion losses. Under-expansion and over-expansion losses occur when the pressure at the end of the isentropic expansion process is greater and lower, respectively, than the discharge pressure (Figure 3.11).

The pressure at the end of the isentropic expansion depends on the intake stroke ratio, α, representing the relative volume swept by the piston between the opening and closing of the admission valve, V_2, and it is equal to the inverse of the built-in volume ratio, $r_{v_{exp}}$ (Eq. (3-10)):

$$\alpha_v = \frac{V_2}{V_0 + V_s} = \frac{1}{r_{v_{exp}}} \tag{3-10}$$

where V_0 is the clearance volume and V_s is the displacement. By adjusting the value of α_v, for instance through a variable valve timing (VVT) system, it is possible to align the internal volumetric expansion ratio with the internal pressure ratio ($p_3 = p_4$).

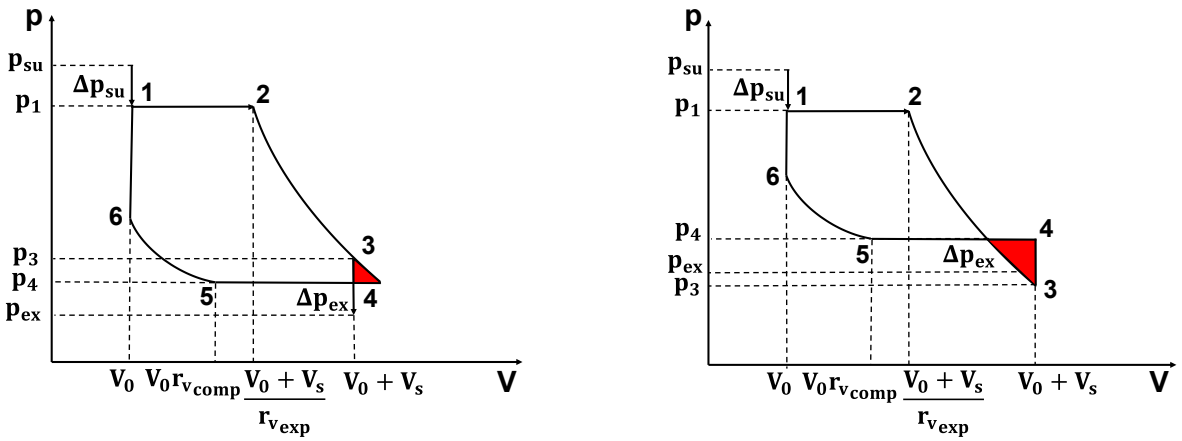

Figure 3.11 - Expander model indicated diagram in case of (a) under-expansion and (b) over-expansion.

3.3.5. Pump

The pump's operating point is determined by the intersection of the circuit's resistance curve (Eq. (3-11)) with the pump's characteristic curve (Eq. (3-12)) [146]. The resistance curve is influenced by the load, as an increase in the expander's resisting load leads to a higher resisting load across the entire circuit, and it also depends on the fluid density, ρ. On the other hand, the pump's characteristic curve varies with its rotational speed, N_{pump}, and the fluid's dynamic viscosity, μ. Both the pump and resistance characteristics can be described by the relationship between the pump pressure rise, Δp, and the volumetric flow rate, $\dot{V}_{wf}$.

$$\Delta p = (const_1 \cdot N_{pump} + const_2 \cdot \dot{V}_{wf}) \cdot \mu \tag{3-11}$$

$$\Delta p = (const_3 \cdot load + const_4) \cdot \dot{V}_{wf} \cdot \rho \tag{3-12}$$

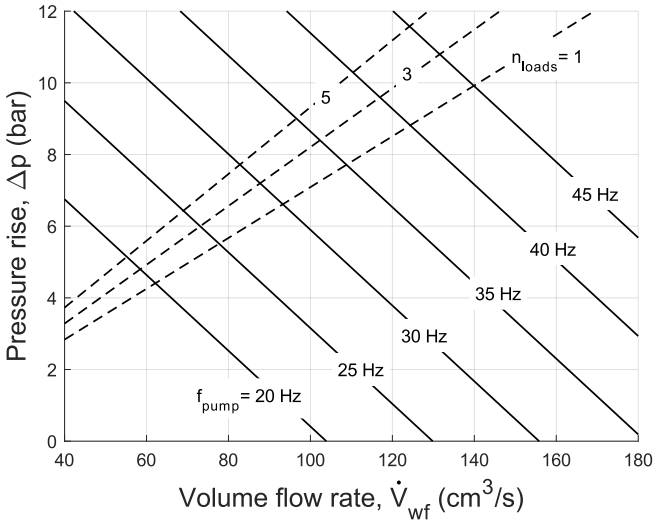

Figure 3.12 - Pump characteristic and circuit resistance extrapolated curves.

The coefficients $const_1$, $const_2$, $const_3$, $const_4$ are calibrated parameters. The extrapolated curves for

the examined gear pump are shown in Figure 3.12, depicting pressure rise versus volumetric flow rate.

3.3.6. Fluid dependent parameters correction

Although most of the empirical parameters requiring calibration are linked to the components' geometry, some are influenced by the thermodynamic properties of the working fluid. Specifically, global heat transfer coefficients are dependent on the working fluid and need to be adjusted when using fluids other than R134a. To address this, the global heat transfer coefficients are recalculated using the procedure proposed by Giuffrida [147] when different fluids are considered. The global heat transfer coefficient is defined by:

$$UA = \frac{Nu \cdot \lambda}{L} \tag{3-13}$$

where Nu is the Nusselt number, λ is the thermal conductivity, and L is the characteristic length. For a new fluid, the global heat transfer coefficient, UA_{fluid}, can be determined in relation to the reference global heat transfer coefficient, UA_{R134a}, and the properties of the fluids, as given by:

$$\frac{UA_{fluid}}{UA_{R134a}} = \frac{Nu_{fluid} \cdot \lambda_{fluid}}{Nu_{R134a} \cdot \lambda_{R134a}} \tag{3-14}$$

3.3.7. Calibration and validation

The calibration procedure for the empirical parameters is a critical step in successfully implementing the semi-empirical model. Essentially, this process involves identifying the values of the empirical parameters that minimize the error between the model's predictions and the experimental data across the entire training data set. Various methods can be used to approach this problem. In this work, the calibration issue is tackled as a minimization problem, with the objective function being the global error function (GEF) on the model output predictions. The empirical parameters serve as the variables. The GEF (Eq. (3-15)) is defined as a type of mean relative error, where x_{out} represents the generic model output variable. The index i enumerates the operating points included in the experimental data training set, n_{train}. The subscripts $calc$ and $meas$ distinguish the variables calculated by the model from those measured during the experimental tests.

$$GEF = \sqrt{\frac{1}{n_{train}} \sum_{i=1}^{n_{train}} \left(\frac{x_{out,meas} - x_{out,calc}}{x_{out,meas}} \right)^2} \tag{3-15}$$

Results of the calibration process of the heat exchangers empirical correlations for the global heat transfer coefficients calculation are included in Table 3.3. The calibration procedure is carried out for two different data set groups, one including experimental data collected in high-temperature (> 60 °C) heat source operation, and the other including experimental data collected in low-temperature (< 50 °C) heat source operation.

The model's validation was conducted using the entire set of available experimental data, divided in the two groups based on the heat source temperature level. To demonstrate the model's accuracy in predicting output variables, the GEF was quantified. The results of the validation process are highlighted in the Figure 3.13. The parity plots compare the calculated values of the output variables (i.e., the thermal power

exchanged in each heat exchanger) with the measured values. The GEF was found to be 1.7 % for the evaporator, 0.13 % for the condenser, and 1.2 % for the recuperator.

Table 3.3 - Heat exchangers models' calibrated coefficients.

Coefficients	**Evaporator**		**Condenser**		**Recuperator**	
	Low T	**High T**	**Low T**	**High T**	**Low T**	**High T**
U_{ref} $[W/(m \cdot K)]$	6.35e+04	0.4046	3.92e+03	0.0015	9.23e+02	3.7914
a $[-]$	1.026	0.9153	0.611	0.8894	0.546	0.4636
b $[-]$	-0.877	-0.9607	0.041	-0.8284	0.468	-0.0186
c $[-]$	-0.023	-0.0214	0.326	-0.0014	-	-
d $[-]$	-0.010	0.1881	-1.479	-0.0024	-	-
e $[-]$	1.117	1.2056	0.261	1.9046	-	-

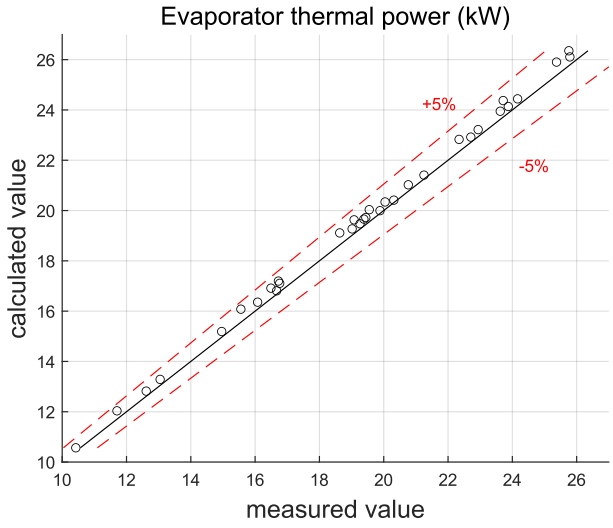

(a)

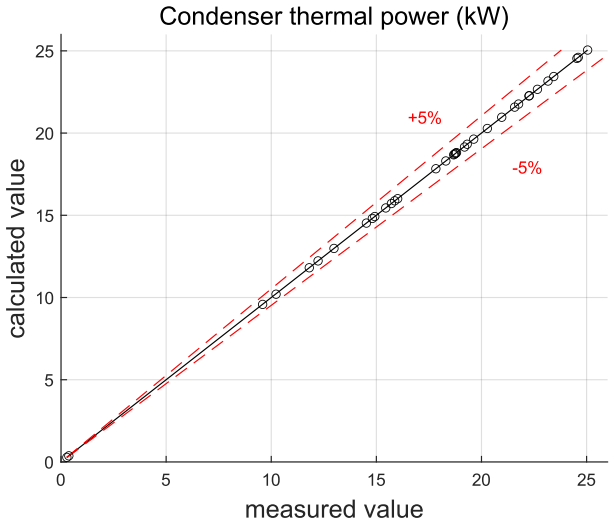

(b)

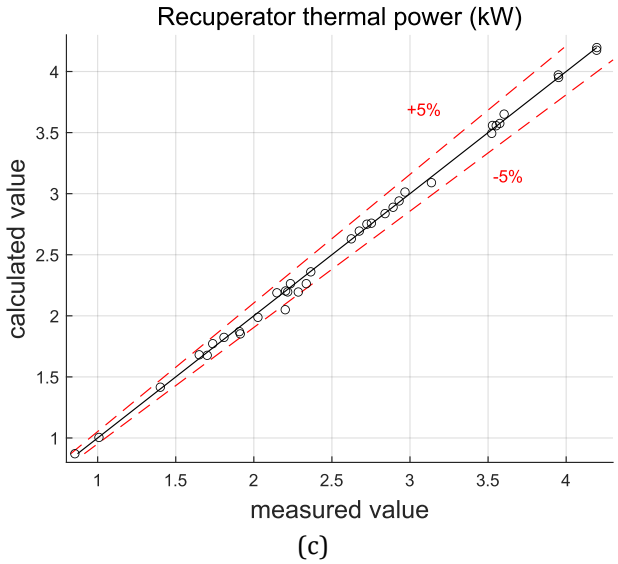

Figure 3.13 - Heat exchangers models' parity plots of the thermal power exchanged in the (a) evaporator, (b) condenser, and (c) recuperator.

3.4. Partial-evaporation micro-ORC

To enhance the technological innovation of ORC systems, the implementation of advanced cycle designs, such as the partial-evaporation cycle, is required. Indeed, the reduction of the isothermal heat of vaporization occurring in PE-ORC improves the temperature match between the heat source and the working fluid, leading to higher conversion efficiency because of reduced heat transfer losses, and increased heat exchanger effectiveness. This advantage is particularly significant with low-temperature heat sources.

Numerous articles explore the theoretical assessment of TFC and PE-ORC for optimization, design, and techno-economic analysis. Lai et al. [148] presented a thermodynamic model comparing the optimal performance of ORC and TFC with different working fluids at 80 °C-heat source temperature, finding 30 % higher net power output for TFC. McGinty et al. [149] conducted a techno-economic analysis of a 2 MW-size TFC, varying the working fluid and heat source temperature, and developed a scaled pilot test bench with a twin-screw expander and R245fa as working fluid, achieving a maximum power output of 6.2 kW and a cycle efficiency of around 4 %. Skiadopoulos et al. [150] used a semi-empirical approach to model TFC with a twin-screw expander and R113 as working fluid. Wang et al. [151] proposed a thermodynamic model of a two-phase reciprocating expander using water with a flash chamber for TFC applications, highlighting the linear increase in intake losses with the intake ratio and a corresponding decrease in isentropic efficiency. White [152] investigated a two-phase ORC system with a radial-inflow turbine, optimizing the cycle and turbine performance with various working fluids, finding that two-phase expansion can improve power output from waste-heat recovery systems by up to 30 %. Braimakis and Karellas [153] examined exergy efficiency improvements in wet expansion ORCs using zeotropic mixtures and pure fluids for waste heat temperatures between 80 °C and 200 °C. They found that partial evaporation and trilateral cycles generally achieve higher exergy efficiency compared to standard ORCs, especially with R1233zd(E)-R1234ze(E) mixtures. Despite technical challenges with zeotropic cycles, they show superior efficiency, particularly at lower temperatures. Dual-phase cycles remain competitive with isentropic efficiencies around 60 %, needing efficiencies above 50 % to compete with saturated vapor cycles. Lecompte et al. [154] compared the subcritical ORC and the PE-ORC under time-dependent operating conditions. While subcritical ORC is the industry standard due to its simplicity and low costs, PE-ORC has

shown higher power outputs in theoretical studies. Results showed that PE-ORC has an annually averaged net power output 9.6 % higher than subcritical ORC. However, using time-averaged input conditions overestimates the net power output and reduces the relative improvement of PE-ORC to 6.8 %, suggesting that comparisons should avoid time-averaged conditions. Bellos et al. [155] focused on PE-ORC for efficient utilization of low-temperature heat sources, specifically a solar-fed system using evacuated flat plate collectors and a sensible storage tank. The thermodynamic analysis, complemented by a transient analysis using TRNSYS tool, calculated annual mean efficiencies as 45.0 % for the solar field, 8.71 % for the thermodynamic cycle, and 3.68 % for the overall system.

Experimental data on two-phase expansion is limited, especially for Rankine cycles with wet expansion, which primarily focus on screw expanders. Steidel et al. [156] tested a twin-screw expander with geothermal water, achieving a maximum efficiency of 53 % with varying vapor quality between 0.08 and 0.27. Smith et al. [157] analysed a twin-screw machine using R113, concluding that isentropic efficiency can reach up to 70 % for systems below 25 kW, and over 80 % for larger systems with two-phase expansion. Öhman and Lundqvist [158] compared Lysholm turbine performance with R134a under superheated, saturated, and two-phase conditions, achieving an expander efficiency of nearly 80 % with a vapor quality of 0.7. Iqbal et al. [159] investigated a TFC-based system with isopentane, using a converging-diverging nozzle and a Pelton turbine, achieving thermal efficiency up to 14 % with heat source temperatures between 64 °C and 75 °C. Dawo et al. [160] experimentally compared ORC and PE-ORC using the same test rig and R1233zd(E), finding that ORC with fixed 10 K superheating degree presents higher thermal efficiency, while PE-ORC offers better heat transfer efficiency, especially at lower heat source temperatures.

Few studies focus on reciprocating piston expanders with wet expansion. Kanno and Shikazono [161] conducted an experimental analysis on two-phase adiabatic expansion in a single cylinder, achieving isentropic efficiencies of 86 % and 82 % with water and ethanol, respectively. Löffler [162] experimented with a flash process in a cyclone, which separates steam that is then expanded in a piston engine cylinder.

3.4.1. Contribution

To fill the literature poorness of experimental data, an experimental investigation involving the reference micro-ORC test bench operating in partial evaporation and two-phase expansion is performed. The analysis is conducted under steady-state conditions, varying the hot water temperature. For each heat source condition, the feed-pump speed is adjusted to increase the working fluid mass flow rate, thereby affecting the vapor quality at the expander inlet. Results are compared with the test bench performance regular operation, i.e., in dry expansion conditions. The main novelties introduced by this study include:

- a detailed experimental investigation of a residential-scale ORC system operating in PE mode, focusing on both the overall cycle and key components such as the expander, pump, and evaporator. Existing literature primarily examines the expansion process. The comprehensive experimental dataset is included in [163] and can serve researchers for model validation or design purposes.
- the use of very low-quality heat, testing the system with heat source temperatures ranging from 40 °C to 75 °C.
- the implementation and validation of a method to compute the working fluid quality at the outlet of the evaporator.
- the experimental demonstration of two-phase expansion using a kW-scale piston expander, while experimental studies have predominantly used different types of expanders (particularly screw expanders).
- a deep investigation of the influence of the hot secondary fluid mass flow rate on the distribution of heat transferred in the economizer and the vaporizer.

- The evaluation of effect on the condensing pressure.

3.4.2. Tests methodology

The experimental analysis involves varying the hot water temperature at the evaporator inlet. While maintaining a constant heat source temperature and hot water flow rate, the mass flow rate of the working fluid is altered by adjusting the feed-pump frequency, which in turn sets the pump's rotational speed. The shift from dry expansion (DE) to PE operation is qualitatively depicted in the temperature-entropy diagrams of Figure 3.14. These diagrams contrast the vaporization process across three scenarios with a fixed heat source temperature, TH_{in} (indicated by the yellow dashed line). Figure 3.14(a) illustrates a dry expansion scenario characterized by low mass flow rate, low evaporation pressure, and a high degree of superheating (ΔT_{SH}) at the expander inlet. As the mass flow rate increases, the evaporation pressure rises and the superheating degree diminishes, as shown in Figure 3.14(b), where ΔT_{SH} is minimized to just ensure dry expansion. Further increases in the mass flow rate lead to the condition depicted in Figure 3.14(c) (PE mode), where the vaporization process halts and the working fluid at the expander inlet is in a two-phase state. In PE mode, continuing to increase the mass flow rate will lower the vapor quality of the working fluid at the expander inlet while keeping the evaporation pressure constant.

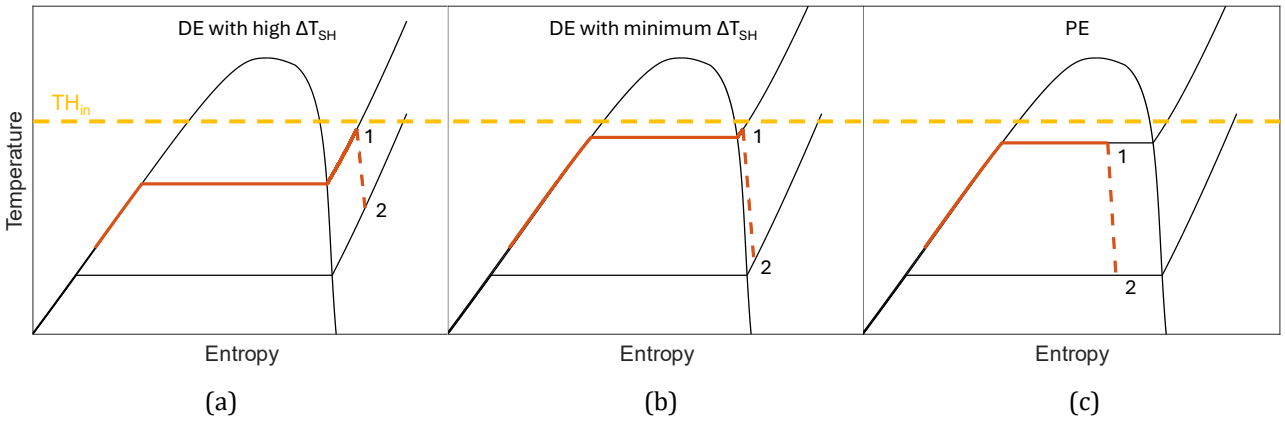

Figure 3.14 - Transition from dry expansion to partial evaporation operation: (a) dry expansion with high superheating degree, (b) dry expansion with minimum superheating degree, and (c) partial evaporation operation.

The vaporization temperature and pressure in PE mode are influenced by the hot water temperature, the working fluid flow rate, and the hot water flow rate. Assuming a constant temperature difference at the evaporator pinch point, an increase in the hot water flow rate reduces the slope of the water curve in the heat transfer diagram of the evaporator, thereby increasing the evaporation temperature and pressure. However, under the operating conditions tested in this study, the hot water flow rate has a limited impact on the cycle pressure compared to the effect of the temperature.

In this test setup, the minimum achievable vapor quality is limited by three main factors: i) the maximum pump rotating frequency, which affects the maximum flow rate of the working fluid, ii) the heat source temperature, which influences the evaporation temperature and pressure, and iii) the maximum pressure within the circuit. For example, at heat source temperatures above 80°C, the evaporating pressure exceeds 26 bar, which is the safety valve limit set to protect the test bench components. Additionally, the maximum feed-pump frequency restricts the ability to achieve near-zero vapor quality (saturated liquid) at high heat source temperatures.

The experimental test points are defined by the heat source temperature, which ranges from 40 °C to 75 °C, and the feed-pump frequency, which varies from 15 Hz to 60 Hz, corresponding to a pump shaft rotational speed between 75 rpm and 300 rpm. Figure 3.15 shows the set of boundary conditions in terms

of heat source temperature and pump frequency. The cross markers indicate the operating points in DE mode, all characterized by a superheating degree at the expander inlet between 3 K and 7 K. The dot markers indicate the operating points in PE mode.

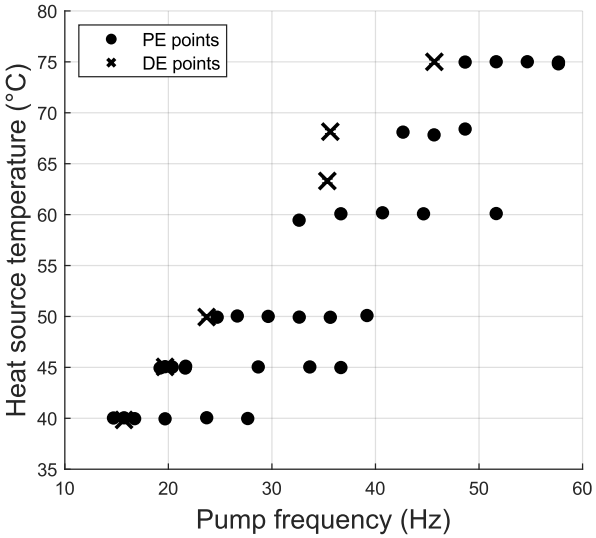

Figure 3.15 - Experimental tests controlled boundary conditions: heat source temperature and pump frequency.

3.4.3. Quality assessment and performance indexes

To determine the thermodynamic state of the working fluid when it is in single-phase conditions (either subcooled liquid or superheated vapor), the CoolProp function [27] is used, utilizing temperature and pressure as inputs. This is described in Eq. (3-16), where $CPfun$ signifies the CoolProp function, and the subscript i refers to specific sections of the ORC system as depicted in the layout in Figure 3.2.

$$h_i = CPfun(p_i, T_i) \qquad i = 4, 5, 6, 7 \tag{3-16}$$

When the ORC operates under PE conditions, direct measurements do not provide complete thermodynamic data for the working fluid at points 1, 2, and 3 (corresponding respectively to the expander inlet, expander outlet, and recuperator outlet). In the two-phase region, temperature and pressure alone are insufficient to determine enthalpy or vapor quality.

Therefore, to fully ascertain the thermodynamic states in PE mode, a thermal balance approach is used for the heat exchangers to calculate enthalpy values in the two-phase region. Specifically, the specific enthalpy of the working fluid at the evaporator outlet (or expander inlet, h_1) is determined by applying a thermal balance at the evaporator, as shown in Eq. (3-17). The enthalpy of the fluid entering the evaporator (h_7) is calculated using CoolProp (through Eq. (3-16)), based on measured temperature and pressure (T_7 and p_7), as the fluid is in the subcooled phase at the evaporator inlet.

$$h_1 = h_7 + \frac{\dot{V}H \cdot \rho H}{\dot{m}_{wf}} \cdot c_p H \cdot (TH_{in} - TH_{out}) \tag{3-17}$$

In Equation (3-17), $\dot{V}H$, ρH, and $c_p H$ represent the volume flow rate, density, and specific heat of the water, respectively. These values are accurately computed using CoolProp as functions of the measured temperature and pressure of the hot water.

Similarly, the enthalpy at the condenser inlet (h_3) is calculated through a thermal balance at the condenser, as indicated in Eq. (3-18). The enthalpy of the subcooled liquid at the condenser outlet (h_4) is

determined using CoolProp (through Eq. (3-16)), based on temperature and pressure measurements. Finally, the enthalpy at the expander outlet (h_2) is obtained from the thermal balance in the recuperator, as shown in Eq. (3-19), assuming a constant mass flow rate of the working fluid throughout the ORC circuit.

$$h_3 = h_4 + \frac{\dot{V}C \cdot \rho C}{\dot{m}_{wf}} \cdot c_p C \cdot (TC_{out} - TC_{in}) \tag{3-18}$$

$$h_2 = h_3 + (h_7 - h_6) \tag{3-19}$$

Heat losses are excluded from the balance Eqq. (3-17), (3-18), and (3-19) under the assumption that the evaporator and recuperator are thermally insulated and that the condenser operates near ambient temperature, making thermal losses negligible.

Once enthalpy values are calculated for all sections of the circuit, the complete thermodynamic cycle of the PE-ORC is determined. The vapor quality at the two-phase points (1, 2, and 3) is then derived using pressure and enthalpy as inputs to the CoolProp library, as described in Eq. (3-20).

$$x_i = CPfun(p_i, h_i) \qquad i = 1,2,3 \tag{3-20}$$

To validate the accuracy of the energy balance method used to determine the thermodynamic states of the organic fluid in the two-phase sections, the same approach was applied to experimental data obtained under DE operating mode. The specific enthalpies in sections 1, 2, and 3 of the cycle were calculated using the thermal balance at the heat exchangers (following Eqq. (3-17), (3-18), and (3-19)), and these results were compared with the values provided by the CoolProp library, based on measured temperatures and pressures. Figure 3.16 and Figure 3.17 demonstrate that the accuracy achieved with the energy balance method is sufficient for this study. The parity plot of specific enthalpy at the expander inlet in DE mode, shown in Figure 3.16, indicates that the error in the energy balance calculation is consistently below 5 % compared to the direct evaluation via CoolProp. Additionally, Figure 3.17 illustrates that the more accurate value computed using CoolProp falls within the uncertainty range of the value obtained through the thermal balance.

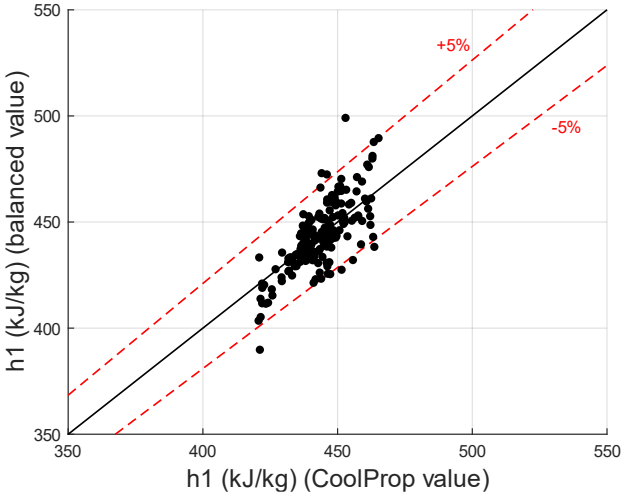

Figure 3.16 - Parity of the specific enthalpy at the expander inlet (h_1) in DE mode: h_1 computed through the thermal balance of the evaporator versus h_1 from CoolProp.

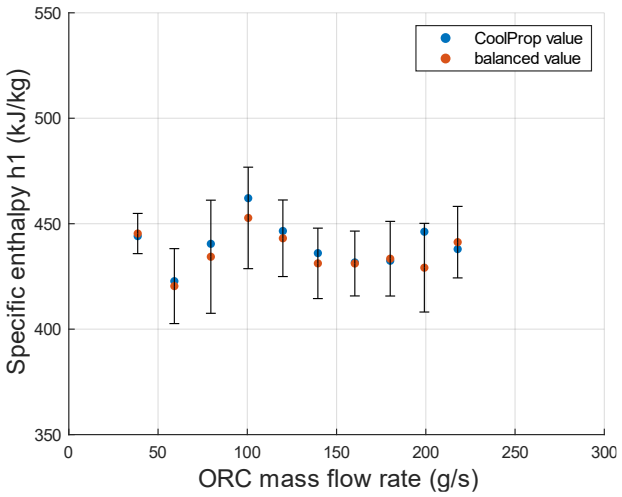

Figure 3.17 - Specific enthalpy at the expander inlet (h_1) in DE mode versus working fluid mass flow rate.

With all the thermodynamic states established, the system performance can be evaluated.

The working fluid behaviour in the evaporator is crucial for understanding the operation of the ORC system under partial evaporation conditions. Key observations are related to the trend of the thermal power transferred in the evaporator ($\dot{Q}_{ev}$) and the working fluid's specific enthalpy rise in the component ($\Delta h_{ev} = h_1 - h_7$). Furthermore, the evaporator's performance is evaluated using the concept of heat transfer effectiveness, considering the plate evaporator as a counter-flow heat exchanger with no heat losses to the environment. Generally, the effectiveness of a heat exchanger is the ratio of the actual heat transferred to the maximum possible heat transferable if the surface area were infinite ($\varepsilon = {\dot{Q}}/{\dot{Q}_{max}}$) [164]. Given the phase change process, the evaporator is effectively split into two sections: the economizer (eco) and the vaporizer (vap), corresponding to the flow direction inside the heat exchanger. The effectiveness for each section is calculated using Eq. (3-21) and Eq. (3-22). Both equations stem from the same definition but differ in their final forms: for the economizer, effectiveness is calculated from the perspective of the organic fluid side, whereas for the vaporizer, it is based on the water side [165]. In Eq. (3-21), $h_{ev,L}$ represents the enthalpy of the saturated liquid at the vaporization pressure, and h_7 denotes the enthalpy at the evaporator inlet. The term $h_{\Delta Tpp=0}$ indicates the liquid enthalpy at a saturation temperature equal to the water temperature at the pinch point, TH_{pp}, assuming an ideal zero temperature difference at the pinch point. Eq. (3-22) calculates the effectiveness of the vaporizer section using the terminal temperature difference, assuming constant values for water's specific heat (c_pH), volume flow rate ($\dot{V}H$), and density (ρH). A comprehensive effectiveness for the evaporator is then derived using Eq. (3-23), which employs the average effectiveness of the economizer and vaporizer sections (ε_{eco} and ε_{vap}), weighted by their respective ideal thermal powers ($\dot{Q}_{eco}$ and $\dot{Q}_{vap}$). The parameter UA, representing the product of the overall heat transfer coefficient and the heat transfer surface area, is calculated for both the economizer and vaporizer sections using Eqq. (3-24) and (3-25).

$$\varepsilon_{eco} = \frac{\dot{Q}_{eco}}{\dot{Q}_{eco,max}} = \frac{\dot{m}_{wf}\cdot(h_{ev,L}-h_7)}{\dot{m}_{wf}\cdot(h_{\Delta Tpp=0}-h_7)} = \frac{(h_{ev,L}-h_7)}{(h_{\Delta Tpp=0}-h_7)} \tag{3-21}$$

$$\varepsilon_{vap} = \frac{\dot{Q}_{vap}}{\dot{Q}_{vap,max}} = \frac{\dot{V}H\cdot\rho H\cdot c_pH\cdot(TH_{in}-TH_{pp})}{\dot{V}H\cdot\rho H\cdot c_pH\cdot(TH_{in}-T_{vap})} = \frac{TH_{in}-TH_{pp}}{TH_{in}-T_v} \tag{3-22}$$

$$\varepsilon_{ev} = \frac{\dot{Q}_{eco}+\dot{Q}_{vap}}{\dot{Q}_{eco,max}+\dot{Q}_{vap,max}} = \frac{\varepsilon_{eco}\cdot\dot{Q}_{eco,max}+\varepsilon_{vap}\cdot\dot{Q}_{vap,max}}{\dot{Q}_{eco,max}+\dot{Q}_{vap,max}} \tag{3-23}$$

$$UA_{\mathrm{eco}} = \frac{\dot{Q}_{\mathrm{eco}}}{LMTD_{eco}} = \frac{\dot{m}_{wf}\cdot(h_{ev,L}-h_7)}{(TH_{pp}-T_v)-(TH_{out}-T_7)}\cdot\ln\left(\frac{TH_{pp}-T_v}{TH_{out}-T_7}\right) \tag{3-24}$$

$$UA_{\mathrm{vap}} = \frac{\dot{Q}_{\mathrm{vap}}}{LMTD_{vap}} = \frac{\dot{m}_{wf}\cdot(h_1-h_{ev,L})}{(TH_{in}-T_v)-(TH_{pp}-T_v)}\cdot\ln\left(\frac{TH_{in}-T_v}{TH_{pp}-T_v}\right) \tag{3-25}$$

Expander efficiency (η_{exp}) is computed using Eq. (3-26), with $\dot{W}_{exp,el}$ and $h_{2,is}$ representing respectively the electric power generated by the expander and the specific enthalpy at the expander outlet under ideal (isentropic) conditions. The expander filling factor (FF) is defined in Eq. (3-27), where ρ_1 is the density at the expander inlet, N_{exp} is the rotating speed in rpm, and V_{exp} is the expander's total displacement. The feed-pump's total efficiency (η_{pump}) is calculated using Eq. (3-28), as the ratio of the ideal hydraulic power to the electric power consumed by the pump ($\dot{W}_{pump,el}$). The density at the pump inlet (ρ_5) is directly measured by a Coriolis flow meter. Finally, the pump's volumetric efficiency

($\eta_{pump,vol}$) is determined using Eq. (3-29), where N_{pump} and V_{pump} represent the pump's rotational speed in rpm and its displacement, respectively.

$$\eta_{exp} = \frac{\dot{W}_{exp,el}}{\dot{m}_{wf} \cdot (h_1 - h_{2,is})} \tag{3-26}$$

$$FF = \frac{\dot{m}_{wf}}{\rho_1 \cdot N_{exp}/60 \cdot V_{exp}} \tag{3-27}$$

$$\eta_{pump} = \frac{\dot{m}_{wf} \cdot (p_6 - p_4)}{\rho_5 \cdot \dot{W}_{pump,el}} \tag{3-28}$$

$$\eta_{pump,vol} = \frac{\dot{m}_{wf}}{\rho_5 \cdot N_{pump}/60 \cdot V_{pump}} \tag{3-29}$$

The overall ORC efficiency (η_{ORC}) is computed using Eq. (3-30) as the ratio of net electric power ($\dot{W}_{net}$) to the thermal power transferred in the evaporator ($\dot{Q}_{ev}$). The second law efficiency (η_{II}) is calculated using Eq. (3-31), which is the ratio of the overall efficiency to the Carnot efficiency (η_{Carnot}), based on the same hot source and cold sink temperatures. The back work ratio (BWR), defined in Eq. (3-32) as the ratio of the pump power consumption to the expander power output, is particularly important in small-scale ORCs with low-critical temperature fluids, where pump consumption significantly affects net power output, even exceeding 10 % in well-designed systems [4].

$$\eta_{ORC} = \frac{\dot{W}_{net}}{\dot{Q}_{ev}} = \frac{\dot{W}_{exp,el} - \dot{W}_{pump,el}}{\dot{m}_{wf} \cdot (h_1 - h_7)} \tag{3-30}$$

$$\eta_{II} = \frac{\eta_{ORC}}{\eta_{Carnot}} = \frac{\dot{W}_{exp,el} - \dot{W}_{pump,el}}{\dot{Q}_{ev}} \cdot \frac{1}{1 - {TC_{in}}/{TH_{in}}} \tag{3-31}$$

$$BWR = \frac{\dot{W}_{pump,el}}{\dot{W}_{exp,el}} \tag{3-32}$$

In the whole analysis, the uncertainty contributions are calculated according to the methodology illustrated in subsection 3.2.2 and shown in the results. Indeed, in the figures presented in the next subsection, the experimental data are represented with their corresponding error bands obtained applying the above-mentioned procedure.

3.4.4. Experimental results

The results in this subsection are based on steady-state experimental tests, presented as average values over time periods where key variables remain stable. The steady-state detection method follows the approach depicted in subsection 3.2.1. The comparison between experimental results from PE mode and DE mode, both at the same heat source temperatures, is shown with DE mode data marked by cross markers in the figures. Since the test rig is not optimized for PE, the results should be viewed qualitatively, focusing on trends and performance variable dependencies compared to DE mode.

In PE conditions, the mass flow rate of the working fluid ($\dot{m}_{wf}$) as a function of pump frequency (f_{pump}) mirrors the trend observed in DE operation, though there is a slight increase in $\dot{m}_{wf}$ at constant frequencies in PE mode (refer to Figure 3.18). The flow rate rises with increasing pump frequency, ranging from a minimum of about 40 g/s at 15 Hz to a maximum of nearly 250 g/s at 58 Hz. Additionally, the heat source temperature has a secondary effect on the mass flow rate, where higher temperatures slightly decrease the flow rate at the same pump frequency.

Figure 3.19 illustrates the relationship between evaporation pressure (p_1) and mass flow rate across different hot water temperatures. It is evident that p_1 is primarily influenced by the heat source temperature, fluctuating between 9 bar and 21 bar as the temperature increases from 40 °C to 75 °C. This contrasts with DE operation, where increasing the flow rate typically raises the evaporation pressure. In PE mode, the evaporation pressure remains nearly constant despite variations in the mass flow rate when the heat source temperature (TH_{in}) is fixed.

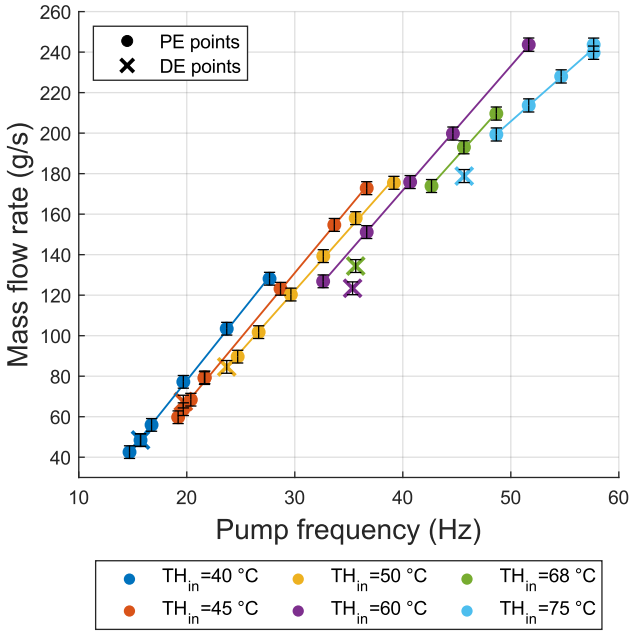

Figure 3.18 - Working fluid mass flow rate ($\dot{m}_{wf}$) versus pump frequency (f_{pump}), varying the heat source temperature (TH_{in}).

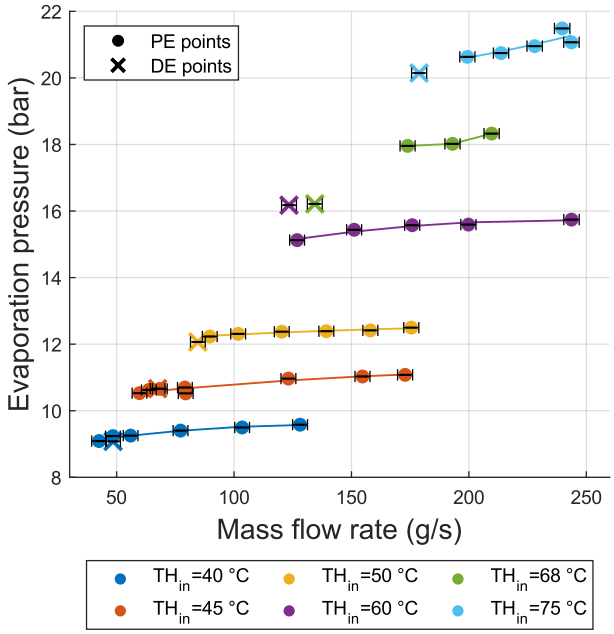

Figure 3.19 - Evaporation pressure (p_1) versus working fluid mass flow rate ($\dot{m}_{wf}$), varying the heat source temperature (TH_{in}).

Experimental observations also show that the condensation pressure (p_4) does not significantly change with different pump frequencies (see Figure 3.20), so the pressure difference across the expander is mainly affected by the heat source temperature.

As the flow rate increases in PE mode, the vapor quality at the expander inlet (x_1) decreases, as depicted in Figure 3.21, which shows vapor quality as a function of mass flow rate and hot water temperature. Different trends are associated with each TH_{in} value: at a constant mass flow rate, lower vapor qualities are achieved with lower hot water temperatures. When the hot water temperature is constant, increasing the working fluid mass flow rate decreases the vapor quality. At the maximum tested heat source temperature, i.e., at 75 °C, the saturation condition is reached with a flow rate around 200 g/s, while the minimum vapor quality is slightly above 0.7 when close to 250 g/s (corresponding to a pump frequency of 58 Hz, near the maximum setting of 60 Hz). The lowest vapor quality, approximately 0.20, is achieved with low hot water temperature values (around 40 °C) and mass flow rates in the range of 130-170 g/s. Higher hot water temperatures necessitate a higher minimum mass flow rate to operate in PE mode. It is noted that with heat source temperatures of 40 °C and 45 °C, even the minimum pump frequency (16-18 Hz) induces a two-phase condition at the expander inlet, with vapor quality ranging from 0.95 to 1.0.

Consequently, for the ORC system under analysis, partial evaporation may be the only operational mode if the evaporator is supplied with temperatures below 45 °C.

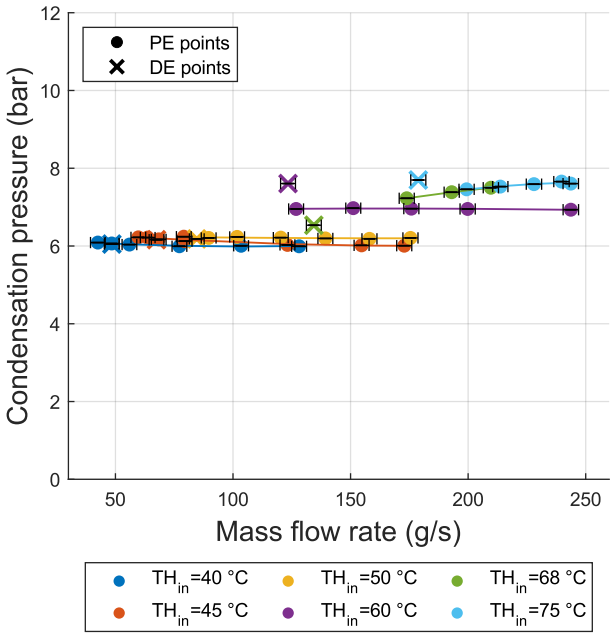

Figure 3.20 - Condensation pressure (p_4) versus working fluid mass flow rate ($\dot{m}_{wf}$), varying the heat source temperature (TH_{in}).

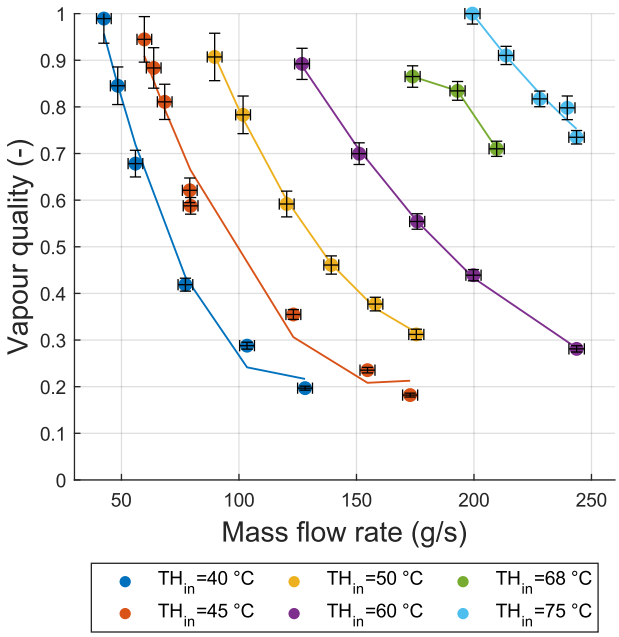

Figure 3.21 - Vapor quality (x_1) versus working fluid mass flow rate ($\dot{m}_{wf}$), varying the heat source temperature (TH_{in}).

Analysing the variables related to the evaporator, Figure 3.22 shows that the exchanged thermal power primarily depends on the heat source temperature, with minimal impact of the working fluid mass flow rate. This contrasts with DE mode operation, where the thermal power exchanged in the evaporator and condenser is almost linearly related to the mass flow rate, with little influence from the water temperature [129]. This contrast is linked to the working fluid enthalpy (Δh_{ev}) trend in the evaporator (Figure 3.23).

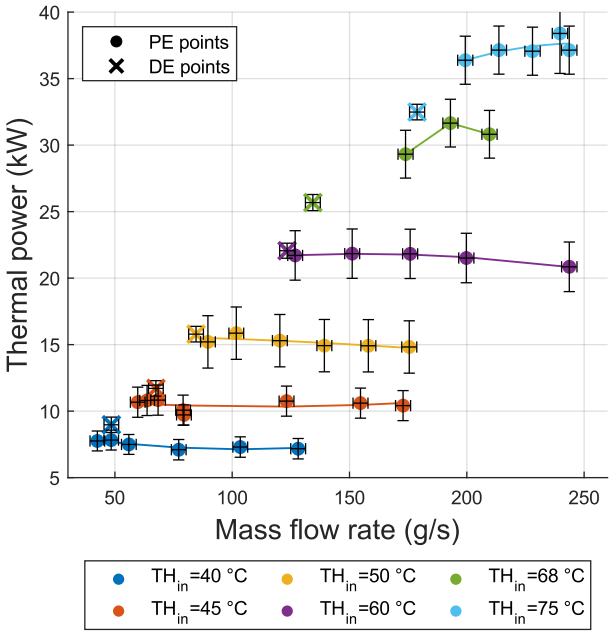

Figure 3.22 - Thermal power exchanged in the evaporator ($\dot{Q}_{ev}$) versus working fluid mass flow rate ($\dot{m}_{wf}$), varying the heat source temperature (TH_{in}).

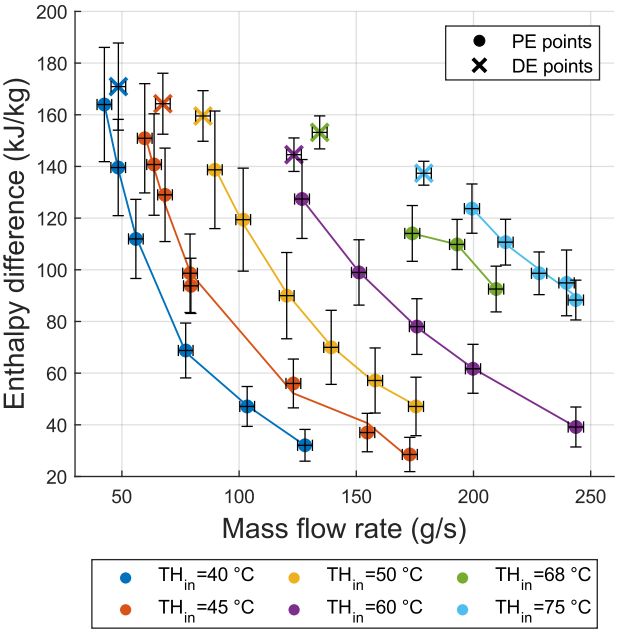

Figure 3.23 – Working fluid enthalpy rise in the evaporator (Δh_{ev}) versus working fluid mass flow rate ($\dot{m}_{wf}$), varying the heat source temperature (TH_{in}).

In DE mode, Δh_{ev} remains relatively stable (between 140 kJ/kg and 170 kJ/kg) across various heat source temperatures and working fluid flow rates. However, in PE operation, Δh_{ev} decreases with increasing mass flow rate and decreasing vapor quality, ranging from 30 to 160 kJ/kg. This decrease offsets the mass flow rate increase, leading to minor variations in transferred thermal power at constant temperatures, as seen in Figure 3.22. The thermal power ranges from a minimum of around 7 kW at lower temperatures to a maximum of just over 37 kW at higher temperatures.

Figure 3.24 illustrates the effectiveness trends for individual zones and the overall evaporator effectiveness as functions of the working fluid mass flow rate. The economizer effectiveness (ε_{eco}, blue markers) remains nearly constant, close to unity under all tested PE conditions, with a slight dip below 0.85 at low flow rates (below 100 g/s). The vaporizer effectiveness (ε_{vap}, red markers) ranges from 0.6 to 0.7 for most operating conditions, showing a slight decrease at lower flow rates. Consequently, the overall effectiveness (ε_{ev}, yellow markers) peaks slightly above 0.8 and generally stays between 0.65 and 0.75 under the tested conditions. Comparing these values with those from DE mode (cross markers in Figure 3.24, and more in detail in [129]) some observations can be highlighted. First, in DE mode, the evaporator effectiveness varies widely, increasing with the flow rate and decreasing with the heat source temperature. This trend is due to the pinch point temperature difference, which is larger when the superheating degree is high, typically at high temperatures and low evaporation pressures (and low flow rates). The significant increase in effectiveness under PE conditions, where values range from 0.1 to 0.6 in dry conditions, is largely due to improvements in the performance of the economizer and vaporizer zones, rather than the absence of a superheater in PE mode. In DE conditions, the superheated working fluid temperature at the outlet of the evaporator (T_1) is nearly equal to the hot water inlet temperature (TH_{in}), resulting in a superheater effectiveness close to 1. The thermal power exchanged in the superheater is relatively small compared to that in the economizer and vaporizer due to the generally low superheating degree. The positive effect in PE mode is attributed to the increase in economizer effectiveness, which is more pronounced at high mass flow rates, rising from 0.8–0.9 in DE conditions to nearly 1 in PE mode. Additionally, the proportion of heat transferred by the economizer increases significantly, reaching up to 50 % of the total evaporator thermal power, which enhances the overall effectiveness. The vaporizer effectiveness also shows an improvement, averaging around 0.65 in PE mode.

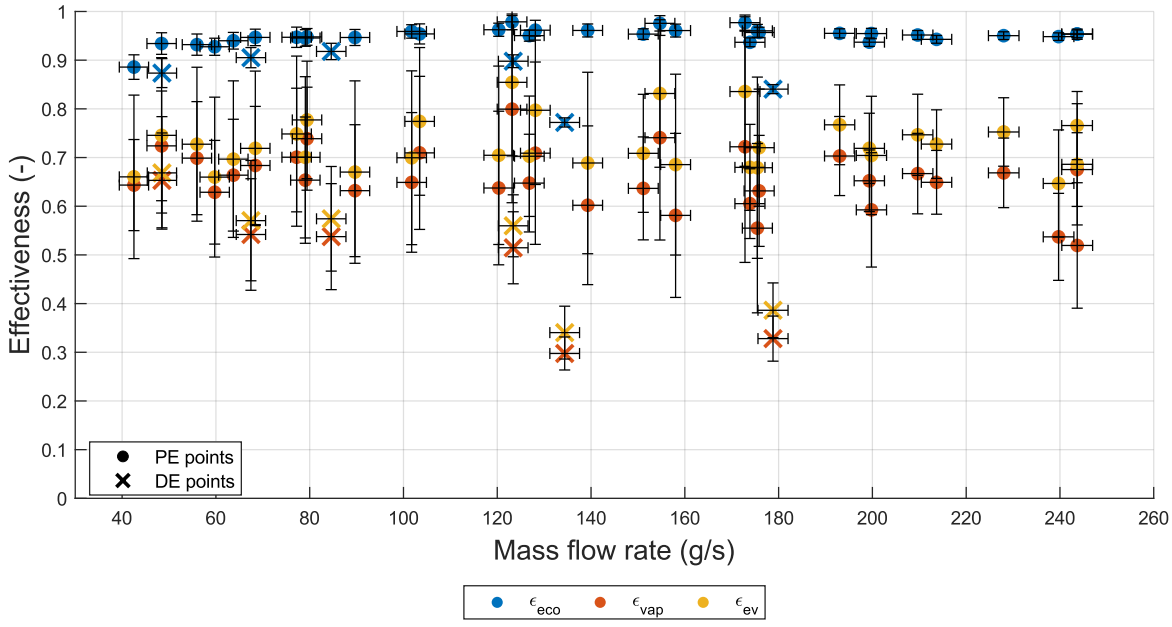

Figure 3.24 - Evaporation process effectiveness (ε_{eco}, ε_{vap} and ε_{ev}) versus working fluid mass flow rate ($\dot{m}_{wf}$).

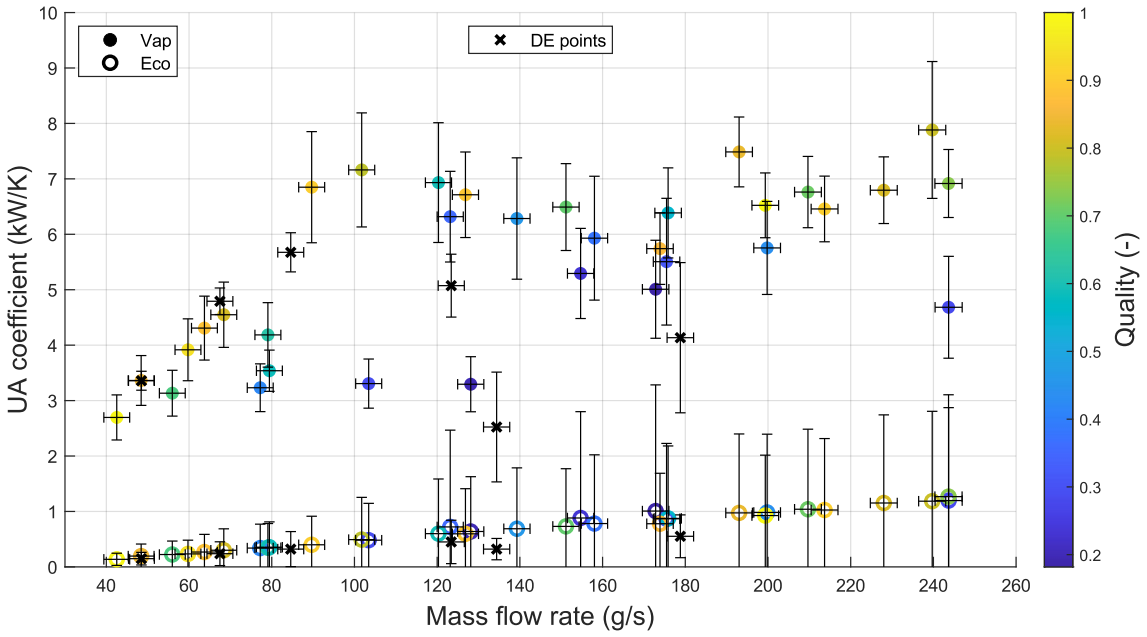

Figure 3.25 - UA coefficients for the evaporator economizer and vaporizer sections versus working fluid mass flow rate ($\dot{m}_{wf}$) and vapor quality (x_1).

Both improvements result from a substantial reduction in the temperature difference between the water and working fluid at the pinch point ($\Delta\tau_{pp}$). The benefits of PE operation on economizer and vaporizer effectiveness are more significant when compared to DE points with a high superheating degree, as this condition increases $\Delta\tau_{pp}$. Figure 3.25 presents the UA coefficient for both the economizer and vaporizer, indicating higher average values in PE conditions, especially at working fluid flow rates above 80 g/s. The economizer UA coefficient (UA_{eco}) increases almost linearly with mass flow rate, ranging from 0.2 kW/K to 1.2 kW/K. The vaporizer UA coefficient (UA_{vap}) varies between 3 and 5 kW/K at low mass flow rates and between 5 and 8 kW/K at medium to high flow rates. It is also noted that UA_{vap} values exceeding 6 kW/K are achieved with vapor qualities above 0.5.

The influence of changes in the hot water flow rate and the organic fluid flow rate is illustrated in the heat transfer diagrams of Figure 3.26.

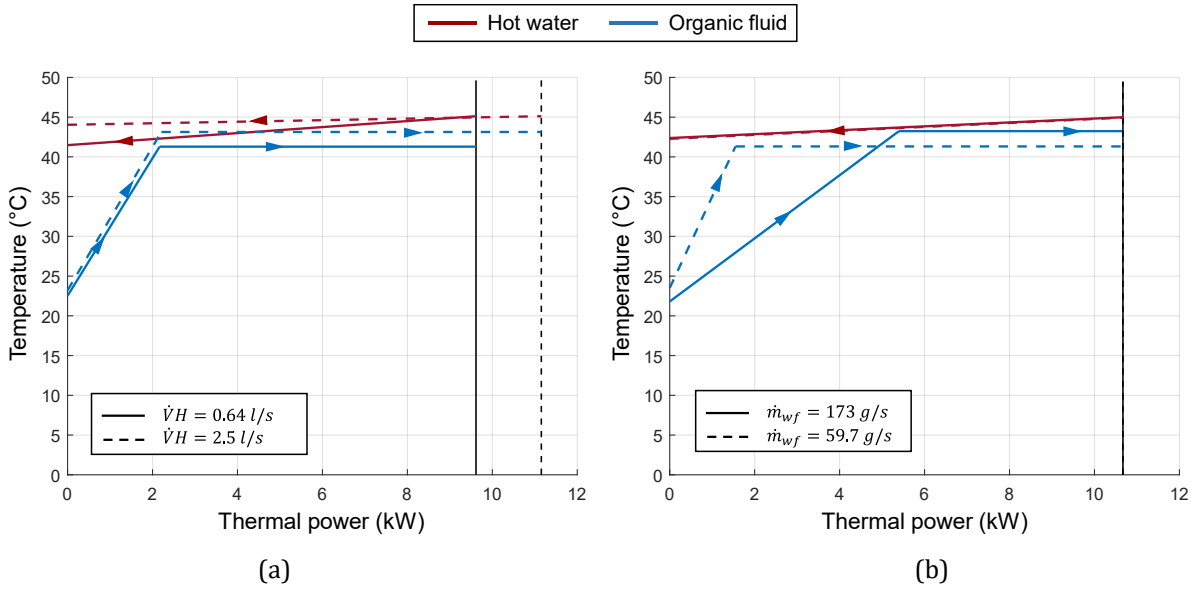

Figure 3.26 - Effect of the variation of the (a) hot water flow rate ($\dot{V}H$) and (b) working fluid flow rate ($\dot{m}_{wf}$) in the heat transfer diagram, at constant heat source temperature (TH_{in}) of 45 °C.

In Figure 3.26(a), two operating conditions are shown with the same heat source temperature ($TH_{in} \cong 45\ °C$) and the mass flow rate of the organic fluid constant at 80 g/s. The hot water flow rate ($\dot{V}H$) is varied from 0.64 l/s (solid line) to 2.5 l/s (dashed line), resulting in an increase in the evaporation temperature by nearly 2 K and a corresponding rise in the evaporation pressure by about 0.5 bar, from 10.5 bar to 11.0 bar. This increase in p_1 is due to the slope reduction of the water curve in the diagram as the water flow rate increases, while the pinch point temperature difference remains around 1 K. Consequently, the transferred thermal power rises from 9.7 kW to 11.3 kW, as shown in Figure 3.26(a). Since the pinch point position does not change, the thermal power increase is attributed to the higher power exchanged in the vaporization zone, with the economizer heat remaining constant. This indicates that the vapor quality at the evaporator outlet varies between the two conditions, decreasing as the water flow rate decreases. Specifically, in Figure 3.26(a), the quality x_1 changes from 0.6 to 0.75.

In Figure 3.26(b), a different scenario is presented where the temperature and flow rate of the hot water are kept constant at 45 °C and 1.0 l/s, respectively. Instead, the feed-pump speed is adjusted increasing the organic fluid mass flow rate from 60 g/s to 170 g/s (solid and dashed lines, respectively). The increase in $\dot{m}_{wf}$ leads to a change in the evaporation temperature by nearly 2 K, raising the pressure from 10.5 bar to 11.1 bar. Differently from the case in Figure 3.26(a), the rise in evaporation pressure here is linked to a decrease in the pinch point temperature difference, which drops from 1.3 K to 0.5 K as the mass flow rate increases. The pinch point position shifts to the right in the diagram, reducing the heat transferred in the vaporizer zone while increasing the thermal power exchanged in the economizer. As a result, the vapor quality x_1 decreases, dropping from 0.94 to 0.2 in the case shown in Figure 3.26(b), as the mass flow rate increases.

Figure 3.27, displaying the expander's electric power ($\dot{W}_{exp,el}$) trend, reveals that the expander's performance in PE mode diverges significantly from the dry expansion operation. At a constant heat source temperature, the electric power diminishes as the mass flow rate increases due to the decreased vapor quality at the expander inlet, resulting in less vapor expansion within the cylinders. The highest values obtained for $\dot{W}_{exp,el}$ are around 130 W at 40 °C, nearly 580 W at 60 °C, and approximately 1160 W at 75 °C. The rotational speed of the expander (N_{exp}) follows a similar trend to the power output, as illustrated in Figure 3.28. The decrease in N_{exp} with increasing mass flow rate (and simultaneous decreasing vapor quality) can be attributed to the higher density of the working fluid at the expander inlet. The variation range of N_{exp} is 190–240 rpm at 40 °C, 400–500 rpm at 60 °C, and 700–850 rpm at 75 °C.

Figure 3.29 presents the expander filling factor (FF), calculated according to Eq. (3-27). FF results show a general decreasing trend with the working fluid mass flow rate and the heat source temperature. The highest FF values in PE mode (0.9–1.0) are achieved at temperatures up to 45 °C, while the average FF for temperatures from 50 °C to 68 °C is between 0.7 and 0.8. The minimum average FF value of 0.6 occurs at 75 °C. Compared to the DE mode, in PE mode there is a noticeable improvement in the filling factor, likely due to the lower expander speed at the same TH_{in}, as it was also observed in DE operation where the filling factor generally decreases with increased expander speed [72]. The expander total efficiency (η_{exp}), calculated according to Eq. (3-26) and depicted in Figure 3.30, increases with the expander speed. As the temperature rises, the average η_{exp} decreases, ranging from 0.30–0.38 at 40 °C, 0.26–0.34 at 60 °C, and 0.26–0.31 at 75 °C. The reduction in vapor quality when increasing the working fluid mass flow rate penalizes η_{exp} by increasing expansion losses and reducing power output.

In general, expander performance is penalized in wet expansion compared to dry expansion. This penalty is more pronounced for vapor quality values below 0.5 and at high heat source temperatures, especially at 75 °C, where efficiency remains below 30 % regardless of vapor quality x_1. At constant temperature, the efficiency reduction between the DE and PE experimental points at the highest vapor quality is limited in most cases (within 5 percentage points). This suggests that working conditions with high vapor quality (above 0.8) may result in limited penalization of expander performance, which could

be beneficial for systems designed for DE operation but forced to work in PE mode.

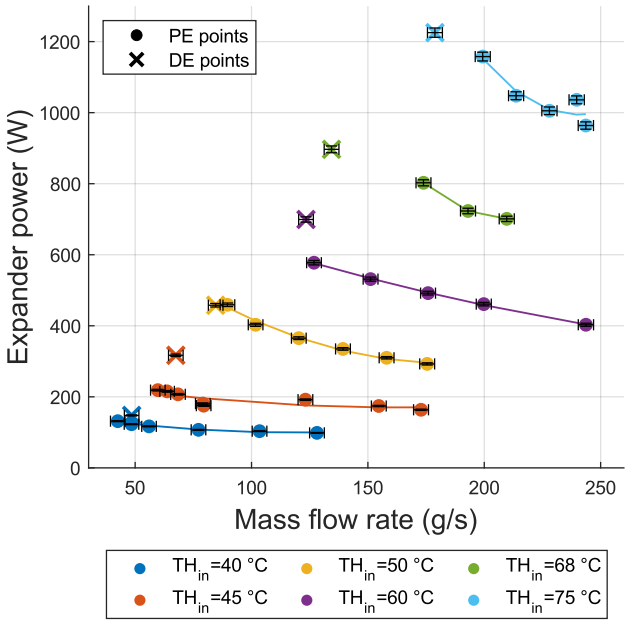

Figure 3.27 - Electrical power generated by the expander ($\dot{W}_{exp,el}$) versus working fluid mass flow rate ($\dot{m}_{wf}$), varying the heat source temperature (TH_{in}).

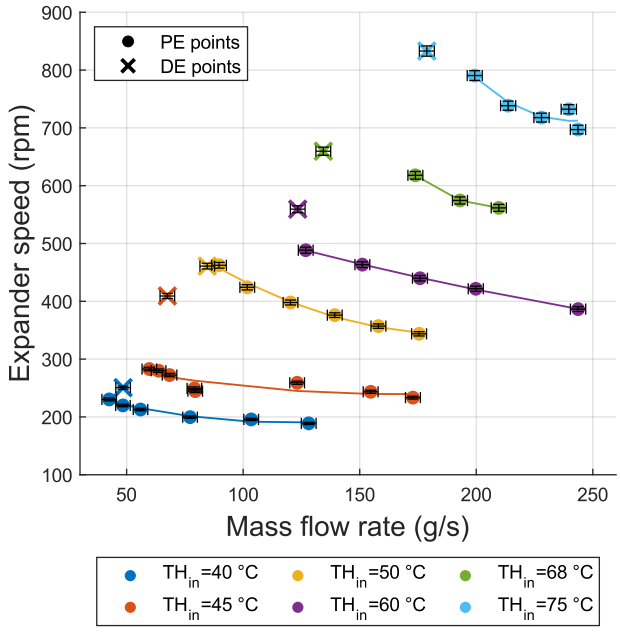

Figure 3.28 - Expander speed (N_{exp}) versus working fluid mass flow rate ($\dot{m}_{wf}$), varying the heat source temperature (TH_{in}).

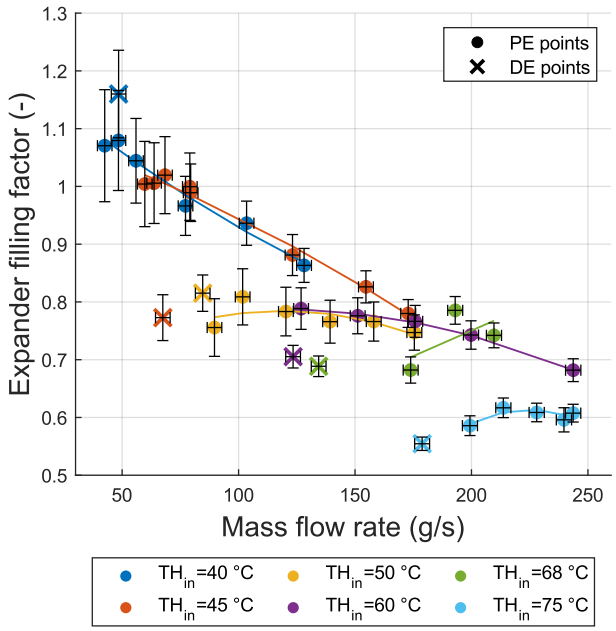

Figure 3.29 - Expander filling factor (FF) versus working fluid mass flow rate ($\dot{m}_{wf}$), varying the heat source temperature (TH_{in}).

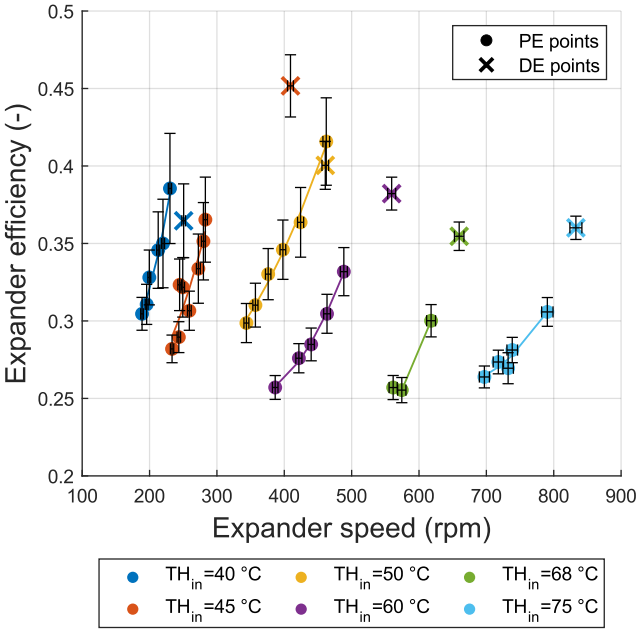

Figure 3.30 - Expander total efficiency (η_{exp}) versus expander speed (N_{exp}), varying the heat source temperature (TH_{in}).

The analysis of the feed-pump results indicates that PE mode operation leads to better performance in terms of volumetric efficiency and total efficiency, compared to DE mode. The pump volumetric efficiency ($\eta_{pump,vol}$), calculated according to Eq. (3-28) and shown in Figure 3.31, increases with the mass flow rate, reaching the maximum values (around 73 %) at the minimum vapor quality for each heat source temperature up to 60 °C. At higher temperatures (68 °C and 75 °C, green and light blue markers,

respectively), the maximum $\eta_{pump,vol}$ is around 65 %. In dry expansion, the maximum pump volumetric efficiency is about 60 %, with the minimum below 45 %. The total efficiency of the feed pump (η_{pump}), calculated according to Eq. (3-28) and depicted in Figure 3.32, shows a general increasing trend with the working fluid mass flow rate, with the curves shifting up as the heat source temperature increases. The maximum η_{pp} in PE conditions is around 37 %, significantly higher than the maximum efficiency in dry expansion, close to 30 %. At a constant heat source temperature, the improvement in η_{pump} is mainly due to the higher mass flow rate achieved in PE conditions, as η_{pump} increases almost linearly with $\dot{m}_{wf}$.

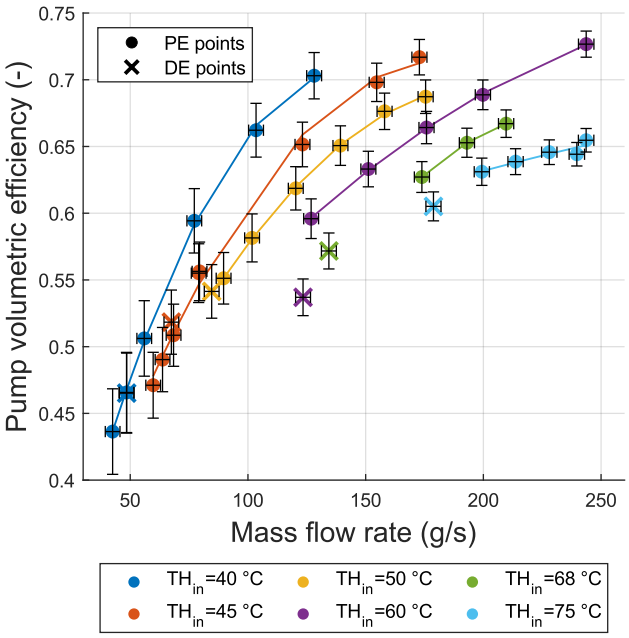

Figure 3.31 - Pump volumetric efficiency ($\eta_{pump,vol}$) versus working fluid mass flow rate ($\dot{m}_{wf}$), varying the heat source temperature (TH_{in}).

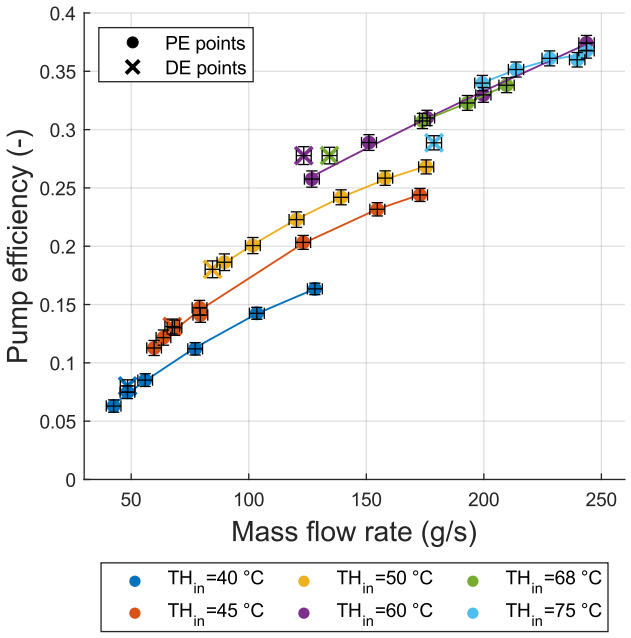

Figure 3.32 - Pump total efficiency (η_{pump}) versus working fluid mass flow rate ($\dot{m}_{wf}$), varying the heat source temperature (TH_{in}).

The combination of the power plant's very small size, the relatively low performance of the machines, and the system not being optimized for partial evaporation mode significantly impacts the net power output, despite the pump's total efficiency improvement in PE mode. This is particularly noticeable at the lowest tested heat source temperature values. Indeed, the comparison between the expander production and the feed-pump consumption trends, in Figure 3.33, and the back work ratio (BWR) trend, in Figure 3.34, shows that the pump consumes more power compared to the expander production when the temperature is below 45 °C. The optimal condition ($BWR \approx 50\%$) is achieved at nearly superheated vapour (hence minimal flow rate) with temperatures ranging from 50 °C to 75 °C.

The overall performance, shown as second law efficiency (η_{II}, Eq. (3-31)), is depicted in Figure 3.35 (this figure only includes points with a positive η_{II}). At a constant heat source temperature, efficiency decreases as the working fluid mass flow rate increases. η_{II} values are quite low, never overcoming 15 %. Even in DE mode, the feed-pump consumption significantly lowers the second law efficiency, ranging between 10 % and 15 %. At a heat source temperature of 40 °C, the micro-ORC system produces no net power, even in DE mode.

Figure 3.36 illustrates the relative variations of key performance indicators in PE operation compared to dry expansion. The selected indicators are the expander power ($\dot{W}_{exp,el}$), efficiency (η_{exp}), and filling factor (FF); the pump total and volumetric efficiency (η_{pump} and $\eta_{pump,vol}$); the evaporator effectiveness (ε_{ev}); the back work ratio (BWR); and the second law efficiency (η_{II}). For PE mode, the relative variation is calculated using the most favourable conditions, i.e., the highest value for all variables except BWR, for

which the minimum value is considered the best. A positive variation indicates a higher value in PE mode.

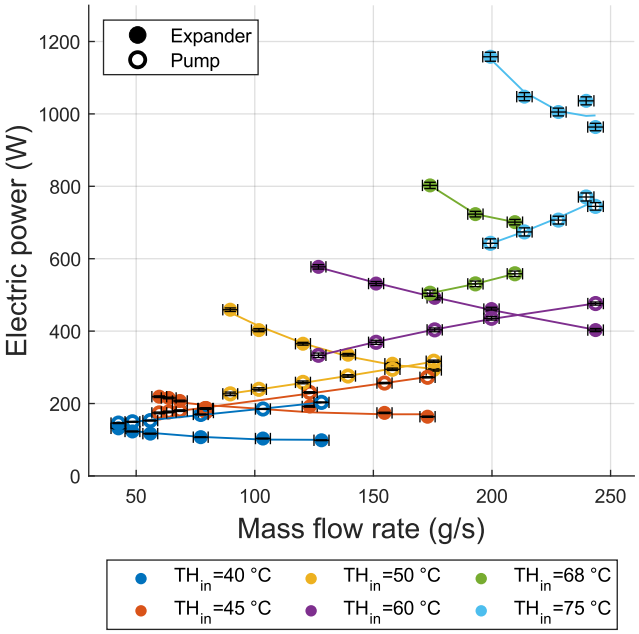

Figure 3.33 – Expander electric power production ($\dot{W}_{exp,el}$) and pump electric power consumption ($\dot{W}_{pump,el}$) versus working fluid mass flow rate ($\dot{m}_{wf}$), varying the heat source temperature (TH_{in}).

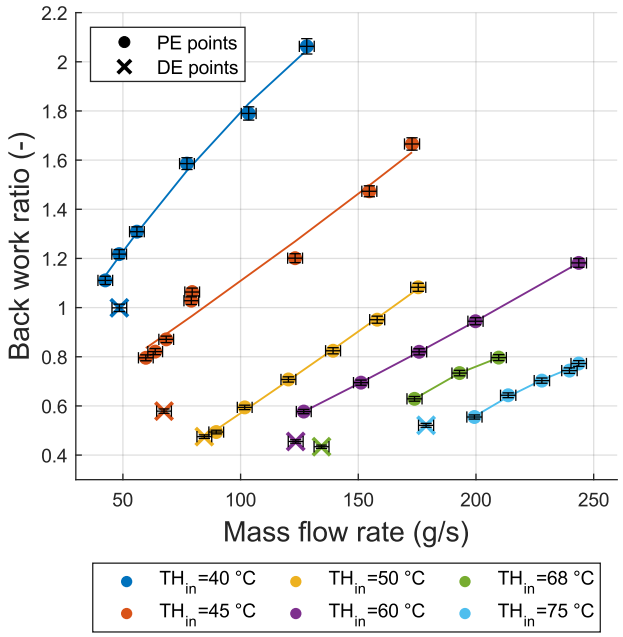

Figure 3.34 – Back work ratio (BWR) versus working fluid mass flow rate ($\dot{m}_{wf}$), varying the heat source temperature (TH_{in}).

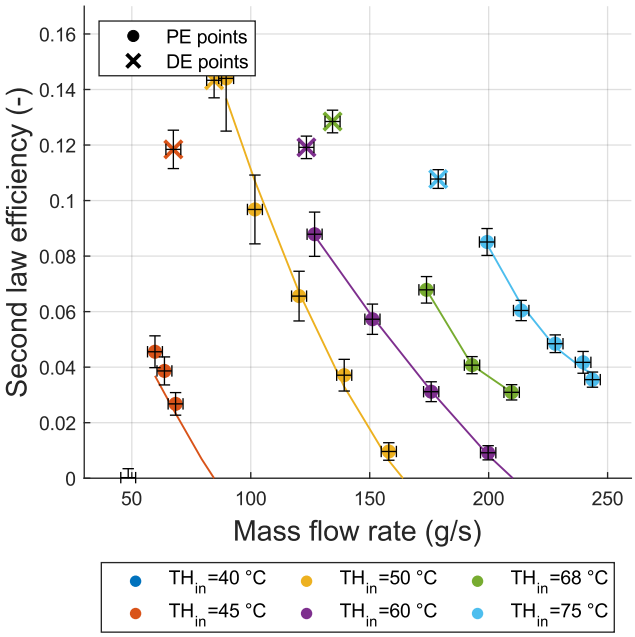

Figure 3.35 - Second law efficiency (η_{II}) versus working fluid mass flow rate ($\dot{m}_{wf}$), varying the heat source temperature (TH_{in}).

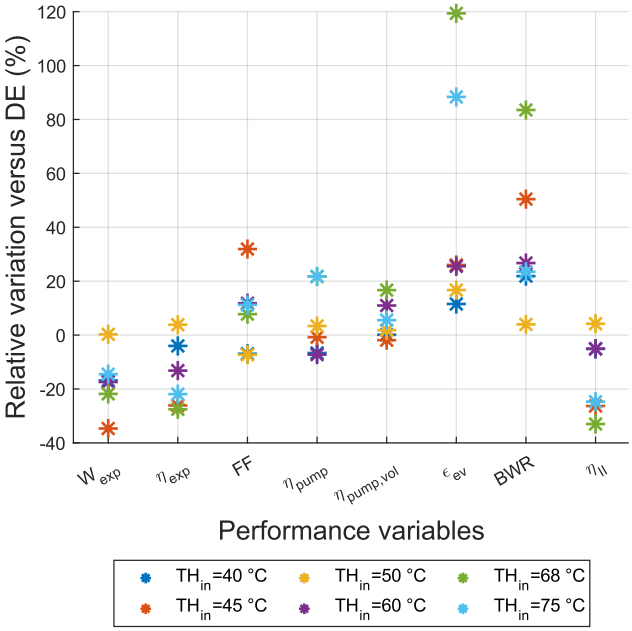

Figure 3.36 - Relative variation for the key performance variables: a positive variation indicates that the index is higher in PE mode compared to DE mode.

Figure 3.36 shows that pump efficiency improves for all tested heat source temperatures, with a minimum increase of 25 % for $TH_{in} = 75\,°C$ and a maximum slightly above 100 % for $TH_{in} = 40\,°C$. Notably, the pump efficiency is generally low at low mass flow rates, which characterizes DE operation at low heat source temperatures. The relative improvement in pump volumetric efficiency ranges from 8 %

to 51 %, increasing as the heat source temperature decreases. Evaporator effectiveness also significantly improves under all tested conditions, with relative variations from 20 % to 125 %. Expander power output and total efficiency are lower in PE mode under most heat source conditions, with a maximum relative reduction of around –23 % and –19 %, respectively. Conversely, an improvement of up to 32 % in the expander filling factor is observed in PE mode. The BWR is consistently higher in PE conditions, with a relative increase between 4 % and 37 %. Despite the pump's better efficiency (increasing with mass flow rate) in most PE mode conditions, pump consumption also rises with mass flow rate while expander power decreases (see Figure 3.33). The second law efficiency is penalized in PE mode under all considered conditions due to the impact of BWR and the significantly reduced contribution of the recuperator to the required thermal input compared to DE mode.

3.4.5. Conclusions

An extensive experimental analysis on a micro-ORC system designed for low-temperature heat recovery, using partial evaporation and wet expansion was performed. The system was originally developed for dry expansion operation, therefore the experiments aimed to test the micro-ORC cycle, and in particularly the piston expander, under challenging off-design conditions. Despite these very off-design conditions, the cycle operation remained stable, with continuous electrical power production. The study achieved the lowest vapor quality values (0.2–0.3) with heat source temperatures between 40 °C and 60 °C and high fluid mass flow rates. At higher temperatures (68 °C and 75 °C), the minimum quality was above 0.6 due to test bench limitations. Overall, the system performance decreases at low vapor quality, while optimal performance occurs at vapor qualities between 0.8 and 1, where the evaporator's efficiency improves due to the absence of superheating.

The main key findings include:

- in PE mode, vaporization pressure is mainly influenced by heat source temperature, with minimal impact from the working fluid mass flow rate.
- the condensation pressure is not affected by variations in working fluid flow rate.
- the pump performance shows significant improvement in PE conditions compared to DE, with substantial increases in volumetric and total efficiencies.
- the evaporator heat transfer effectiveness increases by up to 125 % compared to DE mode, and the temperature difference at the pinch point is reduced to 1-2 K in PE mode.
- the recuperator contribution is minimal in PE mode.
- although suitable for wet expansion, the expander performance decreases as vapour quality reduces, especially at higher heat source temperatures (above 60 °C), with efficiency penalties up to -19 % compared to DE mode. The efficiency reduction is smaller at vapour quality above 0.8.
- in some PE conditions, BWR exceeds 1.

In conclusion, the system's performance is generally poor below 60 °C, even with dry expansion, but partial evaporation could be beneficial for ultra-low-temperature waste heat. Indeed, PE mode enhances heat source utilization and evaporator effectiveness due to reduced pinch point temperature difference. A system specifically designed for partial evaporation mode, with an optimized expander and component sizes, could improve evaporator performance and eliminate the need for the recuperator, simplifying the system and reducing costs and pressure losses. Adjusting expander parameters, such as valve timing and displacement, could help maintain performance.

Feed-pump consumption remains a significant issue, especially at low temperatures. Redesigning the pump and motor could reduce the back work ratio to acceptable levels (below 30 %) and improve overall efficiency. The results also suggest that partial evaporation may be used as an off-design condition for ORC systems designed for dry expansion. This approach is more suitable for systems with low superheating

degrees and fluctuating heat source temperatures. It helps maintain higher evaporation pressure and expansion ratio, reducing the efficiency penalty and enhancing overall efficiency through improved evaporator performance. Regulating parameters to optimize the filling process is essential for maximizing expander performance under varying conditions.

3.5. Conclusions

In this chapter, the micro-ORC test bench, located at the University of Bologna, is presented. The test rig was utilized for experimental campaigns to assess performance with very low-temperature sources and under specific off-design operating conditions. The data collected was used to calibrate and validate a semi-empirical model, extensively employed throughout the thesis to analyse various micro-ORC applications.

The system, developed by StarEngine for residential use, features a nominal power of ~3 kW and utilizes thermal power from a low-temperature source (< 100 °C). It consists of three primary circuits: the internal ORC circuit and two external circuits supplying the evaporator and condenser. The ORC circuit utilizes HFC-134a as the working fluid, chosen for its suitable thermodynamic properties, chemical and thermal stability, and low toxicity. The system main components include a reciprocating piston expander, an external gear pump, a brazed plate heat exchanger evaporator, a brazed plate heat exchanger recuperator, a shell and tube condenser, and a liquid receiver. The heat source circuit features an electric water heater with delivering thermal power capacity up to 42 kW, while the cooling system is maintained by water extracted from a well and circulated to the condenser. The test rig is equipped with sensors to measure temperatures, pressures, and flow rates of the working fluid and secondary fluids, as well as to capture the electric power generated and consumed by the system. The methodology adopted to perform the experimental campaign, includes extracting the steady state operation intervals, and evaluating the uncertainty of the experimental data is highlighted.

A semi-empirical model of the micro-ORC test bench is developed based on the physical equations, incorporating empirical correlations to predict the system's performance under different operating conditions. The model calibration process is crucial, involving the adjustment of empirical parameters to minimize the error between model predictions and experimental observations. The calibration is approached as a minimization problem, using a global error function that quantifies the discrepancy between calculated and measured values.

Eventually, the results of an experimental campaign, aiming at assessing the thermodynamic performance of an advanced ORC cycle operating with partial evaporation and wet expansion, are provided as a part of the present thesis experimental activity. The micro-ORC test bench, originally designed for dry expansion, has proven to maintain stable operation and continuous power production even under these challenging off-design conditions. Although the system's overall performance is generally poor for temperature levels below 60 °C, PE mode can improve ultra-low-temperature waste heat recovery by increasing heat source utilization and evaporator efficiency through a lower pinch point temperature difference. A system tailored for PE, with optimized components, could boost performance, remove the need for a recuperator, simplify the design, and cut costs and pressure losses. Adjusting expander settings like valve timing and displacement could maintain an acceptable efficiency. However, high feed-pump consumption at low temperatures remains a concern, requiring redesign to lower the back work ratio below 30 % and enhance efficiency. The results suggest that PE can be used as an off-design condition for ORC systems intended for dry expansion (especially those with low superheating degrees and varying heat source temperatures), to maintain higher evaporation pressure and improve overall efficiency.

4. Micro-ORC applications for low-grade heat valorisation

Summary. In this chapter, two distinct applications of small-scale ORC technology for harnessing low-temperature heat are explored and presented. The first application focuses on the residential sector, utilizing thermal solar as the heat source. The study investigates the integration of a kW-sized recuperated ORC system with a commercial solar thermal collector to meet the annual electricity demand of a single-family user. The second investigation pertains to industrial waste heat recovery, assessing the feasibility and energy-saving potential of integrating a micro-ORC system into data centers to recover cooling waste heat. Both studies include a sensitivity analysis that varies the ORC working fluid to examine the potential of low environmental-impact alternatives.

4.1. Solar driven micro-ORC system for residential application

ORC systems are a promising technology for harnessing solar radiation to generate thermal energy via solar collectors. Dickes et al. [166] examined and summarized some of the most advanced and innovative solar ORC technologies. Solar thermal energy is particularly suitable for residential areas [167], where micro-generation technologies, such as micro-ORC, are targeted. Solar thermal energy offers several benefits: medium-low temperatures (< 130 °C), high reliability, user-friendliness, low maintenance, compact size, and the ability to use various fluids for heat exchange.

However, solar applications face challenges such as the unpredictability of the energy source and fluctuations in its intensity. Soulis et al. [168] discovered that solar radiation variation is influenced not only by latitude but also by altitude, affecting climate variability. This spatial variability significantly impacts the efficiency and power output of systems that combine solar collectors with ORC setups.

Research on solar thermal and ORC technology integration is quite topical. Lombardo et al. [169] developed a dynamic model of a small-scale trigeneration system for residential use, including a solar collector, the micro-ORC test rig presented in this thesis, and an absorption refrigeration system. Their findings highlight the potential of ORC technology in trigeneration plants, achieving an overall efficiency of 63 %. Calise et al. [170] conducted a detailed techno-economic analysis of a small-scale solar combined heating and power (CHP) system, combining evacuated flat-plate solar thermal collectors with a small ORC, and found it economically viable for many Mediterranean locations. Roumpedakis et al. [171] evaluated the exergetic and economic performance of a small-scale solar-driven ORC for the South-East Mediterranean region, considering various scenarios, collector types, working fluids, and installation sites. Kutlu et al. [172] proposed a domestic solar-ORC system coupled with a vapor compression cycle (VCC) that operates in three modes, i.e., producing electricity and cooling in summer, and either power and heating or just heating in winter. Quoilin et al. [173] introduced a novel reversible energy conversion system for houses that can function as either an ORC unit or a heat pump, depending on weather conditions and heating needs. Liu et al. [174] developed a dynamic fuzzy logic control strategy to optimize solar radiation absorption, enhance electric power output, and improve thermal efficiency. They modelled their 1-kWe ORC test facility using Dymola software in the Modelica environment and linked it virtually with the thermal output of a solar field simulated in Simulink. Ciani Bassetti et al. [175] designed a hybrid geothermal-solar power plant with a parabolic trough collector solar field and an air-cooled binary cycle geothermal plant, demonstrating increased system efficiency and annual net power output. Gao et al. [176] proposed a solar-driven ORC system with a two-stage thermal collection and accumulation, design to

address performance issues caused by variable solar irradiance. Using non-concentrating solar plants and two-stage energy accumulators, the system reduces power output fluctuations by 70 % and improves overall efficiency by 43.85 %, outperforming conventional ORC systems in thermal performance. Qureshi et al. [177] examined a refrigeration system combining solar-based ORC and vapor compression refrigeration using natural hydrocarbons to reduce environmental impact. The system operates efficiently with solar thermal energy between 90 and 315 °C. Alghamdi et al. [178] assessed a hybrid energy system combining a supercritical Brayton Cycle and an ORC, using solar parabolic trough collector by day and biogas by night. The system's exergy destruction and efficiency were analysed, along with an exergo-economic evaluation of investment rates and returns. Findings indicate that integrating solar parabolic trough collector with biogas effectively enhances heat delivery and overall system performance. Chen et al. [179] presented a hybrid energy system combining solar ORC and ground source HP technologies for heating and power supply. By sharing a ground heat exchanger and utilizing waste heat from the ORC condenser, the system achieves a COP of 6.5, outperforming the stand-alone HP COP of 2.8. Optimal design for a 3000 m^2 building results in 180 kW net power output, 27.5 % thermal efficiency, and 9.2 % exergy efficiency. Yang et al. [180] presented a combined cooling, heating and power (CCHP) system powered by biomass and solar energy, integrated with an ORC. They examined exergy, exergoeconomic, and exergoenvironmental performances using Aspen Plus simulations. Key findings show varying costs and environmental impacts for domestic hot water, electricity, and chilled/heated water. Improving solar collector performance and optimizing components like the absorption chiller, heat exchanger, and engines can enhance system efficiency and reduce environmental impact. Pezo et al. [181] introduced two technologies for residential buildings: a HP/ORC system with solar thermal collectors and a HP with photovoltaic panels. The study compares these systems in terms of performance, emissions, operational cost, and Net Zero Energy Building potential in Santiago, Concepción, and Temuco (Chile). Costs and CO_2 emissions reductions are significant for both systems compared to traditional natural gas boilers. Valencia Ochoa et al. [182] compared the use of solar energy for electricity generation in buildings using two configurations, i.e., a regenerative ORC and a simple ORC. Results indicated that while the regenerative ORC performed better in energy management, the simple ORC achieved a higher annual benefit (39833 USD/year vs. 39604 USD/year). Particle swarm optimization, used to enhance economic and environmental outcomes, improved economic indicators for both configurations, though environmental impact reductions were minimal. Qi et al. [183] proposed an integrated energy system combining biomass, solar, and a two-stage ORC to meet rising energy demands. The analysis highlights specific areas for performance enhancement and environmental impact reduction, emphasizing the need for targeted improvements in system components. Rodriguez-Pastor et al. [184] explored the potential of integrating hybrid solar ORCs in residential buildings, focusing on their annual performance and economic feasibility. Evaluations highlight their suitability for cogeneration in isolated installations and retrofits of existing solar heating systems. Results indicate a positive internal rate of return of 8.61 % for a Seville-based installation operating the ORC 15 % annually, effectively mitigating overheating issues by 20 % during warm months. Li et al. [185] proposed a novel cogeneration system combining compressed air energy storage, an ORC, and solar collectors. It achieves an output power of 389.19 kW and heat output of 985.18 kW with efficiencies including 24.63 % for power, 86.96 % for energy, and 67.57 % for exergy. The solar collector system contributes the highest energy destruction (199.43 kW), and total system investments amount to 6471.35 k$, with the solar collectors and turbine representing the largest investment costs at 30.72 % and 27.87 % respectively. The system has a simple payback period of 17.68 years and a dynamic payback period of 11.56 years. Eventually, from the review by Nguyen et al. [186] emerges the potential of solar-driven ORC for applications such as water desalination, water pumping, and power generation, focusing on working fluid selection, component choices, challenges, and avenues for future research. Solar ORC appears as a promising pathway for sustainable energy system development.

4.1.1. Contribution

Based on the above literature review, the application of the ORC technology to the solar thermal energy source occurs as a promising solution for residential targets. In the light of that, the purpose of this study, in the context of the present thesis, is to enrich the current literature on investigating the performance of new generation fluids (HFOs) and their mixtures when used in solar applications at very low temperatures. The performance model, calibrated and validated over the experimental data of a real ORC system, is coupled with a simplified model of commercial thermal solar collector to compare the techno-economic performance that can be reached with low-GWP working fluids.

In this study, the semi-empirical model of the ORC test bench is adapted to simulate the considered application. An overall assessment of the yearly energy output for a residential building located in Bologna (Italy) is conducted. Using historical solar radiation data, the average monthly irradiation profile is estimated to evaluate the system's performance throughout the year. A comparison is made between the system's performance using R134a, the current fluid in the plant, and five low-GWP alternatives (R1234yf, R1234ze(E), R1243zf, R513A, R515A) as working fluids. The models for the solar collector, hot water circuit, and regulation strategy are incorporated into the calculation code. The selection of the working fluid, a critical aspect of ORC technology design, is also discussed. Simulations consider the average daily profiles of irradiation and ambient temperature for each month in Bologna. A parametric analysis is conducted by varying the solar collector surface area and storage dimensions to determine the optimal parameters for maximum electricity output. Finally, a performance comparison using different fluids and mixtures is presented, comparing performance indexes and the annual electricity production for each fluid.

4.1.2. The integrated solar-ORC energy system

The designed energy system features a micro-ORC intended to provide electrical power to a single-family household. This setup utilizes solar radiation through an external circuit consisting of a commercial thermal solar collector and a thermal energy storage unit (Figure 4.1).

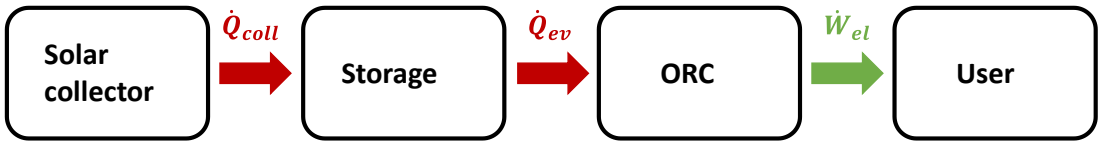

Figure 4.1 - Solar-ORC energy system conceptual scheme.

The system configuration, depicted in Figure 4.2, integrates the micro-ORC model with a heat source circuit model, including a flat plate thermal solar collector and two storage tanks. The storage unit decouples the thermal power production of the solar collector from the ORC evaporator's thermal demand, based on the user's electricity consumption. Water is used as the heat transfer medium, conveying thermal power from the collector to the storage unit and from the storage to the ORC evaporator.

The solar collector is designed to operate at nominal conditions of 800 W/m^2 irradiance and an ambient temperature of 20 °C. To optimize ORC performance, the system is designed with a 2 °C water temperature glide through the evaporator and a water flow rate of 2 L/s, resulting in approximately 16 kW of thermal power. Given these parameters, a solar collector with a surface area of about 32.25 m^2 is selected. The storage tanks are sized at 6000 L, striking a balance between mitigating solar radiation fluctuations and limiting the system's overall size for residential application.

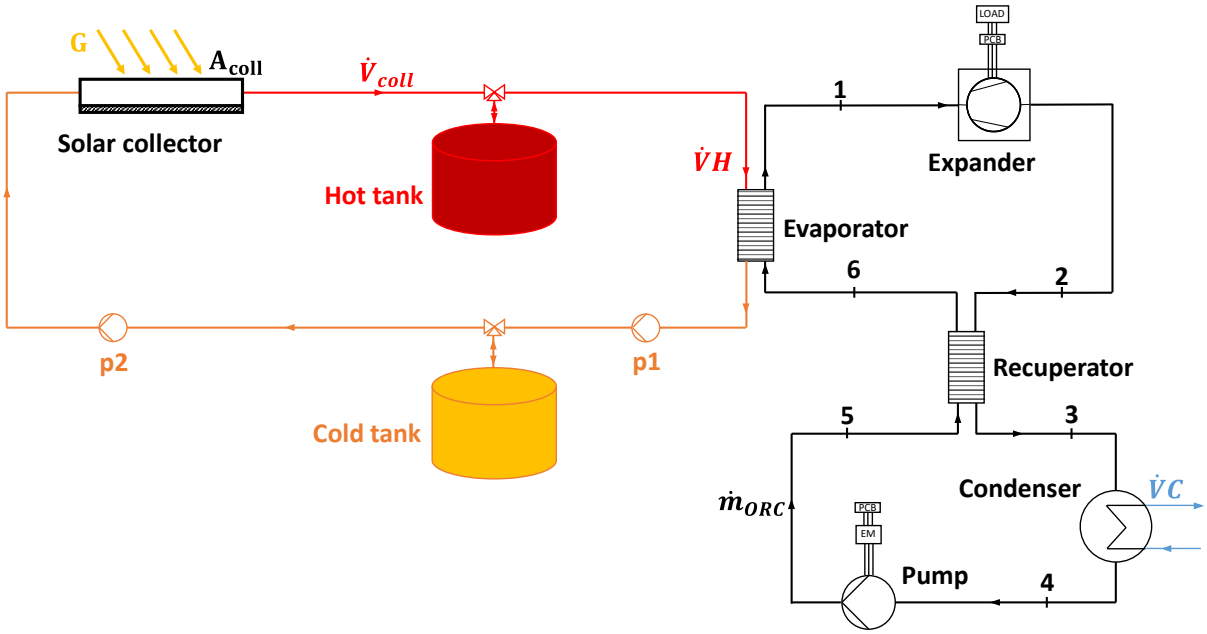

Figure 4.2 - The integrated solar-ORC energy system layout.

4.1.3. Solar collector model

Based on Garcia-Saez et al. [187], a 0-dimensional method was used to model the performance of the flat solar collector under quasi-static equilibrium conditions. The thermal solar collector model simulates the energy balance between the incident solar radiation (G) on the absorbing surface (A_{coll}) and the thermal energy transferred to the water flowing through the component (Figure 4.3).

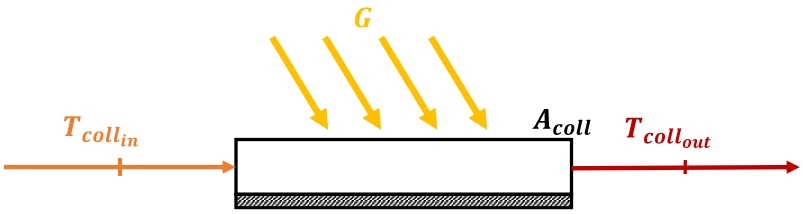

Figure 4.3 - Scheme of the flat-plate solar thermal collector.

The thermal energy absorbed at the collector surface, $\dot{Q}_{coll}$, is calculated using Eq. (4-1):

$$\dot{Q}_{coll} = \eta_{coll} \cdot G \cdot A_{coll} \tag{4-1}$$

The collector efficiency, η_{coll}, is determined by the following equation:

$$\eta_{coll} = \eta_0 - a_1 \cdot \frac{T_{coll_{in}} - T_{amb}}{G} - a_2 \cdot \left(\frac{T_{coll_{in}} - T_{amb}}{G}\right)^2 \tag{4-2}$$

where η_0, a_1, and a_2 are parameters from the collector catalogue [188] residential; $T_{coll_{in}}$ is the water temperature at the solar collector inlet, equal to the water temperature at the evaporator outlet; and T_{amb} is the ambient temperature.

Table 4.1 lists the primary specifications of the solar collector for a single panel, including the mentioned parameters. The collector capturing surface area (approximately 32.25 m^2) is achieved by assembling 15 panels of the selected model. The characteristic curve of the solar collector, derived from Eq. (4-2), is shown in Figure 4.4.

Table 4.1 - Thermal solar collector single panel specifications.

Surface (m^2)		Absorber			Stagnation Temperature (°C)	Dimensions (mm)			Weight (kg)
Total	Absorbent	η_0	a_1 (W/(m^2K))	a_2 (W/(m^2K^2))		L	H	P	
2.57	2.15	0.839	3.47	0.0106	214	2077	1238	100	46

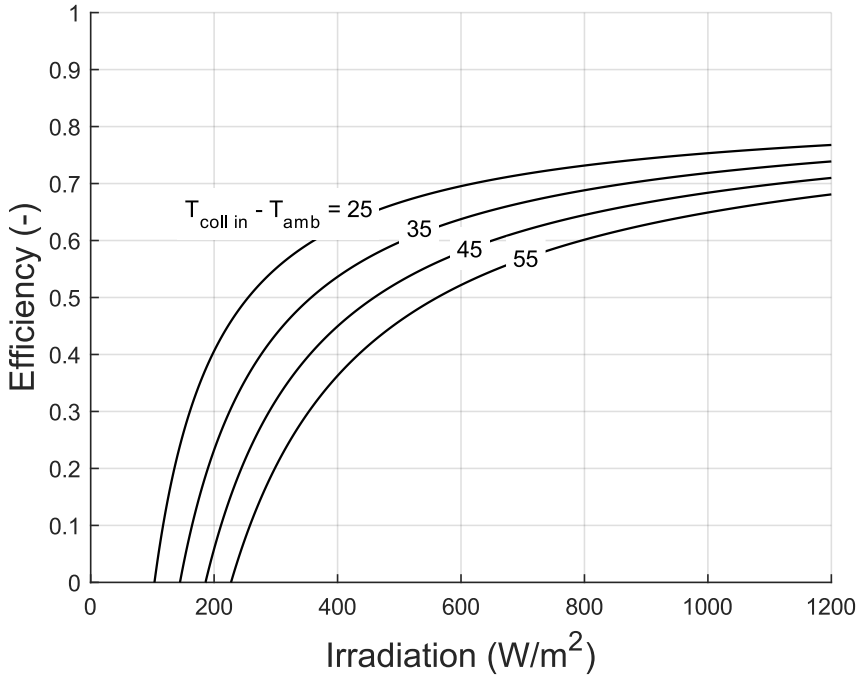

Figure 4.4 - Thermal solar collector characteristic curves.

The energy balance on the collector provides the water temperature at the evaporator inlet, which is equal to the water temperature at the solar collector outlet, $T_{coll_{out}}$ (Eq. (4-3)):

$$T_{coll_{out}} = T_{coll_{in}} + \frac{\dot{Q}_{coll}}{\dot{V}H \cdot \rho H \cdot c_p H} \tag{4-3}$$

4.1.4. Storage model and regulation strategy

The storage tanks are simulated as containers that are filled or emptied based on the mass balance between incoming and outgoing flow rates, according to the operation of the solar collector and the evaporator. Specifically, when the water flow rate through the solar collector ($\dot{V}_{coll}$) exceeds the flow rate required by the evaporator ($\dot{V}H$), the hot tank gains water while the cold tank loses an equivalent volume. Conversely, if the solar collector's water flow rate drops below the evaporator's demand, the hot tank starts to empty and the cold tank begins to fill. According to the mass balances in Eqq. (4-4) and (4-5), the volumes of water in the hot tank ($\dot{V}H_{tank,0}$) and cold tank ($\dot{V}C_{tank,0}$) are recalculated to new volumes ($\dot{V}H_{tank}$ and $\dot{V}C_{tank}$) after the time period $t_{filling/empting}$:

$$\dot{V}H_{tank} = \dot{V}H_{tank,0} + (\dot{V}_{coll} - \dot{V}H) \cdot t_{filling/empting} \tag{4-4}$$

$$\dot{V}C_{tank} = \dot{V}C_{tank,0} + (\dot{V}H - \dot{V}_{coll}) \cdot t_{filling/empting} \quad (4\text{-}5)$$

A constraint is set to cease filling or emptying when a tank is fully filled or emptied. Heat losses through the storage tanks are assumed to be negligible.

The water flow rate through the solar collector is adjusted based on solar radiation, while the evaporator's water flow rate is maintained as close as possible to the nominal condition, within the storage tank's capacity limits. A control system regulates both flow rates ($\dot{V}_{coll}$ and $\dot{V}H$), considering the current solar radiation level and the storage tank's fill status.

Specifically, the hot water control system first checks if the irradiance is zero or not:

- If there is no solar radiation, the system checks if the hot storage tank is empty. If it is, no flow rates are set. Otherwise, a nominal flow rate ($\dot{V}H_{nom}$) is set in the evaporator loop until the hot tank is empty.
- If solar radiation is present, the control system adjusts the hot water flow rate through the solar collector to maintain a fixed temperature glide. The evaporator's flow rate matches the collector's flow rate if the latter is in between the lower ($\dot{V}H_{min}$) and upper ($\dot{V}H_{max}$) limits for the evaporator's flow rate. If the collector's flow rate is below $\dot{V}H_{min}$, the ORC is either turned off or operates with a flow rate above $\dot{V}H_{min}$, depending on the storage fill level. If the collector's flow rate exceeds $\dot{V}H_{max}$, the ORC operates at $\dot{V}H_{max}$, and the hot tank is filled.

In summary, the control system strives to keep ORC operation near $\dot{V}H_{nom}$ to maximize the efficiency. If solar irradiance is high, the thermal power transferred to water in the collector overcomes the power exchanged in the evaporator, leading to a higher collector flow rate than evaporator flow rate, and the excess energy is stored in the hot tank. Conversely, when solar radiation is low or absent, the evaporator demands a higher flow rate than the collector provides, causing the hot tank emptying to meet the demand, with excess water stored in the cold tank.

Figure 4.5 illustrates the storage tanks' fill and empty cycle, showing variable state of charge throughout the day. In the early morning, as thermal power rises but irradiation remains low, the ORC system stays off, and heated water is collected in the hot tank (while the cold tank empties). The ORC starts when minimum output conditions are met, with the hot tank filling during midday and emptying in the afternoon and evening.

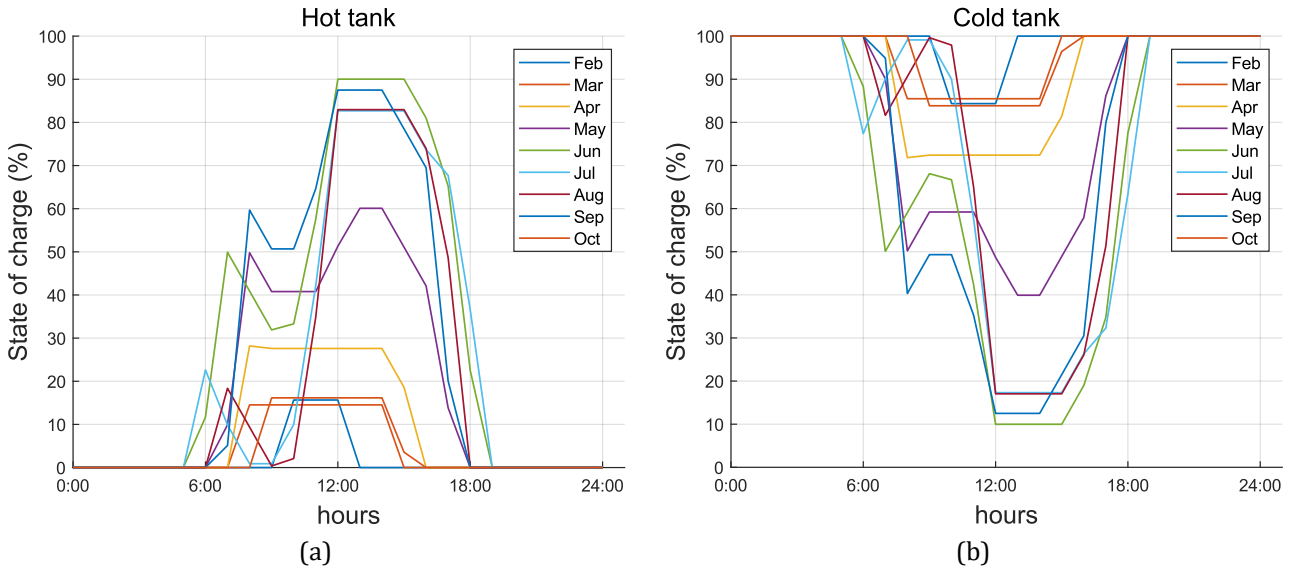

Figure 4.5 - Typical daily profiles of the (a) hot and (b) cold tanks state of charge, for each month of the year.

4.1.5. Working fluid selection

To explore the use of low-GWP working fluids [30] in this micro-ORC application as alternatives to the standard R134a (GWP = 1470 [189]) [190], a comparative analysis of various fluids was conducted. The alternative working fluids selected for this study, in accordance with current low-GWP refrigerant technology, include three different HFOs (GWP < 1 [191]), i.e., R1234yf, R1234ze(E), and R1243zf, along with R513A (GWP = 647), a mixture of 56 % R1234yf and 44 % R134a, and R515A (GWP = 320), a blend of 88 % R1234ze(E) and 12 % R227.

These fluids present very similar thermodynamic properties, including saturation limit curves in the T-s diagram (Figure 4.6), critical temperature and pressure, density, viscosity, and latent heat. However, slight differences among them impact system performance. Specifically, density and viscosity influence losses due to leakage, while the heat transfer coefficient affects thermal power dissipation to the environment. Table 4.2 provides the density (ρ), viscosity (μ), and latent heat (Δh_{lat}) for each of the fluids at typical condensing and evaporating temperatures, corresponding to ambient and source temperatures, respectively.

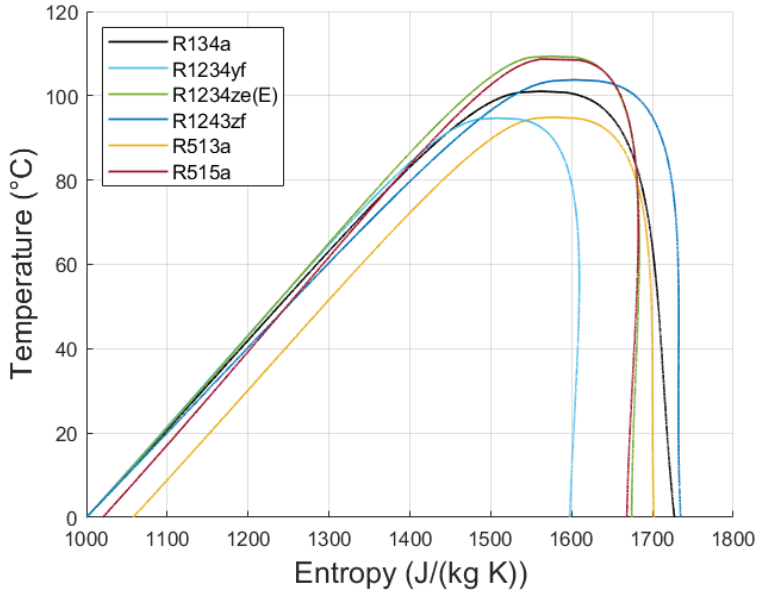

Figure 4.6 - Temperature-entropy diagram for selected working fluids comparison.

Table 4.2 - Selected working fluids thermodynamic properties on saturated curves at typical condensing and evaporating temperatures.

	ρ (T=18 °C) (kg/m^3)		ρ (T=65 °C) (kg/m^3)		μ (T=18 °C) (Pa·s·10^4)		μ (T=65 °C) (Pa·s·10^4)		Δh_{lat} (T=18 °C) (kJ/kg)	Δh_{lat} (T=65 °C) (kJ/kg)
	sat. liq.	sat. vap.	sat. liq.	sat. vap.	sat. liq.	sat. vap.	sat. liq.	sat. vap.		
R134a	1233	26.1	1026	100	2.13	0.114	1.15	0.140	184	132
R1234yf	1117	30.9	914	115	1.66	0.111	0.899	0.141	151	104
R1234ze(E)	1186	21.2	1010	80.1	2.08	0.118	1.15	0.148	172	130
R1243zf	999	21.9	837	78.8	1.71	0.111	0.981	0.136	187	138
R513A	1160	30.6	949	116	1.81	0.113	0.966	0.142	162	112
R515A	1210	21.9	1030	82.9	2.12	0.118	1.17	0.147	165	124

4.1.6. Boundary conditions and performance indexes

To calculate the annual electrical energy output of the system under analysis, simulations with the monthly-averaged daily hourly profiles of solar radiation are performed. The solar radiation profiles derive from historical data for Bologna (around 44.5°N latitude), provided by the UNI 10349 standards [192] for the months of July and September. These profiles refer to solar panels with a 30° inclination (in Italy, the optimal tilt angle for maximum electricity production ranges between 30° and 35°, depending on the location of installation), and south oriented. Typically, solar thermal panels are installed with an inclination equal to the latitude increased by 15° or 20° to maximize hot water production during winter [193]. However, in this scenario where hot water is utilized for electricity generation, it is more beneficial to have an inclination that optimizes production year-round. Hence, the inclination typically used for photovoltaic panels is preferred.

The monthly-averaged daily hourly profiles of solar radiation are calculated for every month of the year (Figure 4.7(a)) using the available profiles for July and September, along with the daily solar radiation's monthly average values, provided by ENEA [194].

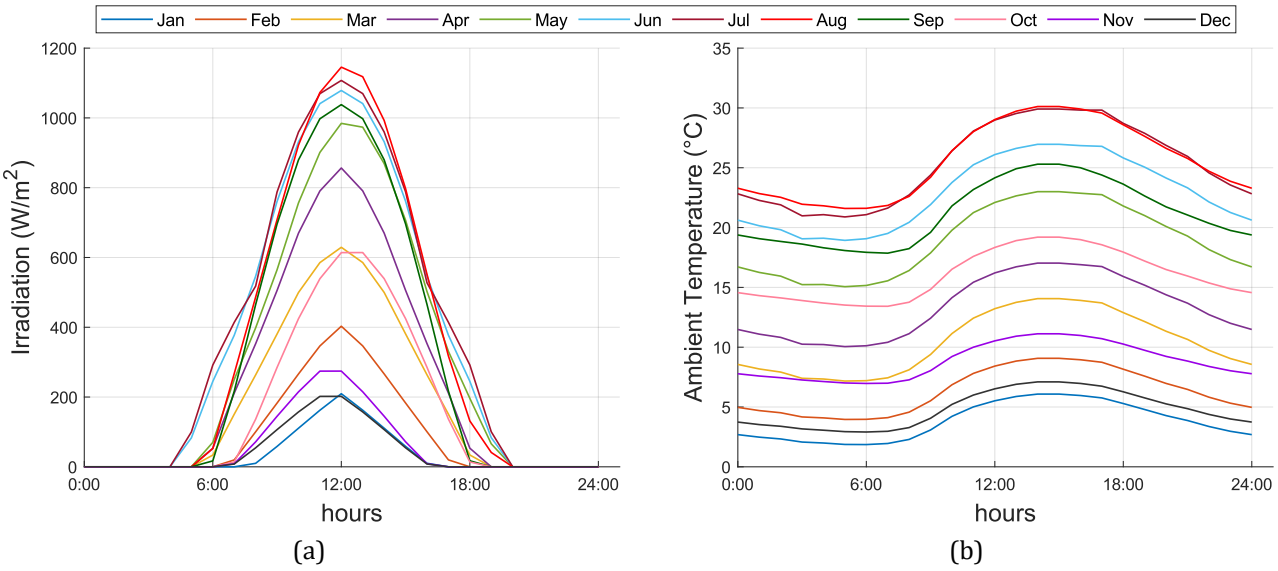

Figure 4.7 - Monthly-averaged (a) irradiation and (b) ambient temperature daily profiles.

Table 4.3 - Boundary conditions and controlled variables.

Variable	Value					
$load$	3000 W					
TC_{in}	18 °C					
$\dot{V}C$	2.77 L/s					
TH_{in}	53 - 65 °C					
ΔTH	2 °C					
$\dot{V}H_{nom}$	1.0 L/s					
$\dot{V}H_{min}$	0.4 L/s					
$\dot{V}H_{max}$	2.0 L/s					
ΔT_{SC}	0.5 °C					
ΔT_{SH}	R134a	R1234yf	R1234ze(E)	R1243zf	R513A	R515A
	3°C	15°C	10°C	10°C	20°C	10°C

The corresponding monthly average profiles of the daily hourly ambient temperature are depicted in Figure 4.7(b). Then, the ORC's performance is simulated using the model for each representative day of the month, based on the input variables outlined in Table 4.3.

The ORC's regulation strategy is designed to optimize the ORC system's overall efficiency during each operating hour with variable input thermal power from the renewable source. It's important to note that the degree of superheating at the expander inlet (ΔT_{SH}) remains constant during the monthly simulations, but it varies depending on the selected fluid to optimize the electric power output ($\dot{W}_{net}$). The evaporator water temperature glide ($\Delta TH = TH_{in} - TH_{out}$) is consistently maintained at 2 °C, while the evaporator water inlet temperature (TH_{in}) remains constant throughout the month, but it assumes a different value each month based on the average monthly irradiance.

The system performance and electricity production are computed on an hourly basis, striking a balance between the need to capture daily and yearly variability and the need to minimize computational costs. Indeed, hourly data enable the detection of the daily trend of solar radiation (and the electric power output) without significantly increasing the computational time and cost. Moreover, the available irradiation and ambient temperature data are monthly averages, so a finer discretization would not enhance the accuracy of the simulated electricity production. As seen in Figure 4.7, the hourly discretization allows for the appreciation of daily variations, and the monthly averages adequately capture yearly variations.

The performance indexes, rated to compare the application of the selected working fluids in the reference scenario, include the key indexes for typical ORCs performance evaluation: the expander electric output power ($\dot{W}_{exp,el}$); the pump electric consumption ($\dot{W}_{pump,el}$); the net output power ($\dot{W}_{net}$, see Eq. (3-30)); the back work ratio (BWR, Eq. (3-32)); the ORC efficiency (η_{ORC}, Eq. (3-30)). The monthly and yearly values of the electricity production (E_{el}) are also included in the analysis and calculated as it follows:

$$E_{el} = \sum \dot{W}_{net} \cdot t_{on} \tag{4-6}$$

where t_{on} represents the amount of time the ORC is operating.

4.1.7. Performance results

A parametric analysis is run to determine the optimal size of the solar collector surface and examine performance variations when altering the hot storage tank sizes for a specific micro-ORC system. Initially, a reference solar collector area of 32.25 m^2 (15 panels of the selected model) is chosen. To ensure that both smaller and larger collector surfaces would reduce the system's electricity output, results with solar collector areas of 21.5 m^2 (10 panels) and 64.5 m^2 (30 panels) are assessed. Additionally, the storage tanks volume is varied from 0 to 12 m^3 with a step of 3 m^3 to study the impact of tank size on performance.

Figure 4.8 illustrates the simulated annual electric energy produced by the system under consistent conditions (Table 4.3) using R134a as working fluid, with varying storage tank volumes and collector surface areas. Increasing the hot storage tank volume gradually decouples the ORC loop operation from the hot circuit conditions, benefiting ORC performance and electricity production. When irradiance is high, the buffer receives the surplus thermal energy, which is then released during lower irradiance periods. This helps maintain optimal ORC conditions for as long as possible.

Furthermore, Figure 4.8 shows that annual electricity production is nearly independent of storage tank volume when the collector area is small (21.5 m^2). In this scenario, the thermal power produced by the collector never overcomes the nominal thermal power exchangeable at the evaporator, so the heat from the collector is directly sent to the evaporator, with the storage thermal inertia being minimally used (except during very low irradiance). Among the simulated collector sizes, a surface area of 32.25 m^2 yields

the highest production. However, even in this case, electricity production approaches an asymptotic value as storage capacity becomes too large to be fully utilized. A storage volume of around 6 m^3 thus strikes a good balance between size and performance.

Increasing the solar collector surface to 64.5 m^2, while maintaining a constant water temperature glide, leads to a higher water flow rate to handle the increased thermal power input. However, due to limited storage size, fully decoupling the hot circuit from the ORC operation becomes impossible. Consequently, the organic fluid mass flow rate must also rise to accommodate the increased thermal power input. Under these conditions, the ORC operates in off-design conditions, resulting in decreased system performance (mainly due to increased expander under-expansion losses and higher pump consumption). The reduction in electric energy production is more pronounced with smaller storage volumes due to reduced storage thermal inertia.

It is important to note that these collector size parametric analysis results are specific to the case study of a kW-size ORC. Combining a larger collector surface with a larger ORC would increase electricity production, but the dimensions would no longer be suitable for residential applications.

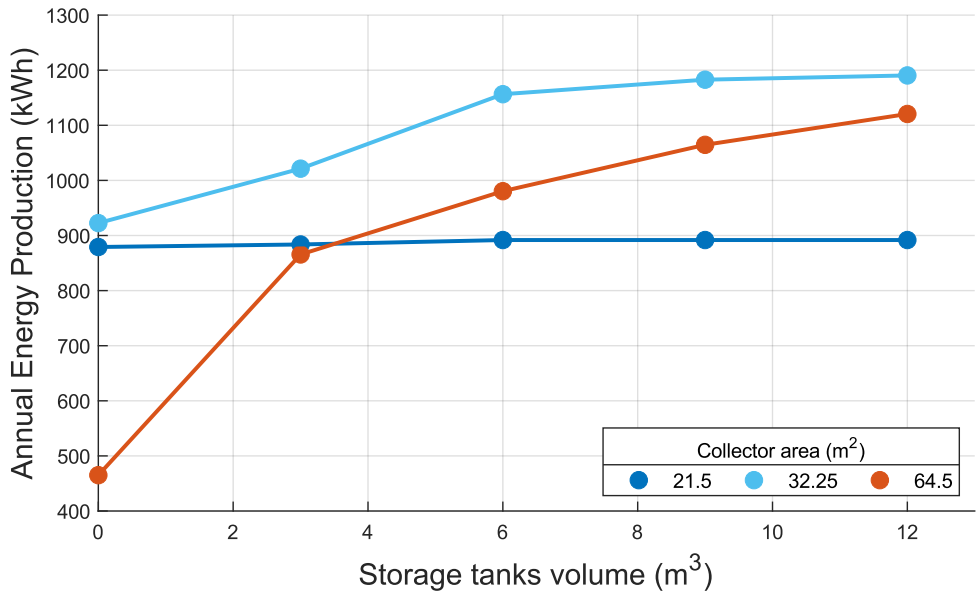

Figure 4.8 - Annual electricity production when varying the storage tanks volume and the solar collector surface.

The assessment of various fluids indicates that using R134a as the working fluid results in the highest expander electric power output (Figure 4.9), owing to its larger isentropic enthalpy drop during expansion. R134a's higher liquid density and viscosity (Table 4.2) contribute to a reduced pressure drop through the expander inlet valve. Consequently, an average expander power output exceeding 1000 W can be achieved between April and October with R134a, whereas low-GWP fluids yield less than 600 W. In the winter months (November, December, and January), the solar radiation is insufficient for generating electric power.

Regarding pump performance, R134a, having the highest liquid viscosity (2.06 $x10^{-4}$ Pa·s), experiences minimal leakage losses at the pump meatus, affecting volumetric flow. Additionally, pump consumption inversely correlates with fluid density (Eq. (3-28)), favouring R134a. However, R134a leads to higher pump consumption (Figure 4.10) due to the increased working fluid mass flow rate required by the lower superheating degree (Figure 4.11). Consequently, the net power output of the system is significantly higher with R134a (Figure 4.12), reaching up to 500 W, while low-GWP fluids yield under 300 W throughout the year. The back work ratio (Figure 4.13) is quite high (over 40 %) for all analysed fluids due to considerable pump consumption, aligning with typical ORC system values. The highest efficiency (Figure 4.14) is achieved with R134a (over 2 %). It's important to note that the system is specifically designed for R134a,

and its redesigning for a different fluid might improve performance. However, the Carnot efficiency of the ORC system remains below 14 % due to the very low operating temperature levels of the application.

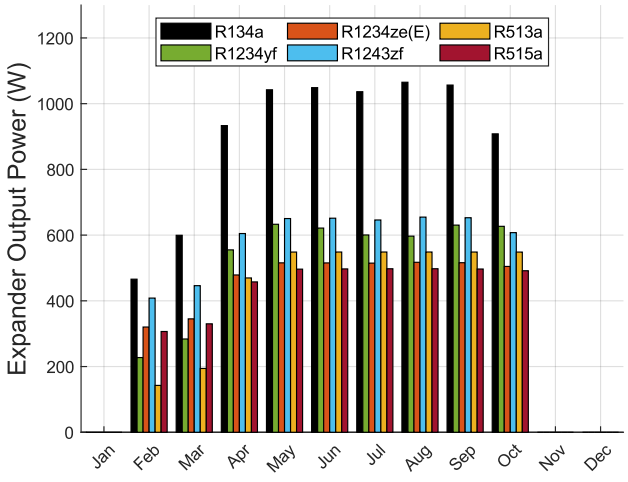

Figure 4.9 - Monthly average expander output power.

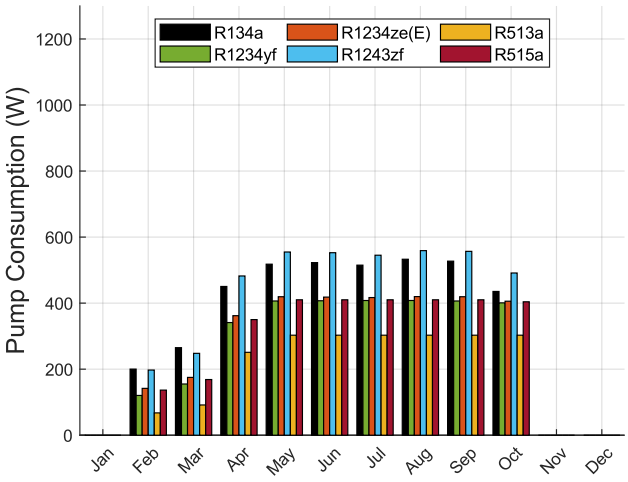

Figure 4.10 - Monthly average pump consumption.

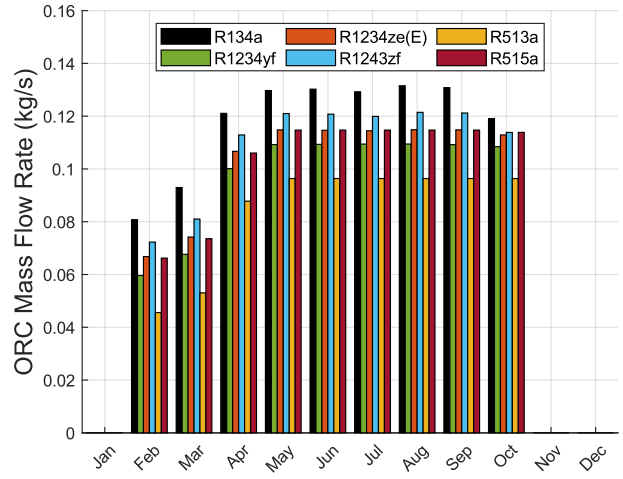

Figure 4.11 - Monthly average ORC mass flow rate.

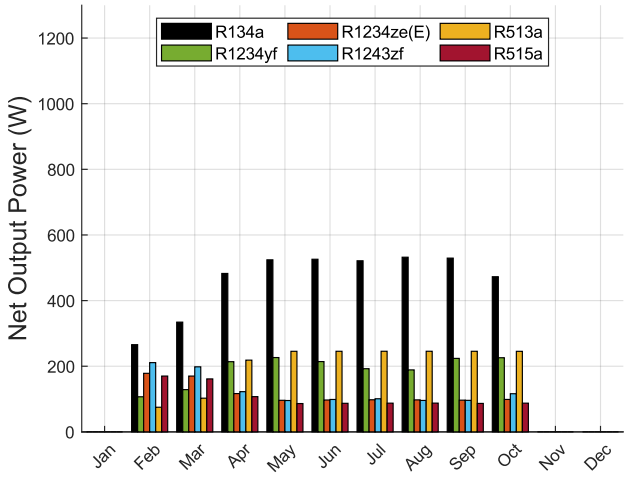

Figure 4.12 - Monthly average ORC net output power.

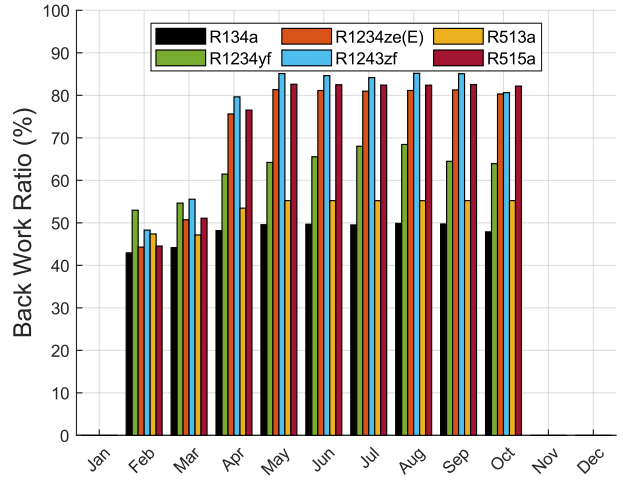

Figure 4.13 - Monthly average back work ratio.

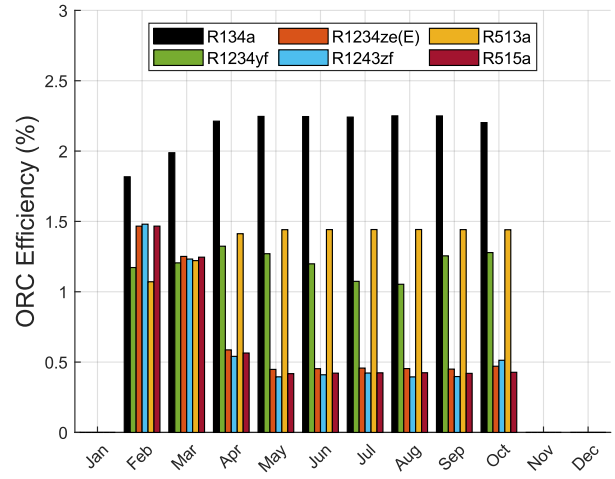

Figure 4.14 - Monthly average ORC net efficiency.

Figure 4.15 illustrates the estimated monthly energy produced by the system. Using R134a, an annual electricity production of 1156 kWh is calculated, which is approximately 30 % more than the value without hot water storage tanks (878 kWh per year, see Figure 4.8). For a single-family user's annual consumption of 2996 kWh [195], the system would cover about 39 % of the demand (29 % without thermal storage). With the average electricity price in Italy in 2019 (24.21 c€/kWh [196]), this results in an annual saving of € 280.

The micro-ORC test bench in this study is a prototype, making investment cost estimation challenging. A market survey using web information and commercial component costs estimates the cost of micro-ORC system at approximately 10000 $/kWe [40], the storage tanks and the solar collector at respectively 6000 € and 4000 € [197]. As a result, the complete system investment cost would be around € 17000-19000. With an estimated payback period exceeding 60 years, the system is currently not market competitive. Enhancing system efficiency and output power could reduce the payback period to a few years.

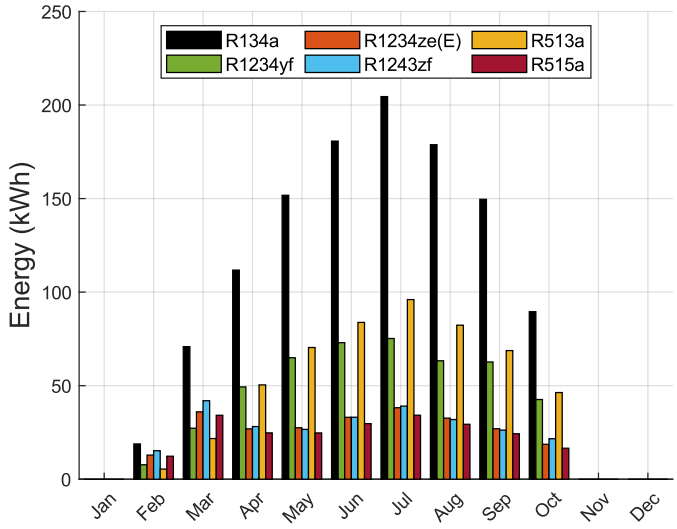

Figure 4.15 - ORC electric energy production for each month of the year.

Table 4.4 - Annual electricity production obtainable with each of the considered working fluids and related estimated covered demand.

Working fluid	Electricity (kWh/year)	% of the satisfied demand
R134a	1156.44	39.0 %
R1234yf	466.01	16.0 %
R1234ze(E)	252.92	8.0 %
R1243zf	263.97	8.8 %
R513A	525.21	17.5 %
R515A	230.11	7.7 %

An alternative solution could involve modifying the hot water circuit and increasing the solar radiation capturing surface to supply electric power together with thermal power. A promising layout could include tapping hot water for thermal use from the storage tanks, reintegrating the hot circuit with cold water upstream of the thermal solar collector, and regulating the flow rate to ensure the desired evaporator inlet temperature. Incorporating thermal production allows the ORC subsystem to be turned off at lower solar radiation levels, optimizing the system for thermal requests.

Using low-GWP fluids results in lower annual electric energy production and savings, summarized in Table 4.4. The performance comparison underscores that while low-GWP fluids offer environmental

benefits, they incur an energy production penalty compared to conventional HFCs. This highlights the ongoing need for research into fluids that balance low environmental impact with acceptable performance. Understanding the causes of low performance with low-GWP fluids encourages further investigation.

4.1.8. Conclusions of the solar driven micro-ORC system application

This study proposes the coupling of the semi-empirical steady-state simulation model of the reference kW-size micro-ORC test bench with a commercial solar thermal collector. A performance comparison of the estimated yearly electricity production for residential use, when using low-GWP working fluids as alternatives to HFC-134a, is provided. Simulations consider typical daily irradiation and temperature profiles for Bologna (Italy), identifying the optimal storage tank size and solar collector area for maximum electricity generation.

The performance of the system using the current working fluid, R134a, is compared with five low-GWP alternatives: R1234yf, R1234ze(E), R1243zf, and the blends R513A and R515A. Results show that net power output is higher with R134a (over 500 W) due to a larger isentropic enthalpy drop and lower pump consumption. As a consequence, the low-GWP fluids result in higher BWR values and lower overall efficiency. The highest efficiency is assessed to be over 2 % with R134a.

Redesign and optimization of the micro-ORC system could enhance performance with alternative fluids. The yearly electricity production with R134a is estimated to be over 1150 kWh, meeting almost 40 % of a single-family household's annual electricity demand. Although low-GWP fluids currently perform worse than HFC-134a, the environmental benefits necessitate further research to improve their performance.

Future studies could include a detailed economic analysis, performance optimization based on state-of-art machine efficiencies, and the integration of thermal power production. Expanding the solar collector surface and redesigning the system regulation could meet a thermal demand, especially at lower solar radiation levels, improving overall system efficiency.

4.2. Micro-ORC system for data center waste heat recovery

In the attempt to improve waste energy recovery, DCs are becoming of crucial importance due to the huge amount of low-grade heat generated and released by computer racks. ORC power systems represent a viable solution for recovering this waste heat.

Numerous studies in literature explore cooling technologies and low-grade waste heat recovery systems for DCs. Nadjahi et al. [25] conducted an in-depth analysis of various DC cooling technologies, including free cooling, liquid cooling, two-phase technologies, and building envelopes, comparing their effectiveness. Ljungdahl et al. [198] developed a decision support model demonstrating potential energy performance efficiencies when liquid cooling and latent thermal energy storage replace traditional air-based cooling systems, which dominate over 90 % of the DC industry [199]. The model also provides design parameters, usable for future applications, allowing proper selection of various system parameters, yearly energy savings, yearly cost savings, and efficiency gains through the Power Usage Effectiveness (PUE) and the Energy Reuse Effectiveness (ERE). The Authors used the model to analyse the case of the high-performance computing cluster at the University of Southern Denmark, showing a reduction in the electricity consumption and a waste heat recovery potential. Orò et al. [200] demonstrated a 30 % reduction in overall DC consumption by applying liquid cooling in a swimming pool case study. Zhang et al. [201] created an economic evaluation model to promote DC waste heat recovery in China, while Yu et al. [202] conducted a numerical analysis of a DC in Harbin, China. Deymi-Dashtebayaz and Valipour-Namanlo [203] explored the technical and economic viability of using an air source HP to recover waste

heat for space heating in a DC in Mashhad, Iran. Ebrahimi et al. [24] reviewed low-grade waste heat recovery technologies applicable to DC cooling, identifying absorption refrigeration [204] and ORC as the most promising options, considering the thermodynamic conditions and operational requirements of DCs. Gupta and Puri [205] provided a technical and economic analysis of a hybrid DC infrastructure with water-cooled high-density computing racks and air-cooled low-density server racks. Ding et al. [206] proposed an integrated system combining free cooling and heat recovery from DCs, operating in four modes based on cooling and heating demands, and experimentally validated its feasibility in northern cold cities. Lin et al. [207] suggested an integrated system using DC waste heat to meet annual heating, cooling, and hot water demands by combining a CO_2-HP with a lithium bromide-water absorption refrigeration system: in winter data centers waste heat is upgraded by the HP to provide direct heating, besides sanitary hot water; during summer the absorption refrigeration cycle produces cooling.

A significant challenge in reusing DC waste energy is the low quality of the heat, typically below 60 °C. ORC technology shows promise for exploiting low-grade heat sources [208], despite inherent thermodynamic limits on electricity production due to low Carnot efficiency. To the Authors knowledge, only few studies have addressed this application, even fewer experimentally. Ebrahimi et al. [209] conducted a numerical study on integrating an ORC system into DC cooling, developing a steady-state thermodynamic model to evaluate performance and a preliminary economic analysis predicting a 4–8-year payback period. Marshall and Duquette [210] offered a techno-economic analysis of using HP-assisted ORC systems for DC waste heat reuse, as an efficient and less costly alternative to conventional air-source chiller systems. Jawad Al-Tameemi et al. [211] performed a steady-state thermodynamic evaluation of an integrated system providing DC cooling and hot water for central heating, featuring an ORC, HP, and gas burner. Temiz and Dincer [212] simulated an ammonia trilateral Rankine cycle in a standalone DC system, including a bifacial photovoltaic power plant, hydrogen storage for renewable intermittency, and the trilateral Rankine cycle for cooling and providing additional electricity from waste heat. They also proposed a system for DC cooling and electricity needs [213], integrating a parabolic trough solar plant with a Rankine cycle, a bifacial photovoltaic plant, a hydrogen storage system, and a Li-Br absorption refrigeration cycle. Eventually, Corigliano et al. research [214] shows that ORC systems can achieve electric efficiencies over 5 % using fluids like pentane and isopentane, with significant energy and environmental benefits. The study outlines the design and analysis framework for such systems, emphasizing the selection of working fluids and optimization of components. The findings suggest ORC integration can provide notable improvements in energy efficiency and greenhouse gas savings for DCs.

4.2.1. Contribution

In this context, the objective of this study is to demonstrate the feasibility of utilizing ORC technology to recover very low-grade heat generated by servers. An experimental campaign is conducted using the reference micro-ORC test bench, with hot source boundary conditions replicated to align with typical values observed in DCs. The experimental data are employed to recalibrate and validate the semi-empirical steady-state model of the test bench. Additionally, the optimization of the expander's built-in volume ratio is performed to enhance the machine's filling performance under significantly off-design conditions. Finally, a parametric analysis with variable boundary conditions and a performance comparison with low-GWP alternative fluids is conducted.

4.2.2. Data center and ORC integration

The proposed configuration, depicted in Figure 4.16, integrates an ORC system in parallel with the DC cooling system to recover part of the DC discharged thermal energy, reducing the cooling load. This

application is intended to generate electric energy for DC feeding from its waste heat. Water is used as the heat transfer medium, conveying thermal power from the DC rack to the ORC evaporator.

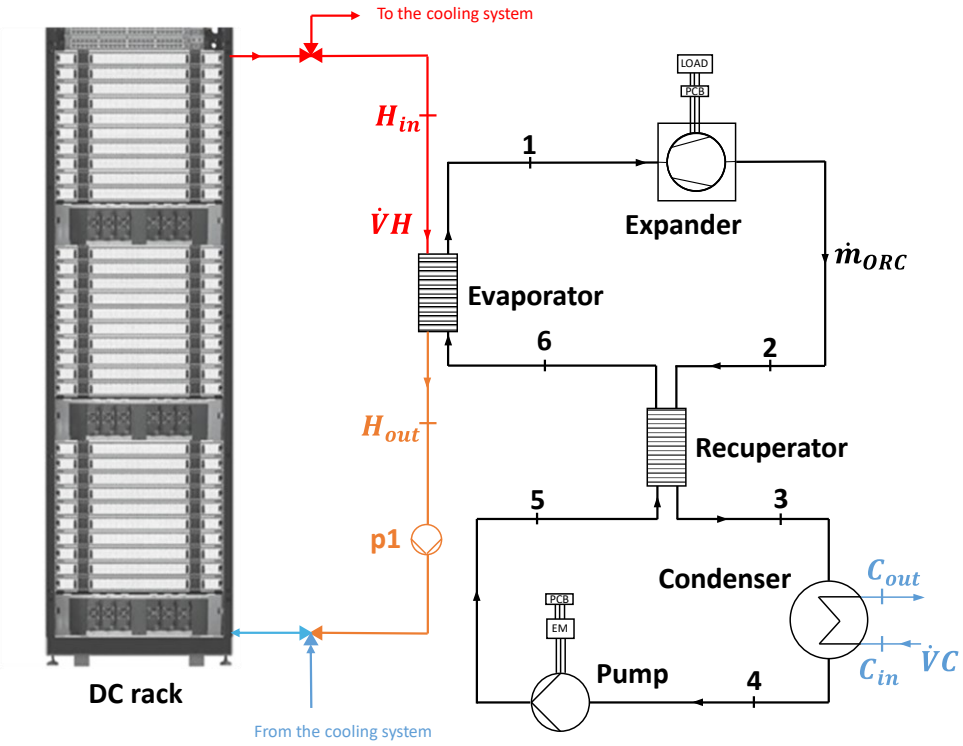

Figure 4.16 - The integrated DC-ORC energy system layout.

4.2.3. Experimental analysis and model validation with very low-temperature heat source

The primary goal of the experimental campaign is to evaluate the performance of the micro-ORC test bench under significantly off-design conditions, typical of DCs. A summary of the experimental boundary conditions is provided in Table 4.5: the hot source temperature and flow rate are varied, while the cold sink conditions are kept constant for the sake of a homogeneous comparison on the variability of the heat source conditions.

Table 4.5 - Experimental campaign boundary conditions.

Hot source temperature (°C)	40 – 55	Varied
Hot source flow rate (L/s)	0.556 – 1.45	
Cold sink temperature (°C)	16	Constant
Cold sink flow rate (L/s)	1.94	

Figure 4.17 illustrates the thermal power input delivered to the evaporator during each test condition, showing a linear trend with the ORC mass flow rate. At lower hot source temperatures, the ORC mass flow rate is constrained by the minimum pinch point and a required minimum superheating degree at the evaporator outlet (further increasing the mass flow rate would result in incomplete evaporation that is not desired in this analysis).

The experimental campaign demonstrates the system's operational feasibility even under highly off-design conditions, as evidenced by the electric power production. The expander electric power output (Figure 4.18) increases with both ORC mass flow rate and hot source temperature, ranging from a

minimum of about 200 W at TH_{in} = 40 °C to a maximum of nearly 550 W at TH_{in} = 50 °C.

Carnot efficiency is around 10 % under the tested conditions due to the low temperature difference between the heat source and the cold sink. The second law efficiency (η_{II}, Eq. (3-31)) varies between 5 % and 13 % (Figure 4.19 and Figure 4.20), increasing with the ORC mass flow rate, and hot source temperature and flow rate.

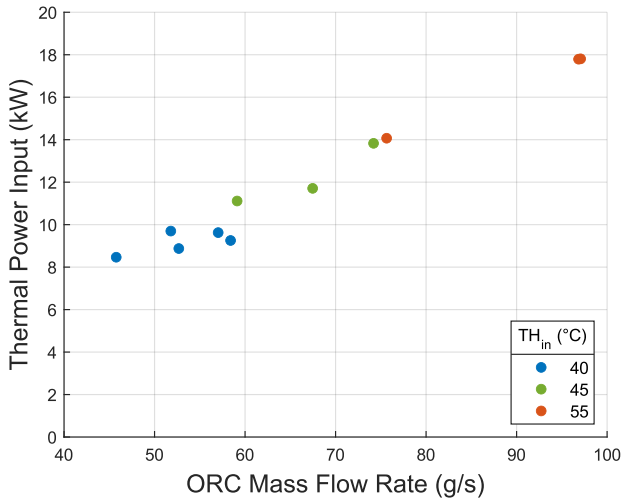

Figure 4.17 - Thermal power input versus ORC mass flow rate varying the heat source temperature in the experimental campaign.

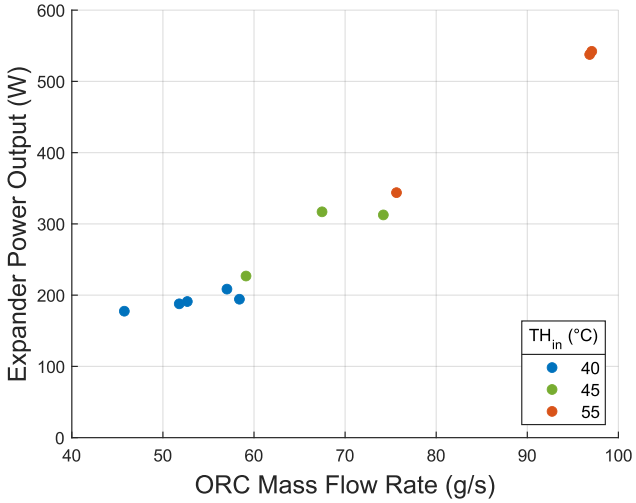

Figure 4.18 - Expander electric power output versus ORC mass flow rate varying the heat source temperature in the experimental campaign.

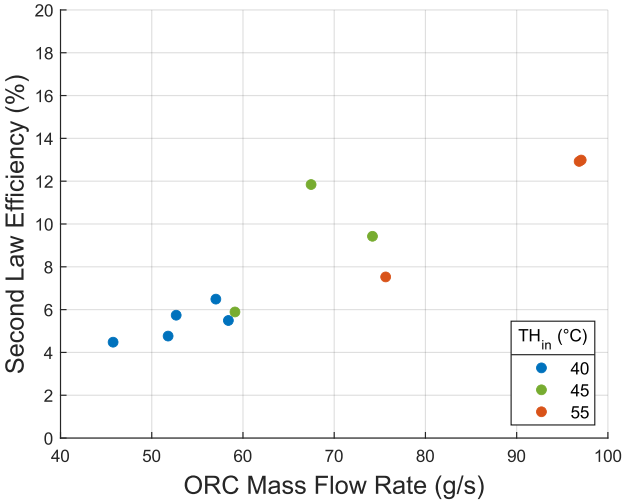

Figure 4.19 - Second law efficiency versus ORC mass flow rate varying the heat source temperature in the experimental campaign.

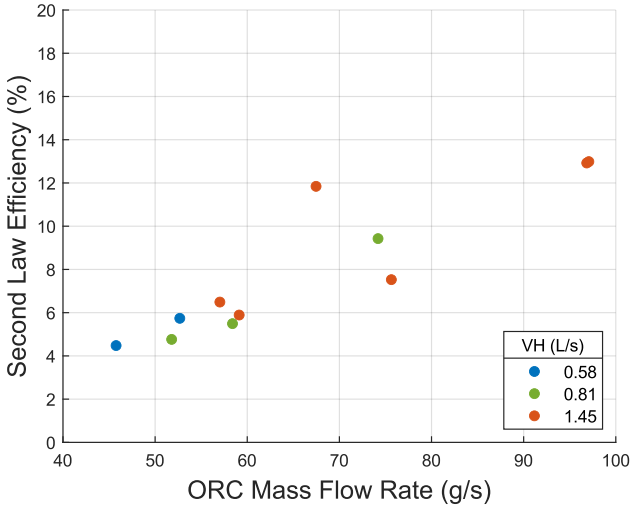

Figure 4.20 - Second law efficiency versus ORC mass flow rate varying the heat source volume flow rate in the experimental campaign.

Although the system's performance is modest, the experimental campaign confirms the feasibility of recovering waste heat from data centers through the ORC technology. Additionally, since the reference system was not specifically designed for this application, there is substantial room for further improvement.

The experimental data are utilized to recalibrate and validate the semi-empirical model of the reference micro-ORC system for applications involving very low heat source temperatures (see Figure 4.21).

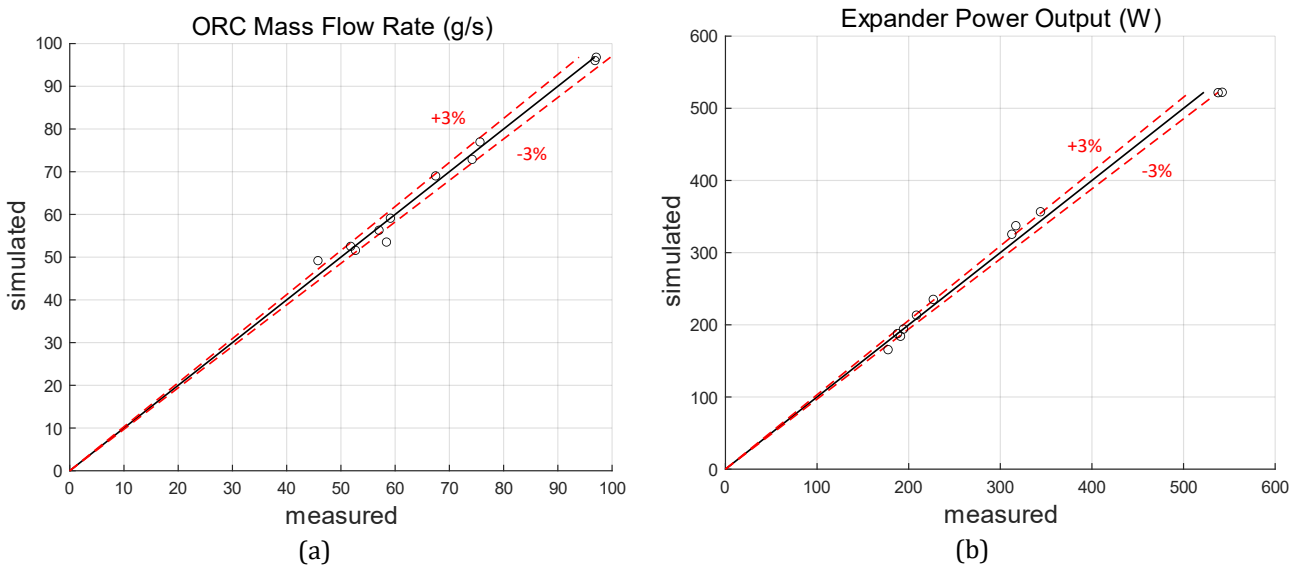

Figure 4.21 – Recalibrated model's parity plots of (a) ORC mass flow rate and (b) expander electric power output.

4.2.4. Optimization of the expander intake stroke ratio

Since in the considered application the reference ORC system performance is strongly affected by the operation in very off-design conditions, an optimization of the expander design is numerically carried out to better match the operating conditions. The purpose is to assess the performance that an ORC, specifically designed for the DC waste heat temperature levels, would show. In the light of the above, a numerical method is implemented to optimize the expander's built-in volume ratio for each tested condition, aiming to improve its design and enhance filling efficiency. In a previous study, Bianchi et al. [215] demonstrated significant improvements in expander performance through optimization of the built-in volume ratio. Indeed, the built-in volume ratio strongly influences the expander under- and over-expansion losses, and thus the machine power output, as explained in the subsection 3.3.4.

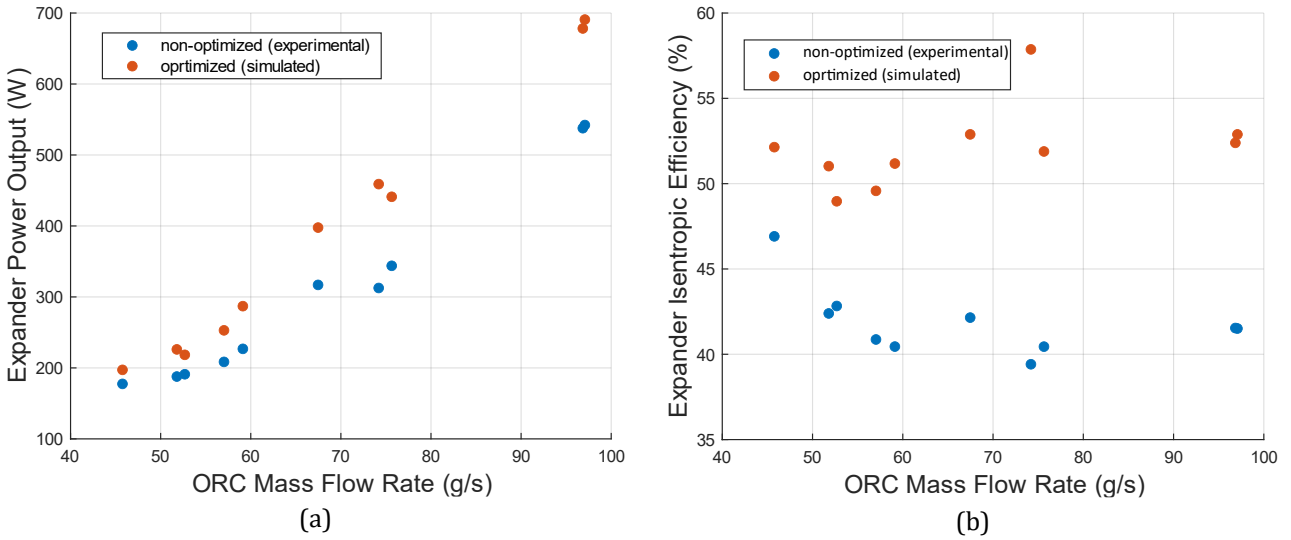

Figure 4.22 - Expander performance comparison with and without the built-in volume ratio optimization: expander (a) power output and (b) isentropic efficiency versus ORC mass flow rate.

Implementing an optimization procedure for the expander built-in volume ratio, $r_{v_{exp}}$ (see Eq. (3-10)), enables a comparison of the performance achievable with different working fluids. Figure 4.22 presents the results of this procedure, demonstrating that a slight increase in expander power output and isentropic

efficiency can be achieved by optimizing the value of $r_{v_{exp}}$. The improvement becomes more noticeable with an increase in the ORC mass flow rate, which is proportional to the expander speed. Indeed, at higher speeds, the filling process becomes less efficient, making the regulation of the built-in volume ratio more impactful on performance.

4.2.5. Performance comparison with low-GWP working fluids

The optimized model is employed to run a parametric analysis by varying the hot source temperature (TH_{in}) and flow rate ($\dot{V}H$) in line with typical DC conditions. Additionally, the analysis includes three different cold sink temperatures (TC_{in}) to evaluate the impact of ambient conditions on performance. The input variables used in the simulations are detailed in Table 4.6.

Table 4.6 - Parametric analysis input variables' values.

Hot source temperature (°C)	40 – 50
Hot source flow rate (L/s)	0.6 – 1.4
Superheating degree (K)	3
Cold sink temperature (°C)	5 - 25
Cold sink flow rate (L/s)	2
Subcooling degree (K)	3
Load (-)	3

Figure 4.23 illustrates that the thermal power input primarily depends on TH_{in}, while $\dot{V}H$ has a limited effect, especially at lower TH_{in}. As the hot source temperature increases from 40 °C to 55 °C, the thermal power rises from 10 kW to over 20 kW. This is due to pinch point constraints. Indeed, increasing $\dot{V}H$ slightly decreases the slope of the hot source heat transfer curve, which is already nearly flat (see Figure 4.24(a)), allowing only a minor increase in the ORC mass flow rate (and evaporating pressure), because of the minimum pinch point constraint. Conversely, increasing TH_{in} shifts the hot source heat transfer curve, enabling a higher ORC mass flow rate (see Figure 4.24(b)) while keeping the pinch point constraint.

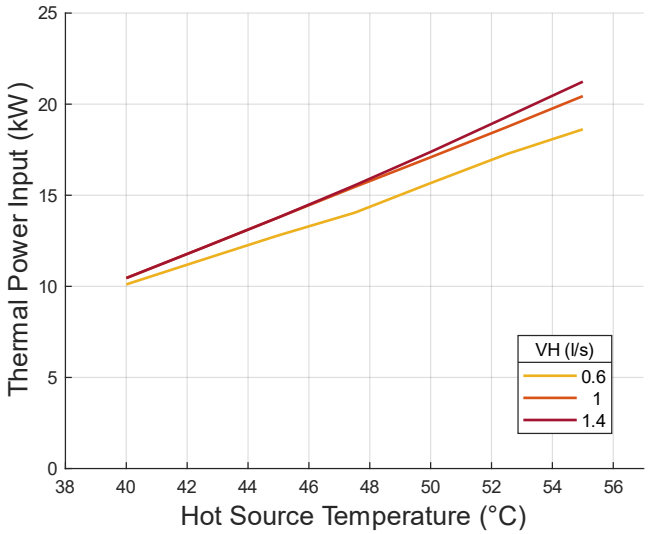

Figure 4.23 - Thermal power input versus hot source temperature (TH_{in}) varying the hot source volume flow rate in the parametric analysis.

The system's performance also varies significantly with TC_{in}. Figure 4.25 depicts the trend of net power production as a function of TH_{in} at different TC_{in}. At the maximum TH_{in} (55 °C), net power production overcomes 1 kW at the minimum TC_{in} (5 °C), but drops below 300 W at TC_{in} = 25 °C. Furthermore, at

lower TH_{in} values and higher TC_{in} conditions, the system fails to produce net power. The second law efficiency (Figure 4.26) is approximately 30 % in the most favourable scenario with $TC_{in} = 5$ °C.

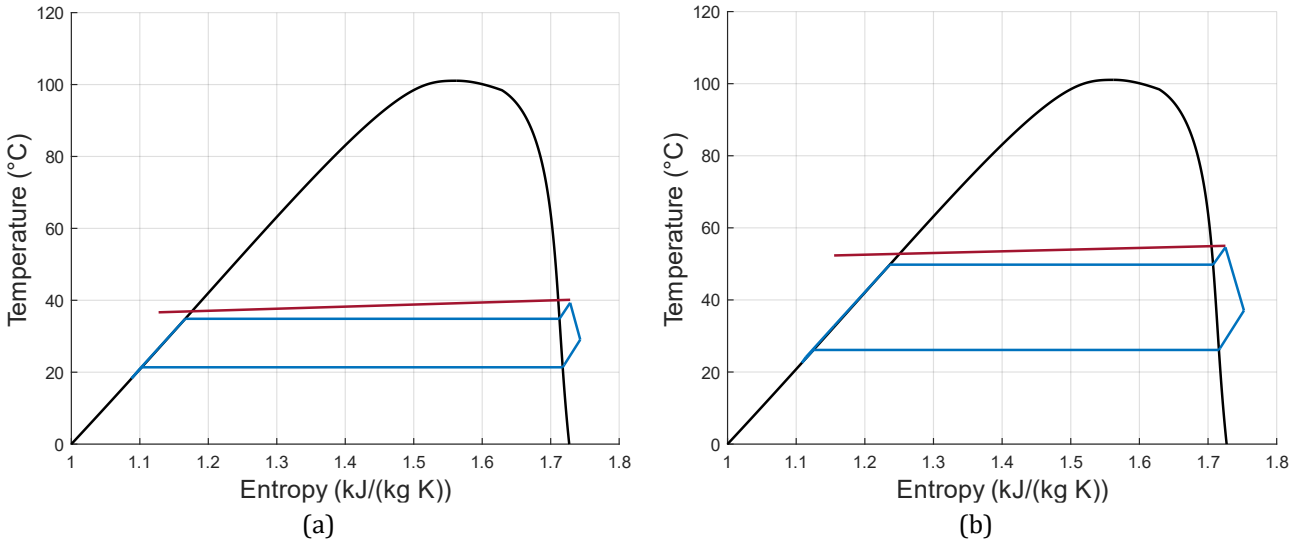

Figure 4.24 - ORC cycle and hot source heat transfer diagram at (a) $TH_{in} = 40\ °C$ and (b) $TH_{in} = 55\ °C$.

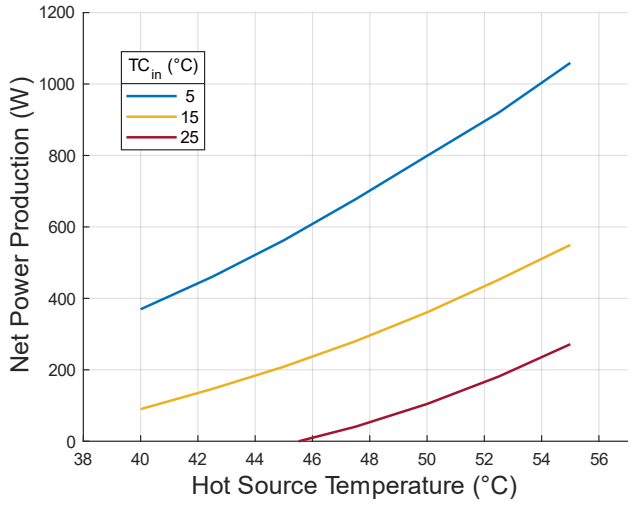

Figure 4.25 - Net electric power production versus hot source temperature (TH_{in}) varying the cold source temperature (TC_{in}) in the parametric analysis.

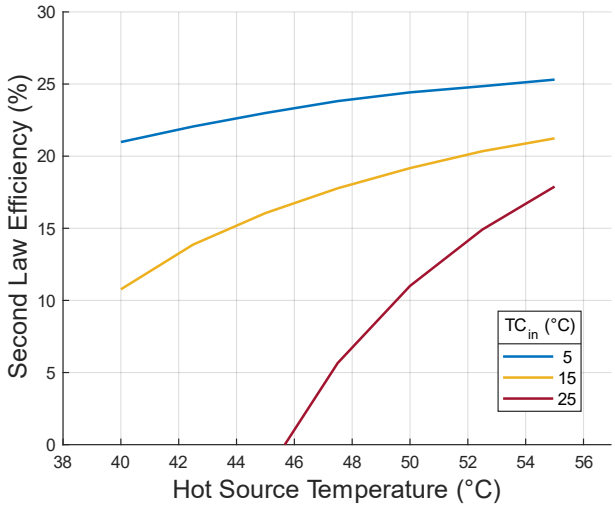

Figure 4.26 - Second law efficiency versus hot source temperature (TH_{in}) varying the cold source temperature (TC_{in}) in the parametric analysis.

The optimized model was utilized to compare the performance of two low-GWP working fluids, i.e., R1234yf and R1234ze(E), against R134a. Both olefines are considered suitable replacements for R134a due to their similar thermodynamic properties but with a significantly lower environmental impact (see Table 4.7). The system's performance with these low-GWP fluids is comparable to that with R134a (Figure 4.28 and Figure 4.29). In the most favourable scenario ($TC_{in} = 5$ °C and $\dot{V}H = 1.4$ L/s), R134a produces slightly higher net output power (Figure 4.28). Regarding cycle efficiency (Figure 4.29), R1234ze(E) achieves the highest net efficiency of nearly 4.5 %, corresponding to a second law efficiency of almost 30 %, compared to around 27 % with R1234yf and slightly over 25 % with R134a. The higher net power production with R134a is due to a greater isentropic enthalpy drop in the expander. Indeed, R134a has higher density and viscosity, resulting in lower pressure drops through the expander inlet valve. However, cycle efficiency does not follow the same trend because the low-GWP fluids show lower thermal power input in the evaporator (Figure 4.30). For R1234ze(E), this is due to a lower mass flow rate (Figure 4.31),

and for R1234yf, it is due to lower vaporization latent heat (Figure 4.27).

Table 4.7 - Selected working fluids' properties.

Fluid Name	Critical Temperature (°C)	Critical Pressure (bar)	GWP 100 (-)
R134a	101.06	40.593	1430
R1234yf	94.70	33.82	4
R1234ze(E)	109.37	36.36	6

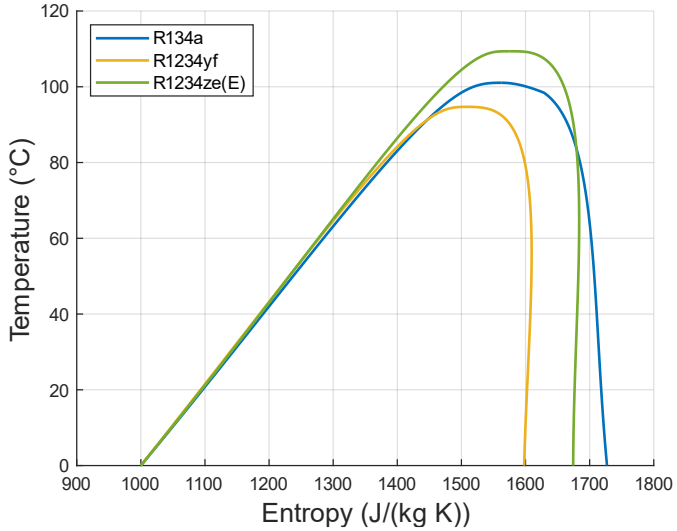

Figure 4.27 - Selected working fluids' saturation curves.

The analysis is carried out with constant hot source temperature (50 °C) and superheating degree (3 K), as described in Table 4.6, determining the evaporating temperature and pressure. Similarly, the condensing pressure is set by the cold sink temperature and subcooling degree, applied equally to all three fluids. Consequently, the ORC mass flow rate, calculated in the pump model, depends solely on the fluid's thermodynamic properties, particularly density and viscosity [215]. The lower density of R1234ze(E), due to lower operating pressures from the set evaporating and condensing temperatures, results in a lower ORC mass flow rate.

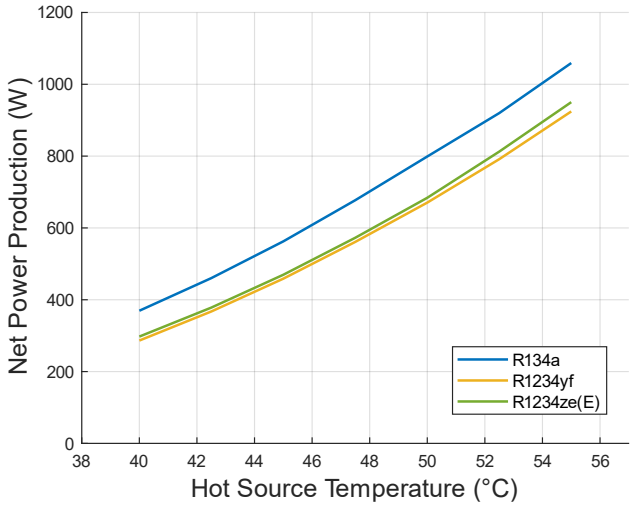

Figure 4.28 - Net electric power production versus hot source temperature (TH_{in}) in the working fluid sensitivity analysis.

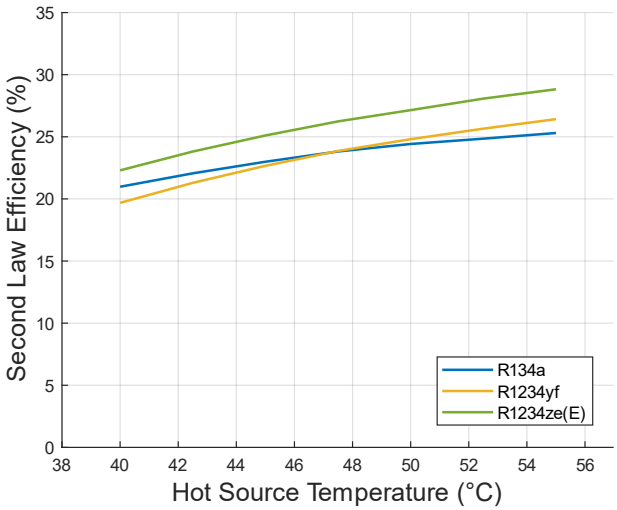

Figure 4.29 - Second law efficiency versus hot source temperature (TH_{in}) in the working fluid sensitivity analysis.

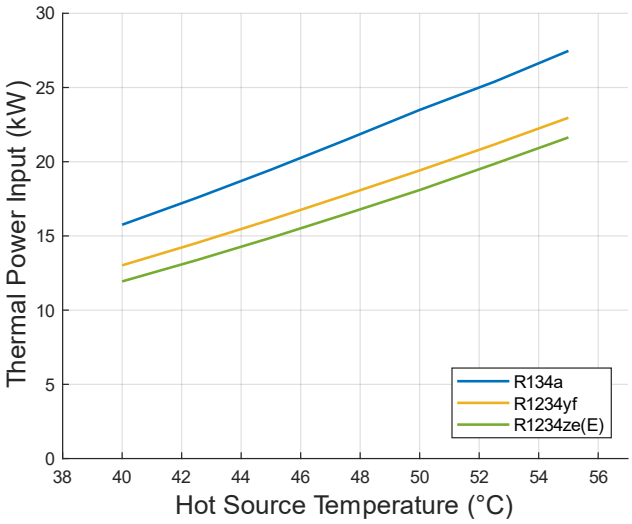

Figure 4.30 - Thermal power input versus hot source temperature (TH_{in}) in the working fluid sensitivity analysis.

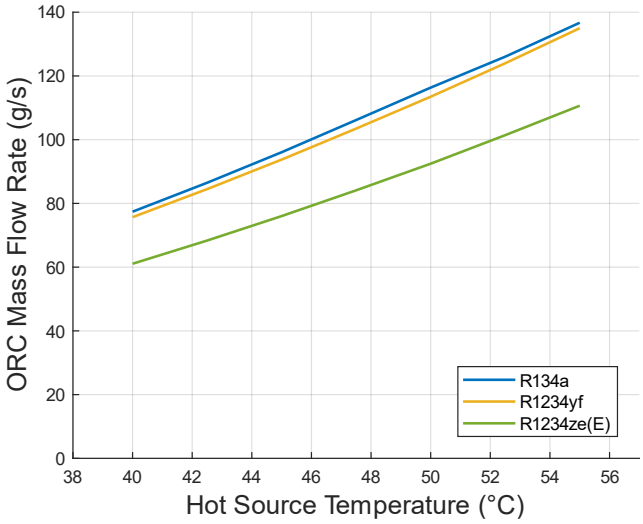

Figure 4.31 - Working fluid mass flow rate versus hot source temperature (TH_{in}) in the working fluid sensitivity analysis.

Considering that approximately 70 % of the power supplied to DCs must be dissipated [20], and thus can be used as thermal power input to the system, R1234ze(E) can recover 3 % of the electric power required by DCs, followed by R1234yf at 2.8 %, and R134a at 2.7 %.

This study's results demonstrate the promising potential of R1234yf and R1234ze(E) as environmentally friendly alternatives to HFC-134a. The optimization of the expander's built-in volume ratio ensures that the performance comparison is not affected by expander filling inefficiencies, improving system performance with all three fluids. However, it is noteworthy that previous studies [215], [216] reported significantly lower performance for HFOs compared to R134a, while in this study, performances are comparable. Therefore, the performance improvement due to the built-in volume ratio optimization is more pronounced with low-GWP fluids. Figure 4.32 shows the intake stroke ratio, α_v (Eq. (3-10)), which slightly increases with both hot source temperature (and expander inlet temperature) and ORC mass flow rate (Figure 4.31).

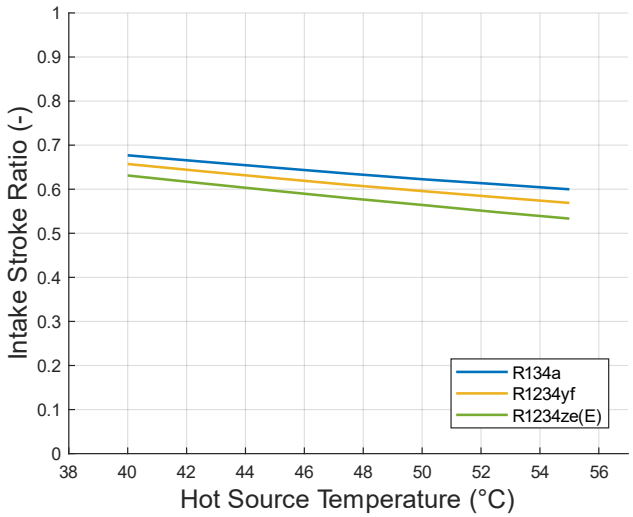

Figure 4.32 - Intake stroke ratio versus hot source temperature (TH_{in}) in the working fluid sensitivity analysis.

4.2.6. Conclusions of micro-ORC system application to data centers

This study proposes a feasibility analysis of integrating a micro-ORC system to recover cooling waste heat from servers in DCs. Given that DCs are highly energy-intensive converting most supplied electricity into heat, ORC technology offers a promising solution to enhance efficiency by reconverting some of this waste heat back into electrical energy.

The study combines both experimental and numerical investigations. The available ORC test bench is utilized to demonstrate the feasibility of recovering very low-grade heat, replicating heat source temperatures between 40 and 55 °C, typical for DCs. The semi-empirical model of the reference micro-ORC is then recalibrated and optimized in the expander built-in volume ratio. The optimized model is used to perform a parametric analysis, varying both heat source and ambient conditions, estimating around 1 kW production in the most favourable scenario, with a net efficiency close to 4.5 %.

Additionally, the study compares performance using the reference working fluid (HFC-134a) with low-GWP alternatives (HFO-1234yf and HFO-1234ze(E)). The results highlight comparable performance in power production and second law efficiency among the three fluids. While R134a produces the maximum electric power, it shows the lowest second law efficiency (25 %), whereas R1234ze(E) and R1234yf achieve second law efficiencies of 29 % and 27 %, respectively, with slightly less than 1 kW of power production.

Considering that approximately 70 % of the power supplied to DCs must be removed, the present study demonstrates that recovering this wasted energy can save a portion of the required electric power. In terms of electricity savings, R1234ze(E) is the most effective working fluid, recovering about 3 % of the power required by data center servers, followed by R1234yf and R134a, which recover 2.8 % and 2.7 %, respectively. Thus, the numerical analysis confirms the viability of the two HFOs as environmentally friendly alternatives to HFC-134a. Moreover, the reference system, although it includes prototype machines, is not specifically designed for very low temperatures, leaving significant potential for performance improvement.

Future works could explore replacing the water condenser with an air condenser to increase system flexibility and eliminate the need for a cooling tower, although this would raise condensing pressure and auxiliary consumption due to the fan. Additionally, using the organic fluid to directly cool the servers could be investigated to reduce thermal losses and increase the available temperature for heat recovery. Finally, partial evaporation might better match the heat source and WHR system, but it would require specialized design and optimization studies.

4.3. Conclusions

In this chapter, two different applications of small-scale ORC technology for low-temperature heat harnessing are investigated and presented. The first application involves the residential sector and the heat source is provided by thermal solar. The second investigation is related to waste heat recovery in an industrial application. In both the studies, a sensitivity analysis varying the ORC working fluid is assessed with the aim of exploring the potential of environmental-friendly working fluids.

More in detail, the first study explores the potential of integrating a kW-sized recuperated ORC system with a commercial solar thermal collector to reduce the annual electricity consumption of a single-family household. Using the detailed semi-empirical steady-state model presented in the previous chapter (section 3.3) and validated against experimental data, the analysis is performed considering daily and seasonal solar irradiation and ambient temperature profiles typical for Bologna (Italy). The first aim of the study is to design the sizes for both the solar collector surface and the storage tanks for the considered

application. Then, a performance comparison using different low-GWP fluids and blends as alternatives to the reference HFC-134a fluid for low-temperature ORCs is provided. Results indicate that the integrated system using R134a can meet about 39 % of the annual electricity demand, producing over 1150 kWh. In contrast, using alternative fluids like R1234yf and R513A leads to significantly lower electricity production, covering only 16 % (466 kWh) and 17.5 % (525 kWh) of the annual demand, respectively.

Despite the lower performance of low-GWP fluids, their adoption is essential for reducing greenhouse gas emissions. The study underscores the need for further research to optimize ORC systems for these alternative fluids, suggesting future work could include detailed economic analyses, system redesigns for efficiency improvement, and investigations into thermal power production. These steps could enhance the viability and performance of low-GWP fluids in ORC systems, making them a more effective solution for reducing the environmental impact of energy consumption in households.

The second study evaluates the feasibility and potential energy savings of integrating a micro-ORC system into DCs to recover cooling waste heat. DCs generate huge amount of heat from computer racks, and the ORC technology can exploit this waste heat, available at very low temperatures, to improve energy efficiency. The research involves both experimental and numerical investigations. An experimental analysis is conducted on the reference ORC test bench (described in section 3.1 of the previous chapter) using R134a as the working fluid. The heat is supplied at temperatures ranging from 40 to 55 °C and flow rates between 1.8 and 5 m^3/h, reflecting typical DC conditions. The second law efficiency varies between 5 % and 13 % in these experimental tests. Additionally, the reference model of the micro-ORC (section 3.3) is recalibrated and validated with experimental data. The reciprocating piston expander's built-in volume ratio is optimized to enhance the machine's filling performance. A parametric analysis is performed, varying the boundary conditions and the ORC working fluids (R1234yf and R1234ze(E) are explored). Performance comparisons among R134a and low-GWP alternatives (R1234yf and R1234ze(E)) indicate similar results in terms of power production and second law efficiency. R134a allows the production of the maximum electric power but shows the lowest second law efficiency (25 %). In contrast, R1234ze(E) and R1234yf achieve higher second law efficiencies of 29 % and 27 % respectively, with slightly lower power production. R1234ze(E) emerged as the most effective fluid for electricity savings, recovering about 3 % of the power required by data center servers. R1234yf and R134a followed, with savings of 2.8 % and 2.7 %, respectively. The reference system, not optimized for very low temperatures, suggests potential for performance improvements. Furthermore, direct cooling of servers with the organic fluid could reduce thermal losses and increase available heat recovery temperatures.

This study highlights the potential of ORC technology in enhancing DC energy efficiency by recovering waste heat, and underscores the need for further optimization and economic analysis to maximize the benefits of using low-GWP fluids in ORC systems.

5. HTHP in the ceramic tiles manufacturing sector

Summary. In this chapter, the use of a HTHP to enhance energy efficiency in ceramic tile manufacturing, by upgrading waste heat streams to process heat, is explored. Indeed, the production of ceramic tiles is an industrial process that consumes a significant amount of energy and generates considerable carbon emissions, yet it offers substantial opportunities for harvesting low-grade thermal energy. Two distinct WHR configurations are examined to convert unused waste heat streams into useful process heat, thereby lowering natural gas usage and cutting CO_2 emissions.

5.1. Ceramic tiles process

The ceramic industry, a significant energy-consuming manufacturing sector, accounts for 28 % of industrial energy use and produces 19 million tons of CO_2 annually [10]. Fossil fuel combustion is responsible for 66 % of these emissions, while electricity and process-related emissions contribute 18 % and 16 %, respectively. Various strategies to reduce carbon emissions in ceramic production have been investigated through European [217] and UK Roadmaps [218], as well as a collaborative industry-government action plan [219]. The identified technologies to cut CO_2 emissions fall into four primary categories [11]: i) improving energy efficiency, ii) electrification, iii) substituting fossil fuels with renewable energy or low-carbon hydrogen (or other synthetic fuels), and iv) carbon capture and storage. Among these strategies, enhancing energy efficiency by optimizing processes and technologies is the most feasible for immediate implementation. Natural gas remains indispensable in the short term and will continue to be the main fuel during the energy transition. Additionally, the lack of specific infrastructure significantly hinders the adoption of fuel switching, electrification, and carbon capture methods.

5.1.1. Process description

The ceramics industry includes the production of ceramic tiles, sanitary ceramics, tableware, and refractories. The primary category within this sector is "ceramic tiles for flooring and cladding," encompassing a variety of products with diverse formats, aesthetic and mechanical properties, and manufacturing methods. Regardless of the end product type, six common stages can be identified in the ceramic tile manufacturing process [48], as illustrated in Figure 5.1:

1. Grinding. Raw materials needed for the mixture are stored, measured, and sent to the grinding process. Wet grinding, the most common method, produces a powder with specific particle size and water content suitable for the intended product. This results in a "slip" with a water content of about 30-40 %.
2. Spray drying. The slip is transferred to a spray dryer. A strong jet of hot air (500-600 °C) rapidly reduces the water content from 35 % to 6-7 %. This phase primarily consumes thermal energy.
3. Pressing. The mixture is compacted through extrusion or pressing. Continuous pressing is widely used, allowing the creation of large-format and variable-thickness ceramic slabs.
4. Drying. Excess water is removed from the product using hot air (160-200 °C) in the drying phase. This strengthens the product for handling and reduces the firing cycle time, accounting for 9 % of the total thermal energy consumption in the process.
5. Glazing. Glazes are prepared by wet grinding specific components to create an aqueous suspension.

The glaze is then applied to the raw ceramic support, giving the final product its aesthetic characteristics and low water absorption.

6. Firing. Tiles and glazes are fired in roller kilns at temperatures up to 1200 °C. This phase imparts the desired mechanical strength to the finished product. Firing is the most energy-intensive stage, consuming 55 % of the total thermal energy in the production process. The necessary thermal energy is typically provided by natural gas combustion.
7. Cooling. After the firing stage, the tiles are cooled down before any additional operations, which may include rectification, cutting, lapping, or chamfering.
8. Sorting, Packaging, and Shipping. Finally, tiles are classified based on quality, followed by sorting, packaging, and shipping.

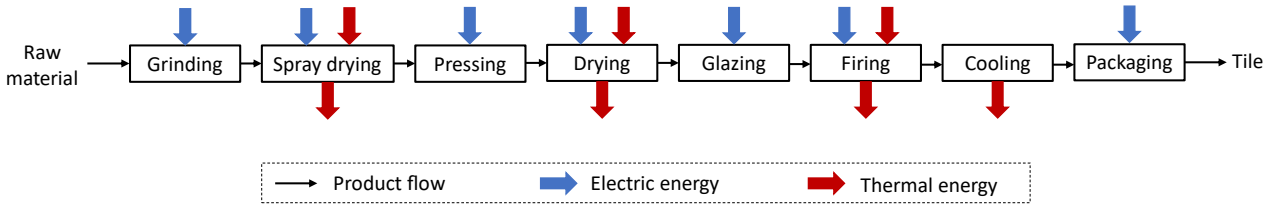

Figure 5.1 - Ceramic tiles manufacturing process line with highlighted energy vectors.

5.1.2. Energy efficiency solutions state of the art

Energy efficiency aims to produce the same products using less energy without altering the production process itself. Current estimates indicate that, with the technologies available today, additional energy savings of 15-25 % could be achieved by 2050 [11]. In the ceramic industry, efforts to improve energy efficiency have mainly focused on enhancing kiln efficiency, recovering waste heat from kiln flue gases and cooling air, improving thermal insulation, using high-speed flame burners, and continuously monitoring working conditions and process parameters [48]. Given the simultaneous need for electricity and heat in ceramic tile production, CHP technologies have been widely adopted since the 1990s [220]. Even CCHP generation has been explored through simulations [221]. Despite these advancements, energy costs still represent about 30 % of total production costs [222], which significantly contributes to production-related emissions.

To further boost the ceramic industry's energy efficiency, Mezquita et al. [223] introduced a calculation methodology based on specific kiln operating parameters to quantify energy savings achieved by recovering part of the cooling gases in the firing chamber rather than exhausting them into the atmosphere. Their study estimates up to 17 % energy savings in the examined case. Delpech et al. [224] investigated the use of a heat-pipe-based heat exchanger (HX) to reduce fuel consumption in a ceramic kiln. Their findings indicate that integrating the heat-pipe HX into the kiln's cooling stack could recover over 863 MWh of thermal energy annually, saving approximately 110600 Sm^3 of natural gas, preventing 164 tonnes of CO_2 emissions, and yielding cost savings of over € 22000. Another study [225] assessed the feasibility of recovering waste heat during the cooling stage using a system involving a radiative heat-pipe, kiln, and ceramics heater, demonstrating the capability to recover up to 4 kW of heat through radiation and natural convection in an enclosed kiln. Brough et al. [226] applied a multi-pass heat-pipe HX to a lab-scale ceramic kiln to transfer heat from the kiln exhaust to water, achieving a heat recovery rate of up to 63 kW and predicting a 33-month payback period for a full-scale unit preheating water for space heating. Jouhara et al. [227] demonstrated that a heat-pipe HX positioned adjacent to the cooling section exhaust stack could recover up to 100 kW at steady state without cross-contamination or excess fouling, with a return on investment estimated at 16 months and annual savings of £ 30000. Milani et al. [228] developed a lumped parameters model to simulate kiln performance under real operating conditions, exploring

various design options for kiln components and comparing different control strategies. Their analysis includes evaluating a novel burner type with internal heat recovery capabilities, showing approximately 10 % fuel savings and reduced CO_2 emissions compared to standard burners. In a subsequent work [229], the model was enhanced to minimize residual stresses in tiles and improve product quality. Venturelli et al. [230] used a 0D/1D numerical analysis and transient system simulation to examine energy efficiency gains from using a heat-pipe-based HX in the ceramic industry. Numerical results are validated against experimental measurements from a real ceramic facility, demonstrating the model's effectiveness in assessing energy efficiency improvements and exploring different configurations to meet industry requirements. Peris et al. [231] diverged from other studies by focusing on waste heat recovery to power an ORC. Based on experimental characterization, they developed a system model to predict net electrical production over a typical operational year. Their results show total energy production exceeding 115 MWh, saving approximately 237 MWh of primary energy, and preventing around 31 tons per year of equivalent CO_2 emissions, with a payback period of less than 5 years.

5.2. HTHP for ceramic tiles process waste heat upgrade

The push for decarbonization in the energy sector is driving the adoption of RES and the electrification of energy systems. This evolving landscape highlights the importance of exploring new synergies between renewable electricity generation and heat-intensive processes, particularly in industries, but also in residential and commercial sectors. HTHP technology emerges as a promising solution in this context. HTHPs enable the electrification of heat demand and utilize process waste heat as a 'renewable energy' source, potentially offering higher performance compared to applications relying primarily on outdoor air, ground heat, or groundwater. HTHP technology represents a viable strategy for decarbonizing sectors traditionally dependent on combustion.

5.2.1. Contribution

In the light of the above, as part of this thesis, this study aims to explore the potential of implementing HTHP technology in the ceramic industry to enhance energy efficiency. To the best of the Author's knowledge, there is a lack of studies in the literature investigating the feasibility of using HTHPs to improve waste heat quality and utilize it to supply thermal energy to the most heat-demanding tiles production stages. With this objective, an HTHP is designed to match the waste heat temperatures from the tiles production process, providing thermal energy to the most energy-demanding stages. During the design process, the layout of the HTHP is determined, the working fluid is selected, the compressor and HXs are sized, and the primary energy savings and prevented CO_2 emissions are calculated.

5.2.2. Energy recovery configuration

Based on Figure 5.1, thermal energy is needed for the spray drying, drying, and firing stages. Waste heat is generated in the same stages, including also the cooling step. The temperature levels at which thermal energy is needed ($T_{in,i}$) and released ($T_{out,i}$) vary across these stages and are listed in Table 5.1, along with the thermal consumption ($\dot{Q}_{in,i}/\dot{Q}_{in,tot}$) and waste heat ($\dot{Q}_{out,i}/\dot{Q}_{out,tot}$) ratios [49]. According to the data in Table 5.1, more than half of the total thermal demand is attributed to the firing stage (kiln), while the spray drying stage releases the highest amount of waste heat (50 % of the total).

Table 5.1 - Temperature levels and thermal power ratios required and released in the most energy-intensive stages [49].

	Spray dryer	**Dryer**	**Kiln**	**Cooler**
$T_{in,i}$ (°C)	500	200	1200	15
$T_{out,i}$ (°C)	100	130	250	70
$\dot{Q}_{in,i}/\dot{Q}_{in,tot}$ (-)	0.35	0.10	0.53	0
$\dot{Q}_{out,i}/\dot{Q}_{out,tot}$ (-)	0.50	0.12	0.21	0.17

Assuming a tile production rate of 5 t/h [228], a kiln-specific consumption of 550 kcal/kg [48], and an ambient temperature of 15 °C, the thermal power required ($\dot{Q}_{in,i}$) and released ($\dot{Q}_{out,i}$) in each stage are calculated through Eqq. (5-1)-(5-4) are reported in Table 5.2. The mass flow rate ($\dot{m}_i$) of hot air or fumes exchanging thermal energy in each stage is determined (see Table 5.2) through an energy balance across each stage (Eq. (5-5)).

$$\dot{Q}_{in,kiln} = q_{in,kiln} \cdot 4.186 \cdot \dot{m}_{tile}/3600 \tag{5-1}$$

$$\dot{Q}_{in,i} = \frac{\dot{Q}_{in,i}/\dot{Q}_{in,tot}}{\dot{Q}_{in,kiln}/\dot{Q}_{in,tot}} \cdot \dot{Q}_{in,kiln} \tag{5-2}$$

$$\dot{Q}_{out,kiln} = \frac{c_{p,out,kiln} \cdot (T_{out,kiln} - T_{amb})}{c_{p,in,kiln} \cdot (T_{in,kiln} - T_{amb})} \tag{5-3}$$

$$\dot{Q}_{out,i} = \frac{\dot{Q}_{out,i}/\dot{Q}_{out,tot}}{\dot{Q}_{out,kiln}/\dot{Q}_{out,tot}} \cdot \dot{Q}_{out,kiln} \tag{5-4}$$

$$\dot{m}_i = \frac{\dot{Q}_{in,i} - \dot{Q}_{out,i}}{\bar{c}_p (T_{in,i} - T_{out,i})} \tag{5-5}$$

Table 5.2 - Required and released thermal power, and mass flow rate in the most energy-intensive stages for a facility with a tiles production capacity of 5 t/h.

	Spray dryer	**Dryer**	**Kiln**	**Cooler**
$\dot{Q}_{in,i}$ (kW)	2111	603	3196	0
$\dot{Q}_{out,i}$ (kW)	1638	393	688	557
$\dot{m}_i$ (kg/s)	1.12	2.94	2.36	10.1

The explored energy recovery configuration applied to the ceramic tiles manufacturing is illustrated in Figure 5.2. The cooling air flow rate ($\dot{m}_{cooler}$), which enters the system at ambient conditions and after the cooling stage is at approximately 70 °C (refer to Table 5.1), is split in two fluxes. In one branch, the equivalent of the hot air flow rate required in the dryer and kiln ($\dot{m}_{dryer} + \dot{m}_{kiln}$) is preheated in two recovery heat exchangers, named RH1 and RH2, using waste heat from the drying and firing stages respectively. In the other branch, the enthalpy content of the remaining cooling air is utilized by the HTHP to raise the temperature of the hot air needed in the drying and firing stages. Considering that heat recovery technologies for the kiln waste stream are still under ongoing research [49], two scenarios are examined: one with RH2 (Figure 5.2) and one without (Figure 5.3). The goal of the analysis is to assess the

feasibility and design a HTHP to further preheat the air required in the drying and firing stages. Therefore, the hot sink flow rate ($\dot{m}_{sfH}$) is defined as the sum of the dryer and kiln flow rates (Eq. (5-6)), while the cold source flow rate ($\dot{m}_{sfC}$) is determined by subtracting the hot sink flow rate from the cooler flow rate (Eq. (5-7)).

$$\dot{m}_{sfH} = \dot{m}_{dryer} + \dot{m}_{kiln} \tag{5-6}$$

$$\dot{m}_{sfC} = \dot{m}_{cooler} - \left(\dot{m}_{dryer} + \dot{m}_{kiln}\right) = \dot{m}_{cooler} - \dot{m}_{sfH} \tag{5-7}$$

The cold source temperature at the inlet (TC_{in}) of the HTHP evaporator corresponds to the air temperature at the outlet of the cooler ($TC_{in} = T_{out,cooler}$). The hot sink temperature at the inlet (TH_{in}) of the HTHP condenser is calculated using THERMOFLEX [232], a commercial software specialized in energy systems modelling.

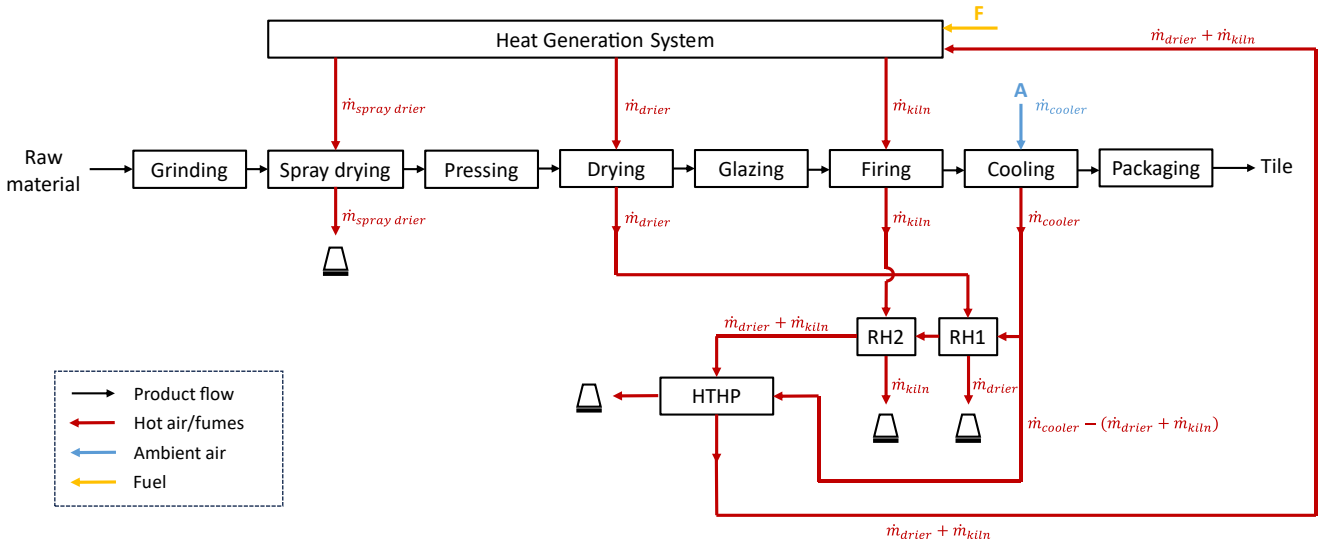

Figure 5.2 - Waste heat recovery setup applied to the ceramic tiles manufacturing - case with both RH1 and RH2.

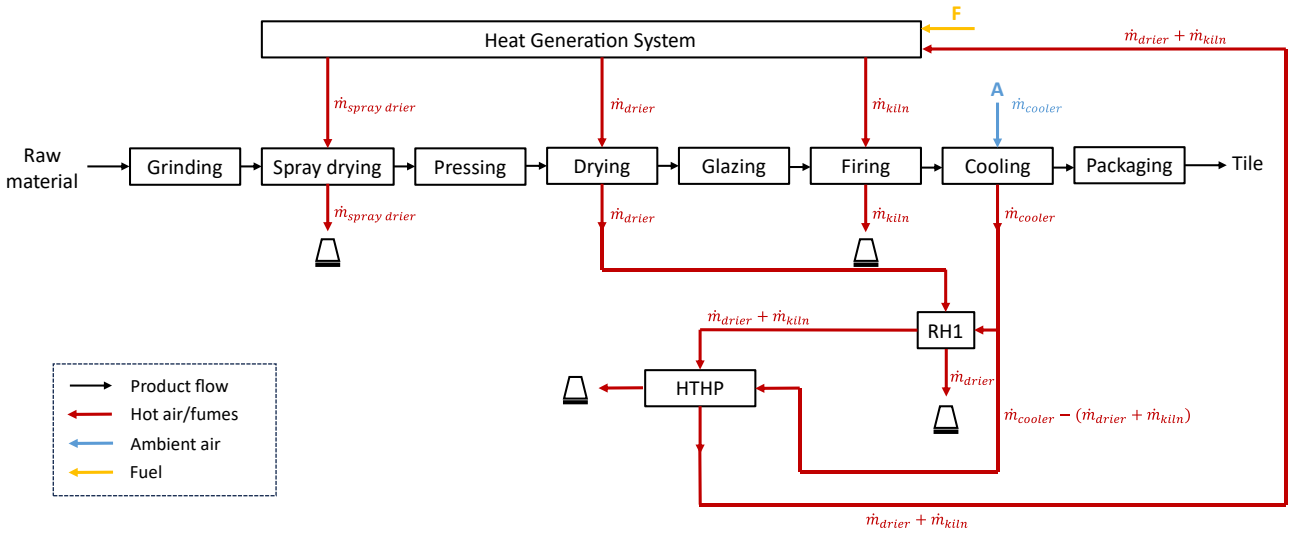

Figure 5.3 - Waste heat recovery setup applied to the ceramic tiles manufacturing - case with RH1 only.

The waste heat released by the spray drying is not exploited for multiple reasons: i) it is a very 'dirty'

high-wet air exhaust, which should be filtered before letting it pass through a heat exchanger; ii) it is available at a too low temperature compared to the air temperature at the outlet of the cooling stage; iii) the spray dryer does not work continuously, differently from the dryers, the kilns and coolers. Furthermore, some smaller companies do not have their own spray dryer, but they prefer buying the slip. Due to these considerations, the spray drying stage is not accounted for in the current study.

Specifically, the energy recovery setup includes the HTHP and the two heat exchangers, RH1 and RH2, as shown in Figure 5.4 (or only RH1, as shown in Figure 5.5). A single-stage cycle with an IHX is selected for the HTHP, consistent with most studied cycles and those achieving the highest sink temperatures [47].

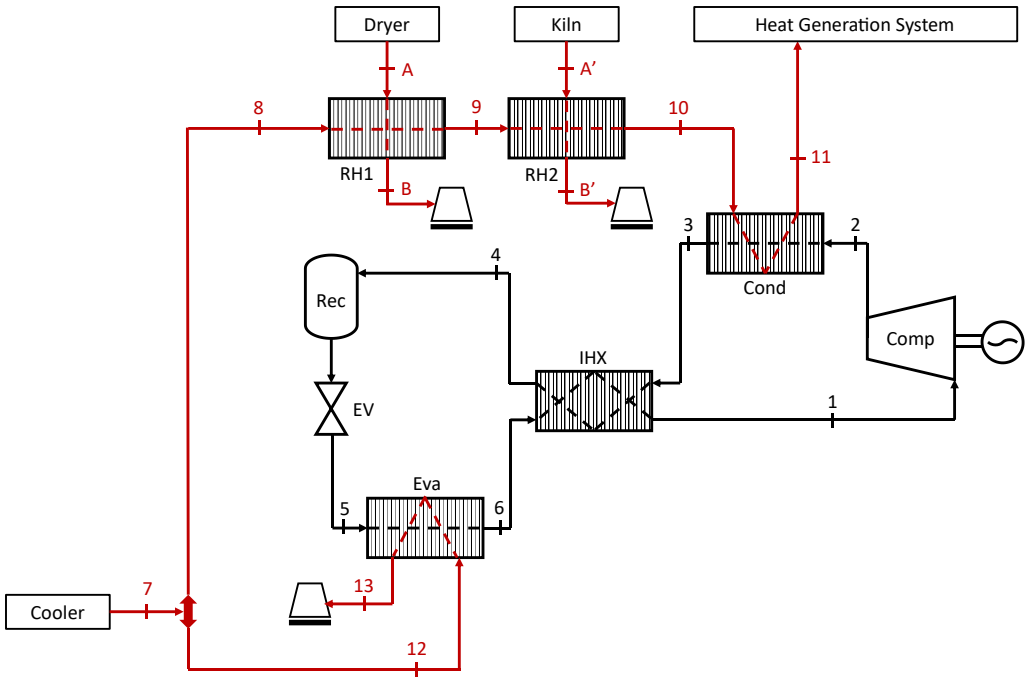

Figure 5.4 - Waste heat recovery setup layout - case with both RH1 and RH2.

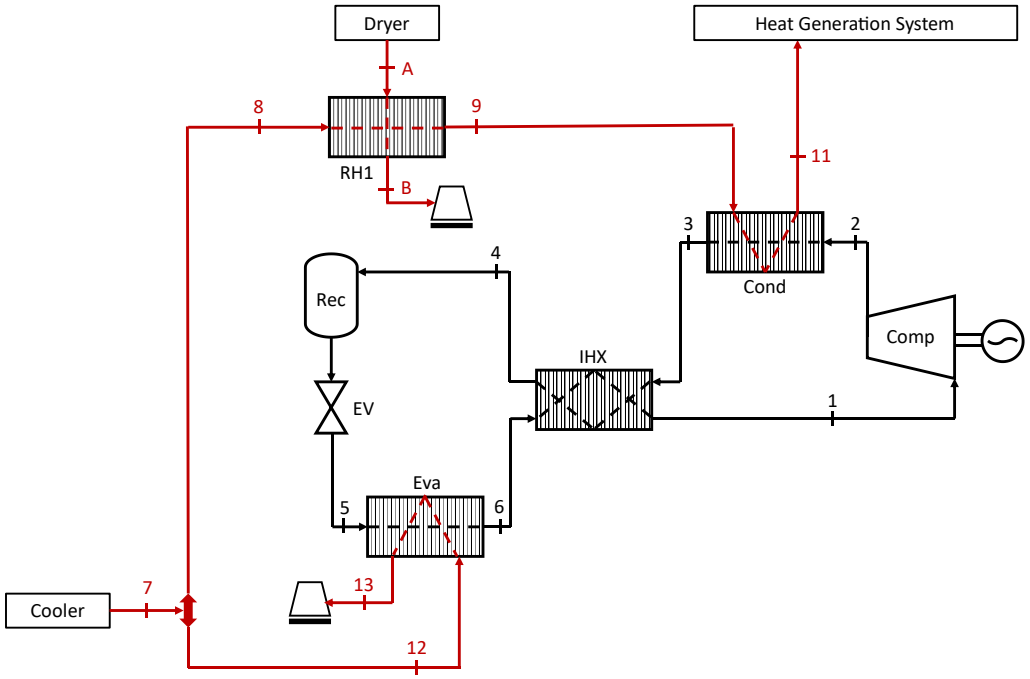

Figure 5.5 - Waste heat recovery setup layout - case with RH1 only.

5.2.3. Modelling approach for the working fluid selection

A general HX component from THERMOFLEX built-in library is chosen to model RH1 and RH2, assuming air-to-air cross-flow HXs with a thermal effectiveness of 75 % [233]. Heat losses of 1%, pressure losses of 2 %, and a minimum pinch point of 2.78 °C are considered. With these input values, RH1 allows to heat up the recovered air to 95 °C (point 9 in Figure 5.4), and RH2 pushes it to nearly 150 °C.

The first step for the HTHP design consists of selecting a suitable working fluid. A systematic comparison of thermodynamic performance for various working fluids is conducted using a lumped-parameters thermodynamic model developed in MATLAB [234]. The cycle model runs with a selection of fluids from the CoolProp library [27], chosen based on their critical temperatures suitable for the considered application. Indeed, the critical temperatures of the chosen fluids range between the outlet temperatures of RH1 and RH2 (in the respective scenarios with and without RH2) and up to 300 °C. Specifically, fluids with critical temperatures above 165 °C are considered suitable for both cases involving RH1 alone and the combination of RH1 and RH2. Conversely, fluids with critical temperatures below 165 °C and above 120 °C are suitable for the scenario including RH1 only. Additionally, any fluids with high critical pressures (> 50 bar), high GWP (GWP100 > 150), and non-zero ODP are excluded. Table 5.3 lists the selected fluids, along with their critical temperatures and pressures, GWP100, and their applicability to the RH1-only and combined RH1 and RH2 cases.

Table 5.3 - Working fluids selected set.

Fluid Name	T_{crit} (°C)	p_{crit} (bar)	GWP100 (-)	Case
1-Butene	146.14	40.051	-	RH1
cis-2-Butene	162.60	42.255	-	RH1
Cyclopentane	238.57	45.712	-	RH1 and RH2
Isobutane	134.67	36.290	-	RH1
Isobutene	144.94	40.098	-	RH1
Isohexane	224.55	30.400	-	RH1 and RH2
Isopentane	187.20	33.780	-	RH1 and RH2
n-Butane	151.98	37.960	3	RH1
n-Hexane	234.67	30.340	3.1	RH1 and RH2
n-Pentane	196.55	33.700	-	RH1 and RH2
Neopentane	160.59	31.960	-	RH1
R123	183.68	36.720	77	RH1 and RH2
R1233zd(E)	166.45	36.236	0	RH1 and RH2
R1234ze(Z)	150.12	35.330	0	RH1
trans-2-Butene	155.46	40.273	-	RH1

The cycle routine determines the evaporation pressure (p_v) and the condensation pressure (p_k) for each working fluid, utilizing input values such as the cold source and hot sink secondary fluids flow rates ($\dot{m}_{sfC}$, $\dot{m}_{sfH}$), the cold source inlet temperature (TC_{in}), and the hot sink inlet and outlet temperatures (TH_{in}, TH_{out}). Also included among the inputs are the minimum pinch point temperature difference (ΔT_{pp}), the superheating degree at the compressor inlet (ΔT_{SH}), the subcooling degree at the condenser outlet (ΔT_{SC}), and the temperature difference in the IHX (ΔT_{IHX}). These inputs allow for the calculation of thermal production. The equations used to model the HTHP cycle are detailed in Table 5.4, where dT_v and dT_k represent the increments of the iterative variables, and the state points correspond to those on the layout in Figure 5.4. The input parameters are detailed in Table 5.5. Additional assumptions include

constant isentropic efficiency for compression, constant electromechanical efficiency, and negligible pressure losses in the HXs. The thermodynamic properties of the fluids are derived from CoolProp library [27]. This cycle model is employed to compare the thermodynamic performance of various fluids, identifying the one with the highest COP for the given application (Eq. (5-23)).

Table 5.4 - HTHP lumped-parameters thermodynamic model equations.

Inputs	$\eta_{is,comp}$, η_{em} , ΔT_{pp} , ΔT_{SH} , ΔT_{SC} , ΔT_{IHX} , TH_{in} , TH_{out} , TC_{in} , $\dot{m}_{sfH}$, $\dot{m}_{sfC}$	
Pressures (iterative)	$p_v = p(T_v = TC_{in} - \Delta T_{pp} - dT_v, x = 1)$	(5-8)
	$p_k = p(T_k = TH_{out} + \Delta T_{pp} \mp dT_k, x = 0)$	(5-9)
State point 1	$h_1 = h(p_v, T_v + \Delta T_{SH})$	(5-10)
	$s_1 = h(p_v, h_1)$	(5-11)
State point 2	$h_{2,is} = h(p_k, s_1)$	(5-12)
	$h_2 = h_1 + (h_{2,is} - h_1)/\eta_{is,comp}$	(5-13)
State point 3	$h_3 = h(p_k, T_k - \Delta T_{SC})$	(5-14)
State point 4	$h_4 = h(p_k, T_v + \Delta T_{IHX})$	(5-15)
State point 5	$h_5 = h_4$	(5-16)
State point 6	$h_6 = h_1 - (h_3 - h_4)$	(5-17)
Hot sink	$\dot{Q}_{sink} = \dot{m}_{sfH} \cdot c_p H \cdot (TH_{out} - TH_{in})$	(5-18)
Working fluid	$\dot{m}_{wf} = \dot{Q}_{sink}/(h_2 - h_3)$	(5-19)
Cold source	$\dot{Q}_{source} = \dot{m}_{wf} \cdot (h_6 - h_5)$	(5-20)
	$TC_{out} = TC_{in} - \dot{Q}_{source}/\dot{m}_{sfC}/c_p C$	(5-21)
Electric consumption	$\dot{W}_{el} = \dot{m}_{wf} \cdot (h_2 - h_1)/\eta_{em}$	(5-22)
Coefficient Of Performance	$COP = \dot{Q}_{sink}/\dot{W}_{el}$	(5-23)

Table 5.5 - HTHP lumped-parameters thermodynamic model inputs.

$\eta_{is,comp}$ (-)	η_{em} (-)	ΔT_{pp} (K)	ΔT_{SH} (K)	ΔT_{SC} (K)	ΔT_{IHX} (K)	TH_{in} (°C)	TH_{out} (°C)	TC_{in} (°C)	$\dot{m}_{sfH}$ (kg/s)	$\dot{m}_{sfC}$ (kg/s)
0.70	0.90	3	10	20	5	95/145 (RH1/RH2)	120/165 (RH1/RH2)	70	5.3	4.8

The COP values (Eq. (5-23)) obtained from the lumped-parameters model for the selected fluids (Table 5.3) are utilized to determine the most suitable working fluid for the reference application, considering both scenarios, i.e., with and without direct waste heat recovery from the kiln stream. The achievable COP values for each fluid, using the same inputs (Table 5.5), are presented in Figure 5.6 and Figure 5.7 for the two cases, respectively (with both RH1 and RH2, and with RH1 only). The COP values are higher in the case involving waste heat recovery only from the drying stage (only RH1 – Figure 5.7) compared to the case including also direct waste heat recovery from the kiln stream (both RH1 and RH2 – Figure 5.6). This is due to the lower temperature lift between the cold source and hot sink of the HTHP, which results in a lower pressure ratio required to the compressor, and thus to a reduced electric consumption. This initial analysis indicates that cyclopentane is the most effective working fluid in both scenarios, reaching a COP of 2.1 in the first case (Figure 5.6) and 3.4 in the second case (Figure 5.7). Consequently, cyclopentane is selected as the working fluid for the reference application in both the cases.

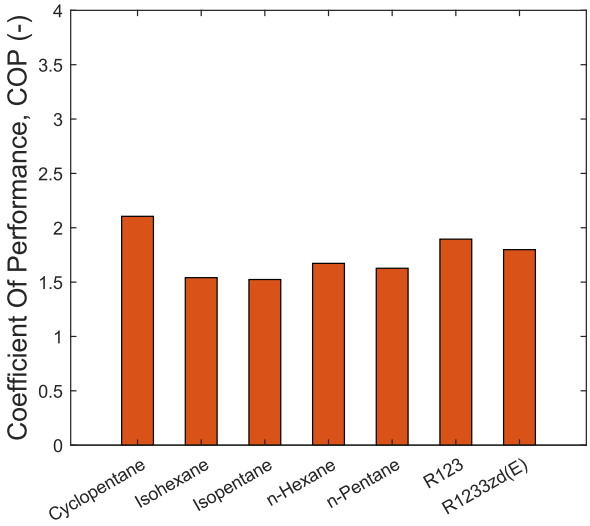

Figure 5.6 – COP results with the working fluids set selected for the case including waste heat recovery from both the drying and the firing stages (both RH1 and RH2).

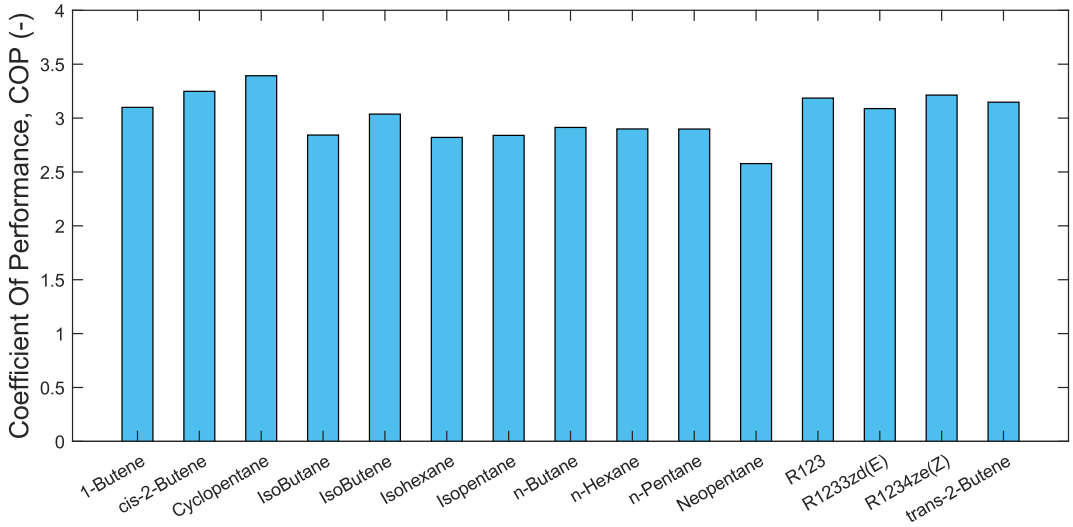

Figure 5.7 - COP results with the working fluids set selected for the case involving waste heat recovery only from the drying stage (only RH1).

5.2.4. HTHP components design and performance assessment

The selected working fluid is employed in a more detailed and accurate model, developed using THERMOFLEX, to design the compressor and HXs in the HTHP, as well as RH1 and RH2. The COP, the waste heat recovered at low temperature ($\dot{Q}_{source}$) and introduced into the heat generation system (HGS) at higher temperature by the HTHP ($\dot{Q}_{sink}$), and the compressor's electric consumption ($\dot{W}_{el}$) are used to assess the HTHP performance. Additionally, the temperature achieved by the hot air sent to the HGS (state point 11 in Figure 5.4 and Figure 5.5) indicates the HTHP's contribution to thermal production. The performance analysis and design of the HXs and the compressor in the energy recovery configuration are presented for the reference application in both analysed cases, i.e., with both RH1 and RH2 (Figure 5.4), and with RH1 only (Figure 5.5).

For the heat exchangers, the overall heat transfer coefficients (UA) are calculated using Eq. (5-24), while the compressor size ($\dot{W}_{comp}$) is determined using Eq. (5-25).

$$UA_{HXi} = \frac{\dot{Q}_{HXi}}{\Delta T_{HXi}} \tag{5-24}$$

$$\dot{W}_{comp} = \dot{m}_{wf} \cdot (h_2 - h_1) \tag{5-25}$$

In these equations, $\dot{Q}_{HXi}$ represents the thermal power exchanged in the i-th HX, ΔT_{HXi} is the positive temperature difference of the secondary fluid between the inlet and outlet of the i-th HX, and $(h_2 - h_1)$ is the enthalpy difference of the working fluid across the compressor.

As for RH1 and RH2, a general HX component from THERMOFLEX built-in library is chosen to model the HTHP's HXs. A thermal effectiveness of 80 % is set, assuming counter-flow HXs [233]. Heat losses of 1 %, pressure losses of 2 %, and a minimum pinch point of 2.78 °C are considered also for these HXs. Regarding the efficiencies, a design point isentropic compression efficiency of 70 %, a mechanical efficiency of 99 %, and an electric motor nameplate efficiency of 94 % are imposed. Eventually, a pressure ratio of 12 is assumed for the case with both RH1 and RH2, and a pressure ratio of 9.5 is set for the case with only RH1. These values are chosen to align with the pressure ratio values derived from the lumped-parameters thermodynamic model, which aims to achieve optimal performance of the HTHP unit.

The features of the WHR system setup and the main components design represent part of the results from THERMOFLEX modelling. The fluids' conditions at each state point in the WHR setup layout (Figure 5.4 and Figure 5.5), including mass flow rate ($\dot{m}$), pressure (p), and temperature (T), are detailed in Table 5.6 for both scenarios, with both RH1 and RH2, and with only RH1. Table 5.7 presents the design of the main components in terms of the overall heat transfer coefficient (UA) for the heat exchangers and the size of the compressor ($\dot{W}_{comp}$).

Table 5.6 - Thermodynamic conditions of the state points in the two waste heat recovery setups.

	RH1 and RH2				**RH1 only**			
	fluid	**$\dot{m}$ (kg/s)**	**p (bar)**	**T (°C)**	**fluid**	**$\dot{m}$ (kg/s)**	**p (bar)**	**T (°C)**
1	cyclopentane	0.41	0.965	68.0	cyclopentane	0.28	0.965	95.9
2			17.7	190			15.6	210
3			17.3	149			15.3	130
4			17.0	51.2			15.0	51.2
5			1.00	49.0			1.00	49.0
6			0.985	48.4			0.984	48.4
7	air	10.0	1.08	70.0	air	10.0	1.05	70.0
8			1.08	70.0			1.05	70.0
9		5.35	1.05	94.8		5.35	1.03	95.3
10			1.03	147				
11			1.01	173			1.01	119
12		4.65	1.08	70.0		4.65	1.05	70.0
13			1.05	53.2			1.03	53.2
A	low wet air	3.00	1.03	130	low wet air	3.00	1.03	130
B			1.01	85.0			1.01	85.0
A'	fumes	2.40	1.03	250	-	-	-	-
B'			1.01	134			-	-

Table 5.7 - Waste heat recovery components size for a facility with a tiles production capacity of 5 t/h.

	RH1 and RH2					**RH1 only**			
UA (kW/K)	RH1	RH2	Cond	IHX	Eva	RH1	Cond	IHX	Eva
	5.62	4.22	16.0	3.23	7.46	5.78	2.19	2.19	7.46
$\dot{W}_{comp}$ (kW)	69.0					49.9			

The overall system performance outcomes are summarized in Table 5.8 for both scenarios, i.e., with

both RH1 and RH2, and with only RH1. In each scenario, the COP is slightly lower than the values obtained from the thermodynamic analysis due to the THERMOFLEX model accounting for pressure and heat losses, HXs' efficiencies, and components' technical limitations. Additionally, while the MATLAB model fixes the thermal production $\dot{Q}_{sink}$ for performance comparison between different fluids, in the THERMOFLEX model, $\dot{Q}_{sink}$ is a variable output.

Table 5.8 - HTHP performance outcomes for a facility with a tiles production capacity of 5 t/h.

	RH1 and RH2	**RH1 only**
Coefficient of performance, COP (-)	2.0	2.4
Thermal power recovered, $\dot{Q}_{source}$ (kW)	79.4	79.4
Thermal production, $\dot{Q}_{sink}$ (kW)	146	128
Electric consumption, $\dot{W}_{el}$ (kW)	73.4	53.3
Hot air temperature, T_{11} (°C)	173	119

The effectiveness of the WHR setup in capturing thermal waste is measured by comparing the amount of heat actually recovered to the total recoverable waste heat. Temperature limits for each waste flow's atmospheric emissions are set based on the composition. Therefore, the effectiveness (ε_{WHR}) of the two WHR configurations is calculated as the proportion of waste heat recovered in the given scenario ($\dot{Q}_{WH,max} - \dot{Q}_{WH}$) relative to the total waste heat ($\dot{Q}_{WH,max}$) produced by the ceramic tile manufacturing process (Eq. (5-26)).

$$\varepsilon_{WHR} = \frac{\dot{Q}_{WH,max} - \dot{Q}_{WH}}{\dot{Q}_{WH,max}} = \frac{\sum \dot{Q}_{WH,max,i} - \sum \dot{Q}_{WH,i}}{\sum \dot{Q}_{WH,max,i}} \tag{5-26}$$

The total waste heat ($\dot{Q}_{WH,max}$) produced by the process is the sum of the waste heat released by each manufacturing stage ($\dot{Q}_{WH,max,i}$) when there is no energy recovery strategy, namely in the scenario represented in Figure 5.8. $\dot{Q}_{WH,max,i}$ is calculated according to Eq. (5-27):

$$\dot{Q}_{WH,max,i} = \dot{m}_i \cdot \left(h_{out,i} - h_{out,lim,i}\right) \tag{5-27}$$

in which $\dot{m}_i$ is the mass flow rate of the hot air/fumes crossing the i-th stage, $h_{out,i}$ is its enthalpy at the outlet of the i-th stage, and $h_{out,lim,i}$ is the enthalpy associated with the minimum (limit) temperature at which the hot air/fumes is allowed to be released in the atmosphere.

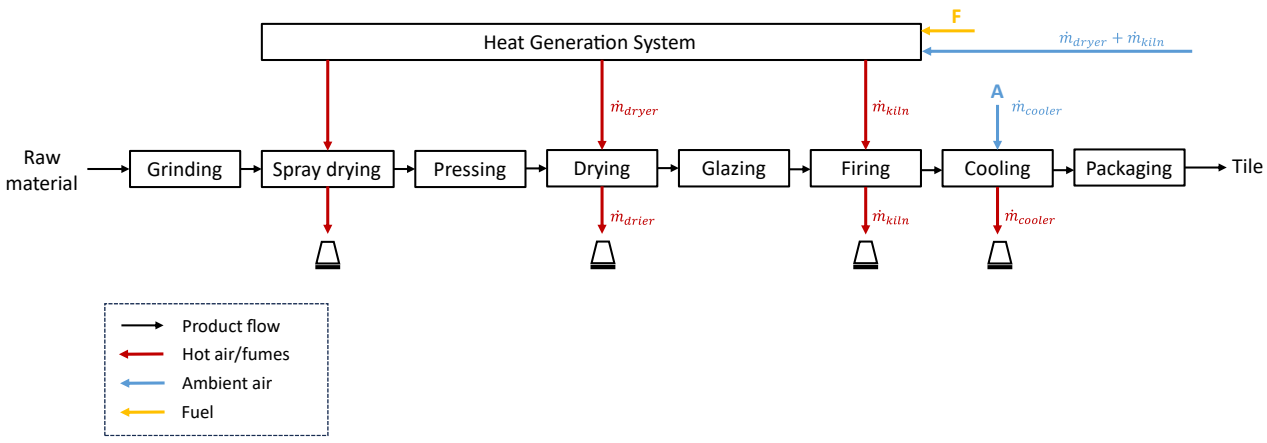

Figure 5.8 - Ceramic tiles manufacturing process without any waste heat recovery application.

Different temperature limits are set for each waste flow according to the proper composition and listed in Table 5.9: the air at the cooler outlet is almost pure, so the temperature limit is set equal to the assumed ambient air temperature (15 °C); the fumes at the kiln outlet are combustion exhaust fumes, therefore the minimum temperature at which they are allowed to be released into the ambient is 120 °C [235]; the air at the dryer outlet is wet with a humidity content of 0.1 kg_{water}/kg_{air} [236], thus the temperature limit is calculated imposing a maximum relative humidity of 60 %.

Table 5.9 - Limits for atmospheric emission of ceramic tiles waste streams.

	Dryer	**Kiln**	**Cooler**
Temperature limits for atmospheric emission (°C)	65	120	15
Absolute humidity (kg_{water}/kg_{air})	0.1	-	-

The recirculation of the hot air from the cooler outlet to the HGS (see Figure 5.9) allows to recover 26.5 % of the process waste heat.

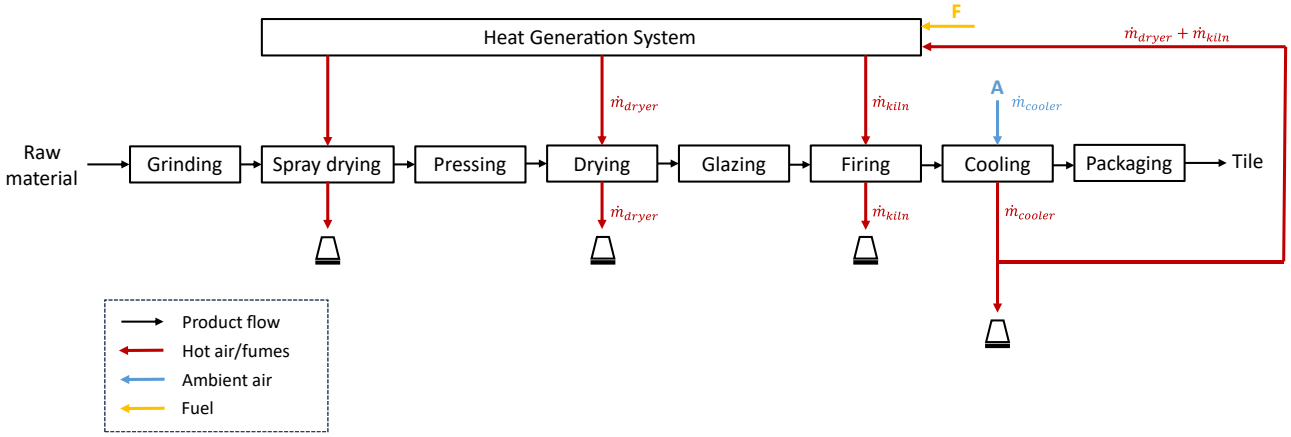

Figure 5.9 - Ceramic tiles manufacturing process with cooler hot air recirculation.

The implementation of a direct heat recovery from the dryer waste stream (RH1), as represented in Figure 5.10, increases ε_{WHR} to 40.9 %. Including also the HTHP (see the case layout in Figure 5.3) the fraction of recovered waste heat goes up to 47.9 %.

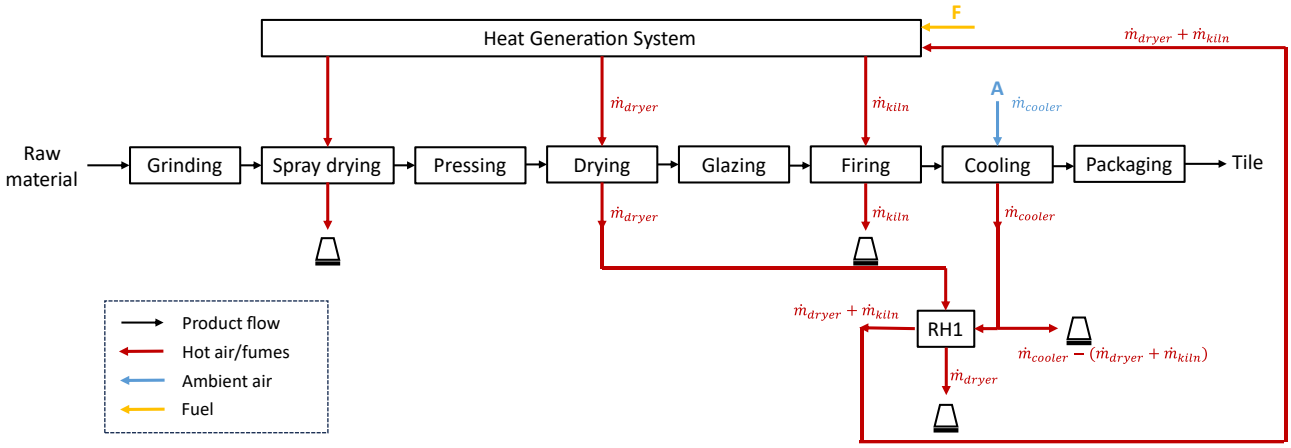

Figure 5.10 - Ceramic tiles manufacturing process with cooler hot air recirculation and direct heat recovery from the dryer waste stream.

The implementation of direct heat recovery both from the drying (RH1) and the kiln (RH2) waste streams, as depicted in Figure 5.11, allows to recover 67.8 % of the process waste heat. Including also the HTHP (see

the case layout in Figure 5.2) the fraction of recovered waste heat increases to 74.8 %.

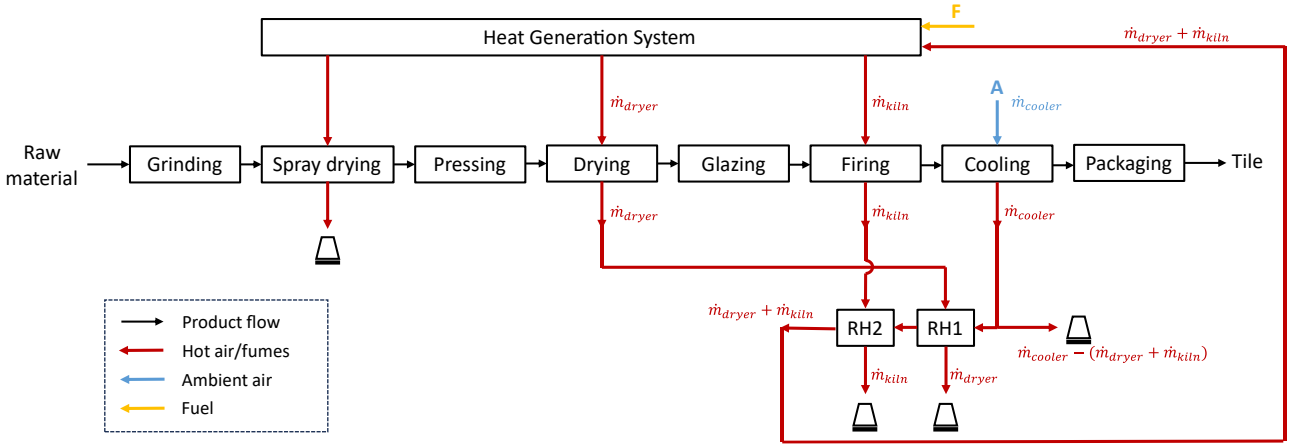

Figure 5.11 - Ceramic tiles manufacturing process with cooler hot air recirculation and direct heat recovery from the dryer and the kiln waste streams.

5.2.5. Fuel consumption and CO_2 emissions savings

Considering the environmental impact, the WHR configurations' benefits on thermal production are assessed by measuring reductions in fuel consumption and CO_2 emissions. The amount of fuel saved ($\dot{m}_F$) is determined by assuming that the thermal energy ($\dot{Q}_{sink}$), supplied by the HTHP to the hot air directed to the HGS (state point 11 in Figure 5.4 and Figure 5.5), does not need to be generated by a boiler combustion process:

$$\dot{m}_F = \frac{\dot{Q}_{sink}}{LHV \cdot \eta_{comb}} \tag{5-28}$$

In Eq. (5-28), LHV is the fuel's lower heating value, and η_{comb} is the assumed combustion efficiency of the boiler. The two scenarios in which the electricity used by the HTHP is i) sourced from renewable energy or ii) provided by the grid are evaluated (in this case, a reference electric conversion efficiency of 46 % is considered).

The avoided CO_2 emissions ($\dot{m}_{CO2}$) are calculated based on the molar mass ratio of CO_2 to the fuel, reflecting the mass of CO_2 produced from burning 1 kg of fuel during stoichiometric combustion. Methane (CH_4) is assumed to be the fuel used for thermal energy production, with an LHV of 50 MJ/kg and a molar mass ratio of 2.75. A combustion efficiency of 90 % is set according to [221].

Table 5.10 summarizes the results for fuel reduction and associated avoided CO_2 emissions per tonne of tiles produced, for the configurations with both RH1 and RH2, and with RH1 only, and in the two scenarios in which electricity is provided by renewables or by the grid. In brackets, the first term is associated with the HTHP thermal production contribution, the second term is associated with the direct heat recovery contribution (RH1 and RH2), the third term (negative) refers to the HTHP electric consumption in the scenario in which the electricity is provided by the grid (this term is null in case of renewable electricity). Results show that the HTHP implementation makes sense only in presence of renewable energy availability. Furthermore, the findings indicate that, despite the lower performance of the HTHP in the case with waste heat recovery from both the dryer and kiln (RH1 and RH2 scenario), the primary energy savings and associated avoided emissions are greater, not only because of the higher fraction of recovered waste heat, but also due to the HTHP delivering higher thermal power (Table 5.8).

Table 5.10 - Fuel consumption and CO_2 emissions savings per ton of tiles produced.

		HTHP, RH1 and RH2 (case with both RH1 and RH2)	**HTHP and RH1** (case with RH1 only)
Fuel consumption savings, $\dot{m}_F$ ($kg_{fuel}/h/t_{tiles}$)	Scenario 1: electricity from renewables	13.6 (2.34 + 11.3)	8.89 (2.05 + 6.84)
	Scenario 2: electricity provided by the grid	11.3 (2.34 + 11.3 – 2.30)	7.22 (2.05 + 6.84 – 1.67)
CO2 avoided emissions, $\dot{m}_{CO2}$ ($kg_{CO2}/h/t_{tiles}$)	Scenario 1: electricity from renewables	37.5 (6.42 + 31.1)	24.4 (5.63 + 18.8)
	Scenario 2: electricity provided by the grid	31.2 (6.42 + 31.1 – 6.33)	19.8 (5.63 + 18.8 – 4.59)

Compared to the thermal demand of the drying and firing stages (Table 5.2), the WHR configuration incorporating RH1, RH2, and the HTHP achieves fuel savings of 18.6 %, whereas the configuration with RH1 and the HTHP alone ensures fuel savings of 14.7 %.

5.3. Conclusions

This chapter proposes the application of HTHP technology to improve energy efficiency in the ceramic industry, specifically targeting waste heat recovery from key energy-intensive stages (spray drying, drying, kiln firing, and cooling) in ceramic tile production. The study employs a comprehensive methodology encompassing thermodynamic modelling, fluid selection, and detailed system design. Unlike previous studies that focus on enhancing kiln energy efficiency, this research proposes an energy recovery configuration incorporating an HTHP to pre-heat the air needed for the drying and firing stages after recovering waste heat from cooling, drying, and firing processes.

Fluid selection, evaluated using a lumped-parameters model developed in MATLAB, identifies cyclopentane as the most appropriate working fluid for the application. A detailed model of the HTHP system is implemented in the THERMOFLEX environment, using inputs based on cyclopentane and data from technical literature. The HTHP achieves a COP of 2.0 and pre-heats air to 173 °C when recovering waste heat from drying, firing, and cooling stages. A COP of 2.4 and air pre-heat temperature of 119 °C are achieved when recovering waste heat from drying and cooling stages only. Additionally, the detailed model determines the sizes of the heat exchangers and compressor for a reference tile production capacity of 5 t/h. The two WHR configurations allow to recover respectively 75 % and 48 % of the total waste heat produced by the ceramic tiles manufacturing process.

Ultimately, the study assesses fuel consumption savings and associated avoided CO_2 emissions. Estimating savings are of approximately 13.6 kg/h of fuel (and 37.5 kg/h of CO_2) per ton of tiles produced, which corresponds to 18.6 % of the stages demand, when recovering waste heat from drying, firing, and cooling stages. Fuel savings are of approximately 8.89 kg/h of fuel (and 24.4 kg/h of CO_2) per ton of tiles produced, corresponding to 14.7 % of the demand, when recovering waste heat from drying and cooling stages only. In conclusion, the research underscores the potential of HTHP technology as a decarbonization strategy in hard-to-abate industrial sectors. Future research could explore scalability and economic viability in real-world ceramic production facilities.

PART II

Carnot battery technology integration for energy storage applications

6. Carnot battery reference test benches

Summary. This chapter introduces the two reversible HP/ORC test benches located at the Thermodynamics Laboratory of the University of Liège (Belgium). The experimental facilities are described in their main components, including the acquisition and control system. The first test bench is a 1.5 kW-size CB, designed as a proof of concept to validate CB technology, demonstrating the system's components and performance in both HP and ORC modes. The second, a larger 10 kW-sixed setup, is currently under development and designed for integration with the lab's district heating substation, focusing on energy storage and peak shaving. The control and acquisition system for this larger test bench is developed as part of this thesis and described in the last part of this chapter.

6.1. University of Liège 1.5 kW-sized reversible HP/ORC test bench

Carnot batteries obtained from the integration of ORC and HTHP technologies represents a promising way to push the penetration of renewables in the energy sector. Indeed, integrated in complex energy systems, CBs allow to smooth the mismatch between energy demand and renewable energy production, typically intermittent, improving the grid stability and providing a sustainable energy storage solution.

As mentioned in subsection 1.4.4, CB technology (PTES in particular) is still in its early stages. As a result, much of the research in this area has been theoretical, concentrating on laying the groundwork for the technology. Recently, however, with growing momentum toward carbon-zero goals, some experimental studies and pilot projects have started to emerge.

With the aim of contributing to the literature and experimental research on this topic, numerical and experimental activities were pursued, and reported in this second part of the thesis. Two CB prototypes, located at the Thermodynamics Laboratory of the University of Liège (Belgium), are considered as reference for the aforementioned activities. The first prototype, a 1.5 kW-sized reversible HP/ORC pilot plant, is described in this section (0). The second prototype, a 10 kW-sized reversible HP/ORC test bench still under development, is described in the next section (6.2).

Designed, built and tested at the Thermodynamics Laboratory [107], the 1.5 kW-sized reversible HP/ORC pilot plant is intended as a proof of concept to prove the technical feasibility of the CB technology by showing acceptable performance of components (heat exchangers and volumetric machine) working in very different conditions depending on the operating mode (i.e., HP or ORC mode). The development of the test bench, including external heat supply circuits, cold sink circuits, and the acquisition and control system, was completed by Thermodynamics Laboratory personnel [237].

The experimental data, based on the experimental campaign conducted on the 1.5 kW-sized pilot plant [107], were used to calibrate and validate the HP/ORC model developed by Torricelli [136]. The HP/ORC model is extensively employed throughout this thesis, which is mainly focused on the development of strategies to improve the management of CBs in complex energy systems involving different energy fluxes. The following subsections describe the experimental setup of the test bench and the reversible HP/ORC model.

6.1.1. Experimental setup

The reference 1.5 kW-sized prototype is a reversible HP/ORC power plant, sharing the same heat exchangers and the same volumetric machine in both the operating modes. The hydraulic layout, including

all components and sensors, is depicted in Figure 6.1. The primary circuit, shown in green, represents the refrigerant loop, which includes a high-pressure heat exchanger, a scroll volumetric machine capable of functioning as both a compressor and an expander, a low-pressure heat exchanger, and two parallel branches equipped with an expansion valve and a plunger pump. These allow the system to alternate between HP mode and ORC mode. In ORC mode, the refrigerant flows clockwise, while in HP mode, it flows counterclockwise. Additionally, the test bench incorporates two external circuits (blue loops) with water circulating through them to simulate the hot and cold sources, feeding the high-pressure and low-pressure heat exchangers, respectively. The hot source loop contains two storage tanks to maintain a perfect stratification between the hot and cold zones, with a pump ensuring the water moves from the hot tank to the cold one during ORC mode, and the reverse during HP mode, through a four-way valve. A similar reversible configuration is applied to the cold source loop, although it lacks storage tanks. To simulate varying temperature levels, both the hot and cold sides are equipped with external heat sources.

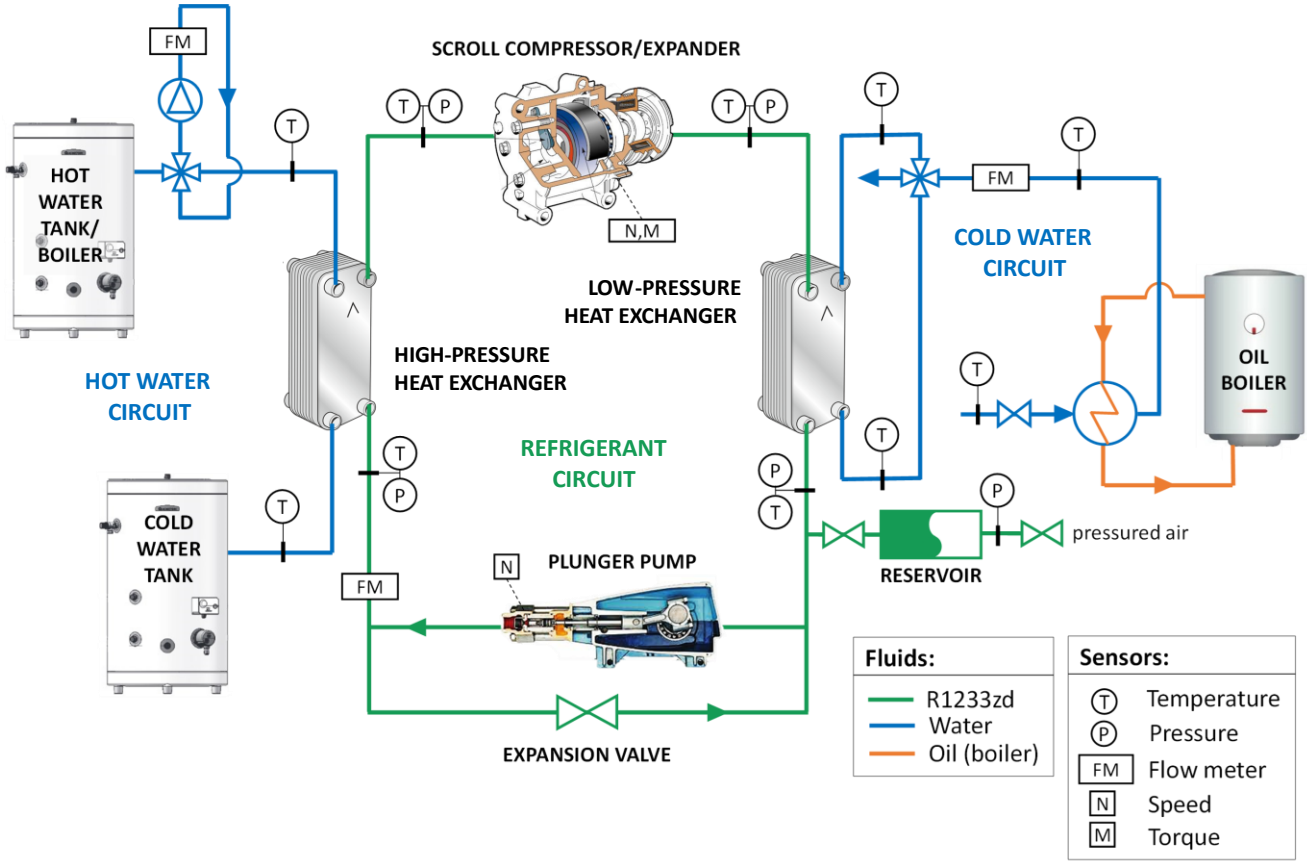

Figure 6.1 - Layout of the 1.5 kW-sized reversible HP/ORC pilot plant at the Thermodynamics Laboratory of the University of Liège [136].

The volumetric machine is a modified scroll compressor from the automotive industry, designed to operate reversibly as an expander. The ORC plunger pump was selected for its high volumetric and isentropic efficiency. A solenoid valve serves as the expansion valve to adjust the compressor's suction superheating in HP mode. Two storage tanks, each with a 900-liter capacity, store 10 kWh of energy on the hot water side. The condenser and evaporator are plate heat exchangers, designed to maintain a pinch point below 2 K. The test rig is fully equipped with high-accuracy sensors to monitor the thermodynamic state of the fluids at various cycle points and the associated power levels. Detailed specifications of the components can be found in Table 6.1.

Table 6.1 - 1.5 kW-sized reversible HP/ORC pilot plant components' technical data [107].

Component	Parameter	Value
Scroll Compressor Sanden TRSA09	Swept volume (cm^3)	85.7
	Shaft speed (rpm)	500-8000
	Volume ratio	2.2
Plunger pump Hyproplunger 2220B-P	Flow rate (l/s)	0.159
	Shaft speed (rpm)	1725
	Maximum pressure (bar)	137
Expansion Valve Asco 290	Flow coefficient – Kv (m^3/h)	2.7
	Maximum temperature (°C)	90
	Maximum differential pressure (bar)	6
Auxiliary pump (HP) Grundfos CRE1-4	Maximum flow (l/s)	0.5
	Head (m)	15
	Maximum temperature (°C)	95
Liquid tank	Maximum pressure (bar)	10
	Volume (l)	5
	Maximum temperature (°C)	110
Storage (x2)	Volume (m^3)	0.9 (x2)
Low-pressure heat exchanger B85Hx44	Area (m^2)	2.52
	Number of plates (-)	44
High-pressure Heat Exchanger B26Hx060	Area (m^2)	2.38
	Number of plates (-)	60

The prototype's sizing and working fluid selection were based on target boundary conditions that are representative of many industrial applications, with the goal of balancing electrical production and consumption [237]:

- Ambient temperature set to 15 °C and waste heat temperature to 75 °C.
- Storage capacity around 10 kWh.
- Hot source temperature glide through the HP heat exchanger at 10 °C.
- Nominal electrical power of the volumetric machine approximately 3 kW.

Given these conditions, HFO-1233zd(E) was selected as the refrigerant due to its high performance. It has a critical temperature of 165 °C and a critical pressure of 35.7 bar. HFO-1233zd(E) is a non-flammable refrigerant with an ultra-low GWP (GWP = 1), originally developed as a replacement for R-123 in low-pressure centrifugal chillers. Its thermodynamic properties are illustrated in the pressure-enthalpy diagram in Figure 6.2.

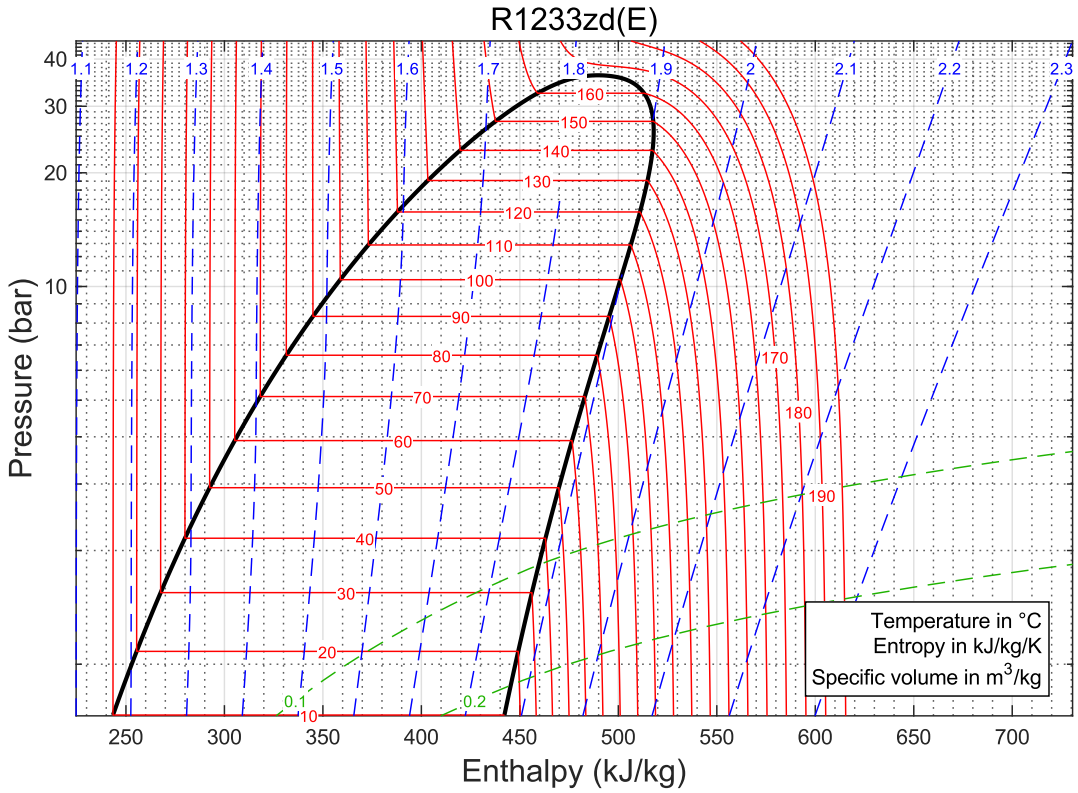

Figure 6.2 - R1233zd(E) pressure-enthalpy thermodynamic diagram (obtained by means of Refprop thermodynamic database [132]).

6.1.2. ORC and HP models

The HP's and ORC's components sub-models, developed by Torricelli [136], are summarized in this subsection. For further information, the interested reader is invited to consult Torricelli's thesis [136] and the associated work [71]. The HP and ORC semi-empirical models are here described due to their extensive use in the numerical activity carried out as a part of this thesis and detailed in the next two chapters.

Separate models for the ORC and HP are used to predict the performance of the system operating in each mode under various boundary conditions and control variables. The look up tables obtained with these models represent the HP/ORC performance maps, which can be combined into a comprehensive CB model, including also a TES tank.

The ORC and HP main components are modelled using a semi-empirical approach, drawing on methods described in the section 3.3 of this document. The key components include:

- the heat exchangers, modelled using the moving boundaries method, with corrected versions of Cooper's and Gnielinski's correlations to evaluate heat transfer coefficients;
- the scroll compressor, modelled using a lumped parameter approach that accounts for various losses and mechanical inefficiencies but excludes recompression losses, unlike in piston expanders;
- the ORC pump, whose performance is modelled based on operating conditions like rotational speed and pressure rise, with empirical parameters influencing power consumption;
- the HP expansion valve, represented by isenthalpic expansion between condensing and evaporating pressure values;
- pressure drops, calculated using an empirical equation;
- auxiliary pumps, whose power consumption is modelled based on fluid flow and pressure drops with a constant efficiency.

These sub-models are time-independent, meaning that it is assumed they operate in steady-state

conditions during the considered time intervals. The models are linked each other to simulate the overall system performance, considering boundary conditions and control variables. The boundary conditions are influenced by the location and the specific processes involved, with key factors being the state of the hot and cold source fluids and the surrounding ambient temperature. On the other hand, the control variables are those adjustable by an operator, including the secondary fluids temperature glide through the heat exchangers, the flow rate of the working fluid, the degree of superheating at the evaporator, and the degree of subcooling at the condenser. By iterating over cycle pressures, the part-load model can output the fluid state at each cycle point, the thermal power exchanged within the heat exchangers, the flow rate of secondary fluids, and the power either consumed or generated by the machines. The empirical parameters were calibrated using experimental data obtained from the experimental campaign documented by Dumont et al. in [107].

The HP and ORC models were used to simulate the system, in each mode, when working in a wide range of boundary conditions and control variables. With this aim, look up tables representing the HP's and ORC's performance, were built up to provide the optimal operating conditions according to the available boundary conditions. The target is to maximize the net efficiency/COP in ORC/HP mode under given boundary conditions. More in detail, the strategy involves:

1. Creating lookup tables through simulations that explore the entire range of possible boundary and control variable conditions. These tables relate net efficiency (or COP) to variables like hot source temperature, glide, and working fluid flow rate.
2. From these, new lookup tables are generated to identify the optimal values of glide and working fluid flow rate for maximum efficiency (or COP) at various hot source temperatures and power levels.
3. Interpolating this data to determine the best settings for operating the system at maximum efficiency.

Basically, this strategy ensures that the HP/ORC operates at its most efficient point, depending on the current storage temperature (hot sink/source) and the power required/available. The goal is to achieve maximum efficiency, even if it does not always correspond to maximum power production in ORC mode or minimum power consumption in HP mode.

6.2. University of Liège 10 kW-sized reversible HP/ORC test bench

Still under construction, the 10 kW-sized reversible HP/ORC Carnot battery test bench [238] is intended to be coupled with the district heating (DH) substation serving the Thermodynamics Laboratory building, equipped with photovoltaic (PV) panels. The purpose of this application is to provide both electrical and thermal peaks shaving. Integrating a CB with a DH system, utilizing a hot water tank for thermal energy storage, enables the reduction of thermal demand in the building by directly using the stored hot water. Additionally, surplus renewable energy generation elevates the temperature of the hot water in the tank by converting thermal energy from the DH system. When the building's electricity consumption overcomes its renewable energy production, the CB in ORC mode converts the stored thermal energy into electricity to meet electrical demand peaks.

The following subsections describe the experimental setup of the test bench and illustrate the connection with the DH substation.

6.2.1. Experimental setup

As the 1.5 kW-sized prototype, also the 10 kW-sized power plant shares the same heat exchangers in both the HP and ORC modes, and the volumetric machines can operate both as compressors and expanders.

Figure 6.3 presents the hydraulic layout, which includes all components and sensors. The primary loop, shown in green, is the refrigerant circuit. This circuit consists of two brazed plate heat exchangers, namely a high-pressure HX and a low-pressure HX, three scroll machines operating as either compressors or expanders, and two parallel branches equipped with an expansion valve and a pump respectively. These allow for alternating operation between HP mode and ORC mode. A liquid receiver is incorporated within the expansion valve branch. The refrigerant flows clockwise during ORC mode and counterclockwise during HP mode.

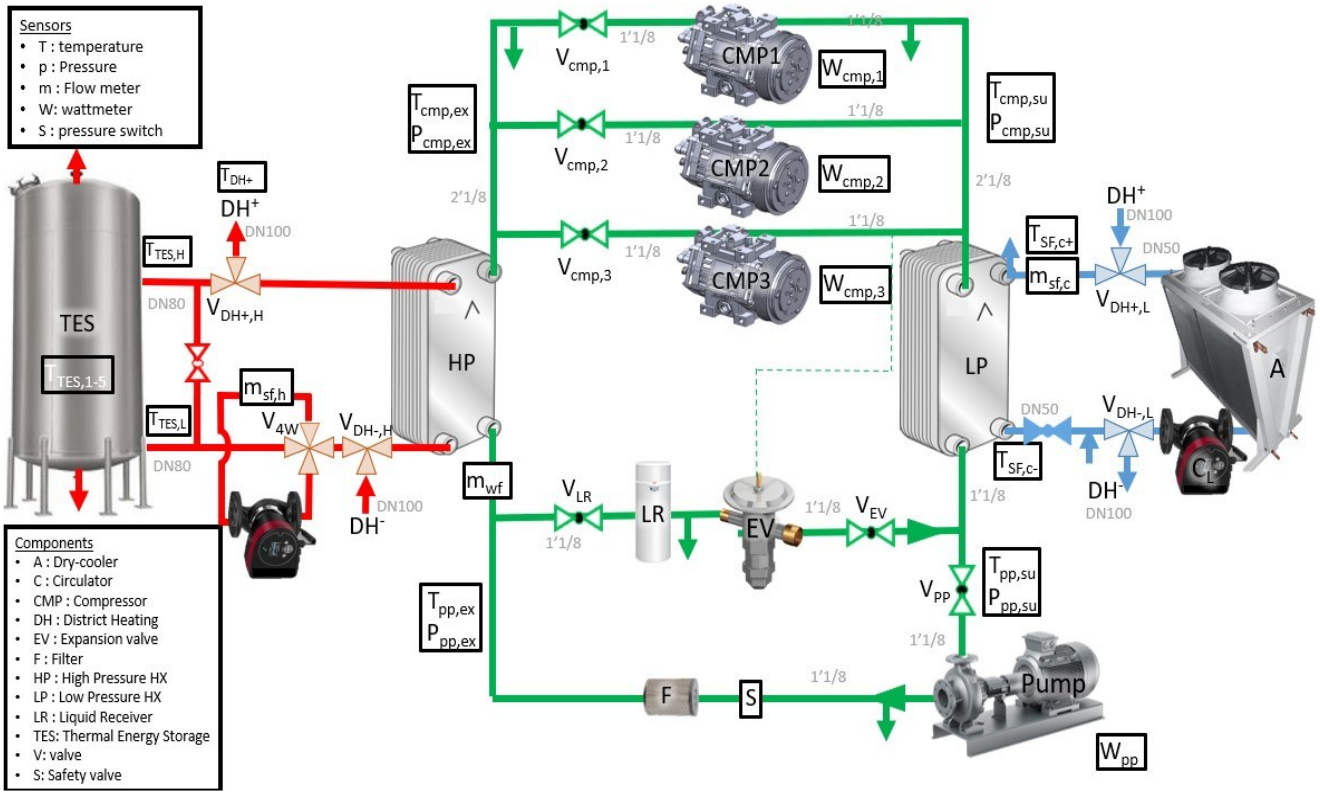

Figure 6.3 - Layout of the 10 kW-sized reversible HP/ORC Carnot Battery at the Thermodynamics Laboratory of the University of Liège [238].

The test bench also features two external circuits (represented by red and blue loops), which circulate water to simulate the hot and cold sources, feeding the HXs. In this bench, instead of two tanks, the hot circuit includes only one stratified tank, with a pump facilitating water circulation from the top to the bottom of the tank in ORC mode, and in reverse during HP mode, using a four-way valve. A dry cooler is included in the cold circuit. Detailed specifications of the components are listed in Table 6.2.

In HP mode, two scroll compressors handle the compression, while in ORC mode, three scroll machines are utilized due to the higher volumetric flow rate. The scroll compressors have been modified for reversible operation as expanders and operate at a constant speed. The compressors' motors can operate as generators (in ORC mode) by changing their rotation verse inverting two of the three phases. Furthermore, each machine is provided with a clutch to be decoupled from the motor. A centrifugal pump was selected for its robustness, as volumetric pumps require greater sub-cooling and are less durable. The condenser and evaporator are plate heat exchangers, designed to maintain a pinch point below 2 K. The HP expansion valve is electronically regulated. The liquid receiver has a 10-liter capacity to achieve charge adjustments based on the operating mode. The refrigerant charge is managed via the V_{LR} and V_{EV} valves. During HP mode, V_{LR} and V_{EV} are open, while V_{PP} is closed. In ORC mode, V_{PP} is open, and V_{LR} and V_{EV} are typically closed but can be briefly opened to adjust the charge.

The selected working fluid is R1233zd(E) (Figure 6.2) also for this test rig.

Table 6.2 - 10 kW-sized reversible HP/ORC Carnot battery components' technical data [238].

Component	Parameter	Value
Scroll compressors Sanden TRSA12B3457	Swept volume (cm^3)	121
	Shaft speed (rpm)	6000
	Volume ratio	1.7
Pump Sawa MP73-RKFE	Flow rate (l/s)	0.5
	Shaft speed (rpm)	3000
	Temperature range (°C)	-30 - 120
	Nominal pressure (bar)	63
	Pressure head (m)	100
Expansion valve Danfoss ICM20	Flow coefficient – K_v (m^3/h)	2.4
	Temperature range (°C)	-60 - 120
	Maximum differential pressure (bar)	52
Auxiliary pump (HP) Wilo Stratos 2.0-I 50/1-20/1,5	Flange nominal diameter (mm)	50
	Nominal pressure (bar)	16
	Pressure head (m)	37
	Temperature range (°C)	-20 - 140
Liquid tank OCSCOLD RF194X395A	Maximum pressure (bar)	48
	Volume (l)	10
	Temperature range (°C)	-10 - 100
Storage	Volume (m^3)	8.1
	Thermal isolation thickness (PU) (mm)	125
Low pressure heat exchanger Swep P200THx140/1P-SC-H	Area (m^2)	15.2
	Number of plates (-)	120
	Maximum pressure (bar)	50
High pressure heat exchanger Swep P200THx140/1P-SC-H	Area (m^2)	17.8
	Number of plates (-)	140
	Maximum pressure (bar)	50

6.2.2. District heating connection

In Figure 6.3, 'DH-' refers to the exhaust pipe of the district heating system (cold branch), while 'DH+' denotes the supply pipe (hot branch).

During thermal discharge (TD), the hot water circulator moves cold water from the district heating system (DH-) to the hot water tank and, at the same time, hot water from the tank is channelled into the hot supply line of the district heating system (DH+). Valves $V_{DH+,H}$ and $V_{DH-,H}$ are open. No other components are active in this mode.

In HP mode, the evaporator (low-pressure HX) absorbs heat from the district heating system (DH+). Valves $V_{DH+,L}$ and $V_{DH-,L}$ are open. The heated water is then further warmed in the condenser (high-pressure HX) and directed to the top of the hot water tank (valves $V_{DH+,H}$ and $V_{DH-,H}$ are closed).

In ORC mode, the DH system is bypassed (valves $V_{DH+,L}$ and $V_{DH-,L}$ are closed). Instead, the evaporator

(high-pressure HX) draws hot water from the top of the hot water tank (valves $V_{DH+,H}$ and $V_{DH-,H}$ are closed), while the condenser dissipates heat through the dry cooler.

Nominal working conditions in the operating modes are summarized in Table 6.3.

Table 6.3 - 10 kW-sized reversible HP/ORC Carnot battery nominal operating conditions.

Mode	**Thermal charge (HP mode)**	**Thermal discharge (TD mode)**	**Electric discharge (ORC mode)**
Electrical power (kW)	10.7	-	5.6
Condenser power (kW)	82.5	400	94.6
Evaporator power (kW)	67.3		100
Glide (K)	14	14	8
Cold temperature (°C)	62	76	62
Hot temperature (°C)	76	62	70
Scroll efficiency (%)	69.5	-	61.8
COP/efficiency (-/%)	7.69	-	5.5
Optimal volume ratio (-)	1.68	-	3.04
Evaporator pressure (bar)	3.34	-	4.05
Condenser pressure (bar)	6.02	-	1.18
Condenser flow (sf) (l/s)	1.4	-	2.6
Evaporator flow (sf) (l/s)	3.2	6.8	2.99
Working fluid mass flow rate (kg/s)	0.422	-	0.449

6.3. Acquisition and control system development

The 10 kW-sized CB test rig is outfitted with high-precision sensors to monitor the thermodynamic state of the fluids at various points in the three circuits and measure the associated powers. Recorded variables include temperatures, pressures, and mass flow rates in the main (organic fluid) circuit, as well as temperatures and volume flow rates in the hot and cold water circuits, and the electric current and voltage of the machines and pump for power and frequency analysis. For a comprehensive thermodynamic characterization and thorough performance analysis of the system, temperature and pressure sensors are positioned at the inlet and outlet of each component in the three circuits. Temperatures are recorded using Pt100 thermoresistances, while pressures are measured with ceramic pressure transducers. The working fluid mass flow rate is measured by a Coriolis flow meter located at the outlet of the high-pressure HX. For acquiring the electric power absorbed/generated by the compressors/expanders and consumed by the pump motor, wattmeters are employed.

All signals are transmitted to a workstation via Siemens LOGO! Modular microcontrollers which include modules for analogue and digital input and output. The development of the test bench control and acquisition system is part of this PhD thesis, therefore it is comprehensively illustrated in the following subsections.

6.3.1. Contribution

The acquisition and control system of the 10 kW-sized CB test bench located at the University of Liège is implemented in two levels (three in the future developments). The lower level is developed on the LOGO! Soft Comfort software, which is run in the LOGO! Modular microcontrollers (Siemens), adopted to switch on/off and regulate the actuators, and to read the sensors measurements. The higher level of the control and acquisition system is developed in Python, and it involves the manual or automatic control of each of the Carnot battery operating modes (HP mode, ORC mode, TD mode), and the acquisition of the physical quantities (temperatures, pressures, flow rates) converted in the LOGO!. The further level of the control and acquisition system, as a future development, is going to be developed in MATLAB, and it involves the optimization of the scheduling strategy and the calculation of other thermodynamic quantities (i.e., enthalpy, entropy…). The ruled-based scheduling strategy is already defined and optimized (it is described in detail in the next chapter of this thesis), but the communication with the Python level needs to be implemented. This last level will be included in the whole control and acquisition system after the validation of the middle and low levels that requires finalizing the test bench setup.

6.3.2. Lower-level acquisition and control system

The control and acquisition system of the reference test rig is developed in three LOGO! Modular microcontrollers (Siemens), connected to a user interface developed in Python environment. The communication between Python and LOGO! Soft Comfort is based on a S7 protocol (ethernet protocol). A Server connection is configurated to allow the connection between LOGO and the host pc through Snap7Client for reading and writing the LOGO memory. In this way, by using the Python library 'snap7', it is possible to read the LOGO memory cells in which the sensors measurements signals are acquired (input), and to write in the LOGO memory cells which send the signals to the actuators (output), directly from the Python interface. Furthermore, the communication with the DH computer, to obtain the temperature values, is established through Modbus protocol using the Python library 'pymodbus' (pymodbus.client.ModbusTCPClient).

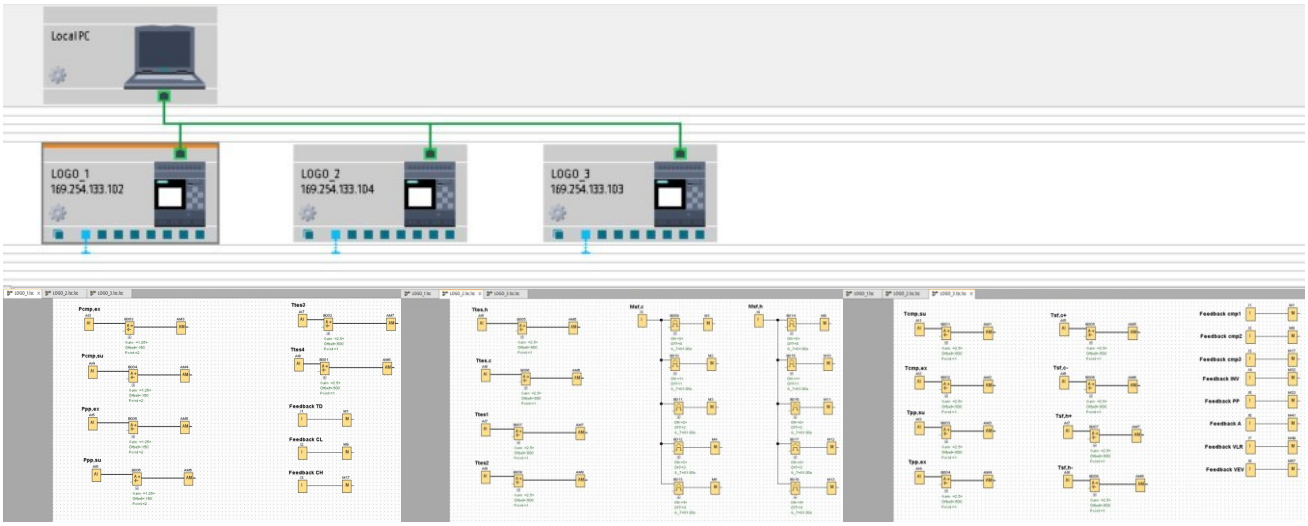

Figure 6.4 - LOGO! Soft Comfort signal acquisition program.

In the lower level of the control and acquisition system, developed on the LOGO! Soft Comfort (Figure 6.4), there is only the conversion of the current/voltage signals provided by the sensors into the respective physical quantities (temperature, pressure, flow rate). These physical quantities are directly read and transferred to Python, in which the whole control routine is developed. In the same way, the Server

connection allows to overwrite the LOGO memory cells directly from Python to send signals to the actuators. Therefore, the control and acquisition routine is almost entirely developed in Python, in functions associated with the buttons, the sliders, and the live graphs created on the user interface, which is developed using the Python library 'tkinter'.

6.3.3. Higher-level acquisition and control system

The higher level of the control and acquisition system is fully developed in Python and it consists of defining and launching different control routines according to the set operating mode and the measured variables' values. The control interface is shown in Figure 6.5. The orange button on the top allows to decide the operating mode (HP mode, ORC mode, TD mode): this button allows i) to send an electric signal to invert two of the three phases of the motors/generators connected to the volumetric machines, ii) to adjust the four-way valve opening that determines the hot water flow direction, iii) to set the three-way valves opening in the cold circuit.

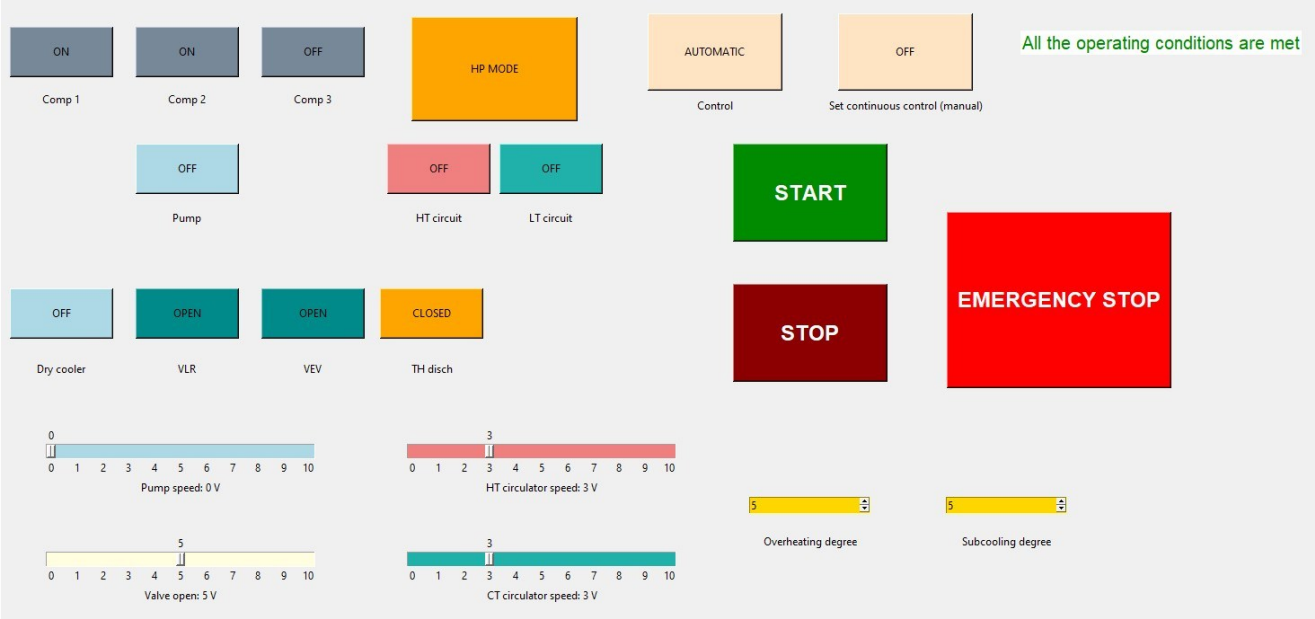

Figure 6.5 – Control window of the user interface for the 10 kW-size reversible HP/ORC Carnot battery test bench.

The start-up can be performed in an automatic way or in a manual way using the 'control' button. In the automatic condition, the system allows the user to set a priori i) the number of machines to switch on, pressing on the 'comp' buttons (otherwise the system will switch on two machines in HP mode and three in ORC mode), ii) the circulator(s and the pump) starting speed (otherwise the routine will set the default values) and iii) the overheating and subcooling degree targets. To launch the start-up, the user needs to press the green 'START' button. At this point, according to the set mode, the routine follows the start-up procedure, described below for each mode. At the end of the start-up procedure, the routine will keep checking all the operating conditions and controlling the system according to the overheating and subcooling degree targets. In case the user set the control in 'manual' condition, she/he is allowed to open/close the valves, regulate the pump and circulators speed, and switch on all the actuators manually whenever she/he wants. However, some security measures are taken to avoid an improper use of the test rig (i.e., the pump is not allowed to be switched on if the system in not in ORC mode, the machines are not allowed to be switched on in TD mode, no more than two machines can be switched on as compressors in HP mode, the machines are not allowed to be switched on in ORC mode if the pump is off, the pump and the machines are not switched on if the water circulators are off…). After the manual start-up, while the

system is running, it is possible to set a continuous automatic control using the button 'set continuous control'.

More in detail, the automatic start-up is performed according to the following routine, for each mode:

- ORC mode (Figure 6.6): first there is a pre-check of the operating conditions. Pressure and temperature in all the three circuits must be in their operating ranges (0.7 < pressure < 11; 10 < temperature < 95; overheating = subcooling = 0). The temperature in the storage must be higher than 60 °C (minimum temperature to run the ORC) and higher than the DH temperature. If these conditions are met, it is possible to start the auxiliaries. First the ORC mode is set and the expansion valve is fully open, the dry cooler is started and the circulator starting speed is set. When the dry cooler is running and the expansion valve is completely open, the circulators in the hot and cold circuits are started, and the continuous control on the hot and cold water flow rates is launched. After that, it is possible to start the main circuit. The pump starting speed is set, then the pump is started, and the continuous control on the working fluid mass flow rate is launched. When the pump is running, the continuous control on the subcooling degree is launched: if the subcooling degree is lower than the target, the valve V_{EV} is open, otherwise, if the subcooling degree is higher the valve V_{LR} is open (Figure 6.3). Eventually, the expanders can be started, one after the other. The overheating degree is controlled by a PI controller, while the water glide in the hot circuit is controlled modifying the circulator speed in order to match the water glide at the evaporator with the water glide in the storage.

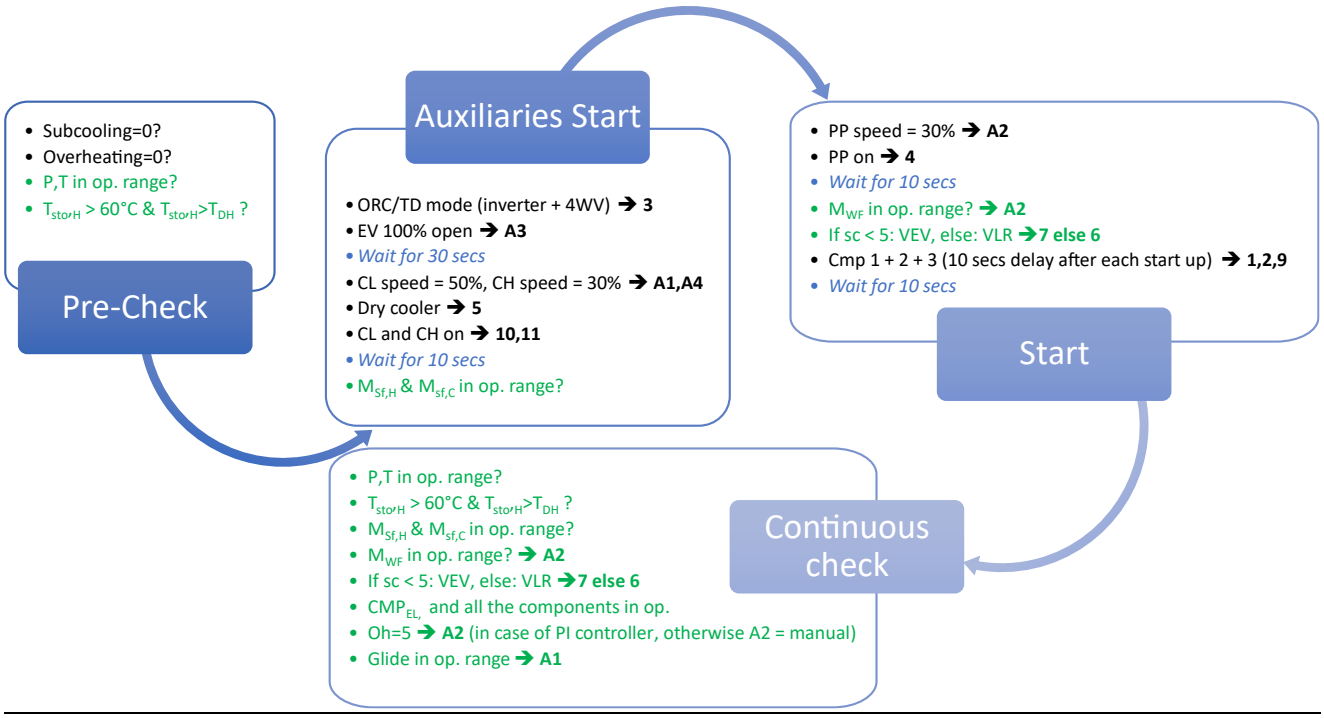

Figure 6.6 - ORC mode automatic start up procedure.

- HP mode (Figure 6.7): as in ORC mode, first there is a pre-check of the pressure and temperature values and of the subcooling and overheating degree. Furthermore, the storage temperature must be higher than the DH temperature. If these conditions are met, it is possible to start the auxiliaries. The HP mode is set and the expansion valve is open at the starting opening (50 % is the default value). The water circulators starting speed is set, then they are switched on, and the continuous control on the hot and cold water flow rates is launched. After that, the compressors can be started, one after the other. As in ORC mode, also in HP mode the overheating degree is controlled by a PI controller, while the water glide in the hot circuit is controlled modifying the circulator speed in order to match the water glide at the condenser with the water glide in the storage.

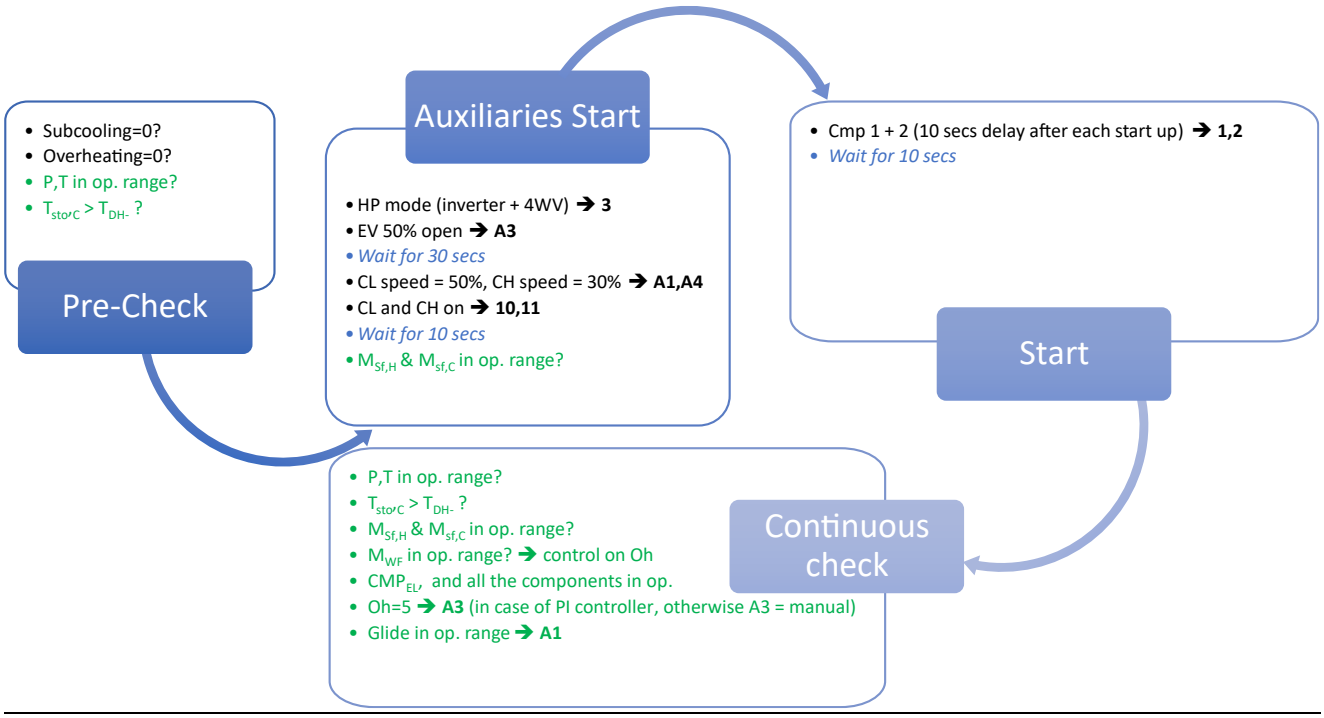

Figure 6.7 - HP mode automatic start up procedure.

- TD mode (Figure 6.8): in this mode, the pre-check is on the storage temperature that must be between 50 and 85 °C, and higher than the DH temperature. If these conditions are met, it is possible to open the thermal discharge valves ($T_{DH+/-}$ in Figure 6.3) and switch on the hot water circulator. After that, the continuous control on the water flow rates is launched. Also in this case, the water glide is controlled modifying the circulator speed.

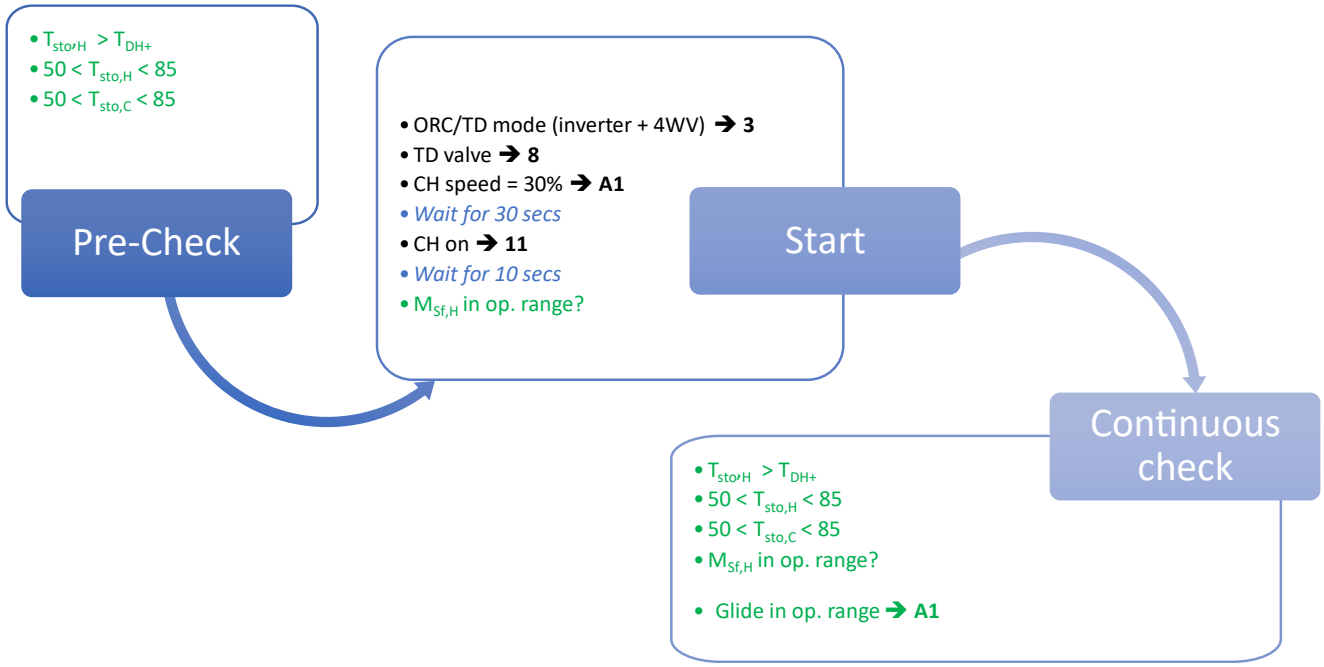

Figure 6.8 - TD mode automatic start up procedure.

The automatic stop procedure (Figure 6.9) is unique for the three modes and it starts when the red 'STOP' button is pressed. First the volumetric machines are stopped one after the other; then the pump (if

it is on) and the hot water circulator are switched off; eventually the cold water circulator and the dry cooler (if they are on) are switched off. An 'emergency stop' procedure (Figure 6.10) is available pressing the emergency button. In this case everything is suddenly stopped at the same time. The emergency stop procedure is automatic when at least one of the operating conditions is not met during the stationary operations. In this case, a message will pop up describing which condition is not met.

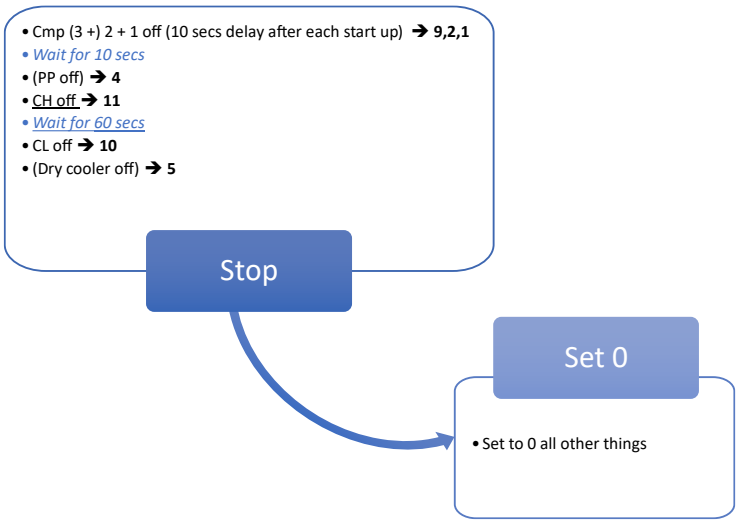

Figure 6.9 – Stop automatic procedure.

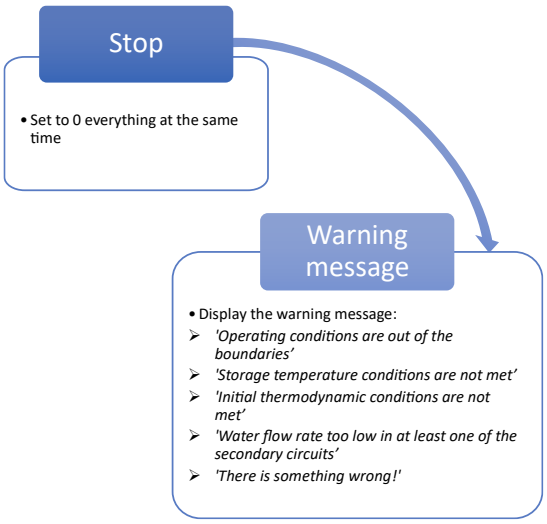

Figure 6.10 - Emergency stop procedure.

6.4. Conclusions

The Thermodynamics Laboratory at University of Liège has developed two reversible HP/ORC test benches of different size to advance research on CBs. CBs are considered a promising method for enhancing the penetration of renewable energy into the grid, by providing a solution for energy storage that can compensate the mismatch between energy supply and demand.

The 1.5 kW-sized test bench was designed and built as a proof of concept to validate the practical feasibility of CB technology. This setup aims to demonstrate the technical viability of CBs by showing that the system's components, like heat exchangers and a volumetric machine, can perform effectively under different conditions, depending on whether the system is operating in HP or ORC mode. The test bench development included setting up external circuits for heat supply and cold sinks, along with a sophisticated data acquisition and control system. The test bench is based on a reversible HP/ORC power plant prototype that uses the same heat exchangers and a modified scroll compressor in both operating modes. The primary circuit, which circulates refrigerant, includes a high-pressure heat exchanger, a volumetric machine that can operate as both a compressor and an expander, and two parallel branches equipped with an expansion valve and a plunger pump. Additionally, two external water circuits simulate hot and cold sources, feeding the heat exchangers. The system also includes two storage tanks to maintain thermal stratification, ensuring efficient energy use depending on the operating mode. The volumetric machine is adapted from an automotive scroll compressor, modified for reversible operation as an expander. The system uses HFO-1233zd(E) as a refrigerant due to its high performance and ultra-low GWP. The test bench is equipped with high-precision sensors to monitor various parameters such as temperature, pressure, and flow rates, which are critical for analysing the system thermodynamic performance.

The experimental data gathered from this setup was used to validate semi-empirical models of the HP and ORC systems. These models are used to simulate the system performance under various operating

conditions and to create lookup tables. These look up tables are implemented in the overall system control strategy, aiming to maximize efficiency in either ORC or HP mode, depending on the boundary conditions.

In addition to the 1.5 kW-sized test bench, the University of Liège is also developing a larger - 10 kW-sized - reversible HP/ORC test bench, which is designed to be integrated with the DH substation of the Thermodynamics Laboratory building. This larger setup aims to provide both electrical and thermal peak shaving by utilizing surplus renewable energy from the building photovoltaic panels and converting it into thermal energy stored in a hot water tank. This stored energy can then be converted back into electricity during periods of high demand.

The control and acquisition system for the 10 kW-sized test bench is being developed in multiple levels as part of this thesis, primarily using Siemens LOGO! microcontrollers for basic control tasks and Python for higher-level control routines. This system allows for both manual and automatic control of the test bench operations, ensuring optimal performance in various modes, namely HP mode, ORC mode, and TD mode. The control system is designed to be ruled by the overall integrated system control strategy.

In summary, the research conducted at the University of Liège on these test benches is crucial for advancing the understanding and practical implementation of CBs. By experimenting with these prototypes, the research contributes valuable data and insights that could lead to more efficient and sustainable energy systems, capable of integrating a higher share of renewable energy sources.

7. Thermally integrated Carnot battery combined with district heating

Summary. This chapter outlines a rule-based control strategy for operating a 10 kWe reversible HP/ORC Carnot battery within an integrated system, which includes a DH substation and a PV power plant, aimed at meeting both thermal and electrical demands of a university campus building. The strategy is designed to maximize economic benefits by leveraging the CB to reduce early morning thermal demand peaks, thus downsizing the DH substation and cutting investment costs. Two reference cases are analysed, differing in the HP's cold source, which is free waste heat in the first case, and the return branch of the DH substation in the second case. The study finds that significant savings are achieved in the first case, but no positive economic gain in the second. The study explores the impact of various parameters — such as the PV power plant area, the storage volume, the electricity price profile, and the specific investment cost of the reversible HP/ORC — on the system's techno-economic performance through extensive sensitivity analysis. Results reveal that DH substation downsizing is key to economic gains. The strategy is adaptable for other applications and will be implemented and validated in the new reversible HP/ORC CB prototype at the University of Liège.

7.1. Carnot batteries in integrated energy systems: state of the art

When included in integrated systems for renewable energy storage, CBs necessitate the implementation of effective scheduling strategies to manage multiple energy flows and ensure smooth operation under various conditions. Niu et al. [239] utilized a multi-objective optimization model to integrate a CB with solar collectors. They evaluated the performance of both a basic and a regenerated CB, using different working fluids, during the summer and winter solstices. The study revealed that there are optimal temperatures for the hot and cold reservoirs, as well as ideal combinations of working fluids for each CB configuration, which maximize roundtrip efficiency and minimize the levelized cost of storage. Tassenoy et al. [240] conducted a techno-economic analysis of a CB integrated with a PV power plant for electricity load-shifting in an office building. Their findings suggest that the implementation of a CB in this context is not cost-effective. However, this assessment only considers electricity load-shifting, without exploring the potential benefits of thermal energy load-shifting. This thesis' chapter attempts to broaden the study by [240], by examining the cost-effectiveness of a CB designed to handle thermal energy demand peaks, thereby enabling thermal energy load-shifting. Lin et al. [241] introduced a cross-border integrated energy system incorporating a CB based on phase-change material storage, capable of storing electricity as steam. Their findings indicate 28.57 % reduction in operating costs, 43.49 % decrease in carbon emissions, and 16.49 % reduction in grid power purchase costs when compared to electric batteries in an industrial park case study. Nonetheless, the authors recommend the deployment of steam CBs in integrated energy systems in environments with abundant renewable energy and low-grade heat availability. Scharrer et al. [242] proposed a control strategy for operating a reversible HP/ORC CB, integrated with PV panels, in a domestic setting within a community with varying numbers of houses. Here, the CB is solely used for electricity load-shifting, employing a rule-based strategy to charge the storage when excess electricity is available and discharge it at night. The results show that excessively increasing the PV size or storage capacity is counterproductive once the HP and ORC operate at their nominal conditions. The authors also conducted a financial analysis, considering variations in feed-in tariffs and thermal energy costs. Despite achieving notable power-to-power (P2P) efficiency (≈ 50 %), they concluded that for financial savings of up to 180 € per house per year and a 13-year amortization period, the feed-in

tariff and thermal energy costs would need to be minimal, alongside high electricity prices. Similar to Scharrer's work, this thesis' chapter proposes a control strategy for operating a reversible HP/ORC, but the focus here is primarily on thermal load-shifting and secondarily on electrical load-shifting, revealing significant economic benefits and a shorter amortization period. Thus, this thesis part can be seen as an extension of the analysis in [242], addressing the potential of using the CB for both thermal and electrical load-shifting. Within the CHESTER project [108], a compressed heat energy storage system is planned to be combined with smart DH. As part of this project, three case studies were examined under varying boundary conditions and compared with other storage options, such as lead-acid batteries and hydrogen storage systems. The findings show that the savings from reduced imported electricity are negligible compared to the investment costs of these storage options, which are not always recouped by the increased profits. However, compared to the hydrogen storage solution, the compressed heat energy storage system proved to be economically superior by 15 % to 50 % [243]. The same project also considered scenarios involving both the electricity-only market and the combined electricity and heat markets [244]. The results indicate that scenarios including heat exchange are more robust and less likely to compete with other storage facilities compared to electricity-only scenarios, owing to the integration of multi-energy systems.

Based on the existing literature and the author's expertise, the potential benefits of thermal energy load-shifting have not yet been thoroughly explored in previous research. To address this gap, this study investigates the integration of a reversible HP/ORC CB with DH and assesses the advantages of using the CB for thermal demand peak shaving.

7.2. Contribution

From the literature review, it appears that only a limited number of studies have provided a comprehensive control strategy for managing and scheduling the operation of a CB within an integrated system designed to meet both thermal and electric demands. Therefore, this thesis aims at offering a novel contribution to the existing literature by presenting a techno-economic evaluation of a reversible HP/ORC CB, integrated with a DH substation and a PV power plant, to meet a representative thermal and electrical energy demand. The study focuses on a university campus building (located at the University of Liège), which includes laboratories and offices, as the case study. The integration of the CB with a DH substation is particularly noteworthy because the thermal energy stored in the TES can be used to shave thermal demand peaks, leading to the downsizing of the DH substation and significantly reducing investment costs.

A detailed rule-based control strategy is implemented to optimize the operation of the CB, DH substation, and PV power plant throughout a typical year. For this purpose, the off-design model of the 1.5 kW-sized reversible HP/ORC prototype CB, described in section 6.1 and enhanced with a stratified TES tank model, is utilized in the control strategy. The study aims to evaluate the performance of the entire integrated system under varying boundary conditions over an annual activity, with the goal of maximizing economic benefits from CB operation. Two reference scenarios are examined: in the first, the HP's cold source is assumed to be free waste heat, while in the second, it is thermal energy supplied by the DH. Additionally, a sensitivity analysis is conducted by varying parameters such as the PV panel surface area, the storage volume, the electricity price profile, and the specific cost of the reversible HP/ORC investment, to understand how these factors influence the system's yearly design, operation, and performance.

7.3. The integrated energy system

The energy system investigated in this study comprehends a PV power plant and a DH substation designed to meet respectively the electrical and thermal needs of a university campus building. To enhance the flexible utilization of renewable energy and the thermal capability of the DH substation, a reversible HP/ORC Carnot battery is included into the system. The remaining electrical demand is supplied by the grid. Additionally, an on-site thermal power source is assumed to boost the CB performance. This section details the integrated energy system and emphasizes the benefits of coupling the CB with the DH substation.

7.3.1. The energy system configuration

The explored energy system, along with the interactions between its subsystems, is depicted in Figure 7.1 and briefly outlined below (with components numbered as in the figure).

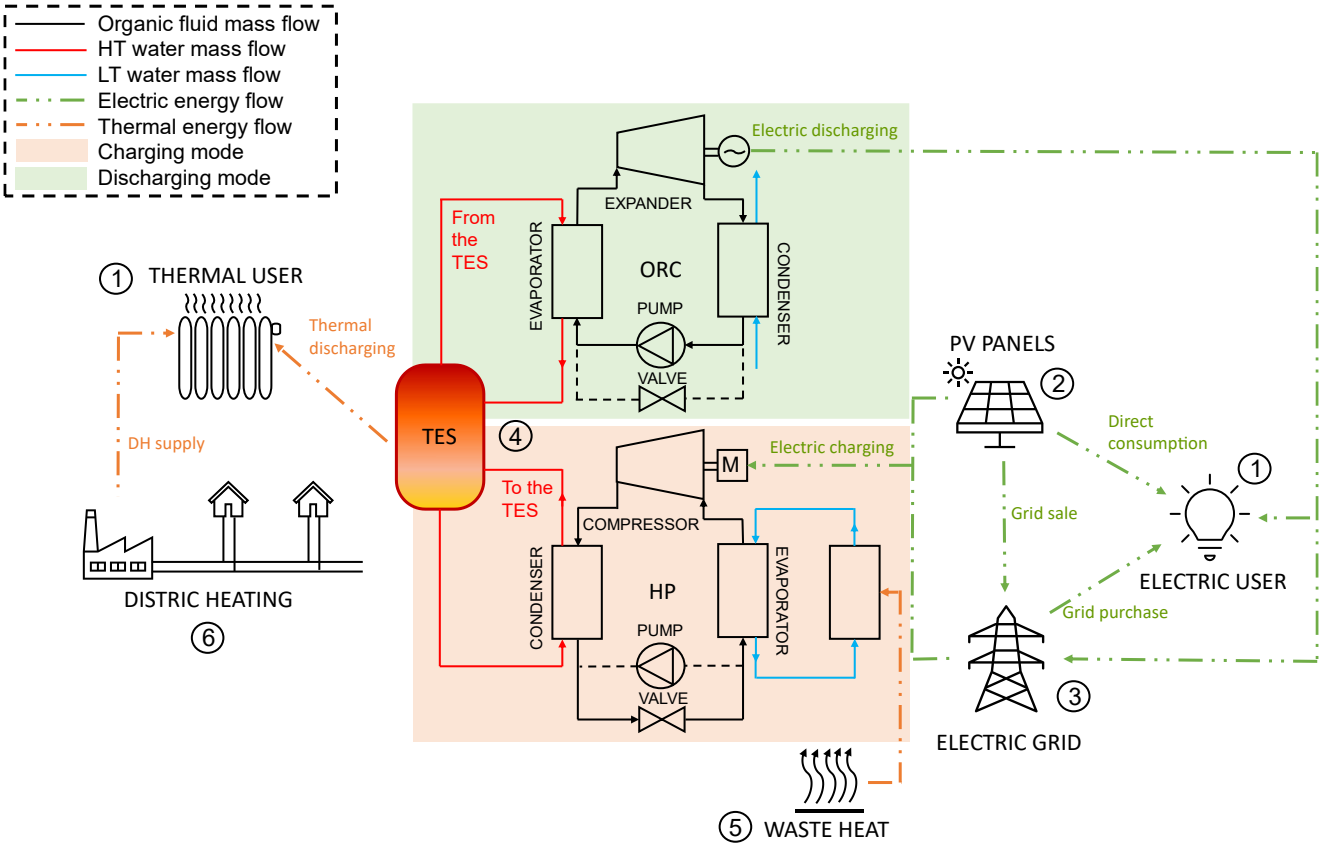

Figure 7.1 - The integrated energy system depicted with the CB charging (HP) and discharging (ORC) modes illustrated as distinct subsystems for clarity. In the real system, the CB operates as a reversible HP/ORC loop.

The key components include:

1 - An on-site electric and thermal power user, raising the demand profiles that must be met by the generation and storage units in the system.

2 - An on-site solar PV power generation plant, serving as the renewable energy source. The electricity generated by the PV plant is dependent on the available solar irradiance at each timestep and is compared against the electricity demand. Excess PV production can either be sold to the grid or stored in the CB. When stored, this energy can later be converted back into electricity during periods of low renewable output or when electricity prices are high.

3 - The electric grid, which can absorb the surplus electricity produced by the PV plant. The grid can also supply electricity to meet demand and produce thermal energy via the HP to satisfy thermal needs.
4 - The CB, consisting of a reversible HP/ORC system and a TES unit. The CB can be charged in HP mode using surplus PV electricity or grid electric energy to run the compressor. In ORC mode, the CB discharges to meet the electric demand. The CB's TES can also be discharged to address peaks in thermal demand by directly utilizing stored thermal energy. Additionally, electricity generated through the ORC may be sold to the grid if renewable production exceeds demand.
5 - An on-site thermal power source, which could be either i) a free waste heat source or ii) a low-temperature DH line. This source supplies heat to the HP, enabling a smaller temperature lift and achieving a higher COP. If using a free waste heat source, the input thermal energy introduces no economic cost. Conversely, using the DH line imposes an economic cost on the CB.
6 - The DH substation, primarily tasked with meeting thermal demand. The DH meets the thermal demand fully as long as it keeps within the substation capacity. When demand exceeds the substation thermal output, the excess is met using the TES.

7.3.2. Carnot battery and district heating coupling

The integration of a Carnot battery with a DH substation enhances flexibility, particularly in managing thermal demand and production. A portion of the thermal energy stored in the CB can be utilized to meet peak thermal power demands, enabling a reduction in the size of the DH substation and thereby significantly lowering investment costs. As illustrated in Figure 7.2, the thermal power demand profile (shown in red) exhibits a daily peak in the morning. Without the CB, the DH system (depicted in yellow) would need to supply the entire thermal demand at all times, necessitating a DH substation sized to match the highest peak demand. In contrast, the CB can handle demand spikes by using the thermal energy stored in the TES (represented in orange), allowing for a smaller DH substation. The amount of thermal power that can be delivered by the TES fluctuates based on the temperature level required by the thermal user. The storage is replenished through the HP when excess renewable electricity from the PV power plant (shown in blue) is available.

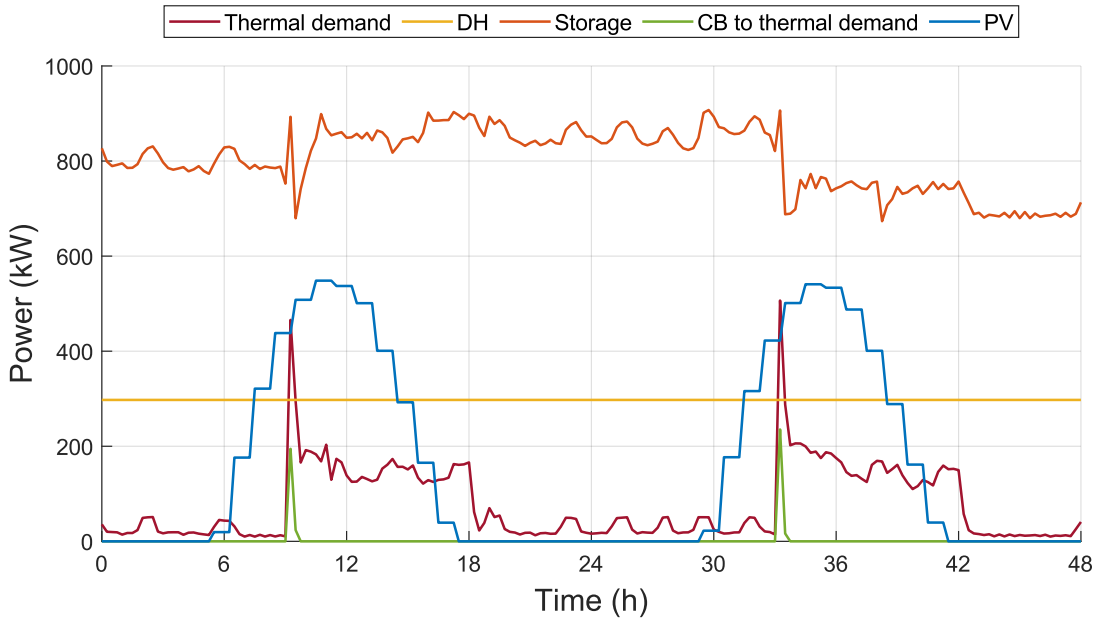

Figure 7.2 - Thermal power profiles for the reference scenario over two consecutive days in March, including the user's thermal demand, the DH substation power capacity, the available thermal power in storage (Eq. (7-12)), the thermal power supplied by the TES to meet thermal demand peaks, and the PV electricity generation profile.

In some scenarios, the thermal energy stored in the TES might be insufficient to meet peak demand, and simultaneously, the renewable energy supply may not be in surplus. In such cases, it may be more cost-effective to purchase electricity from the grid and use the HP to satisfy the peak in the thermal demand, rather than increasing the size of the DH substation. However, this should be a rare occurrence; otherwise, expanding the DH substation would be more advantageous. The DH substation's size must be carefully optimized to minimize total costs, which include both the annualized investment and operating expenses.

The CB, the DH substation, and the thermal user are assumed to be interconnected according to the hydraulic circuit layout depicted in Figure 7.3. In this diagram, black lines indicate water pipes, and brown lines represent the working fluid of the reversible HP/ORC loop. Black arrows show the water flow direction when the DH substation is meeting the thermal demand, independent of CB operation (path 3-4-5-6-7-8 in Figure 7.3). Red arrows illustrate the additional water flows during thermal discharge mode (path 13-19-4-5-6-20-16-17 in Figure 7.3). The key streams and flow directions for the CB in HP and ORC modes are shown by blue and green arrows, respectively. In HP mode, two reference cases are considered: i) the "free waste heat" scenario, where the HP cold side is an external source (circuit represented by dashed lines, following path 21-10-11-22 in Figure 7.3); and ii) the "thermal integration with DH" scenario, where the HP cold side is the DH substation (path 3-4-5-6-7-9-10-11-12-8 in Figure 7.3). In the first case, the HP can operate during the thermal discharge mode, whereas it is restricted from doing so in the second case. The ORC is also prevented from running during thermal discharge mode (and during HP mode). Further details on the constraints governing CB operation are discussed in the next sections. Reference temperature values are provided in Figure 7.3 to assist the reader in following the subsequent analysis.

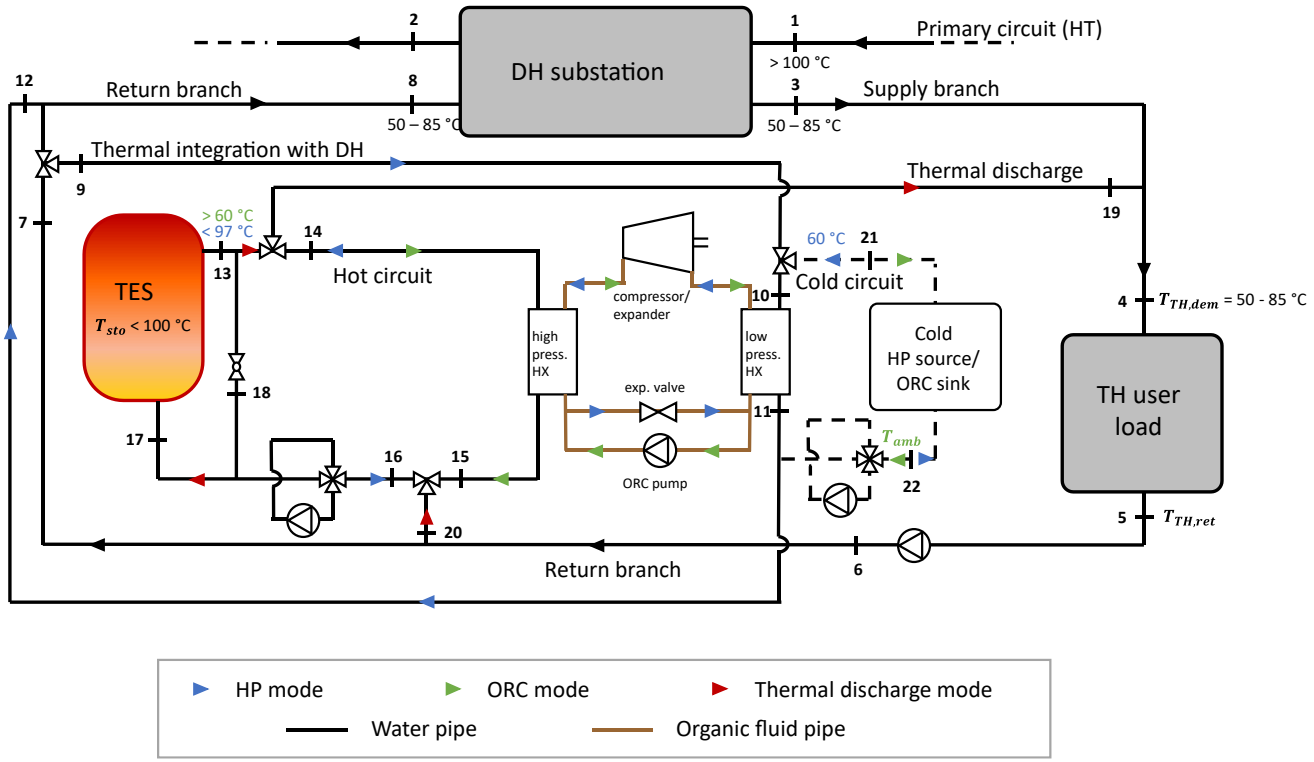

Figure 7.3 – Layout of the hydraulic circuit linking the CB, the DH substation, and the thermal user.

7.4. The Carnot battery management strategy

The problem resolution approach is structured according to a rule-based strategy. To explore how key

design factors and boundary conditions — such as PV and storage sizes, electricity pricing, and environmental variables — impact the system's technical and economic performance, an accurate model is required. This model is required to include numerous details without causing a significant increase in computational time. Due to the high computational demands of detailed thermodynamic models, the control strategy sacrifices some optimization for modelling accuracy, leading to a rule-based scheduling approach. This method provides a sub-optimal solution, with the level of optimization depending on how well the empirical rules fit the specific application. However, the more tailored these rules are to one scenario, the less applicable they become to others, necessitating adjustments in the scheduling strategy for different cases. The management of the CB is driven by cost minimization. The following subsections detail the physical problem and the control algorithm. The CB management strategy is fully implemented within MATLAB environment.

7.4.1. Problem description

The CB management strategy is called to determine the instantaneous load of the HP and ORC at each time step to maximize the economic benefits achieved by integrating the CB into the system. The objective function (Eq. (7-1)) measures the annual gain by comparing scenarios with and without the CB intervention in the integrated energy system.

$$\Delta gain = R_1 + R_2 + R_3 + R_4 - C_1 - C_2(-C_3) \quad (7\text{-}1)$$

This gain is the sum of four revenue components, denoted as R, minus two (or three, if the HP's cold source is the DH instead of waste heat) cost components, denoted as C.

The first two revenue terms (R_1 and R_2), calculated for each time step, are associated with the surplus sale ($E_{ORC,surplus}$) and self-consumption ($E_{ORC,selfcons}$) of the ORC-generated electricity:

$$R_1 = E_{ORC,surplus} \cdot C_{el,sale} \quad (7\text{-}2)$$

$$R_2 = E_{ORC,selfcons} \cdot C_{el,pur} \quad (7\text{-}3)$$

The surplus energy revenue (R_1) is proportional to the electricity sale price ($C_{el,sale}$), as this surplus electricity is sold directly to the grid. The self-consumption gain (R_2) represents the cost savings from generating electricity for internal use rather than purchasing it from the grid. This gain is calculated by multiplying the ORC self-consumed electricity ($E_{ORC,selfcons}$) by the grid purchase price ($C_{el,pur}$), since, without the ORC, this electricity would have been bought from the grid.

The other two positive revenue terms (R_3 and R_4) arise from using the CB to meet part of the thermal demand. R_3 relates to the reduced investment costs from downsizing the DH substation, while R_4 pertains to the thermal energy supplied to the user by the CB (Q_{CB2dem}), which would otherwise be sourced from the DH (operating costs):

$$R_3 = \Delta size_{sub} \cdot C_{I,DH,fee}/lifetime \quad (7\text{-}4)$$

$$R_4 = Q_{CB2dem} \cdot C_{Q,DH} \quad (7\text{-}5)$$

R_3 represents the avoided levelized investment cost of the DH substation. It is proportional to i) the difference ($\Delta size_{sub}$) between the original and new substation size (the original size is equal to the maximum thermal demand peak to be covered by the external thermal energy source), and ii) the specific

investment cost of the DH substation ($C_{I,DH,fee}$ in €/kW). R_4 is proportional to the specific cost of purchasing heat from the DH ($C_{Q,DH}$), as the thermal energy supplied by the CB (Q_{CB2dem}) would otherwise be provided by the DH.

The cost components (C_1 and C_2) are linked to the HP's electricity consumption, and calculated at each time step:

$$C_1 = E_{HP,ren} \cdot C_{el,sale} \tag{7-6}$$

$$C_2 = E_{HP,grid} \cdot C_{el,pur} \tag{7-7}$$

C_1 represents the cost of renewable energy production ($E_{HP,ren}$) that is not sold to the grid but used to power the HP. This cost is proportional to the electricity sale price ($C_{el,sale}$) because, without the CB, the electricity would have been sold to the grid. C_2 is proportional to the grid purchase price ($C_{el,pur}$) for the electricity used by the HP and purchased from the grid ($E_{HP,grid}$).

If the thermal energy for the HP evaporator is provided by the DH (Q_{DH2HP}), an additional cost term, C_3, is included:

$$C_3 = Q_{DH2HP} \cdot C_{Q,DH} \tag{7-8}$$

C_3 is proportional to the specific cost of heat purchased from the DH ($C_{Q,DH}$).

Although producing electricity for self-consumption allows for downsizing the electrical substation, the significant difference in scale between ORC electricity production and electric demand makes the electrical substation downsizing contribution negligible, so it is not included in the objective function for this application.

Maximizing the economic gain ($\Delta gain$) is achieved by optimizing three time-dependent variables at each time step: the HP/ORC electric power input/output ($\dot{W}_{HP}$ and $\dot{W}_{ORC}$) and the thermal power demand satisfied by the CB ($\dot{Q}_{CB2dem}$). The integrals of $\dot{W}_{HP}$, $\dot{W}_{ORC}$, and $\dot{Q}_{CB2dem}$ over the year provide the energy terms ($E_{HP,ren}$, $E_{HP,grid}$, $E_{ORC,surplus}$, $E_{ORC,selfcons}$, and $\dot{Q}_{CB2dem}$) used in the objective function (Eq. (7-1)). Therefore, $\dot{W}_{HP}$, $\dot{W}_{ORC}$, and $\dot{Q}_{CB2dem}$ are regulated to maximize $\Delta gain$.

The problem's instantaneous constraints include the HP/ORC operating limits (Eqq. (7-9) and (7-10)), such as the system's maximum load ($\dot{W}_{max}$), which depends on the storage temperature (T_{sto} (t)), and the minimum technical load ($\dot{W}_{min}$), below which the reversible HP/ORC does not operate. An additional constraint prevents the CB from operating in ORC and HP modes simultaneously. The thermal power demand met by the CB, $\dot{Q}_{CB2dem}$, is restricted by the lowest value between the available storage thermal power, $\dot{Q}_{CB,ava}$ (which depends on the storage temperature profile and the user's thermal demand), and the user's thermal power demand, $\dot{Q}_{dem}$ (Eq. (7-11)):

$$\dot{W}_{HP}(t) = 0 \quad or \quad \in [\dot{W}_{min}, \dot{W}_{max}(T_{sto}(t))] \tag{7-9}$$

$$\dot{W}_{ORC}(t) = 0 \quad or \quad \in [\dot{W}_{min}, \dot{W}_{max}(T_{sto}(t))] \tag{7-10}$$

$$\dot{Q}_{CB2dem}(t) \in [0, min\ (\dot{Q}_{CB,ava}(T_{sto}(t), t), \dot{Q}_{dem}(t))] \tag{7-11}$$

Here, $\dot{Q}_{CB,ava}$ is time-dependent and calculated as shown in Eq. (7-12):

$$\dot{Q}_{CB,ava}(t) = \frac{M_{sto} \cdot c_p \cdot (T_{sto}(t) - T_{TH,dem}(t))}{\Delta t} \quad (7\text{-}12)$$

where M_{sto} is the mass of the secondary fluid in storage, c_p is the fluid's specific heat at constant pressure, $T_{TH,dem}$ is the thermal user's temperature level, and Δt is the time step (15 minutes in this study, to account for system inertia).

Additional operating constraints for the HP/ORC systems are defined by Eq. (7-13) and Eq. (7-14). The HP cannot operate if the storage temperature exceeds the maximum operating temperature ($T_{op,max}$), and the ORC cannot run if the storage temperature drops below the minimum ORC operating temperature ($T_{ORC,min}$):

$$\dot{W}_{HP}(t) > 0 \quad if \quad T_{sto}(t) < T_{op,max}(t) \quad (7\text{-}13)$$

$$\dot{W}_{ORC}(t) > 0 \quad if \quad T_{sto}(t) > T_{ORC,min}(t) \quad (7\text{-}14)$$

7.4.2. The control logic procedure

The problem is solved by iteratively running the routine depicted in Figure 7.4, gradually reducing the size of the DH substation in each iteration. This process continues until the CB can cover all the thermal demand peaks. If the CB fails to meet the demand peaks at any point, the process stops, and the minimum size of the DH substation is determined. As it will be demonstrated in the results section, most of the economic benefits from the CB intervention come from reducing the size of the DH substation. This is due to the significant variation in the thermal demand profile, which exhibits sharp daily peaks. Even with a small volume of the TES, these peaks can be covered, allowing for a substantial reduction in the DH substation size, and therefore, a reduction in investment costs.

Once the DH substation size is established, the routine in Figure 7.4 is run again to assess the economic impact of integrating the CB into the system. The algorithm seeks to maximize annual gain by deciding when to activate the CB and whether to switch between HP and ORC modes at each 15-minute time step, based on user demand profiles and boundary conditions. Starting with an initial solution, the operation of the CB is simulated step-by-step according to the detailed rule-based routine illustrated in Figure 7.4 and described below.

In this control strategy, priority is given to thermal discharge, meaning the focus is on meeting thermal demand peaks using the stored thermal energy. If the thermal demand exceeds the DH substation size, this indicates a peak that should be covered by the thermal energy stored in the CB. Consequently, the DH system covers a portion of the thermal demand equal to its maximum capacity (which corresponds to the substation size), while the remaining demand is met by the thermal power available in the CB TES. This mode of CB operation is referred to as "Thermal discharge" ($Th_{dis} = 1$).

Next, the instantaneous PV electric power production is compared with the actual demand. If the electric demand is not fully met by renewable production, a power deficit occurs. This deficit must be covered by ORC electric production or by purchasing electricity from the grid. The decision to run the CB, and whether to operate it in ORC or HP mode, is made based on the following rules:

1. The routine first checks the instantaneous electricity price and compares it to the average electricity price for the current day (this check is represented in Figure 7.4 by $C_{el} > C_{el,ave}(day)$). The daily average electricity price is calculated as the arithmetic mean of the price values throughout the day up to the current time step. If the instantaneous price is higher than the average, it may be more cost-

effective to run the ORC to minimize the amount of electricity that needs to be purchased from the grid, thus reducing costs. If the electricity price is low, it might be better to buy the required electricity and store thermal energy to use it later when the grid price is higher or for thermal discharge. In this scenario, since electricity is cheap, it may be advantageous to purchase electricity from the grid to charge the storage via the HP. If the HP operating limits (Eq. (7-9)) are met and the storage is not fully charged (Eq. (7-13)), the HP operates according to its "optimal control strategy" (see the next subsection), which maximizes the HP COP.

2. If the electricity price is high, making ORC operation potentially beneficial, the algorithm checks whether thermal discharge is occurring during the current time step (represented in Figure 7.4 by $Th_{dis} = 1$). If thermal discharge is taking place, the ORC is prevented from operating to avoid further depleting the storage, which could jeopardize satisfying the entire thermal demand peak. In essence, discharging the TES through the ORC is avoided to prioritize shaving the thermal demand peak.
3. Before allowing the ORC to discharge the storage, the algorithm also checks whether the available thermal power in the storage is sufficient to cover the thermal demand peaks for the next three days (represented in Figure 7.4 by $\dot{Q}_{CB,ava} < 3 \cdot \Delta\dot{Q}_{peak}$). This heuristic rule, developed through trial and error, aims to strike a compromise by avoiding excessive electricity purchases to cover upcoming thermal demand peaks in the event of prolonged unavailability of renewable energy.

If these three rules are satisfied, along with the ORC operating limits (Eq. (7-10) and Eq. (7-14)), the ORC operates according to its "optimal control strategy" (see the next subsection), which focuses on maximizing ORC efficiency while discharging the TES.

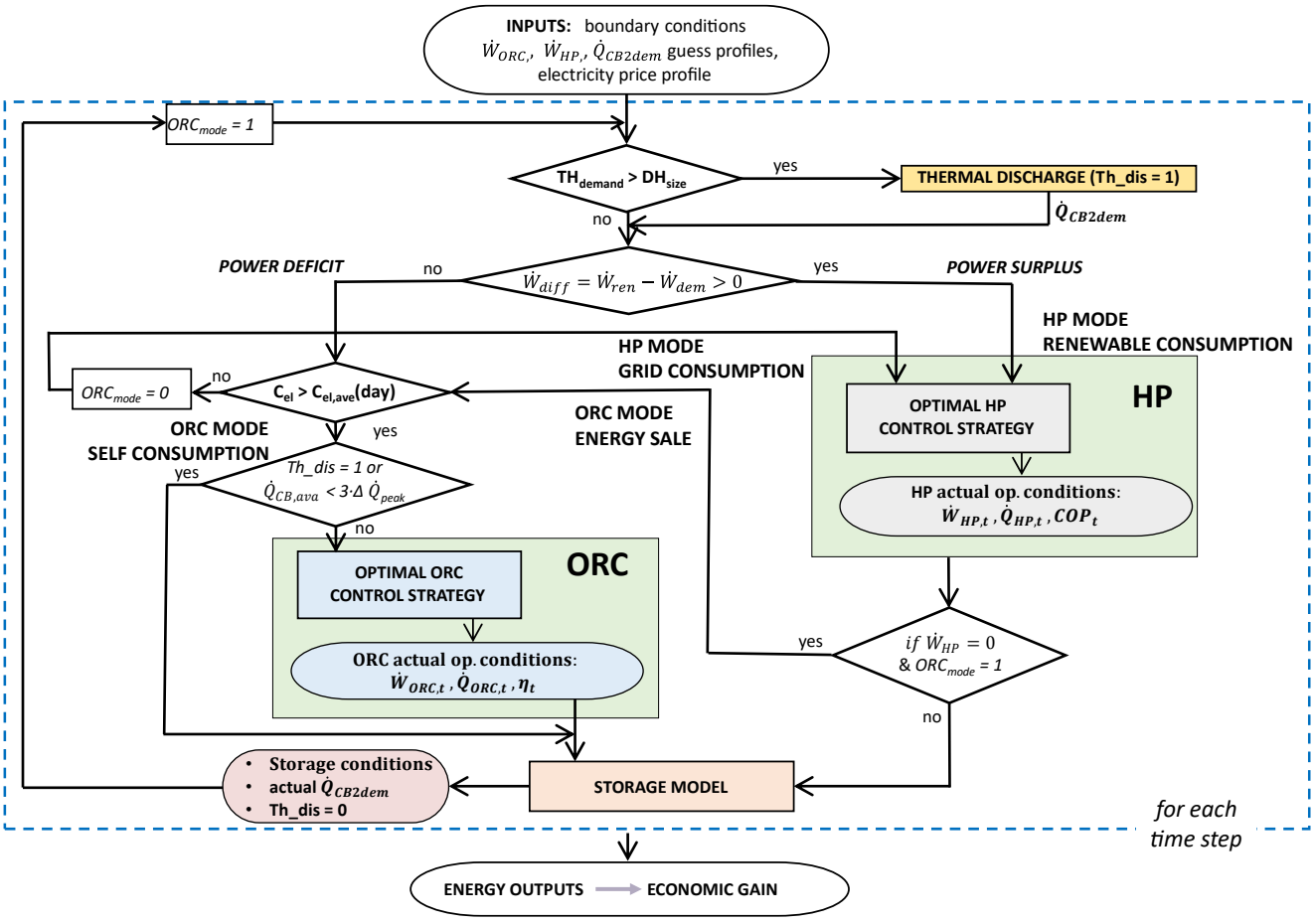

Figure 7.4 - Carnot battery management control logic procedure flowchart.

If renewable production exceeds electric demand, creating a power surplus, and if the HP operating

limits (Eq. (7-9)) are met and the storage is not full (Eq. (7-13)), the HP operates according to its "optimal control strategy," using part or all of the surplus renewable electricity to charge the TES.

In the event of a power surplus, if the HP is not engaged ($\dot{W}_{HP} = 0$, due to fully charged storage or unmet HP operating limits), the algorithm considers running the ORC to generate surplus electricity for sale to the grid. Before permitting the ORC to operate, the algorithm re-evaluates three factors: i) the instantaneous electricity price compared to the day's average price, ii) whether thermal discharge is occurring, and iii) the available thermal power in storage at the current time step and for covering the next three days of thermal demand peaks.

Finally, an energy balance on the TES is performed to update the storage conditions, including the temperature profile and availability of thermal energy. The storage model block is described in detail in the following subsection. Additionally, boundary conditions are assumed to remain constant throughout the time step interval, so although the HP/ORC system operation varies over time, it is considered to be in "quasi-steady state" during each time step.

7.4.3. Components modelling

The operation and performance of the HP/ORC system are determined using lookup tables that represent performance maps of the system. These tables help identify the conditions for achieving maximum efficiency given the imposed boundary conditions. By considering factors such as the storage temperature, the temperature of the cold source or sink, and the availability or demand for electric power, the lookup tables provide the optimal operating conditions for the HP/ORC to maximize its COP/efficiency. The operating conditions provided include details on effective electric power absorption or production, thermal power production or absorption, working fluid mass flow rate, and the temperature differences of secondary fluids between the inlet and outlet of heat exchangers. The lookup tables are generated as described in subsection 6.1.2.

As a crucial element of the CB system, the sensible thermal energy storage is represented by a one-dimensional stratified water tank. In this model, the tank is a vertical cylindrical structure where water temperature changes only along the vertical axis, with no radial temperature gradient. Consequently, the storage volume is divided into a series of n equal-volume horizontal layers (Figure 7.5), and the temperature within each layer is assumed to be uniform [245]. Thermodynamic properties can vary between layers, but remain constant within a single layer, following the principles of the isothermal mixing zone approach. Each layer can exchange energy with its neighbouring layers through convection and diffusion, as well as with the tank wall via conduction. The energy conservation equation applied to each layer results in a system of n ordinary differential equations (Eq. (7-15)) [246].

$$\frac{M_{sto_i} \cdot c_p \cdot \left(T_i(t) - T_i(t-1)\right)}{\Delta t} = \dot{m}_{ch} \cdot c_p \cdot \left(T_{i-1}(t) - T_i(t)\right) + \dot{m}_{dis} \cdot c_p \cdot \left(T_{i+1}(t) - T_i(t)\right) + \alpha_{Th} \cdot M_{sto_i} \cdot c_p \cdot \frac{\left(T_{i+1}(t) + T_{i-1}(t) - 2T_i(t)\right)}{\Delta L^2} - U \cdot A_i \cdot \left(T_i(t) - T_{amb}\right) \quad (7\text{-}15)$$

On the left side of Eq. (7-15), the change in thermal energy within the i-th layer over time is described. Here, M_{sto_i} represents the fluid mass in the layer, c_p is the specific heat capacity at constant pressure, $T_i(t)$ is the temperature in the current time step, $T_i(t-1)$ is the temperature from the previous time step, and Δt is the time interval.

The right side of Eq. (7-15) accounts for all heat transfer mechanisms occurring between nodes and the surroundings. The first two terms describe the convective heat transfer within the i-th layer during both charging and discharging phases (see Figure 7.5). The first term pertains to the charging phase, where fluid

is forced to move from the top to the bottom of the tank at a mass flow rate $\dot{m}_{ch}$. The second term corresponds to the discharging phase, where fluid flows from the bottom to the top, driven by a mass flow rate $\dot{m}_{dis}$. The third term on the right side represents the diffusive heat transfer between the i-th layer and its adjacent layers. Here, α_{Th} is the thermal diffusivity coefficient (in m^2/s), and ΔL is the layer thickness. The final term accounts for heat loss to the environment via conduction through the tank walls, coupled with convection and radiation on the outer surface. U denotes the overall heat transfer coefficient through the wall, A_i is the wall surface area of the i-th layer, and T_{amb} is the ambient temperature.

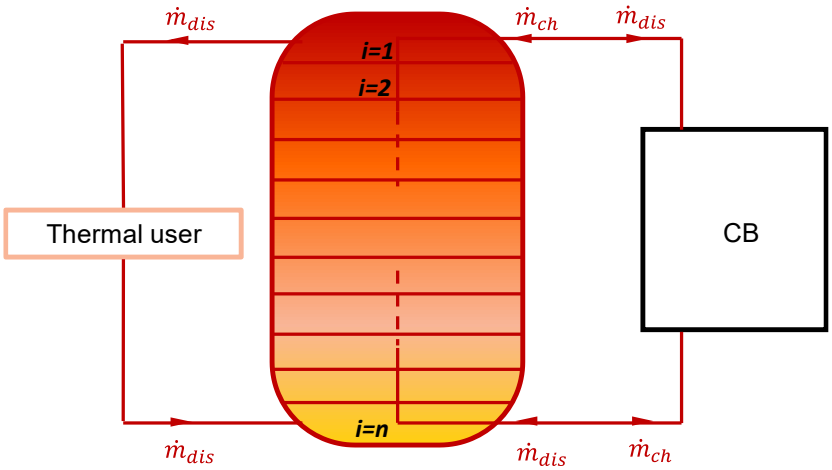

Figure 7.5 - Sensible thermal energy storage discretization scheme.

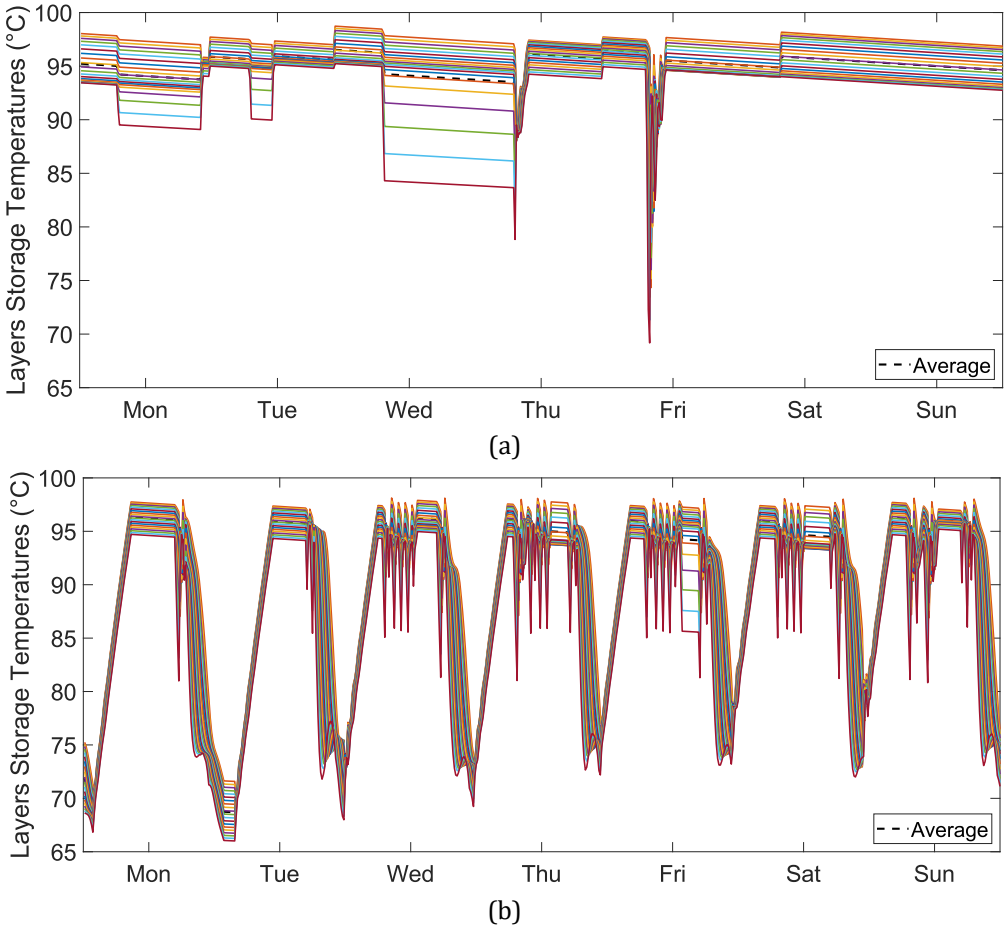

Figure 7.6 - Storage temperature profiles for each layer during a typical week in (a) winter and (b) summer.

The problem is solved numerically using the upwind scheme [247], which provides the temperature distribution in the storage tank as a function of time.

Temperature profiles within the storage are illustrated in Figure 7.6 for typical weeks during winter (a) and summer (b) respectively. Each coloured line represents the temperature profile of a specific layer within the discretized storage volume. In summer, the storage temperature can drop considerably since the stored thermal energy is not required to cover the thermal demand, allowing the ORC to utilize the stored energy whenever the electricity price makes it favourable and technical conditions are met. During winter, priority is given to thermal discharge, and the need to maintain temperatures suitable for the user places significant constraints on ORC operation, thus limiting the range of temperature variation within the TES.

7.5. Boundary conditions and performance indicators

This section outlines the assumptions and parameters used in this study, as detailed in Table 7.1, followed by the performance indicators considered for the systematic analysis.

Table 7.1 – Integrated system simulations assumptions and parameters.

Reversible HP/ORC	Nominal Power (kW)	10
	Max op. Temperature (°C)	97
	ORC min op. Temperature (°C)	60
	ORC cold sink Temperature (°C)	T_{amb}
	HP cold sink (free waste heat) Temperature (°C)	60
TES	Volume (m^3)	10
	Aspect ratio (-)	6
	N° of Mixing Zones (-)	20
	Wall Thermal Resistance ($m^2 \cdot K/W$)	10
	Initial Temperature (°C)	95
	Max Temperature (°C)	100
PV Solar Panels	Area (m^2)	2000
	Efficiency (%)	25
DH	Min Temperature (°C)	50
	Max Temperature (°C)	85
Cost parameters	HP/ORC specific cost (€/kW)	2000
	Storage cost (€)	Eq. (7-16)
	Lifetime (years)	30
	Discount rate (-)	0.04
	DH fee (€/kW)	631
	Thermal energy price (€/kWh)	0.07

7.5.1. User, photovoltaic panels, and district heating energy profiles

The user energy consumption profiles, which include both electrical and thermal demands, are derived from data collected over a year from a 2000 m^2 building at the University of Liège campus, consisting of laboratories and offices. The primary contributors to these demands are the building's lighting and heating systems. Figure 7.7 displays the energy demand profiles with a negative sign to emphasize that they need to be offset by various subsystems (e.g., PV panels, the grid, and the ORC for electricity; the DH substation

and CB storage for thermal energy). Electrical power is required year-round, with peak demands during working hours. Thermal demand is minimal during summer months but spikes significantly in the early mornings of winter workdays.

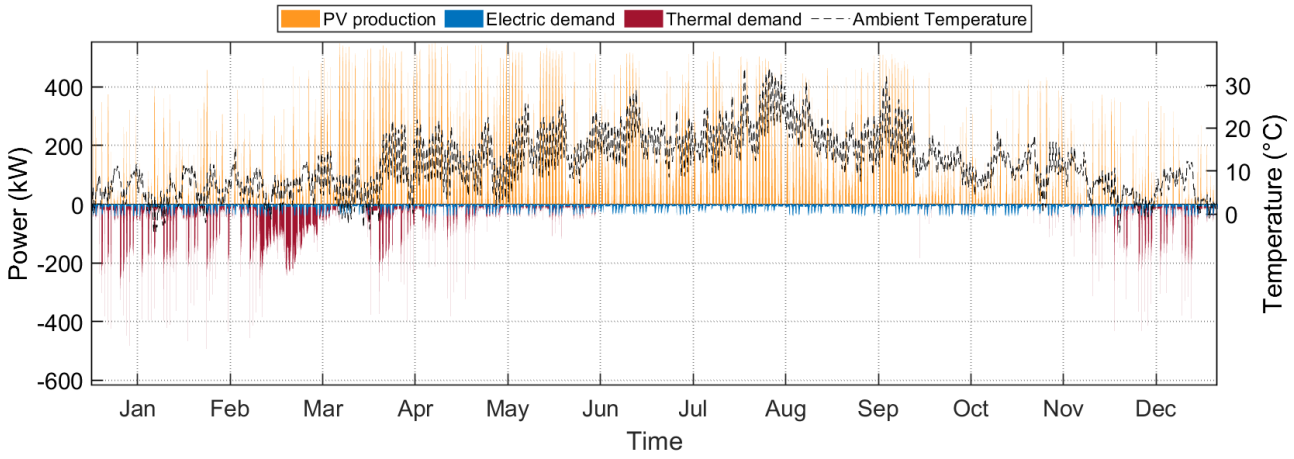

Figure 7.7 - Renewables production, user electric and thermal energy, and ambient temperature annual profiles.

The renewable energy source is represented by a photovoltaic solar power plant with a surface area of 2000 m^2. The solar panels are oriented with an optimal tilt and azimuth angle for Liège's coordinates (40-degree slope and -5-degree azimuth), and a constant efficiency of 25 % is assumed for the PV system. The renewable energy production (Figure 7.7) is simulated using the solar irradiance data from Liège in 2020 [248]. For simplicity and given the study's focus on the economic feasibility of integrating the CB into a more complex system, the PV plant is not modelled in detail. Instead, the renewable electricity generation is directly proportional to the irradiance profile, with a constant value equal to the product of PV efficiency and surface area. Any reduction in PV efficiency can be compensated by increasing the surface area. In this initial analysis, a constant PV efficiency is assumed. While variable efficiency would alter instantaneous electricity production compared to a constant efficiency assumption, reducing the PV surface area does not significantly affect the overall economic gain (as discussed in the next section). However, this simplification could be removed in future studies by implementing a detailed model of the PV plant to assess the impact of efficiency variability on annual operating costs.

An interesting alternative is the use of photovoltaic thermal (PV-T) panels instead of conventional PV technology. PV-T panels typically have higher efficiency and can supply both electricity for the user's needs and thermal energy to enhance the HP performance. The use of PV-T panels in DH systems combined with HPs is a subject of extensive research [249], as PV-T alone cannot reach the temperature levels required by conventional DH networks like the one in the reference campus. For example, Obalanlege et al. [250] analysed an integrated system of PV-T panels, a water tank, and a HP for residential heating and electricity generation. Mi et al. [251] explored the economic feasibility of integrating a PV-T system with a HP to supply a DH network in Dalian, China, demonstrating significant improvements in system efficiency and costs. Their study showed that the PV-T HP system required only 30 % of the energy consumption of an air-source heat pump and 12 % of an electric boiler. Therefore, PV-T technology is a promising upgrade for meeting both thermal and electric demands in tertiary sector applications. In such a scenario, adopting a CB for energy storage is highly suitable. Although Li-ion batteries offer higher roundtrip efficiency, energy density, and lower long-term costs, they also come with higher medium-term costs and sustainability concerns related to manufacturing and recycling. Parra et al. [252], in a techno-economic comparison, found that hot water storage tanks are the most cost-effective option for PV storage systems in the UK, compared to Li-ion and lead-acid batteries. Similarly, Pakere et al. [253] concluded that converting excess electricity into heat is economically advantageous when electricity prices are low. If

different EES systems were used in the reference university building, it would also necessitate the inclusion of an additional thermal production system (e.g., a solar thermal collector) to support the DH system during periods of high thermal demand.

The DH substation serving the reference building operates at temperatures between 50 and 85 °C, which are lower than the primary circuit temperatures of the campus DH system (> 100 °C), as illustrated in Figure 7.3. Therefore, the temperature level for thermal users is capped at 85 °C. The temperature profiles for the DH supply (upstream of the thermal user) and return (downstream of the thermal user) branches are based on data collected from the reference building on the university campus (see Figure 7.8).

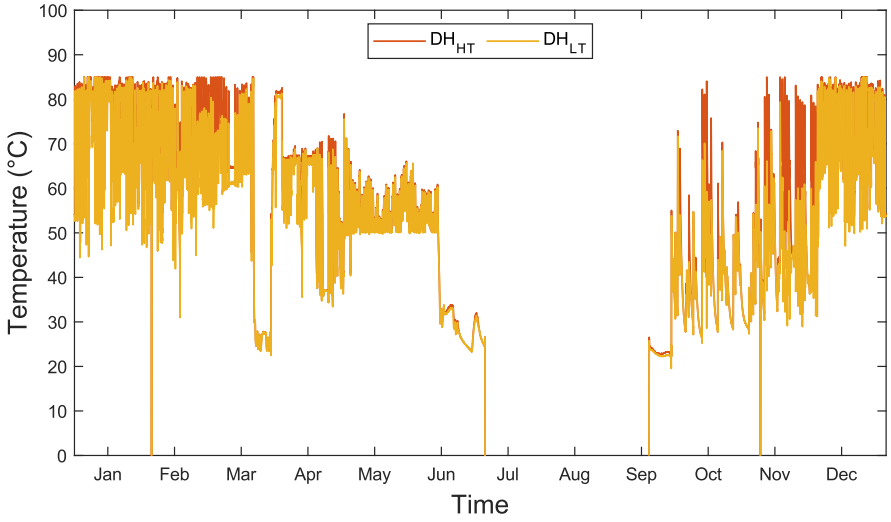

Figure 7.8 - DH supply (HT) and return (LT) branches temperature.

7.5.2. The Carnot battery system and free waste heat

The reversible HP/ORC system (for further details read section 6.2) has a nominal electrical power output of 10 kWe and operates using HFO-1233zd(E), a high-performance, non-flammable refrigerant with an ultra-low GWP (< 1 [27]). The hot source/HP sink temperature for the ORC ranges from 60 to 97 °C. The upper limit is set to prevent water boiling inside the TES tank. The lower limit corresponds to the minimum temperature at which the ORC can operate effectively, avoiding very low conversion efficiency. The cold ORC sink temperature is determined by the ambient temperature profile in Liège in 2020 [248] (see Figure 7.7). To improve performance, the HP operates with a smaller temperature lift (the difference between the hot sink and cold source temperatures), resulting in a thermally integrated CB. In HP mode, the evaporator uses thermal energy available at 60 °C, sourced either from free waste heat or the DH substation (both scenarios are analysed in the results section). The free waste heat source could come from various sources at a university campus, with one of the most abundant being the thermal energy released by data centers, which are prevalent in the reference campus. DCs operate almost continuously, and liquid cooling systems typically produce return water temperatures of 50-60 °C [254], which align with the requirements for the reference application.

The storage system is a cylindrical water tank with a volume of 10 m^3 and an aspect ratio of 6. The tank volume is divided into 20 layers, striking a balance between accuracy in the TES temperature profile and computational effort. The wall's thermal resistance is set at 10 $m^2 \cdot K/W$, according to [255]. The maximum storage temperature is capped at 97 °C, consistent with the constraints imposed on the HP/ORC system, while the initial temperature is set to 95 °C.

7.5.3. Costs correlations and electricity price profiles

To conduct the economic analysis, estimations for the investment costs of the reversible HP/ORC system and the storage tank are made. A specific cost of 2000 €/kWe is assumed for the reversible HP/ORC plant, based on a 10 kWe capacity in HP mode, in line with the capacity exponent ratio method for estimating costs of heat recovery ORC systems [256]. While the assumed HP/ORC investment cost is higher than those estimated for ORC projects in previous studies [256], it is consistent with the price range for HP and ORC technologies considered in recent research on CB systems [60]. The assumed costs reflect the anticipated expenses of industrial production, rather than prototype costs, considering potential system scaling to larger sizes. To account for this, a sensitivity analysis has been performed, varying the specific cost of the reversible HP/ORC system.

The investment cost of the storage system is calculated using Eq. (7-16) [257], where V is the TES volume in cubic meters:

$$C_{I,TES} = \log(V) - 0.002745 \cdot V^2 + 902.6 \cdot V + 7061 \quad (7\text{-}16)$$

The CB is assumed to have a lifetime of 30 years, with a discount rate of 0.04 [258]. The specific investment cost for the DH substation ($C_{DH,fee}$) is set at 631 €/kWth, applicable for substation sizes between 200 and 1200 kW [259]. This value, multiplied by the difference between the original and new DH substation sizes ($\Delta size_{sub}$), represents the potential savings in substation investment costs. Additionally, the cost of purchasing DH thermal energy is assumed to be constant at 0.07 €/kWh, as stipulated by the grid regulator [259].

For electricity pricing, the hourly spot market profile in Belgium for 2021 [260] is used as reference. The first part of that year saw daily average prices similar to those in previous years, while the latter part experienced a significant increase, reaching average values observed in 2022. Consequently, 2021 is chosen as a compromise year between the lower prices of previous years and the higher prices of 2022. The electricity purchase price ($C_{el,pur}$) is increased by 0.12 €/kWh ($\Delta C_{el,ref} = C_{el,pur} - C_{el,sale}$) compared to the electricity sale price ($C_{el,sale}$), which is aligned with the spot market profile. These data are specific to the reference case study, but a sensitivity analysis exploring variations in electricity costs is included and discussed in the results section. The electricity price profiles for 2021 are shown in Figure 7.9.

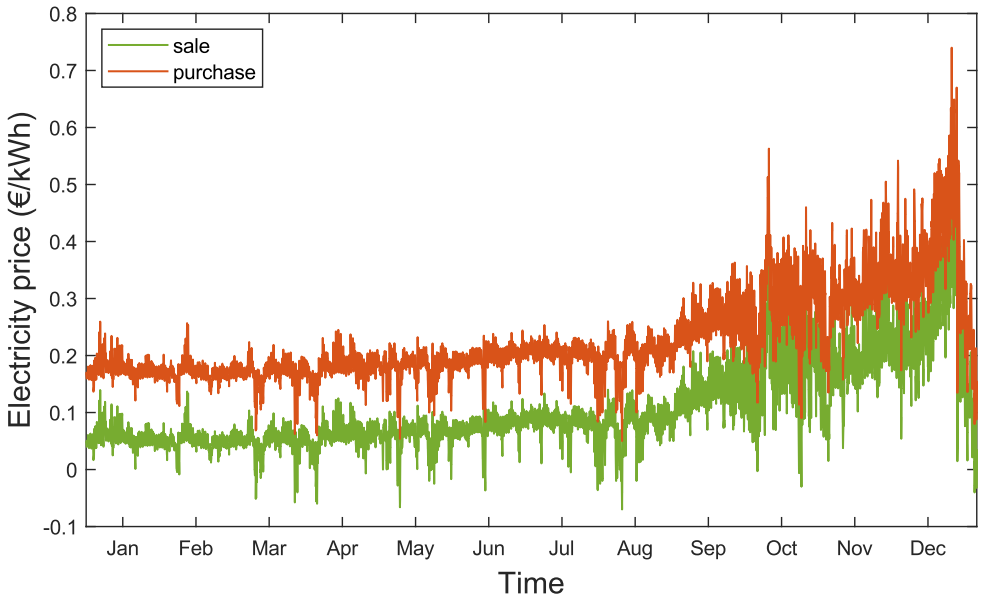

Figure 7.9 - Electricity price profiles for selling and purchasing.

7.5.4. Carnot battery performance indicators

The performance indexes introduced to assess the CB operation are defined as follows:

- The annual electric energy consumption by the HP (E_{HP}) and the annual electric energy generation by the ORC (E_{ORC}) are calculated as the sum of the electric power consumed ($\dot{W}_{HP}$) during HP operation and the electric power generated ($\dot{W}_{ORC}$) during ORC operation:

$$E_{HP} = \sum \dot{W}_{HP} \cdot \frac{\Delta t}{3600} \tag{7-17}$$

$$E_{ORC} = \sum \dot{W}_{ORC} \cdot \frac{\Delta t}{3600} \tag{7-18}$$

- The annual thermal energy output by the HP (Q_{HP}) and the thermal energy absorbed by the ORC (Q_{ORC}) are obtained by summing the thermal power output ($\dot{Q}_{HP}$) during HP operation and the thermal power input ($\dot{Q}_{ORC}$) during ORC operation:

$$Q_{HP} = \sum \dot{Q}_{HP} \cdot \frac{\Delta t}{3600} \tag{7-19}$$

$$Q_{ORC} = \sum \dot{Q}_{ORC} \cdot \frac{\Delta t}{3600} \tag{7-20}$$

- The average coefficient of performance (COP_{ave}) for HP mode and the average efficiency (η_{ave}) for ORC mode are calculated using Eqq. (7-21) and (7-22). The COP is the ratio of the thermal energy output by the HP (Q_{HP}) to the electric energy consumed by the HP (E_{HP}), and the efficiency is the ratio of the electric energy generated by the ORC (E_{ORC}) to the thermal energy absorbed by the ORC (Q_{ORC}):

$$COP_{ave} = \frac{Q_{HP}}{E_{HP}} \tag{7-21}$$

$$\eta_{ave} = \frac{E_{ORC}}{Q_{ORC}} \tag{7-22}$$

- Another important performance indicator is the thermal energy directly supplied to the user (Q_{CB2dem}) from the CB. Additionally, the thermal energy consumed by the HP from the DH system (Q_{DH2HP}) is also significant, especially if the HP cold source is not free waste heat but thermal energy purchased from the DH system:

$$Q_{CB2dem} = \sum \dot{Q}_{CB2dem} \cdot \frac{\Delta t}{3600} \tag{7-23}$$

$$Q_{DH2HP} = \sum \dot{Q}_{DH2HP} \cdot \frac{\Delta t}{3600} \tag{7-24}$$

- The CB running hours are the total amount of hours the CB runs in both HP and ORC modes.
- The CB roundtrip efficiency (η_{rt}) is defined as the ratio of the electricity generated by the ORC (E_{ORC}) to the portion of electricity stored in the CB that is reconverted by the ORC ($(Q_{HP} - Q_{CB2dem})/COP_{ave}$):

$$\eta_{rt} = \frac{E_{ORC}}{(Q_{HP} - Q_{CB2dem})/COP_{ave}} \quad (7\text{-}25)$$

7.5.5. Integrated system performance indicators

The effectiveness of integrating the CB with PV panels to minimize the mismatch between electric power production and user demand is evaluated using the following indicators [261]:

- The self-consumption rate (γ_{cons}) is the fraction of electric energy consumed by the user, including the HP's consumption, that is covered by renewable energy production, including the electricity reconverted by the ORC:

$$\gamma_{cons} = \frac{\sum \min(E_{cons}, E_{prod})}{\sum E_{cons}} \quad (7\text{-}26)$$

- The self-production rate (γ_{prod}) is the fraction of electric energy produced by renewable sources, including ORC production, that is consumed by the user and the HP:

$$\gamma_{prod} = \frac{\sum \min(E_{cons}, E_{prod})}{\sum E_{prod}} \quad (7\text{-}27)$$

Here, E_{cons} represents the total electric demand including the HP electric consumption, while E_{prod} represents the combined output of the PV panels and the ORC. The values of γ_{cons} and γ_{prod} are compared to a scenario without CB intervention in the results section.

7.5.6. Economic performance indicators

The economic advantage of implementing the CB into the integrated system, which includes a PV power plant and a DH substation to meet the user's thermal needs, is highlighted by:

- The downsizing of the DH substation ($\Delta size_{sub}$), which is the difference between the size of the DH substation without the CB ($DHsize_{sub,woCB}$) and with the CB ($DHsize_{sub,wCB}$) (Eq. (7-28)). This provides an economic benefit in terms of savings on the DH substation's investment cost ($\Delta C_{I,DH}$), proportional to the DH fee ($C_{I,DH,fee}$) (Eq. (7-29)):

$$\Delta size_{sub} = DHsize_{sub,woCB} - DHsize_{sub,wCB} \quad (7\text{-}28)$$

$$\Delta C_{I,DH} = \Delta size_{sub} \cdot C_{I,DH,fee}/lifetime \quad (7\text{-}29)$$

- The annual differential economic gain, $\Delta gain$, (Eq. (7-1)), which is the difference in economic benefits between scenarios with and without the CB in the integrated system.

The simple payback period (SPB) [262] and the discounted payback period (DPB) are determined by equating the CB investment cost ($C_{I,HP/ORC}$) and the storage investment cost ($C_{I,TES}$) to the differential economic gain (Eq. (7-30)) and the discounted differential economic gain (Eq. (7-31)), where the discount rate (r) is taken into account for the actualization of the value:

$$SPB = \frac{C_{I,HP/ORC} + C_{I,TES}}{\Delta gain} \quad (7\text{-}30)$$

$$\sum_{i=1}^{DPB} \frac{\Delta gain}{(1+r)^i} = C_{I,HP/ORC} + C_{I,TES} \quad (7\text{-}31)$$

7.6. Annual results

Results are provided and compared for two reference cases, each differing in the HP cold source: the first case utilizes "free waste heat", and the second case involves "thermal integration with DH." In the first case, the HP evaporator absorbs thermal energy from available free waste heat, while in the second case, the evaporator receives thermal energy from the DH return branch. Additionally, the control optimization for the first case is discussed, highlighting the outcomes when altering certain rules in the control flowchart. A sensitivity analysis is also presented, considering variations in the PV plant surface area, storage volume, electricity price profile, and the investment cost of the reversible HP/ORC system.

7.6.1. Reference cases

In the first reference case (free waste heat as HP cold source), the additional revenues and expenses from integrating the CB with a PV power plant and a DH substation, to meet the thermal and electric demands of the user, are illustrated in Figure 7.10. The majority of the revenues stem from the reduction in the DH substation size, leading to significantly lower investment costs. Specifically, out of over € 7000 in annual revenues, more than € 5000 is attributed to the downsizing of the DH substation. Conversely, the gain directly associated with the CB thermal energy, used to meet the demand instead of purchasing it from the DH, is almost negligible. Consequently, the economic benefit from CB intervention with the DH primarily arises from the substantial reduction in DH investment costs rather than operating costs. Additional revenues come from the ORC production for self-consumption, with a smaller portion from electricity sold back to the grid. On the expense side, costs are linked to the CB investment and the electricity consumption of the HP, both from the grid and PV production, which is not sold to the grid.

Table 7.2 highlights the CB annual performance, detailing the contributions from the three modes of operation: HP mode, ORC mode, and TD mode. Over a year of operation, the HP charges the storage for approximately 1630 hours, producing 78843 kWh of thermal energy. Most of this thermal production is utilized by the ORC, reconverted into 5280 kWh of electricity. The ORC operates for around 1506 hours with an average efficiency of 8.42 %. A small portion of the stored heat (1943 kWh) is directly delivered to the thermal user in TD mode to cover early morning thermal demand peaks. This thermal peak shaving effect (illustrated in Figure 7.12) allows for the downsizing of the DH substation. Specifically, the $\Delta size_{sub}$ term is 269.5 kW, which is almost half of the peak demand of 575.1 kW (the size required to meet the entire thermal demand without the CB). Regarding the plant's electricity balance, approximately 44 % of the electricity demand is met by renewable production, with 9.5 % of PV production consumed by the user. Both the self-consumption and self-production rates improve compared to a scenario without the CB (41.8 % and 8.03 %, respectively). This demonstrates that the CB operates as an electricity storage device, effectively reducing the mismatch between renewable production and user consumption. In this reference case, the SPB is calculated to be 8.5 years, and the DPB results to be close to 10 years. Figure 7.11 and Figure 7.12 show the power profiles occurring during typical weeks in summer and winter respectively.

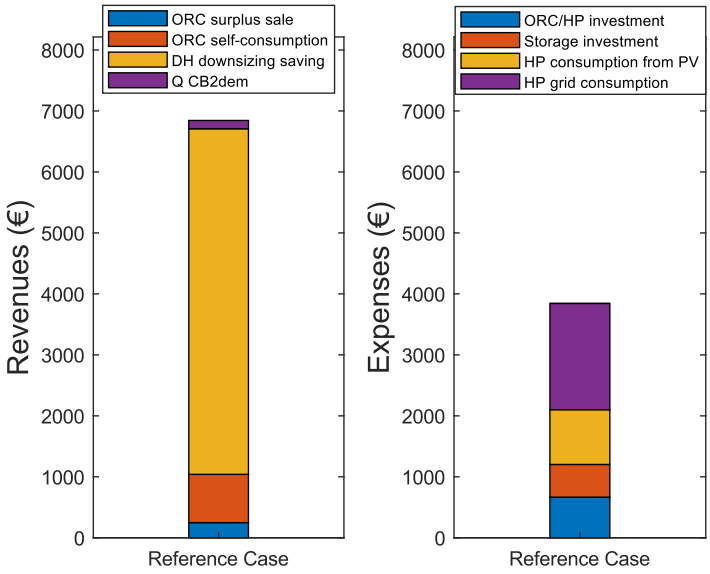

Figure 7.10 – CB annual revenues and expenses for the 1st reference case: R1 – ORC surplus sale, R2 – ORC self-consumption, R3 – DH downsizing saving, R4 – Q CB2dem, C1 – HP consumption from PV, C2 – HP grid consumption.

Table 7.2 – Annual average performance for the 1st reference case.

Mode	**Charge - HP**	**Discharge - ORC**	**Thermal discharge**
COP/efficiency (-)/(%)	4.84	8.42	-
Electrical energy (kWh)	16300	5280	-
Thermal energy (kWh)	78843	62735	1943
Running hours (h)	1630	1506	28.5
Roundtrip efficiency, η_{rt} (%)	33.2		-
DH downsizing, $\Delta size_{sub}$ (kW)	269.5 *(size without the CB intervention: 575.1)*		
Self-consumption rate, γ_{cons} (%)	44.3 *(41.8 without the CB intervention)*		
Self-production rate, γ_{prod} (%)	9.49 *(8.03 without the CB intervention)*		
SPB (years)	8.59		
DPB (years)	10.2		

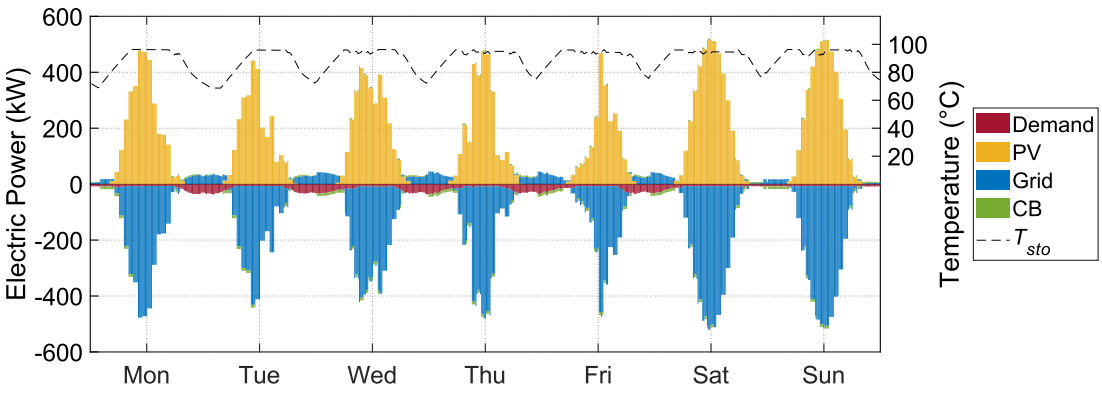

Figure 7.11 – Electric power profile in a typical week in summertime.

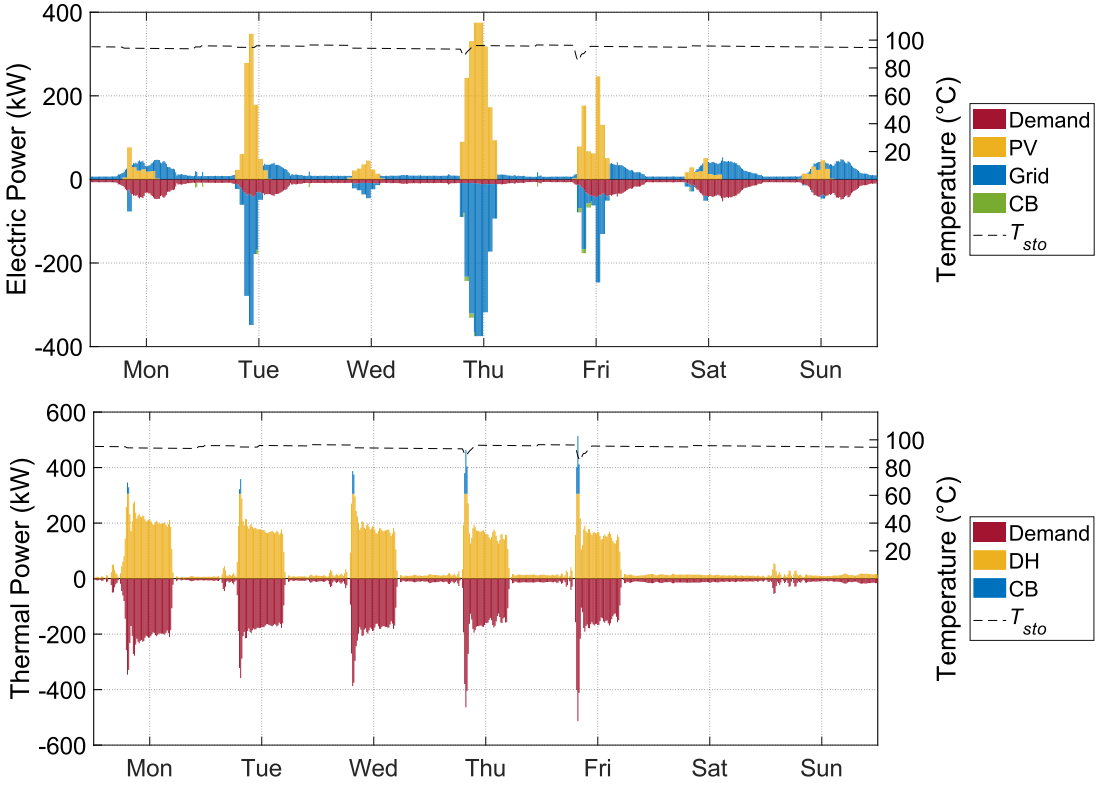

Figure 7.12 – Electric and thermal power profiles in a typical week in wintertime.

In the "thermal integration with DH" case (second reference case), the economic benefit of the CB is influenced by the cost of purchasing heat from the DH. As shown in Figure 7.13, the thermal energy consumption of the HP represents the largest expense, resulting in costs more than double those of the first case. A reduction in revenues also occurs due to a smaller downsizing of the DH substation. Since the CB draws thermal energy from the DH during HP operation, the HP cannot operate when the system is in TD mode. The DH substation, already operating at nominal power, cannot supply thermal energy to the HP during this mode. As a result, the HP cannot provide a boost to the TES during thermal discharge, which limits the extent of DH substation downsizing.

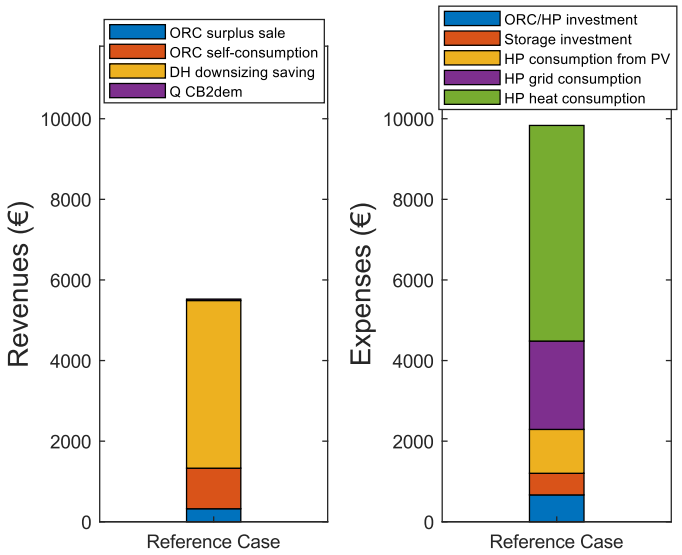

Figure 7.13 – CB annual revenues and expenses for the 2nd reference case: R1 – ORC surplus sale, R2 – ORC self-consumption, R3 – DH downsizing saving, R4 – Q CB2dem, C1 – HP consumption from PV, C2 – HP grid consumption, C3 – HP heat consumption.

Table 7.3 – Annual average performance for the 2nd reference case.

Mode	Charge - HP	Discharge - ORC	Thermal discharge
COP/efficiency (-)/(%)	4.85	8.49	-
Electrical energy (kWh)	19860	6701	-
Thermal energy (kWh)	96294	78919	510
Running hours (h)	1986	1849	12
Roundtrip efficiency, η_{rt} (%)	33.9		-
DH downsizing, $\Delta size_{sub}$ (kW)	197.8		
Self-consumption rate, γ_{cons} (%)	44.8		
Self-production rate, γ_{prod} (%)	9.79		
SPB (years)	-		
DPB (years)	-		

As detailed in Table 7.3, the DH substation downsizing is reduced to 198 kW. However, the larger size of the DH substation means the CB only needs to cover the highest peaks, leaving more thermal energy available throughout the day for ORC operation. This increases the ORC production in the second case, compared to the first. To compensate for the increased ORC running hours, the HP running hours and consumption also rise.

The analysis of the second case indicates that integrating the CB with a DH substation, when waste heat is unavailable and the HP draws thermal energy from the DH, is not economically viable (i.e., expenses exceed revenues under the given conditions). Therefore, this case is not further explored in the rest of the study.

7.6.2. Effect of the control optimization

This subsection examines the benefits of including constraints on electricity price and HP grid consumption into the control strategy. A comparison is made to the annual economic performance when the CB is integrated with the reference system (1st case).

Figure 7.14(a) illustrates the annual revenues and expenses when the constraint on electricity prices ($C_{el} < C_{el,ave}(day)$) is removed (refer to Figure 7.4). Allowing the ORC to discharge the storage immediately, without waiting for higher electricity prices, slightly increases ORC production due to fewer operational constraints. Specifically, the economic gain from self-consumption decreases, while the gain from ORC electricity sales slightly rises (see Figure 7.10 for comparison). However, the cost of HP electricity increases significantly to support higher ORC production, especially since electricity is purchased even when prices are high. The HP consumption of renewable electricity also increases as the removal of the electricity cost constraint allows both the HP and ORC to operate more frequently. Consequently, the ORC production for sale increases. However, the DH substation downsizing remains unaffected by this change in the control algorithm. Overall, the removal of the electricity cost constraint reduces the economic benefit provided by CB intervention, extending the SPB period to approximately 11 years (Table 7.4).

To avoid increasing HP costs, the option of purchasing electricity from the grid to power the HP could be eliminated. Figure 7.14(b) shows the annual revenues and expenses when both the electricity price constraint and the ability to feed the HP with grid electricity are removed. In this scenario, the DH substation downsizing decreases significantly (see Table 7.4), resulting in a lower economic benefit compared to the reference case (Figure 7.10). This decrease is due to the CB impossibility to charge storage and boost thermal production when solar radiation is low or absent, limiting the CB operation to shave thermal demand peaks. As a result, a larger DH substation size is required, and less thermal energy is

available from the CB to cover peaks in the thermal demand, leaving more energy available for ORC operation, which increases its production (Figure 7.14(b)). Moreover, the absence of HP grid consumption reduces overall HP costs, but it also increases self-consumption of electricity produced by PV panels. With these adjustments in the control algorithm, the SPB period exceeds 12 years.

Removing the constraints on electricity prices and HP grid consumption increases both self-consumption and self-production rates (Table 7.4) due to larger utilization of renewable energy by the HP.

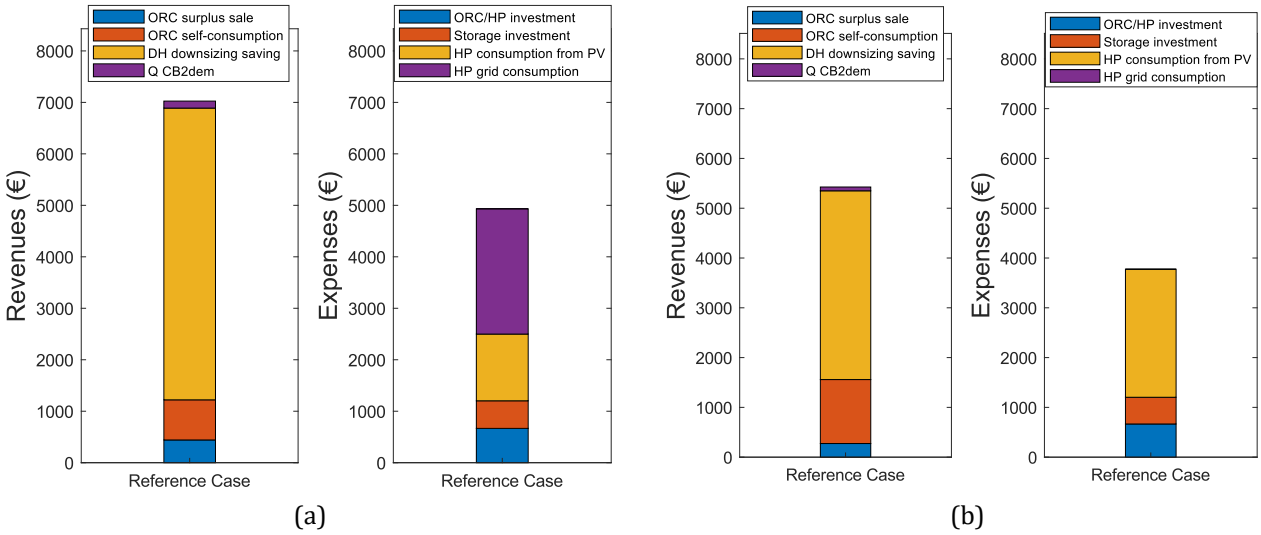

Figure 7.14 - CB annual revenues and expenses removing (a) the electricity price constraint and (b) the possibility of feeding the HP with electricity from the grid.

Table 7.4 – Annual economic performance modifying the CB control strategy.

	Without electricity price constraint	**Without the possibility of feeding the HP with electricity from the grid**
DH downsizing, $\Delta size_{sub}$ (kW)	269.5	180.3
Self-consumption rate, γ_{cons} (%)	46.1	53.9
Self-production rate, γ_{prod} (%)	10.3	12.2
SPB (years)	10.9	12.6
DPB (years)	13.9	17.0

In conclusion, despite the increase in self-consumption, a reduction in economic profit is observed when the instantaneous electricity price is not considered in the regulation strategy and the HP is prevented from drawing electricity from the grid.

7.6.3. Effect of the photovoltaics panels surface

A parametric analysis is conducted to examine how varying the PV power plant surface area affects system performance by altering the renewable energy input. This analysis focuses on the 1st reference case, with the PV panels area ranging from 250 to 2000 m^2 with a step of 250 m^2. Smaller surfaces are excluded from the analysis due to their insufficient size to provide economic benefits with the reference CB. Larger surfaces are not considered because the goal is to explore reductions in the PV area relative to the reference cases, thereby lowering the PV investment cost.

Figure 7.15 presents the annual revenues and expenses associated with the CB when varying the PV panels area, specifically when free waste heat is available as the HP cold source. Both revenues and expenses remain nearly constant. Only when the PV panel area is 250 m^2 the HP consumption slightly

increases compared to other scenarios. Expanding the PV surface leads to higher renewable energy production, which can be stored in the CB until the HP reaches its full capacity. In the first two scenarios with the smallest PV surface, the percentage of HP renewable consumption relative to total HP consumption is lower than in the other cases, where this value tends to stabilize. Specifically, with a PV panels area of 250 m^2, HP renewable consumption accounts for 22 % of total HP consumption. Increasing the PV panel area to 500 m^2 raises HP renewable consumption to 29 %, and with larger PV surfaces this ratio is kept between 31 % and 34 %.

Furthermore, as shown in Table 7.5, the self-consumption rate increases with the PV surface area, while the self-production rate decreases. This is due to the rise in renewable energy production, which can cover a larger portion of the electric demand.

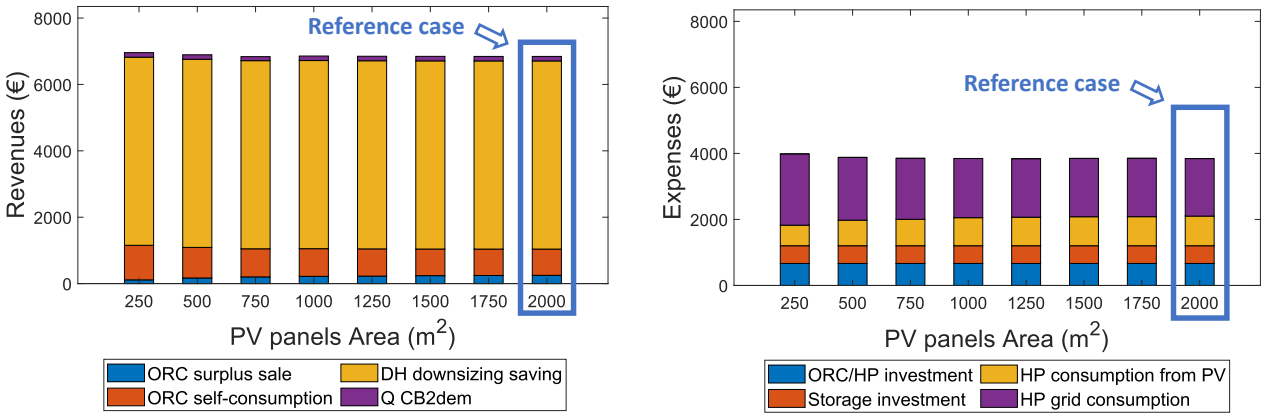

Figure 7.15 - CB annual revenues and expenses varying the PV surface for the 1st reference case.

Table 7.5 - Annual results varying the PV surface for the 1st reference case.

PV surface (m^2)	**250**	**500**	**750**	**1000**	**1250**	**1500**	**1750**	**2000**
DH downsizing, $\Delta size_{sub}$ (kW)	269.5	269.5	269.5	269.5	269.5	269.5	269.5	269.5
Self-consumption rate, γ_{cons} (%)	30.9	36.9	39.7	41.3	42.4	43.2	43.8	44.4
Self-production rate, γ_{prod} (%)	50.2	30.8	22.3	17.5	14.4	12.3	10.7	9.49
SPB (years)	8.64	8.56	8.57	8.57	8.57	8.59	8.60	8.59
DPB (years)	10.3	10.2	10.2	10.2	10.2	10.2	10.2	10.2

When removing HP grid consumption, the reduction in DH substation size is only affected by the PV panel area for the two smallest surface scenarios (Figure 7.16).

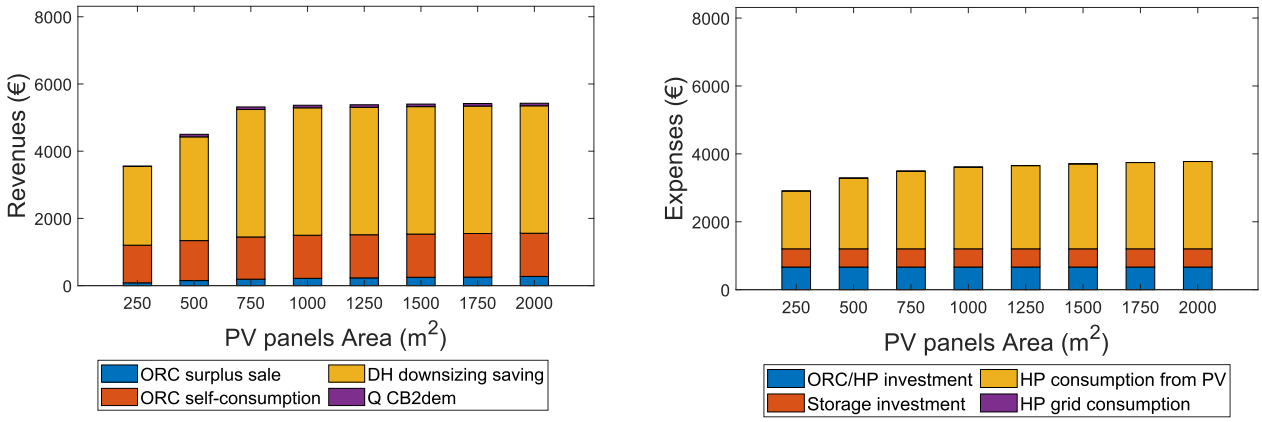

Figure 7.16 - CB annual revenues and expenses varying the PV surface for the 1st reference case, and removing the electricity price constraint and the possibility of feeding the HP with electricity from the grid.

In these two scenarios, the limited availability of renewable electricity prevents the HP from operating at full capacity to generate the required thermal energy to further reduce the DH substation size. Both HP consumption and ORC production show a slight increase from the first case, that then tend to stabilize. The CB SPB period decreases until the DH substation downsizing occurs, after which it slightly increases due to higher HP consumption, which is not fully offset by the minor increase in ORC production (Table 7.6).

Table 7.6 - Annual results varying the PV surface for the 1st reference case, and removing the electricity price constraint and the possibility of feeding the HP with electricity from the grid.

PV surface (m^2)	**250**	**500**	**750**	**1000**	**1250**	**1500**	**1750**	**2000**
DH downsizing, $\Delta size_{sub}$ (kW)	111.3	146.7	180.3	180.3	180.3	180.3	180.3	180.3
Self-consumption rate, γ_{cons} (%)	37.9	44.8	48.4	50.5	51.7	52.6	53.4	53.9
Self-production rate, γ_{prod} (%)	61.9	38.5	28.3	22.4	18.5	15.8	13.8	12.2
SPB (years)	19.5	14.9	11.9	12.2	12.3	12.4	12.5	12.6
DPB (years)	35.2	21.7	15.6	16.1	16.4	16.6	16.8	17.0

In summary, the CB techno-economic performance is relatively insensitive to variations in the PV panel surface area. This is because the CB energy performance largely depends on temperature levels, while its economic performance is strongly tied to the DH substation downsizing, which is unaffected by renewable electricity production, especially when HP grid consumption is considered.

7.6.4. Effect of the storage volume

Given that the CB operates as an energy storage system and its capacity is closely linked to the TES volume, a sensitivity analysis is performed to assess how varying the storage volume impacts overall system performance and economic viability. The storage volume is adjusted from 7 to 16 m^3 with a step of 3 m^3. The results are discussed for the 1st case.

Figure 7.17 illustrates the annual revenues and expenses associated with the CB when varying the storage volume. Increasing the TES capacity allows for storing more thermal energy, which can be used to meet a greater portion of thermal demand peaks, thereby further reducing the DH substation size and associated investment costs. However, the reduction in DH substation size does not increase linearly with storage volume (Table 7.7). It stops once the CB can cover the entire early morning peak, with further downsizing requiring the CB to meet part of the thermal demand throughout the winter days. HP consumption (from both PV production and the grid) and ORC production rise as the storage capacity increases, allowing the HP to produce more thermal energy for peak shaving and ORC discharge phases.

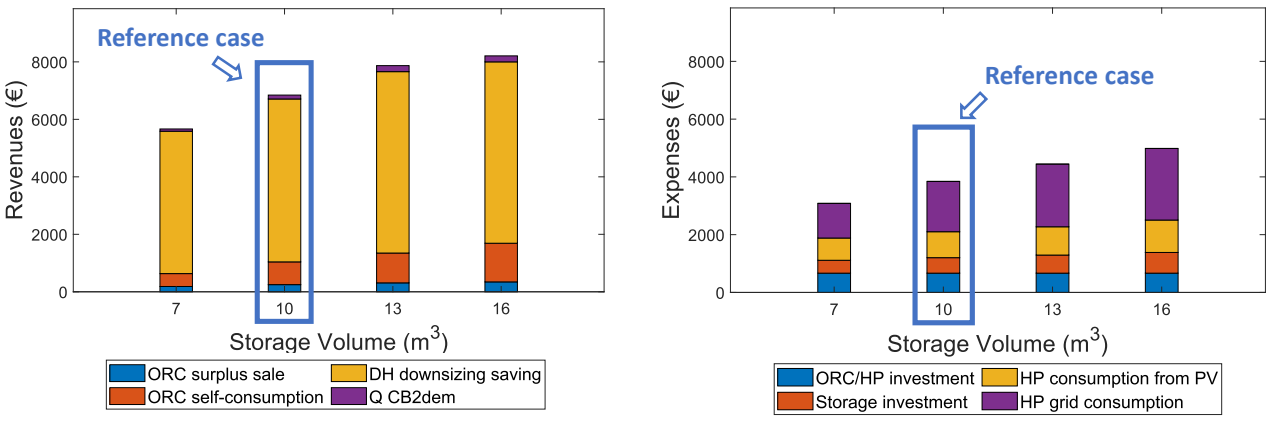

Figure 7.17 - CB annual revenues and expenses varying the storage volume for the 1st reference case.

Additionally, annual expenses grow with storage volume due to higher investment costs. As shown in Table 7.7, the SPB period decreases with increasing storage volume until a reduction in DH substation size occurs; afterward, it increases due to higher storage investment costs, which are not offset by a significant increase in annual gain. Ultimately, both self-consumption and self-production rates slightly rise: the former due to increased HP consumption, and the latter due to higher ORC production.

Table 7.7 - Annual results varying the storage volume for the 1st reference case.

Storage volume (m^3)	**7**	**10**	**13**	**16**
DH downsizing, $\Delta size_{sub}$ (kW)	235.5	269.5	300.0	300.0
Self-consumption rate, γ_{cons} (%)	43.7	44.4	44.7	45.6
Self-production rate, γ_{prod} (%)	9.12	9.49	9.71	10.1
SPB (years)	9.04	8.59	8.22	9.01
DPB (years)	10.9	10.2	9.70	10.8

In conclusion, there is an optimal storage size that minimizes the SPB period for each application. In this case, the optimal storage size is 13 m^3, representing a balance between the benefits of increased storage capacity and the corresponding rise in investment costs. The optimal size is closely related to both the CB nominal power and the intensity of the thermal demand peaks that need to be shaved.

7.6.5. Effect of the electricity price profiles

An additional sensitivity analysis is conducted by altering the electricity price profiles to simulate two different scenarios.

In the first scenario, the objective is to assess the impact of increasing or decreasing the average electricity price while maintaining a consistent difference ($\Delta C_{el,ref}$) between purchasing and selling prices. This adjustment is implemented by applying an offset ($\Delta C_{el,sens1}$) to both the purchasing and selling electricity price profiles, as described by Eq. (7-32):

$$C_{el,sale} = reference\ spot\ market\ profile\ (2021) + \Delta C_{el,sens1} \quad (€/kWh)$$
$$C_{el,pur} = reference\ spot\ market\ profile\ (2021) + \Delta C_{el,ref} + \Delta C_{el,sens1} \quad (€/kWh) \tag{7-32}$$

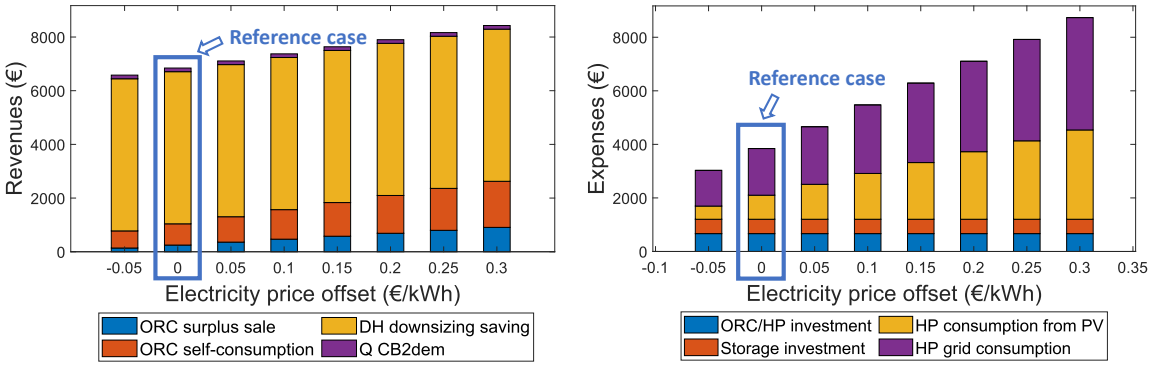

Figure 7.18 - CB annual revenues and expenses varying the electricity price of an offset for the 1st reference case.

Figure 7.18 illustrates the annual revenues and expenses for the first reference case when electricity price profiles are adjusted according to Eq. (7-32). The size reduction of the DH substation remains unaffected by changes in electricity prices, resulting in a constant associated gain. This consistency is due

to the DH substation downsizing profit being directly proportional to the DH fee, which is assumed to be constant throughout the analysis.

As the average electricity price increases, both the revenues from ORC production and the costs associated with HP consumption rise. However, the increase in HP consumption costs overcomes the revenue growth from ORC production since the HP consumes more energy than the ORC produces. This leads to a decrease in the annual economic gain and an extension of the SPB period, as detailed in Table 7.8. Moreover, if the DH fee and thermal energy price remain unchanged, the economic advantage provided by the CB thermal flexibility diminishes with higher electricity prices.

Table 7.8 - CB payback period varying the electricity price of an offset for the 1st reference case.

Electricity price offset (€/kWh)	**-0.05**	**0**	**0.05**	**0.1**	**0.15**	**0.2**	**0.25**	**0.3**
SPB (years)	7.59	8.59	9.88	11.6	14.1	18.0	24.9	-
DPB (years)	8.81	10.2	12.2	15.1	20.0	30.2	-	-

In the second scenario, the analysis focuses on the effects of altering the price difference ($\Delta C_{el,sens2}$) between electricity purchasing and selling prices. Here, the selling price profile remains unchanged, identical to the reference case, while the purchasing price is modified by varying $\Delta C_{el,sens2}$ as per Eq. (7-33):

$$C_{el,sale} = reference\ spot\ market\ profile\ (2021) \qquad (€/kWh)$$
$$C_{el,pur} = reference\ spot\ market\ profile\ (2021) + \Delta C_{el,sens2} \qquad (€/kWh) \qquad (7\text{-}33)$$

Figure 7.19 presents the outcomes of this sensitivity analysis for the first reference case. Similar to the previous scenario, the DH substation size reduction, the portion of thermal demand met by the CB, and the CB investment cost remain constant. Since the selling price profile is unaltered, revenues from ORC surplus sales and HP renewable consumption also stay consistent. The variables affected by changes in $\Delta C_{el,sens2}$ are the revenues from ORC production used for self-consumption and the expenses from HP grid consumption. As the purchasing price increases, expenses grow more significantly than revenues due to the HP higher energy consumption compared to ORC production. This results in decreased overall gains and a prolonged SPB period, as shown in Table 7.9. Consequently, when purchasing and selling prices are closely aligned, the economic benefit increases, primarily driven by the DH substation downsizing.

Overall, this analysis indicates that increasing electricity prices negatively impact the economic viability of the CB system because i) the contribution of thermal-side flexibility to economic gains becomes less significant, and ii) HP consumption costs increase more rapidly than ORC production revenues.

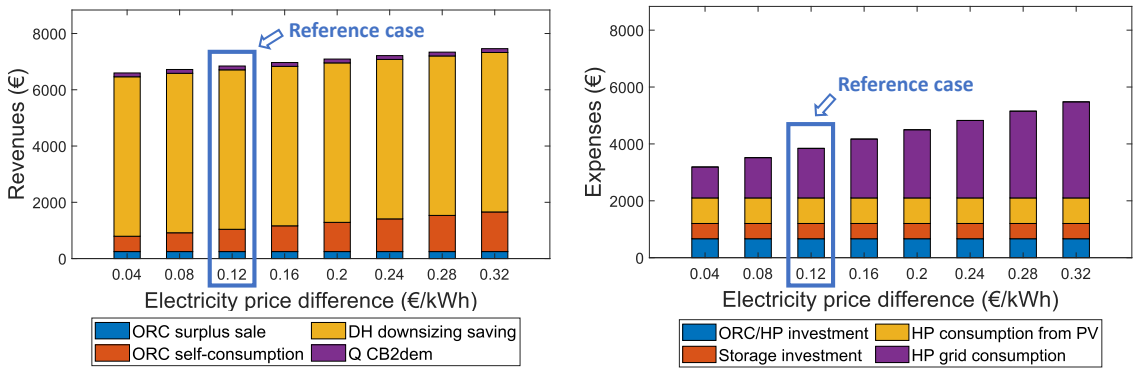

Figure 7.19 - CB annual revenues and expenses varying the electricity price difference between purchase and sale for the 1st reference case

Table 7.9 - CB payback period varying the electricity purchase and sale price difference for the 1st reference case.

Electricity price difference (€/kWh)	0.04	0.08	0.12	0.16	0.20	0.24	0.28	0.32
SPB (years)	7.83	8.19	8.59	9.02	9.51	10.0	10.6	11.3
DPB (years)	9.13	9.65	10.2	10.9	11.6	12.5	13.4	14.6

7.6.6. Effect of the HP/ORC investment cost

A final sensitivity analysis is performed by varying the specific investment cost of the reversible HP/ORC system between 500 and 5000 €/kW. Since the system's investment cost represents a fixed capital expenditure, it does not influence the operational scheduling or performance of the CB within the integrated system. Therefore, while the CB annual operational gain remains unchanged, variations in investment cost directly affect the simple and discounted payback periods. Table 7.10 summarizes the SPB and DPB periods corresponding to different specific investment costs, assuming a constant storage investment cost.

Table 7.10 - CB payback period varying the reversible HP/ORC specific investment cost

HP/ORC investment cost (€/kW)	500	1000	1500	2000	2500	3000	3500	4000	4500	5000
SPB (years)	5.02	6.21	7.40	8.59	9.77	11.1	12.2	13.3	14.5	15.7
DPB (years)	5.47	6.95	8.54	10.2	12.0	14.0	16.1	18.4	20.9	23.7

Although the CB's investment cost does not alter the control strategy outlined in this study, it plays a crucial role in determining the economic feasibility of the proposed integration. Indeed, since HP and ORC technologies are mature and well-established, their commercial adoption is primarily constrained by investment costs.

7.7. Conclusions

This chapter presents a detailed rule-based control strategy for scheduling the operation of a 10 kWe reversible HP/ORC CB within an integrated system. This system includes a DH substation and a PV power plant, and it is designed to meet both the thermal and electrical demands of a user. The control strategy is developed to maximize the economic benefits of the CB when integrated into the system over the course of a year, taking into account the daily fluctuations in electricity spot market prices.

The thermal energy stored in the CB enables the shaving of early morning peaks in thermal demand, facilitating a significant reduction in the size of the DH substation, which translates to substantial savings in investment costs. To assess overall performance, variable boundary conditions are assumed. The electric and thermal energy profiles of the user are based on data collected from a building at the University of Liège campus, while the solar irradiance and ambient temperature profiles are derived from records in Liège during 2020. The electricity price data are sourced from the Belgian spot market profile for 2021. Additionally, two reference system cases, differing in the HP cold source, are examined. In the first case, the HP extracts thermal energy from free waste heat at a constant temperature, assumed to be continuously available and without cost. In the second case, the HP evaporator draws thermal energy from the return branch of the DH substation, incurring an additional cost.

The main outcomes of this study are as follows:

- In the 1st reference case, simulation results indicate that a significant portion of the revenues,

approximately 47 %, comes from the reduction in DH substation size, leading to annual savings of about € 5000. There is 6 % increase in the electricity demand met by renewable production and 18 % increase in renewable production consumed by the user. The reversible HP achieves an annual average COP of 4.8, while the ORC average discharge efficiency is around 8.4 %. From an economic perspective, the CB has a SPB period of less than 9 years.

- In the 2nd reference case, the HP is not allowed to operate during TD mode, as the DH substation is already used at full capacity. This restriction prevents the HP from boosting the TES, negatively impacting the DH substation downsizing and associated economic benefits. As a result, the integration of the CB does not yield a positive economic gain in this case.
- Some control rules applied in the strategy are evaluated, demonstrating their impact on performance. For instance, if the ORC is allowed to discharge the storage immediately without waiting for higher electricity prices later in the day, and if the HP is permitted to draw electricity from the grid even when prices are high, the economic gain is reduced, and the CB SPB period extends to around 11 years. This underscores the importance of optimal system management for maximizing profits.
- Eliminating the option of purchasing electricity from the grid to power the HP, further reduces economic gains because it hampers the DH substation downsizing. In situations with low or no solar radiation, HP-driven thermal production is diminished, resulting in less thermal energy available to shave demand peaks. In this case, the SPB period is approximately 12.6 years.
- Sensitivity analyses varying the PV power plant's surface area and the storage volume are conducted. The results indicate that the PV panel area has minimal impact on gains and CB operation, as the system's energetic performance primarily depends on temperature levels. Economic gains are closely linked to the DH substation downsizing, which remains unaffected by renewable electricity production when grid electricity is available for the HP. Conversely, increasing storage volume significantly influences DH substation downsizing, as well as other revenues and expenses. However, despite the rise in both revenues and expenses with larger storage, there is no substantial change in economic gains or PB period. The optimal storage volume for the application is identified as 13 m^3, corresponding to the shortest PB period.
- A sensitivity analysis is also performed by adjusting the electricity price profile with a certain offset, either increasing or decreasing the average value. Two scenarios are examined: one where both purchasing and selling price profiles are varied, and another where only the purchasing price profile is adjusted. In both scenarios, though to varying degrees, an increase in electricity prices led to a reduction in economic gains. This is primarily because HP operating costs are significantly higher than ORC revenues (as HP consumption far exceeds ORC production) due to the HP primarily generating thermal energy to meet peak thermal demand. Thus, higher electricity prices result in increased HP costs, while the economic benefit from DH substation downsizing remains constant, unaffected by electricity prices.

The rule-based control strategy developed for managing CB operations in an integrated system, as presented in this study, can be adapted for other applications. While the specific rules may need modification to suit different case studies, the overall approach is transferable. Indeed, the techno-economic assessment of a thermally integrated reversible HP/ORC CB applied to a DC cooling system is presented in the next chapter of this thesis.

The control strategy outlined and numerically tested in this study will be implemented in the control and acquisition system of the new 10 kWe prototype of the reversible HP/ORC CB, currently under construction at the Thermodynamics Laboratory of the University of Liège and described in chapter 6 of this thesis. This prototype is directly connected to the lab's DH substation for thermal integration. A comprehensive experimental campaign will follow to fully characterize the CB test bench, validate the control strategy, and provide guidelines for the future development of efficient CBs.

8. Carnot battery thermally integrated with a data center

Summary. This chapter explores the integration of a reversible HP/ORC CB into into DC's cooling systems powered by PV electricity. The research includes a thermodynamic performance analysis, identifying R1233zd(E) as the most efficient working fluid. Then, the semi-empirical off-design model of the reference CB test bench is employed in a rule-based control strategy to manage the CB operations, optimizing the available renewable electricity and reducing the cooling system load. A sensitivity analysis explores the effects of varying storage volume and energy prices. Results indicate that CB integration is economically viable in high energy price scenarios, especially when the system is not allowed to sell electricity to the grid. The study suggests there is room to enhance both system performance and economic benefits, given the conservative operational assumptions and the validation on a non-optimized prototype. Furthermore, a comparison of CB integration with a simpler alternative where DC waste heat is recovered using only an ORC system is carried out, highlighting the advantages of the more complex CB system for waste heat recovery.

8.1. Carnot batteries for data centers energy efficiency enhancement

Multiple solutions to improve the energy management in DC systems, and proposed in literature, are presented at the beginning of section 4.2 of this thesis. The majority of those suggestions rely on cooling improvement technologies and ORC applications in integrated system and often boosted by technologies to increase the temperature level of the thermal energy in input to the ORC as, for instance, HP systems.

An alternative approach to utilize and recover waste heat from DCs involves redirecting the released thermal energy to contribute meeting the heating demands of residential users. Jang et al. [263] introduced an innovative water-source HP system designed to recover waste heat from DCs, thereby reducing overall energy consumption. Hou et al. [264] explored the optimal control strategies for heat prosumers utilizing DC waste heat, employing a model predictive control scheme. Their research includes the integration of short-term TES in a water tank, which enhances the flexibility in the utilization of thermal energy. More broadly, Liu et al. [265] offered a comprehensive review of TES technologies integrated with cooling systems, highlighting their potential to achieve energy and cost savings when applied to DCs.

Considering the literature discussed above, the integration of a CB into DC cooling systems emerges as an intriguing area of study. As far as the author is concerned, the application of CB technology to DCs has only been explored by Laterre et al. [266]. Their study evaluates the potential for incorporating an electric booster-assisted CB into DCs to enhance electrical storage efficiency through WHR. The research examines multiple scenarios and climatic conditions using multi-criteria optimization and thermodynamic modelling. Although the findings suggest that PB periods may be extended, reducing CB capital costs could accelerate economic returns. The study also underscores that the choice between HPs and resistive heaters is contingent upon the temperature of the heat sources. A key insight from the research is the trade-off between efficiency and charging capacity, indicating the need for more effective booster configurations to enhance the techno-economic performance of thermally integrated CB systems. Laterre et al. also offer several recommendations for future research and developments, which are addressed in this thesis' chapter: i) investigating more efficient system configurations during the charging phase, ii) addressing constraints related to flexibility and part-load operations, iii) lowering CB capital costs through the adoption of reversible HP/ORC systems and the use of a single stratified tank as TES, and iv) incorporating additional revenue streams into the integrated system.

8.2. Contribution

Starting from the recommendations by Laterre et al. [266], this study intends to address some of the identified gaps by exploring the feasibility of incorporating a reversible HP/ORC CB into the cooling system of a DC powered by a PV power plant. As one of the pioneering efforts to apply CB technology within the DC sector, this research introduces a novel approach to tackle the challenges of waste heat recovery and enhance electrical storage efficiency in a sector known for significant energy consumption, where heat is typically lost entirely.

The initial part of the study focuses on the comprehensive design of the proposed system, which includes selecting the most appropriate working fluid for both the HP and the ORC. After conducting an initial thermodynamic assessment of well-established working fluids used in HP and ORC applications, the study identifies the most suitable fluid for DC applications through a sensitivity analysis using constant-efficiency models for the HP and ORC. These models, combined with the chosen working fluid, guide the design of the CB and the sizing of the PV plant for the specific application.

Following this essential design phase, a detailed semi-empirical model of a reversible HP/ORC system (the model is the one related to the reference 10 kW-sized prototype under development at the University of Liège, detailed in chapter 6 of this thesis), along with a stratified TES model, is employed to simulate the CB performance under off-design conditions. A rule-based management strategy is then developed to optimize the operation of the CB, with the goal of maximizing economic returns over a year of operation. The strategy involves partially recovering DC waste heat via the HP when PV generation exceeds DC demand, storing this heat at a higher temperature within a sensible TES. When PV output falls below DC electricity needs, the stored thermal energy is used to power the ORC, reducing reliance on grid electricity. Additionally, the possibility of directing high-temperature thermal energy to a thermal user during winter is considered as an additional revenue stream.

The integration of the CB with the DC's cooling system offers dual benefits. First, it prevents the thermal energy released by the servers from being wasted by upgrading its quality via the HP. This energy can either be converted into electricity through the ORC for on-site use when renewable energy is insufficient or used to meet the thermal demands of a user. Second, the proposed system reduces the cooling load on the DC's cooling system, thereby decreasing electricity consumption, as the HP cold source partially replaces the original DC's cooling system.

This study differs from previous research by adopting a comprehensive approach to the design and optimization of the integrated system. It includes the selection of optimal working fluids for the HP and ORC, sizing the CB and PV components, and developing a rule-based management strategy aimed at maximizing economic benefits. The research explores the integration of multiple revenue streams by harnessing previously untapped low-temperature heat and surplus PV electricity to generate high-temperature heat. The double possibility of using this high-temperature heat either to meet the DC's electricity demand via the ORC during PV deficit or to supply thermal energy to a user enhances both the efficiency and revenue potential of the proposed solution. Two distinct scenarios involving electricity and thermal energy prices are analysed and compared. Additionally, the proposed configuration is evaluated against a simpler alternative consisting of a standalone ORC of equivalent size and characteristics, which solely recovers waste heat from the DC. This comparative analysis offers a thorough assessment of the advantages and limitations of different WHR strategies within DC environments.

8.3. The integrated system configuration

The integration of a reversible HP/ORC CB with a sensible TES within a DC's cooling system is outlined

below, with references to the numbered elements in Figure 8.1:

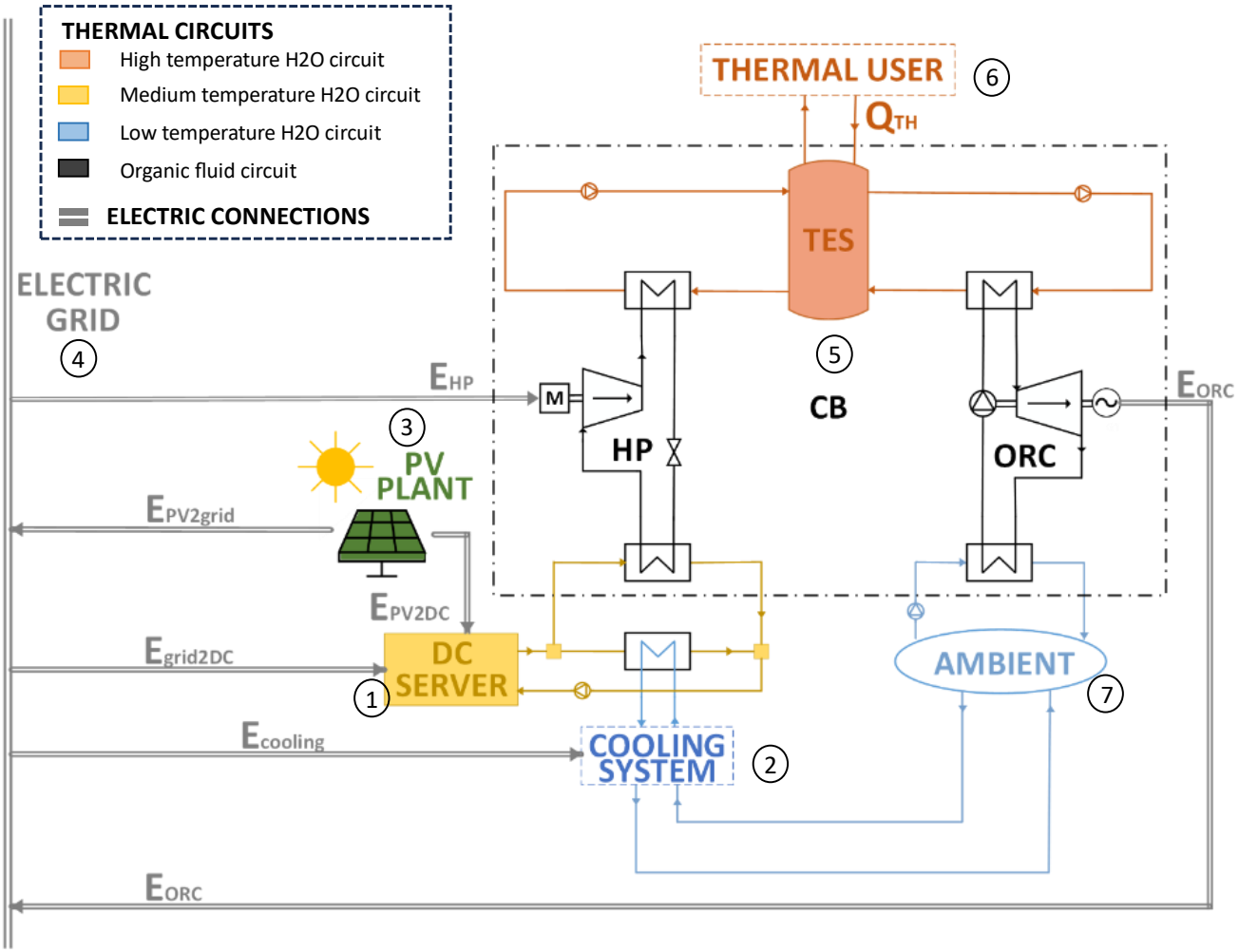

Figure 8.1 - Integrated system configuration scheme, in which main components, thermal circuits, and electric connections are highlighted.

1 - The on-site DC servers, which present a constant electricity demand over time.
2 - The DC's cooling system, which includes direct air cooling and water cooling via a chiller, ensures the servers temperature remains within acceptable limits.
3 - An on-site solar PV power plant that supplies electricity to both the DC and its cooling system. Its output varies with solar irradiance and can either exceed or not the DC's electrical demand.
4 - The electric grid, which serves as a backup, supplying electricity when the PV and integrated system cannot meet demand and absorbing any excess electricity generated by the PV plant. This ensures stable DC operations despite the variability of PV output.
5 - The HP/ORC CB, which is charged operating in HP mode to store excess energy from the PV plant and recover waste heat from the DC, and discharged operating in i) ORC mode to convert the stored energy back into electricity or ii) TD mode to provide direct thermal energy to a user. Waste heat from the DC is recovered bypassing some of the hot water, typically sent to the chiller, into the HP evaporator, thereby reducing the load on the cooling system.
6 - A high-temperature thermal user, such as a DH substation, that can absorb any surplus thermal energy produced by the HP, exceeding the TES capacity, thereby reducing the need for conventional heating systems.
7 - The environment, at ambient air temperature, serves as a cold sink for both the DC's cooling system and the ORC unit.

8.4. Preliminary thermodynamic investigation

To achieve an optimal design for the CB components and select the most appropriate working fluid for the explored application, a systematic thermodynamic performance comparison is conducted. A set of fluids is chosen from the CoolProp library [27], selecting those with a critical temperature slightly above the DC waste heat temperature, and with low environmental impact. The CB thermodynamic performance is evaluated considering the COP in HP mode, the net efficiency in ORC mode, and the overall roundtrip efficiency. This is accomplished using a lumped-parameters thermodynamic model that simulates a basic HP cycle and a simple ORC configuration, both operating in subcritical conditions with the minimum necessary components.

8.4.1. HP and ORC thermodynamic performance

The thermodynamic cycles for the HP and ORC are depicted in Figure 8.2, using R1233zd(E) as the working fluid.

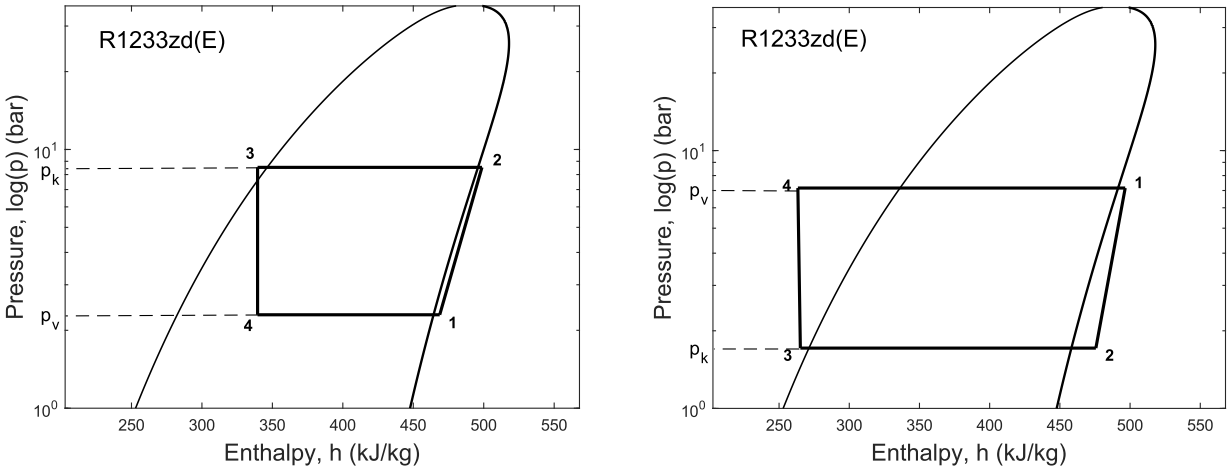

Figure 8.2 - Semi-logarithmic pressure-enthalpy diagrams depicting the (a) HP cycle and (b) ORC, with R1233zd(E).

A calculation routine developed in the MATLAB environment determines the evaporation pressure (p_v) and condensation pressure (p_k) for a given working fluid. Input values include the cold and hot source inlet temperatures (TC_{in}, TH_{in}), the secondary fluids' glide terms ($\Delta T_{glide,sfC}$, $\Delta T_{glide,sfH}$), and the pinch point temperature difference (ΔT_{pp}). The equations and assumptions used to model the HP and ORC cycles are detailed in Table 8.1. The model assumes constant isentropic efficiency for compression (in both modes) and expansion (in ORC mode), isenthalpic expansion (in HP mode), isobaric evaporation and condensation (in both modes), and negligible pressure drops in the HXs. The thermodynamic properties of the fluids under investigation are derived from the CoolProp database [27]. The HP performance is assessed via the thermodynamic COP (COP_{th}, as defined in Eq. (8-11)), which is the ratio of the specific thermal energy produced to the specific work consumed during the compression process. The ORC efficiency is evaluated using the net thermodynamic efficiency ($\eta_{ORC,th}$, defined in Eq. (8-22)), which is the ratio of the cycle's net specific work output (the specific work produced during expansion minus the specific work required for liquid compression) to the cycle's specific thermal energy input. In addition to these performance indicators, the thermodynamic roundtrip efficiency ($\eta_{rt,th}$, as defined in Eq. (8-23)) accounts for the CB thermodynamic performance. In Eq. (8-23), the storage efficiency is considered to be unitary for the sake of simplicity, as assuming a completely insulated (adiabatic) storage tank.

Table 8.1 - Lumped-parameters thermodynamic model equations for HP and ORC performance assessment.

Inputs	$\eta_{is,comp}$, $\eta_{is,exp}$, $\eta_{is,pump}$, ΔT_{pp} , ΔT_{SH} , ΔT_{SC} , TH_{in} , TC_{in} , $\Delta T_{glide,sfH}$, $\Delta T_{glide,sfC}$	
HP mode		
Secondary fluids	$TC_{out} = TC_{in} - \Delta T_{glide,sfC}$	(8-1)
	$TH_{out} = TH_{in} + \Delta T_{glide,sfH}$	(8-2)
Pressures	$p_v = p(TC_{out} - \Delta T_{pp}, x = 1)$	(8-3)
	$p_k = p(TH_{out} + \Delta T_{pp}, x = 0)$	(8-4)
State point 1	$h_1 = h(p_v, TC_{out} - \Delta T_{app} + \Delta T_{SH})$	(8-5)
	$s_1 = h(p_v, h_1)$	(8-6)
State point 2	$h_{2,is} = h(p_k, s_1)$	(8-7)
	$h_2 = h_1 + (h_{2,is} - h_1)/\eta_{is,comp}$	(8-8)
State point 3	$h_3 = h(p_k, TH_{out} + \Delta T_{pp} + \Delta T_{SC})$	(8-9)
State point 4	$h_4 = h_3$	(8-10)
Thermodynamic COP	$COP_{th} = (h_2 - h_3)/(h_2 - h_1)$	(8-11)
ORC mode		
Secondary fluids	$TH_{out} = TH_{in} - \Delta T_{glide,sfH}$	(8-12)
	$TC_{out} = TC_{in} + \Delta T_{glide,sfC}$	(8-13)
Pressures	$p_v = p(TH_{out} - \Delta T_{pp}, x = 1)$	(8-14)
	$p_k = p(TC_{out} + \Delta T_{pp}, x = 0)$	(8-15)
State point 1	$h_1 = h(p_v, TH_{out} - \Delta T_{pp} + \Delta T_{SH})$	(8-16)
	$s_1 = h(p_v, h_1)$	(8-6)
State point 2	$h_{2,is} = h(p_k, s_1)$	(8-7)
	$h_2 = h_1 - \eta_{is,exp}(h_1 - h_{2,is})$	(8-17)
State point 3	$h_3 = h(p_k, TC_{out} + \Delta T_{pp} - \Delta T_{SC})$	(8-18)
	$s_3 = h(p_k, h_3)$	(8-19)
State point 4	$h_{4,is} = h(p_v, s_3)$	(8-20)
	$h_4 = h_3 + (h_{4,is} - h_3)/\eta_{is,pump}$	(8-21)
Net thermodynamic efficiency	$\eta_{ORC,th} = [(h_1 - h_2) - (h_4 - h_3)]/(h_1 - h_4)$	(8-22)
HP and ORC integration in CB		
Thermodynamic roundtrip efficiency	$\eta_{rt,th} = COP_{th} \cdot \eta_{ORC,th}$	(8-23)

To design the CB for a specific HP input electric power ($\dot{W}_{el,HP}$), the working fluid flow rate ($\dot{m}_{wf}$) is calculated, assuming a constant electromechanical conversion efficiency (η_{em}). From this, the thermal power absorbed in the evaporator ($\dot{Q}_{source,HP}$) and released in the condenser ($\dot{Q}_{sink,HP}$) can be evaluated using the following equations:

$$\dot{m}_{wf} = \dot{W}_{el,HP} \cdot \eta_{em}/(h_2 - h_1) \quad (8\text{-}24)$$

$$\dot{Q}_{source,HP} = \dot{m}_{wf} \cdot (h_1 - h_4) \quad (8\text{-}25)$$

$$\dot{Q}_{sink,HP} = \dot{m}_{wf} \cdot (h_2 - h_3) \quad (8\text{-}26)$$

Given that the HP source in this application corresponds to the waste heat discharged by the DC, the reversible HP/ORC is designed to maximize the utilization of this waste heat. This involves calculating $\dot{Q}_{source,HP}$ for various values of $\dot{W}_{el,HP}$ and comparing it with the thermal power released by the DC.

8.4.2. Working fluid selection

The thermodynamic analysis involves comparing a selection of fluids with thermodynamic and environmental properties suitable for the intended application. Given that the DC waste heat is available at 50 °C, and considering a realistic temperature lift for the HP [47] along with the characteristics of the reference CB [107], fluids are chosen with critical temperatures ranging from 90 °C to 200 °C. Fluids with high critical pressure (greater than 50 bar) are excluded for the sake of technical simplicity. Only environmentally friendly fluids, characterized by low GWP and zero ODP, are included in the final selection. Additionally, R134a and R245fa, which are conventional HFCs used as reference fluids for the given ORC operating temperature range [139], are also part of the selected set for the sake of comparison.

Table 8.2 - Working fluid selected set [27] for the explored application.

Fluid Name	T_{crit} (°C)	p_{crit} (bar)	ODP (-)	GWP100 (-)
HFE143m	104.77	36.350	0	0
Isobutane	134.67	36.290	-	-
Isobutene	144.94	40.098	-	-
Isopentane	187.20	33.780	-	-
n-Butane	151.98	37.960	-	3
n-Pentane	196.55	33.700	-	-
n-Propane	96.74	42.512	-	3
Neopentane	160.59	31.960	-	-
Novec649	168.66	18.690	-	-
R1233zd(E)	166.45	36.236	0	0
R1234yf	94.70	33.822	-	4
R1234ze(E)	109.37	36.363	-	6
R1234ze(Z)	150.12	35.330	0	0
R13I1	123.29	39.526	-	0.4
R134a	101.06	40.593	-	1430
R152A	113.26	45.200	-	124
R245ca	174.42	39.407	-	-
R245fa	153.86	36.510	-	1030

Table 8.2 presents the selected fluids, along with their critical temperature and pressure, ODP and GWP (at 100 years) values.

Table 8.3 lists the input parameters used in the thermodynamic constant-efficiency model. These values are chosen to align with the application of the CB in the DC's cooling system, based on the operating conditions of the reference prototype [107], and are consistent with those used in similar thermodynamic models [47]. Specifically, the temperatures of the cold source and sink are set to match the DC waste heat

temperature (50 °C) during HP operation and an average ambient temperature (25 °C) during ORC operation. The hot sink/source temperature values are determined by the temperature available in the TES in the prototype [140], as well as the isentropic efficiency values, and the secondary fluids glides. Minimum pinch point, superheating, and subcooling degrees are selected to align with similar thermodynamic models [47].

Table 8.3 - Constant values and boundary conditions set in the lumped-parameters thermodynamic model.

$\eta_{is,comp}$ (-)	$\eta_{is,exp}$ (-)	$\eta_{is,pump}$ (-)	ΔT_{pp} (K)	ΔT_{SH} (K)	ΔT_{SC} (K)	TH_{in} (°C)	TC_{in} (°C)	$\Delta T_{glide,sfH}$ (K)	$\Delta T_{glide,sfC}$ (K)
0.70	0.75	0.65	3	5	5	85/90 (HP/ORC)	50/25 (HP/ORC)	5	5

8.5. Carnot battery control algorithm

The integration of a CB into a complex system with multiple components necessitates the implementation of an effective scheduling strategy to manage the CB operation. The control algorithm, developed to address this requirement, is based on a rule-based strategy (Figure 8.3).

It establishes when to activate or deactivate the CB and switch between HP and ORC modes. This decision-making process begins with an initial solution attempt and considers the boundary conditions, such as PV electric production, DC electricity demand, weather conditions, and electricity prices. The CB scheduling is guided by an economic objective function (Eq. (8-27)), designed to maximize financial gain ($\Delta gain$) by comparing scenarios with and without CB intervention in the system.

$$\Delta gain = E_{ORC} \cdot C_{el} + \Delta E_{cooling} \cdot C_{el} + Q_{TH} \cdot C_Q - E_{HP} \cdot C_{el} \quad (8\text{-}27)$$

$\Delta gain$ accounts for the energy produced by the ORC (E_{ORC}), the electricity savings from the cooling system ($\Delta E_{cooling}$) due to the DC waste heat removal by the HP, and the revenue from selling thermal energy (Q_{TH}) to a thermal user. These positive contributions are curtailed by the negative impact of using surplus renewable energy to power the HP (E_{HP}) instead of selling it to the grid.

The algorithm first assesses the availability of renewable electricity relative to the DC energy demand. When the PV production is insufficient to meet the DC needs (PV deficit), the algorithm checks the current electricity price (C_{el}). If the price exceeds the average for the day and the TES temperature is above the minimum operating temperature for the ORC, the ORC is activated to discharge the storage. Conversely, when PV production exceeds the demand (PV surplus), the HP is activated to store the excess electricity as thermal energy in the TES. If the HP cannot operate (due to a full storage or insufficient electricity to run the HP above its technical minimum), the algorithm considers the economic viability of using the ORC to generate surplus electricity for sale. The possibility of operating the HP in power deficit conditions, drawing electricity from the grid when prices are low, is not included in this conservative approach.

Afterwards, the energy balance in the storage is updated, reflecting the new conditions in terms of temperature (T_{TES}) and thermal power ($\dot{Q}_{TES}$) availability. Additionally, during the winter season, any excess thermal energy stored above $T_{TH,min}$ can be sold to an external thermal user (such as a DH substation), leading to a thermal discharge and an update of the storage conditions. The main rules for activating or deactivating the CB and switching its modes are summarized in Table 8.4.

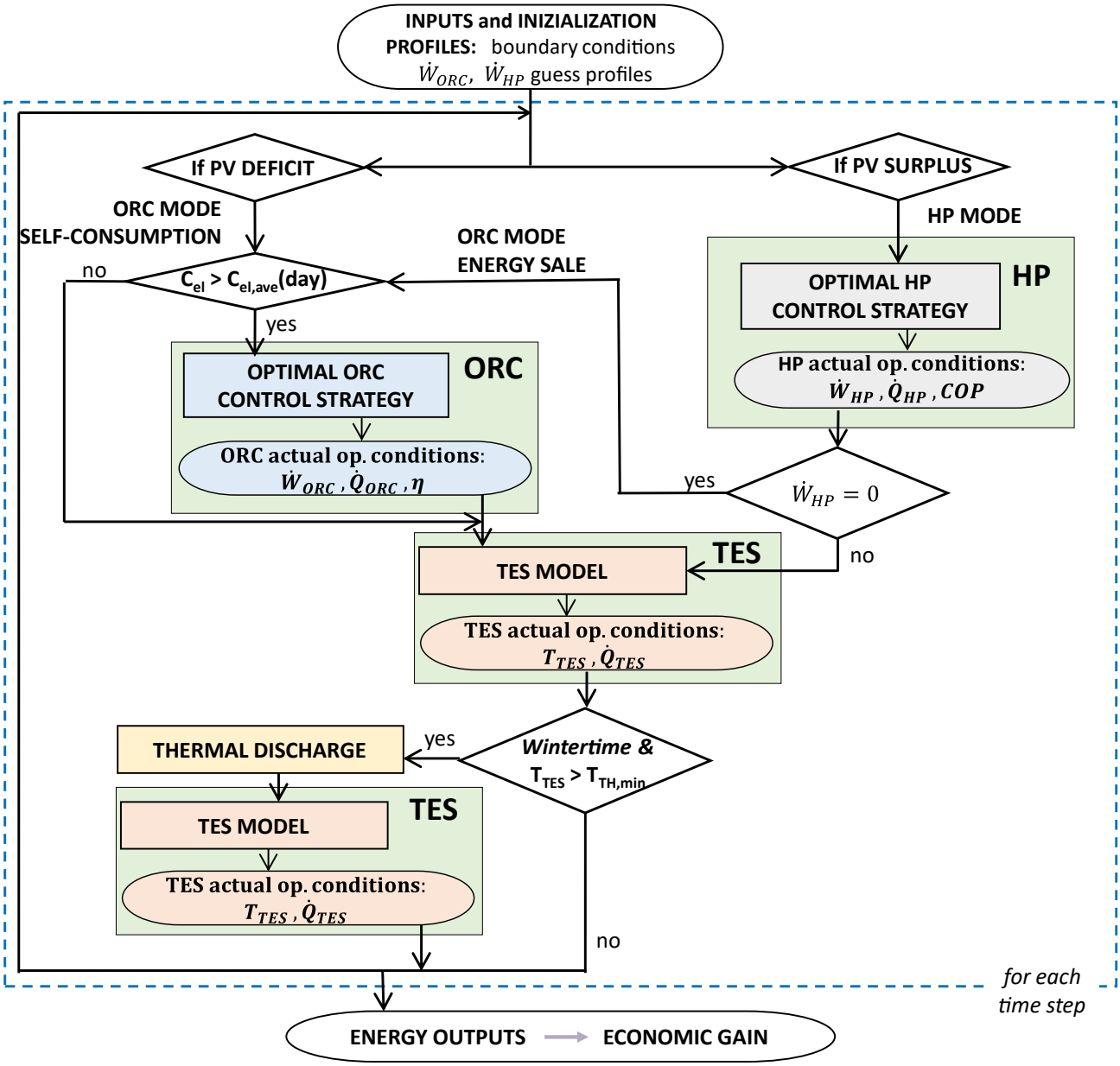

Figure 8.3 - Carnot battery management procedure flowchart.

Although the algorithm initially considers activating the ORC, priority is implicitly given to thermal discharge. Specifically, when there is a renewable production surplus, the HP is activated to charge the storage. Two alternative scenarios then disclose, depending on the season: in winter, once the storage temperature reaches $T_{TH,min}$, the HP production is directed to the thermal user, allowing the HP to continue operating as long as there is a surplus. In summer, the HP operates until the storage is fully charged ($T_{TES} < T_{TES,max}$), after which the storage is discharged via the ORC when it becomes economically advantageous in terms of electricity prices. Following the discharge period, the HP resumes charging the storage, thereby reducing the DC's cooling load. In the case of power deficit, the storage can be discharged through the ORC to generate electricity to meet the DC additional demand, a scenario more common in summer when the storage remains fully charged. In winter, however, HP production is promptly directed to the thermal user, and the storage is not maintained at full charge for ORC operation.

The reversible HP/ORC system model is the one described in subsection 6.1.2, and adopted for the study presented in chapter 7. The sensible TES is modelled as a one-dimensional, vertically stratified water tank, as detailed in subsection 7.4.3 in the present thesis.

Table 8.4 - List of the main rules for each mode activation.

Mode	Rule
Th. Charge (HP mode)	HP is activated only in case of: PV surplus ($\dot{W}_{el,PV} > \dot{W}_{el,dem}$) & $T_{TES} < T_{TES,max}$
Th. Discharge	In wintertime, priority of heat from TES to thermal user when $T_{TES} > T_{TH,min}$
El. Discharge (ORC mode)	ORC is activated in case of: PV deficit ($\dot{W}_{el,PV} < \dot{W}_{el,dem}$) & $T_{TES} > T_{ORC,min}$ & $C_{el} > C_{el,ave}(day)$ *OR* if: PV surplus ($\dot{W}_{el,PV} > \dot{W}_{el,dem}$) & HP off (due to full TES or low PV surplus) & $C_{el} > C_{el,ave}(day)$

8.6. ORC-only configuration

Another approach to enhance the energy efficiency of a DC is through the direct recovery of waste heat to power an ORC, generating electricity to help meeting the DC's power requirements (Figure 8.4).

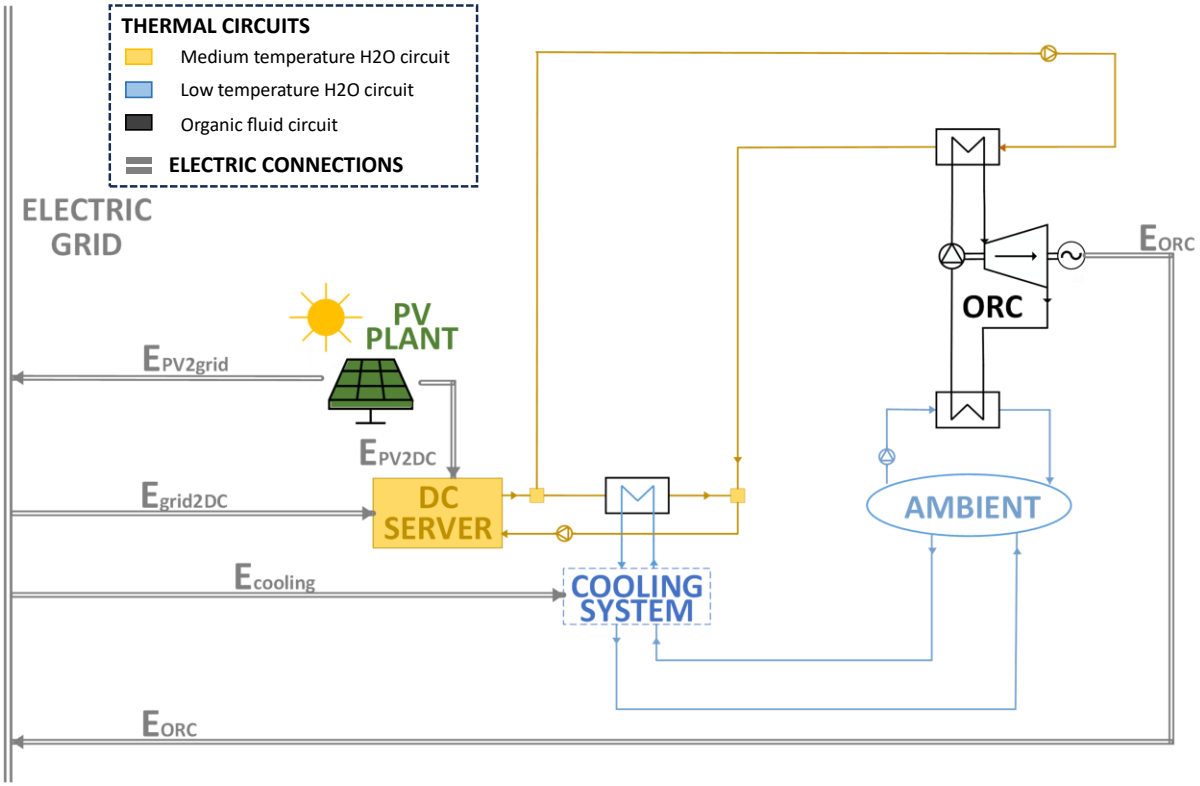

Figure 8.4 - ORC-only configuration scheme, in which main components, thermal circuits, and electric connections are highlighted.

In this scenario, the ORC is linked to a heat source, namely the waste heat from the DC, that remains constantly available at a fixed temperature. However, the ORC is deactivated when the ambient temperature, which serves as the cold sink, becomes too high. The same performance maps that outline ORC operations within the CB management strategy are also applied to assess the ORC performance in this ORC-only configuration.

8.7. Boundary conditions and performance indicators

This section outlines the hypotheses and boundary conditions used in this study, followed by the performance indicators considered for the techno-economic analysis.

8.7.1. Data center, cooling system, and photovoltaic power plant

The DC electric demand is assumed to be steady at 200 kW (Figure 8.5), consistently with the information provided by Ajayi and Heyman [267]. Of the total electricity consumed by the DC, 97 % is converted into waste heat [268], which is released at 50 °C and must be dissipated via a cooling system. This system is assumed to use passive free cooling technologies, such as direct airside and waterside economization (utilizing a chiller), depending on the instantaneous ambient temperature. These methods align with the most efficient passive cooling strategies identified in a review by Nadjahi et al. [25]. The cooling system fans are activated only when the outside air temperature is below 15 °C [268], and they operate at an assumed constant COP of 20 [25]. This equivalent COP is defined as the ratio of thermal energy removed to the electricity consumed by the fans, similar to the chiller's COP, which is also assumed constant at 4, according to data from Sathesh and Shih [269].

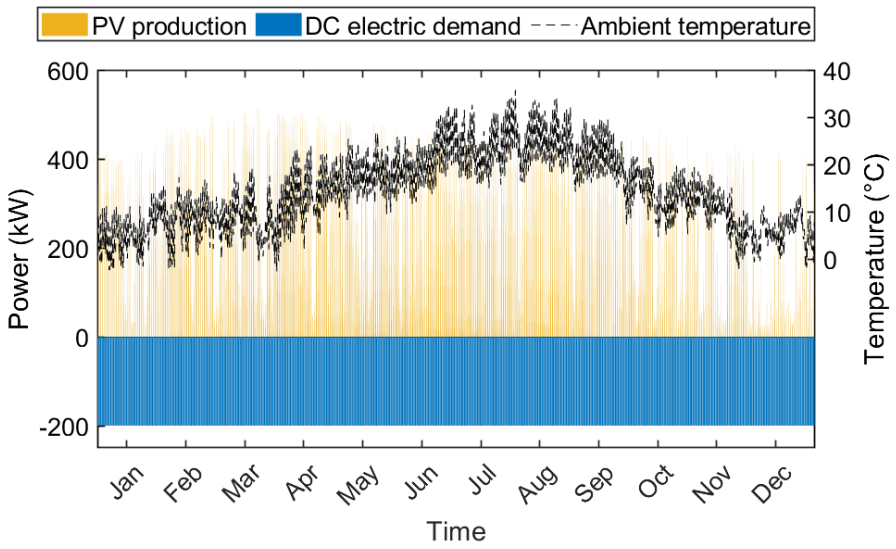

Figure 8.5 - Boundary conditions: PV power production, DC electric demand, and ambient temperature annual profiles.

PV solar panels with a total surface area of 2000 m^2 are considered as the renewable energy source in this study. The PV system is designed to fully meet the DC energy requirements. Indeed, as shown in chapter 7, the sensitivity analysis on the PV size revealed that the size of the PV system does not significantly impact the CB performance. The PV energy production (Figure 8.5) is calculated at 15-minute intervals using the irradiance profile, G, occurred in Bologna (Italy) in 2020, as the assumed ambient temperature profile [248]. The ambient temperature, T_{amb} (Figure 8.5), influences the temperature of the PV panels, T_{PV}, as described by Eq. (8-28) [270], which also affects the ORC performance and thermal losses from the TES to the environment.

$$T_{PV} = T_{amb} + \frac{G}{G_{ref}}\left(T_{NOCT} - T_{ref}\right) \tag{8-28}$$

In this equation, the reference irradiance, G_{ref}, and temperature, T_{ref}, are set at 800 W/m^2 and 20 °C,

respectively [270]. The nominal operating cell temperature, T_{NOCT}, is assumed to be 45 °C [271]. The temperature of the PV panels, T_{PV}, also influences their efficiency, η_{PV}, which is calculated using the general equation [270]:

$$\eta_{PV} = \eta_{ref}\left[1 - \beta_{ref}\left(T_{PV} - T_{ref}\right) + \gamma_G \, log(G)\right] \quad (8\text{-}29)$$

Here, η_{ref} is the nominal PV efficiency, set at 25 % [271], β_{ref} is the temperature coefficient, at 0.26 %/°C [271], and γ_G is the irradiance coefficient, assumed to be zero [272].

In the reference system, the thermal user is assumed to require energy at 80 °C. All assumptions and boundary conditions used in this study are summarized in Table 8.5.

Table 8.5 - DC, cooling system, PV plant, and thermal user hypotheses and parameters.

Data Center	
IT + lighting and auxiliaries electric consumption (kW)	200
Electricity converted into waste heat (%)	97
Waste heat temperature (°C) - T_{WH}	50
Cooling System	
COP chiller (-)	4
COP fans (-)	20
Maximum temperature to use fans (°C)	15
PV Solar Panels	
Area (m^2)	2000
Nominal efficiency (%)	25
TH user	
Minimum temperature (°C) - $T_{TH,min}$	80

8.7.2. The Carnot battery system

The parameters and constraints for the HP/ORC system, listed in Table 8.6, are based on the reference CB test bench (see section 6.2).

The chosen electric power size of 25 kW represents a compromise between the HP size, which allows for the absorption of all the thermal energy released by the DC in HP mode (calculated following the methodology outlined in subsection 8.4.1), and feasible storage sizes. Considering R1233zd(E) as the working fluid (as in the reference test bench), the electric power required by the HP to fully utilize the DC thermal energy would be 50 kW (Figure 8.6). The CB size in the model has been adjusted accordingly, maintaining the same efficiencies under the same boundary conditions.

A cylindrical tank with a height-to-diameter ratio of 6 is considered for the TES to enhance charging and discharging efficiency, as suggested by [273]. The storage volume is varied between 5 and 30 m^3, with a step of 5 m^3, and it is divided into 20 layers (Table 8.6).

Table 8.6 - CB assumptions and parameters.

Reversible HP/ORC	
Nominal electric Power (kW)	25
Maximum operating temperature (°C) - $T_{TES,max}$	95
ORC minimum operating temperature (°C) - $T_{ORC,min}$	60
HP cold sink temperature (°C)	50
TES	
Volume (m^3)	from 5 to 30
Aspect ratio (-)	6
Number of Mixing Zones (-)	20
Wall thermal resistance ($m^2 \cdot K/W$)	10
Initial temperature (°C)	95
Operating temperature range (°C)	60-95

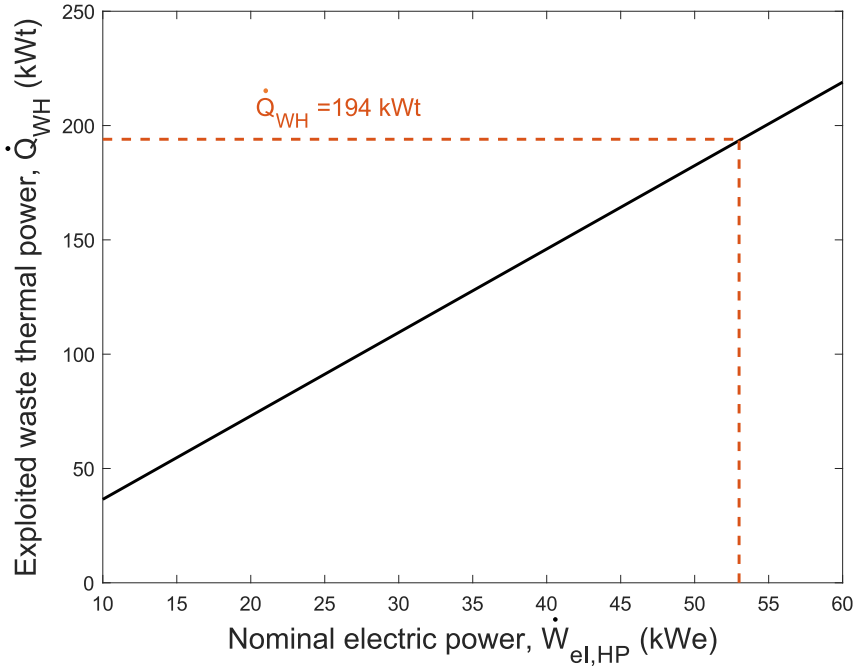

Figure 8.6 – Absorbed thermal power versus HP electric consumption in nominal conditions.

Table 8.7 lists the cost parameters, including the CB investment cost, the system's lifetime, the discount rate used for investment actualization, and the thermal energy price, which is assumed to remain constant throughout the year. Specifically, for the reversible HP/ORC system, an investment cost of 2500 €/kWe is used, based on Lemmens [256] for a system size of 25 kW. The investment cost of a HP/ORC system can vary depending on several design factors, including the invertibility of the machine, component size, thermodynamic settings, and the adopted working fluid. However, in this study, the electric power size is considered the primary determinant of the specific investment cost, using the correlation provided by [256]. The storage investment cost is dependent on volume and is calculated according to Shamoushaki et al. [257]. The values for system lifetime and discount rate are sourced from [262].

The thermal energy price is assumed to be 0.08 €/kWh and 0.16 €/kWh for the years 2018 and 2022, respectively, based on the average DH prices in Bologna during those years [274]. The electricity price profile is derived from hourly spot market data from Northern Italy in 2018 and 2022 [275]. Two distinct scenarios, characterized by very different energy prices (Figure 8.7), are analysed in this study. These will be referred to as the "low energy price" scenario and the "high energy price" scenario in the following of the chapter.

Table 8.7 - Costs assumed parameters.

Cost parameters	
HP/ORC investment cost (€/kWe)	2500
Storage investment cost (€)	[257]
Lifetime (years)	20
Discounted rate (%) - r	6
Thermal energy price (€/kWh)	0.08 / 0.16

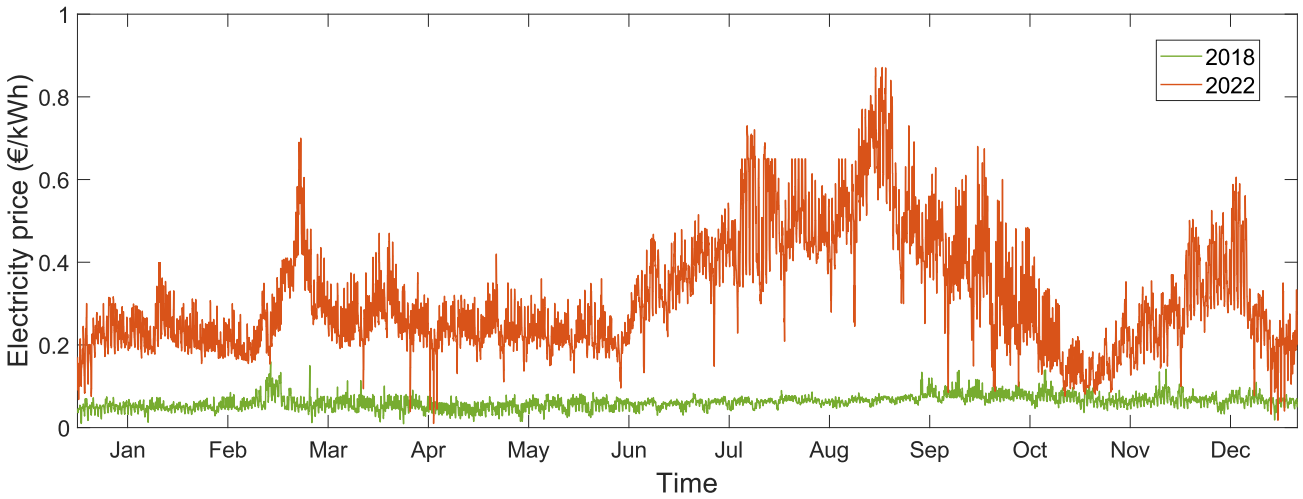

Figure 8.7 – Annual electricity price profiles occurred in Italy during years 2018 and 2022.

In the ORC-only scenario, all assumptions and parameter values remain unchanged, except for the removal of the constraint on the ORC minimum operating temperature ($T_{ORC,min}$), since the heat source is consistently available at 50 °C. The technical feasibility of ORCs operating at such low heat source temperatures has already been experimentally validated for test benches with capacities of 3 kWe (as detailed in section 4.2) and 11 kWe [130].

8.7.3. Carnot battery performance indicators

The operation of the CB in the reference application is evaluated by considering the following key performance indicators:

- The annual electrical energy consumed by the HP (E_{HP}) and generated by the ORC (E_{ORC}).
- The total annual thermal energy produced by the HP (Q_{HP}) and absorbed by the ORC (Q_{ORC}).
- The total running hours of the CB in both HP and ORC modes over the year.
- The annual average COP (COP) for the HP and the efficiency (η_{ORC}) for the ORC, calculated using Eqq. (8-30) and (8-31) respectively.

$$COP = \frac{\sum Q_{HP}}{\sum E_{HP}} \tag{8-30}$$

$$\eta_{ORC} = \frac{\sum E_{ORC}}{\sum Q_{ORC}} \tag{8-31}$$

- The overall performance is summarized by the yearly average roundtrip efficiency, η_{rt}, as defined in Eq. (8-32). The efficiency of the TES, η_{TES}, is given by Eq. (8-33).

$$\eta_{rt} = COP \cdot \eta_{ORC} \cdot \eta_{TES} \tag{8-32}$$

$$\eta_{TES} = \frac{\sum Q_{ORC} + \sum Q_{TH}}{\sum Q_{HP}} \tag{8-33}$$

8.7.4. Overall performance indicators

The techno-economic assessment of the integrated system is performed by analysing the additional revenues and costs associated with the CB integration.

- The annual economic gain, $\Delta gain$ (Eq. (8-27)), is the difference in economic benefits between scenarios with and without the CB in the integrated system.
- The payback period is determined using both the simple payback period (SPB) and the discounted payback period (DPB), calculated according to Eqq. (8-34) and (8-35).

$$SPB = \frac{C_{I,HP/ORC} + C_{I,TES}}{\sum \Delta gain} \tag{8-34}$$

$$\sum_{i=1}^{DPB} \frac{\sum \Delta gain}{(1+r)^i} = C_{I,HP/ORC} + C_{I,TES} \tag{8-35}$$

where $C_{I,HP/ORC}$ and $C_{I,TES}$ represent the investment costs for the HP/ORC and the storage tank respectively, r is the discount rate, and $\Delta gain$ is the annual economic differential gain.

- The performance improvement of the DC and its cooling system is evaluated by calculating the Power Usage Effectiveness (PUE) and the Energy Reuse Effectiveness (ERE) as described by Eqq. (8-36) and (8-37), following the method outlined in [25].

$$PUE = \frac{E_{cooling} + E_{light\&loss} + E_{IT}}{E_{IT}} \tag{8-36}$$

$$ERE = \frac{E_{cooling} + E_{light\&loss} + E_{IT} - E_{reuse}}{E_{IT}} \tag{8-37}$$

Here, $E_{cooling}$ represents the electricity required for server cooling, $E_{light\&loss}$ accounts for the electricity lost in the energy distribution system, as well as other infrastructure losses (e.g., UPS or PDU), and lighting in the DC. E_{IT} is the energy input to the IT equipment, while E_{reuse} is the amount of recovered thermal energy.

- The reduction in the cooling system load, due to the partial use of the HP for cooling the DC, is quantified by the utilization factor (UF). This is the ratio between the cooling energy associated with the chiller and fans in scenarios with ($E_{cooling,chiller/fans,wCB}$) and without ($E_{cooling,chiller/fans,woCB}$) the CB intervention.

$$UF_{chiller/fans} = \frac{E_{cooling,chiller/fans,wCB}}{E_{cooling,chiller/fans,woCB}} \tag{8-38}$$

The technical feasibility of the ORC-only configuration is assessed by comparing its performance — considering annual electricity production, thermal consumption, average efficiency, and operating hours — with the ORC performance when integrated into the CB. Additionally, the annual economic gain for the

ORC-only scenario, $\Delta gain_{ORC}$ (Eq. (8-39)), along with the PUE (Eq. (8-36)), ERE (8-37), and UF (Eq. (8-38)) indexes, are also evaluated.

$$\Delta gain_{ORC} = \sum_{year} E_{ORC} \cdot C_{el} \tag{8-39}$$

8.8. Results and discussion

This section details and analyses the results obtained from the present study. The thermodynamic performance of the selected fluids is evaluated based on indicators such as thermodynamic COP, ORC efficiency, and roundtrip efficiency. Additionally, the techno-economic performance of a CB integrated with a DC cooling system powered by a PV plant is assessed across various storage volume sizes and under two distinct energy price scenarios. The analysis also examines how the CB operation enhances the overall performance of the integrated system. Moreover, the financial advantage of integrating the CB is compared to the potential gain from using a stand-alone ORC instead of a CB (ORC-only configuration).

8.8.1. Thermodynamic design analysis

The fluids deemed suitable for DC applications (as outlined in Table 8.2) are analysed for thermodynamic performance using the model described in section 8.4. Figure 8.8 presents the thermodynamic COP, ORC efficiency, and roundtrip efficiency achieved with the selected fluids, along with the inputs and parameters detailed in Table 8.3.

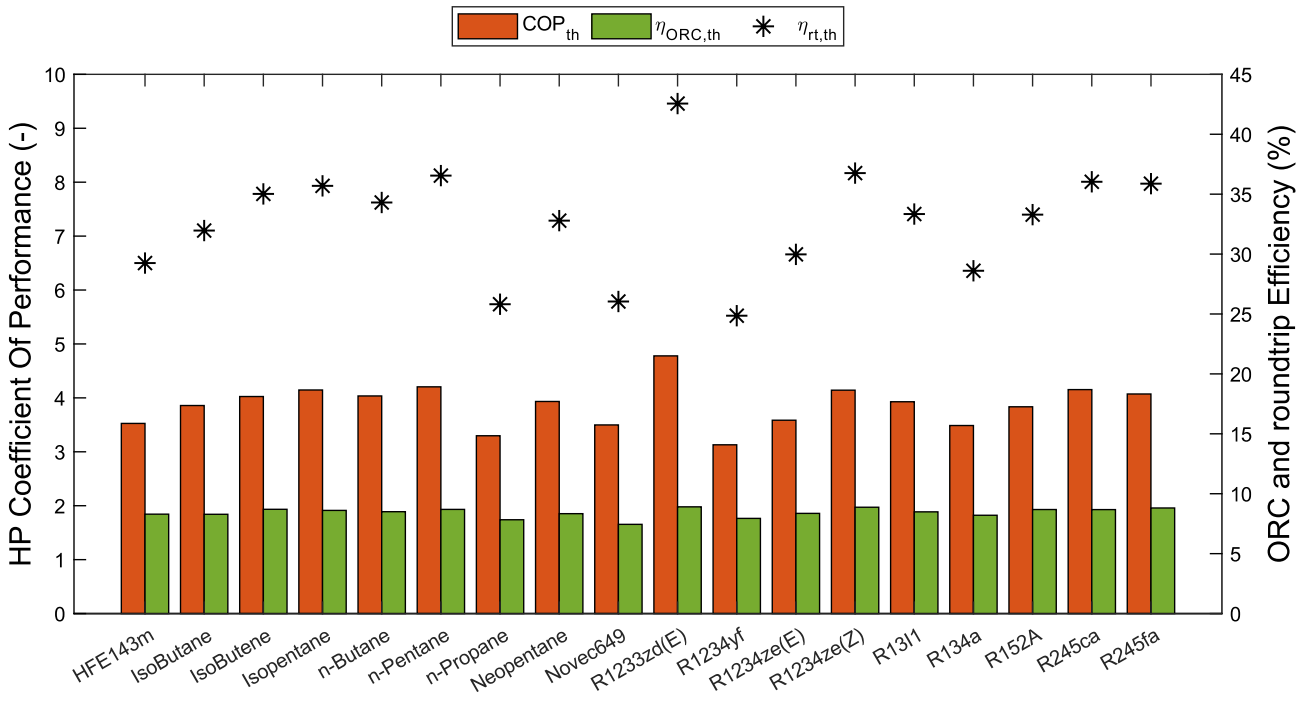

Figure 8.8 - Thermodynamic performance comparison among the selected working fluids for DC applications.

The thermodynamic COP (COP_{th}) falls within the range of 3.2 to 4.8, while the ORC efficiency ($\eta_{ORC,th}$) spans from 7.4 % to 8.9 %. Consequently, the roundtrip efficiency ($\eta_{rt,th}$) varies between 25 % and 43 %. The findings highlight that the olefin R1233zd(E) outperforms the other fluids in both HP and ORC modes,

demonstrating the highest thermodynamic COP (4.78) and ORC efficiency (8.91 %). Therefore, it is not advantageous to employ different working fluids for the HP and ORC modes. The corresponding roundtrip efficiency ($\eta_{rt,th}$) for R1233zd(E) reaches 42.6 %. Although this roundtrip efficiency is lower than that of other storage technologies like PHES, chemical batteries, flywheel energy storage, and CAES [89], it is comparable to the roundtrip efficiencies of hydrogen energy storage systems reported in the literature [276]. The pressure and temperature values for the HP and ORC cycles using R1233zd(E) are provided in Table 8.8.

Table 8.8 - Pressure and temperature values resulting from HP and ORC models when simulated with R1233zd(E).

	p_v (bar)	p_k (bar)	T_1 (°C)	T_2 (°C)	T_3 (°C)	T_4 (°C)
HP	2.3	8.5	47	94	86	42
ORC	7.2	1.7	90	53	28	26

8.8.2. Integrated system weekly operation

Figure 8.9 and Figure 8.10 illustrate the energy flows within the integrated system, depicting both electric (a) and thermal (b) power during two representative weeks – one in winter (Figure 8.9) and one in summer (Figure 8.10). In these figures, energy production within the system is indicated by positive bars, whereas energy demand or consumption is represented by negative bars.

Figure 8.9(a) and Figure 8.10(a) present the electrical energy flows in the system. The PV power generation (shown in yellow) is driven by solar radiation levels, while the DC electricity demand (depicted in blue) remains constant. The electrical consumption of the chiller (in light blue) and fans (in purple) is embedded for summer and winter, respectively. The CB electrical power (represented in orange) shows negative values during HP consumption and positive values when ORC production occurs. The power exchanged with the grid (in green) is positive when the system draws electricity from the grid to meet the demand (electric power in input to the system), and negative when excess electricity is generated and fed back into the grid (electric power in output from the system). Figure 8.9(b) and Figure 8.10(b) display the thermal energy flows in the integrated system. The constant production of waste heat from the DC is shown in blue. The thermal energy removed by the chiller (in light blue), fans (in purple), and HP (in green) is depicted as negative, as it represents heat being extracted from the system. The CB associated thermal power (in orange) is positive when representing the HP thermal production – thermal power filling the system – and negative when absorbed by the ORC – thermal power drained from the system. Thermal energy delivered to the thermal user is shown in red, while energy entering or leaving the TES is illustrated in yellow, with signs opposite to those of the CB thermal output.

During the winter, when PV output is low, most of the DC energy needs must be supplied by the grid (Figure 8.9(a)). When there is an excess of PV production, the HP (in orange) is activated, first to charge the storage (negative yellow bars in Figure 8.9(b)) and then to produce thermal energy for the thermal user (in red). This approach is designed to reduce the load on the cooling system by maximizing HP usage and optimizing the recovery of DC waste heat. As PV generation decreases, the ORC (in orange) operates until the storage is depleted (positive yellow bars in Figure 8.9(b) representing the release of stored thermal energy). In summer, when there is no thermal demand, the HP (in orange) remains inactive during periods of excess electricity (Figure 8.10(a)) as the storage reaches its full capacity (in yellow in Figure 8.10(b)). The ORC is then alternated with the HP to generate surplus electricity for grid sales, discharging the storage and allowing the HP to resume operation later. When the HP operates, it reduces the load on the cooling system (green in both Figure 8.9(b) and Figure 8.10(b)). Moreover, during winter, when ambient temperatures are low (typically below 15 °C), only the fans are engaged for cooling (Figure 8.9), while in summer, the chiller is necessary, resulting in higher electricity consumption (Figure 8.10).

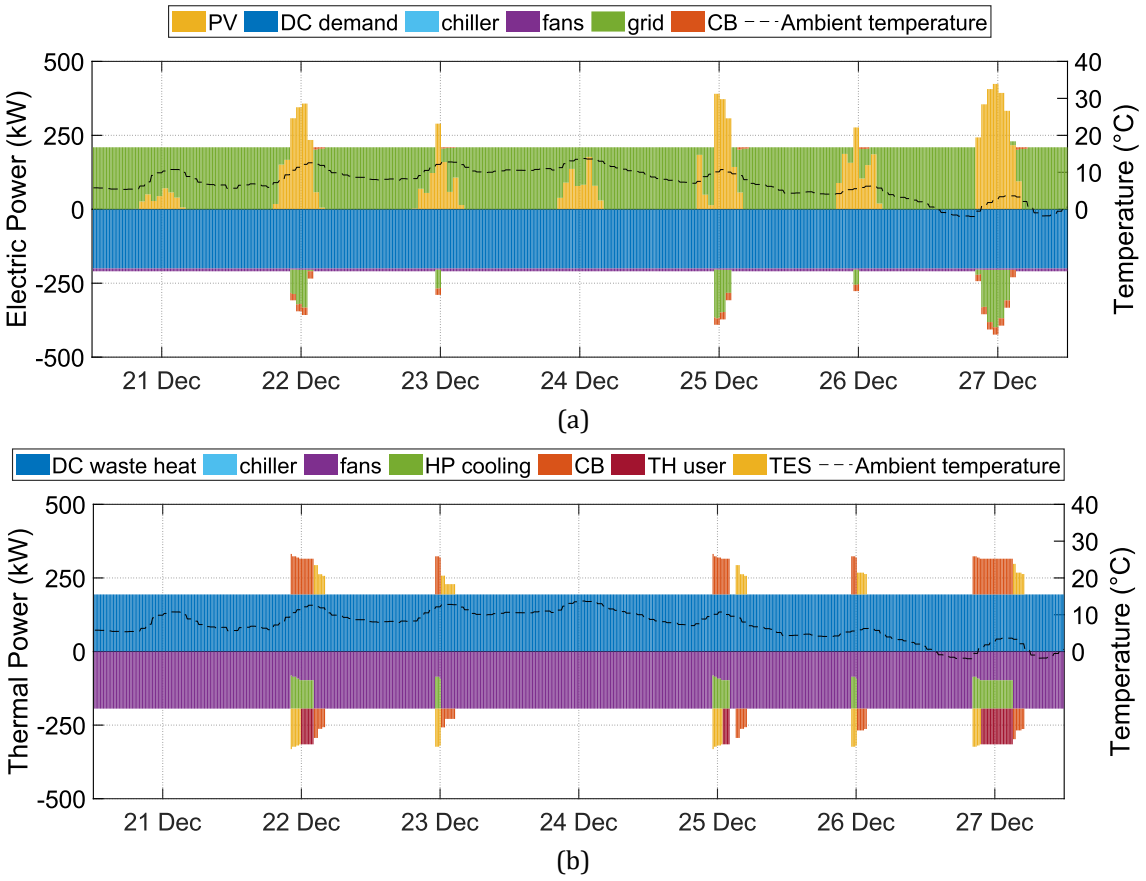

Figure 8.9 – Typical winter week (a) electric and (b) thermal energy flows.

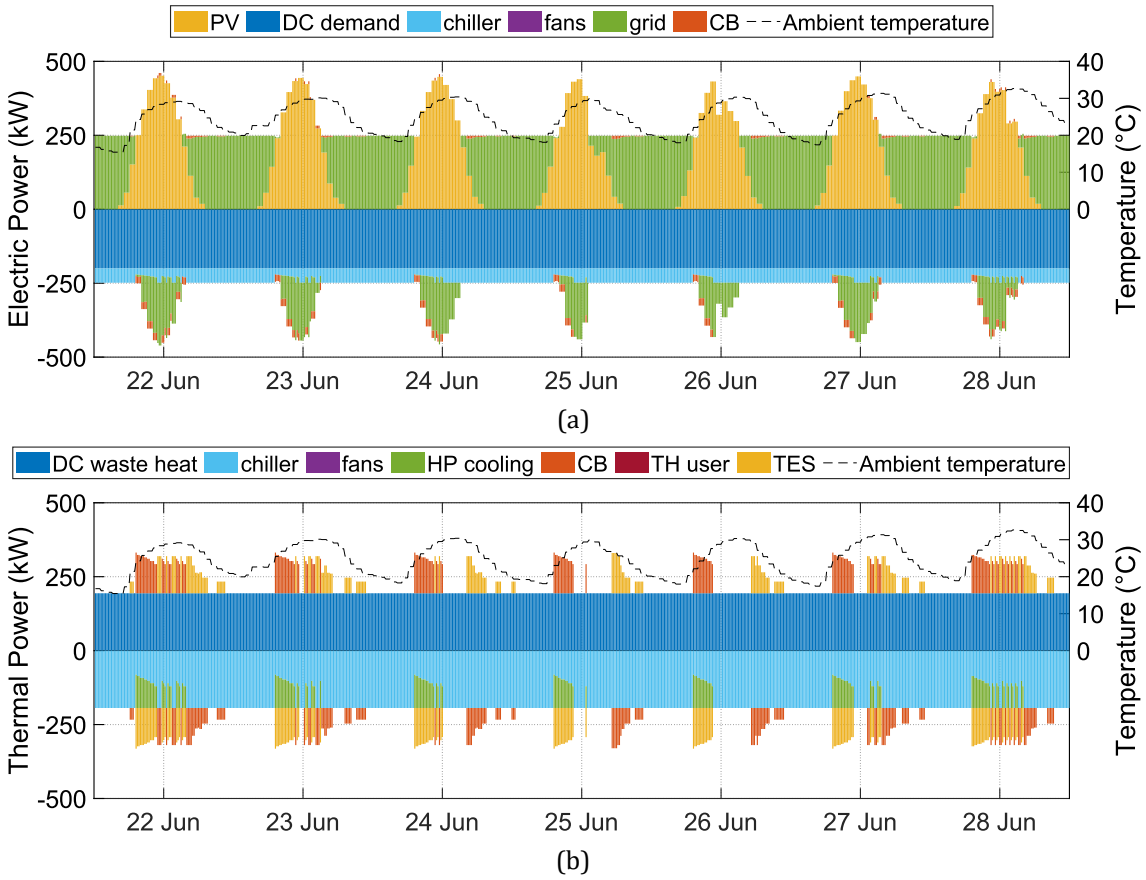

Figure 8.10 - Typical summer week (a) electric and (b) thermal energy flows.

8.8.3. Carnot battery techno-economic performance

The additional yearly revenues and costs arising from the integration of the CB into the reference system are illustrated in Figure 8.11 and Figure 8.12, corresponding to the two energy price scenarios. Increasing the storage volume enhances the energy storage capacity, which extends the operational duration of the CB, thereby improving the decoupling between the DC electric demand and the PV power generation. As a result, the expansion of storage capacity enables the availability of more thermal energy, leading to a significant increase in ORC output. The HP electricity consumption sees a slight rise up to a specific storage volume (25 m^3), after which it levels off. This plateau occurs because the HP reaches its maximum output potential based on the surplus renewable electricity available. To better clarify, when the storage volume is below 25 m^3, HP operation might be restricted if the storage is full during periods of surplus renewable energy. With a larger storage capacity (30 m^3), HP operation is no longer limited by storage size but is instead dependent on the availability of surplus renewable power and temperature constraints. The increase in ORC output corresponds with a reduction in thermal energy production as storage volume expands. Savings from the cooling system, achieved when the HP is used to absorb DC waste heat, increase with both HP output and storage volume. In the high energy price scenario (Figure 8.12), these savings become more significant due to a notable rise in electricity prices.

The annual economic benefits (resulting from operating revenues and expenses), along with SPB and DPB values for the two energy price scenarios, are detailed in Table 8.9 and Table 8.10, respectively. Values for SPB and DPB that exceed the CB's lifetime (20 years) are not included in the tables. Under low energy price conditions, integrating a CB into the system is economically disadvantageous, requiring an extended period to recoup the investment costs (Table 8.9). On the other hand, as energy prices rise, the integrated system with the CB becomes a more appealing option, particularly for smaller storage capacities. The PB period is significantly reduced, reaching attractive levels, especially for smaller storage volumes (Table 8.10). Table 8.11 compares the performance of the CB in the two energy price scenarios, focusing on a storage volume of 10 m^3, which optimizes the annual economic gain ($\Delta gain$) in the high energy price scenario (7744 €/year).

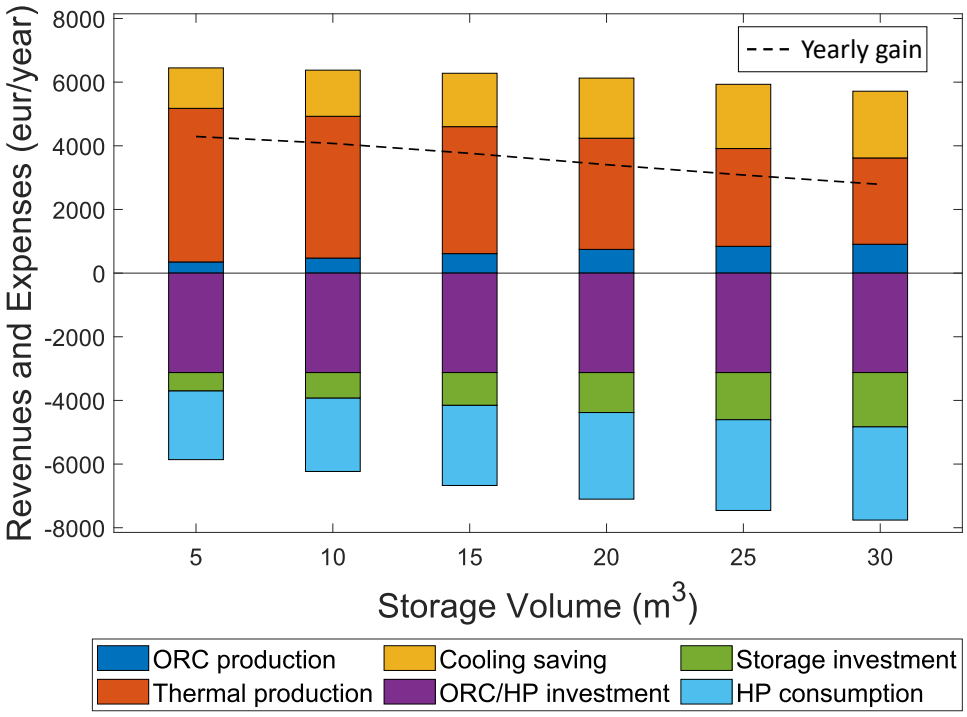

Figure 8.11 – Yearly economic gain associated with the CB integration (low energy price scenario).

Table 8.9 - Yearly economic gain, simple and discounted payback period (low energy price scenario).

Storage volume (m³)	5	10	15	20	25	30
Yearly gain (€/year)	4292	4075	3763	3407	3082	2788
SPB (years)	17.3	19.3	> 20	> 20	> 20	> 20
DPB (years)	> 20	> 20	> 20	> 20	> 20	> 20

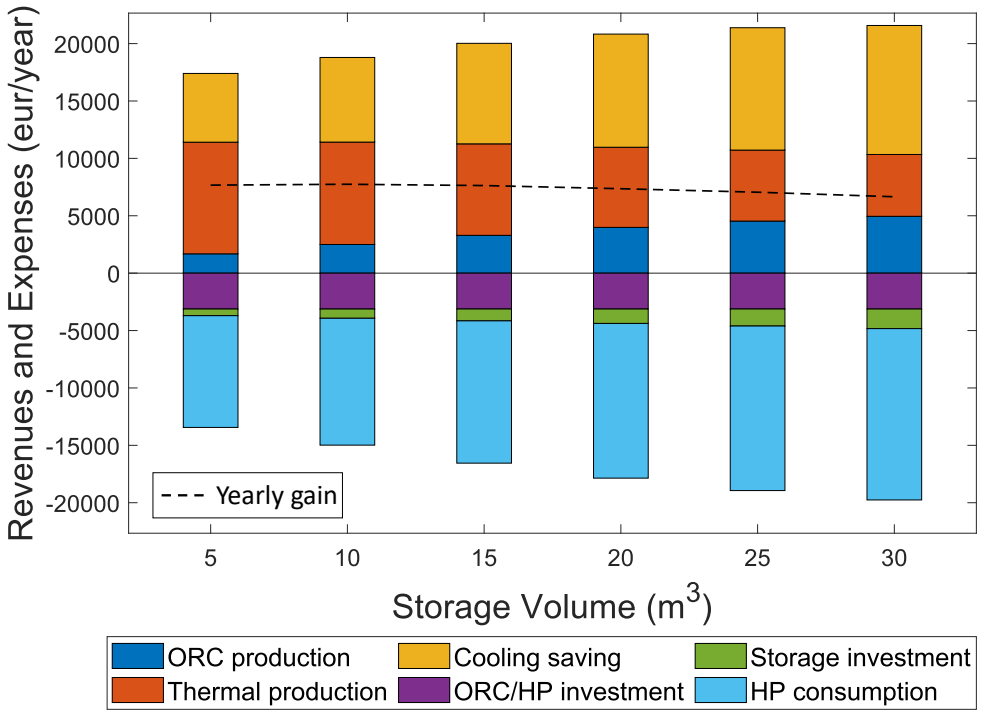

Figure 8.12 - Yearly economic gain associated with the CB integration (high energy price scenario).

Table 8.10 - Yearly economic gain, simple and discounted payback period (high energy price scenario).

Storage volume (m³)	5	10	15	20	25	30
Yearly gain (€/year)	7668	7744	7631	7356	7051	6655
SPB (years)	9.66	10.1	10.9	11.9	13.1	14.5
DPB (years)	13.6	14.7	16.5	19.2	> 20	> 20

Table 8.11 - CB annual average performance for a storage volume of 10 m³.

	Low energy price scenario			High energy price scenario			PV
	HP	ORC	TD	HP	ORC	TD	
Annual average COP/efficiency (-)/(%)	4.88	7.05	-	4.90	7.16	-	20.5
Annual electrical energy (kWh)	36543	7140	-	34778	6774	-	870769
Annual thermal energy (kWh)	178247	101292	55667	170410	94656	55761	-
Annual running hours (h)	1497	1230	459	1425	1169	460	4267
Annual average storage efficiency (%)	88.1		-	88.3		-	-
Annual average roundtrip efficiency (%)	30.3		-	31.0		-	-

More favourable values for annual economic gain, SPB, and DPB are observed in both energy price scenarios when the option to sell electricity to the grid is removed (Table 8.12 and Table 8.13). In this scenario, HP consumption is no longer considered a cost since the associated energy would otherwise be

wasted without the CB, and ORC production would be limited to self-consumption. These findings are particularly noteworthy in the high energy price scenario (Table 8.13), where the PB period ranges between 4 and 5 years, making the proposed CB integration economically viable.

Table 8.12 - Yearly economic gain, simple and discounted payback period when selling the electricity to the grid is not possible (low energy price scenario).

Storage volume (m3)	**5**	**10**	**15**	**20**	**25**	**30**
Yearly gain (€/year)	6337	6306	6232	6091	5909	5703
SPB (years)	11.7	12.4	13.3	14.4	15.6	16.9
DPB (years)	18.6	> 20	> 20	> 20	> 20	> 20

Table 8.13 - Yearly economic gain, simple and discounted payback period when selling the electricity to the grid is not possible (high energy price scenario).

Storage volume (m3)	**5**	**10**	**15**	**20**	**25**	**30**
Yearly gain (€/year)	16988	18491	19820	20691	21283	21524
SPB (years)	4.36	4.25	4.19	4.23	4.33	4.49
DPB (years)	4.87	4.73	4.66	4.71	4.83	5.03

8.8.4. Integrated system performance

The CB integration leads to improvements in both the DC PUE and ERE, as shown in Figure 8.13. This enhancement is driven by the HP contributing to part of the cooling power, with roughly 30 % of the HP electrical consumption (that is not utilized as thermal energy) being recovered by the ORC, as detailed in Table 8.11 (where η_{rt} is nearly 30 %). As the CB operates, the number of running hours increases with the expansion of the storage capacity, resulting in corresponding enhancements in both PUE and ERE.

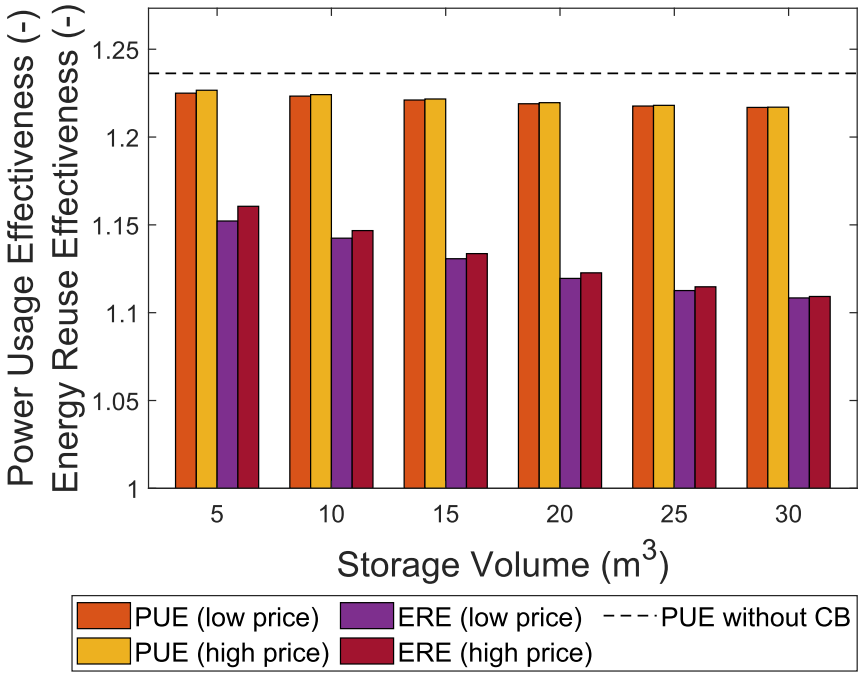

Figure 8.13 - DC power usage effectiveness and energy reuse effectiveness with the CB integration in the two scenarios with low and high energy price, and compared with the system configuration without the CB.

Moreover, the increase in storage capacity helps reduce the power needed by the cooling system,

particularly for the chiller, which consumes more energy due to its lower COP. This is further emphasized in Figure 8.14 through the UF. Furthermore, the overall efficiency of the integrated system benefits from the CB usage, regardless of the energy pricing scenario.

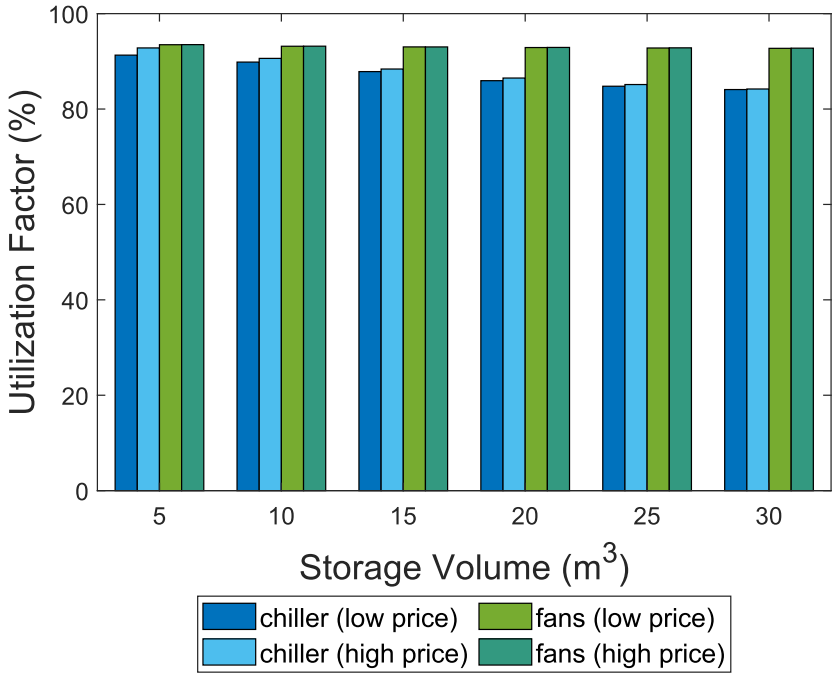

Figure 8.14 - Cooling system utilization factor in the two scenarios with low and high energy price.

8.8.5. ORC-only configuration performance

In the ORC-only configuration, the ORC is consistently required to operate under heavily off-design conditions due to the very low temperature of the heat source. Additionally, during the summer months, high ambient temperatures largely prevent the ORC from operating, particularly between June and September. Table 8.14 presents the ORC performance in the ORC-only setup, compared with its performance when integrated into the CB.

Table 8.14 - ORC performance comparison when integrated into the CB or working in ORC-only configuration.

	Low energy price scenario		**High energy price scenario**	
	ORC in CB	**ORC-only**	**ORC in CB**	**ORC-only**
Annual average efficiency (%)	7.05	1.53	7.16	1.53
Annual electrical energy (kWh)	7140	4366	6774	4366
Annual thermal energy (kWh)	101292	126512	94656	126512
Annual running hours (h)	1230	3971	1169	3971

The findings indicate that the ORC annual average efficiency drops significantly in the ORC-only configuration, primarily due to the suboptimal operating conditions. Although the ORC operates for more than three times as many hours in the ORC-only setup compared to when integrated into the CB, the much lower temperature of the heat source restricts the amount of recoverable thermal energy, resulting in only slightly higher annual thermal energy input. Moreover, the reduced efficiency leads to a lower electricity production compared to the CB configuration.

Figure 8.15 illustrates the revenues and expenses associated with the ORC-only setup. The revenues come from the electricity generated by the ORC, which helps meet the DC energy needs, and from the

reduction in cooling system load achieved by the ORC evaporator, which absorbs a portion of the waste heat. The expenses are tied to the ORC investment costs (shown as a levelized value in Figure 8.15). In both energy price scenarios, although to different extents, the annual expenses exceed the revenues. Consequently, the SPB and DPB exceed the ORC lifespan. Table 8.15 details the ORC annual economic gain, factoring in operating costs, for the two energy price scenarios. The DC PUE and ERE, as well as the cooling system UF, are identical in both scenarios since they are unaffected by energy prices.

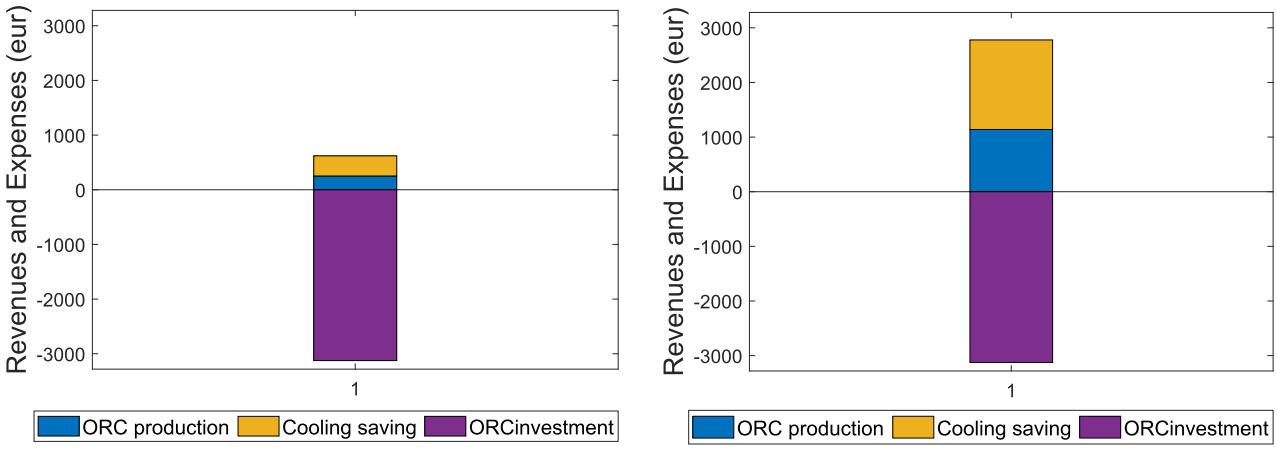

Figure 8.15 - Economic gain with the ORC-only configuration in (a) low and (b) high energy price scenarios.

Table 8.15 - ORC-only configuration overall performance.

	Low energy price scenario	High energy price scenario	Case without ORC
Yearly economic gain (€/year)	620	2778	-
SPB (years)	> 20	> 20	-
DPB (years)	> 20	> 20	-
PUE (-)	1.233		1.236
ERE (-)	1.160		-
UF chiller (-)	1		1
UF fans (-)	0.86		1

8.9. Conclusions

This study makes a valuable contribution to the existing research on utilizing CBs in waste heat recovery technologies for data centers applications. The work involves simulating the integration of a reversible HP/ORC CB within the cooling system of a DC, powered by electricity generated from a PV power plant.

The first phase of this research focuses on conducting a thermodynamic performance analysis to identify the most suitable working fluid for the application. R1233zd(E) emerges as the top-performing fluid in both the HP cycle and ORC, enabling the system to achieve a thermodynamic roundtrip efficiency of 43 % under typical operating conditions for the specified application.

In the second phase, the detailed semi-empirical off-design model of the reference CB test bench is employed, along with a rule-based control strategy, to manage the operations of the ORC and HP within the integrated system. When the PV panels generate excess electricity, this surplus can be stored in the CB through the HP, effectively reducing the load and energy consumption of the cooling system. When energy

demand exceeds the renewable energy supply, the stored thermal energy is utilized to activate the ORC. Furthermore, during winter, there is the option to sell the stored thermal energy to an external thermal user. A sensitivity analysis is performed, varying both the storage volume and energy price, to determine the optimal storage size and assess the impact of these variables on the integrated system performance. The findings suggest that integrating the CB can be economically viable in scenarios with high energy prices, even under the conservative assumption that the CB cannot absorb electricity from the grid while operating in HP mode. With a storage capacity of 10 m^3, the additional annual profit is estimated to be around € 7744, with a SPB period of approximately 10 years. More favourable results are observed when the system is not allowed to sell electricity to the grid. In this scenario, a PB period of less than 5 years is achieved, with an annual economic gain of nearly € 18500, using the same storage size in a high energy price scenario. Moreover, the conservative assumptions in the CB operation, along with the validation of the model on a non-optimized prototype, suggest there is potential to further improve both the system's performance and its economic benefits. The thermal integration allows for roundtrip efficiencies exceeding 30 %, even under very low operating temperatures. Since the HP helps meeting the cooling demand and a portion of the HP electric consumption is recovered by the ORC, the DC PUE and ERE indicators improve with the CB integration.

In the final part of the study, the CB integration is compared with a simpler alternative where the DC waste heat is continuously recovered using only an ORC system. In this setup, the integrated ORC is identical in size and characteristics to the ORC used in the CB configuration (the semi-empirical off-design model is the same of the reference CB test bench ORC). The comparison reveals a significant decline in both the ORC technical performance and the overall economic viability of the system. The ORC average annual efficiency drops to 1.5 % due to two main factors: i) the very low temperature of the heat source, which drastically reduces thermodynamic efficiency, and ii) the off-design operating conditions that the ORC must endure. Moreover, even though the ORC is designed to run continuously throughout the year, for over half of the year, the ambient temperature remains too high to maintain an adequate temperature difference between the heat source and the cold sink, preventing the ORC from functioning. These results underscore the advantages of using a more complex system like a CB, rather than a simple ORC, for DC waste heat recovery applications. However, it is also important to note that a CB functions as an energy storage system, making it a viable option only in scenarios where renewable electricity generation is available.

Looking ahead, future research will explore the possibility of purchasing electricity from the grid during periods of low prices to power the HP. This strategic approach aims to further enhance the system energy efficiency and financial performance. Additionally, the dynamic behaviour of the system during transitions between different CB operating modes will be included into the system modelling. This adjustment is essential for achieving a smoother and more responsive adaptation to changing conditions, thereby improving the overall reliability and performance of the integrated system.

9. Combined Heat and Power reversible Brayton PTES system

Summary. This chapter compares the thermodynamic performance of a closed Brayton-PTES in its base and recuperated configurations. The recuperated version, with an internal heat exchanger, achieves higher cycle temperatures (over 500 °C) and roundtrip efficiencies of 20-30 %, but the base configuration shows a higher COP (up to 3.5) due to a lower temperature lift. Cogeneration performance is also analysed, showing that at least 25 % of the stored heat should be supplied to a thermal user to be beneficial in terms of primary energy savings when compared to conventional separate production. At the highest temperature level, thermal production needs to exceed 60 % of the total energy to be competitive compared to conventional separate production. Investment cost analysis indicates that the base configuration is more sensitive to thermal energy price changes, while the recuperated version is influenced by both electricity and thermal price variations.

9.1. Brayton PTES: state of the art

In the last few years, Brayton-based CB technology has drawn remarkable attention in the PTES research field. Indeed, it is a promising alternative to Rankine-based CB systems, specifically for larger applications with higher temperature levels. The state of the art of Brayton-based PTES technology is described below.

Cascetta et al. [277] examined the performance of a novel PTES system integrated with a concentrated solar power plant, using a closed-loop Brayton-Joule cycle. The system, designed for 5 MW output and 6 hours of storage, uses argon as the working fluid and granite pebbles for storage. MATLAB-Simulink simulations were conducted to assess the system performance and thermocline profile during charging and discharging. A control strategy was developed to optimize operations based on grid demand, solar availability, and TES levels. While the integrated system is feasible for energy arbitrage, it achieves a lower exergy round-trip efficiency (54 %) compared to a standalone PTES system (60 %). Ghilardi et al. [278] examined the economic benefits of using a Brayton-based PTES system as a multi-energy device rather than just for electricity storage. The PTES system, which can discharge energy for heating, cooling, or electricity, is analysed in an urban district with both thermal and electrical needs. The research shows that using PTES's multi-energy functions can reduce operational costs by 5–10 % annually. However, relying only on direct heating leads to thermal losses of 6–10 %, which can be reduced to 3 % by adding direct cooling capabilities. Zhang et al. [279] introduced a new CCHP system using Brayton-cycle PTES. An unsteady model simulates the system performance for energy storage and delivery, revealing it to be effective for an office building in Norway. The system achieved COP values of 63.5 % for electrical storage, 137.9 % for CHP, and 188.1 % for full CCHP. It also showed 1.4 % increase in exergetic efficiency compared to traditional electricity storages, demonstrating strong potential for practical use. In a second study [280], the same Authors introduced a 10-MW PTES system with indirect TES and compares it to a direct TES system. The research focuses on reducing investment costs while maintaining technical and economic performance. The findings reveal that indirect PTES offers lower installation costs for electricity storage durations exceeding 6 hours, despite a slight reduction in roundtrip efficiency, suggesting it as a cost-effective option for long-duration electricity storage. In another study [281], the same Authors optimized and analysed the Joule-Brayton cycle-based PTES system. By exploring various charging-to-discharging duration ratios, the research optimizes key parameters like reservoir dimensions and discharge

compression ratios. The study finds that longer charging/discharging durations improve economic performance, achieving a round-trip efficiency of 70.97 % and a levelized cost of storage of 0.190 ± 0.043 $/kWh for a 60-MWh system. Wang et al. [282] explored the optimization of PTES systems, focusing on the effects of various factors and losses during charge, storage, and discharge processes. The findings reveal that higher maximum working temperatures and efficient turbomachines enhance both roundtrip efficiency and energy storage density. The study also emphasizes the importance of selecting an optimal pressure ratio to balance efficiency and storage density. The Joule-Brayton PTES system can achieve round-trip efficiencies up to 88.2 % at 1300 K with high turbomachine efficiency. Even with typical component losses, a round-trip efficiency of 59 % and a storage density of 60 kWh/m^3 are attainable. The same Authors, in a later work [283], introduced a novel PTES system that incorporates a liquid piston to enhance performance. The liquid piston improves cold energy quality in the cold reservoir and maximizes heat release from the hot reservoir. A mathematical model was developed to analyse the system dynamic thermodynamic performance. Results indicate that the system achieves a round-trip efficiency of 58.97 % and an energy storage density of 170.88 kWh/m^3, showing improvements compared to conventional PTES systems.

Yang et al. [284] investigated how a PTES system can adjust its net power output to match varying load demands, making it suitable for large-scale energy storage. The researchers developed a dynamic model for a 5 MW PTES system, incorporating off-design models for turbomachinery and heat exchangers. They simulated disturbances in user-side load and analysed the system's response. An inventory control strategy for the working fluid was introduced to regulate power output. Using a traditional PI controller, the system effectively responded to load changes, demonstrating its ability to adapt its power output to meet demand variations. In another work [285], the same Authors analysed the effects of power input fluctuations: due to thermal inertia, the temperature response lagged behind the power changes. An inventory control strategy was used to stabilize the thermal storage temperature, minimizing energy losses. Shi et al. [286] addressed the need for effective load variation methods in PTES systems, which are essential for stabilizing grid fluctuations. Five innovative variable load strategies for a closed Brayton cycle PTES system with liquid-phase storage were proposed and simulated. The findings reveal that rotor speed fluctuation rates and load regulation ranges vary across these methods. Modes with smaller rotor speed fluctuations offer smaller load regulation ranges, while those with larger fluctuations provide broader load regulation. The study suggests selecting load variation modes based on the desired balance between rotor stability and load regulation.

Belik's study [287] examined the integration of P2H into Brayton cycle-based PTES systems to improve cost efficiency and flexibility. While P2H integration reduces component size and capital costs by up to 23 %, it also leads to a loss in roundtrip efficiency of up to 5 %. The research provides a thermodynamic and economic analysis, offering design solutions for the novel P2H component that balance efficiency and cost in utility-scale electricity storage. McTigue et al. [288] developed a techno-economic model for PTES systems using recuperated Joule-Brayton cycles and two-tank liquid storage. The model focuses on optimizing heat exchangers and evaluating economic metrics like capital costs and levelized cost of storage. The study finds that heat exchangers with up to 0.95 effectiveness are cost-effective, and using high-temperature chloride salts slightly improves efficiency but may not justify the extra cost. Optimal designs achieve round-trip efficiencies of 59-72 % and storage costs competitive with lithium-ion batteries for durations over 6 hours.

Zhao et al. [289] focused on optimizing Joule-Brayton PTES systems using solid thermal reservoirs and liquid thermal storages. Thermo-economic models and parametric analyses show that higher charging temperatures improve both efficiency and cost-effectiveness. Helium is identified as the best working fluid, with magnetite and a mix of Hitec XL, Therminol 66, and Butane being ideal storage materials for solid thermal reservoirs and liquid thermal stores systems, respectively. PTES systems with solid thermal reservoirs are found to be more cost-effective than those with liquid thermal stores, achieving a roundtrip

efficiency of 71.8 % at a lower purchase cost. Shamsi et al. [290] explored a TI-PTES system using supercritical CO_2 (sCO_2) for both heat pumps and power cycles. The use of sCO_2 offers benefits like compact design and a smaller footprint. The research evaluates the thermo-economic performance of sCO_2-based TI-PTES, considering the integration of industrial and renewable heat sources and utilizing available thermal energy storage options through a mapping approach.

9.2. Contribution

In the light of the above state of the art, this study, as a final chapter of the present thesis, aims to evaluate the thermodynamic efficiency of a closed Brayton cycle-based PTES system utilizing sCO_2, a fluid identified in prior research as highly effective. A detailed parametric analysis was conducted using a commercial-based software, THERMOFLEX [232], to assess the potential of the investigated energy conversion and storage system. The analysis not only explores the system potential as an energy storage solution but also examines its role in enhancing flexibility in aligning thermal production with demand. In the performance assessment, first, the thermodynamic performance results are discussed during the charging and discharging phases, and second, the system cogeneration potentialities are illustrated when employed in a CHP arrangement to meet both thermal and electric needs. Finally, an economic evaluation is accomplished to determine the maximum allowable specific investment cost that ensures a reasonable return on investment.

9.3. System configuration layout

This study explores the performance of a reversible closed-cycle sCO_2 Brayton-based PTES system when integrated with a renewable energy source. The system is designed to operate in a CHP setup, producing both thermal and electric energy based on the demand. As illustrated in Figure 9.1, surplus electricity from the renewable source is converted into heat using an inverse Brayton cycle. This stored heat can either be delivered to a thermal user or converted back into electricity if the RES production falls in deficit compared to the demand. The Brayton-based PTES system comprises a TES, an inverse Brayton (BI) cycle, and a direct Brayton (BD) cycle.

Specifically, when RES production exceeds electricity demand, the surplus electric power is sent in input to the system operating the cycle in inverse mode (BI cycle), storing thermal energy in a hot reservoir (charging phase). When electricity demand overtakes RES output, the system switches to the direct cycle mode (BD cycle), releasing thermal energy from the TES to generate additional electrical output (discharging phase). Operating the BI cycle with a smaller temperature difference compared to the BD cycle can enhance the indirect cycle performance without compromising the direct cycle efficiency. The availability of a cold source for the BI cycle at a higher temperature than the cold sink of the BD cycle, as well as free waste heat that is not otherwise usable, could make this option viable. When the system total production is not enough to cover the demand, the deficit is supplied by the grid. Additionally, high-temperature heat in the TES can partially meet the demand of a thermal user (thermal discharge - TD), operating as a CHP system by storing energy to address both electrical and thermal needs.

Thus, the system can operate in either charging or discharging modes on the electrical side (BI and BD cycles respectively), while TD can occur independently of the electrical mode. Even when the Brayton cycle is inactive, the CB can still function in pure TD mode. This study considers two Brayton-based PTES configurations: a basic Brayton cycle (B-PTES) and a recuperated Brayton cycle (RECB-PTES).

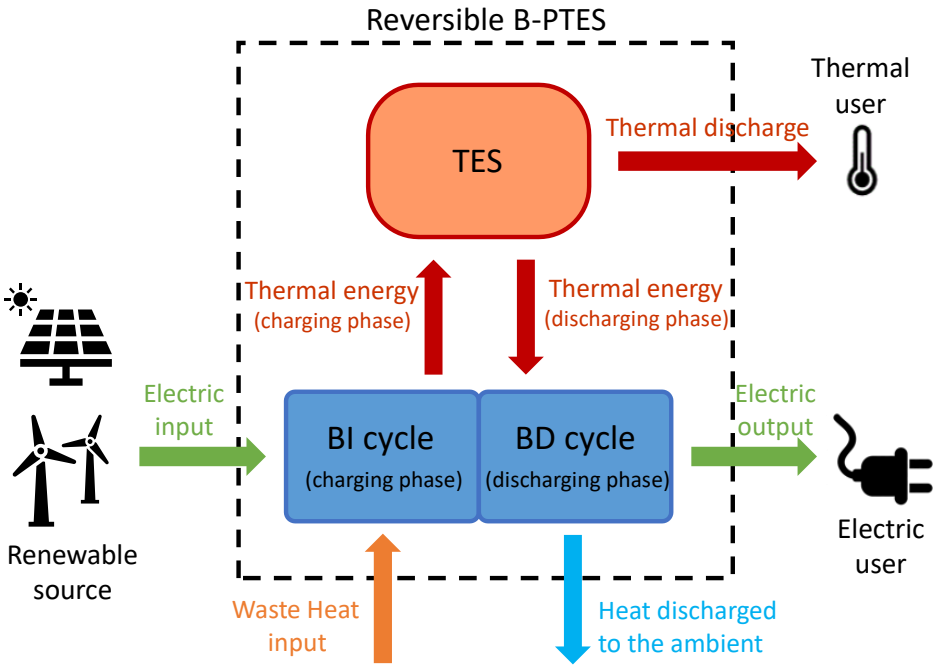

Figure 9.1 – Conceptual scheme of the Brayton-based PTES system.

9.3.1. B-PTES configuration

Figure 9.2 depicts the components and flow streams of the B-PTES system. During the charging phase (Figure 9.2(a)), the working fluid is first preheated at low pressure by a cold source in the cold heat exchanger (Cold HX). As suggested in [63], the exploitation of available low-temperature waste heat, which would otherwise go unused (e.g., residual low-enthalpy heat from many industrial processes), is preferable for enhancing the indirect cycle efficiency. Indeed, this approach reduces the temperature lift in the BI cycle, with a consequent reduction of the required compression work. Next, the working fluid is compressed in the Compressor and then transfers high-temperature thermal energy to the TES via the Hot HX. Finally, in the last stage, the fluid is expanded back to the low-pressure level in the Turbine, recovering part of the compression work.

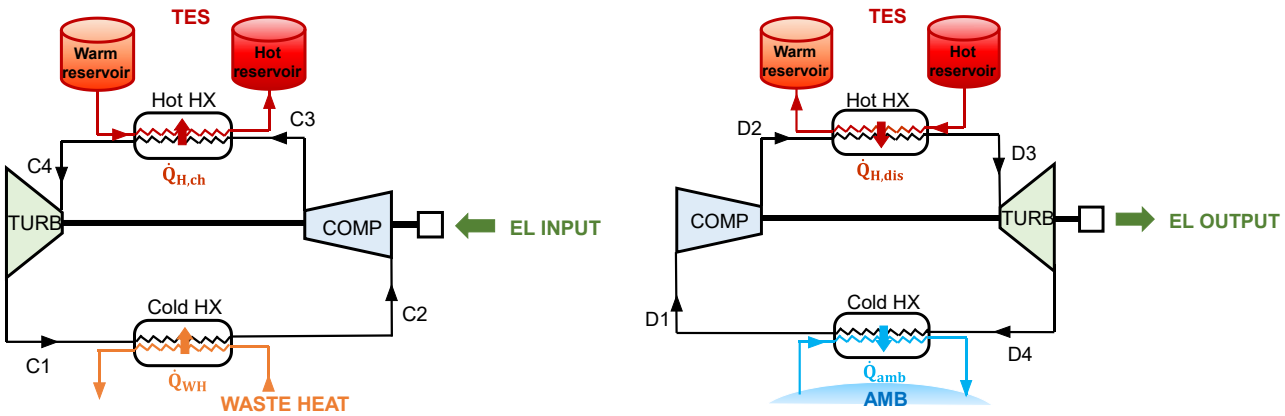

Figure 9.2 - B-PTES layout in (a) charging mode - BI cycle - and (b) discharging mode - BD cycle.

In the discharging phase (Figure 9.2(b)), the cycle operates in reverse mode. The working fluid is compressed in the Compressor, heated by the hot source in the Hot HX, and then expanded in the Turbine

to produce mechanical power. Eventually, the fluid is cooled in the Cold HX, completing the closed BD cycle.

The TES comprises two reservoirs (Warm and Hot) where a heat transfer fluid (HTF) facilitates heat exchange and storage.

Figure 9.3 presents qualitative temperature-entropy diagrams of the BI and BD cycles. The fluid state at key cycle points is indicated, alongside variations in Hot and Cold source temperatures for comparison purposes. To maintain general applicability, no specific numerical values for temperatures, pressures, or other thermodynamic properties are provided.

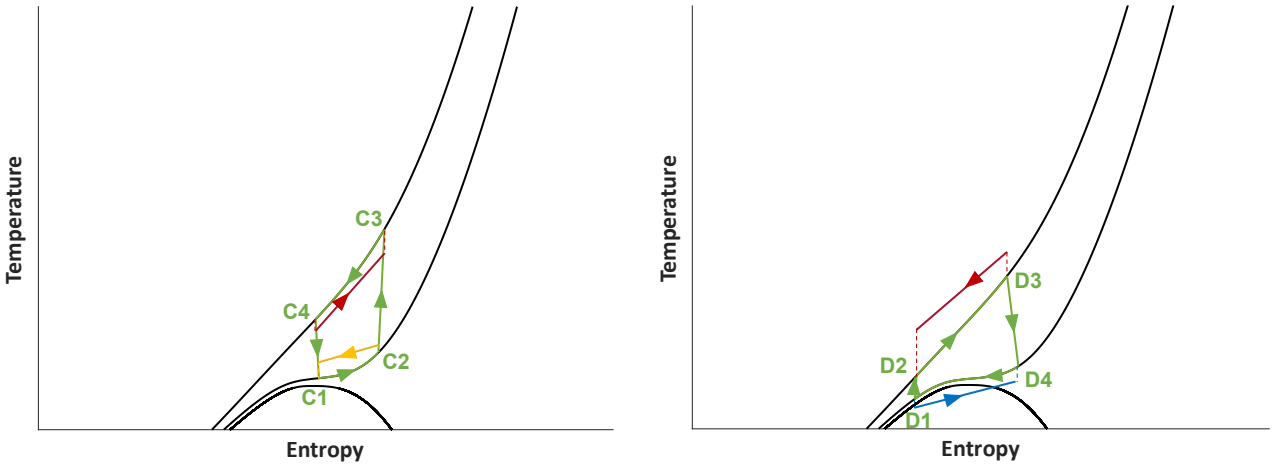

Figure 9.3 - B-PTES qualitative T-s diagram in (a) charging mode - BI cycle - and (b) discharging mode - BD cycle.

9.3.2. RECB-PTES configuration

In the RECB-PTES configuration, a Recuperator (Rec HX) is added, as shown in Figure 9.4. In the BI cycle (Figure 9.4(a)), the Recuperator increases the temperature at the Compressor inlet (point RC3) by further heating the working fluid exiting the Cold HX (RC2) with the fluid exiting the Hot HX (RC5). In the BD cycle (Figure 9.4(b)), the Recuperator preheats the working fluid at the Hot HX inlet (RD3) using the residual enthalpy of the fluid exiting the Turbine (RD5), which improves the BD cycle conversion efficiency.

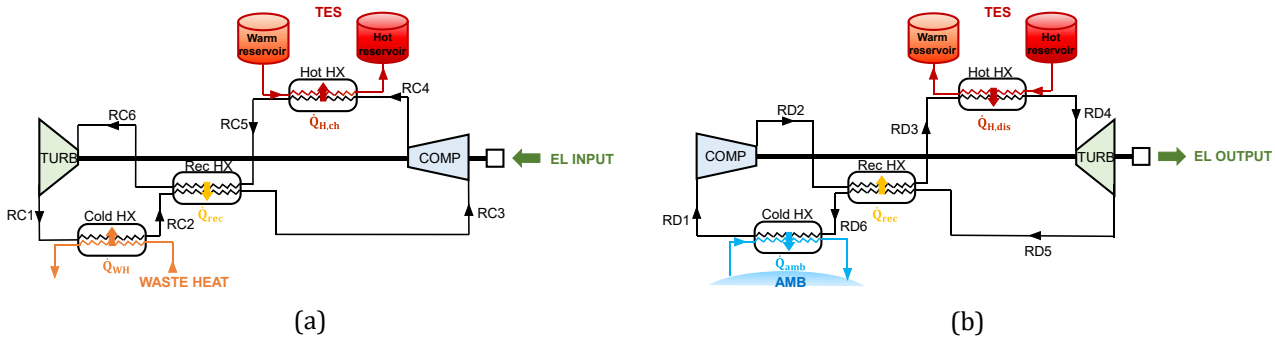

Figure 9.4 – RECB-PTES layout in (a) charging mode - BI cycle - and (b) discharging mode - BD cycle.

Figure 9.5 presents qualitative temperature-entropy diagrams of the BI and BD cycles. Similarly to the B-PTES temperature-entropy diagrams, also for this configuration, no specific numerical values for thermodynamic properties are given to keep the analysis broadly applicable.

Supercritical CO_2 is selected as the working fluid for this analysis due to a balance of performance, availability, and cost considerations. With a critical temperature of approximately 31 °C, it can utilize low-grade cold sources and sinks in the BI and BD cycles, respectively. However, its critical pressure (73.8 bar)

necessitates relatively high pressures to keep the cycle in the supercritical regime, thereby influencing the cycle pressure ratio to maintain maximum pressure within current technical limits. This limitation impacts the cycle maximum temperature, especially in the basic configuration (Figure 9.3). The inclusion of the Recuperator increases the separation between expansion and compression processes (Figure 9.5), allowing for higher maximum cycle temperatures and TES temperature levels.

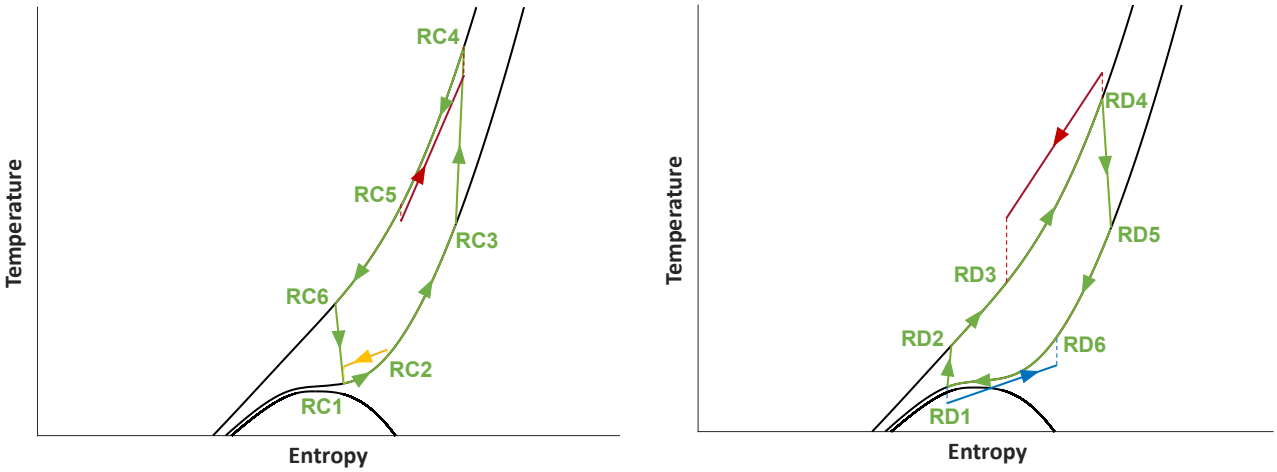

Figure 9.5 - RECB-PTES qualitative T-s diagram in (a) charging mode - BI cycle - and (b) discharging mode - BD cycle.

9.4. The THERMOFLEX model

The power plant under analysis is modelled using the commercial-based software THERMOFLEX [232], which facilitates the thermodynamic simulation of complex energy systems by assembling components from a built-in library through a lumped-parameters approach. This tool utilizes Refprop thermodynamic database [132] to evaluate the properties of CO_2 and secondary fluids.

A sensitivity analysis is conducted to assess the thermodynamic performance variations of the B-PTES and RECB-PTES system configurations under different design parameters, focusing primarily on the temperature levels of heat sources and the pressure ratio of the turbomachines.

9.4.1. Boundary conditions and system specifics

Regarding the hot source temperature, the inlet temperature of the HTF at the Hot HX (from the TES warm reservoir) is set as an input, with the outlet temperature calculated accordingly. In the base configuration, three HTF inlet temperature levels are considered: 70 °C, 85 °C, and 100 °C. These TES temperature values align with medium/low-grade heat demands and are compatible with the maximum temperature achieved at the compressor outlet (C3 point) during the charging phase of the B-PTES (not exceeding 200 °C within the pressure range studied). In the RECB-PTES configuration, the HTF inlet temperature is varied to 150 °C, 250 °C, and 350 °C, allowing the cycle's maximum temperature (RC4 point) to reach up to 550 °C due to the recuperator. These TES temperature levels are suitable for industrial medium/high-grade heat users. HTFs were selected based on their temperature limits and compatibility with the cycle's operating temperatures:

- Duratherm 630 (maximum operating temperature of 329 °C) is chosen for the base configuration, where temperatures do not exceed 200 °C.

- Helisol 5A (maximum operating temperature of 450 °C) is used in the recuperated configuration for the first two temperature levels (150 °C and 250 °C).
- Nitrate salt (operating between 260 °C and 593 °C) is selected for the highest temperature level.

Water is used as the external fluid for the cold side, with inlet temperatures of 60 °C during charging phase and 20 °C during discharging phase. In charging mode, low-grade heat is assumed to be recovered from an external waste heat source, serving as a free energy source. In discharging mode, water at near-ambient conditions is used as the cold sink. The decision to differentiate the low-temperature levels between the BI and BD cycles is based on the justification that the storage system is valuable only when applied to existing technologies to reduce waste energy. Thermal integration enables the recovery of waste heat, which would otherwise be lost to the environment, and enhances charging phase performance by reducing the temperature lift required by the compressor, thus lowering electrical consumption.

All assumptions and boundary conditions for the hot and cold sources/sinks are detailed in Table 9.1.

Table 9.1 - Hypotheses and boundary conditions concerning the hot and cold sides.

Hot and Cold sources/sinks	**B-PTES**		**RECB-PTES**	
	charging	**discharging**	**charging**	**discharging**
Hot sink/source fluid	Duraterm630		Helisol5A / Nitrate Salt (60% $NaNO_3$ - 40% KNO_3)	
Inlet temperature (°C)	70–85–100	-	120–250–350	-
Outlet temperature (°C)	-	70–85–100	-	120–250–350
Cold source/sink fluid	Water		Water	
Mass flow rate (kg/s)	1.5		1.5	
Inlet temperature (°C)	60	20	60	20

Concerning the reversible Brayton cycles operating pressure levels, a parametric analysis is conducted with the following assumptions:

- The low-pressure level is set at 80 bar (slightly above the CO_2 critical pressure) to maintain supercritical conditions throughout the cycle in both charging and discharging phases.
- The high-pressure level is varied to identify the optimal pressure ratio value.
- The maximum pressure for both the BI and BD cycles is limited at 350 bar to meet current technological limitations. Consequently, the pressure ratio value is varied systematically from 1.5 to 4.25, with increments of 0.25.
- For simplicity, the pressure ratio values for the BI and BD cycles are assumed to be equal in the same thermodynamic design.

The polytropic efficiencies of the turbine and compressor are kept constant at 85 %, consistent with literature values [80], [291]. The effectiveness, minimum pinch point, normalized heat loss, and pressure drop values for all heat exchangers are set equally for both configurations and are summarized in Table 9.2, together with the system main specifics.

Regarding the economic analysis, the maximum investment cost was calculated for a 10-year return period, assuming a discount rate of 0.06 [262]. Cash flows were based on 1500 equivalent working hours of the RES [292], with an average electricity price of 0.30 €/kWh [275] and an average thermal energy price of 0.18 €/kWh [274], reflecting the 2022 averages in several European countries. The maximum investment cost was estimated by varying the electricity and thermal energy prices, with the former ranging from 0.05 to 0.40 €/kWh and the latter from 0.03 to 0.24 €/kWh. The assumptions for the

economic analysis are summarized in Table 9.3.

Table 9.2 - B-PTES and RECB-PTES main specifics.

Operating fluid	Carbon Dioxide
Mass flow rate (kg/s)	1
Compressor inlet pressure (bar)	80
Maximum pressure limit (bar)	350
Pressure ratio (-)	from 1.5 to 4.25 with a step of 0.25
Compressor polytropic efficiency (%)	85
Turbine polytropic efficiency (%)	85
Mechanical efficiency (%)	99
Auxiliary efficiency (%)	99
Generator / Motor electric efficiency (%)	90
Heat exchangers thermal effectiveness (%)	90
Heat exchangers minimum pinch point (°C)	5
Heat exchangers normalized heat loss (%)	1
Pressure drops across heat exchangers (%)	2

Table 9.3 - Hypothesis and boundary conditions concerning the economic analysis.

Time for the return of the investment (years)	10
Discount rate (%)	6
RES equivalent working hours (h)	1500
Reference electricity price (€/kWh)	0.30
Reference thermal energy price (€/kWh)	0.18
Electricity price variation range (€/kWh)	from 0.05 to 0.40 with a step of 0.05
Thermal energy price variation range (€/kWh)	from 0.03 to 0.24 with a step of 0.03

9.5. Performance assessment

This section outlines and analyses the comparative results between the B-PTES and RECB-PTES systems. First, the thermodynamic performance during both the charging and discharging phases is presented, followed by an evaluation of the overall system thermodynamic efficiency. A comparison with the ideal system is also carried out. The achievable temperature in the hot reservoir for each system is discussed to provide insight into the temperature level at which thermal energy is delivered to the user. Next, thermal and electrical output in the charging and discharging phases are compared for both configurations. The cogeneration capabilities of the integrated system are then assessed and analysed. Finally, the maximum investment cost required for a 10-year return on investment is calculated, considering variations in electricity and thermal energy prices.

9.5.1. Thermodynamic performance

A systematic analysis to assess the operation of the Brayton PTES system and compare both configurations requires the definition of key performance indicators. They are introduced, distinguishing among ones referring to the charging phase, discharging phase, and overall system performance, as detailed below.

For the charging phase (BI cycle), the performance indicators include:

- The amount of thermal energy output per unit mass flow rate of the working fluid (QH_{ch}) stored in the hot reservoir. This represents the thermal energy produced during the charging phase.
- The net specific electric work input ($W_{net,ch}$) for the inverse cycle, calculated as it follows:

$$W_{net,ch} = \frac{(W_{comp} - W_{turb})}{\eta_{aux}} \tag{9-1}$$

where W_{turb} is the turbine specific output work, W_{comp} is the compressor specific input work, and η_{aux} represents auxiliary plant efficiency, accounting for losses in electric and mechanical systems. This measures the renewable electric energy stored in the CB in case of surplus.

- The coefficient of performance (COP) assesses the thermodynamic efficiency of the inverse cycle and is calculated as:

$$COP = \frac{QH_{ch}}{W_{net,ch}} \tag{9-2}$$

where $W_{net,ch}$ is the net specific electricity consumption and QH_{ch} is the system thermal output during charging. If free waste heat is available above ambient temperature, it lowers the compressor's temperature lift, reducing $W_{net,ch}$ and improving COP.

The COP values are compared with the ideal coefficient of performance (COP_{id}), calculated as:

$$COP_{id} = \frac{TH_{eq}}{TC_{eq} - TC_{eq}} \tag{9-3}$$

where TH_{eq} and TC_{eq} represent the working fluid's average temperatures during heat release and absorption phases.

For the discharging phase (BD cycle), performance indicators include:

- The thermal energy delivered from the hot reservoir into the direct cycle per unit mass flow rate (QH_{dis}), representing the thermal energy stored during charging phase that is reconverted into electricity.
- The net specific electrical work output ($W_{net,dis}$) during the direct cycle, calculated as it follows:

$$W_{net,dis} = (W_{turb} - W_{comp}) \cdot \eta_{aux} \tag{9-4}$$

This reflects the system electric output during the discharging phase.

- The net electrical efficiency (η_{dis}) of the direct cycle, calculated as:

$$\eta_{dis} = \frac{W_{net,dis}}{QH_{dis}} \tag{9-5}$$

η_{dis} can be compared to Carnot efficiency (η_{Carnot}), defined as:

$$\eta_{Carnot} = 1 - \frac{TC_{eq}}{TH_{eq}} \tag{9-6}$$

To evaluate the overall storage and return process performance, the following indicators are considered:

- The roundtrip efficiency (η_{rt}), which measures the amount of electric energy reconverted after the storage process with reference to the electric input, can be calculated as a function of COP, η_{dis}, and the TES efficiency (η_{TES}), which accounts for energy losses during storage:

$$\eta_{rt} = \frac{W_{net,dis}}{W_{net,ch}} = COP \cdot \eta_{dis} \cdot \eta_{TES} \tag{9-7}$$

  A constant TES efficiency of 99 % is assumed for simplicity. The ideal roundtrip efficiency ($\eta_{rt,id}$) is also calculated for comparison using:

$$\eta_{rt,id} = COP_{id} \cdot \eta_{Carnot} \tag{9-8}$$

- The time ratio (Δt_{ratio}), defined as the ratio of discharging time (Δt_{dis}) to charging time (Δt_{ch}), is expressed as:

$$\Delta t_{ratio} = \frac{\Delta t_{dis}}{\Delta t_{ch}} = \frac{QH_{ch}}{QH_{dis}} \tag{9-9}$$

  This ratio assumes that the thermal energy stored during charging equals the energy released during discharging.

The thermodynamic analysis is carried out for different values of pressure ratio and at different levels of the storage temperature (three for the base configuration and three for the recuperated one). Figure 9.6 displays the inverse cycle output thermal energy (QH_{ch}) and the thermal energy delivered from the hot reservoir to the direct cycle (QH_{dis}).

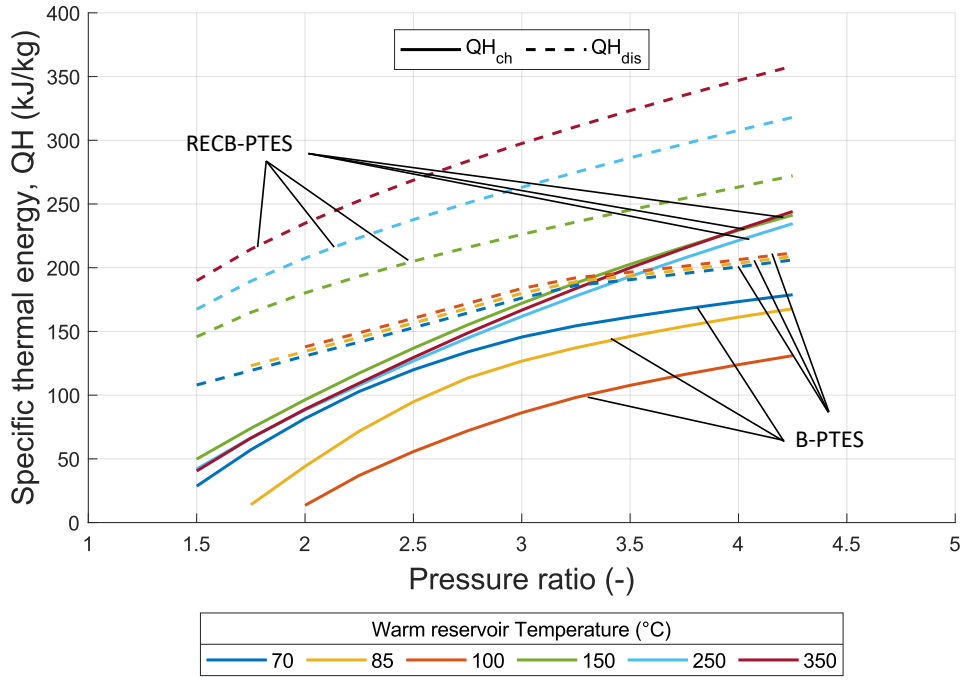

Figure 9.6 - Specific thermal energy produced in charging mode (QH_{ch}) and absorbed in discharging mode (QH_{dis}), versus pressure ratio.

Figure 9.7 shows the input net specific electric work ($W_{net,ch}$), which is the amount of renewable electricity in surplus, during the charging phase and the output net specific electric work ($W_{net,dis}$) during discharging phase. The results reveal that QH_{ch} is consistently lower than QH_{dis}. This means that with the

same unitary working fluid mass flow rate, the time necessary to charge the storage is always higher than the time needed to completely discharge it. This aspect is quantified by the time ratio, shown in Figure 9.8.

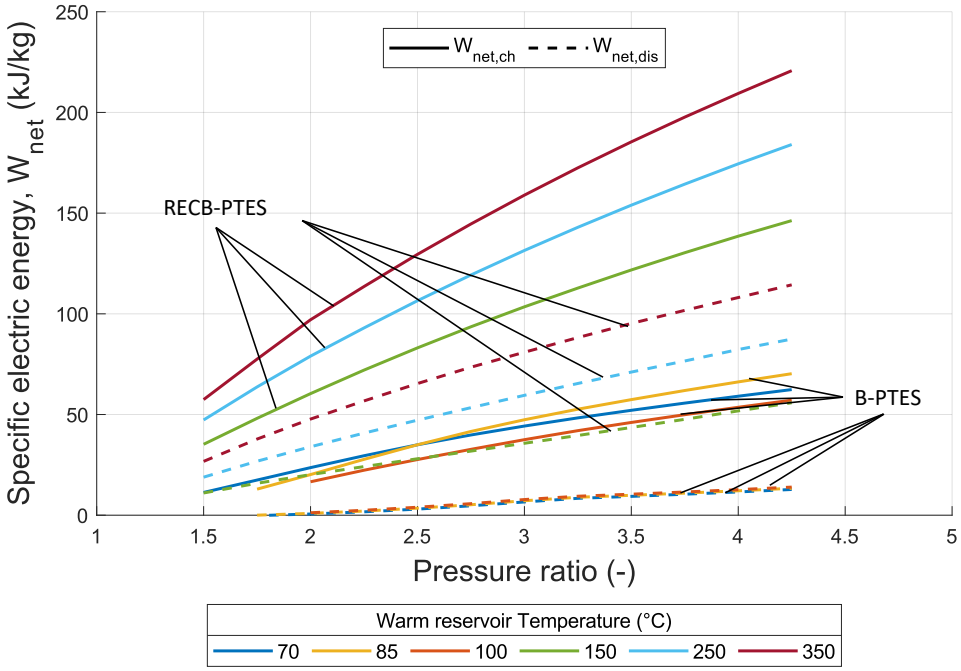

Figure 9.7 - Specific electric energy absorbed in charging mode ($W_{net,ch}$) and produced in discharging mode ($W_{net,dis}$), versus pressure ratio.

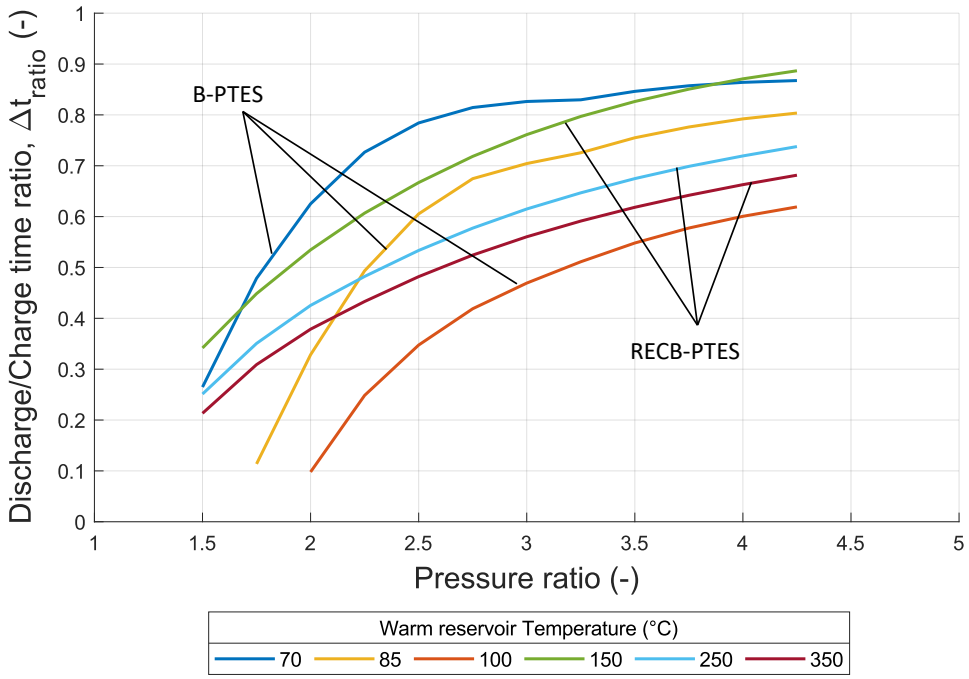

Figure 9.8 - Discharge/charge time ratio versus pressure ratio, for the six levels of warm reservoir temperature.

The Δt_{ratio} increases with pressure ratio and decreases with the storage temperature for each configuration. Indeed, it rises above 0.8 for the lowest temperature levels (Figure 9.9) in both configurations (70 °C and 150 °C, respectively). These cases feature the highest COP values (see Figure 9.10), with the maximum QH_{ch} in both B-PTES and RECB-PTES and the lowest QH_{dis} during discharging. Thus, Figure 9.8 and Figure 9.9 indicate that the time ratio decreases with increasing warm reservoir

temperature and rises with increasing pressure ratio. This variation is more pronounced in the B-PTES configuration than in the RECB-PTES, especially at low pressure ratio values.

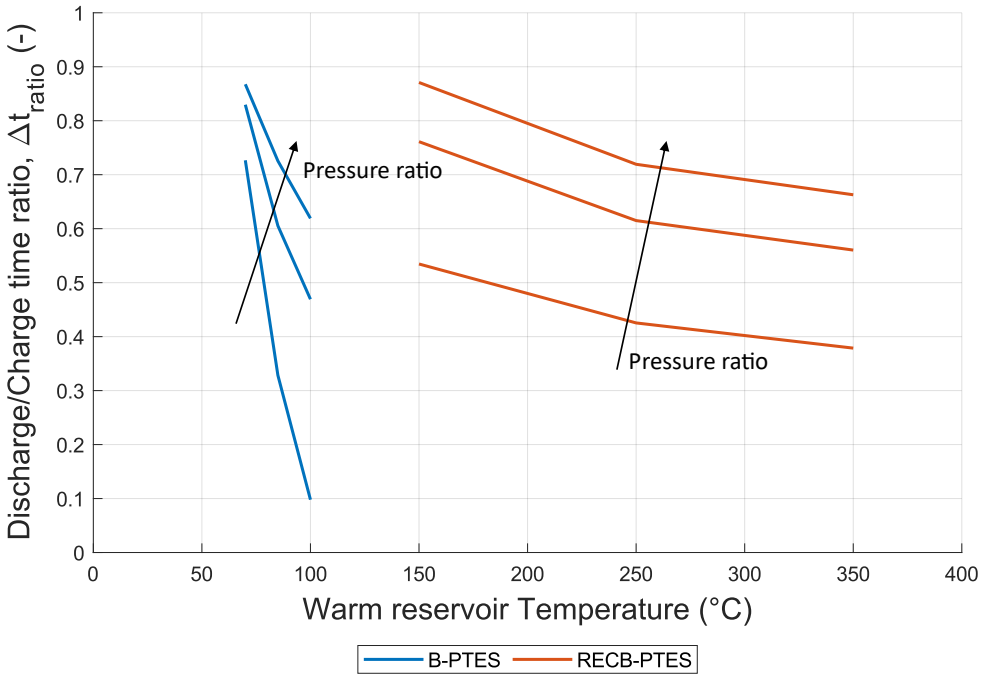

Figure 9.9 - Discharge/charge time ratio versus the warm reservoir temperature, for different values of the pressure ratio, for the two analyzed configurations.

In Figure 9.10, the COP of the BI cycle, the discharging efficiency of the BD cycle, and the roundtrip efficiency are compared between the B-PTES (Figure 9.10(a)) and RECB-PTES (Figure 9.10(b)) configurations. The COP is higher in the base configuration because the temperature difference between the cold source and hot sink is significantly smaller compared to the recuperated setup. However, the lower maximum temperature in the base case negatively impacts the discharging efficiency, as it remains limited to relatively low levels. Indeed, η_{dis} reaches more acceptable values in the RECB-PTES.

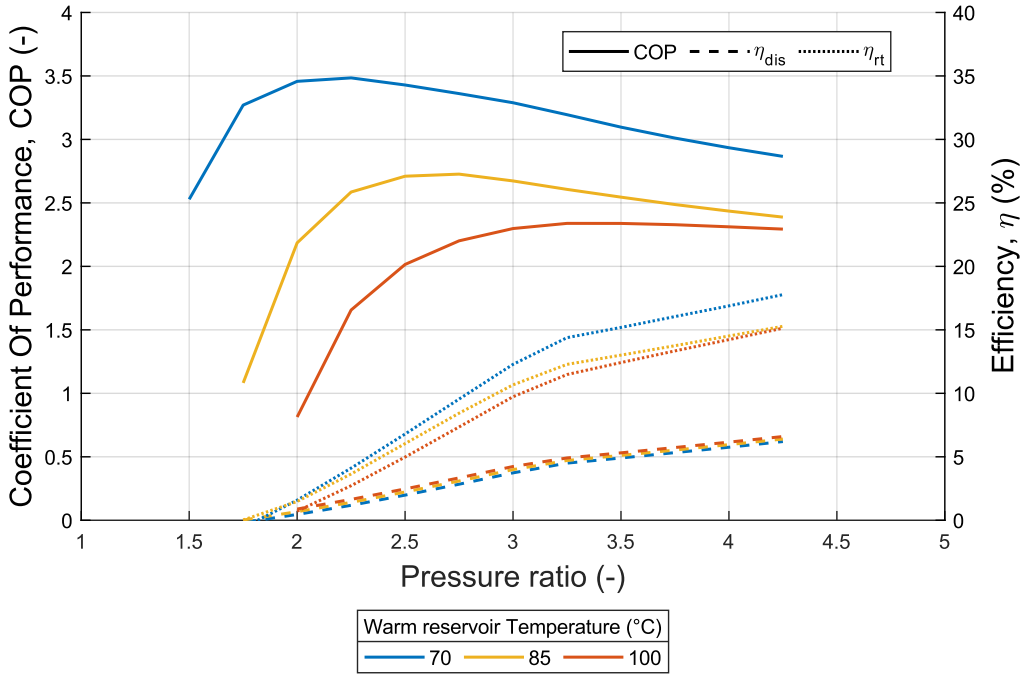

(a)

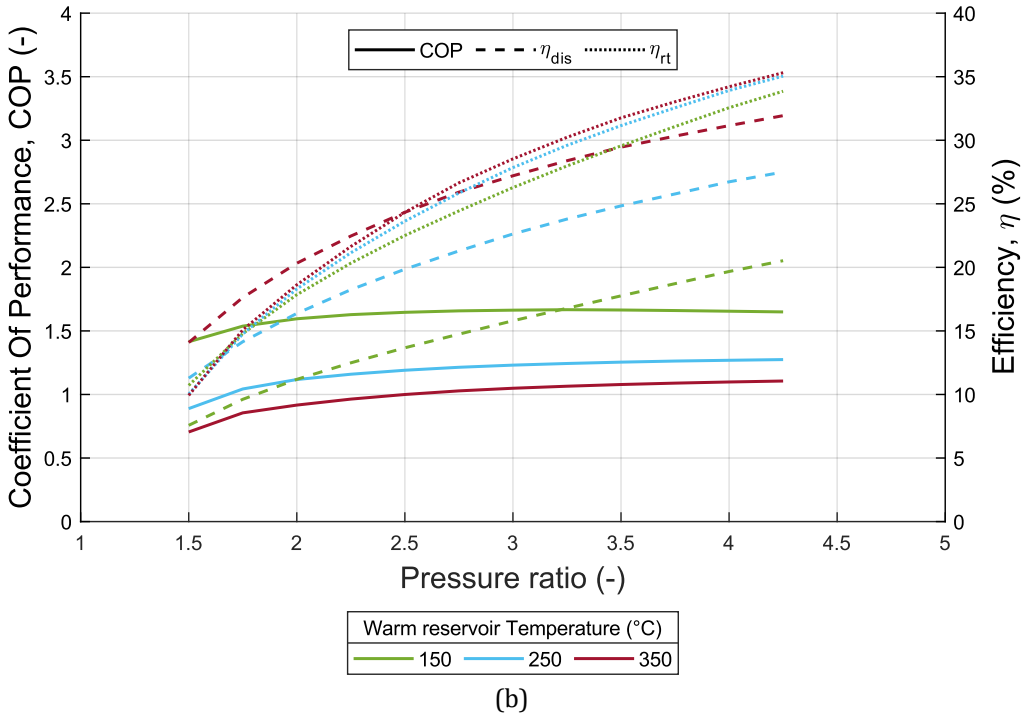

(b)

Figure 9.10 - Coefficient of performance (COP), net electric efficiency (η_{dis}), roundtrip efficiency (η_{rt}) in (a) B-PTES and (b) RECB-PTES configurations, versus pressure ratio.

Additionally, since the temperature ranges explored in the B-PTES are quite similar, η_{dis} curves almost overlap. The cycle pressure ratio has a greater effect on the COP in the base configuration, with optimal values found between 2.25 and 3.25 (depending on the temperature level), whereas in the recuperated setup, charging performance remains relatively stable. As expected, η_{dis} increases with the pressure ratio in both the simple and recuperated cycles. Furthermore, the roundtrip efficiency is higher in the RECB-PTES configuration, where it reaches a maximum of around 35 % at the highest pressure ratio. In comparison, the maximum η_{rt} in the B-PTES configuration is below 20 %. η_{rt} is more influenced by η_{dis} than by COP, especially in the B-PTES configuration, where COP values align with HTHP literature [47].

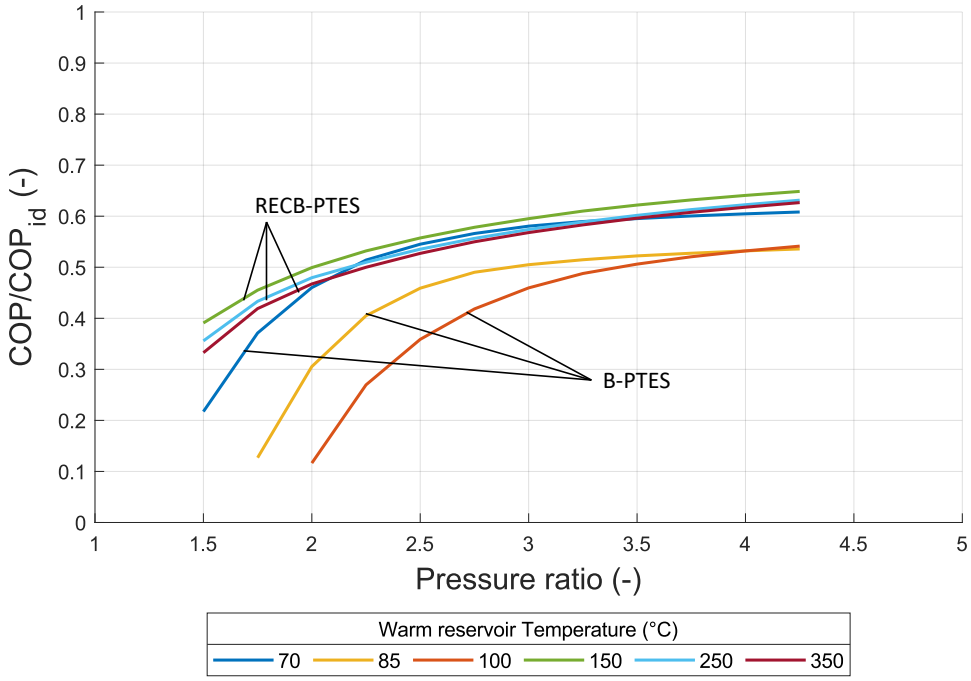

Figure 9.11 - Performance comparison: ratio between the COP and the ideal COP, versus pressure ratio.

Figure 9.11 demonstrates that in most cases, the COP value is at least 50 % of the ideal COP, except for cases with very low pressure ratio values. In contrast, Figure 9.12 reveals that the discharging efficiency in the base configuration is significantly lower than Carnot efficiency, never reaching 40 % of η_{Carnot}. Moreover, in the B-PTES configuration, even the ideal roundtrip efficiency (Figure 9.13) fails to reach high values, particularly at low pressure ratio values. In all scenarios, $\eta_{rt,id}$ remains below 100 %, although other studies [66] have shown that thermal integration can exceed this value. This discrepancy is likely due to the very low temperature (< 60 °C) of the waste heat provided to the inverse cycle.

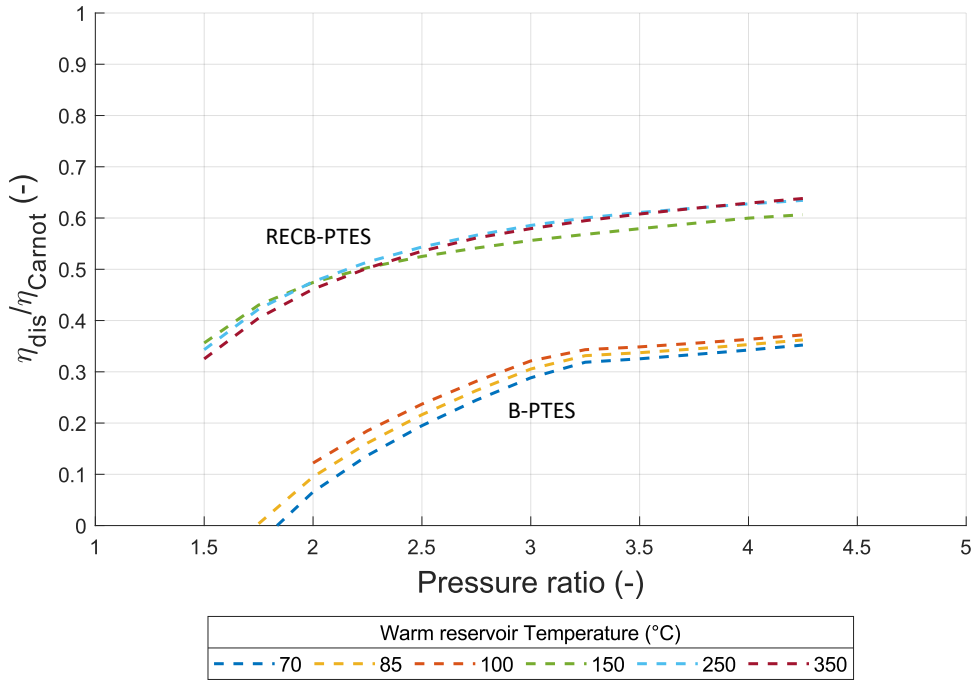

Figure 9.12 - Performance comparison: ratio between the discharging efficiency and the Carnot efficiency, versus pressure ratio.

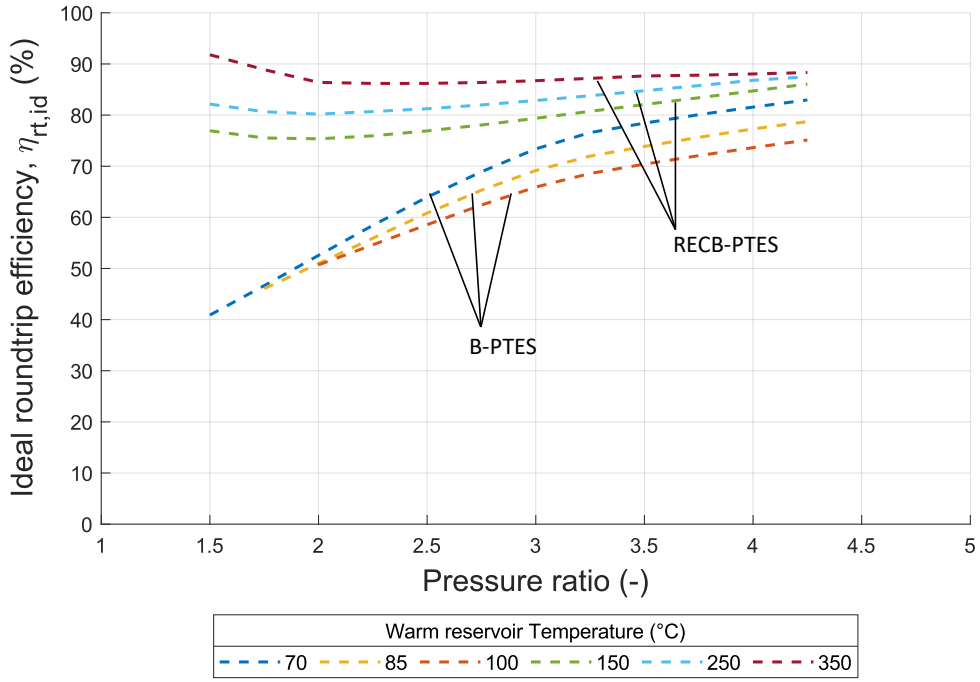

Figure 9.13 - Ideal roundtrip efficiency versus pressure ratio.

Figure 9.14 illustrates the TES hot reservoir temperatures achievable across the six temperature levels considered (three for B-PTES and three for RECB-PTES) plotted against the pressure ratio. In the base configuration, the maximum temperature of the heat stored in the hot reservoir remains below 200 °C and appears to depend almost exclusively on the pressure ratio rather than the temperature level of the heat sink (warm reservoir). Conversely, in the recuperated configuration, the temperature of the heat stored during the charging phase is highly influenced by the HTF temperature in the warm reservoir, especially at the onset of heat transfer process. In the RECB-PTES configuration, the maximum temperature achieved exceeds 550 °C.

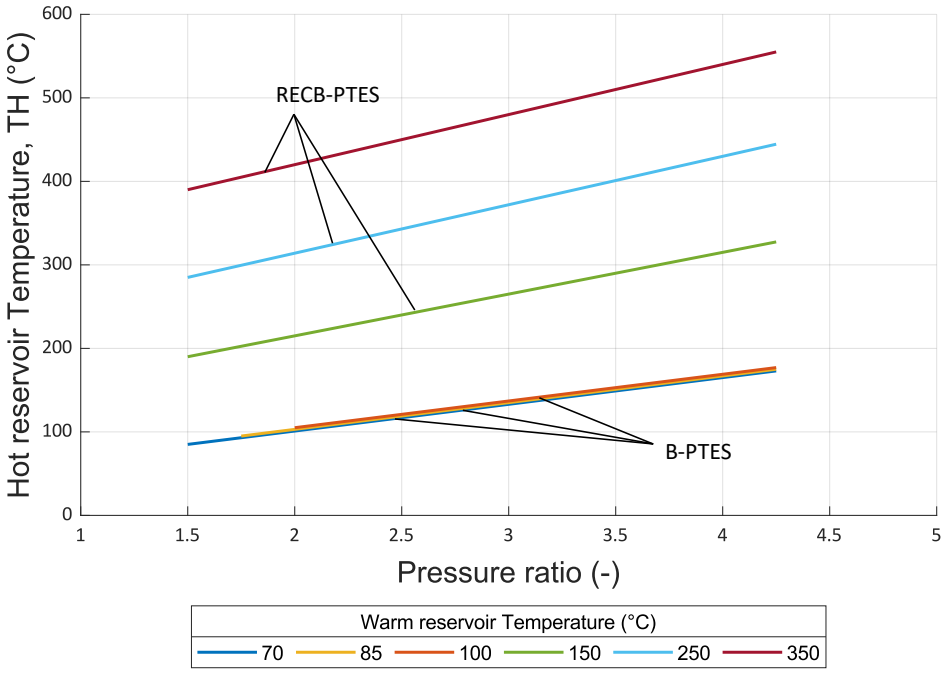

Figure 9.14 - Hot reservoir temperature obtainable for each analyzed level of warm reservoir temperature, in both the configurations, versus the pressure ratio.

9.5.2. Cogeneration performance evaluation

The system performance is also analysed for CHP applications, where stored heat may be used for thermal demand or converted back into electricity. Indeed, a portion of the thermal energy stored in the TES can be diverted to a thermal user rather than being converted back into electricity. This increases system flexibility, allowing better alignment between energy production and demand in specific applications. More in detail, depending on the demand profiles of the user, the energy stored in the TES can be allocated differently between thermal and electric users (with electricity generated via the BD cycle). So, the thermal energy directly sent to the thermal user and the thermal energy absorbed in the discharging phase, are complementary, and their sum is equal to the thermal energy produced in the charging phase (Eq. (9-10)). This results in various CHP scenarios.

$$QH_{net} + QH_{dis} = QH_{ch} \tag{9-10}$$

where QH_{net} is the net thermal energy provided to the thermal user from the hot reservoir, calculated as:

$$QH_{net} = QH_{ch} - QH_{dis} = QH_{ch} - \frac{W_{net,dis}}{\eta_{dis}} \quad (9\text{-}11)$$

The cogeneration performance is evaluated comparing the system energy production with conventional generation of heat and power. For this purpose, a simplified energy saving index (I_{es}) is introduced:

$$I_{es} = \frac{E_{P,Th} + E_{P,el} - W_{ren}}{W_{ren}} \quad (9\text{-}12)$$

where, W_{ren} represents the primary energy input, assumed to be renewable ($W_{net,ch}$), while $E_{P,Th}$ (Eq. (9-13)) and $E_{P,el}$ (Eq. (9-14)) are the reference primary energy consumption for thermal output and electric output respectively.

$$E_{P,Th} = \frac{QH_{net}}{\eta_{Th,ref}} \quad (9\text{-}13)$$

$$E_{P,el} = \frac{W_{net,dis}}{\eta_{el,ref}} \quad (9\text{-}14)$$

The reference thermal efficiency ($\eta_{Th,ref}$) and reference electrical efficiency ($\eta_{el,ref}$) are set at 90 % and 52.5 %, respectively, according to EU regulations [293] for CHP plants.

I_{es} reflects the normalized primary energy savings when producing heat and power with the system compared to conventional separate systems. An index greater than zero indicates a gain in primary energy efficiency. I_{es} is evaluated under different energy allocation scenarios - either fully to thermal demand, fully to electricity production, or split between both (in several partitioning solutions). Indeed, to maintain general applicability, a parametric analysis is carried out in this study, exploring various heat-to-power production ratios. The full range of possible values is considered by adjusting the allocation of available thermal energy in the TES - from 100 % of the thermal energy being sent directly to the thermal user (and 0 % converted into electricity) to 100 % of the thermal energy being used for electricity generation to meet electric demand.

For each scenario, the specific energy saving index is calculated to evaluate the advantages of adopting the proposed system, integrated with a renewable energy source (e.g., photovoltaic panels), in comparison with traditional systems that generate heat and power separately. Figure 9.15 presents the calculated I_{es} values for each temperature level in both configurations. A pressure ratio value corresponding to the maximum COP (as shown in Figure 9.10) is used for each PTES configuration.

The results depicted in Figure 9.15 reveal that when a higher percentage of the stored heat is reconverted into electricity, the system becomes less favourable in terms of I_{es} compared to conventional separate production methods. In fact, to achieve a positive I_{es} in both configurations and across all temperature levels, at least 60 % of the available TES heat must be directed to the thermal user, leaving a maximum of 40 % for reconversion into electricity. Specifically, the B-PTES configuration exhibits higher I_{es} values than the RECB-PTES. In the case of B-PTES, benefits can be observed even when up to 70–75 % of the stored thermal energy is reconverted into electricity at all three temperature levels. In contrast, the RECB-PTES system is only marginally advantageous compared to separate production methods when a maximum of 65 % of the stored thermal energy is reconverted into electricity at the lowest temperature level (150 °C), 50 % and 60 % at 250 °C and 350 °C, respectively.

Thus, Figure 9.15 shows that as the temperature level increases, a larger portion of the stored thermal energy must be allocated to the thermal user. Additionally, cases involving lower warm reservoir temperatures yield higher values for the primary energy saving index.

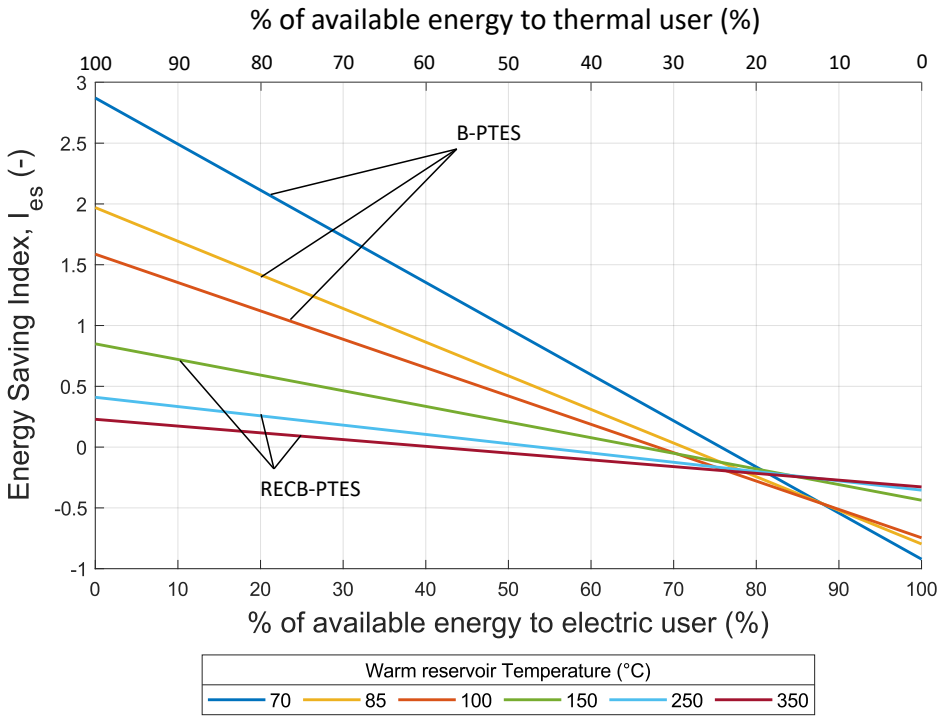

Figure 9.15 - Energy saving index evaluated in the whole range of stored energy partitioning between electric user and thermal user, for the six temperature levels.

9.5.3. Economic analysis

The economic viability of the system is assessed by calculating the maximum specific investment cost that would ensure a return on investment within a reasonable period, which is set at 10 years. The maximum specific investment cost (C_I) is calculated nullifying the net present value (NPV):

$$NPV = \sum_{i=1}^{\tau} \frac{CF_i}{(1+r)^i} - C_I \tag{9-15}$$

where CF_i is the cash flow for year i, r is the discount rate (see Table 9.3), and τ is the 10-year investment period. CF_j is obtained assuming 1500 equivalent working hours (h_{eq}) for the renewable energy source (in line with the average yearly working hours of the wind power plants in Italy [292]), according to Eq. (9-16):

$$CF_i = \frac{(W_{net,dis} \cdot C_{el} + QH_{net} \cdot C_{Th}) \cdot h_{eq}}{W_{net,ch}} \tag{9-16}$$

where C_{el} and C_{Th} are the electricity and thermal energy price respectively (detailed in Table 9.3).

The analysis is conducted for both configurations (B-PTES and RECB-PTES) at all temperature levels, selecting an appropriate pressure ratio value for each scenario. The maximum specific investment cost is calculated under two conditions: i) one where 30 % of the heat stored in the TES is converted back into electricity, and ii) another where 70 % of the TES heat is reconverted into electricity. The investment cost is evaluated by independently varying the prices of electricity and thermal energy, leading to a sensitivity analysis on energy price fluctuations.

Figure 9.16 illustrates the maximum specific investment cost (C_I) for each case as the average electricity price is varied. In Figure 9.16(a), when the majority of the available energy is allocated to the thermal user,

the maximum specific investment cost remains largely unaffected by changes in electricity prices. The highest C_I value is found in the B-PTES configuration at the lowest temperature level, reaching approximately 5000 €/kW. In contrast, when 70 % of the available energy is converted into electricity (Figure 9.16(b)), the variation in electricity prices has a slightly greater impact on the specific investment cost, especially in the recuperated configuration, where C_I ranges from about 1000 to 2000 €/kW. By comparing both graphs in Figure 9.16, it becomes evident that the system is more cost-effective, and can support a higher specific investment cost, when most of the thermal energy produced is used directly. This finding aligns with the linear trend of the energy-saving index (Figure 9.15). The trend in I_{es} also supports the greater cost-effectiveness of the B-PTES configuration compared to the RECB-PTES. The reasons behind this lie in the more significant influence of the charging phase (and the COP) on improving the roundtrip efficiency in B-PTES, as shown in Figure 9.10. In the recuperated configuration, the discharging phase (and its efficiency) plays a larger role in enhancing the roundtrip efficiency, meaning that changes in electricity prices have a more substantial effect on the return on investment. Nonetheless, an increase in electricity prices makes systems with higher specific investment costs more attractive.

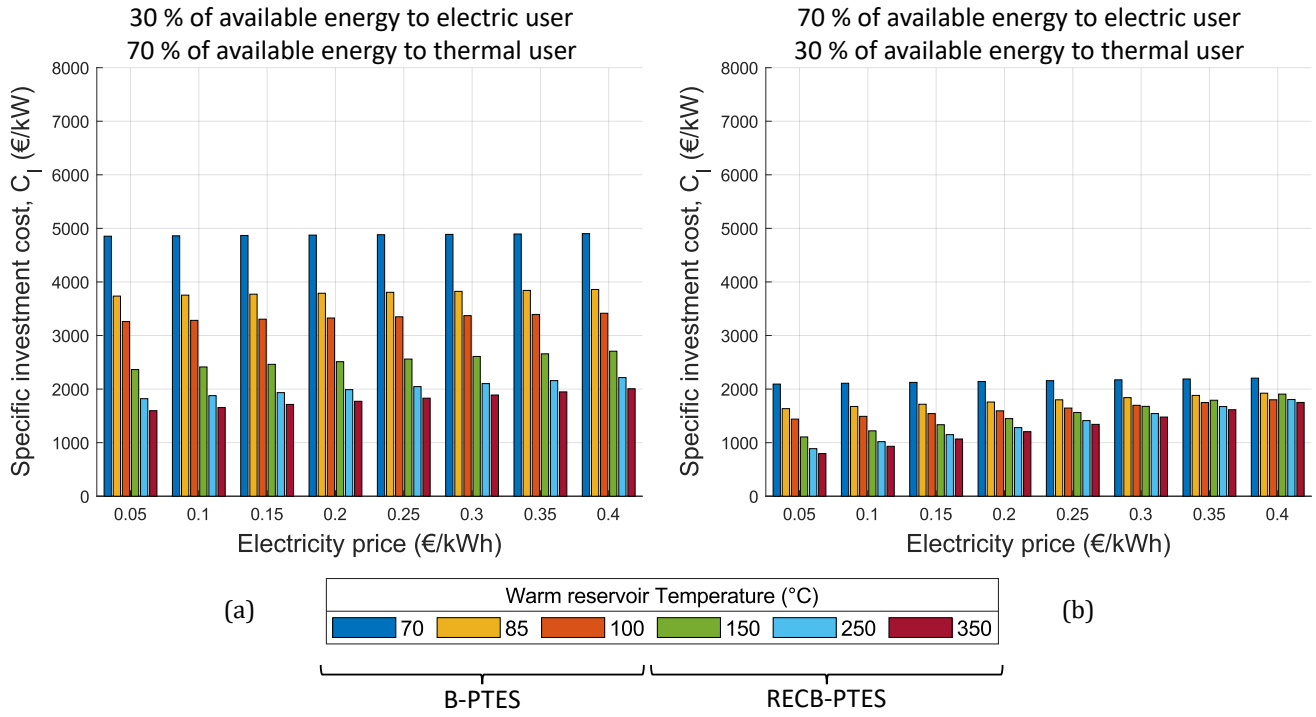

Figure 9.16 - Maximum specific investment cost of the Brayton-based PTES to ensure 10-year return of the investment, when varying the average electricity price.

Figure 9.17 depicts the maximum C_I as the average thermal energy price varies. The economic feasibility of a system with this specific investment cost depends heavily on the thermal energy price, particularly for the B-PTES configuration, where thermal production has a greater impact on overall performance. In this case, at the lowest temperature level, C_I ranges from below 1000 €/kW to over 6000 €/kW, depending on the thermal energy price. Additionally, when most of the available thermal energy is converted into electricity (Figure 9.17(b)), and if thermal energy price is low, the RECB-PTES configuration achieves a higher maximum specific investment cost (exceeding 1000 €/kW) compared to the B-PTES (which remains below 500 €/kW). This difference is due to the major importance of the discharging phase and, consequently, of the electricity production in the system performance.

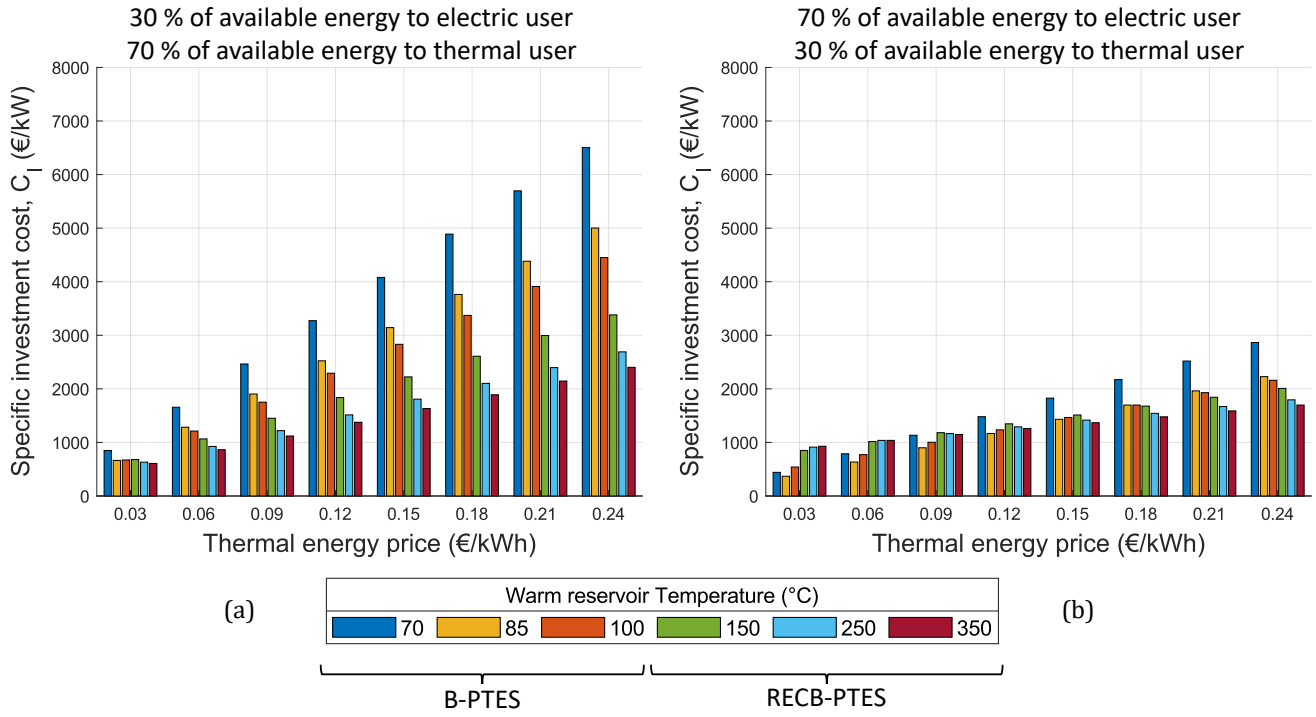

Figure 9.17 - Maximum specific investment cost of the Brayton-based PTES to ensure 10-year return of the investment, when varying the average thermal energy price.

9.6. Conclusions

In the ongoing effort to decarbonize the energy sector and increase the share of renewable energy sources, strategies must be developed to manage their inherent instability and fluctuations, enabling more flexible utilization. PTES technology based on the reversible Joule-Brayton cycle can be considered among these solutions.

This chapter provides a systematic thermodynamic comparison between a closed sCO_2 Brayton-PTES in its base configuration and a recuperated version. In the latter, an additional heat exchanger (the recuperator) is employed to achieve higher cycle maximum temperatures (even exceeding 500 °C), thus increasing the temperature difference between the expansion and compression processes. Although the recuperated configuration achieves the highest roundtrip efficiencies (ranging from 20 % to 30 %), primarily due to improved discharging efficiencies, the base configuration demonstrates a higher COP in the inverse cycle, attributed to a lower temperature lift. Indeed, the base configuration achieves COP values as high as 3.5, compared to values below 2 in the recuperated configuration.

The analysis also includes the system cogeneration performance, recognizing that part of the heat stored in the TES can be directly supplied to a thermal user. The results indicate that, in the most favourable case (with a heat temperature level of 70 °C), at least 25 % of the stored heat must be allocated to the thermal user for the integrated system, to be beneficial in terms of primary energy savings when compared to conventional separate production. At the highest temperature level (350 °C), thermal production must account for at least 60 % of the total energy to yield a positive specific energy saving index.

Lastly, the maximum specific investment cost of the system for both configurations (B-PTES and RECB-PTES) is evaluated, with the goal of achieving a return on investment within 10 years. This is done by alternately varying the average electricity and thermal energy prices. The findings reveal that an increase in both electricity and thermal energy prices allows for a higher maximum specific investment cost.

However, the B-PTES configuration is primarily impacted by changes in the thermal energy price, while the RECB-PTES configuration is also notably influenced by fluctuations in electricity prices.

The results of this study provide a base for further investigation into the system integration in specific applications, accounting for predefined electric and thermal demand profiles, as well as the characteristics of a given RES power plant.

CONCLUSIONS

10. Thesis conclusions overview

Summary. In this final chapter, the methodology and the main outcomes of this thesis are summarized. Eventually, remarks and suggestions for future developments are provided.

This thesis aims to address key topics in the Power-To-Heat-To-Power field, encompassing experimental data collection, the development of reliable models based on experimental data, and the integration of these models into complex energy systems. The study includes technological analyses, environmental considerations, and economic assessments. The thesis is divided into two main parts: "PART I – ORC and HTHP for Stand-Alone Electric and Thermal Energy Generation" and "PART II – Carnot Battery Technology Integration for Energy Storage Applications". Various methodologies are applied across different applications, and the results are categorized by topic as follows:

PART I – ORC and HTHP for Stand-Alone Electric and Thermal Energy Generation

- Experimental analysis of ORC performance in partial evaporation mode for ultra-low-temperature waste heat recovery.
- Performance assessment of ORC technology applied to i) solar thermal in residential sector and ii) data center waste heat recovery, using a semi-empirical model experimentally validated.
- Performance assessment and preliminary design of HTHP technology for waste heat recovery in the ceramic industry.

PART II – Carnot Battery Technology Integration for Energy Storage Applications

- Preliminary development of the acquisition and control system for a 10 kW-sized reversible HP/ORC Carnot battery.
- Design of a rule-based control strategy for managing Carnot battery operations within complex energy systems, with applications i) in the residential sector and ii) to enhance data center energy efficiency.
- Investigation of a Brayton cycle-based Carnot battery for combined heat and power applications.

The final conclusions of this work are structured and discussed according to these topics.

10.1. PART I – ORC and HTHP for stand-alone electric and thermal energy generation

Experimental analysis of ORC performance in partial evaporation mode for ultra-low-temperature waste heat recovery.

An in-depth experimental campaign, with a focus on partial evaporation and wet expansion for ultra-low-temperature heat recovery, was conducted on the micro-ORC test bench located at the University of Bologna. The ORC test rig is presented and the methodology adopted for the experimental campaign and the data acquisition is described in detail. Originally built for dry expansion, the system - particularly the piston expander - was tested under challenging off-design conditions. Despite these challenges, the system demonstrated stable operation and continuous electrical power production. Vapor quality values as low as 0.2–0.3 were achieved at heat source temperatures between 40 °C and 60 °C with high mass flow rates,

while higher temperatures (68 °C and 75 °C) resulted in minimum vapor quality values above 0.6, due to test bench limitations. The system performed best at vapor qualities between 0.8 and 1, where the evaporator efficiency improved as superheating was eliminated.

Key results show that in PE mode, the vaporization pressure was primarily dictated by the heat source temperature, with little influence from the fluid flow rate. Condensation pressure remained stable regardless of flow rate variations, while pump efficiency significantly improved in PE conditions. Additionally, evaporator heat transfer effectiveness increased by up to 125 % compared to dry expansion, with the pinch point temperature difference narrowing to 1-2 K in PE mode. The recuperator's role became negligible under these conditions. While the expander handled wet expansion well, its performance dropped as vapor quality decreased, especially at higher heat source temperatures, with efficiency losses of up to 19 % compared to DE mode. However, at vapor qualities above 0.8, the efficiency penalty was less severe. In some PE scenarios, the back work ratio exceeded 1, indicating high energy consumption by the pump. Overall, the system performance was weak at temperatures below 60 °C, even under dry expansion, but partial evaporation showed promise for ultra-low-temperature waste heat recovery. Indeed, PE mode improved heat source utilization and evaporator effectiveness due to the reduced pinch point temperature difference. However, feed-pump consumption remains a significant concern, especially at lower temperatures.

The experimental results suggests that partial evaporation could serve as a valuable off-design condition for ORC systems originally intended for dry expansion, particularly those operating with low superheating and fluctuating heat source temperatures. By maintaining higher evaporation pressure and expansion ratio, the efficiency penalty is reduced, leading to better evaporator performance and overall system efficiency.

Performance assessment of ORC technology applied to i) solar thermal in residential sector and ii) data center waste heat recovery, using a semi-empirical model experimentally validated.

An available off-design model to simulate micro-ORCs was recalibrated and validated versus experimental data collected for the test bench available at the University of Bologna, to be applied in the simulations of specific ORC applications. This model, developed in MATLAB, incorporates physical equations alongside empirical correlations to accurately predict system performance across various conditions. Calibration involved fine-tuning empirical parameters to minimize the discrepancy between model predictions and experimental measurements, approached as a global minimization problem. The off-design model is used in the performance assessment of two applications of small-scale ORC technology for harnessing low-temperature heat, one focuses on residential solar thermal integration and the other on industrial waste heat recovery. Both studies include sensitivity analyses to explore the potential of environmentally friendly working fluids.

The first investigation focuses on integrating a small-scale, recuperated ORC system with a commercial solar thermal collector to reduce the annual electricity consumption of a single-family house. In the study, first the solar collector and storage tanks sizes are designed, second a performance comparison of various low-GWP fluids as alternatives to the standard working fluid, R134a, is carried out. Results show that the system using R134a meets about 39 % of the annual electricity demand, generating over 1150 kWh of electricity. However, when switching to low-GWP fluids like R1234yf and R513A, electricity production significantly drops, covering only 16 % and 17.5 % of annual demand, respectively. Despite the lower efficiency of these low-GWP fluids, their use is crucial for minimizing greenhouse gas emissions.

The second study examines the potential for integrating a micro-ORC system into data centers to recover waste heat from cooling processes. Data centers generate substantial heat from their operations, and ORC technology could exploit this low-temperature waste heat to improve energy efficiency. Experimental investigations were conducted, using the micro-ORC test bench available at the University

of Bologna. Heat was supplied at temperatures between 40 °C and 55 °C, simulating typical data center conditions. In experimental tests, second law efficiency ranged between 5 % and 13 %. Then, the ORC model was recalibrated based on these results, optimizing the piston expander's built-in volume ratio for better performance. Furthermore, a numerical parametric analysis is performed, varying boundary conditions and comparing the performance of R134a with low-GWP alternatives such as R1234yf and R1234ze(E). While R134a produces the highest amount of electric power, it shows the lowest second law efficiency (25 %). Conversely, R1234ze(E) achieves the highest second law efficiency (29 %) with slightly lower power output. This fluid also proved to be the most effective for electricity savings, recovering about 3 % of the power required by data center servers, compared to 2.8 % and 2.7 % for R1234yf and R134a, respectively. Although the system was not optimized for very low-temperature operations, the study demonstrates that direct cooling of servers with organic fluids could enhance heat recovery and reduce thermal losses. The research highlights the significant potential of ORC technology in improving data center energy efficiency through waste heat recovery.

Performance assessment and preliminary design of HTHP technology for waste heat recovery in the ceramic industry.

For the modelling of HTHPs, due to the lack of experimental data, the simulation software THERMOFLEX, designed for analysing complex power plants in both design and off-design conditions, was selected as the primary simulation tool. Special care was taken in the selection of model parameters to ensure accuracy and reliability. The application of HTHP technology to enhance energy efficiency in the ceramic industry is explored, focusing on waste heat recovery from energy-intensive processes such as spray drying, drying, kiln firing, and cooling to provide thermal energy to the most energy-demanding stages. More in detail, an innovative energy recovery configuration that incorporates an HTHP to preheat the air required for the drying and firing stages, capturing waste heat from the cooling, drying, and firing processes, is proposed. The analysis is performed adopting a comprehensive approach that includes thermodynamic modelling, fluid selection, and detailed system design.

Fluid selection plays a critical role, and using a lumped-parameters thermodynamic model developed in MATLAB, the study identifies cyclopentane as the most suitable working fluid for the application. A detailed model of the HTHP system is then implemented in the THERMOFLEX environment, using cyclopentane and data from technical literature and thermodynamic optimization as inputs. The HTHP demonstrates significant performance, achieving a COP of 2.0 while preheating air to 173 °C by recovering waste heat from drying, firing, and cooling stages. In a configuration where waste heat is recovered solely from the drying and cooling stages, the system achieves a COP of 2.4 and air preheat temperature of 119 °C. The detailed model also provides key insights into the sizing of essential components such as heat exchangers and compressor, optimized for a reference ceramic tile production capacity of 5 tons per hour. The study examines two distinct waste heat recovery configurations: i) one that recovers waste heat from drying, firing, and cooling stages for a total amount of 75 % of the waste heat generated by the ceramic production process; ii) another that recovers waste heat solely from the drying and cooling stages for a total amount of 48 % of the entire process waste heat. These configurations yield substantial benefits in terms of fuel consumption savings and reductions in CO_2 emissions. When waste heat from drying, firing, and cooling stages is recovered, the system saves approximately 13.6 kg/h of fuel and avoids 37.5 kg/h of CO_2 emissions per ton of tiles produced. In the configuration that only recovers waste heat from drying and cooling stages, the savings amount to approximately 8.89 kg/h of fuel and 24.4 kg/h of CO_2 emissions per ton of tiles produced.

In conclusion, this research highlights the potential of HTHP technology as a promising decarbonization strategy for key energy-intensive industrial sectors such as ceramic manufacturing. By effectively recovering and utilizing waste heat, HTHP systems offer a pathway to significantly reduce energy

consumption and emissions.

10.2. PART II – Carnot battery technology integration for energy storage applications

Preliminary development of the acquisition and control system for a 10 kW-sized reversible HP/ORC Carnot battery.

The acquisition and control system for a reversible HP/ORC Carnot battery test bench under development at the University of Liège is designed in two levels, with a third planned for future development. The lower level is implemented using LOGO! Soft Comfort software and runs on Siemens LOGO! Modular microcontrollers. This level manages basic functions such as turning actuators on and off, regulating their operation, and reading sensor measurements. The higher level of the system is developed in Python and is responsible for both manual and automatic control of the Carnot battery different operating modes, namely HP mode, ORC mode, and thermal discharge mode. It also handles the acquisition of key physical quantities, such as temperatures, pressures, and flow rates, which are first processed by the LOGO! microcontrollers. Both the acquisition and control levels are described in detail, including the start and stop procedure for each of the three operating modes.

A 10 kW-sized Carnot battery test bench is being developed for integration with the district heating substation of the Thermodynamics Laboratory building. This larger system aims to provide electrical and thermal peak shaving by converting surplus renewable energy from the building's photovoltaic panels into stored thermal energy, which can later be converted back into electricity during periods of high demand.

Design of a rule-based control strategy for managing Carnot battery operations within complex energy systems, with applications i) in the residential sector and ii) to enhance data center energy efficiency.

A comprehensive rule-based control strategy was developed in MATLAB for optimizing the operation of the reversible HP/ORC Carnot battery in an integrated system that includes a district heating substation and a photovoltaic power plant. The control strategy aims to maximize the economic benefits of the CB over a year, considering daily fluctuations in electricity prices from the spot market. By using the CB to store thermal energy, the system effectively reduces early morning thermal demand peaks, allowing a significant downsizing of the DH substation and substantial investment savings.

The study considers variable boundary conditions, with user energy profiles based on data from a University of Liège building, and solar radiation and ambient temperature profiles from 2020 records. Two system configurations are explored: one in which the HP extracts free waste heat at a constant temperature, and another one in which the HP draws heat from the DH substation return branch, incurring additional costs. The first configuration shows that the CB can reduce the DH substation size significantly, generating annual savings of approximately € 5000, with 47 % of revenues stemming from the substation downsizing, resulting in a payback period of less than 9 years. In contrast, the second configuration restricts the HP operation, preventing thermal discharge mode and negatively affecting the system economic feasibility, yielding no positive financial gain. The study also evaluates some control rules and their impact on system performance. For example, discharging the ORC storage immediately, rather than waiting for higher electricity prices, and allowing the HP to draw from the grid when prices are high, extends the PB period to 11 years. Removing the option to purchase grid electricity for the HP further reduces economic gains, particularly during periods of low solar radiation, leading to a PB of approximately 12.6 years. This analysis proves the benefits of rules and constraints imposed in the control strategy. Sensitivity analyses reveal that the PV power plant's surface area has minimal impact on

economic gains and system operation, as the system performance is more closely tied to temperature levels. However, increasing storage volume significantly affects the DH substation downsizing and overall revenues and expenses, although the net economic gain and PB period remain relatively unchanged. The optimal storage volume for this application is identified as 13 m^3, offering the shortest PB period. Additional sensitivity analysis explores how varying electricity prices affects performance. As electricity prices increase, economic gains decrease due to the HP higher operating costs, which outweigh the ORC's revenues. The economic benefit from DH substation downsizing remains unaffected by electricity prices.

The control strategy developed in this study is adaptable to other applications, with adjustments to suit different case studies. Indeed, the same approach is adopted to investigate the integration of a reversible HP/ORC Carnot battery into data centers cooling systems, powered by electricity from a PV power plant. This study explores the potential for enhancing both energy efficiency and economic performance.

First, the study focuses on analysing thermodynamic performance to identify the most suitable working fluid for the system. R1233zd(E) is selected as the optimal fluid for both the HP and ORC systems, allowing the CB to achieve a thermodynamic roundtrip efficiency of 43 % under nominal conditions. This result highlights the CB potentiality to handle the energy demands of DC cooling systems while making effective use of renewable energy. Second, a detailed semi-empirical off-design model of the CB test bench is employed alongside a rule-based control strategy to manage the integration of the ORC and HP into the system. When the PV plant generates excess electricity, the surplus is stored in the CB via the HP, reducing the energy demand of the cooling system. When renewable energy is insufficient to meet demand, the stored thermal energy activates the ORC. Additionally, in winter, the system can sell stored thermal energy to an external user, providing further economic opportunities. A sensitivity analysis examines variations in storage volume and energy prices, leading to the conclusion that CB integration can be financially viable, particularly in high energy price environments. With a storage capacity of 10 m^3, the system can generate an additional annual profit of around € 7744, with a payback period of approximately 10 years. Even more favourable results emerge when the system operates without selling electricity to the grid, achieving a PB period of less than 5 years and an annual economic gain of nearly € 18500. The study suggests that the conservative assumptions made in the CB operation, coupled with the validation of the model on a non-optimized prototype, indicate potential for further improvement in both performance and profitability. Thermal integration enables roundtrip efficiencies exceeding 30 %, even at low temperatures, and the CB enhances the DC performance metrics, i.e., PUE and ERE, by recovering part of the HP electric consumption via the ORC. The final part of the research compares the CB integration with a simpler alternative that continuously recovers DC waste heat using only an ORC system. This comparison highlights the limitations of a stand-alone ORC, where the average annual efficiency drops to 1.5 %. This decline is due to the low temperature of the heat source and the off-design conditions under which the ORC operates. Furthermore, the ORC is unable to run continuously because, for more than half the year, the ambient temperature is too high to maintain the necessary temperature difference between the hot source and the cold sink. These findings underscore the clear advantage of the CB system, which, unlike the ORC, also serves as an energy storage solution and is particularly beneficial in systems with renewable energy generation.

Investigation of a Brayton cycle-based Carnot battery for combined heat and power applications.

As a promising alternative to Rankine-based CB systems, Brayton-based CB technology has drawn remarkable attention in the PTES research field for larger applications with higher temperature levels. A comprehensive thermodynamic assessment of a closed Brayton cycle-based PTES system utilizing supercritical CO_2 was performed comparing base configuration and a recuperated version, with the latter featuring an additional heat exchanger, known as a recuperator. The recuperator enables the system to achieve higher maximum temperatures, exceeding 500 °C, which in turn increases the temperature difference between the expansion and compression processes, enhancing cycle efficiency. A detailed parametric analysis is performed using the simulation software THERMOFLEX to assess the energy

conversion and storage potential of this system. This analysis not only examines the system potential as an energy storage solution, but also investigates its role in providing flexibility, enabling thermal production to be more closely aligned with demand.

The thermodynamic performance during both the charging and discharging phases of the PTES system are analysed. The results demonstrate the system efficiency in energy conversion and storage under varying operating conditions, highlighting its potential for achieving high thermodynamic performance. The recuperated configuration achieves the highest roundtrip efficiencies, ranging from 20 % to 30 %, primarily due to improved discharging efficiencies. This improvement is driven by the enhanced temperature difference between hot and cold sides, making the recuperated system more effective during the energy discharge phase. However, the base configuration exhibits a higher COP during the inverse cycle because it operates with a lower temperature lift. The base configuration can reach COP values as high as 3.5, while the recuperated version shows values below 2. This contrast underscores the trade-off between efficiency in discharging mode and COP in charging mode, depending on the chosen system configuration.

The analysis also considers the cogeneration performance of the system, emphasizing the ability to supply part of the stored heat directly to a thermal user. In this scenario, the system, capable of addressing both thermal and electrical needs, offers a more integrated and flexible approach to energy management. The results indicate that, under the most favourable conditions (with a heat temperature level of 70 °C), at least 25 % of the stored heat must be allocated to the thermal user for the integrated system to yield significant primary energy savings compared to conventional separate production methods. At higher temperature levels, such as 350 °C, thermal production must account for at least 60 % of the total energy output to deliver a positive specific energy saving index. These findings highlight the importance of optimizing the thermal output allocation in cogeneration applications to maximize the system overall energy efficiency.

In addition to the technical analysis, the study includes an economic evaluation aimed at determining the maximum allowable specific investment cost that would ensure a reasonable return on investment. This financial assessment is crucial for understanding the system economic viability and identifying the conditions under which such a PTES system could be commercially competitive. The findings from this evaluation provide valuable insights into the potential for broader implementation of sCO2-based Brayton cycle PTES systems as part of a sustainable energy strategy, helping to meet both thermal and electrical demands while enhancing overall energy system flexibility. The economic evaluation is conducted by varying average electricity and thermal energy prices. The results reveal that increases in both electricity and thermal energy prices allow for a higher maximum specific investment cost. However, the economic performance of the two configurations differs: while the B-PTES configuration is primarily influenced by changes in thermal energy prices, the RECB-PTES system is significantly impacted by fluctuations in both electricity and thermal energy prices. This underscores the different sensitivities of each configuration to market conditions, with the recuperated system more responsive to changes in the electricity market.

10.3. Perspectives

In addition to the original objective, the value of this work lies in disclosing new challenges and opportunities that emerged throughout the problem-solving process. From the author's perspective, the following observations and suggestions could be valuable for further research.

Concerning the ORC and HTHP for stand-alone electric and thermal energy generation:

- The development of an ORC system specifically designed for partial evaporation, with an optimized expander and component sizes would likely improve the evaporator performance and streamline the system by removing the need for a recuperator, thus reducing both costs and pressure losses. Further

refinement of the expander's parameters, such as adjusting valve timing and displacement, could help maintain high performance levels. Additionally, optimizing the filling process is crucial to ensure the expander operates effectively under different conditions. The modification of the valve timing for the reciprocating piston expander could be implemented and tested to assess its actual benefits. When designing a new volumetric expander, a preliminary analysis is recommended to determine the optimal built-in volume ratio for the specific application. Another area of potential improvement lies in redesigning the pump to reduce the back work ratio to below 30 %, which would enhance the overall efficiency of the system.

- Due to the phase out of high-environmental impact fluids additional research should focus on i) the identification of new high-performance low-GWP fluids through simulations, and ii) the optimization of ORC systems for these fluids. To address the first target, research should focus on fluids and mixtures that operate at pressures enabling the highest possible enthalpy drop at the expander and own high viscosity to minimize pump leakage. Furthermore, fluids with a high latent heat of vaporization could also enhance micro-ORC system performance by recovering more heat at the evaporator, as revealed by findings in this thesis. Experimental validation would further support the conclusions. To address the second target, future investigations should include comprehensive economic analysis, system redesign aimed at improving efficiency, and explorations into thermal power production. These measures are crucial to enhance the viability and performance of low-GWP fluids in ORC systems, positioning them as a more sustainable solution for reducing household and industrial energy consumption.
- Future research on HTHPs could explore the scalability and economic viability of integrating this technology into actual ceramic production facilities, as well as other energy-intensive industrial sectors. Such investigations have the potential to revolutionize energy efficiency within the industry, offering a path toward more sustainable and cost-effective manufacturing processes.

Regarding the Carnot battery technology integration for energy storage applications, instead:

- Future integration plans regarding the CB test bench, under construction at the Thermodynamics Laboratory of the University of Liège, include the development of a third advanced level in MATLAB, aimed at optimizing the scheduling strategy and calculating additional thermodynamic quantities such as enthalpy and entropy. While the rule-based scheduling strategy is already optimized, its integration with the Python control layer will be necessary before full implementation. This advanced level will be incorporated into the overall control and acquisition system once the middle and lower levels will be fully validated, which will be achieved after completing the test bench setup. Experimental tests on the CB prototype will contribute to a deeper practical understanding of this technology, offering experimental data and insights that could pave the way for more efficient and sustainable energy systems, better suited for renewable energy sources incorporation.
- For what concerns the development of efficient and optimized management strategy for CB operations in integrated systems, future research should explore strategies like purchasing electricity from the grid during low-price periods to power the HP, aiming to improve both energy and financial efficiency. Additionally, the dynamic behaviour of the CB system during transitions between different operating modes could be worthy of being integrated into future models, enhancing the system adaptability, reliability, and overall performance in fluctuating conditions.
- Additional research should focus on optimizing the performance and cost-effectiveness of PTES technology by considering detailed and realistic electric and thermal demand profiles, along with the specific characteristics of renewable energy source power plants. This approach could enhance the applicability of PTES systems in real-world scenarios.

References

[1] G. Lentze, "The year 2022 was the second warmest on record in Europe," ECMWF. Accessed: Mar. 13, 2024. [Online]. Available: https://www.ecmwf.int/en/about/media-centre/news/2023/year-2022-was-second-warmest-record-europe

[2] H. Ritchie, M. Roser, and P. Rosado, "Renewable Energy," *Our World in Data*, Mar. 2024, Accessed: Mar. 13, 2024. [Online]. Available: https://ourworldindata.org/renewable-energy

[3] H. Ritchie, P. Rosado, and M. Roser, "Energy Mix," *Our World in Data*, Jan. 2024, Accessed: Mar. 13, 2024. [Online]. Available: https://ourworldindata.org/energy-mix

[4] S. Quoilin, M. V. D. Broek, S. Declaye, P. Dewallef, and V. Lemort, "Techno-economic survey of Organic Rankine Cycle (ORC) systems," *Renewable and Sustainable Energy Reviews*, vol. 22, pp. 168–186, Jun. 2013, doi: 10.1016/j.rser.2013.01.028.

[5] A. Colmenar-Santos, D. Gómez-Camazón, E. Rosales-Asensio, and J.-J. Blanes-Peiró, "Technological improvements in energetic efficiency and sustainability in existing combined-cycle gas turbine (CCGT) power plants," *Applied Energy*, vol. 223, pp. 30–51, Aug. 2018, doi: 10.1016/j.apenergy.2018.03.191.

[6] K. Rahbar, S. Mahmoud, R. K. Al-Dadah, N. Moazami, and S. A. Mirhadizadeh, "Review of organic Rankine cycle for small-scale applications," *Energy Conversion and Management*, vol. 134, pp. 135–155, Feb. 2017, doi: 10.1016/j.enconman.2016.12.023.

[7] SIEMENS, "Waste Heat Recovery with Organic Rankine Cycle Technology - Power Generation with the Siemens ORC-Module." [Online]. Available: https://www.researchgate.net/profile/Sathish_Dhandapani2/post/what_is_the_scope_of_Waste_heat_Recovery_through_Organic_Rankine_cycle/attachment/59d63fca79197b807799c1e5/AS:428525447585792@1479179836620/download/brochure-orc-organic-Rankine-cycle-technology_EN.pdf

[8] C. Ononogbo *et al.*, "Opportunities of waste heat recovery from various sources: Review of technologies and implementation," *Heliyon*, vol. 9, no. 2, Feb. 2023, doi: 10.1016/j.heliyon.2023.e13590.

[9] *COMMUNICATION FROM THE COMMISSION TO THE EUROPEAN PARLIAMENT, THE EUROPEAN COUNCIL, THE COUNCIL, THE EUROPEAN ECONOMIC AND SOCIAL COMMITTEE AND THE COMMITTEE OF THE REGIONS A New Industrial Strategy for Europe*. 2020. Accessed: Feb. 06, 2024. [Online]. Available: https://eur-lex.europa.eu/legal-content/EN/TXT/?qid=1593086905382&uri=CELEX%3A52020DC0102

[10] D. D. Furszyfer Del Rio *et al.*, "Decarbonizing the ceramics industry: A systematic and critical review of policy options, developments and sociotechnical systems," *Renewable and Sustainable Energy Reviews*, vol. 157, p. 112081, Apr. 2022, doi: 10.1016/j.rser.2022.112081.

[11] "Policy Department for Economic, Scientific and Quality of Life Policies Directorate-General for Internal Policies, Energy-intensive industries - Challenges and opportunities in energy transition, PE 652.717–July 2020, available at: Highlights | Supporting analyses | Committees | European Parliament (europa.eu)."

[12] V. Pethurajan, S. Sivan, and G. C. Joy, "Issues, comparisons, turbine selections and applications – An overview in organic Rankine cycle," *Energy Conversion and Management*, vol. 166, pp. 474–488, Jun. 2018, doi: 10.1016/j.enconman.2018.04.058.

[13] A. Redko, O. Redko, and R. DiPippo, "9 - Industrial waste heat resources," in *Low-Temperature Energy Systems with Applications of Renewable Energy*, A. Redko, O. Redko, and R. DiPippo, Eds., Academic Press, 2020, pp. 329–362. doi: 10.1016/B978-0-12-816249-1.00009-1.

[14] A. K. S. Al-Sayyab, A. Mota-Babiloni, and J. Navarro-Esbrí, "Renewable and waste heat applications for heating, cooling, and power generation based on advanced configurations," *Energy Conversion and Management*, vol. 291, p. 117253, Sep. 2023, doi: 10.1016/j.enconman.2023.117253.

[15] J. S. Pereira, J. B. Ribeiro, R. Mendes, G. C. Vaz, and J. C. André, "ORC based micro-cogeneration systems for residential application – A state of the art review and current challenges," *Renewable and Sustainable Energy Reviews*, vol. 92, pp. 728–743, Sep. 2018, doi: 10.1016/j.rser.2018.04.039.

[16] G. Kosmadakis, "Industrial waste heat potential and heat exploitation solutions," *Applied Thermal Engineering*, p. 122957, Mar. 2024, doi: 10.1016/j.applthermaleng.2024.122957.

[17] H. S. Sun and S. E. Lee, "Case study of data centers' energy performance," *Energy and Buildings*, vol. 38, no. 5, Art. no. 5, May 2006, doi: 10.1016/j.enbuild.2005.08.012.

[18] K. Kant, "Data center evolution: A tutorial on state of the art, issues, and challenges," *Computer Networks*, vol. 53, no. 17, Art. no. 17, Dec. 2009, doi: 10.1016/j.comnet.2009.10.004.

[19] Jonathan G Koomey, "Estimating Total Power Consumption by Servers in the US and the World," Mar. 2007.

[20] J. Cho, T. Lim, and B. S. Kim, "Viability of datacenter cooling systems for energy efficiency in temperate or subtropical regions: Case study," *Energy and Buildings*, vol. 55, pp. 189–197, Dec. 2012, doi:

10.1016/j.enbuild.2012.08.012.
[21] Q. Huang, S. Shao, H. Zhang, and C. Tian, "Development and composition of a data center heat recovery system and evaluation of annual operation performance," *Energy*, vol. 189, p. 116200, Dec. 2019, doi: 10.1016/j.energy.2019.116200.
[22] Y. Luo, J. Andresen, H. Clarke, M. Rajendra, and M. Maroto-Valer, "A framework for waste heat energy recovery within data centre," *Energy Procedia*, vol. 158, pp. 3788–3794, Feb. 2019, doi: 10.1016/j.egypro.2019.01.875.
[23] Y. Luo, J. Andresen, H. Clarke, M. Rajendra, and M. Maroto-Valer, "A decision support system for waste heat recovery and energy efficiency improvement in data centres," *Applied Energy*, vol. 250, pp. 1217–1224, Sep. 2019, doi: 10.1016/j.apenergy.2019.05.029.
[24] K. Ebrahimi, G. F. Jones, and A. S. Fleischer, "A review of data center cooling technology, operating conditions and the corresponding low-grade waste heat recovery opportunities," *Renewable and Sustainable Energy Reviews*, vol. 31, pp. 622–638, Mar. 2014, doi: 10.1016/j.rser.2013.12.007.
[25] C. Nadjahi, H. Louahlia, and S. Masson, "A review of thermal management and innovative cooling strategies for data center," *Sustain. Comput. Informatics Syst.*, 2018, doi: 10.1016/J.SUSCOM.2018.05.002.
[26] J. Bao and L. Zhao, "A review of working fluid and expander selections for organic Rankine cycle," *Renewable and Sustainable Energy Reviews*, vol. 24, pp. 325–342, Aug. 2013, doi: 10.1016/j.rser.2013.03.040.
[27] I. H. Bell, J. Wronski, S. Quoilin, and V. Lemort, "Pure and Pseudo-pure Fluid Thermophysical Property Evaluation and the Open-Source Thermophysical Property Library CoolProp," *Ind. Eng. Chem. Res.*, vol. 53, no. 6, Art. no. 6, Feb. 2014, doi: 10.1021/ie4033999.
[28] O. US EPA, "Understanding Global Warming Potentials." Accessed: Apr. 10, 2024. [Online]. Available: https://www.epa.gov/ghgemissions/understanding-global-warming-potentials
[29] "Regulation (EU) No 517/2014 of the European Parliament and of the Council of 16 April 2014 on fluorinated greenhouse gases and repealing Regulation (EC) No 842/2006," p. 36.
[30] Y. Heredia-Aricapa, J. M. Belman-Flores, A. Mota-Babiloni, J. Serrano-Arellano, and J. J. García-Pabón, "Overview of low GWP mixtures for the replacement of HFC refrigerants: R134a, R404A and R410A," *International Journal of Refrigeration*, vol. 111, pp. 113–123, Mar. 2020, doi: 10.1016/j.ijrefrig.2019.11.012.
[31] ASHRAE Standards Committee, "Designation and Safety Classification of Refrigerants", [Online]. Available: https://www.ashrae.org/File%20Library/Technical%20Resources/Standards%20and%20Guidelines/Standards%20Addenda/34_2016_g_20180628.pdf
[32] "Classe sicurezza gas refrigeranti." Accessed: Apr. 18, 2024. [Online]. Available: https://www.interfred.it/Aziende/Refrigeranti/Classificazione/Tabella_sicurezza.asp
[33] C. Tammone, R. Pili, S. Indrehus, and F. Haglind, "TECHNO-ECONOMIC ANALYSIS OF PARTIAL EVAPORATION ORGANIC RANKINE CYCLE SYSTEMS FOR GEOTHERMAL APPLICATIONS," p. 10, 2021.
[34] R. Cipollone, G. Bianchi, M. Di Bartolomeo, D. Di Battista, and F. Fatigati, "Low grade thermal recovery based on trilateral flash cycles using recent pure fluids and mixtures," *Energy Procedia*, vol. 123, pp. 289–296, Sep. 2017, doi: 10.1016/j.egypro.2017.07.246.
[35] J. Fischer, "Comparison of trilateral cycles and organic Rankine cycles," *Energy*, vol. 36, no. 10, Art. no. 10, Oct. 2011, doi: 10.1016/j.energy.2011.07.041.
[36] M. Imran, M. Usman, B.-S. Park, and D.-H. Lee, "Volumetric expanders for low grade heat and waste heat recovery applications," *Renewable and Sustainable Energy Reviews*, vol. 57, pp. 1090–1109, May 2016, doi: 10.1016/j.rser.2015.12.139.
[37] E. Macchi and M. Astolfi, Eds., *Organic Rankine cycle (ORC) power systems: technologies and applications*. in Woodhead Publishing series in energy, no. number 107. Duxford ; Cambridge, Massachusetts ; Kidlington: Woodhead Publishing is an Imprint of Elsevier, 2017.
[38] T. Tartière and M. Astolfi, "A World Overview of the Organic Rankine Cycle Market," *Energy Procedia*, vol. 129, pp. 2–9, Sep. 2017, doi: 10.1016/j.egypro.2017.09.159.
[39] M. Bianchi *et al.*, "Feasibility of ORC application in natural gas compressor stations," *Energy*, vol. 173, pp. 1–15, Apr. 2019, doi: 10.1016/j.energy.2019.01.127.
[40] A. Squared, "Introducing the Plug and Play Micro-ORC," Air Squared Scroll Technology. Accessed: Apr. 29, 2024. [Online]. Available: https://airsquared.com/news/introducing-plug-play-micro-orc/
[41] F. Campana *et al.*, "ORC waste heat recovery in European energy intensive industries: Energy and GHG savings," *Energy Conversion and Management*, vol. 76, pp. 244–252, Dec. 2013, doi: 10.1016/j.enconman.2013.07.041.
[42] X. Li, B. Xu, H. Tian, and G. Shu, "Towards a novel holistic design of organic Rankine cycle (ORC) systems operating under heat source fluctuations and intermittency," *Renewable and Sustainable Energy Reviews*, vol. 147, p. 111207, Sep. 2021, doi: 10.1016/j.rser.2021.111207.
[43] K. Hamid *et al.*, "Potential evaluation of integrated high temperature heat pumps: A review of recent advances," *Applied Thermal Engineering*, vol. 230, p. 120720, Jul. 2023, doi: 10.1016/j.applthermaleng.2023.120720.
[44] S. Bouckaert *et al.*, "Net Zero by 2050: A Roadmap for the Global Energy Sector," 2021, Accessed: Oct. 28, 2022. [Online]. Available: https://trid.trb.org/view/1856381
[45] X. Ma, Y. Du, T. Zhao, T. Zhu, B. Lei, and Y. Wu, "A comprehensive review of compression high-temperature heat

pump steam system: status and trend," *International Journal of Refrigeration*, Apr. 2024, doi: 10.1016/j.ijrefrig.2024.04.024.
[46] K.-M. Adamson *et al.*, "High-temperature and transcritical heat pump cycles and advancements: A review," *Renewable and Sustainable Energy Reviews*, vol. 167, p. 112798, Oct. 2022, doi: 10.1016/j.rser.2022.112798.
[47] C. Arpagaus, F. Bless, M. Uhlmann, J. Schiffmann, and S. S. Bertsch, "High temperature heat pumps: Market overview, state of the art, research status, refrigerants, and application potentials," *Energy*, vol. 152, pp. 985–1010, Jun. 2018, doi: 10.1016/j.energy.2018.03.166.
[48] GSE, "Allegato 1 del Decreto Direttoriale 30 aprile 2019 - Guida operativa.pdf." Apr. 30, 2019. [Online]. Available: https://www.gse.it/documenti_site/Documenti%20GSE/Servizi%20per%20te/CERTIFICATI%20BIANCHI/MANUALI/Allegato%201%20del%20Decreto%20Direttoriale%2030%20aprile%202019%20-%20Guida%20operativa.pdf
[49] B. Egilegor *et al.*, "ETEKINA: Analysis of the potential for waste heat recovery in three sectors: Aluminium low pressure die casting, steel sector and ceramic tiles manufacturing sector," *International Journal of Thermofluids*, vol. 1–2, p. 100002, Feb. 2020, doi: 10.1016/j.ijft.2019.100002.
[50] D. Wu, J. Jiang, B. Hu, and R. Z. Wang, "Experimental investigation on the performance of a very high temperature heat pump with water refrigerant," *Energy*, vol. 190, p. 116427, Jan. 2020, doi: 10.1016/j.energy.2019.116427.
[51] J. Jiang, B. Hu, R. Z. Wang, N. Deng, F. Cao, and C.-C. Wang, "A review and perspective on industry high-temperature heat pumps," *Renewable and Sustainable Energy Reviews*, vol. 161, p. 112106, Jun. 2022, doi: 10.1016/j.rser.2022.112106.
[52] Z. Hao, Z. Yanting, X. Jingyu, W. Lin, and H. Zheng, "Performance Analysis of Internal Heat Exchanger-Based Quasi-Two-Stage Vapor Compression Heat Pump System for High-Temperature Steam Production," *Energy Technology*, vol. 8, no. 12, p. 2000623, 2020, doi: 10.1002/ente.202000623.
[53] B. Hu, D. Wu, L. W. Wang, and R. Z. Wang, "Exergy analysis of R1234ze(Z) as high temperature heat pump working fluid with multi-stage compression," *Front. Energy*, vol. 11, no. 4, pp. 493–502, Dec. 2017, doi: 10.1007/s11708-017-0510-6.
[54] Z.-R. Peng, G.-B. Wang, and X.-R. Zhang, "Thermodynamic analysis of novel heat pump cycles for drying process with large temperature lift," *International Journal of Energy Research*, vol. 43, no. 8, pp. 3201–3222, 2019, doi: 10.1002/er.4394.
[55] H. Yan, B. Hu, and R. Wang, "Air-Source Heat Pump for Distributed Steam Generation: A New and Sustainable Solution to Replace Coal-Fired Boilers in China," *Advanced Sustainable Systems*, vol. 4, no. 11, 2020, doi: 10.1002/adsu.202000118.
[56] "Task 1 - Technologies," Annex 58. Accessed: May 08, 2024. [Online]. Available: https://heatpumpingtechnologies.org/annex58/task1/
[57] F. Schlosser, M. Jesper, J. Vogelsang, T. G. Walmsley, C. Arpagaus, and J. Hesselbach, "Large-scale heat pumps: Applications, performance, economic feasibility and industrial integration," *Renewable and Sustainable Energy Reviews*, vol. 133, p. 110219, Nov. 2020, doi: 10.1016/j.rser.2020.110219.
[58] H. C. Becker, Ed., *Methodology and Thermo-Economic Optimization for Integration of Industrial Heat Pumps*. Lausanne: EPFL, 2012. doi: 10.5075/epfl-thesis-5341.
[59] A. Vecchi *et al.*, "Carnot Battery development: A review on system performance, applications and commercial state-of-the-art," *Journal of Energy Storage*, vol. 55, p. 105782, Nov. 2022, doi: 10.1016/j.est.2022.105782.
[60] O. Dumont, G. F. Frate, A. Pillai, S. Lecompte, M. De paepe, and V. Lemort, "Carnot battery technology: A state-of-the-art review," *Journal of Energy Storage*, vol. 32, p. 101756, Dec. 2020, doi: 10.1016/j.est.2020.101756.
[61] A. Vecchi, Y. Li, Y. Ding, P. Mancarella, and A. Sciacovelli, "Liquid air energy storage (LAES): A review on technology state-of-the-art, integration pathways and future perspectives," *Advances in Applied Energy*, vol. 3, p. 100047, Aug. 2021, doi: 10.1016/j.adapen.2021.100047.
[62] E. Thiele, "The Lamm-Honigmann Thermochemical Energy Storage," in *Encyclopedia of Energy Storage*, L. F. Cabeza, Ed., Oxford: Elsevier, 2022, pp. 159–172. doi: 10.1016/B978-0-12-819723-3.00060-3.
[63] G. F. Frate, L. Ferrari, and U. Desideri, "Multi-criteria investigation of a pumped thermal electricity storage (PTES) system with thermal integration and sensible heat storage," *Energy Conversion and Management*, vol. 208, p. 112530, Mar. 2020, doi: 10.1016/j.enconman.2020.112530.
[64] O. Dumont and V. Lemort, "Mapping of performance of pumped thermal energy storage (Carnot battery) using waste heat recovery," *Energy*, vol. 211, p. 118963, Nov. 2020, doi: 10.1016/j.energy.2020.118963.
[65] K. Ökten and B. Kurşun, "Thermo-economic assessment of a thermally integrated pumped thermal energy storage (TI-PTES) system combined with an absorption refrigeration cycle driven by low-grade heat source," *Journal of Energy Storage*, vol. 51, p. 104486, Jul. 2022, doi: 10.1016/j.est.2022.104486.
[66] G. F. Frate, M. Antonelli, and U. Desideri, "A novel Pumped Thermal Electricity Storage (PTES) system with thermal integration," *Applied Thermal Engineering*, vol. 121, pp. 1051–1058, Jul. 2017, doi: 10.1016/j.applthermaleng.2017.04.127.
[67] Z. Su, L. Yang, J. Song, X. Jin, X. Wu, and X. Li, "Multi-dimensional comparison and multi-objective optimization of geothermal-assisted Carnot battery for photovoltaic load shifting," *Energy Conversion and Management*, vol. 289,

p. 117156, Aug. 2023, doi: 10.1016/j.enconman.2023.117156.
[68] X. Zhang *et al.*, "The Carnot batteries thermally assisted by the steam extracted from thermal power plants: A thermodynamic analysis and performance evaluation," *Energy Conversion and Management*, vol. 297, p. 117724, Dec. 2023, doi: 10.1016/j.enconman.2023.117724.
[69] R. Xia *et al.*, "Comprehensive performance analysis of cold storage Rankine Carnot batteries: Energy, exergy, economic, and environmental perspectives," *Energy Conversion and Management*, vol. 293, p. 117485, Oct. 2023, doi: 10.1016/j.enconman.2023.117485.
[70] E. Bellos, "Thermodynamic analysis of a Carnot battery unit with double exploitation of a waste heat source," *Energy Conversion and Management*, vol. 299, p. 117844, Jan. 2024, doi: 10.1016/j.enconman.2023.117844.
[71] N. Torricelli, L. Branchini, A. De Pascale, O. Dumont, and V. Lemort, "Optimal Management of Reversible Heat Pump/Organic Rankine Cycle Carnot Batteries," *Journal of Engineering for Gas Turbines and Power*, vol. 145, no. 4, Apr. 2023, doi: 10.1115/1.4055708.
[72] M. Bianchi *et al.*, "Experimental analysis of a micro-ORC driven by piston expander for low-grade heat recovery," *Applied Thermal Engineering*, vol. 148, pp. 1278–1291, Feb. 2019, doi: 10.1016/j.applthermaleng.2018.12.019.
[73] B. Eppinger, D. Steger, C. Regensburger, J. Karl, E. Schlücker, and S. Will, "Carnot battery: Simulation and design of a reversible heat pump-organic Rankine cycle pilot plant," *Applied Energy*, vol. 288, p. 116650, Apr. 2021, doi: 10.1016/j.apenergy.2021.116650.
[74] O. Dumont and V. Lemort, "Thermo-technical approach to characterize the performance of a reversible heat pump/organic Rankine cycle power system depending on its operational conditions," in *ECOS 2019*, 2019.
[75] M. Abarr, J. Hertzberg, and L. D. Montoya, "Pumped Thermal Energy Storage and Bottoming System Part B: Sensitivity analysis and baseline performance," *Energy*, vol. 119, pp. 601–611, Jan. 2017, doi: 10.1016/j.energy.2016.11.028.
[76] X. Yu, H. Qiao, B. Yang, and H. Zhang, "Thermal-economic and sensitivity analysis of different Rankine-based Carnot battery configurations for energy storage," *Energy Conversion and Management*, vol. 283, p. 116959, May 2023, doi: 10.1016/j.enconman.2023.116959.
[77] A. White, G. Parks, and C. N. Markides, "Thermodynamic analysis of pumped thermal electricity storage," *Applied Thermal Engineering*, vol. 53, no. 2, pp. 291–298, May 2013, doi: 10.1016/j.applthermaleng.2012.03.030.
[78] G. F. Frate, M. Pettinari, E. Di Pino Incognito, R. Costanzi, and L. Ferrari, "Dynamic Modelling of a Brayton PTES System," presented at the ASME Turbo Expo 2022: Turbomachinery Technical Conference and Exposition, American Society of Mechanical Engineers Digital Collection, Oct. 2022. doi: 10.1115/GT2022-83445.
[79] L. Wang, X. Lin, L. Chai, L. Peng, D. Yu, and H. Chen, "Cyclic transient behavior of the Joule–Brayton based pumped heat electricity storage: Modeling and analysis," *Renewable and Sustainable Energy Reviews*, vol. 111, pp. 523–534, Sep. 2019, doi: 10.1016/j.rser.2019.03.056.
[80] J. McTigue, P. Farres-Antunez, K. Ellingwood, T. Neises, and A. White, "Pumped thermal electricity storage with supercritical CO2 cycles and solar heat input," *AIP Conference Proceedings*, vol. 2303, no. 1, p. 190024, Dec. 2020, doi: 10.1063/5.0032337.
[81] A. Benato, "Performance and cost evaluation of an innovative Pumped Thermal Electricity Storage power system," *Energy*, vol. 138, pp. 419–436, Nov. 2017, doi: 10.1016/j.energy.2017.07.066.
[82] J. D. McTigue, A. J. White, and C. N. Markides, "Parametric studies and optimisation of pumped thermal electricity storage," *Applied Energy*, vol. 137, pp. 800–811, Jan. 2015, doi: 10.1016/j.apenergy.2014.08.039.
[83] N. R. Smith *et al.*, "The Design of a Small-Scale Pumped Heat Energy Storage System for the Demonstration of Controls and Operability," presented at the ASME Turbo Expo 2022: Turbomachinery Technical Conference and Exposition, American Society of Mechanical Engineers Digital Collection, Oct. 2022. doi: 10.1115/GT2022-83424.
[84] C. S. Lai and M. D. McCulloch, "Levelized cost of electricity for solar photovoltaic and electrical energy storage," *Applied Energy*, vol. 190, pp. 191–203, Mar. 2017, doi: 10.1016/j.apenergy.2016.12.153.
[85] Z. Song *et al.*, "Multi-objective optimization of a semi-active battery/supercapacitor energy storage system for electric vehicles," *Applied Energy*, vol. 135, pp. 212–224, Dec. 2014, doi: 10.1016/j.apenergy.2014.06.087.
[86] F. Díaz-González, A. Sumper, O. Gomis-Bellmunt, and F. D. Bianchi, "Energy management of flywheel-based energy storage device for wind power smoothing," *Applied Energy*, vol. 110, pp. 207–219, Oct. 2013, doi: 10.1016/j.apenergy.2013.04.029.
[87] M. C. Massaro, R. Biga, A. Kolisnichenko, P. Marocco, A. H. A. Monteverde, and M. Santarelli, "Potential and technical challenges of on-board hydrogen storage technologies coupled with fuel cell systems for aircraft electrification," *Journal of Power Sources*, vol. 555, p. 232397, Jan. 2023, doi: 10.1016/j.jpowsour.2022.232397.
[88] P. Hendrick, "Introduction to Hydro Energy Storage," in *Encyclopedia of Energy Storage*, L. F. Cabeza, Ed., Oxford: Elsevier, 2022, pp. 100–103. doi: 10.1016/B978-0-12-819723-3.00158-X.
[89] M. Amir *et al.*, "Energy storage technologies: An integrated survey of developments, global economical/environmental effects, optimal scheduling model, and sustainable adaption policies," *Journal of Energy Storage*, vol. 72, p. 108694, Nov. 2023, doi: 10.1016/j.est.2023.108694.
[90] Y. Han, H. Cui, H. Ma, J. Chen, and N. Liu, "Temperature and pressure variations in salt compressed air energy

storage (CAES) caverns considering the air flow in the underground wellbore," *Journal of Energy Storage*, vol. 52, p. 104846, Aug. 2022, doi: 10.1016/j.est.2022.104846.
[91] E. R. Barbour and D. L. F. Pottie, "Adiabatic Compressed Air Energy Storage Systems," in *Encyclopedia of Energy Storage*, L. F. Cabeza, Ed., Oxford: Elsevier, 2022, pp. 188–203. doi: 10.1016/B978-0-12-819723-3.00061-5.
[92] M. Gimeno-Gutiérrez and R. Lacal-Arántegui, "Assessment of the European potential for pumped hydropower energy storage based on two existing reservoirs," *Renewable Energy*, vol. 75, pp. 856–868, Mar. 2015, doi: 10.1016/j.renene.2014.10.068.
[93] W. He, M. King, X. Luo, M. Dooner, D. Li, and J. Wang, "Technologies and economics of electric energy storages in power systems: Review and perspective," *Advances in Applied Energy*, vol. 4, p. 100060, Nov. 2021, doi: 10.1016/j.adapen.2021.100060.
[94] M. Fürsch, S. Hagspiel, C. Jägemann, S. Nagl, D. Lindenberger, and E. Tröster, "The role of grid extensions in a cost-efficient transformation of the European electricity system until 2050," *Applied Energy*, vol. 104, pp. 642–652, Apr. 2013, doi: 10.1016/j.apenergy.2012.11.050.
[95] A. Smallbone, V. Jülch, R. Wardle, and A. P. Roskilly, "Levelised Cost of Storage for Pumped Heat Energy Storage in comparison with other energy storage technologies," *Energy Conversion and Management*, vol. 152, pp. 221–228, Nov. 2017, doi: 10.1016/j.enconman.2017.09.047.
[96] S. Georgiou, N. Shah, and C. N. Markides, "A thermo-economic analysis and comparison of pumped-thermal and liquid-air electricity storage systems," *Applied Energy*, vol. 226, pp. 1119–1133, Sep. 2018, doi: 10.1016/j.apenergy.2018.04.128.
[97] G. F. Frate, L. Ferrari, and U. Desideri, "Critical review and economic feasibility analysis of electric energy storage technologies suited for grid scale applications," *E3S Web Conf.*, vol. 137, p. 01037, 2019, doi: 10.1051/e3sconf/201913701037.
[98] J. Howes, "Concept and Development of a Pumped Heat Electricity Storage Device," *Proceedings of the IEEE*, vol. 100, no. 2, pp. 493–503, Feb. 2012, doi: 10.1109/JPROC.2011.2174529.
[99] V. Novotny, V. Basta, P. Smola, and J. Spale, "Review of Carnot Battery Technology Commercial Development," *Energies*, vol. 15, no. 2, Art. no. 2, Jan. 2022, doi: 10.3390/en15020647.
[100] "Barmeier, T. Electric Thermal Energy Storage (ETES) Transition of Energy Supply. 26. Wind. Warn., Warnemünde, Germany. 2017. Available online: https://windenergietage.de/wp-content/uploads/sites/2/2017/11/26WT0811_F11_1120_Dr_Barmeier.pdf."
[101] "Witold, A. StoreToPower Pilot Plant for the Development of a Heat Storage Power Plant. 2nd Int. Work. Carnot Batter; DLR: Stuttgart, Germany, 2020."
[102] "E2S Power |." Accessed: May 30, 2024. [Online]. Available: https://e2s-power.com/
[103] "Schäfer, T. Thermo-MechanischerSpeicher (CARNOT-Batterie). Zittau, Germany. 2020. Available online: https://www.cleantechost.
de/fileadmin/user_upload/chefredakteur1/AK_Energiespeicher/IV_IPM_Thermomechanischer_Speicher_Schaefer.pdf."
[104] D. Steger, J. Karl, and E. Schlücker, "LAUNCH AND FIRST EXPERIMENTAL RESULTS OF A REVERSIBLE HEAT PUMP-ORC PILOT PLANT AS CARNOT BATTERY," 2021. Accessed: May 30, 2024. [Online]. Available: https://www.semanticscholar.org/paper/LAUNCH-AND-FIRST-EXPERIMENTAL-RESULTS-OF-A-HEAT-AS-Steger-Karl/c1eaacfdf09d7a7495608b5bfaaab26fe5ceb88e
[105] V. Palomba, E. Borri, A. Charalampidis, A. Frazzica, L. F. Cabeza, and S. Karellas, "Implementation of a solar-biomass system for multi-family houses: Towards 100% renewable energy utilization," *Renewable Energy*, vol. 166, pp. 190–209, Apr. 2020, doi: 10.1016/j.renene.2020.11.126.
[106] F. Kaufmann, C. Schifflechner, C. Wieland, and S. Hartmut, "DESIGN AND CONSTRUCTION OF A REVERSIBLE ORC TEST RIG FOR GEOTHERMAL CHP APPLICATIONS," Sep. 2023.
[107] O. Dumont, A. Charalampidis, and V. Lemort, "Experimental Investigation Of A Thermally Integrated Carnot Battery Using A Reversible Heat Pump/Organic Rankine Cycle," *International Refrigeration and Air Conditioning Conference*, May 2021, [Online]. Available: https://docs.lib.purdue.edu/iracc/2085
[108] "The Project » CHESTER Project," CHESTER Project. Accessed: Jan. 25, 2023. [Online]. Available: https://www.chester-project.eu/about-chester/the-project/
[109] FutureBay, "FutureBay," FutureBay. Accessed: May 30, 2024. [Online]. Available: https://futurebay.uk.com/
[110] "Karthäuser, J. The Low Tempeature (80–120 _C) Carnot Battery and its Potential for the Integrated Energy System. 2nd Int. Work. Carnot Batter; DLR: Stuttgart, Germany, 2020."
[111] V. Novotny, S. Mach, M. Rathan, V. Bašta, and J. Špale, *Modelling and experimental development of a waste heat upgrade integrated ORC Carnot battery with stone dust thermal storage*. 2021. doi: 10.13140/RG.2.2.31010.76486/1.
[112] L. Sanz Garcia, E. Jacquemoud, and P. Jenny, "Thermo-economic heat exchanger optimization for Electro-Thermal Energy Storage based on transcritical CO2 cycles," *3rd European Conference on Supercritical CO2 (sCO2) Power Systems 2019: 19th-20th September 2019*, pp. 353–362, Oct. 2019, doi: 10.17185/duepublico/48917.
[113] "EPS100 | Echogen Power Systems." Accessed: Jan. 11, 2021. [Online]. Available:

https://www.echogen.com/our-solution/product-series/eps100/
[114] M. Astolfi, D. Rizzi, E. Macchi, and C. Spadacini, "A Novel Energy Storage System Based on Carbon Dioxide Unique Thermodynamic Properties," presented at the ASME Turbo Expo 2021: Turbomachinery Technical Conference and Exposition, American Society of Mechanical Engineers Digital Collection, Sep. 2021. doi: 10.1115/GT2021-59487.
[115] "Projects," Highview Power. Accessed: May 30, 2024. [Online]. Available: https://highviewpower.com/projects/
[116] "Aga, V.; Conte, E.; Carroni, R.; Burcker, B.; Ramond, M. Supercritical CO2-Based Heat Pump Cycle for Electrical Energy Storage for Utility Scale Dispatchable Renewable Energy Power Plants. In Proceedings of the 5th International Symposium—Supercritical CO2 Power Cycles, San Antonio, TX, USA, 28–31 March 2016."
[117] "Anderson, B.N. Modular Solar Systems for 24/7 Scalable, Flexible, Affordable Electricity. In Proceedings of the ASME Power Conference, Charlotte, NC, USA, 26–30 June 2017; Volume 2, p. V002T09A002."
[118] J. Parham, P. Vrettos, and N. Levinson, "Chapter 13 - Commercialisation of ultra-high temperature energy storage applications: the 1414 Degrees approach," in *Ultra-High Temperature Thermal Energy Storage, Transfer and Conversion*, A. Datas, Ed., in Woodhead Publishing Series in Energy. , Woodhead Publishing, 2021, pp. 331–346. doi: 10.1016/B978-0-12-819955-8.00013-2.
[119] "Technology - Peregrine Turbine Technologies Info." Accessed: May 30, 2024. [Online]. Available: https://www.peregrineturbine.com/technology/
[120] X. J. Xue, H. N. Wang, J. H. Wang, B. Yang, J. Yan, and C. Y. Zhao, "Experimental and numerical investigation on latent heat/cold stores for advanced pumped-thermal energy storage," *Energy*, vol. 300, p. 131490, Aug. 2024, doi: 10.1016/j.energy.2024.131490.
[121] "The GridScale technology explained | Stiesdal." Accessed: May 30, 2024. [Online]. Available: https://www.stiesdal.com/storage/the-gridscale-technology-explained/
[122] "WindTP – Wind Driven Thermal Pumping." Accessed: May 30, 2024. [Online]. Available: https://www.windtp.com/
[123] G. Schneider, H. Maier, J. Häcker, and S. Siegele, "Electricity Storage With a Solid Bed High Temperature Thermal Energy Storage System (HTTES) - A Methodical Approach to Improve the Pumped Thermal Grid Storage Concept," Jan. 2021. doi: 10.2991/ahe.k.210202.005.
[124] R. B. Laughlin, "Pumped thermal grid storage with heat exchange," *Journal of Renewable and Sustainable Energy*, vol. 9, no. 4, p. 044103, Aug. 2017, doi: 10.1063/1.4994054.
[125] S. Hamdy, T. Morosuk, and G. Tsatsaronis, "Exergetic and economic assessment of integrated cryogenic energy storage systems," *Cryogenics*, vol. 99, pp. 39–50, Apr. 2019, doi: 10.1016/j.cryogenics.2019.02.009.
[126] S. Sharma and M. Mortazavi, "Pumped thermal energy storage: A review," *International Journal of Heat and Mass Transfer*, vol. 213, p. 124286, Oct. 2023, doi: 10.1016/j.ijheatmasstransfer.2023.124286.
[127] F. Nitsch, M. Wetzel, H. C. Gils, and K. Nienhaus, "The future role of Carnot batteries in Central Europe: Combining energy system and market perspective," *Journal of Energy Storage*, vol. 85, p. 110959, Apr. 2024, doi: 10.1016/j.est.2024.110959.
[128] G. Zampieri, "'Closed-cycle plant' U.S. Patent US2016/0032786A1, Feb. 4, 2016," US20160032786A1, Feb. 04, 2016 Accessed: May 05, 2020. [Online]. Available: https://patents.google.com/patent/US20160032786/en
[129] S. Ottaviano, "TEST BENCH DEVELOPMENT, EXPERIMENTAL ANALYSIS AND MODELLING OF MICRO-ORGANIC RANKINE CYCLE FOR LOW-GRADE HEAT RECOVERY," Università di Bologna, 2020.
[130] M. Bianchi *et al.*, "Performance and operation of micro-ORC energy system using geothermal heat source," *Energy Procedia*, vol. 148, pp. 384–391, Aug. 2018, doi: 10.1016/j.egypro.2018.08.099.
[131] "R-134a, its properties and alternatives - Infraserv.com." Accessed: Jun. 03, 2024. [Online]. Available: https://www.infraserv.com/en/services/facility-management/expertise/f-gas/refrigerant/specific-refrigerant/r-134a.html
[132] Eric W. Lemmon, Ian H. Bell, Marcia L. Huber, and Mark O. McLinden, *REFPROP 10.0 Standard Reference Database 23*. National Institute of Standards and Technology, Boulder, Colorado, United States.
[133] S. Lecompte, H. Huisseune, M. van den Broek, B. Vanslambrouck, and M. De Paepe, "Review of organic Rankine cycle (ORC) architectures for waste heat recovery," *Renewable and Sustainable Energy Reviews*, vol. 47, pp. 448–461, Jul. 2015, doi: 10.1016/j.rser.2015.03.089.
[134] B. Saleh, G. Koglbauer, M. Wendland, and J. Fischer, "Working fluids for low-temperature organic Rankine cycles," *Energy*, vol. 32, no. 7, Art. no. 7, Jul. 2007, doi: 10.1016/j.energy.2006.07.001.
[135] M. Kim, S. H. Yoon, P. A. Domanski, and W. Vance Payne, "Design of a steady-state detector for fault detection and diagnosis of a residential air conditioner," *International Journal of Refrigeration*, vol. 31, no. 5, Art. no. 5, Aug. 2008, doi: 10.1016/j.ijrefrig.2007.11.008.
[136] N. Torricelli, "Modelling of ORC components and systems for low-medium temperature heat recovery applications with reduced environmental impact," Doctoral Thesis, Alma Mater Studiorum - Università di Bologna, 2022. doi: 10.48676/unibo/amsdottorato/10034.
[137] "Bianchi, M., Branchini, L., Casari, N., Pascale, A.D., Fadiga, E., Melino, F., Ottaviano, S., Peretto, A., Pinelli, M.,

Spina, P.R., Suman, A., 2019. Uncertainty quantification of performance parameters in a small scale ORC test rig. Proceedings of the 5th International Seminar on ORC Power Systems 9 - 11 September 2019, Athens, Greece."
[138] M. Bianchi *et al.*, "Performance prediction of a reciprocating piston expander with semi-empirical models," *Energy Procedia*, vol. 158, pp. 1737–1743, 2019.
[139] M. Bianchi *et al.*, "Performance and total warming impact assessment of pure fluids and mixtures replacing HFCs in micro-ORC energy systems," *Applied Thermal Engineering*, vol. 203, p. 117888, Feb. 2022, doi: 10.1016/j.applthermaleng.2021.117888.
[140] R. Dickes, O. Dumont, R. Daccord, S. Quoilin, and V. Lemort, "Modelling of organic Rankine cycle power systems in off-design conditions: An experimentally-validated comparative study," *Energy*, vol. 123, pp. 710–727, Mar. 2017, doi: 10.1016/j.energy.2017.01.130.
[141] D. Ziviani *et al.*, "Development and a Validation of a Charge Sensitive Organic Rankine Cycle (ORC) Simulation Tool," *Energies*, vol. 9, no. 6, Art. no. 6, Jun. 2016, doi: 10.3390/en9060389.
[142] R. Dickes, O. Dumont, L. Guillaume, S. Quoilin, and V. Lemort, "Charge-sensitive modelling of organic Rankine cycle power systems for off-design performance simulation," *Applied Energy*, vol. 212, pp. 1262–1281, Feb. 2018, doi: 10.1016/j.apenergy.2018.01.004.
[143] D. Ziviani, R. Dickes, V. Lemort, and J. E. B. and E. A. Groll, "Effects of the Working Fluid Charge in Organic Rankine Cycle Power Systems: Numerical and Experimental Analyses," *Organic Rankine Cycle Technology for Heat Recovery*, Nov. 2018, doi: 10.5772/intechopen.78026.
[144] M. Bianchi *et al.*, "Application and comparison of semi-empirical models for performance prediction of a kW-size reciprocating piston expander," *Applied Energy*, vol. 249, pp. 143–156, Sep. 2019, doi: 10.1016/j.apenergy.2019.04.070.
[145] Y. Glavatskaya, P. Podevin, V. Lemort, O. Shonda, and G. Descombes, "Reciprocating Expander for an Exhaust Heat Recovery Rankine Cycle for a Passenger Car Application," *Energies*, vol. 5, no. 6, Art. no. 6, Jun. 2012, doi: 10.3390/en5061751.
[146] M. Bianchi *et al.*, "Performance modelling and greenhouse impact assessment of a micro-ORC energy system working with HFCs, low GWP fluids and mixtures," presented at the 100RES 2020 – Applied Energy Symposium (ICAE), Virtual, Online, Oct. 2020.
[147] A. Giuffrida, "Modelling the performance of a scroll expander for small organic Rankine cycles when changing the working fluid," *Applied Thermal Engineering*, vol. 70, no. 1, Art. no. 1, Sep. 2014, doi: 10.1016/j.applthermaleng.2014.06.004.
[148] K.-Y. Lai, Y.-T. Lee, M.-R. Chen, and Y.-H. Liu, "Comparison of the Trilateral Flash Cycle and Rankine Cycle with Organic Fluid Using the Pinch Point Temperature," *Entropy*, vol. 21, no. 12, Art. no. 12, Dec. 2019, doi: 10.3390/e21121197.
[149] R. McGinty *et al.*, "Techno-economic survey and design of a pilot test rig for a trilateral flash cycle system in a steel production plant," *Energy Procedia*, vol. 123, pp. 281–288, Sep. 2017, doi: 10.1016/j.egypro.2017.07.242.
[150] A. Skiadopoulos, X. van Heule, G. Kosmadakis, D. Manolakos, M. D. Paepe, and S. Lecompte, "THERMODYNAMIC LOW-ORDER MODEL FOR THE SIMULATION OF TWO- PHASE EXPANSION IN A TFC UNIT," p. 10, 2021.
[151] Q. Wang, W. Wu, Z. He, and D. Ziviani, "Analysis of the intake process and its influence on the performance of a two-phase reciprocating expander," *Applied Thermal Engineering*, vol. 160, p. 113943, Sep. 2019, doi: 10.1016/j.applthermaleng.2019.113943.
[152] M. T. White, "Cycle and turbine optimisation for an ORC operating with two-phase expansion," *Applied Thermal Engineering*, vol. 192, p. 116852, Jun. 2021, doi: 10.1016/j.applthermaleng.2021.116852.
[153] K. Braimakis and S. Karellas, "Exergy efficiency potential of dual-phase expansion trilateral and partial evaporation ORC with zeotropic mixtures," *Energy*, vol. 262, p. 125475, Jan. 2023, doi: 10.1016/j.energy.2022.125475.
[154] S. Lecompte, M. A. Chatzopoulou, C. N. Markides, and M. De Paepe, "Off-design comparison of subcritical and partial evaporating ORCs in quasi-steady state annual simulations," *Energy Procedia*, vol. 158, pp. 2064–2069, Feb. 2019, doi: 10.1016/j.egypro.2019.01.477.
[155] E. Bellos, P. Lykas, C. Sammoutos, A. Kitsopoulou, D. Korres, and C. Tzivanidis, "Thermodynamic investigation of a solar-driven organic Rankine cycle with partial evaporation," *Energy Nexus*, vol. 11, p. 100229, Sep. 2023, doi: 10.1016/j.nexus.2023.100229.
[156] R. F. Steidel Jr., H. Weiss, and J. E. Flower, "Performance Characteristics of the Lysholm Engine as Tested for Geothermal Power Applications in the Imperial Valley," *Journal of Engineering for Power*, vol. 104, no. 1, pp. 231–240, Jan. 1982, doi: 10.1115/1.3227255.
[157] I. K. Smith, N. Stošič, and C. A. Aldis, "Development of the Trilateral Flash Cycle System Part 2: Increasing Power Output with Working Fluid Mixtures," *Proc. Inst. Mech. Eng. Part A J. Power Energy*, vol. 210, no. 1, pp. 75–93, 1996.
[158] H. Öhman and P. Lundqvist, "Experimental investigation of a Lysholm Turbine operating with superheated, saturated and 2-phase inlet conditions," *Applied Thermal Engineering*, vol. 50, no. 1, Art. no. 1, Jan. 2013, doi:

10.1016/j.applthermaleng.2012.08.035.
[159] A. Iqbal, "Experimental study on the prospect of low-temperature heat to power generation using Trilateral Flash Cycle (TFC)," *Applied Thermal Engineering*, p. 13, 2020.
[160] F. Dawo, J. Buhr, C. Wieland, and H. Spliethoff, "EXPERIMENTAL INVESTIGATION OF THE PARTIAL EVAPORATED ORGANIC RANKINE CYCLE FOR VARIOUS HEAT SOURCE CONDITIONS," p. 9, 2021.
[161] H. Kanno and N. Shikazono, "Experimental and modeling study on adiabatic two-phase expansion in a cylinder," *International Journal of Heat and Mass Transfer*, vol. 86, pp. 755–763, Jul. 2015, doi: 10.1016/j.ijheatmasstransfer.2015.02.059.
[162] M. K. Löffler, "Flash Evaporation in Cyclones," *Chemical Engineering & Technology*, vol. 31, no. 7, pp. 1062–1065, 2008, doi: 10.1002/ceat.200700470.
[163] S. Ottaviano, C. Poletto, M. A. Ancona, and F. Melino, "Experimental investigation on micro-ORC system operating with partial evaporation and two–phase expansion," *Energy Conversion and Management*, vol. 274, p. 116415, Dec. 2022, doi: 10.1016/j.enconman.2022.116415.
[164] W. C. Reynolds and H. C. Perkins, *ENGINEERING THERMODYNAMICS*, Second. McGraw-Hill, Inc., 1977.
[165] F. P. Incropera, D. P. Dewitt, T. L. Bergman, and A. S. Lavine, *Introduction to Heat Transfer*, Fifth. John Wiley & Sons, Inc., 2007.
[166] R. Dickes, A. Desideri, E. Casati, and S. Quoilin, "From 1885 To Nowadays: A (Short) Techno-historical Review Of Solar Organic Rankine Cycle Systems," presented at the 6th International Seminar on ORC Power Systems, Technical University of Munich, 2021. Accessed: Jul. 04, 2024. [Online]. Available: https://orbi.uliege.be/handle/2268/302909
[167] P. A. Østergaard, N. Duic, Y. Noorollahi, and S. Kalogirou, "Latest progress in Sustainable Development using renewable energy technology," *Renewable Energy*, vol. 162, pp. 1554–1562, Dec. 2020, doi: 10.1016/j.renene.2020.09.124.
[168] K. Soulis, D. Manolakos, E. Ntavou, and G. Kosmadakis, "Preliminary operation assessment of a two-stage ORC engine combined with evacuated tube solar collectors throughout Greece," presented at the ORC, Munich, Germany, 2021.
[169] W. Lombardo, S. Ottaviano, L. Branchini, S. Vasta, A. De Pascale, and A. Sapienza, "A dynamic model of a solar driven trigeneration system based on micro-ORC and adsorption chiller prototypes," *AIP Conference Proceedings*, vol. 2191, no. 1, p. 020098, Dec. 2019, doi: 10.1063/1.5138831.
[170] F. Calise, M. D. d'Accadia, M. Vicidomini, and M. Scarpellino, "Design and simulation of a prototype of a small-scale solar CHP system based on evacuated flat-plate solar collectors and Organic Rankine Cycle," *Energy Conversion and Management*, vol. 90, pp. 347–363, Jan. 2015, doi: 10.1016/j.enconman.2014.11.014.
[171] T. C. Roumpedakis, G. Loumpardis, E. Monokrousou, K. Braimakis, A. Charalampidis, and S. Karellas, "Exergetic and economic analysis of a solar driven small scale ORC," *Renewable Energy*, vol. 157, pp. 1008–1024, Sep. 2020, doi: 10.1016/j.renene.2020.05.016.
[172] C. Kutlu, M. T. Erdinc, J. Li, Y. Wang, and Y. Su, "A study on heat storage sizing and flow control for a domestic scale solar-powered organic Rankine cycle-vapour compression refrigeration system," *Renewable Energy*, vol. 143, pp. 301–312, Dec. 2019, doi: 10.1016/j.renene.2019.05.017.
[173] S. Quoilin, O. Dumont, K. Hansen, and V. Lemort, "Design, Modeling, and Performance Optimization of a Reversible Heat Pump/Organic Rankine Cycle System for Domestic Application," *Journal of Engineering for Gas Turbines and Power*, vol. 138, Jul. 2015, doi: 10.1115/1.4031004.
[174] Z. Liu, A. Romagnoli, P. Sapin, C. Markides, and M. Mersch, "Dynamic control strategies for a solar-ORC system using first-law dynamic and data-driven machine learning models," presented at the ORC, Munich, Germany, 2021.
[175] M. Ciani Bassetti, D. Consoli, G. Manente, and A. Lazzaretto, "Design and off-design models of a hybrid geothermal-solar power plant enhanced by a thermal storage," *Renewable Energy*, vol. 128, pp. 460–472, Dec. 2018, doi: 10.1016/j.renene.2017.05.078.
[176] D. Gao, J. Li, Y. Hao, and G. Pei, "A novel solar-driven Organic Rankine Cycle system based on the two-stage solar thermal collection and accumulation," *Applied Thermal Engineering*, vol. 234, p. 121249, Nov. 2023, doi: 10.1016/j.applthermaleng.2023.121249.
[177] M. F. Qureshi, M. W. Chandio, A. A. Memon, L. Kumar, and M. M. Awad, "Thermal analysis of solar energy based organic Rankine cycle cascaded with vapor compression refrigeration cycle," *Energy Nexus*, vol. 14, p. 100291, Jul. 2024, doi: 10.1016/j.nexus.2024.100291.
[178] A. Alghamdi, J. Jose Ponnore, A. M Hassan, S. Alqahtani, S. Alshehery, and A. E Anqi, "Exergy-economic analysis of a hybrid combined supercritical Brayton cycle-organic Rankine cycle using biogas and solar PTC system as energy sources," *Case Studies in Thermal Engineering*, vol. 50, p. 103484, Oct. 2023, doi: 10.1016/j.csite.2023.103484.
[179] L. Chen *et al.*, "Thermodynamic analysis of a hybrid energy system coupling solar organic Rankine cycle and ground source heat pump: Exploring heat cascade utilization," *Energy*, vol. 284, p. 129228, Dec. 2023, doi: 10.1016/j.energy.2023.129228.

[180] K. Yang *et al.*, "Exergy, exergoeconomic, and exergoenvironmental analyses of novel solar- and biomass-driven trigeneration system integrated with organic Rankine cycle," *Energy*, vol. 301, p. 131605, Aug. 2024, doi: 10.1016/j.energy.2024.131605.
[181] M. Pezo, C. Cuevas, E. Wagemann, and A. Cendoya, "Net Zero Energy Building technologies – Reversible Heat Pump/Organic Rankine Cycle coupled with Solar Collectors and combined Heat Pump/Photovoltaics – Case study of a Chilean mid-rise residential building," *Applied Thermal Engineering*, vol. 252, p. 123683, Sep. 2024, doi: 10.1016/j.applthermaleng.2024.123683.
[182] G. Valencia Ochoa, E. V. Ortiz, and J. D. Forero, "Thermo-economic and environmental optimization using PSO of solar organic Rankine cycle with flat plate solar collector," *Heliyon*, vol. 9, no. 3, p. e13697, Mar. 2023, doi: 10.1016/j.heliyon.2023.e13697.
[183] X. Qi *et al.*, "Conventional and advanced exergy-exergoeconomic-exergoenvironmental analyses of an organic Rankine cycle integrated with solar and biomass energy sources," *Energy*, vol. 288, p. 129657, Feb. 2024, doi: 10.1016/j.energy.2023.129657.
[184] D. A. Rodriguez-Pastor, J. A. Becerra, and R. Chacartegui, "Adaptation of residential solar systems for domestic hot water (DHW) to hybrid organic Rankine Cycle (ORC) distributed generation," *Energy*, vol. 263, p. 125901, Jan. 2023, doi: 10.1016/j.energy.2022.125901.
[185] Y. Li, S. Teng, and H. Xi, "3E analyses of a cogeneration system based on compressed air energy storage system, solar collector and organic Rankine cycle," *Case Studies in Thermal Engineering*, vol. 42, p. 102753, Feb. 2023, doi: 10.1016/j.csite.2023.102753.
[186] V. N. Nguyen *et al.*, "Combination of solar with organic Rankine cycle as a potential solution for clean energy production," *Sustainable Energy Technologies and Assessments*, vol. 57, p. 103161, Jun. 2023, doi: 10.1016/j.seta.2023.103161.
[187] I. Garcia-Saez, J. Méndez, C. Ortiz, D. Loncar, J. A. Becerra, and R. Chacartegui, "Energy and economic assessment of solar Organic Rankine Cycle for combined heat and power generation in residential applications," *Renewable Energy*, vol. 140, pp. 461–476, Sep. 2019, doi: 10.1016/j.renene.2019.03.033.
[188] "Residential Heating Residential Cooling Heat Pumps Solar Thermal and Cylinders Commercial Heating Commercial Cooling System Complementary Items PRODUCT CATALOGUE 2015 INTERNATIONAL MARKETS, (2015). www.riello.com."
[189] "Global warming potential (GWP) of HFC refrigerants." Accessed: Jul. 10, 2024. [Online]. Available: https://iifiir.org/en/encyclopedia-of-refrigeration/global-warming-potential-gwp-of-hfc-refrigerants
[190] I. H. Bell, P. A. Domanski, M. O. McLinden, and G. T. Linteris, "The hunt for nonflammable refrigerant blends to replace R-134a," *International Journal of Refrigeration*, vol. 104, pp. 484–495, Aug. 2019, doi: 10.1016/j.ijrefrig.2019.05.035.
[191] "Thermophysical properties of HFO refrigerants." Accessed: Jul. 10, 2024. [Online]. Available: https://iifiir.org/en/encyclopedia-of-refrigeration/thermophysical-properties-of-hfo-refrigerants
[192] "UNI 10349-1:2016 - UNI Ente Italiano di Normazione." Accessed: Jul. 12, 2024. [Online]. Available: https://store.uni.com/uni-10349-1-2016
[193] M. Bernardini, "Inclinazione e orientamento dei pannelli fotovoltaici e solari termici," Aggiustatutto. Accessed: Jul. 12, 2024. [Online]. Available: https://www.aggiustatutto.it/inclinazione-pannelli-fotovoltaici-solari-termici/
[194] "Atlante italiano della radiazione solare." Accessed: Jul. 12, 2024. [Online]. Available: http://www.solaritaly.enea.it/CalcRggmmOrizz/Calcola.php
[195] E. Macchi, S. Campanari, and P. Silva, *La climatizzazione a gas naturale e ad azionamento termico*. Polipress, 2012.
[196] "Come vanno i prezzi dell'energia elettrica in Italia: i dati dell'Autorità | QualEnergia.it." Accessed: Jul. 12, 2024. [Online]. Available: https://www.qualenergia.it/articoli/come-vanno-i-prezzi-dellenergia-elettrica-in-italia-i-dati-dellautorita/
[197] S. A. Kalogirou, R. Agathokleous, G. Barone, A. Buonomano, C. Forzano, and A. Palombo, "Development and validation of a new TRNSYS Type for thermosiphon flat-plate solar thermal collectors: energy and economic optimization for hot water production in different climates," *Renewable Energy*, vol. 136, pp. 632–644, Jun. 2019, doi: 10.1016/j.renene.2018.12.086.
[198] V. Ljungdahl, M. Jradi, and C. Veje, "A decision support model for waste heat recovery systems design in Data Center and High-Performance Computing clusters utilizing liquid cooling and Phase Change Materials," *Applied Thermal Engineering*, vol. 201, p. 117671, Jan. 2022, doi: 10.1016/j.applthermaleng.2021.117671.
[199] E. Oró, P. Taddeo, and J. Salom, "Waste heat recovery from urban air cooled data centres to increase energy efficiency of district heating networks," *Sustainable Cities and Society*, vol. 45, pp. 522–542, Feb. 2019, doi: 10.1016/j.scs.2018.12.012.
[200] E. Oró, R. Allepuz, I. Martorell, and J. Salom, "Design and economic analysis of liquid cooled data centres for waste heat recovery: A case study for an indoor swimming pool," *Sustainable Cities and Society*, vol. 36, pp. 185–203, Jan. 2018, doi: 10.1016/j.scs.2017.10.012.

[201] C. Zhang, H. Luo, and Z. Wang, "An economic analysis of waste heat recovery and utilization in data centers considering environmental benefits," *Sustainable Production and Consumption*, vol. 31, pp. 127–138, May 2022, doi: 10.1016/j.spc.2022.02.006.
[202] J. Yu, Y. Jiang, and Y. Yan, "A simulation study on heat recovery of data center: A case study in Harbin, China," *Renewable Energy*, vol. 130, pp. 154–173, Jan. 2019, doi: 10.1016/j.renene.2018.06.067.
[203] M. Deymi-Dashtebayaz and S. Valipour-Namanlo, "Thermoeconomic and environmental feasibility of waste heat recovery of a data center using air source heat pump," *Journal of Cleaner Production*, vol. 219, pp. 117–126, May 2019, doi: 10.1016/j.jclepro.2019.02.061.
[204] K. Ebrahimi, G. F. Jones, and A. S. Fleischer, "Thermo-economic analysis of steady state waste heat recovery in data centers using absorption refrigeration," *Applied Energy*, vol. 139, pp. 384–397, Feb. 2015, doi: 10.1016/j.apenergy.2014.10.067.
[205] R. Gupta and I. K. Puri, "Waste heat recovery in a data center with an adsorption chiller: Technical and economic analysis," *Energy Conversion and Management*, vol. 245, p. 114576, Oct. 2021, doi: 10.1016/j.enconman.2021.114576.
[206] J. Ding, H. Zhang, D. Leng, H. Xu, C. Tian, and Z. Zhai, "Experimental investigation and application analysis on an integrated system of free cooling and heat recovery for data centers," *International Journal of Refrigeration*, Jan. 2022, doi: 10.1016/j.ijrefrig.2022.01.003.
[207] X. Lin, L. Zuo, L. Yin, W. Su, and S. Ou, "An idea to efficiently recover the waste heat of Data Centers by constructing an integrated system with carbon dioxide heat pump, mechanical subcooling cycle and lithium bromide-water absorption refrigeration cycle," *Energy Conversion and Management*, vol. 256, p. 115398, Mar. 2022, doi: 10.1016/j.enconman.2022.115398.
[208] B.-S. Park, M. Usman, M. Imran, and A. Pesyridis, "Review of Organic Rankine Cycle experimental data trends," *Energy Conversion and Management*, vol. 173, pp. 679–691, Oct. 2018, doi: 10.1016/j.enconman.2018.07.097.
[209] K. Ebrahimi, G. F. Jones, and A. S. Fleischer, "The viability of ultra low temperature waste heat recovery using organic Rankine cycle in dual loop data center applications," *Applied Thermal Engineering*, vol. 126, pp. 393–406, Nov. 2017, doi: 10.1016/j.applthermaleng.2017.07.001.
[210] Z. M. Marshall and J. Duquette, "A techno-economic evaluation of low global warming potential heat pump assisted organic Rankine cycle systems for data center waste heat recovery," *Energy*, vol. 242, p. 122528, Mar. 2022, doi: 10.1016/j.energy.2021.122528.
[211] M. R. Jawad Al-Tameemi, Y. Liang, and Z. Yu, "Combined ORC-HP thermodynamic cycles for DC cooling and waste heat recovery for central heating," *Energy Procedia*, vol. 158, pp. 2046–2051, Feb. 2019, doi: 10.1016/j.egypro.2019.01.471.
[212] M. Temiz and I. Dincer, "A unique bifacial PV and hydrogen-based cleaner energy system with heat recovery for data centers," *Applied Thermal Engineering*, vol. 206, p. 118102, Apr. 2022, doi: 10.1016/j.applthermaleng.2022.118102.
[213] M. Temiz and I. Dincer, "A newly developed solar-based cogeneration system with energy storage and heat recovery for sustainable data centers: Energy and exergy analyses," *Sustainable Energy Technologies and Assessments*, vol. 52, p. 102145, Aug. 2022, doi: 10.1016/j.seta.2022.102145.
[214] O. Corigliano, A. Algieri, and P. Fragiacomo, "Turning Data Center Waste Heat into Energy: A Guide to Organic Rankine Cycle System Design and Performance Evaluation," *Applied Sciences*, vol. 14, no. 14, Art. no. 14, Jan. 2024, doi: 10.3390/app14146046.
[215] M. Bianchi *et al.*, "Performance modelling and greenhouse impact assessment of a micro-ORC energy system working with HFCs, low GWP fluids and mixtures," vol. 238, p. 10002, Oct. 2021, doi: 10.1051/e3sconf/202123810002.
[216] C. M. Invernizzi, P. Iora, M. Preißinger, and G. Manzolini, "HFOs as substitute for R-134a as working fluids in ORC power plants: A thermodynamic assessment and thermal stability analysis," *Applied Thermal Engineering*, vol. 103, pp. 790–797, Jun. 2016, doi: 10.1016/j.applthermaleng.2016.04.101.
[217] "Ceramic Industry Roadmap: Paving the way to 2050 | Cerame-Unie - The European Ceramic Industry Association." Accessed: Feb. 06, 2024. [Online]. Available: https://cerameunie.eu/topics/cerame-unie-sectors/cerame-unie/ceramic-industry-roadmap-paving-the-way-to-2050/
[218] J. I. Chowdhury, Y. Hu, I. Haltas, N. Balta-Ozkan, G. Jr. Matthew, and L. Varga, "Reducing industrial energy demand in the UK: A review of energy efficiency technologies and energy saving potential in selected sectors," *Renewable and Sustainable Energy Reviews*, vol. 94, pp. 1153–1178, Oct. 2018, doi: 10.1016/j.rser.2018.06.040.
[219] "BEIS, 2017. British Ceramic Confederation. Joint Industry - Government Industrial Decarbonisation and Energy Efficiency Roadmap Action Plan. Department for Business, Energy and Industrial Strategy, London."
[220] L. Branchini *et al.*, "Cogeneration Supporting the Energy Transition in the Italian Ceramic Tile Industry," *Sustainability*, vol. 13, no. 7, Art. no. 7, Jan. 2021, doi: 10.3390/su13074006.
[221] H. Ershadi and A. Karimipour, "Present a multi-criteria modeling and optimization (energy, economic and environmental) approach of industrial combined cooling heating and power (CCHP) generation systems using the genetic algorithm, case study: A tile factory," *Energy*, vol. 149, pp. 286–295, Apr. 2018, doi:

10.1016/j.energy.2018.02.034.
[222] M. A. Ancona *et al.*, "Energy and Environmental Assessment of Cogeneration in Ceramic Tiles Industry," *Energies*, vol. 16, no. 1, Art. no. 1, Jan. 2023, doi: 10.3390/en16010182.
[223] A. Mezquita, J. Boix, E. Monfort, and G. Mallol, "Energy saving in ceramic tile kilns: Cooling gas heat recovery," *Applied Thermal Engineering*, vol. 65, no. 1, pp. 102–110, Apr. 2014, doi: 10.1016/j.applthermaleng.2014.01.002.
[224] B. Delpech *et al.*, "Energy efficiency enhancement and waste heat recovery in industrial processes by means of the heat pipe technology: Case of the ceramic industry," *Energy*, vol. 158, pp. 656–665, Sep. 2018, doi: 10.1016/j.energy.2018.06.041.
[225] B. Delpech, B. Axcell, and H. Jouhara, "Experimental investigation of a radiative heat pipe for waste heat recovery in a ceramics kiln," *Energy*, vol. 170, pp. 636–651, Mar. 2019, doi: 10.1016/j.energy.2018.12.133.
[226] D. Brough *et al.*, "An experimental study and computational validation of waste heat recovery from a lab scale ceramic kiln using a vertical multi-pass heat pipe heat exchanger," *Energy*, vol. 208, p. 118325, Oct. 2020, doi: 10.1016/j.energy.2020.118325.
[227] H. Jouhara *et al.*, "Investigation on a full-scale heat pipe heat exchanger in the ceramics industry for waste heat recovery," *Energy*, vol. 223, p. 120037, May 2021, doi: 10.1016/j.energy.2021.120037.
[228] M. Milani, L. Montorsi, M. Stefani, R. Saponelli, and M. Lizzano, "Numerical analysis of an entire ceramic kiln under actual operating conditions for the energy efficiency improvement," *Journal of Environmental Management*, vol. 203, pp. 1026–1037, Dec. 2017, doi: 10.1016/j.jenvman.2017.03.076.
[229] M. Milani, L. Montorsi, M. Venturelli, J. M. Tiscar, and J. García-Ten, "A numerical approach for the combined analysis of the dynamic thermal behaviour of an entire ceramic roller kiln and the stress formation in the tiles," *Energy*, vol. 177, pp. 543–553, Jun. 2019, doi: 10.1016/j.energy.2019.04.037.
[230] M. Venturelli, D. Brough, M. Milani, L. Montorsi, and H. Jouhara, "Comprehensive numerical model for the analysis of potential heat recovery solutions in a ceramic industry," *International Journal of Thermofluids*, vol. 10, p. 100080, May 2021, doi: 10.1016/j.ijft.2021.100080.
[231] B. Peris, J. Navarro-Esbrí, F. Molés, and A. Mota-Babiloni, "Experimental study of an ORC (organic Rankine cycle) for low grade waste heat recovery in a ceramic industry," *Energy*, vol. 85, pp. 534–542, Jun. 2015, doi: 10.1016/j.energy.2015.03.065.
[232] *Thermoflex*. (2023). Thermoflow Inc., Jeckconville FL.
[233] "Air-to-Air Heat Exchangers For Healthier Energy-efficient Homes — Publications." Accessed: Feb. 08, 2024. [Online]. Available: https://www.ag.ndsu.edu/publicationS/energy/air-to-air-heat-exchangers-for-healthier-energy-efficient-homes
[234] *MATLAB 2019b*. © 1994-2020 The MathWorks, Inc., Natick, Massachusetts, United States.
[235] M. Monari, A. Montefusco, and F. Roveri, "Sicurezza degli impianti termici: camini, condotti e canne fumarie." Oct. 12, 2009. [Online]. Available: https://www.ausl.bologna.it/servt/dipt/dsp/uo/uoia/download-file-utili-istruzioni-operative/Sicurezza-degli-impianti-termici-camini-condotti-e/Sicurezza-degli-impianti-termici-camini-condotti-e/files/Sicurezza-degli-impianti-termici-camini-condotti-e.pdf
[236] A. Mezquita *et al.*, *ENERGY OPTIMISATION IN CERAMIC TILE MANUFACTURE BY USING THERMAL OIL*. 2012.
[237] O. Dumont, A. Reyes, and V. Lemort, "Modelling of a thermally integrated Carnot battery using a reversible heat pump/organic Rankine cycle," presented at the ecos conference, Japan, Oct. 2020.
[238] O. Dumont, C. Poletto, O. Thomé, and V. Lemort, "Methodology for the sizing of a Carnot battery based on a Rankine cycle and application to a 10 kWe system for district heating application," presented at the Proceedings of ECOS 2023 - The 36thInternational Conference on Efficiency, Cost, Optimization, Simulation and Environmental Impact of Energy Systems, Las Palmas De Gran Canaria, Spain, Jun. 2023.
[239] J. Niu, J. Wang, X. Liu, and L. Dong, "Optimal integration of solar collectors to Carnot battery system with regenerators," *Energy Conversion and Management*, vol. 277, p. 116625, Feb. 2023, doi: 10.1016/j.enconman.2022.116625.
[240] R. Tassenoy, K. Couvreur, W. Beyne, M. De Paepe, and S. Lecompte, "Techno-economic assessment of Carnot batteries for load-shifting of solar PV production of an office building," *Renewable Energy*, vol. 199, pp. 1133–1144, Nov. 2022, doi: 10.1016/j.renene.2022.09.039.
[241] X. Lin, P. Sun, W. Zhong, and J. Wang, "Thermodynamic analysis and operation investigation of a cross-border integrated energy system based on steam Carnot battery," *Applied Thermal Engineering*, vol. 220, p. 119804, Feb. 2023, doi: 10.1016/j.applthermaleng.2022.119804.
[242] D. Scharrer, P. Bazan, M. Pruckner, and R. German, "Simulation and analysis of a Carnot Battery consisting of a reversible heat pump/organic Rankine cycle for a domestic application in a community with varying number of houses," *Energy*, vol. 261, p. 125166, Dec. 2022, doi: 10.1016/j.energy.2022.125166.
[243] "CHESTER_D6.2_Business-cases-definition-and-baseline-for-Business-models."
[244] "CHESTER-D6.6-Market-replicability-potential.pdf." [Online]. Available: https://www.chester-project.eu/wp-content/uploads/2023/02/CHESTER-D6.6-Market-replicability-potential.pdf
[245] K. M. Powell and T. F. Edgar, "An adaptive-grid model for dynamic simulation of thermocline thermal energy storage systems," *Energy Conversion and Management*, vol. 76, pp. 865–873, Dec. 2013, doi:

10.1016/j.enconman.2013.08.043.
[246] A. L. Nash, A. Badithela, and N. Jain, "Dynamic modeling of a sensible thermal energy storage tank with an immersed coil heat exchanger under three operation modes," *Applied Energy*, vol. 195, pp. 877–889, Jun. 2017, doi: 10.1016/j.apenergy.2017.03.092.
[247] S. Patankar, *Numerical Heat Transfer and Fluid Flow*. Boca Raton: CRC Press, 2018. doi: 10.1201/9781482234213.
[248] "JRC Photovoltaic Geographical Information System (PVGIS) - European Commission." Accessed: Feb. 10, 2023. [Online]. Available: https://re.jrc.ec.europa.eu/pvg_tools/it/#MR
[249] A. Kang, I. Korolija, and D. Rovas, "Photovoltaic Thermal District Heating: A review of the current status, opportunities and prospects," *Applied Thermal Engineering*, vol. 217, p. 119051, Nov. 2022, doi: 10.1016/j.applthermaleng.2022.119051.
[250] M. A. Obalanlege, Y. Mahmoudi, R. Douglas, E. Ebrahimnia-Bajestan, J. Davidson, and D. Bailie, "Performance assessment of a hybrid photovoltaic-thermal and heat pump system for solar heating and electricity," *Renewable Energy*, vol. 148, pp. 558–572, Apr. 2020, doi: 10.1016/j.renene.2019.10.061.
[251] P. Mi, J. Zhang, Y. Han, and X. Guo, "Study on energy efficiency and economic performance of district heating system of energy saving reconstruction with photovoltaic thermal heat pump," *Energy Conversion and Management*, vol. 247, p. 114677, Nov. 2021, doi: 10.1016/j.enconman.2021.114677.
[252] D. Parra, G. S. Walker, and M. Gillott, "Are batteries the optimum PV-coupled energy storage for dwellings? Techno-economic comparison with hot water tanks in the UK," *Energy and Buildings*, vol. 116, pp. 614–621, Mar. 2016, doi: 10.1016/j.enbuild.2016.01.039.
[253] I. Pakere, D. Lauka, and D. Blumberga, "Solar power and heat production via photovoltaic thermal panels for district heating and industrial plant," *Energy*, vol. 154, pp. 424–432, Jul. 2018, doi: 10.1016/j.energy.2018.04.138.
[254] X. Yuan, Y. Liang, X. Hu, Y. Xu, Y. Chen, and R. Kosonen, "Waste heat recoveries in data centers: A review," *Renewable and Sustainable Energy Reviews*, vol. 188, p. 113777, Dec. 2023, doi: 10.1016/j.rser.2023.113777.
[255] W. Villasmil, L. J. Fischer, and J. Worlitschek, "A review and evaluation of thermal insulation materials and methods for thermal energy storage systems," *Renewable and Sustainable Energy Reviews*, vol. 103, pp. 71–84, Apr. 2019, doi: 10.1016/j.rser.2018.12.040.
[256] S. Lemmens, "Cost Engineering Techniques and Their Applicability for Cost Estimation of Organic Rankine Cycle Systems," *Energies*, vol. 9, no. 7, Art. no. 7, Jun. 2016, doi: 10.3390/en9070485.
[257] M. Shamoushaki, P. H. Niknam, L. Talluri, G. Manfrida, and D. Fiaschi, "Development of Cost Correlations for the Economic Assessment of Power Plant Equipment," *Energies*, vol. 14, no. 9, Art. no. 9, Jan. 2021, doi: 10.3390/en14092665.
[258] O. Dumont, C. Carmo, E. Georges, S. Quoilin, and V. Lemort, "Economic assessment of electric energy storage for load shifting in positive energy building," *Int J Energy Environ Eng*, vol. 8, no. 1, pp. 25–35, Mar. 2017, doi: 10.1007/s40095-016-0224-2.
[259] M. T. Résimont, "Strategic outline and sizing of district heating networks using a geographic information system." Accessed: Apr. 18, 2023. [Online]. Available: https://www.fsa.uliege.be/cms/c_7790914/en/strategic-outline-and-sizing-of-district-heating-networks-using-a-geographic-information-system
[260] "Market data." Accessed: Feb. 10, 2023. [Online]. Available: https://www.nordpoolgroup.com/en/Market-data1/Dayahead/Area-Prices/be/hourly/
[261] R. Baetens *et al.*, "Assessing electrical bottlenecks at feeder level for residential net zero-energy buildings by integrated system simulation," *Applied Energy*, vol. 96, pp. 74–83, Aug. 2012, doi: 10.1016/j.apenergy.2011.12.098.
[262] S. Lecompte, "Performance evaluation of organic Rankine cycle architectures : application to waste heat valorisation," dissertation, Ghent University, 2016. Accessed: Mar. 09, 2023. [Online]. Available: http://hdl.handle.net/1854/LU-7223134
[263] Y. Jang, D. Lee, J. Kim, S. H. Ham, and Y. Kim, "Performance characteristics of a waste-heat recovery water-source heat pump system designed for data centers and residential area in the heating dominated region," *Journal of Building Engineering*, vol. 62, p. 105416, Dec. 2022, doi: 10.1016/j.jobe.2022.105416.
[264] J. Hou, H. Li, N. Nord, and G. Huang, "Model predictive control for a university heat prosumer with data centre waste heat and thermal energy storage," *Energy*, vol. 267, p. 126579, Mar. 2023, doi: 10.1016/j.energy.2022.126579.
[265] L. Liu, Q. Zhang, Z. (John) Zhai, C. Yue, and X. Ma, "State-of-the-art on thermal energy storage technologies in data center," *Energy and Buildings*, vol. 226, p. 110345, Nov. 2020, doi: 10.1016/j.enbuild.2020.110345.
[266] A. Laterre, O. Dumont, V. Lemort, and F. Contino, "Is waste heat recovery a promising avenue for the Carnot battery? Techno-economic optimisation of an electric booster-assisted Carnot battery integrated into different data centres," *Energy Conversion and Management*, vol. 301, p. 118030, Feb. 2024, doi: 10.1016/j.enconman.2023.118030.
[267] O. Ajayi and R. Heymann, "Data centre day-ahead energy demand prediction and energy dispatch with solar

PV integration," *Energy Reports*, vol. 7, pp. 3760–3774, Nov. 2021, doi: 10.1016/j.egyr.2021.06.062.
[268] M. Wahlroos, M. Pärssinen, S. Rinne, S. Syri, and J. Manner, "Future views on waste heat utilization – Case of data centers in Northern Europe," *Renewable and Sustainable Energy Reviews*, vol. 82, pp. 1749–1764, Feb. 2018, doi: 10.1016/j.rser.2017.10.058.
[269] T. Sathesh and Y.-C. Shih, "Optimized deep learning-based prediction model for chiller performance prediction," *Data & Knowledge Engineering*, vol. 144, p. 102120, Mar. 2023, doi: 10.1016/j.datak.2022.102120.
[270] A. Sohani, M. H. Shahverdian, H. Sayyaadi, and D. A. Garcia, "Impact of absolute and relative humidity on the performance of mono and poly crystalline silicon photovoltaics; applying artificial neural network," *Journal of Cleaner Production*, vol. 276, p. 123016, Dec. 2020, doi: 10.1016/j.jclepro.2020.123016.
[271] "Most efficient solar panels 2023," Clean Energy Reviews. Accessed: Dec. 15, 2023. [Online]. Available: https://www.cleanenergyreviews.info/blog/most-efficient-solar-panels
[272] G. Notton, C. Cristofari, M. Mattei, and P. Poggi, "Modelling of a double-glass photovoltaic module using finite differences," *Applied Thermal Engineering*, vol. 25, no. 17, pp. 2854–2877, Dec. 2005, doi: 10.1016/j.applthermaleng.2005.02.008.
[273] E. Hahne and Y. Chen, "Numerical study of flow and heat transfer characteristics in hot water stores," *Solar Energy*, vol. 64, no. 1, pp. 9–18, Sep. 1998, doi: 10.1016/S0038-092X(98)00051-6.
[274] "Costi e tariffe del teleriscaldamento in Emilia Romagna." Accessed: Mar. 09, 2023. [Online]. Available: https://www.ilteleriscaldamento.eu/teleriscaldamento_emilia_romagna.htm
[275] "GME - Gestore dei Mercati Energetici SpA." Accessed: Mar. 09, 2023. [Online]. Available: https://www.mercatoelettrico.org/It/Tools/Accessodati.aspx?ReturnUrl=%2fIt%2fdownload%2fDatiStorici.aspx
[276] Y. Yang *et al.*, "An overview of application-oriented multifunctional large-scale stationary battery and hydrogen hybrid energy storage system," *Energy Reviews*, p. 100068, Jan. 2024, doi: 10.1016/j.enrev.2024.100068.
[277] M. Cascetta, F. Licheri, R. P. Merchán, and M. Petrollese, "Operating performance of a Joule-Brayton pumped thermal energy storage system integrated with a concentrated solar power plant," *Journal of Energy Storage*, vol. 73, p. 108865, Dec. 2023, doi: 10.1016/j.est.2023.108865.
[278] A. Ghilardi, G. F. Frate, K. Kyprianidis, M. Tucci, and L. Ferrari, "Brayton pumped thermal energy storage: Optimal dispatchment in multi-energy districts," *Energy Conversion and Management*, vol. 314, p. 118650, Aug. 2024, doi: 10.1016/j.enconman.2024.118650.
[279] H. Zhang, L. Wang, X. Lin, and H. Chen, "Combined cooling, heating, and power generation performance of pumped thermal electricity storage system based on Brayton cycle," *Applied Energy*, vol. 278, p. 115607, Nov. 2020, doi: 10.1016/j.apenergy.2020.115607.
[280] H. Zhang, L. Wang, X. Lin, and H. Chen, "Technical and economic analysis of Brayton-cycle-based pumped thermal electricity storage systems with direct and indirect thermal energy storage," *Energy*, vol. 239, p. 121966, Jan. 2022, doi: 10.1016/j.energy.2021.121966.
[281] H. Zhang, L. Wang, X. Lin, and H. Chen, "Parametric optimisation and thermo-economic analysis of Joule–Brayton cycle-based pumped thermal electricity storage system under various charging–discharging periods," *Energy*, vol. 263, p. 125908, Jan. 2023, doi: 10.1016/j.energy.2022.125908.
[282] L. Wang, X. Lin, H. Zhang, L. Peng, X. Zhang, and H. Chen, "Analytic optimization of Joule–Brayton cycle-based pumped thermal electricity storage system," *Journal of Energy Storage*, vol. 47, p. 103663, Mar. 2022, doi: 10.1016/j.est.2021.103663.
[283] H. Wang *et al.*, "Dynamic thermodynamic performance analysis of a novel pumped thermal electricity storage (N-PTES) system coupled with liquid piston," *Journal of Energy Storage*, vol. 84, p. 110836, Apr. 2024, doi: 10.1016/j.est.2024.110836.
[284] H. Yang, J. Li, Z. Ge, L. Yang, and X. Du, "Dynamic performance for discharging process of pumped thermal electricity storage with reversible Brayton cycle," *Energy*, vol. 263, p. 125930, Jan. 2023, doi: 10.1016/j.energy.2022.125930.
[285] H. Yang, J. Li, Z. Ge, L. Yang, and X. Du, "Dynamic characteristics and control strategy of pumped thermal electricity storage with reversible Brayton cycle," *Renewable Energy*, vol. 198, pp. 1341–1353, Oct. 2022, doi: 10.1016/j.renene.2022.08.129.
[286] X. Shi, Q. He, C. Lu, T. Wang, S. Cui, and D. Du, "Variable load modes and operation characteristics of closed Brayton cycle pumped thermal electricity storage system with liquid-phase storage," *Renewable Energy*, vol. 203, pp. 715–730, Feb. 2023, doi: 10.1016/j.renene.2022.12.116.
[287] S. Belik, "Techno-economic evaluation of a Brayton battery configuration with power-to-heat extension," *Journal of Energy Storage*, vol. 68, p. 107416, Sep. 2023, doi: 10.1016/j.est.2023.107416.
[288] J. D. McTigue, P. Farres-Antunez, K. S. J, C. N. Markides, and A. J. White, "Techno-economic analysis of recuperated Joule-Brayton pumped thermal energy storage," *Energy Conversion and Management*, vol. 252, p. 115016, Jan. 2022, doi: 10.1016/j.enconman.2021.115016.
[289] Y. Zhao, J. Song, M. Liu, K. Zhang, C. N. Markides, and J. Yan, "Multi-objective thermo-economic optimisation

of Joule-Brayton pumped thermal electricity storage systems: Role of working fluids and sensible heat storage materials," *Applied Thermal Engineering*, vol. 223, p. 119972, Mar. 2023, doi: 10.1016/j.applthermaleng.2023.119972.

[290] S. S. M. Shamsi, S. Barberis, S. Maccarini, and A. Traverso, "Thermo-economic performance evaluation of thermally integrated Carnot battery(TI-PTES) for freely available heat sources," *Journal of Energy Storage*, vol. 97, p. 112979, Sep. 2024, doi: 10.1016/j.est.2024.112979.

[291] M. A. Ancona *et al.*, "A Comparison Between ORC and Supercritical CO2 Bottoming Cycles for Energy Recovery From Industrial Gas Turbines Exhaust Gas," *Journal of Engineering for Gas Turbines and Power*, Jul. 2021, doi: 10.1115/1.4051950.

[292] GSE, "Rapporto Statistico GSE - FER 2020," 2020. [Online]. Available: https://www.gse.it/documenti_site/Documenti%20GSE/Rapporti%20statistici/Rapporto%20Statistico%20GSE%20-%20FER%202020.pdf

[293] *Directive 2004/8/EC of the European Parliament and of the Council of 11 February 2004 on the promotion of cogeneration based on a useful heat demand in the internal energy market and amending Directive 92/42/EEC*, vol. 052. 2004. Accessed: Dec. 14, 2022. [Online]. Available: http://data.europa.eu/eli/dir/2004/8/oj/eng